IRE Transactions

on ANTENNAS and PROPAGATION

Volume AP-5 **JANUARY, 1957** **Number 1**

Published Quarterly

TABLE OF CONTENTS

News and Views 1

CONTRIBUTIONS

The Impedance Properties of Narrow Radiating Slots in the Broad Face of Rectangular Waveguide:
Part I—Theory 4
Part II—Comparison with Measurements ..... *Arthur A. Oliner* 12
A Luneberg Lens Scanning System ..... *J. S. Hollis and M. W. Long* 21
A Design Procedure for Dielectric Microwave Lenses of Large Aperture Ratio and Large Scanning Angle ..... *F. S. Holt and A. Mayer* 25
Circularly Polarized Slot Radiators ..... *Alan J. Simmons* 31
The Effect of Mutual Impedance on the Spacing Error of an Eight-Element Adcock .... *Douglas N. Travers* 36
Correction to Discussion of the Combined Panel Session on Propagation of Doubly-Refracting Media and Future Directions for Research in Electromagnetic Wave Theory in Modern Physics 39
On the Synthesis of Line-Sources and Infinite Strip-Sources ..... *J. L. Yen* 40
Radiation Characteristics with Power Gain for Slots on a Sphere ..... *Y. Mushiake and R. E. Webster* 47
Cylindrical Radio Waves ..... *Samuel Sensiper* 56
A Study of Radar Elevation-Angle Errors Due to Atmospheric Refraction .. *B. M. Fannin and K. H. Jehn* 71
Solar Flares and Atmospheric Noise ..... *E. I. King and A. W. Sullivan* 78
On Scattering and Reflection of Electromagnetic Waves by Rough Surfaces ..... *Victor Twersky* 81
Radio Communications by Means of Very Short Electric Waves ..... *Guglielmo Marconi* 90
Diffraction of Surface Waves by a Semi-Infinite Dielectric Slab ..... *Carlos M. Angulo* 100
Alternative Field Representations in Regions Bounded by Spheres, Cones, and Planes ..... *Leopold B. Felsen* 109
Plane-Wave Scattering by Small-Angle Cones ..... *Leopold B. Felsen* 121
Theory of the Scintillation Fading of Microwaves ..... *Osamu Tukizi* 130
Ray Theory vs Normal Mode Theory in Wave Propagation Problems ..... *Leslie G. McCracken* 137
Universal Curves for the Vertical Polarization Reflection Coefficient ..... *Gunnar P. Ohman* 140

COMMUNICATIONS

Aircraft Telemetry Antenna ..... *Frank E. Butterfield* 143
The Optimum Aperture Function in a Long Array ..... *Glendon C. McCormick* 144
Variational Principles for Electromagnetic Resonators and Waveguides ..... *Victor H. Rumsey* 146
Symposium on Present and Future Uses of Refractive Index Data for Radio Propagation Purposes ..... *L. J. Anderson* 147

Abstracts of IRE-URSI Symposium, Washington, D. C. 148
Abstracts of IRE-URSI Symposium, Berkeley, Calif. 164

Contributors 169

PUBLISHED BY THE

ofessional Group on Antennas and Propagation

IRE TRANSACTIONS® PGAP IS A QUARTERLY PUBLICATION DEVOTED TO EXPERIMENTAL AND THEORETICAL PAPERS ON ANTENNAS AND WIRELESS PROPAGATION OF ELECTROMAGNETIC WAVES

MANUSCRIPTS should be submitted to John B. Smyth, Editor, SRA, 3930 4th Avenue, San Diego 3, California. Manuscripts should be original typewritten copy, double spaced, plus one carbon copy. References should appear as footnotes and include author's name, title, journal, volume, initial and final page numbers, and date. Each paper must have an abstract of not more than 200 words. News items concerning PGAP members and group activities should be sent to the News Editor, Mr. H. A. Finke, Polytechnic Research and Development Company, 55 Johnson Street, Brooklyn, New York.

ILLUSTRATIONS should be submitted as follows: All line drawings (graphs, charts, block diagrams, cutaways, etc.) should be inked uniformly and ready for reproduction. If commercially printed grids are used in graph drawings, author should be sure printer's ink is of a color that will reproduce. All half-tone illustrations (photographs, wash, airbrush, or pencil renderings, etc.) should be clean and ready to reproduce. Photographs should be glossy prints. Call-outs or labels should be marked on a registered tissue overlay, not on the illustration itself. No illustration should be larger than 8 x 10 inches.

Copies can be purchased from
THE INSTITUTE OF RADIO ENGINEERS
1 East 79 St., New York 21, N.Y.

PRICE PER COPY: members of the Professional Group on Antennas and Propagation, $3.20; members of the IRE, $4.80; nonmembers, $9.60.

ANNUAL SUBSCRIPTION PRICE: PGAP members, included in PGAP assessment of $4.00; IRE members, $8.50; Colleges and public libraries, $10.00; nonmembers, $17.00.

Entered as second-class matter, at the post office at Menasha, Wisconsin, under the act of August 24, 1912. Acceptance for mailing at a special rate of postage is provided for in the act of February 28, 1925, embodied in Paragraph 4, Section 412, P. L. & R., authorized October 26, 1927.

news and views

Administrative News

The last issue of the TRANSACTIONS included a notice from the Editor that some papers which had been originally scheduled for publication in that issue of the TRANSACTIONS had been deleted and rescheduled for the current issue because "the funds of the PGAP were temporarily depleted."

This decision was not easily achieved and represents the outcome of considerable discussion among interested parties in the PGAP and IRE headquarters. The alternate possibilities included the extremes of deleting the material permanently and publishing it all immediately through the assistance of funds from IRE Headquarters. Publication of the issue was held up while this matter was being resolved.

A delay of this kind is, of course, most regrettable and is to be ascribed to the fact that the Professional Group system is still very new and that many important problems bearing, not only on the internal operations of the Groups, but also on their relations with the parent organization, are as yet unresolved. One of the knottiest is the matter of Group financing which, of course, underlies the delay discussed above.

IRE expects that all Groups will be self-supporting eventually. The Professional Groups Manual states: "Basically each Group once established must assume full financial responsibility for its own operation." Until recently, however, IRE policy discouraged and severely restricted advertising in the Group TRANSACTIONS. Recently this was changed. On December 18, 1956 the chairman of the Professional Groups Committee, Dr. W. R. G. Baker, issued the following notice:

"To: All Professional Group Administrative Committees

There have been complaints regarding the advertising policies applying to the TRANSACTIONS. I am glad to advise you that with the approval of the Executive Committee, these policies have been changed as follows:

1) The present restrictions on TRANSACTIONS advertising are removed. It is permissible for all Groups to accept advertising in any category, subject to the following conditions:
   a) The advertising rates for the TRANSACTIONS shall be not less than twice the current rates for the PROCEEDINGS. The rates for the TRANSACTIONS are subject to the approval of the Executive Secretary.
   b) In order to maintain a high order of advertising copy, all advertising material must receive the approval of the Executive Secretary or his appointed representative.

I feel sure that this change in policy will be of assistance to your operations."

This is a most significant change, the ultimate implications of which are difficult to predict. For PGAP with its present financial difficulty, it can be an important step toward obtaining the means to solve some of its problems independently. There is little doubt that had the funds been available, the regular issues of the PGAP TRANSACTIONS would have appeared four times last year instead of twice.

The next meeting of the PGAP Administrative Committee is scheduled for January 11, 1957 and will have been held by the time this issue is published. It is anticipated that this subject of advertising will be an important item on the agenda. Your News and Views Editor believes that the TRANSACTIONS constitute a very attractive place for many kinds of advertising, and that development of this source of revenue can assist substantially in the development of PGAP itself.

The IRE Board of Directors has just approved another policy change which can have considerable effect upon PGAP. It relates to the matter of "Affiliate"

membership in the Professional Groups. This subject has been discussed before by this department. Briefly, the plan is to permit qualified non-IRE members to join the Professional Groups (on an affiliate basis). This, like the change in advertising policy, also will be recognized as a most significant step toward the development of the individual Groups as true societies in themselves.

The workings of the plan can be seen from the following rules (approved by the Board of Directors on January 4, 1957):

1) Each Group interested in initiating such a plan shall submit to the Chairman of the Professional Groups Committee a list of accredited organizations which has been selected and approved by its Administrative Committee, for official approval by the Executive Committee of the IRE.
2) Group affiliation may be maintained only so long as the individual continues membership in an accredited organization approved by the Group and the Executive Committee.
3) An "affiliate" will receive the TRANSACTIONS of the Group with which he is affiliated and that Part of the IRE National Convention Record pertaining to his Group.
4) An individual may affiliate with more than one Group, provided the accredited organization of which he is a member is recognized by the Groups with which he wishes to affiliate.
5) An "affiliate" cannot serve in an elective office in the Group or Group Chapter.
6) An "affiliate" shall not have a vote on any of the elective offices of a Group or Group Chapter.
7) An "affiliate" can serve in any appointive Group or Group Chapter office.
8) An "affiliate" may attend any local or national meetings of the Group by payment of charges assessed Group members.
9) An "affiliate" may not receive any IRE benefits that are derived through IRE membership.
10) An "affiliate" is eligible to receive a Group award.
11) Each Section of the IRE is to receive support for mailing and meeting costs based on the number of "affiliates" residing in the Section, at the rate of fifty cents annually for each such "affiliate."
12) The manner of soliciting individual members of accredited organizations will be left to the discretion of the individual Group management.
13) The annual fee for "affiliates" shall be the Group assessment fee, plus $4.50. The latter covers IRE subsidies to the Group, Professional Group overhead expenses borne by IRE Headquarters, and fifty cents which is to be rebated to the Sections.
14) An applicant for "affiliate" membership shall not have been an IRE member during the five years previous to his application.

LOCAL CHAPTER NEWS

Washington, D. C.

On December 11, PGAP, PGMIL, PGVC, PGCS, and PGBTS Chapters held a joint meeting in Tompkins Hall, George Washington University, at 8:30 P.M. E. W. Allen and H. E. Dinger presented joint papers entitled "Impressions of Poland from the CCIR Warsaw Conference." The International Radio Consultative Committee (CCIR) held its Eighth Plenary Assembly at Warsaw, Poland, between August 9 and September 13, 1956. The conference facilities were described and some of the results discussed. Experiences and impressions gained in and around the cities of Warsaw, Danzig, and Krakow were related, with the assistance of numerous color slides.

A paper entitled "Discussion of NRL Ionospheric Studies with Rockets and of Associated Radio Propagation Problems in the 4 to 50 MC Range," by John E. Jackson, is tentatively scheduled for presentation late in January, 1957.

Los Angeles

The November meeting of the Los Angeles Chapter of the PGAP featured a talk on "Radio Astronomy" by John Bolton, Senior Research Fellow in physics and astronomy at the California Institute of Technology. Mr. Bolton discussed the advantages of radio astronomy over optical methods in detecting and observing extremely distant sources; in more accurately determining the linear dependence of the "red shift" on wavelength (this establishing the phenomena as a Doppler effect in an expanding universe); and in contributing to the understanding of the nature of our own galaxy and the mechanisms by which radiation occurs. He also presented slides of a number of radio astronomy antennas including some early paraboloids which he constructed at the Commonwealth Scientific and Industrial Research organization in Australia.

The next meeting of PGAP will be held on January 29, 1957 (4th Tuesday in alternate months, I.A.S. Building, 7660 Beverly, 8 P.M.) and will be preceded as usual by a dinner at the Encore Restaurant.

PERSONAL AND INDUSTRIAL NOTES

O. G. Villard, Jr., professor at Stanford University, Stanford, Calif., will be awarded the Morris Liebmann Memorial Prize Award for 1957 "for his contributions in the field of meteor astronomy and ionosphere physics which led to the solution of outstanding problems in radio propagation."

Burt J. Bittner is leaving Sandia Corporation after eight years and will form an antenna division of Gulton Industries in Albuquerque. He is past chairman and one of the founders of both the Albuquerque-Los Alamos Section and the Albuquerque Chapter of PGAP. The

division will design and build telemetry antennas including a line of high temperature miniaturized ceramic slots.

David Bowman, well known for his work in the antenna design field for many years, has recently joined the ITE Circuit Breaker Company, Special Products Division, designers and manufacturers of antennas.

Robert Feller, formerly of NRL has resigned to teach at the University of South Carolina.

Donald D. King, a member of the PGAP Administrative Committee, has resigned as Director of the Radiation Laboratories of Johns Hopkins University to join the new firm, Electrical Communications, Inc. in Baltimore, Md.

Raymond H. DuHamel, formerly assistant professor at the University of Illinois, where he was active in the antenna research program of that organization, has resigned to join the Collins Radio Company of Cedar Rapids, Iowa.

Herbert A. Finke became Manager of Operations of the Polytechnic Research and Development Corp. Mr. Finke who was previously Director of Engineering for the same organization, is a former member of the PGAP Administrative Committee and Editor of this Department.

A number of firms active in the antenna field have recently opened, or are currently opening, new facilities to accommodate expanded activity. These include: Dalmo-Victor, Belmont, Calif., Dorne and Margolin, Inc., Westbury, N. Y., Granger Associates, Palo Alto, Calif., and Wheeler Laboratories, Smithtown, N. Y.

Call for Papers

Tore N. Anderson, of the PGMTT has sent the following publicity release in order to encourage the contribution of papers by PGAP members to their annual meeting:

1957 Annual Meeting of the Professional Group on Microwave Theory and Techniques

"Microwave Ferrites and Related Devices and Their Applications"
May 9–10, 1957*
Western Union Auditorium
New York, N. Y.

* If enough contributed papers are received, this may be extended to May 8–10.

On recent advances in the microwave art with special emphasis on microwave ferrite devices and their applications, nonreciprocal propagation in gas media, and microwave solid state devices.

Invited Papers—May 9, 1957

1) State of the Microwave Ferrite Art
2) Review of Nonreciprocal Media Other Than Ferrites
3) Microwave Semiconductors and Ferroelectrics
4) Solid State MASER (Microwave Amplifier).

Contributed Sessions

It is tentatively planned that there will be two sessions of contributed papers.

Round Table Discussion

The last day of the conference will be a round table discussion led by a noted panel on the subject of design limitations of microwave ferrite devices covering the following:

High power effects
Low frequency limits
High frequency limits
Anomalous propagation in ferrite loaded waveguides
Below saturation behavior of ferrites
"Fast" ferrite devices (depending on relaxation time)
Bandwidth problems
Materials and losses

Call for Contributed Papers

The deadline date for contributed papers to this meeting is March 1, 1957. All papers should be forwarded to the Technical Program Chairman, S. Weisbaum, c/o Bell Telephone Laboratories, Murray Hill, N. J.

Committees

Technical Program Committee—S. Weisbaum, Bell Telephone Laboratories, Murray Hill, N. J.
Publicity Chairman—T. N. Anderson, 1539 Deer Path, Mountainside, N. J.
Local Arrangements Committee—M. Wind, Microwave Research Institute, 55 John St., Brooklyn, N. Y.

contributions

The Impedance Properties of Narrow Radiating Slots in the Broad Face of Rectangular Waveguide*

Part I—Theory

ARTHUR A. OLINER†

Summary—**Theoretical results, valid at and away from resonance, for the impedance properties of the rotated series slot, the displaced series slot, and the longitudinal shunt slot have been derived by the use of variational expressions coupled with certain stored power considerations. The additional influence of finite wall thickness, an appreciable factor, is taken into account by a microwave network treatment. The results for the zero-thickness resistive elements become identical with those of Stevenson when the slot length is made equal to a half wavelength.**

The theoretical derivations are presented in Part I. In Part II, comparison is made with experimental data both previously available and specially taken in this connection. The effect of wall thickness and the distinction between slots of rounded and rectangular ends are also considered. The agreement between theory and measurement is reasonably good.

A. Introduction

ALTHOUGH slots cut in the walls of rectangular waveguide are widely employed as radiators of microwave energy, relatively little theoretical material is available on their impedance properties. The well-known results of Stevenson[1] for the slot resistance or conductance apply only at resonance. The less well-known calculations of Pounder,[2] based on Stevenson's formulas, for the resonant length of a longitudinal shunt slot are admittedly extremely tedious and must therefore be considered impractical. Analytical expressions have been obtained by several authors, including Lewin[3] and the group at the Polytechnic Institute of Brooklyn,[4,5] for the impedance properties of *centered* slots of arbitrary aspect ratio located in various positions. Centered slots are not useful as radiators, however, since the conductance changes little with slot shape and therefore does not permit the control that is available with a shift or rotation of the slot. The additional influence of the slot wall thickness on its impedance properties is a significant factor and has been accounted for by the Polytechnic group[5] for certain centered slots. There remains the need, therefore, for a reasonably simple analytical procedure for determining the impedance properties of slots in actual use, including, of course, the effect of wall thickness.

* Manuscript received by the PGAP, September 28, 1955; revised manuscript received, October 13, 1956.

† Microwave Res. Inst., Polytechnic Inst. of Brooklyn, Bklyn., N. Y. This work was begun at the Hughes Aircraft Co. during a three-month leave of absence, and completed as part of consulting services since that time.

[1] A. F. Stevenson, "Theory of slots in rectangular wave-guides," *J. Appl. Phys.*, vol. 19, pp. 24–38; January, 1948.
S. Silver, "Microwave Antenna Theory and Design," vol. 12, M.I.T. Rad. Lab. Ser., McGraw-Hill Book Co., New York, N. Y., pp. 291–295; 1949.

[2] J. R. Pounder, "Theoretical Impedance of a Longitudinal Slot in the Broad Face of a Rectangular Wave Guide (Numerical)," Special Comm. on Appl. Math., Natl. Res. Council of Canada, Radio Rep., September, 1944. Quoted in W. H. Watson, "The Physical Principles of Wave Guide Transmission and Antenna Systems," Clarendon Press, Oxford, England, pp. 199–200; 1947.

[3] L. Lewin, "Advanced Theory of Waveguides," Iliffe and Sons, Ltd., London, England, pp. 88–97, 121–128; 1951.

[4] N. Marcuvitz, "The Representation, Measurement and Calculation of Equivalent Circuits for Waveguide Discontinuities with Application to Rectangular Slots," Polytechnic Inst. of Brooklyn; 1949. The report was a group project.

[5] A. A. Oliner, "Equivalent Circuits for Slots in Rectangular Waveguide," Polytechnic Inst. of Brooklyn; August, 1951. The report was a group project.

It is attempted here to furnish such an impedance description for radiating slots located in several positions in the broad face of rectangular waveguide. The three slot types considered are the rotated series slot, the displaced series slot, and the longitudinal shunt slot, illustrated in Fig. 1. Variational expressions are used to obtain the slot equivalent circuit parameters; the slot conductances are determined directly, while the susceptances are related by certain stored energy considerations to the corresponding *centered* slot result, the latter being obtained from the work of the Polytechnic group.[5] The effect of wall thickness is accounted for by microwave network considerations. It should be added that all theoretical results presented herein assume that the slot radiates into a half space (*i.e.*, bounded by an infinite baffle), and that the slot has rectangular ends. The effects of deviations in practice from these idealized conditions, particularly for rounded rather than rectangular slot ends, are discussed in Part II.

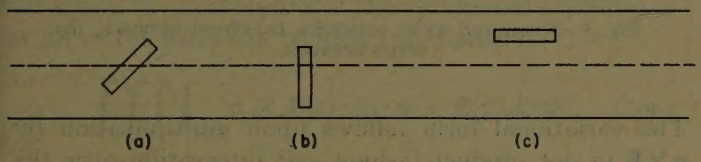

Fig.1—Top view of slots located in the broad face of rectangular waveguide. (a) Rotated series slot, (b) displaced series slot, (c) longitudinal shunt slot.

The variational expressions are derived by following the standard procedure of first obtaining expressions for the magnetic field in the regions inside and outside of the waveguide, and then imposing the condition of continuity of the magnetic field in the slot aperture to obtain the appropriate integral equation. Restricted integral equations are then deduced, following a procedure due to Marcuvitz,[6] by applying antisymmetrical and symmetrical voltage (or electric field) excitation to series and shunt networks, respectively. These restricted integral equations are then cast into variational form in standard fashion. The resulting variational expressions are of the aperture type, thus requiring the insertion of a trial electric field in the slot aperture. The trial field chosen in all cases was cosinusoidal and is expected to be an excellent approximation. The stationary property of these expressions is not proved here since they are in standard form.

Since the conductance and resistance portions of the variational expressions are related only to the radiated power, and do not require the consideration of the rectangular guide Green's function, their determination is relatively simple. The results obtained are valid both at and away from resonance, and reduce identically to the results of Stevenson[1] when the slot length is made equal to a half wavelength.

[6] N. Marcuvitz, "Variational Calculations of Longitudinal Discontinuities," orally presented at URSI-IRE meeting, San Diego, April, 1950.

The direct evaluation of the variational expressions for the reactances and susceptances becomes a formidable task in view of the complexity of the waveguide dyadic Green's function. However, since the susceptance of a *centered* slot is already available,[5] an approach involving so-called "small" aperture or "stored power" considerations is used instead. These considerations relate the susceptance or reactance of the slots of Fig. 1 to the susceptance of the centered slot. The considerations are expected to be very good for rotated and displaced series slots, but are only approximately valid for longitudinal shunt slots.

Under the "small" aperture assumption, the numerators of the variational expressions for all three slots are identical and equal to that corresponding to the centered slot. The denominators, which are always positive definite, vary with the slot location. The implication is, therefore, that all three slots of Fig. 1 possess the same resonant length and the same Q value. A change in slot width will, of course, alter both the Q value and the resonant length. In the case of the rotated series slot, the validity of this conclusion is borne out by the fact that experimentally[7] one finds the resonant length independent of the angle of rotation. Experience with displaced transverse slots coupling identical waveguides indicates that the "small" aperture assumptions should also be very good for the displaced series slot. The dependence of the resonant length on displacement for the longitudinal shunt slot, however, implies that for this case one cannot neglect the influence of the closer side wall and that the "small" aperture results will be valid for small displacements only. Since the present theory does not account for this dependence, there remains the need for an improved theoretical expression for this case.[8] A more detailed evaluation of the usefulness and validity of these theoretical expressions is presented in Part II in connection with the comparisons between these expressions and the measured results.

B. Derivation of the Variational Expressions

Basic to the derivation of aperture type variational expressions are representations for the magnetic fields in the regions interior and exterior to the waveguide. Assuming the slot to radiate into a half space, the magnetic field in the exterior region is given by

$$\mathbf{H}_e(\mathbf{r}) = \iint_{\text{slot}} \mathbf{n} \times \mathbf{E} \cdot \mathcal{Y}_h \, dS \qquad (1)$$

where $\mathbf{E}$ is the electric field in the slot aperture, $\mathbf{n}$ is the normal pointing out of the guide into the half space, and

[7] L. A. Kurtz, "Design Applications of Series Slots," Hughes Aircraft Co. Tech. Memo. No. 273, Fig. 2 or p. 1; December, 1951. Also, see Sec. C, 3, of Part II of the present work.

[8] Since the completion of this work the author has been informed that Dr. W. K. Saunders of the Diamond Ordnance Fuze Labs. has obtained an expression for the longitudinal shunt slot which takes this dependence into account but contains slowly convergent infinite sums.

$\mathcal{Y}_h$ is the half-space dyadic Green's function,[9] or spatial admittance,

$$\mathcal{Y}_h = j\frac{\omega\epsilon}{2\pi}\left(\mathcal{E} + \frac{\nabla\nabla}{k^2}\right)\cdot\frac{e^{-jk|\mathbf{r}-\mathbf{r}'|}}{|\mathbf{r}-\mathbf{r}'|} \tag{2}$$

where $\mathcal{E}$ is the unit dyadic, and $k = 2\pi/\lambda$.

The representation chosen for the magnetic field in the interior region is[10]

$$\mathbf{H}_i(\mathbf{r}) = \tfrac{1}{2}(I_1 + I_2)\mathfrak{H}^{(1)}(\mathbf{r}) - j\tfrac{1}{2}Y_0(V_1 + V_2)\mathfrak{H}^{(2)}(\mathbf{r}) - j\iint_{\text{slot}}(\mathbf{n}\times\mathbf{E})\cdot\mathcal{B}\,dS \tag{3}$$

where the composite (standing wave type) mode functions $\mathfrak{H}^{(1)}$ and $\mathfrak{H}^{(2)}$ are

$$\begin{aligned}\mathfrak{H}^{(1)}(\mathbf{r}) &= \mathbf{h}(\boldsymbol{\rho})\cos\kappa z - j\mathbf{h}_z(\boldsymbol{\rho})\sin\kappa z\\ \mathfrak{H}^{(2)}(\mathbf{r}) &= \mathbf{h}(\boldsymbol{\rho})\sin\kappa z + j\mathbf{h}_z(\boldsymbol{\rho})\cos\kappa z\end{aligned} \tag{4}$$

with $\boldsymbol{\rho} = (x, y)$ and $\kappa = 2\pi/\lambda_g$. The ordinary mode functions are

$$\begin{aligned}\mathbf{h}(\boldsymbol{\rho}) &= \sqrt{\frac{2}{ab}}\cos\frac{\pi x}{a}\mathbf{x}_0,\\ \mathbf{h}_z(\boldsymbol{\rho}) &= j\sqrt{\frac{2}{ab}}\,\frac{\pi}{a\kappa}\sin\frac{\pi x}{a}\mathbf{z}_0\end{aligned} \tag{5}$$

where the geometry is indicated in Fig. 2.

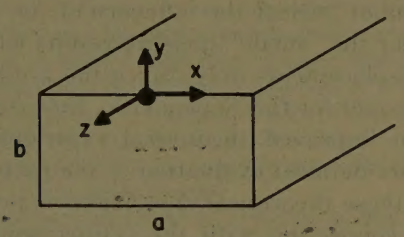

Fig. 2—Geometry of rectangular waveguide.

The voltages and currents V and I are discussed by Marcuvitz and Schwinger[10] and defined in their (3.1) and (3). Y_0 is the characteristic admittance of the dominant mode. The guide (internal) dyadic Green's function, or spatial susceptance, $\mathcal{B}$, is given in (3.41).[10]

Upon application of the condition of continuity of magnetic field in the slot aperture, the following integral equation for the electric field in the aperture is obtained.

$$\tfrac{1}{2}(I_1 + I_2)\mathfrak{H}^{(1)}(\mathbf{r}) - j\tfrac{1}{2}Y_0(V_1 + V_2)\mathfrak{H}^{(2)}(\mathbf{r}) - \iint_{\text{slot}}\mathbf{n}\times\mathbf{E}\cdot(\mathcal{Y}_h + j\mathcal{B})\,dS = 0. \tag{6}$$

[9] H. Levine and J. Schwinger, "On the Theory of Electromagnetic Wave Diffraction by an Aperture in an Infinite Plane Conducting Screen," in "Theory of Electromagnetic Waves, A Symposium," Academic Press, New York, N. Y., pp. S31, S32; 1951.

[10] N. Marcuvitz and J. Schwinger, "On the representation of the electric and magnetic fields produced by currents and discontinuities in wave guides," *J. Appl. Phys.*, vol. 22, pp. 806–819; June, 1951. See (3.38b), (3.39), and (3.41).

The variational expressions are most conveniently deduced from a reduced form of the integral equation obtained by appropriate symmetric or antisymmetric voltage excitation. If the slot is representable by a purely shunt network as in Fig. 3(a), the application of symmetric voltage excitation produces an open circuit bisection of the network, with $I_1 = -I_2$, $V_1 = V_2 = V$. The integral equation then becomes

$$-jY_0V\mathfrak{H}^{(2)} = \iint_{\text{slot}}\mathbf{n}\times\mathbf{E}\cdot(\mathcal{Y}_h + j\mathcal{B})\,dS. \tag{7}$$

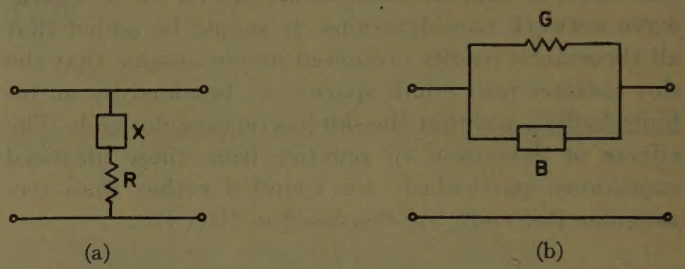

Fig. 3—Shunt and series networks. (a) Shunt network, (b) series network.

The variational form follows upon multiplication by $\mathbf{n}\times\mathbf{E}$ in dot product fashion and integration over the slot aperture, employing[11]

$$2I = jY_0\iint_{\text{slot}}\mathbf{n}\times\mathbf{E}\cdot\mathfrak{H}^{(2)}\,dS \tag{8}$$

and dividing by $(2I)^2$

$$\frac{V}{2I} = R + jX = \frac{\iiiint_{\text{slot}}\mathbf{n}\times\mathbf{E}\cdot(\mathcal{Y}_h + j\mathcal{B})\cdot\mathbf{n}\times\mathbf{E}'\,dS\,dS'}{Y_0^2\left[\iint_{\text{slot}}\mathbf{n}\times\mathbf{E}\cdot\mathfrak{H}^{(2)}\,dS\right]^2} \tag{9}$$

where all integrals are taken over the slot aperture. The normalized value is obtained by dividing both sides by the characteristic impedance $Z_0 (Z_0 = 1/Y_0)$.

If the slot is representable by a purely series network, as in Fig. 3(b), the application of antisymmetric voltage excitation, with $V_1 = -V_2$, $I_1 = I_2 = I$, yields a short circuit bisection of the network so that the integral equation reduces to

$$I\mathfrak{H}^{(1)} = \iint_{\text{slot}}\mathbf{n}\times\mathbf{E}\cdot(\mathcal{Y}_h + j\mathcal{B})\,dS. \tag{10}$$

Again, the multiplication by $\mathbf{n}\times\mathbf{E}$ and integration over the slot aperture, together with the employment of[11]

$$2V = \iint_{\text{slot}}\mathbf{n}\times\mathbf{E}\cdot\mathfrak{H}^{(1)}\,dS \tag{11}$$

[11] *Ibid.* See (3.42b).

and division by $(2V)^2$ casts the integral equation into variational form, *viz.*,

$$\frac{I}{2V} = G + jB$$

$$= \frac{\iiiint_{\text{slot}} \mathbf{n} \times \mathbf{E} \cdot (\mathcal{Y}_h + j\mathcal{B}) \cdot \mathbf{n} \times \mathbf{E}' dS dS'}{\left[\iint_{\text{slot}} \mathbf{n} \times \mathbf{E} \cdot \mathcal{H}^{(1)} dS\right]^2}. \quad (12)$$

Again, the normalized value is obtained upon division by Y_0 on both sides.

C. The Resistance and Conductance Expressions

The resistance and conductance expressions, obtainable from the variational expressions (9) and (12), are particularly simple to evaluate as only the real part of the total dyadic Green's function $(\mathcal{Y}_h + j\mathcal{B})$ need be considered. Since all the slots treated here radiate into a half space, the numerators of the variational expressions for all of the slots will be identical, namely,

$$\iiiint_{\text{slot}} \mathbf{n} \times \mathbf{E}(\mathbf{r}) \cdot \mathcal{G}_h \cdot \mathbf{n} \times \mathbf{E}(\mathbf{r}') dS dS', \quad (13a)$$

where

$$\mathcal{G}_h(\mathbf{r}, \mathbf{r}') = \frac{\omega\epsilon}{2\pi}\left(\mathcal{E} + \frac{\nabla\nabla}{k^2}\right) \cdot \frac{\sin k|\mathbf{r} - \mathbf{r}'|}{|\mathbf{r} - \mathbf{r}'|} \quad (13b)$$

and is the real part of $\mathcal{Y}_h$. The integral (13a), which is related to the power radiated by the slot, has already been evaluated in previous work at the Polytechnic Institute of Brooklyn[12] in connection with a transverse slot radiating from the end of the guide into a half space. The result is

$$\text{"Power Radiated"} = \frac{16}{3\pi}\sqrt{\frac{\epsilon}{\mu}}\frac{1}{\lambda^2}(a'b')^2 \cdot \left[1 - 0.374\left(\frac{a'}{\lambda}\right)^2 + 0.130\left(\frac{a'}{\lambda}\right)^4\right] \quad (14)$$

neglecting terms of the order of $(b'/a')^2$, where a' and b' are the slot length and width, respectively. Eq. (14) is expected to be quite accurate for all narrow slots in general use.

The denominators of the various variational expressions, representing the square of the voltage or current, depending upon the slot in question, will vary with the slot location.

1) *Longitudinal Shunt Slot*

The equivalent network of Fig. 4(b) is valid at the terminal plane T. Appropriate variational expression for normalized resistance R/Z_0 follows from (9) as

$$\frac{R}{Z_0} = \frac{\text{"Power Radiated"}}{Y_0\left[\iint_{\text{slot}} \mathbf{n} \times \mathbf{E}(\mathbf{r}) \cdot \mathcal{H}^{(2)}(\mathbf{r}) dS\right]^2} \quad (15)$$

where the numerator is given in (14). Using (4) and (5), $\mathcal{H}^{(2)}$ is given by

$$\mathcal{H}^{(2)}(x, z) = \sqrt{\frac{2}{ab}}\cos\frac{\pi x}{a}\sin\kappa z\,\mathbf{x}_0 - \sqrt{\frac{2}{ab}}\frac{\pi}{a\kappa}\sin\frac{\pi x}{a}\cos\kappa z\,\mathbf{z}_0. \quad (16)$$

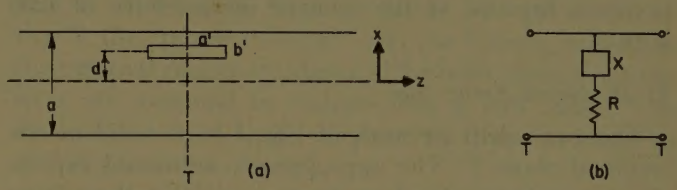

Fig. 4—Longitudinal shunt slot. (a) Physical structure, (b) equivalent network.

Since the dominant mode is an H mode, the characteristic admittance Y_0 is

$$Y_0 = \frac{\kappa}{\omega\mu} = \sqrt{\frac{\epsilon}{\mu}}\frac{\lambda}{\lambda_g}. \quad (17)$$

The trial aperture electric field $\mathbf{E}$ must be chosen as

$$\mathbf{n} \times \mathbf{E} = \mathbf{z}_0 \cos\frac{\pi z}{a'} \quad (18)$$

since that was the value chosen for the numerator in the result (14). For slots in general use this is expected to be an excellent approximation.

The integration over the slot aperture indicated in the denominator of (15) proceeds in straightforward fashion to yield

$$\left[\iint_{\text{slot}} \mathbf{n} \times \mathbf{E} \cdot \mathcal{H}^{(2)} dS\right]^2 = \frac{2}{ab}\left[\frac{2\pi^2 b'}{aa'\kappa}\frac{\sin\frac{\pi d}{a}\cos\frac{\kappa a'}{2}}{\left(\frac{\pi}{a'}\right)^2 - \kappa^2}\right]^2. \quad (19)$$

When (19) is combined with (17) and (14), the result for the normalized resistance becomes

$$\frac{R}{Z_0} = \frac{8\pi a^3 b}{3\lambda^3\lambda_g} \cdot \frac{\left[1 - \left(\frac{2a'}{\lambda_g}\right)^2\right]^2\left[1 - 0.374\left(\frac{a'}{\lambda}\right)^2 + 0.130\left(\frac{a'}{\lambda}\right)^4\right]}{\sin^2\left(\frac{\pi d}{a}\right)\cos^2\left(\frac{\pi a'}{\lambda_g}\right)}. \quad (20)$$

[12] A. A. Oliner, *op. cit.* The particular integral in question was evaluated by H. Kurss.

Stevenson[1] presents a result for the normalized conductance of a longitudinal shunt slot at resonance, *i.e.*, when the network element is purely real, but with the slot length indicated as a half wavelength. If one takes the reciprocal of (20) after substituting $a'=\lambda/2$ and simplifying, one obtains

$$\frac{G}{Y_0} = 2.09\frac{a\lambda_g}{b\lambda}\cos^2\left(\frac{\pi\lambda}{2\lambda_g}\right)\sin^2\left(\frac{\pi d}{a}\right) \tag{21}$$

in exact agreement with Stevenson as quoted in (47) of Silver.[1] Even though the slot is generally not resonant at exactly a half wavelength, Stevenson's result is quite accurate because of the relative insensitivity of (20) with a'.

2) *Displaced Series Slot*

The equivalent network of Fig. 5(b) is valid at the terminal plane T. The appropriate variational expression for the normalized conductance G/Y_0 follows from (12) as

$$\frac{G}{Y_0} = \frac{\text{"Power Radiated"}}{Y_0\left[\iint_{\text{slot}} \mathbf{n}\times\mathbf{E}(\mathbf{r})\cdot\mathfrak{H}^{(1)}(\mathbf{r})dS\right]^2} \tag{22}$$

where the numerator is given in (14), and the mode function $\mathfrak{H}^{(1)}$ is obtained from (4) and (5) as

$$\mathfrak{H}^{(1)}(x,z) = \sqrt{\frac{2}{ab}}\left[\cos\frac{\pi x}{a}\cos\kappa z\,\mathbf{x}_0 + \frac{\pi}{a\kappa}\sin\frac{\pi x}{a}\sin\kappa z\,\mathbf{z}_0\right]. \tag{23}$$

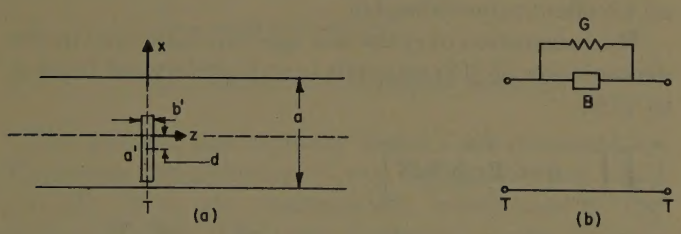

Fig. 5—Displaced series slot. (a) Physical structure, (b) equivalent network.

The trial aperture electric field has the same form as for the longitudinal shunt slot but is oriented at right angles so that

$$\mathbf{n}\times\mathbf{E} = \mathbf{x}_0\cos\frac{\pi x}{a'}. \tag{24}$$

With this trial field, the denominator, which is essentially the square of a voltage, becomes

$$\left[\iint_{\text{slot}} \mathbf{n}\times\mathbf{E}\cdot\mathfrak{H}^{(1)}dS\right]^2$$

$$= \frac{8a^2}{\pi^2}\frac{(a'b')^2}{a^3b}\left[\frac{\cos(\pi a'/2a)}{1-(a'/a)^2}\right]^2\cos^2\frac{\pi d}{a} \tag{25}$$

and, when combined with (14), yields the following result for the normalized conductance

$$\frac{G}{Y_0} = \frac{\lambda_g}{\lambda^3}\frac{32ab}{3\pi}\left[\frac{\pi}{4}\frac{1-(a'/a)^2}{\cos(\pi a'/2a)}\right]^2 \cdot\left[1-0.374\left(\frac{a'}{\lambda}\right)^2+0.130\left(\frac{a'}{\lambda}\right)^4\right]\sec^2\frac{\pi d}{a}. \tag{26}$$

As with the longitudinal shunt slot, agreement with Stevenson's resonant resistance for the displaced series slot is obtained by inverting (26) after a' is set equal to $\lambda/2$. The result is

$$\frac{R}{Z_0} = 0.522\frac{\lambda_g^2}{\lambda ab}\cos^2\frac{\pi\lambda}{4a}\cos^2\frac{\pi d}{a} \tag{27}$$

in agreement with (48) of Silver[1] (the factor there is given as 0.523).

3) *Rotated Series Slot*

The equivalent network of Fig. 6(b) is valid at the terminal plane T. The appropriate variational expression for the normalized conductance is the same as (22) for the displaced series slot, with the numerator again given by (14) and the mode function $\mathfrak{H}^{(1)}$ by (23). The trial aperture electric field has again a cosinusoidal form, but is oriented in the v direction [see Fig. 6(a)], so that

$$\mathbf{n}\times\mathbf{E} = \mathbf{u}_0\cos\frac{\pi u}{a'}. \tag{28}$$

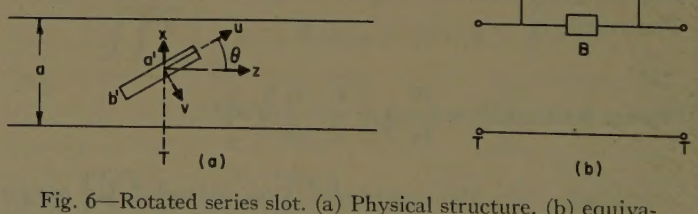

Fig. 6—Rotated series slot. (a) Physical structure, (b) equivalent network.

The angle of rotation of the slot is defined by the angle θ between the u and z axes, with

$$x = u\sin\theta, \qquad z = u\cos\theta$$

so that the voltage term in the denominator of the variational expression becomes

$$\iint_{\text{slot}} \mathbf{n}\times\mathbf{E}\cdot\mathfrak{H}^{(1)}dS$$

$$= \sqrt{\frac{2}{ab}}b'\int_{-a'/2}^{a'/2}\cos\frac{\pi u}{a'}\left[\sin\theta\cos\left(\frac{\pi u}{a}\sin\theta\right)\cos(\kappa u\cos\theta) + \frac{\pi}{a\kappa}\cos\theta\sin\left(\frac{\pi u}{a}\sin\theta\right)\sin(\kappa u\cos\theta)\right]du.$$

Upon performing the integrations and employing (14) the following result is obtained for the normalized conductance

$$\frac{G}{Y_0} = \frac{8\pi}{3}\frac{\lambda_g ab}{\lambda^3}\frac{\left[1 - 0.374\left(\frac{a'}{\lambda}\right)^2 + 0.130\left(\frac{a'}{\lambda}\right)^4\right]}{\left[A(\theta)\sin\theta + \frac{\lambda_g}{2a}B(\theta)\cos\theta\right]^2} \tag{29}$$

where

$$\left.\begin{matrix} A(\theta) \\ B(\theta) \end{matrix}\right\} = \frac{\cos\left(\frac{\pi}{2}\xi\right)}{1-\xi^2} \pm \frac{\cos\left(\frac{\pi}{2}\eta\right)}{1-\eta^2}$$

and

$$\left.\begin{matrix} \eta \\ \xi \end{matrix}\right\} = \left(\frac{a'}{a}\sin\theta \pm \frac{2a'}{\lambda_g}\cos\theta\right).$$

Again, the result of Stevenson for the normalized resistance at resonance may be checked by inversion of (29) after the substitution $a'=\lambda/2$ is made. The result

$$\frac{R}{Z_0} = 0.131\frac{\lambda^3}{\lambda_g ab}\left[A(\theta)\sin\theta + \frac{\lambda_g}{2a}B(\theta)\cos\theta\right]^2 \tag{30}$$

with $A(\theta)$ and $B(\theta)$ defined as in (29), but with

$$\left.\begin{matrix} \eta \\ \xi \end{matrix}\right\} = \frac{\lambda}{2a}\sin\theta \pm \frac{\lambda}{\lambda_g}\cos\theta$$

is in exact agreement with (49) in Silver,[1] upon noting that A and B above are identical with I and J used there.

D. The Reactance and Susceptance Expressions

The evaluation of reactances and susceptances via the variational expressions is generally a rather difficult task. In particular, the difficulty is associated with the integrations in the numerator of the variational expressions, involving the guide (not half space) dyadic Green's function, $\mathfrak{G}$. However, with the recognition that the imaginary portion of the numerator is related to the stored power in the vicinity of the slot, it is sometimes possible to obtain the reactance or susceptance of a slot in a particular location from the corresponding already evaluated result for a slot in some other location. In particular, the available result for the susceptance of a *centered* transverse series slot, located in the broad face of rectangular waveguide, is related below to the corresponding quantity for a rotated series slot, a displaced series slot, and a longitudinal shunt slot.

1. *Rotated Series Slot*

The physical structure and the equivalent network for this slot are given in Fig. 6. The susceptance of this slot will be obtained from that of a centered transverse series slot; the two slots are sketched in Fig. 7. The variational expression for the normalized slot admittance for either slot is obtained from (12) as

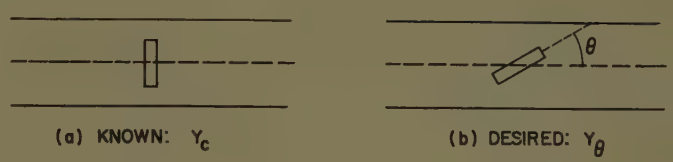

Fig. 7—The centered and rotated series slots.

$$\frac{G}{Y_0} + j\frac{B}{Y_0} = \frac{\text{"Power radiated"} + \text{"Power stored"}}{Y_0\left[\iint \mathbf{n}\times\mathbf{E}\cdot\mathfrak{H}^{(1)}dS\right]^2}. \tag{31}$$

With the highly reasonable assumption that the slot field is of the same form for either slot (a) or (b) of Fig. 7, the "power radiated" and the "power stored" in the external region are identical for both cases, since the slots are assumed to radiate into a half space. The denominators are quite different for the two cases as $\mathfrak{H}^{(1)}$ is a function of angle.

The assumption in the present treatment relates to the "power stored" in the interior, or guide, region. The "stored power," or, considered loosely, the distortion of the field lines in the neighborhood of the slot, will be most strongly affected by the guide walls closest by, which, for both of these slots, is the bottom wall directly opposite the slots. As the slot is rotated through angle θ, the influence of the bottom wall remains constant while that of the side walls changes somewhat. Since the side walls are relatively far away, we assume that the latter effect is negligible. The assumption that the interior "stored power" is independent of the angle of rotation of the slot therefore means that the variational expressions (31) for the two slots have identical numerators, and differ only by the denominators.

With this assumption, the susceptance for arbitrary θ is related to the known susceptance for the centered slot ($\theta=\pi/2$) by equating the numerators in the expressions (31) for the two slots and taking only the imaginary parts

$$\frac{B_\theta}{Y_0} = \frac{B_c}{Y_0}\frac{\left[\iint \mathbf{n}\times\mathbf{E}\cdot\mathfrak{H}_c^{(1)}dS\right]^2}{\left[\iint \mathbf{n}\times\mathbf{E}\cdot\mathfrak{H}_\theta^{(1)}dS\right]^2}. \tag{32}$$

The voltage terms multiplying B_c/Y_0 have already been evaluated in connection with the conductance expressions. Their ratio is denoted in Part II by V_θ^2 and presented as (16). The expression for B_c/Y_0 for a zero-thickness slot is[13]

$$\frac{B_c}{Y_0} = \frac{1}{2}\frac{B_t}{Y_0} + \frac{1}{n_j^2}\frac{B_{rj}}{Y_0} + \frac{2b}{\lambda g}\left[\ln 2 + \frac{\pi b'}{6b} + \frac{3}{2}\left(\frac{b}{\lambda_g}\right)^2\right] \tag{33}$$

[13] A. A. Oliner, *op. cit.* The result presented here for B_c/Y_0 is a modification of the original result evaluated by J. Blass.

where B_t/Y_0, B_{rj}/Y_0, and $1/n_j^2$ are presented in Part II as (8), (6), and (4), respectively. In contrast to the above, the symbol B_c/Y_0 in Part II refers to a centered series slot for which the slot thickness has been taken into account. An expression, analogous to (32), can be written for conductances, but this is unnecessary since the separate conductance expressions for zero-thickness slots are given in Section C.

The quantity B_t/Y_0 represents the normalized susceptance of a zero-thickness transverse slot coupling identical waveguides. It is seen in (8) of Part II that a closed form expression is presented for this quantity despite the fact that the waveguide dyadic Green's function, which occurs in the numerator of the variational expression, involves infinite sums. This result, derived previously,[5] was obtained by first expressing the dyadic Green's function in the form of a dyadic operator operating on a scalar function. This scalar function, an infinite double sum, separates naturally into a sum corresponding to what is obtained for a slot of full width (capacitive), and a sum over the remaining higher modes. The latter sum is then converted by means of a Poisson transformation into a series of Bessel functions of the second kind of imaginary argument; as a result, it converges rapidly enough to be approximated by a single, rather than a double, infinite sum. This transformed kernel, when employed in the variational integrals, will again contribute an infinite series whose sum, however, can be readily approximated. One thereby otains a closed form result which expresses the slot susceptance as that for the full width slot plus correction terms. Lewin's derivation[3] for the same slot also employs a Poisson transformation, but effects an inductive rather than a capacitive separation. The result (8) of Part II for B_t/Y_0 is therefore approximate but has yielded quite good agreement with measured data.

2. *Displaced Series Slot*

The physical structure and equivalent network are given in Fig. 5; one notes that the centered series slot is the centered position of the displaced series slot, *i.e.*, when $d=0$. The variational expression for the admittance of the displaced series slot is also given by (31), and the associated remarks given there apply here also. Since little of the stored field associated with the slot extends beyond the ends of the slot in its long dimension, the proximity of the side wall as the slot is displaced has relatively little influence on the numerator of the variational expression. The assumption made in subsection 1 concerning the constancy of the numerator as the slot is moved, in this case displaced, is therefore applicable.

An expression relating the susceptance of the displaced slot to that of the centered slot is obtained in a fashion similar to that for the rotated slot. The result, identical to (32) with rotated quantities replaced by displaced quantities, becomes, after the appropriate voltage terms are evaluated using (25),

$$\frac{B}{Y_0} = \frac{B_c}{Y_0} \sec^2 \frac{\pi d}{a}. \tag{34}$$

The susceptance B_c/Y_0 of the zero-thickness centered series slot is given in (33).

3. *Longitudinal Shunt Slot*

The physical structure and equivalent network are given in Fig. 4; the variational expression for the normalized slot impedance may be written from (9) as

$$\frac{R}{Z_0} + j\frac{X}{Z_0} = \frac{\text{"Power radiated"} + \text{"Power stored"}}{Y_0\left[\iint \mathbf{n}\times\mathbf{E}\cdot\mathfrak{H}^{(2)}dS\right]^2}. \tag{35}$$

Eq. (35) is to be compared to the corresponding relation (31) for the normalized admittance of the centered series slot in an attempt to relate the reactance of the former to the susceptance of the latter. Since the slot fields are assumed identical for the two cases, the "power stored" in the exterior region and the "power radiated" are identical for both slots since they both radiate into a half space. The assumption will be made now that the "power stored" in the interior region is also identical for both slots. This assumption is not as valid here as it was in the case of the rotated and the displaced series slots since here the side walls exert a nonnegligible influence on the stored power. Since the stored field extends out some distance away from the slot in its narrow dimension, the nearer side wall is expected to exert a noticeable effect here in contrast to the case of the displaced series slot. The effect of the side walls can be accounted for by considering appropriate image terms in the Green's function, but this has not been attempted. The influence of the side walls should manifest itself in a small shift in the resonant frequency of the slot as it is moved off-center; the constancy of the numerator in the case of the rotated and displaced series slots implies a constancy of resonant frequency with angle of rotation or displacement. These effects are borne out by the available experimental data.

With the assumption that the numerators of (31) and (35) are identical, one obtains, upon equating the numerators and taking the imaginary parts (the denominators are always purely real)

$$\frac{X}{Z_0} = \frac{B_c}{Y_0}\frac{\left[\iint \mathbf{n}\times\mathbf{E}\cdot\mathfrak{H}_c^{(1)}dS\right]^2}{\left[\iint \mathbf{n}\times\mathbf{E}\cdot\mathfrak{H}^{(2)}dS\right]^2}. \tag{36}$$

The voltage terms multiplying B_c/Y_0 have already been evaluated and are given in (19) and (25), the latter for the case of $d=0$. Their ratio is denoted in Part II by V_{sh}^2 and presented as (12). The susceptance B_c/Y_0 of the zero-thickness centered series slot is given in (33).

E. Effect of Wall Thickness

The variational expressions and the various slot parameter results obtained above are based on the assumption that the slot walls are of zero thickness. Since, in practice, the finite thickness of the walls exerts a noticeable effect on the slot admittance, this effect is theoretically taken into account here by microwave network considerations. The thick slot is viewed as a composite structure, consisting of a length of waveguide, equal to the slot wall thickness and of cross-sectional dimensions equal to those of the slot, connecting two junctions, one a radiating junction between the slot waveguide and a half space, and the other a Tee junction between the slot waveguide and the main guide. Since the slot wall thickness is usually comparable to the slot width, we can assume negligible higher mode interaction between the junctions and consider them as isolated.

For slots of the same cross-sectional dimensions and thickness, it is evident in this microwave network picture that the radiating junction and the connecting waveguide are identical for all three slot locations, since the slots radiate into a half space. Only the Tee junctions will be different for each.

The radiating junction, common to all three slot locations, is shown in Fig. 8. The Tee junction for the thick centered series slot is the centered E plane Tee pictured in Fig. 9 together with an equivalent network whose simple form is valid since the slot width is small compared to its length. When the component junctions are connected by a length of transmission line equal to the slot thickness, the composite representation of Fig. 10 is obtained for the complete thick centered series slot. In Fig. 10(a), the slot width b' and the thickness t are exaggerated for clarity. The subscripts j signify "junction."

It can be shown[5] that the parameter B_j/Y_0 of the Tee junction of Fig. 9 is given by variational expression (12) when $\mathcal{Y}_h$ is replaced by $j\mathcal{G}_s$, the dyadic Green's function for the stub guide of the Tee, which corresponds here to the slot guide. The term G/Y_0 then drops out, of course. Since the trial aperture electric field was chosen as a cosine, it is orthogonal to all the terms composing $\mathcal{G}_s$, and the stub guide contribution to B_j/Y_0 vanishes. The expression for parameter B_j/Y_0 then becomes identically equal to the interior contribution to B/Y_0 in the zero-thickness case. It is evident that the stored power considerations discussed above apply here in the same fashion, so that we may use the expressions derived in Section D to relate the admittance or impedance of the thick slot of interest to the admittance of the thick centered series slot.

The parameters of the composite representation of Fig. 10(b) are related to those of the over-all representation, the latter being a series network such as that in Fig. 3(b) with parameters G_c and B_c, the subscript signifying "centered," by comparing the two networks and using transmission line relations to reduce the former to the latter. By inspection, one finds

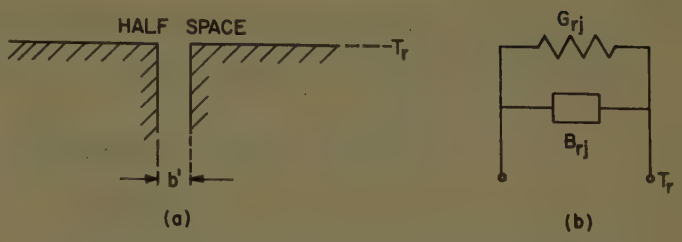

Fig. 8—Radiating junction. (a) Physical structure, (b) equivalent network.

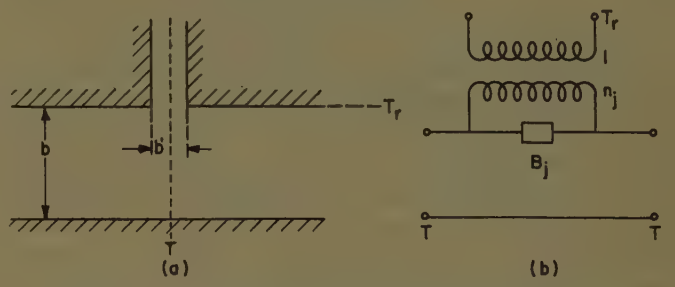

Fig. 9—E plane Tee junction. (a) Physical structure, (b) equivalent network.

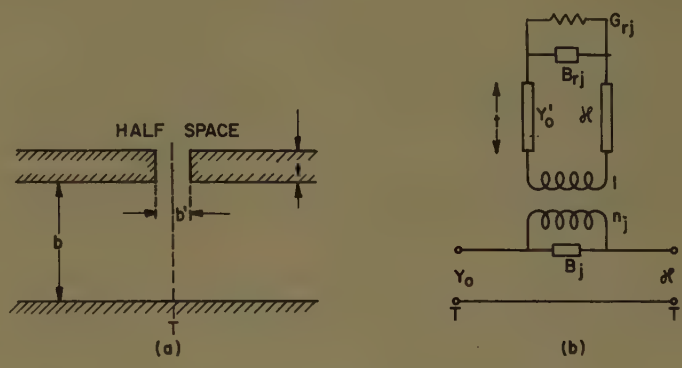

Fig. 10—The thick centered series slot. (a) Physical structure, (b) composite equivalent network.

$$\frac{G_c}{Y_0} + j\frac{B_c}{Y_0} = j\frac{B_j}{Y_0} + \frac{1}{n_j^2}\frac{Y_0'}{Y_0} \cdot \frac{j + \frac{Y_0}{Y_0'}\left(\frac{G_{rj}}{Y_0} + j\frac{B_{rj}}{Y_0}\right)\cot \kappa' t}{\cot \kappa' t + j\left(\frac{G_{rj}}{Y_0} + j\frac{B_{rj}}{Y_0}\right)\frac{Y_0}{Y_0'}} \quad (37)$$

Upon rationalization, the separate expressions presented in the summary, Section B of Part II, for the conductance G_c/Y_0 and the susceptance B_c/Y_0 are obtained. Y_0' and κ' are seen to be the characteristic admittance and propagation wavenumber of the connecting slot waveguide. Theoretical expressions for the component parameters employed above are presented in (4) to (8) of Part II. The relations between G_c/Y_0 and B_c/Y_0 and the parameters of the other slots are also presented in Part II.

The Impedance Properties of Narrow Radiating Slots in the Broad Face of Rectangular Waveguide

Part II—Comparison with Measurement

ARTHUR A. OLINER†

A. Introduction

IN THE companion paper, Part I, theoretical expressions are derived for the equivalent circuit parameters of the slots shown in Fig. 1 of Part I. These slots are the rotated series slot, the displaced series slot, and the longitudinal shunt slot, all located in the broad face of rectangular waveguide. They possess, respectively, a series, a series, and a shunt equivalent network. Both the series and the shunt networks may be put into two alternative forms, as indicated in Fig. 1, below.

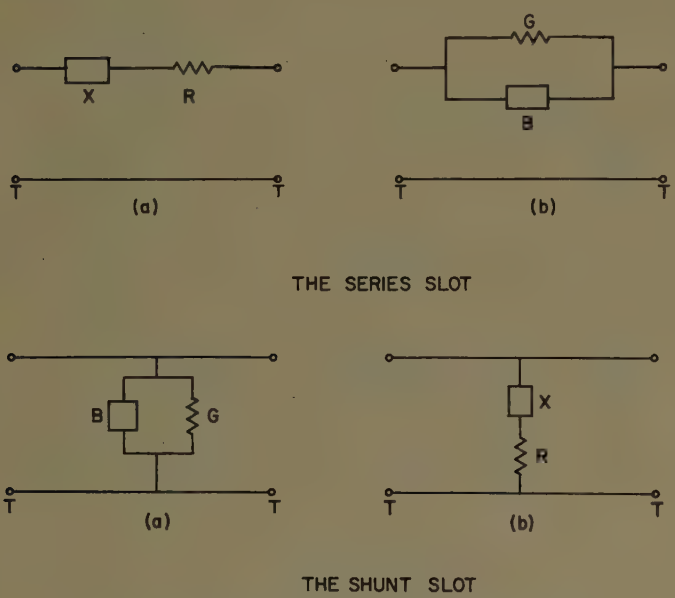

Fig. 1—Alternative forms for the series and shunt slots.

Form (a) for each case is the one that exhibits the resonance properties, and is therefore the one commonly used. The variational expressions of Part I, however, correspond naturally to form (b) in both cases. All parameters in form (b) exhibit monotonic behavior with frequency or slot length; in the neighborhood of resonance the reactances and susceptances have the frequency variation implied by the Foster reactance theorem since they are directly related to the slot stored energy. Whenever network parameters are mentioned in connection with the variational expressions, form (b) is implied. The two forms are, of course, simply related. It is suggested that whenever measurements are taken they be plotted in form (b) since the monotonic behavior of the parameters in this form permits a ready check on the precision of the data.

The section following this introduction presents a summary of theoretical results in the form required for the direct calculation of the equivalent circuit parameters of a slot with finite wall thickness. Included are comments on the simplifications obtained for zero wall thickness. Section C contains the comparison between these theoretical results and the available experimental data for the rotated series slot and the longitudinal shunt slot. The quantitative effect of wall thickness and the difference between rounded and rectangular ends is included.

The measurements to which the theoretical calculations are compared in Section C are obtained from three separate sources. The first source, discussed under C, 1, is the rather comprehensive Hughes Aircraft Company experimental study[1] of the longitudinal shunt slot; the comparison with theory includes the effect of finite wall thickness in the theoretical calculations. The second set of measurements, compared with theory under C, 2, was taken at the suggestion of R. M. Barrett at the Air Force Cambridge Research Center with the purpose of determining the difference between slots of rounded and rectangular ends. These measurements were performed at L band so as to permit careful machining of the slot ends, and in addition furnish a hitherto unavailable systematic set of off-resonance data for a 45° rotated series slot. The third group of measurements was performed at the Polytechnic Institute of Brooklyn on rotated series slots using precision techniques. These measurements, discussed under C, 3, were taken to answer a few remaining questions.

The major conclusions which follow from the discussion under Section C are as follows:

1) Comparison with measurements indicates that the theory is rather good for rotated series slots, and adequate for longitudinal shunt slots of small displacement. For longitudinal shunt slots of large displacement the theory predicts a resonant frequency or slot resonant length which is several per cent too low. Although no measurements were taken on the displaced series slot, the theory as applied to this slot is presumed to be reasonably good.

2) The effect of finite wall thickness is significant. At X band, where the wall thickness is 0.050 inch, its effect is to produce a slot resonant length which is approxi-

† Microwave Res. Inst., Polytechnic Inst. of Brooklyn, Bklyn., N. Y.

[1] R. J. Stegen, "Longitudinal Shunt Slot Characteristics," Hughes Aircraft Co. Tech. Memo. No. 261, Culver City, Calif.; November, 1951.

mately 2 per cent longer than that obtained for zero wall thickness, and also a slightly larger Q value. The slot wall thickness must therefore be included in any calculations based on the formulas given in Section B.

3) The effect of rounding the slot ends is significant. For slots with a length-to-width ratio of about ten, the resonant frequency of slots with rounded ends is about 2 per cent higher than that for slots with rectangular ends but with the same over-all dimensions. The Q value, however, is not influenced by rounding the slot ends, nor is the value of G/Y_0 or R/Z_0 [in form (b) of Fig. 1]. Since the theory presented herein applies to slots with rectangular ends while most slots in general use possess rounded ends, this distinction must be kept in mind.

4) The resonant length of the rotated series slot is substantially independent of the angle of rotation, in accord with the theory presented herein. In contrast, the resonant length of the longitudinal shunt slot may increase by 5 or 10 per cent as the slot is moved from the guide center out to one of the side walls. Because of these effects, the variation of the admittance of a given rotated series slot with angle of rotation may be accurately predicted theoretically, while the corresponding situation does not hold for the longitudinal shunt slot.

5) It is warranted, except for second order effects, to characterize the rotated series slot as a purely series network; *i.e.*, the shunt arms of the more general pi network may be neglected. Further discussion of this point is given under C, 3 and 4.

When the first order effects of finite slot wall thickness and the rounding of the slot ends are taken into account, the theory holds according to the conclusion under 1) above. If an accuracy of better than 1 or 2 per cent in resonant length is desired, it is necessary to consider a number of second order effects. Some of these are discussed under C, 4.

B. Summary of Theoretical Results

1. *Results for Finite Slot Wall Thickness*

The three slots considered here are the longitudinal shunt slot, the inclined or rotated series slot, and the displaced transverse series slot, all located in the broad face of rectangular waveguide. The results are valid for narrow slot widths, and *include the influence of slot wall thickness*. Since the same basic assumption concerning the slot stored power has been made for all three slots, a portion of the calculations for all of the slots will be identical, and this portion is given first.

Let

λ = free space wavelength $= 2\pi/k$
λ_g = guide wavelength $= 2\pi/\kappa$
a = waveguide larger dimension
b = waveguide smaller dimension
a' = long dimension of slot
b' = narrow dimension of slot
t = slot wall thickness.

We wish to compute G_c/Y_0 and B_c/Y_0 as follows:

$$\frac{G_c}{Y_0} = \frac{\dfrac{1}{n_j^2}\left(\dfrac{Y_0'}{Y_0}\right)^2 \dfrac{G_{rj}}{Y_0}(1+\cot^2\kappa' t)}{\left(\dfrac{G_{rj}}{Y_0}\right)^2 + \left[\dfrac{Y_0'}{Y_0}\cot\kappa' t - \dfrac{B_{rj}}{Y_0}\right]^2} \tag{1}$$

$$\frac{B_c}{Y_0} = \frac{B_j}{Y_0} + \frac{\dfrac{1}{n_j^2}\dfrac{Y_0'}{Y_0}\left\{\dfrac{B_{rj}}{Y_0}\dfrac{Y_0'}{Y_0}(\cot^2\kappa' t - 1) + \left[\left(\dfrac{Y_0'}{Y_0}\right)^2 - \left(\dfrac{B_{rj}}{Y_0}\right)^2 - \left(\dfrac{G_{rj}}{Y_0}\right)^2\right]\cot\kappa' t\right\}}{\left(\dfrac{G_{rj}}{Y_0}\right)^2 + \left[\dfrac{Y_0'}{Y_0}\cot\kappa' t - \dfrac{B_{rj}}{Y_0}\right]^2}. \tag{2}$$

The quantities contained in these expressions are given by

$$\kappa' = \sqrt{k^2 - (\pi/a')^2}, \qquad k = 2\pi/\lambda \tag{3}$$

$$\kappa = 2\pi/\lambda_g = \sqrt{k^2 - (\pi/a)^2}$$

$$\frac{Y_0'}{Y_0} = \frac{\kappa'}{\kappa}.$$

When κ' is imaginary, write

$$\kappa = -i\sqrt{\left(\frac{\pi}{a'}\right)^2 - k^2} = -i|\kappa'|;$$

then

$$\cot(\kappa' t) = i\coth(|\kappa'| t).$$

And:

$$\frac{1}{n_j^2} = \frac{ab}{a'b'}\left[\frac{\pi}{4}\frac{1-(a'/a)^2}{\cos(\pi a'/2a)}\right]^2 \tag{4}$$

$$\frac{G_{rj}}{Y_0} = \frac{\lambda_g a' b'}{\lambda^3}\frac{32}{3\pi}\left[1 - 0.374\left(\frac{a'}{\lambda}\right)^2 + 0.130\left(\frac{a'}{\lambda}\right)^4\right] \tag{5}$$

$$\frac{B_{rj}}{Y_0} = \frac{2b'\lambda_g}{\lambda^2}\left\{\left(\frac{\kappa'}{k}\right)^2\left[C + \frac{3}{2} - \ln\frac{\gamma|\kappa'|b'}{2}\right] + \frac{\sin ka'}{ka'} + \left[1 + \left(\frac{\lambda}{2a'}\right)^2\right](S_-) - \frac{2b'}{3a'}\left(\frac{\lambda}{2a'}\right)^2\right\} \tag{6}$$

where

$$\ln\gamma = 0.5772, \qquad \gamma = 1.781$$

κ' is given by (3)

$$C = \frac{Ci(ka' + \pi) + Ci|\, ka' - \pi\,|}{2}$$

$$S_- = \frac{Si(ka' + \pi) - Si(ka' - \pi)}{2\pi},$$

$Ci(x)$ and $Si(x)$ being the cosine and sine integrals:

$$Si(x) = \int_0^x \frac{\sin t}{t}\,dt, \quad Ci(x) = \int_\infty^x \frac{\cos t}{t}\,dt.$$

$$\frac{B_j}{Y_0} = \frac{1}{2}\frac{B_t}{Y_0} + \frac{2b}{\lambda_g}\left[\ln 2 + \frac{\pi}{6}\frac{b'}{b} + \frac{3}{2}\left(\frac{b}{\lambda_g}\right)^2\right] \tag{7}$$

where

$$\frac{B_t}{Y_0} = \frac{4b}{\lambda_g}\left[\ln \csc\frac{\pi b'}{2b} + \frac{1}{2}\left(\frac{b}{\lambda_g}\right)^2 \cos^4\left(\frac{\pi b'}{2b}\right)\right]$$

$$- \frac{4b}{\lambda_g}\left(\frac{\lambda_g}{\lambda_{g3}}\right)^2 \left[\frac{\cos\dfrac{3\pi a'}{2a}}{\cos\dfrac{\pi a'}{2a}} \cdot \frac{1 - \left(\dfrac{a'}{a}\right)^2}{1 - 9\left(\dfrac{a'}{a}\right)^2}\right]^2$$

$$\cdot \left[1 + \left(\frac{\pi b'}{2\lambda_{g3}}\right)^2\right] \ln\left(\frac{4}{\pi\gamma}\,\frac{\lambda_{g3}}{b'}\right) \tag{8}$$

with

$$\gamma = 1.781,$$

$$\lambda_{g3} = \left|\frac{\lambda}{\sqrt{1 - \left(\dfrac{3\lambda}{2a}\right)^2}}\right|.$$

The quantities above have the following physical meanings: G_c/Y_0 and B_c/Y_0 are the normalized conductance and susceptance of a centered transverse series slot in the broad face of rectangular waveguide, when the slot has thickness t; B_j/Y_0 is a susceptance element and n_j^2 a turns ratio in a particular network representing an E plane Tee; G_{rj}/Y_0 and B_{rj}/Y_0 are the conductance and susceptance of the radiating junction between rectangular waveguide and a half space; finally, B_t/Y_0 is the susceptance of a zero-thickness transverse slot coupling identical waveguides.

a) Longitudinal Shunt Slot: The slot shown in Fig. 2 is assumed to be of thickness t. Both equivalent networks are valid at the terminal plane T. Network (b) is the one in standard use for this slot; however, the parameters below apply to network (a) and are related to those of network (b) by

$$\frac{G}{Y_0} = \frac{\dfrac{R}{Z_0}}{\left(\dfrac{R}{Z_0}\right)^2 + \left(\dfrac{X}{Z_0}\right)^2}, \quad \frac{B}{Y_0} = \frac{-\dfrac{X}{Z_0}}{\left(\dfrac{R}{Z_0}\right)^2 + \left(\dfrac{X}{Z_0}\right)^2}. \tag{9}$$

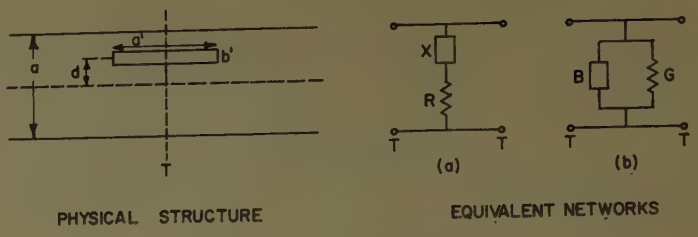

Fig. 2—Longitudinal shunt slot.

The parameters R/Z_0 and X/Z_0 are given by

$$\frac{R}{Z_0} = \frac{G_c}{Y_0} V_{sh}^2 \tag{10}$$

$$\frac{X}{Z_0} = \frac{B_c}{Y_0} V_{sh}^2 \tag{11}$$

where

$$V_{sh} = \left(\frac{2a}{\lambda_g}\right)\left[\frac{\cos\dfrac{\pi a'}{2a}}{\cos\dfrac{\pi a'}{\lambda_g}} \cdot \frac{\left[1 - \left(\dfrac{2a'}{\lambda_g}\right)^2\right]}{\left[1 - \left(\dfrac{a'}{a}\right)^2\right]}\right] \csc\frac{\pi d}{a}. \tag{12}$$

$\dfrac{G_c}{Y_0}$ and $\dfrac{B_c}{Y_0}$ are given by (1) and (2).

b) Rotated Series Slot: The slot shown in Fig. 3 is

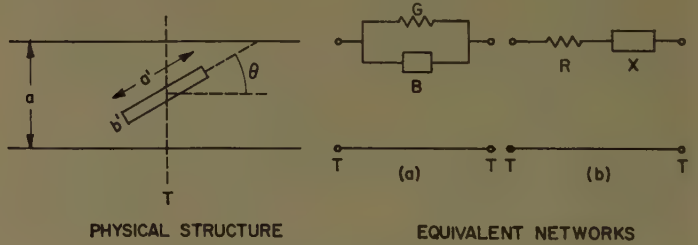

Fig. 3—Rotated series slot.

assumed to be of thickness t. Both equivalent networks are valid at the terminal plane T. Network (b) is the one in standard use for this slot; however, the parameters below apply to network (a) and are related to those of network (b) by

$$\frac{R}{Z_0} = \frac{\dfrac{G}{Y_0}}{\left(\dfrac{G}{Y_0}\right)^2 + \left(\dfrac{B}{Y_0}\right)^2}, \quad \frac{X}{Z_0} = \frac{-\dfrac{B}{Y_0}}{\left(\dfrac{G}{Y_0}\right)^2 + \left(\dfrac{B}{Y_0}\right)^2}. \tag{13}$$

The parameters G/Y_0 and B/Y_0 are given by

$$\frac{G}{Y_0} = \frac{G_c}{Y_0} V_\theta^2, \tag{14}$$

$$\frac{B}{Y_0} = \frac{B_c}{Y_0} V_\theta^2 \tag{15}$$

where G_c/Y_0 and B_c/Y_0 are given by (1) and (2),

$$V_\theta = \left[\frac{\cos\frac{\pi a'}{2a}}{1-(a'/a)^2}\right] \frac{2}{\left[A(\theta)\sin\theta + \frac{\lambda_g}{2a}B(\theta)\cos\theta\right]} \quad (16)$$

where

$$\left.\begin{matrix}A(\theta)\\B(\theta)\end{matrix}\right\} = \frac{\cos\left(\frac{\pi}{2}\xi\right)}{1-\xi^2} \pm \frac{\cos\left(\frac{\pi}{2}\eta\right)}{1-\eta^2}$$

and

$$\left.\begin{matrix}\eta\\\xi\end{matrix}\right\} = \frac{a'}{a}\sin\theta \pm \frac{2a'}{\lambda_g}\cos\theta.$$

c) Displaced Series Slot: The slot shown in Fig. 4 is

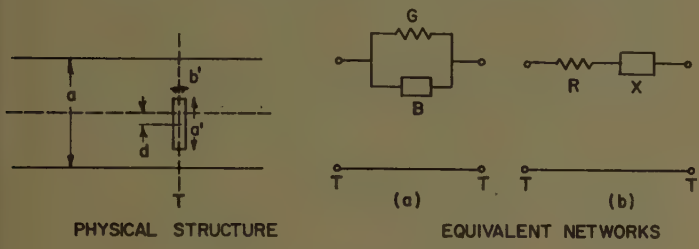

Fig. 4—Displaced series slot.

assumed to be of thickness t. The remarks presented about Fig. 3 concerning the equivalent networks, and including (13), apply here also. The parameters G/Y_0 and B/Y_0 are given by

$$\frac{G}{Y_0} = \frac{G_c}{Y_0} V_d^2 \quad (17)$$

$$\frac{B}{Y_0} = \frac{B_c}{Y_0} V_d^2 \quad (18)$$

where

$$V_d = \sec(\pi d/a). \quad (19)$$

G_c/Y_0 and B_c/Y_0 are given by (1) and (2).

2. *Results for Zero-Thickness Slots*

Results have been obtained for the same three slots considered above when the slots have zero thickness. Since the case of zero-thickness slots is of lesser interest, due to the appreciable influence of slot wall thickness, these results will not be repeated here. Instead, reference will be made to the appropriate equations in Part I.

For the longitudinal shunt slot, parameter R/Z_0 is given by (20), and X/Z_0 by (36). The relations between these parameters and G/Y_0 and B/Y_0 are presented as (9) of Part II. Parameters G/Y_0 and B/Y_0 for the rotated series slot are given by (29) and (32). G/Y_0 and B/Y_0 for the displaced series slot appear as (26) and (34). The relations between these parameters for the last two slots and R/Z_0 and X/Z_0 for these slots are presented as (13) of Part II. The results for X/Z_0 and B/Y_0 are expressed in terms of the normalized susceptance of a zero-thickness centered series slot; the expression for the latter is given as (33).

3. *Restrictions*

All the results are based upon variational expressions and are therefore approximate. However, the choice of a cosinusoidal trial slot electric field is considered to be very good. It is expected that all results for resistances or conductances are quite accurate. The susceptance or reactance results are somewhat more approximate, since they are based on the assumption that the stored power is the same for all three slots. This assumption is expected to be better for the rotated and the displaced series slots than for the longitudinal shunt slot. The results for the latter slot will be better for smaller off-center shifts. The above-mentioned assumption implies that the resonant frequency of the slot, or alternatively the dimensions of the slot for resonance at a given frequency, will be independent of off-center shift or angle of rotation. Further discussion of this point is presented below.

Small slot thickness exerts a negligible effect on the resistance or conductance, for whichever a theoretical expression is directly available. (For example, for the longitudinal shunt slot, small thickness exerts a negligible influence on the resistance, but has an appreciable effect on the conductance.) Both the slot susceptance and reactance are noticeably affected by small slot thickness.

C. Comparison Between Theory and Measurement

In addition to the straightforward comparison between the theoretical and measured results for a number of slots, the discussion below considers such effects as the influence of slot thickness, the distinction between rounded and rectangular slot ends, the variation of resonant length or frequency with off-center shift or angle of rotation, and the presence of small shunt arms in the equivalent pi network of a slot usually characterized as purely series.

While a considerable amount of experimental data exists for slots at resonance, relatively little systematic material is available for off resonance conditions. This is especially true of the rotated and the displaced series slots. Therefore, although the theory described herein is expected to be most reliable for the rotated or displaced series slots, comparison will be made first with the available longitudinal shunt slot data. The remaining portions of this section describe the comparison between the theoretical values and measurements specially taken in connection with this study. These additional measurements also serve to investigate some of the other effects referred to just above.

1. *Hughes Longitudinal Shunt Slot*

The measurements to which the theory is compared are abstracted from the rather comprehensive Hughes Aircraft Company experimental study[1] of the longitudinal shunt slot. One finds, experimentally, that the

resonant length of the longitudinal shunt slot, shown in Fig. 2, varies with the off-center location of the slot. The theory presented herein, however, does not take this variation into account, although, if the off-center displacement is small, the theory is still expected to be reasonably good.

The off-resonance behavior as a function of slot length of a longitudinal shunt slot in X-band waveguide with an off-center displacement of 0.074 inch, and a slot width of 0.0625 inch, at a frequency of 9375 mc, is presented in Fig. 1 of footnote 1, and is chosen as a typical slot for comparison with theory. The experimental and theoretical comparison for the impedance parameters of this slot is given in Figs. 5 and 6. Fig. 5 presents the parameters in form (b) of Fig. 1, while Fig. 6 indicates the behavior for the parameters in form (a). In all curves, the experimental points are indicated and are connected by the dashed curve; the solid lines refer to the theoretical results taking wall thickness into account, while the broken lines correspond to the zero thickness theoretical results. In the curve for R/Z_0, however, the dashed curve is omitted since the experimental points essentially scatter about the theoretical results.

One can infer several interesting results from the curves of Figs. 5 and 6. First, it is clear that the effect of wall thickness is significant, except for R/Z_0, and that substantially better agreement with measurement is obtained when thickness is considered. Quantitatively, the zero-thickness resonant length is approximately 4 per cent shorter than the measured one, while that for the theoretical result including thickness is only 2 per cent shorter. Second, one notes (from the slope of the X/Z_0 curves and from the insensitivity of R/Z_0 to wall thickness) that the Q value for the zero-thickness theoretical result is lower than that for the result including thickness, and that the latter value agrees well with the experimental value. Third, the monotonic behavior of R/Z_0 and X/Z_0 implies that it is preferable to first plot any experimental data in this form as a check on its reliability. Furthermore, a quantitative check is afforded by the insensitivity of R/Z_0 to wall thickness, slot length, etc. It is this insensitivity that permits the Stevenson formula for the conductance at resonance to be valid even though resonance generally does not occur when the slot length is equal to a half-wavelength. One notes, however, that the conductance G/Y_0 is sensitive both to slot length and wall thickness.

The fourth and last point to be noted here is that there still remains a discrepancy between the experimental data and the theoretical results which account for thickness. However, the theoretical results are valid for slots with rectangular ends while the measurements were taken on slots with rounded ends. One would expect that the slot with rounded ends would behave as a somewhat shorter equivalent rectangular-ended slot, thereby requiring a slightly higher frequency or greater

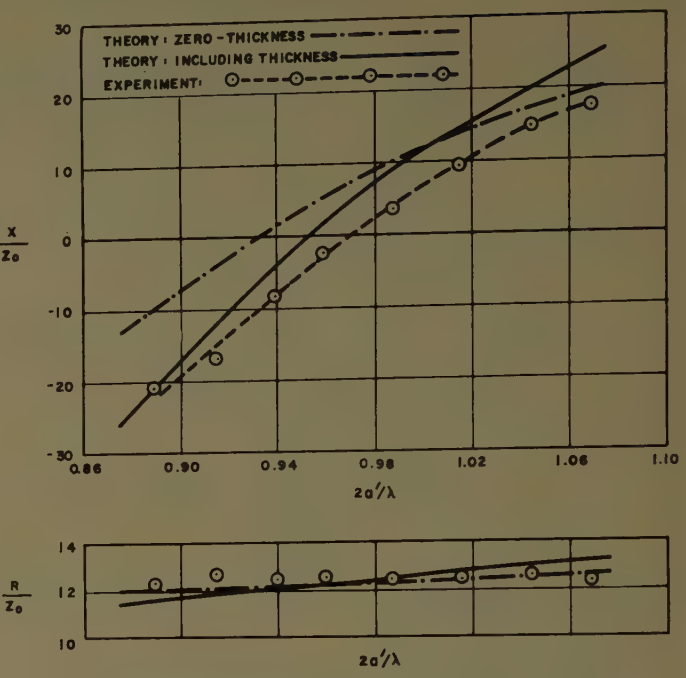

Fig. 5—Impedance of longitudinal shunt slot vs normalized slot length.

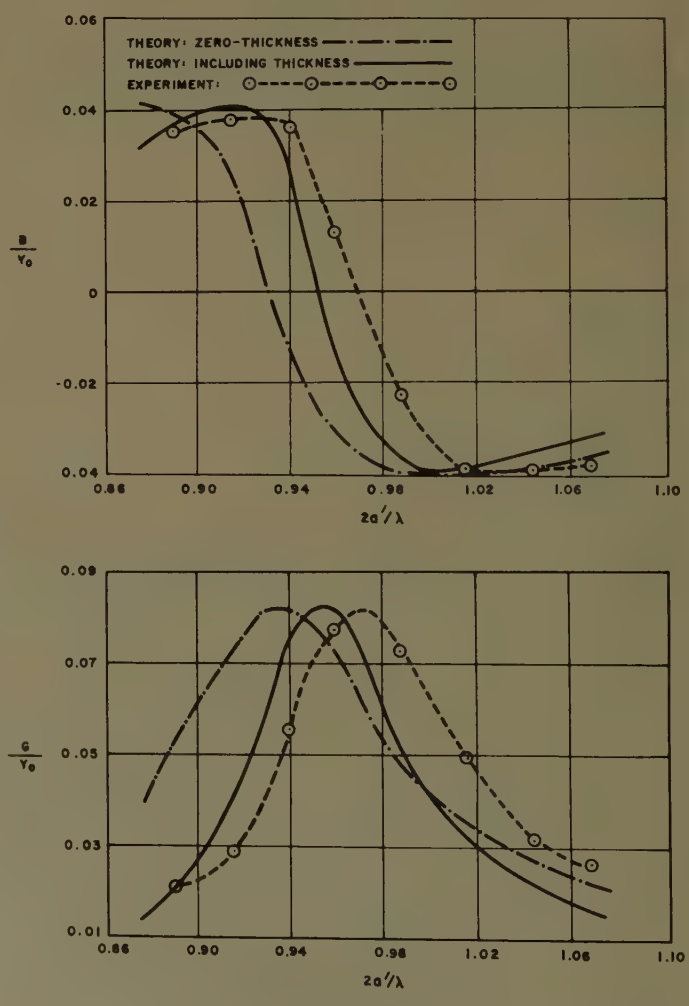

Fig. 6—Admittance of longitudinal shunt slot vs normalized slot length.

slot length for resonance. According to this reasoning, the measurement-theory discrepancy is in the proper direction. As a quantitative check on this effect, the measurements discussed below were taken, and it was found that the above-mentioned discrepancy is almost completely accounted for in this manner. If, however, comparison were to be made with a slot with a much larger off-center displacement, a residual discrepancy would be found due to the variation of slot resonant length with off-center displacement. Further discussion of this point appears in the following section.

2. *AFCRC Rotated Series and Longitudinal Shunt Slots*

As a quantitative check on the distinction between slots of rounded and rectangular ends, measurements have been taken at the Air Force Cambridge Research Center at the suggestion of R. M. Barrett, who made its facilities available for these measurements. The measurements, taken by G. Forbes under the supervision of F. J. Zucker, were performed at L band so as to permit careful machining of the slot ends. Three pairs of slots, one of rotated series slots and two of longitudinal shunt slots, were fabricated and their impedance properties determined as a function of frequency. One slot of each pair possessed rectangular ends; the other slot, of identical over-all dimensions, had rounded ends. Each slot was 4.50 inches in length and 0.45 inch in width, in a rectangular waveguide of dimensions 6.50 inches by 3.25 inches, and of wall thickness 0.080 inch. The measurements on the rotated series slots, of angle 45°, serve the additional purpose of furnishing a hitherto unavailable systematic set of off-resonance data for this slot type.

The experimental data for both of the 45° rotated series slots and the theoretical calculations for the rectangular-ended slot, including the effect of the 0.080 inch wall thickness, are presented in Figs. 7 and 8 (next page). Fig. 7 presents the network parameters in form (b) of Fig. 1, while Fig. 8 indicates the behavior for the parameters in form (a). In all curves, the solid line refers to the theoretical calculation; the measured points for the slots of rounded and rectangular ends are indicated by circles and squares, respectively, surrounding the points, and these points are connected by broken and dashed lines, respectively. An exception is noted in the case of G/Y_0, where the measured points simply scatter about the theoretical values.

It is seen from Figs. 7 and 8 that the rounding of the ends of the slot exerts a decided effect on the resonant frequency of the slot, increasing it by about 2 per cent in this case. Furthermore, the experimental curves seem to be almost identical apart from this frequency shift. In line with the insensitivity of R/Z_0 of Fig. 5, one notes from Fig. 7 that the rounding of the slot ends produces a negligible difference in the G/Y_0 values. In addition, from the slopes of the B/Y_0 curves and the insensitivity of G/Y_0, one concludes that the Q is relatively unaffected by the rounding of the slot ends. This observation agrees with that above concerning the curve shapes.

The theoretical curves of Figs. 7 and 8 are seen to agree very well with the measured values for the rectangular-ended slot. While the theory is expected to agree to within 1 per cent or so, the particularly good correlation here is fortuitous. One should note, finally, in connection with these measurements, that the percentage increase in resonant frequency due to rounding the slot ends is roughly the same as the percentage discrepancy in the resonant lengths obtained between the measurements and the theory, including thickness, in Figs. 5 and 6.

The results for the longitudinal shunt slots exhibit similar differences between slots of rounded and rectangular ends. Again, the slots with rounded ends possess an approximately 2 per cent higher resonant frequency, for both off-center shifts (0.635 inch and 2.00 inches). It is indicated, therefore, that for a slot length to width ratio of ten a 2 per cent increase in resonant frequency is found for rounded as compared to rectangular ends, independent of the slot location in the top wall of the guide.

As regards comparison with theory, the theoretical resonant frequencies as compared to those found for the slot with rectangular ends were 1 per cent high for the 0.635 inch shift and 5 per cent low for the 2.00 inch shift. These results are in agreement with the well known behavior of longitudinal shunt slots, and indicate that the theoretical results will predict resonant frequencies (or lengths) which are slightly high for very small off-center shifts and rather low for very large shifts.

3. *PIB Rotated Series Slot*

Precision measurements were taken on several rotated series slots at the Microwave Research Institute of the Polytechnic Institute of Brooklyn for three reasons: a) to determine whether a purely series network representation for the slots is warranted, or whether the shunt arms of the more general pi network may not be neglected, b) to verify the accuracy of the theoretical expression for the variation with angle of rotation, and c) to check the constancy of resonant length with angle of rotation. In brief, the results of these measurements indicate that a) it is warranted to employ a purely series network for the rotated slot, except for second order effects, b) the theoretical expression accounting for variation with angle is very good, and c) the resonant length is independent of angle of rotation except for very large angles.

In order to maintain the exact slot dimensions as the slot was rotated, the slots were fabricated in a rotatable plate which served as a length of the broad face of the waveguide and which made good electrical contact with the rest of the guide with the aid of a vacuum chuck. The set-up was such that the same slot could be measured for angles of rotation of 0°, 36°, and 72°. In order

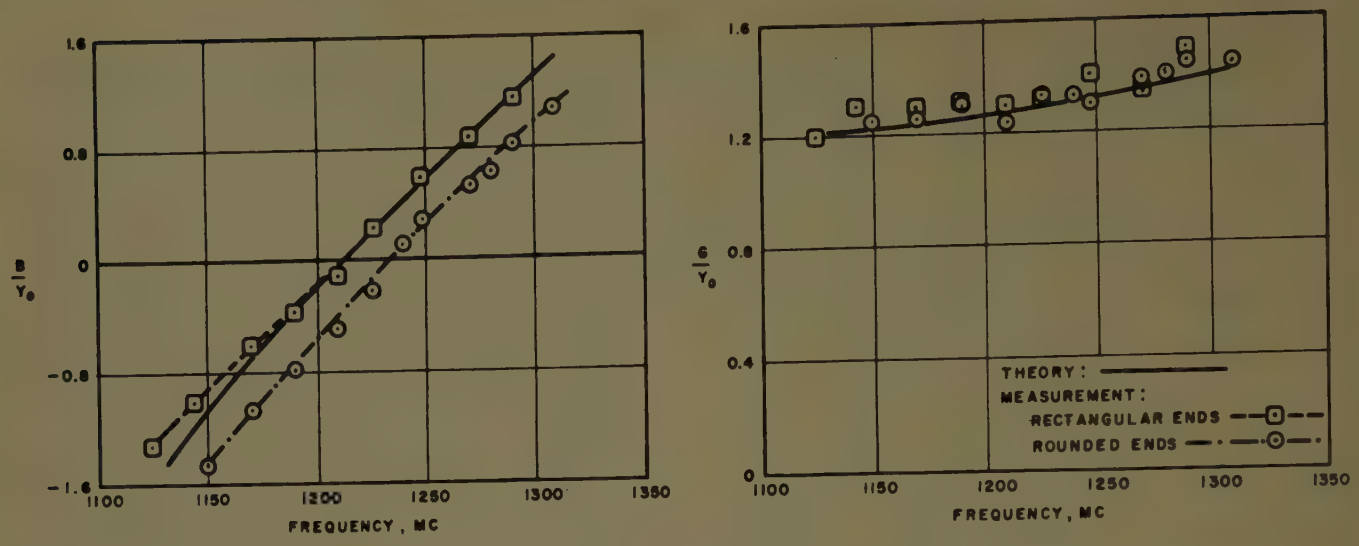

Fig. 7—Admittance of 45° rotated series slot vs frequency.

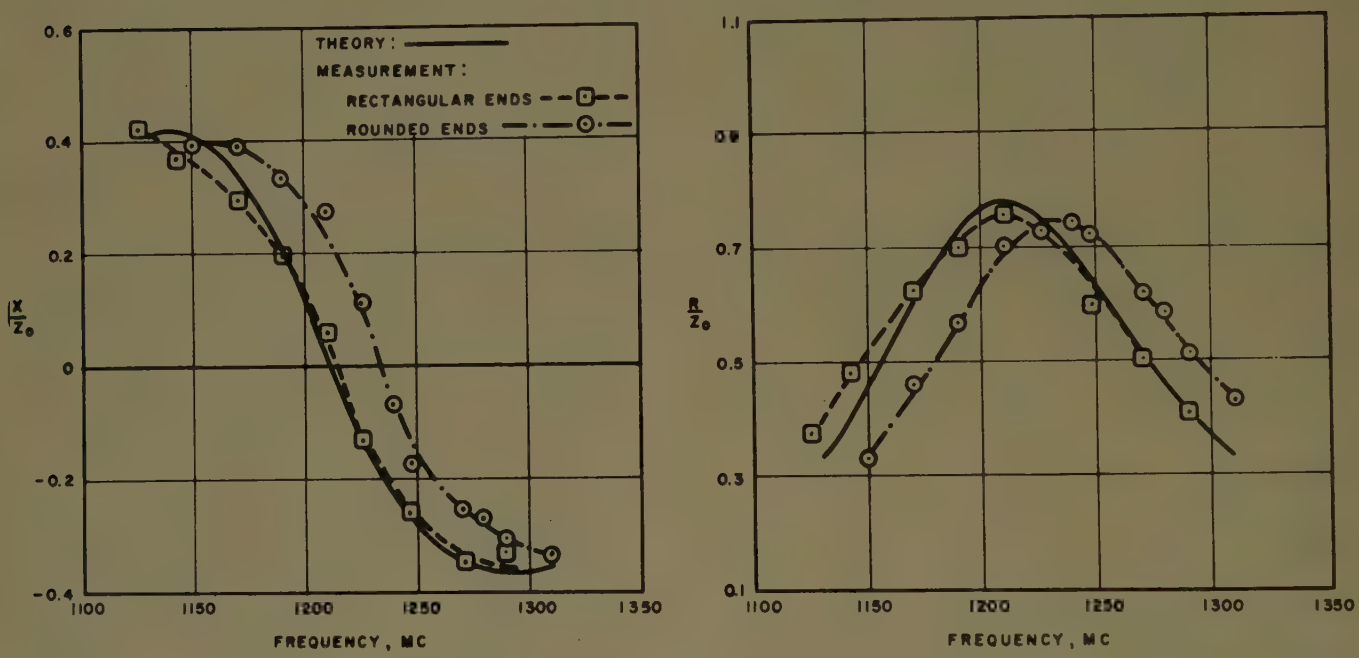

Fig. 8—Impedance of 45° rotated series slot vs frequency.

to go through resonance, the length of the slot was changed by filing the slot with the aid of a mandrel which maintained the slot width constant. Measurement runs were taken on these slots using the variable shorting plunger technique, and the resulting data were analyzed by semiprecision procedures.

The equivalent network results for these measurements were expressed in pi form with terminal planes located at the geometrical symmetry plane of the slot. Although the slot is generally characterized as purely series at these terminal planes, small but nonvanishing shunt arms were found in the pi network representation. These shunt arms contained almost negligible conductive portions and small susceptive contributions which were consistently inductive. While the precision of the measurements was insufficient to permit reliable quantitative interpretation of the results, one can safely conclude that the neglect of these shunt arms would produce errors of second order only. (If the slot length were no longer much greater than the slot width these errors would, of course, become serious.) It is therefore warranted to neglect them in engineering applications, and the discussion that follows assumes a purely series network representation.

As a check on the theoretical expression (16) for the variation of the network parameter values with angle of rotation, the measured values obtained for the unrotated slots (in the transverse position) are inserted as

G_c/Y_0 and B_c/Y_0 in (14) and (15), and V_θ in each case is computed from (16). The resulting theoretical predictions for G/Y_0 and B/Y_0 for any other angle of rotation is then compared with the measured values. To be consistent with the notation for θ in (16) and in Fig. 3, the slot in the transverse position corresponds to $\theta=90°$. As a result, the curves on Figs. 9 and 10, which present this comparison between measurement and theory, are plotted with $90°-\theta$ as the abscissa.

Figs. 9 and 10 indicate clearly that (16) is reliable. The experimental values for large angles of rotation (large values of $90°-\theta$) are less trustworthy because of the steepness of the curves in that range and because of the higher conductance and susceptance values obtained there. It is of interest to note the insensitivity exhibited in the region of small angles of rotation, and, in contrast, the high sensitivity found for large angles. The curve for B/Y_0 for $a'=0.584$ inch is omitted because for this case the value of B_c/Y_0 is almost zero, thereby destroying the precision of the comparison.

The experimental data presented in Figs. 9 and 10 are replotted as a function of slot length in Figs. 11 and 12 (next page). From Fig. 11 it is seen that the conductance values for small angles of rotation are relatively insensitive to changes in slot length; the variation with slot length increases with the angle of rotation. Of greater interest, however, is Fig. 12, in which it is seen that the resonant length is substantially constant for small angles of rotation, and increases very slightly as the angle of rotation is increased. For the $90°-\theta=72°$ case, the resonant length has changed by less than 0.004 inch, or about 0.6 per cent. L. A. Kurtz[2] also found the resonant length for this slot type to be substantially independent of θ. For engineering purposes, it is therefore safe to regard the resonant length of the rotated series slot as independent of the angle of rotation, in accord with the theory presented in Part I.

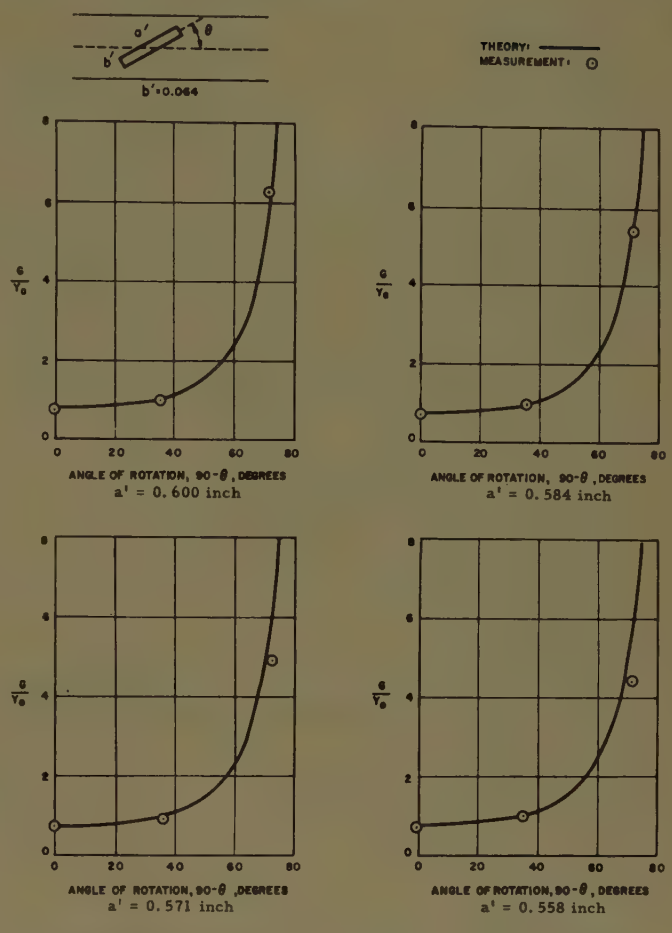

Fig. 9—Conductance of rotated series slot vs angle of rotation.

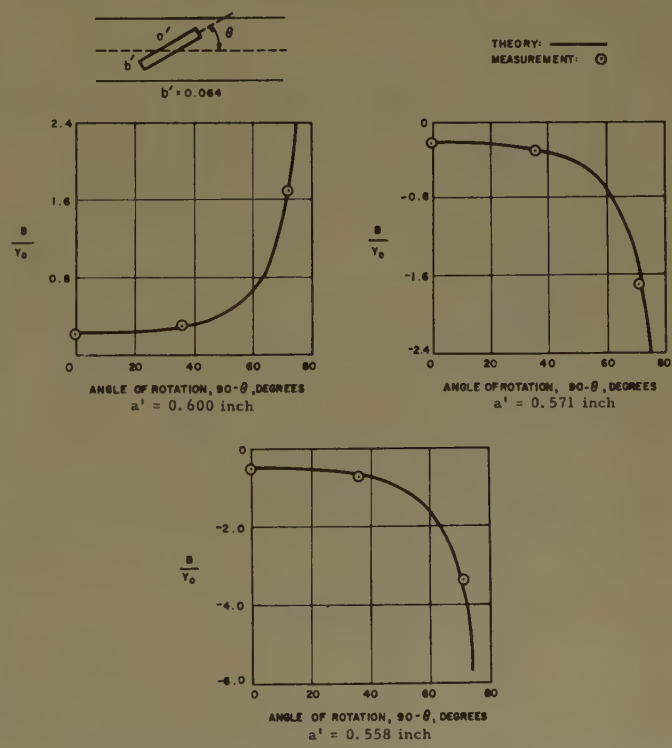

Fig. 10—Susceptance of rotated series slot vs angle of rotation.

4. *Further Discussion*

Discrepancies between the theoretical results and measurements on slots in general use may be due to four factors:

1) The theory is valid for slots with rectangular ends while most slots in general use possess rounded ends. The effect of this difference is considered under subsection 2 above, and its quantitative effect estimated for slots with length to width ratios of ten.

2) The theory assumes the existence of an infinite baffle attached to the slot, while in practice this baffle is absent. However, rough tests made by various people indicate that the effect of a baffle on the impedance is negligible, except for large displacements of the longitudinal shunt slot.

[2] L. A. Kurtz, "Design Applications of Series Slots," Hughes Aircraft Co. Tech. Memo. No. 273, Culver City, Calif.; December, 1951. See Fig. 2 or p. 1.

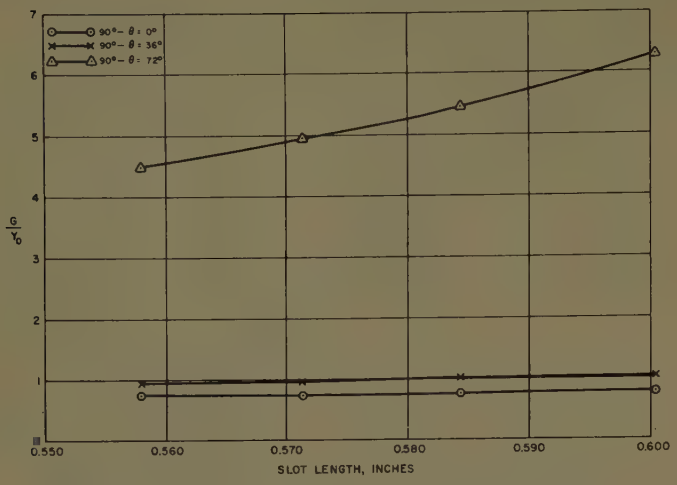

Fig. 11—Conductance vs slot length for rotated series slot.

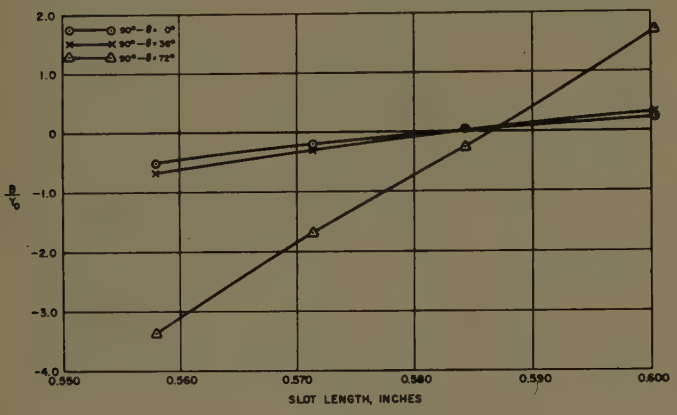

Fig. 12—Susceptance vs slot length for rotated series slot.

3) Both the theory and the measurements assume that the slot is rigorously characterized by a purely shunt or purely series network, depending on the slot location, rather than a complete Tee or pi network, respectively. If the other arms are not negligible, the measured values will be affected differently depending on the method of measurement. The theory would still correctly describe the behavior of the dominant arm, but the evaluation of the other arms, corresponding to a symmetric or antisymmetric electric field excitation of the slot for a basically series or shunt slot, respectively, would be rather formidable and probably not worthwhile. The influence of these other arms increases with an increase in slot width, and will be different for different slot locations. A discussion of this point is given under 3 above for the case of the rotated series slot; it is concluded that while small but nonvanishing shunt arms are present their effect would be of second order.

4) The theory may be inaccurate or inadequate in certain ranges. All of the theoretical reactance and susceptance results are related to the susceptance of the centered slot, which itself may be somewhat in error. Since the result for the centered slot consists essentially of a capacitive term, an inductive term, and correction terms such that at resonance appropriate cancellation occurs, it is easy to see that small errors in any of the constituent terms manifest themselves most critically at resonance. An error of 1 per cent, say, in the resonant length due to this effect is not unreasonable.

It seems, therefore, that a number of second order effects must be considered and taken into account if agreement better than 1 per cent in resonant length is desired. However, one must still check whether or not some of these effects are truly of second order only. It is suggested, for example, that more careful measurements be taken to determine the effect of an attached baffle, and whether or not the neglected arms in the rigorous equivalent network are truly insignificant for the case of the longitudinal shunt slot. The first order effects that must be considered, and which are discussed herein, are the slot thickness and the distinction between rounded and rectangular slot ends.

Since the theory presented herein neglects the presence of the side walls in the longitudinal shunt slot case, it does not account for the experimentally observed variation of the slot resonant length (or frequency) with off-center displacement. There remains, therefore, the need for a theoretical expression which accounts for this variation.

Acknowledgment

The work described herein has been sponsored by the Air Force Cambridge Research Center under Contract No. AF-19(604)-262.

The writer wishes to express his appreciation to Dr. L. C. Van Atta for his encouragement of this work. In connection with the measurements taken at the Air Force Cambridge Research Center, the writer wishes to thank R. M. Barrett for suggesting the measurements and making available the facilities of the AFCRC, G. Forbes for taking the measurements, and particularly F. J. Zucker for correlating and interpreting the data. Thanks are also due Mrs. A. Cordova of the Hughes Aircraft Company for her computing services.

A Luneberg Lens Scanning System*

J. S. HOLLIS† AND M. W. LONG†

Summary—**A 16,000-mc scanner is described which scans a 40° azimuth sector alternately with each of two beams at a rate of 17 scans per beam per second. The beams have half-power vertical and horizontal beamwidths of 0.76° and 1.06° respectively and are separated vertically by an angle of 1.85°. Horizontal collimation of each beam is achieved by a geodesic analog of the two-dimensional Luneberg lens. The lenses feed a section of a semiparabolic cylinder for effecting vertical collimation. Feeding the lenses is a switching system, consisting of two four-way turnstile waveguide switches and a waveguide chopper switch, which gives a scan-time dead-time ratio of 8:1.**

Introduction

THE SCANNING antenna shown in Fig. 1 was designed for use with an experimental K_u-band mortar-location radar. The purpose of this antenna is to alternately scan two pencil-shaped beams of microwave energy across a 40° azimuth sector at a rate of 17 scans per beam per second. The principle of scanning is based on a form of the Luneberg lens. Typical vertical and horizontal beam patterns are shown in Figs. 2 and 3. In Fig. 1 the antenna is shown in the operate position; the reflector folds down over the scanner for storage or transit.

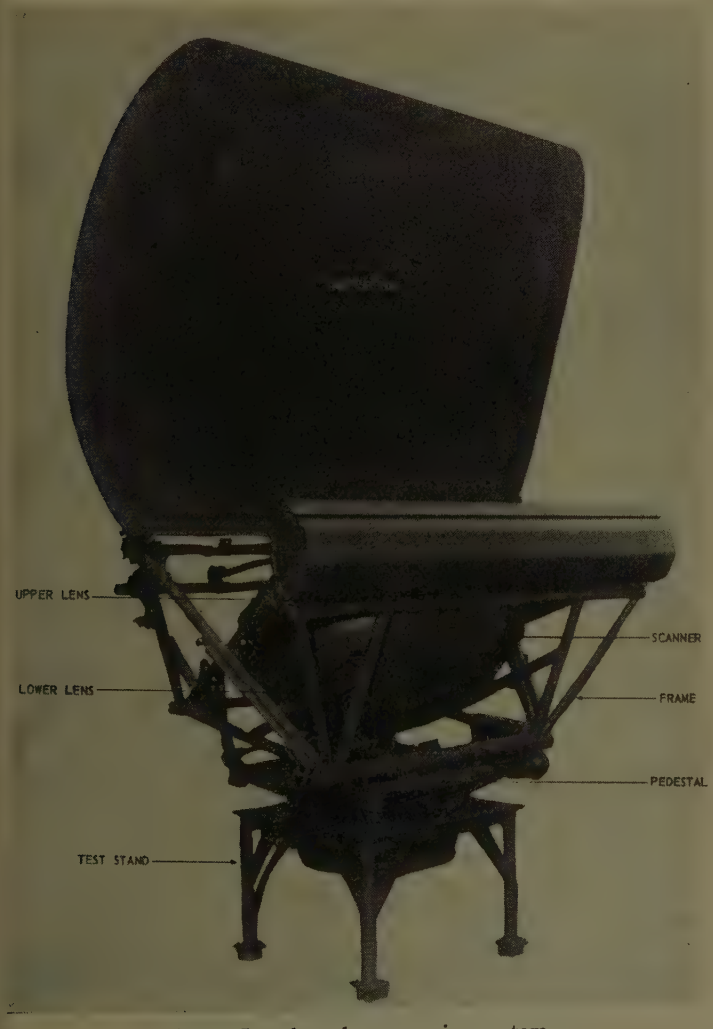

Fig. 1—Luneberg lens scanning system.

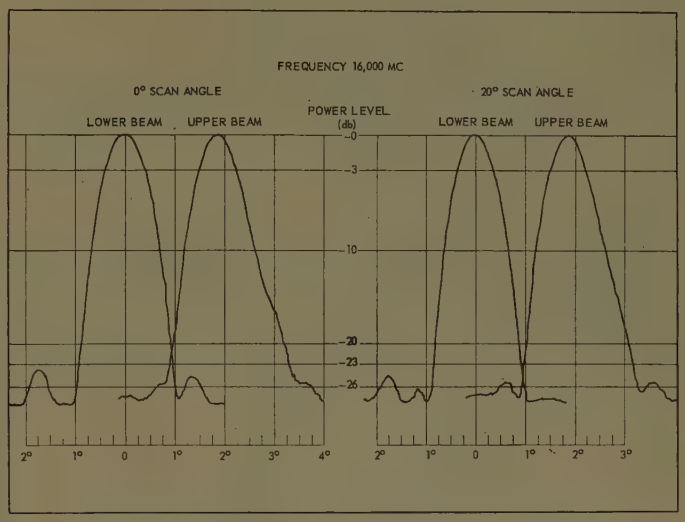

Fig. 2—Typical far-zone vertical-plane beam patterns of the Luneberg lens scanning system.

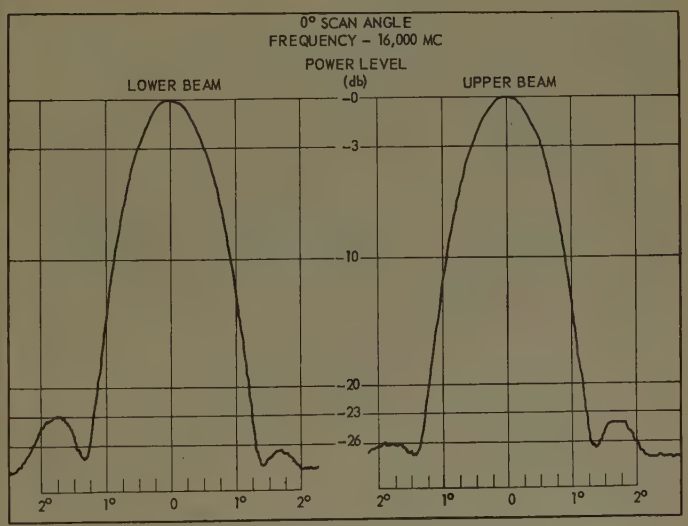

Fig. 3—Typical far-zone horizontal-plane beam patterns of the Luneberg lens scanning system.

Quantitative measurements have not been made of system breakdown power; however, the system has been operated without pressurization at a nominal peak power of 75 kw. The system characteristics are listed in Table I.

* Manuscript received by the PGAP, July 26, 1956. This work was supported by the Signal Corps Eng. Labs., Ft. Monmouth, N. J., under Contract DA-36-039 SC-42707.

† Eng. Experiment Sta., Georgia Inst. Tech., Atlanta, Ga.

TABLE I

System Characteristics

Frequency range	16,000 mc ± 1 per cent
Number of beams	2
Beam separation, vertical	1.85°
Beamwidth, vertical	0.76°
Beamwidth, horizontal	1.06°
Polarization	Vertical
Scan rate	17 scans per beam per second
Scan sector	40°
Maximum side-lobe level	−23 db
Gain	43.6 db
Scanner loss (input waveguide to line-source feed)	1.6 db
Weight of complete system	1250 pounds
Geodesic lenses	130 pounds each
Scanning mechanism	295 pounds

The Luneberg Lens

If the refractive index n of a dielectric sphere varies with the normalized radius ρ according to the relation

$$n(\rho) = \sqrt{2 - \rho^2}, \qquad (1)$$

parallel rays striking the sphere are brought to a focus at a point on the periphery diametrically opposite the tangent plane of entry. A sphere of this type is called a Luneberg lens after R. K. Luneberg.[1] Fig. 4 is a section

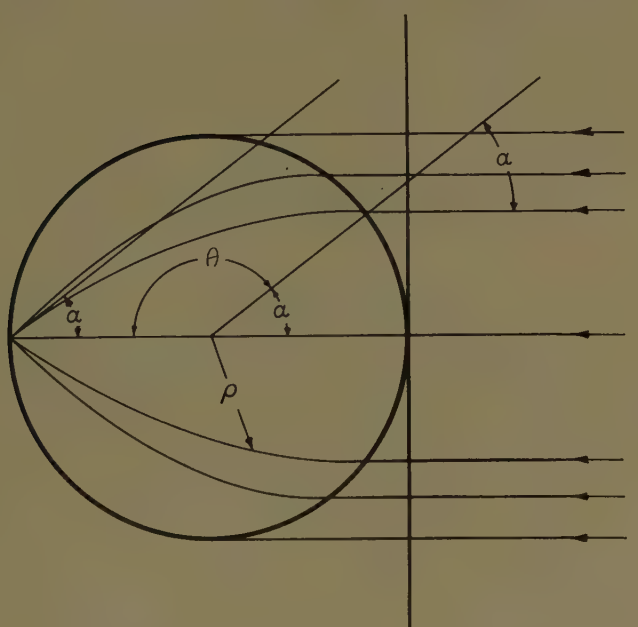

Fig. 4—Luneberg lens geometry.

through the center of such a sphere showing the paths of typical rays. The polar angle θ subtended by a ray in going through the lens is given by the expression

$$\theta = \pi - \alpha, \qquad (2)$$

where α is the angle which the ray makes with the lens diameter at the focal point.

The spherical symmetry of the Luneberg lens permits scanning of a radar beam without deterioration over 4π steradians by moving a feed horn over the surface. This makes the principle of the Luneberg lens applicable to wide-angle rapid scanning. Three-dimensional lenses in which the refractive index approximates that of (1) have been developed, and results of electrical tests are encouraging.[2–4] It is apparent from Fig. 4 that (1) also applies to lenses which focus in a plane. In such lenses, which are called two-dimensional or modified Luneberg lenses, the energy is constrained between two closely spaced conducting plates. Focusing can be accomplished by an actual variation in the index of refraction like that in the three-dimensional lens, by a variation in the effective index of refraction by altering the phase velocity in a dispersive medium,[5] or by application of the geodesic analog principle.[6–8] In the geodesic analog of the modified Luneberg lens the physical lengths of rays, which are along geodesics of the mean surface, are equivalent to the optical lengths of rays in the other two-dimensional Luneberg lenses.

In the antenna[9] of Fig. 1, focusing is accomplished in two steps: a cylindrical reflector brings the incident rays to a line focus, and a geodesic analog[10] of the modified Luneberg lens focuses the line of rays to a point where they are intercepted by a sectoral horn. The lens, of which a plan view and a cross section are shown in Fig. 5, consists of two closely nested aluminum spinnings. Each spinning is made of two sections: a main spinning, and an insert which replaces a section of the main spinning between the periphery and the reinforcing ring. This insert forms an internal feed arc which permits the sectoral feed horns to rotate in a plane about the lens axis. The insert subtends 110° of the periphery of the lens to permit the lens to focus all intercepted parallel rays over the 40° scan sector. Complete circular symmetry, as in ordinary Luneberg lenses, is not required of the lens because only a sector is scanned. Rays

[1] R. K. Luneberg, "Mathematical Theory of Optics," Brown University Press, Providence, R. I., pp. 189–212; 1944.

[2] G. P. Robinson, "Three dimensional microwave lens," *Tele-Tech and Electronic Industries*, vol. 13, pp. 73, 124–25; November, 1954.

[3] W. W. Wright, J. E. Rhodes, and G. P. Robinson, "A Three-Dimensional Luneberg Lens," Final Rep., Contract DA-36-039 SC-56712, Scientific Associates, Inc., Atlanta, Ga.; December 15, 1955.

[4] "Three Dimensional Microwave Luneberg Lens," Tech. Bull. 6-2-3, Emerson and Cuming, Inc., Canton, Mass.

[5] G. D. M. Peeler and D. H. Archer, "A Two-Dimensional Microwave Luneberg Lens," NRL Rep. 4115, Naval Res. Lab., Washington, D. C.; March 2, 1953.

[6] R. F. Rinehart, "A solution to the problem of rapid scanning for radar antennas," *J. Appl. Phys.*, vol. 19, pp. 860–862; September, 1948.

[7] F. G. R. Warren and S. E. A. Pinnell, "The Tin Hat Scanning Antenna," Tech. Rep. No. 6, RCA Victor Co., Ltd., Montreal, Canada; July 16, 1951.

[8] K. S. Kunz, "Propagation of microwaves between a parallel pair of doubly-curved conducting surfaces," *J. Appl. Phys.*, vol. 25, pp. 642–653; May, 1954.

[9] R. M. Goodman, Jr., M. D. Harris, and J. S. Hollis, "A Two-Beam 16,000-Mc Modified Luneberg Lens Scanning System," Final Rep., Vol. II, Contract DA-36-039 SC-42707, Georgia Inst. Tech., Atlanta, Ga.; June 15, 1955.

[10] L. F. Culbreth, Jr., M. W. Long, and A. H. Schaufelberger, "Two-Dimensional Microwave Luneberg Lenses," Final Rep., Vol. I, Contract DA-36-039 SC-42707, Georgia Inst. Tech., Atlanta, Ga.: June 10, 1955.

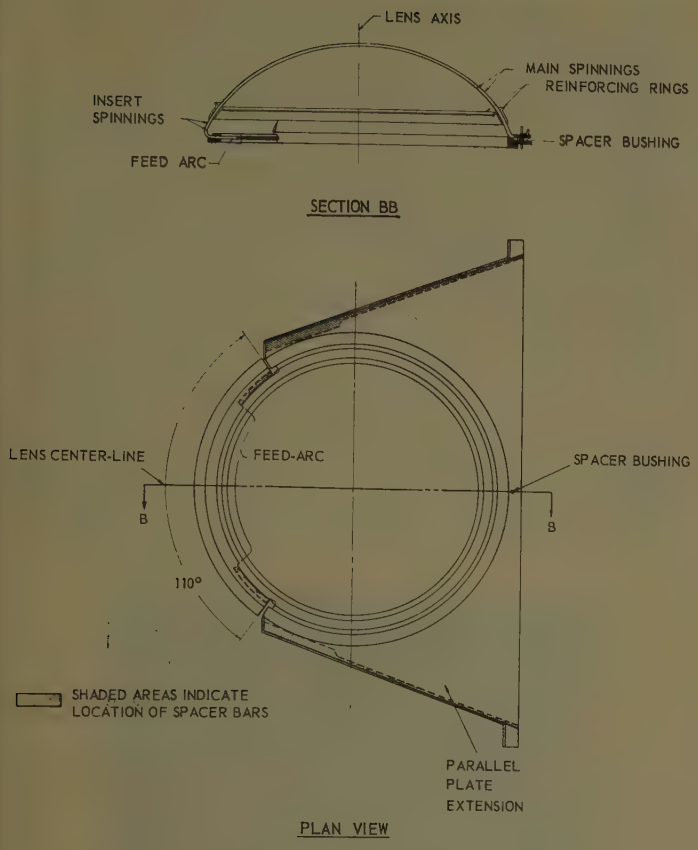

Fig. 5—Geodesic analog of the Luneberg lens.

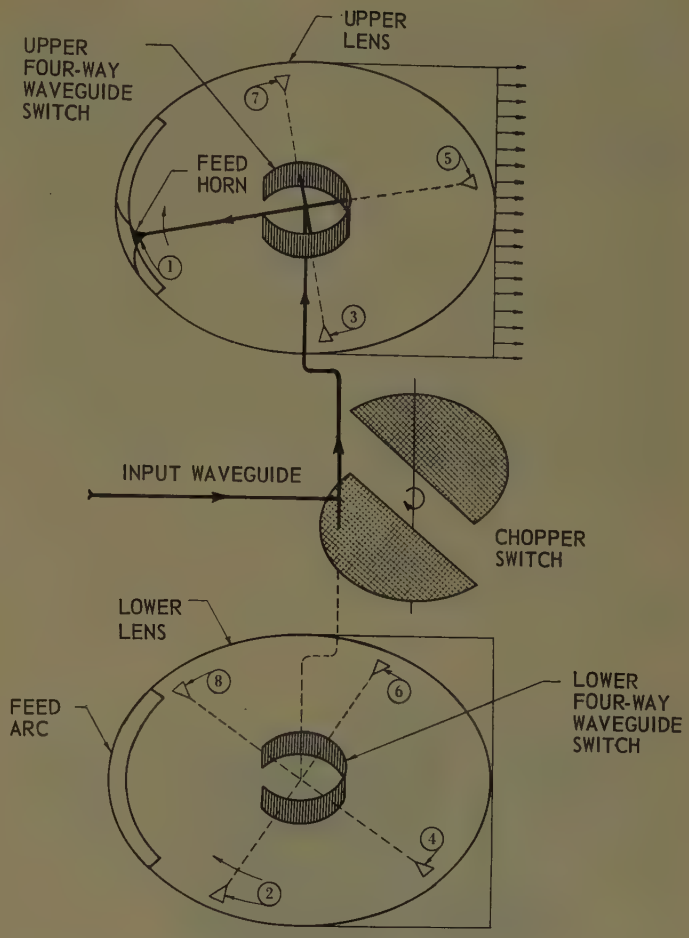

Fig. 6—Functional diagram of the scanning mechanism of the Luneberg lens scanning system.

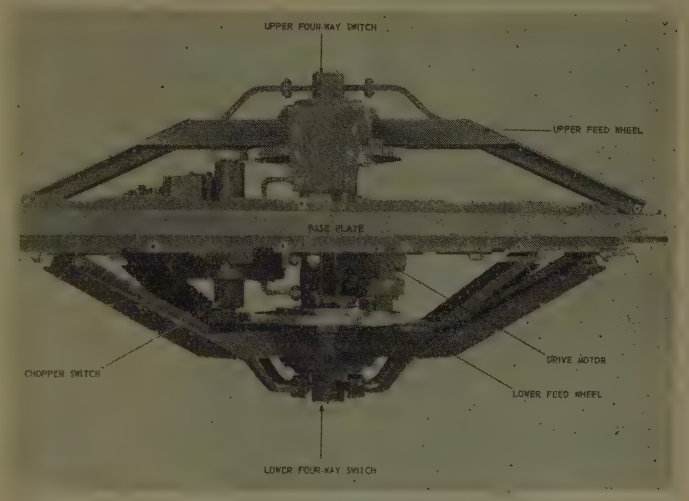

Fig. 7—Scanning mechanism of the Luneberg lens scanning system.

from the focal line of the reflector are guided to the curved periphery of the lens in the TEM mode by non-focusing parallel-plate extensions. The parallel incident rays propagate in air along the mean surface between the spinnings of the lens in such a manner that they are brought to a focus at a point on the focal arc.

The parallel extensions which connect the lenses with the reflector focal line are folded upward to permit mounting the lenses beneath the reflector. To produce the vertical separation angle between the beams, the feed horns are displaced to either side of the focal line of the reflector. The horns are covered by a sandwich-type radome.

The fabrication tolerance for the lens surfaces was set at $\pm 1/32$ inch. Although the lenses are within this tolerance over most of the surface area, deviations exist which are greater than these values. Far-zone beam-pattern measurements of the prototype lens without the reflector indicated a maximum side-lobe level of 25 db below the peak of the main lobe.

The Scanning Mechanism

The scanning mechanism is located in the cavity formed between the two lenses (see Fig. 1). A functional diagram is shown in Fig. 6 and a side view in Fig. 7. Four sectoral feed horns are spaced at intervals of 90° on each of the two feed wheels. The wheels are mounted coaxially and are oriented so that the feed horns of one wheel are spaced at angles of 45° to those of the other. At the center of each feed wheel there is a four-way switch which connects the feed horn that is passing across the feed arc with a two-way chopper switch. The chopper switch rotates at four times the speed of rotation of the feed wheels. Thus, the feed horns of the upper and lower feed wheels are energized sequentially as they pass the internal feed arcs of the lenses. As the

feed wheels rotate, the upper and lower beams alternately scan the 40° azimuth sector at a rate of 17 scans per beam per second. To minimize the lubrication problem, sealed ball-bearings are used throughout and nylon pinions are mated with stainless steel gears on the feed wheels.

The switching system is interesting because the switching angle, the angle through which a feed horn moves during the time that the system is electrically inoperable, is one-fourth that of the chopper switch. The actual chopper switching angle is 14°, which gives an effective switching angle of $3\frac{1}{2}$°. To limit the active scan sector to 40° the switching angle is increased to 5° by blanking the magnetron. This gives a scan-time to dead-time ratio of 8:1.

The Waveguide Switches

An exploded view of the chopper switch is shown in Fig. 8. This type of switch[11] is composed of an E-plane waveguide tee, two output waveguides, and two semi-circular chopper disks. The choppers alternately short each arm of the tee, connecting the input waveguide to the unshorted arm. In addition to its function as a waveguide switch, the chopper serves as a generator for synchronization pulses. Steel inserts in the periphery of the nonmagnetic chopper disks perturb the magnetic fields of reluctance pickups, generating electrical pulses which are synchronized with the beam position.

The four-way waveguide switches are of the turnstile type.[12] Each switch is composed of a stator, a rotor with four waveguide arms, and a thin cylindrical barrier which is attached to the stator and located in a gap between the rotor core and rotor housing, as shown in Fig. 9. A slot in the barrier, called the window, faces the feed arc of its associated lens. The height of the window is that of the E dimension of the waveguide and the length subtends a 90° angle. During the interval in

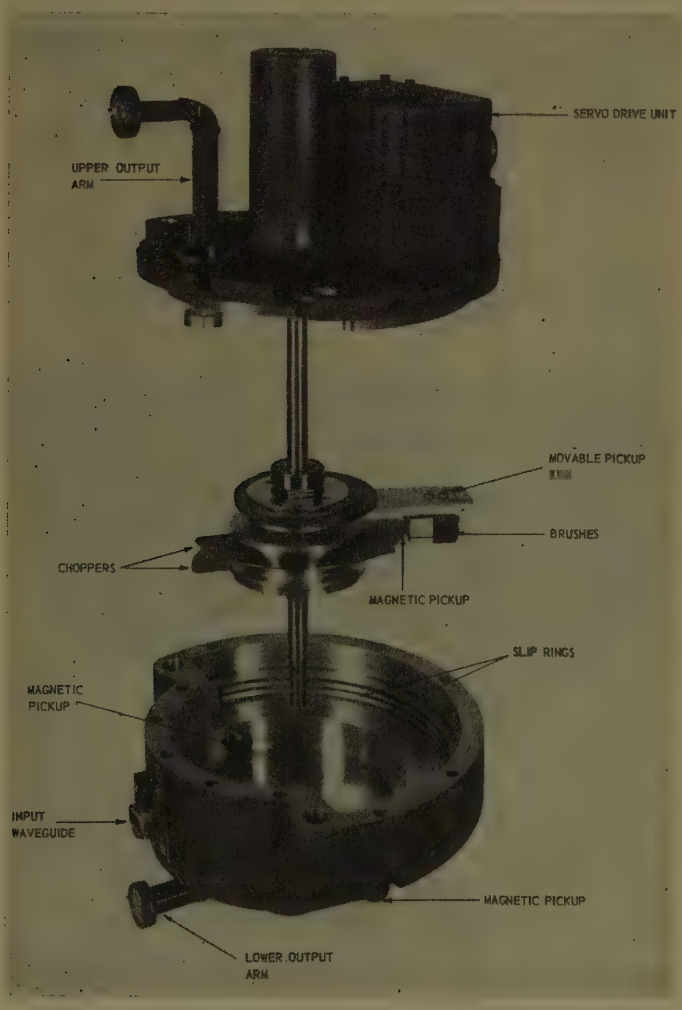

Fig. 8—Exploded view of the waveguide chopper switch of the Luneberg lens scanning system.

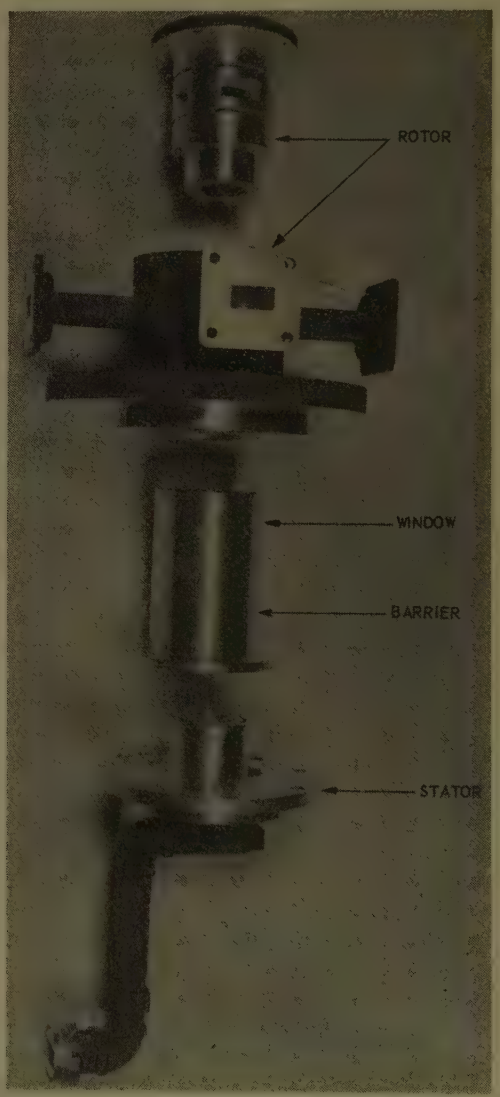

Fig. 9—Exploded view of one of the four-way waveguide switches of the Luneberg lens scanning system.

[11] G. L. Ragan, "Microwave Transmission Circuits," McGraw-Hill Book Co., Inc., New York, N. Y., vol. 9, pp. 533–534; 1948.

[12] M. W. Long, "A high-speed K-band switch," Proc. IRE, vol. 39, pp. 1566–1567; December, 1951.

which a four-way switch is energized by the chopper switch, three of the waveguide outlets of the rotor core are shorted by the barrier. The fourth moves across the window and connects the center waveguide to the feed horn which is passing across the feed arc of the lens.

The vswr of the two-way switch is 1.02 at 16,000 mc and has a maximum value of 1.08 within the two per cent band centered at 16,000 mc. The loss is less than 0.1 db. The maximum vswr of either four-way switch, including two cast E-plane bends, was less than 1.15 over the band. The loss through a four-way switch is about 0.3 db.

Conclusion

The geodesic analog of the modified Luneberg lens is theoretically free of aberration and is not extremely critical with respect to fabrication tolerances. Since the focusing properties of the lens are obtained by the equalization of physical path lengths in a medium which is nondispersive over a wide range of frequencies, it is inherently broadbanded. The scanning system which is described demonstrates that this type of modified Luneberg lens is peculiarly suited to the problem of wide-angle sector scanning.

Acknowledgment

This work was made possible through the combined efforts of a number of people at the Georgia Tech Engineering Experiment Station and at the Signal Corps Engineering Laboratories. Especially significant to the success of the project was the work of A. H. Schaufelberger, who supervised the development of the lens surfaces, and of R. M. Goodman, Jr., who supervised the mechanical design and construction.

A Design Procedure for Dielectric Microwave Lenses of Large Aperture Ratio and Large Scanning Angle*

F. S. HOLT† and A. MAYER‡

Summary—**Methods are given for designing point-source three-dimensional aspheric rotationally-symmetric dielectric lenses and for zoning such lenses. Designs for scan angles and aperture ratios much larger than conventional may be achieved and all computations can be done on a desk calculator. The three-dimensional lens is obtained by first designing an exact two-point corrected cylindrical dielectric lens and then rotating a section of the cylindrical lens about the axis of symmetry of the section. The design procedures for the cylindrical lens are based on ray-tracing techniques. Experimental results indicate that the three-dimensional lenses possess good wide-angle scanning characteristics.**

Introduction

DESIGN procedures for building cylindrical wide-angle lenses of the metal-plate constrained type have been given by Ruze[1] and procedures for designing cylindrical wide-angle dielectric lenses have been given by Gent.[2] In general, the procedures for designing wide-angle dielectric lenses are mathematically much more complicated than procedures for the corresponding metal-plate lenses. Until recently, metal-plate lenses were preferred to dielectric ones not merely because of the simpler design mathematics, but also because of the lack of availability of suitable dielectric materials. With recent advances in the development of lightweight, low-loss dielectric substances, the simpler fabrication techniques (machining) required for dielectric lenses as compared to metal lenses recommend the use of the former. A wide-angle dielectric lens design procedure recently introduced by Sternberg[3] has been successfully applied in the design of many dielectric lenses and has created much interest in this field. The lens design procedures to be presented in this paper are important in that they represent further significant simplifications in wide-angle dielectric lens design theory with resulting appreciable reductions in associated numerical computation. These procedures are based on optical ray-tracing techniques and are capable of high accuracy. Similar techniques have been concurrently and independently worked out by others,[4] but have not as yet been published.

* Manuscript received by the PGAP, February 7, 1956; revised manuscript received August 12, 1956.

† AF Cambridge Res. Ctr., Antenna Lab., Bedford, Mass.

‡ Mass. Inst. of Tech., Lincoln Lab., Lexington, Mass. Formerly with Raytheon Mfg. Co., Bedford, Mass.

[1] J. Ruze, "Wide-angle metal plate optics," Proc. IRE, vol. 38, pp. 53–59; January, 1950.

[2] H. Gent, "Theoretical Design and Performance of a Dielectric Lens for Wide-Angle Scanning," *T.R.E. Tech. Note No. 105*, 1951.

[3] R. L. Sternberg, "Elementary methods in the numerical design of microwave dielectric lenses," *J. of Math. and Phys.*, vol. 34, pp. 209–235; January, 1956.

[4] A. E. Marston and R. M. Brown, Naval Res. Lab., Washington, D. C.; and M. J. Hunt, Gen. Elec. Advanced Electronics Center, Ithaca, N. Y.

Unzoned Binormal Lens[5]

Fig. 1(a) shows a transverse section through a binormal cylindrical dielectric lens. The foci are marked F' and F''; feeds located at the foci produce beams which emerge at the "design scan angles" $\pm\theta$, these being directions measured from the axis of symmetry of the section, that is, the x axis. Fig. 1(b) shows a zoned version of this lens, and Fig. 1(c) is a cutaway view of the spherical lens obtained by rotating the section in Fig. 1(b) about its axis of symmetry.[6]

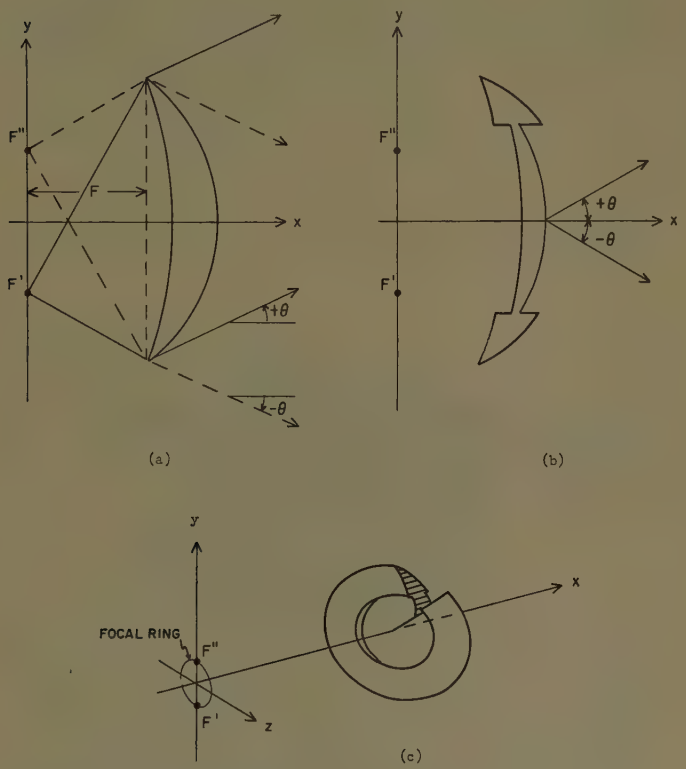

Fig. 1—(a) Unzoned binormal lens.
(b) Same lens zoned.
(c) Spherical lens derived from (b). All cross sections possess mirror symmetry in the X axis.

For the binormal cylindrical lens we define the focal length, F, to be the distance between a line joining the focal points and a line joining the edges of the lens in the same transverse section [see Fig. 1(a)]. Given the four design parameters, focal length F, diameter D, index of refraction n, and design scan angle θ, it is not always possible to design a binormal lens having these specified values. With D, n, and θ given there exists a minimum physically realizable F. We do not know at present how to calculate this minimum F. We merely remark in passing that using polystyrene for design scan angles of as many as 10 half-power beamwidths, F/D values as small as 0.35 are achievable. In the following discussion we will assume that the four parameter values specified in the design problem will lead to a physically realizable lens. To distinguish the unzoned lens from the ones discussed later in connection with zoning, we will use the subscript zero, and define

$$f_0 = F, \qquad s_0 = \frac{D}{2}. \tag{1}$$

Fig. 2 shows a transverse section through the cylindrical lens with the x axis in the plane of symmetry and the y axis passing through the foci. The foci F' and F'' are shown with coordinates $(0, \pm y_f)$, and the lens edge points with coordinates $(f_0, \pm s_0)$. Requiring that the optical path length L_1 for the upper edge ray be equal to the optical path length L_2 for the lower edge ray, each path length being measured from the focal point F' to the reference plane W_0 (see Fig. 2),[7] it can be shown that

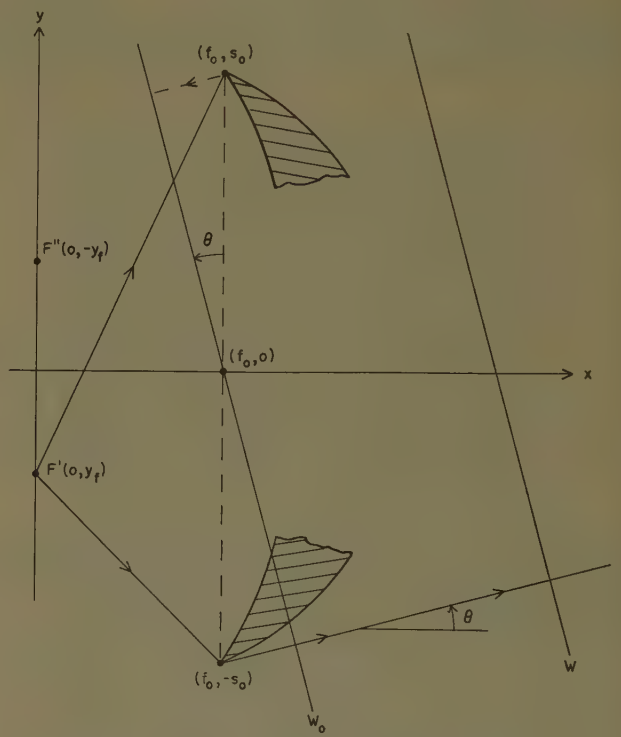

Fig. 2—Coordinate system and reference plane W_0 parallel to wavefront W.

$$y_f = -\sqrt{f_0^2 \tan^2\theta + s_0^2 \sin^2\theta} \tag{2}$$

[5] Binormal (or two point corrected) means that two symmetrically placed focal points exist in any transverse section of such a lens [see Fig. 1(a)]. A cylindrical binormal lens as a whole therefore will have two symmetrically placed focal lines.

[6] The two focal lines have coalesced into a focal ring (see footnote 5).

[7] The plane W_0 in Fig. 2 is for algebraic reasons more convenient to use than the wave front W.

and that

$$w_0 = L_1 = L_2 = -y_f \csc\theta, \tag{3}$$

where w_0 is the optical path constant.

We now have the seven quantities, f_0, s_0, n, θ, x_f (the x coordinate of the foci which is zero in the present coordinate system), y_f, and w_0, which are used in determining points on the lens surfaces. We determine such points by a development of ray lattices.

Ray Lattices[8]

A ray lattice is a set of points and associated slopes which lies on the surfaces of *some* binormal lens. The points and associated slopes of a ray lattice are determined by ray-tracing techniques which involve direct use of six of the seven quantities listed above. The seventh quantity, s_0, is used only as a goal or target to shoot at, as described below. Using the remaining six quantities, an infinite number of ray lattices may be constructed each of which satisfies exactly the optical requirements of the given problem. However, we believe that only one particular lattice out of this infinite number has the additional property that it converges to a knife-edge at the stipulated edge points $(f_0, \pm s_0)$, and we shall call this hypothetical lattice the "ideal lattice." We know of no formal mathematical proof of the existence of such a unique ray lattice; but belief that such an ideal lattice exists is based on our observations of the behavior of the many ray lattices we have computed. We now show how by a method of successive trials we may approach what appears to be the hypothetical ideal lattice.

To each point P_n of a ray lattice (see Fig. 3) there will be associated three coordinates, as follows: two space coordinates, x_n and y_n (the rectangular coordinates of the location of P_n), and one angle coordinate, ψ_n (the angle measured positive in the counter-clockwise direction that the outward normal to the lens at the point P_n makes with the horizontal). We assume that the inner (focal side) surface of the lens intersects the x axis at $x=c(>f_0)$, a trial value, and that there exists a unique value of $c=C$ associated with the ideal lattice. The x axis, being the axis of symmetry of the cross section, is normal to the lens surfaces. Therefore, for the coordinates of the first, we have determined point P_0 of the ray lattice: $x_0=c$, $y_0=0$, and $\psi_0=0$. We now proceed to trace alternately "outgoing" rays which leave the focus and "incoming" rays, which enter the focus, as shown in Fig. 3, all rays being subject to the fundamental condition that their optical path lengths measured from the focal point, through the lens, and thence to the reference plane W_0 shall each be equal to the optical path constant w_0. Tracing the outgoing ray through P_0, we determine the coordinates (x_1, y_1, ψ_0) of the lattice point P_1, a point on the outer surface of the binormal lens. Snell's law plus our knowledge of the six quantities referred to earlier suffice to fix these values; only elementary algebraic calculations are involved. Because of cross-sectional mirror symmetry we now know that the lattice point $\bar{P}_1$, which is the mirror image of P_1 (see Fig. 3), has coordinates $\bar{x}_1=x_1$, $\bar{y}_1=-y_1$

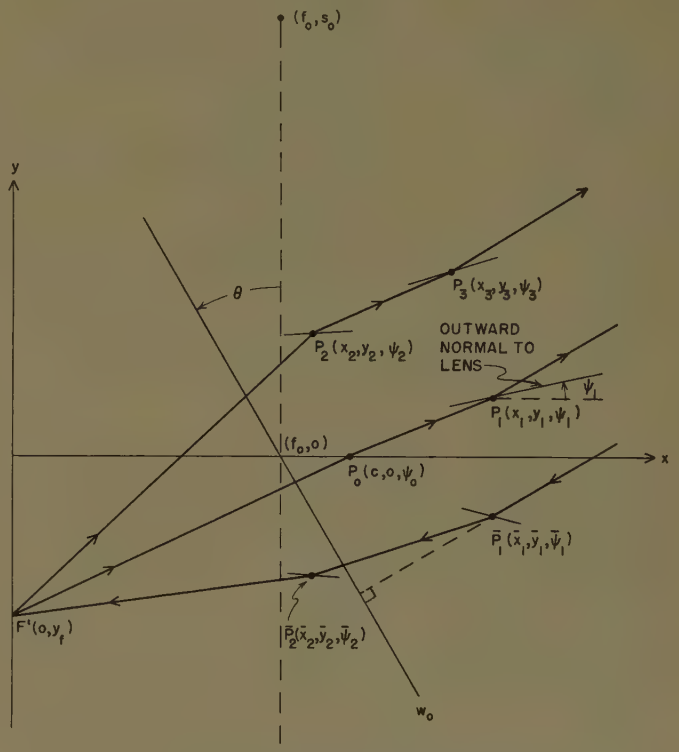

Fig. 3—Development of a ray lattice.

and $\bar{\psi}_1=-\psi_1$. We next trace the incoming ray that makes an angle θ with the positive x axis and is incident on the outer surface of the lens at the point $\bar{P}_1$. Snell's law, the path length condition, and the numerical data on hand again suffice to determine, by elementary algebra, the coordinates $\bar{x}_2$, $\bar{y}_2$, and $\bar{\psi}_2$ of lattice point $\bar{P}_2$, a point on the inner surface of the binormal lens. We then know by symmetry the coordinates of lattice point P_2, the image of $\bar{P}_2$ and may proceed to trace the outgoing ray passing through P_2; etc. Outgoing rays are traced through the upper half of the lens $(y>0)$, incoming rays through the lower half $(\bar{y}<0)$. The ray-tracing of all outgoing rays is describable by a single set of formulas which may be conveniently tabulated for desk machine computations; likewise, the ray-tracing of all incoming rays is describable by a single set of formulas. These sets are given in the next section.

Experience shows that if for a particular trial value c_1 the extremities of the lens bend toward the negative x axis, then C—the value of c we associate with the

[8] Ray lattices were originally used by F. S. Holt in a somewhat different way than here described to design binormal lenses of unspecified F/D.

ideal lattice and assume exists—must be greater than c_1. Conversely, if for a particular trial value c_2 the extremities of the lens bend toward the positive x axis, then C must be less than c_2 and hence $c_1 < C < c_2$. These two cases are illustrated in Fig. 4. The more closely that

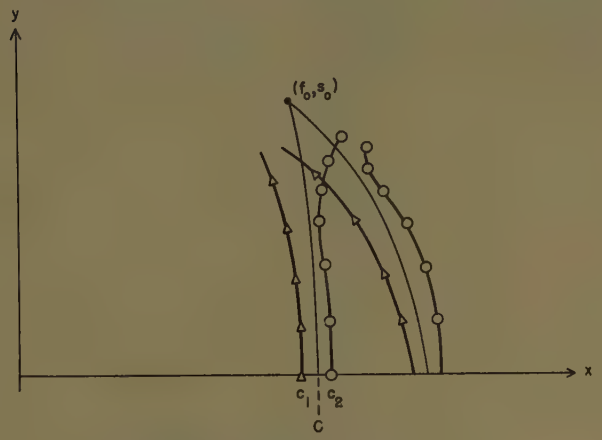

Fig. 4—Bending of ray lattices.

c_1 and c_2 approach each other the more nearly do the corresponding ray lattices condense on the edge points, that is, approach what appears to be the ideal lattice. It is, however, advantageous to approximate C with trial values $c > C$ rather than $c < C$, because in the former case fewer lattice points need be computed in order to determine whether or not the lattice is a good approximation to the ideal. In practice we strive for minimum lens weight—which means, roughly speaking, minimum lens edge thickness—but not necessarily for a true zero edge thickness, as this would be impractical from the point of view of lens mounting.

Ray Tracing Formulas

It simplifies the computation of lattice point coordinates to work in the X, Y coordinate system which is related to the x, y system by $X = x - c$ and $Y = y$; this means placing the origin of the X, Y coordinates at the point P_0 in Fig. 3. Then the focal point coordinates become $X_f = -c$, and $Y_f = y_f$ (see Fig. 5). It becomes convenient to use the plane D_0, which is parallel to W_0, as the optical reference plane. The optical path constant for the lens computed with respect to this plane then

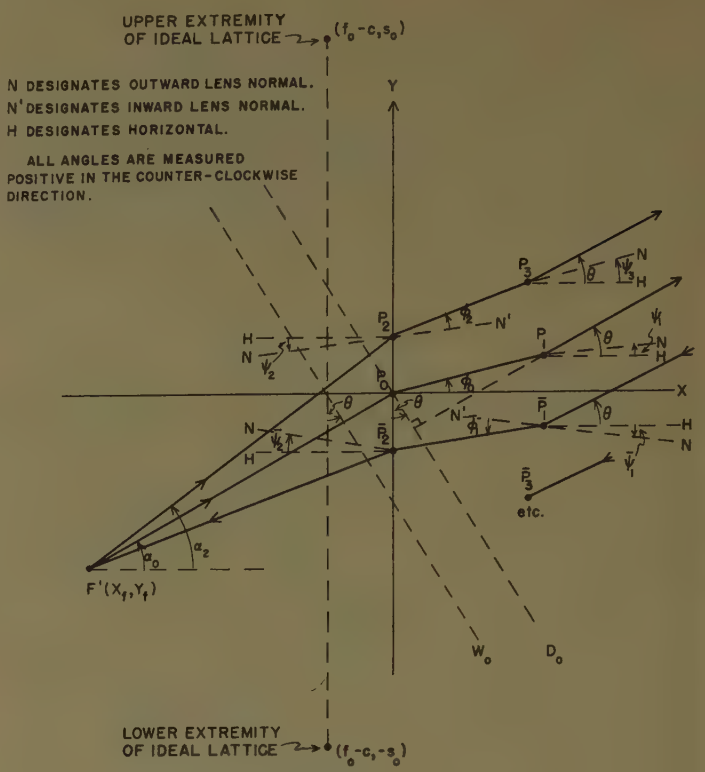

Fig. 5—Symbol meanings for ray tracing formulas.

becomes

$$d_0 = w_0 + (c - f_0)\cos\theta, \tag{4}$$

for the ray lattice corresponding to the trial value c. In Fig. 5, the symbols for coordinates of lattice points lying in the lower half-plane have bars over them; those for lattice points lying in the upper half-plane do not. Inside the lens, the angle between a ray and the inward normal at a lens surface point is denoted by ϕ_n and is measured positive in the counterclockwise direction from the surface normal. α_n denotes the angle a ray makes with the horizontal at the focal point F' and is also measured positive in the counterclockwise direction.

Starting with the point P_0 with coordinates $X_0 = Y_0 = \psi_0 = 0$ we apply alternately the formula sets 1) and 2) below for successive values of $k = 0, 1, 2, \cdots$, etc.

1) Outgoing Ray Formulas for determining the coordinates of lattice points P_{2k+1} and $\bar{P}_{2k+1}$ knowing the coordinates of lattice point P_{2k}.

$$\alpha_{2k} = \tan^{-1}\left(\frac{Y_{2k} - Y_f}{X_{2k} + c}\right) \tag{5a}$$

$$\phi_{2k} = \sin^{-1}\left[\frac{\sin(\alpha_{2k} - \psi_{2k})}{n}\right] \tag{5b}$$

$$X_{2k+1} = X_{2k} = \frac{d_0 + X_{2k}\cos\theta + Y_{2k}\sin\theta - \sqrt{(X_{2k} - X_f)^2 + (Y_{2k} - Y_f)^2}}{n\sec(\psi_{2k} + \phi_{2k}) - \cos\theta - \sin\theta\tan(\psi_{2k} + \phi_{2k})} \tag{5c}$$

$$Y_{2k+1} = Y_{2k} + (X_{2k+1} - X_{2k})\tan(\psi_{2k} - \phi_{2k}) \tag{5d}$$

$$\psi_{2k+1} = \tan^{-1}\left[\frac{n\sin(\psi_{2k}+\phi_{2k}) - \sin\theta}{n\cos(\psi_{2k}+\phi_{2k}) - \cos\theta}\right] \tag{5e}$$

$$\bar{X}_{2k+1} = X_{2k+1} \tag{5f}$$

$$\bar{Y}_{2k+1} = -Y_{2k+1} \tag{5g}$$

$$\bar{\psi}_{2k+1} = -\psi_{2k+1} \tag{5h}$$

2) Incoming Ray Formulas for determining the coordinates of lattice points $\bar{P}_{2k}$ and $\bar{P}_{2k}$ knowing the coordinates of lattice point $\bar{P}_{2k-1}$.

$$\bar{\phi}_{2k-1} = \sin^{-1}\left[\frac{\sin(\theta - \bar{\psi}_{2k-1}}{n}\right] \tag{6a}$$

$$\bar{X}_{2k} = \bar{X}_{2k-1} + \frac{-B + \sqrt{B^2 - AC}}{A} \tag{6b}$$

$$\bar{Y}_{2k} = \bar{Y}_{2k-1} + (\bar{X}_{2k} - \bar{X}_{2k-1})\tan(\bar{\psi}_{2k-1} + \bar{\phi}_{2k-1}) \tag{6c}$$

$$\bar{\psi}_{2k} = \tan^{-1}\left[\frac{n\sin(\bar{\psi}_{2k-1}+\bar{\phi}_{2k-1})\sqrt{(\bar{X}_{2k}-X_f)^2 + (\bar{Y}_{2k}-Y_f)^2} - (\bar{Y}_{2k}-Y_f)}{n\cos(\bar{\psi}_{2k-1}+\bar{\phi}_{2k-1})\sqrt{(\bar{X}_{2k}-X_f)^2 + (\bar{Y}_{2k}-Y_f)^2} - (\bar{X}_{2k}-X_{f,}}\right] \tag{6d}$$

where

$$A = (n^2 - 1)\sec^2(\bar{\psi}_{2k-1} + \bar{\phi}_{2k-1}) \tag{6e}$$

$$B = n(d_0 + \bar{X}_{2k-1}\cos\theta + \bar{Y}_{2k-1}\sin\theta)\tan(\bar{\psi}_{2k-1} + \bar{\phi}_{2k-1}) + (\bar{X}_{2k-1} - X_f) - (\bar{Y}_{2k-1} - Y_f)\tan(\bar{\psi}_{2k-1} + \bar{\phi}_{2k-1}) \tag{6f}$$

$$C = (d_0 + \bar{X}_{2k-1}\cos\theta + \bar{Y}_{2k-1}\sin\theta)^2 - (\bar{X}_{2k-1} - X_f)^2 - (\bar{Y}_{2k-1} - Y_f)^2 \tag{6g}$$

$$X_{2k} = \bar{X}_{2k} \tag{6h}$$

$$Y_{2k} = -\bar{Y}_{2k} \tag{6i}$$

$$\psi_{2k} = -\bar{\psi}_{2k}. \tag{6j}$$

Zoning

To zone the lens which has been designed for the prescribed F, D, n, and θ, we must find other bifocal lenses which are interior to it. The family of lenses, consisting of the original or parent lens as well as the interior lenses, must satisfy the condition that the optical path traced from the focus through the mth interior lens to the wave front labeled W (see Fig. 6) differ from the optical path through the parent lens by the amount $m\lambda$, where λ is the wavelength, and m is an integer denoting the zone. In Fig. 6, the x, y coordinate system is used again. The interior lens shown is assumed to come to a knife-edge at edge points labeled $(f_m, \pm s_m)$. It has its own reference plane W_m which is parallel to W_0. Since the distance between planes W_m and W_0 is required to be $m\lambda$, it follows readily that

$$f_m = f_0 - m\lambda\sec\theta \tag{7}$$

and

$$s_m = \sqrt{y_f^2\csc^2\theta - f_m^2\sec^2\theta}. \tag{8}$$

The optical path through the interior lens when measured to plane W_m may readily be shown to be

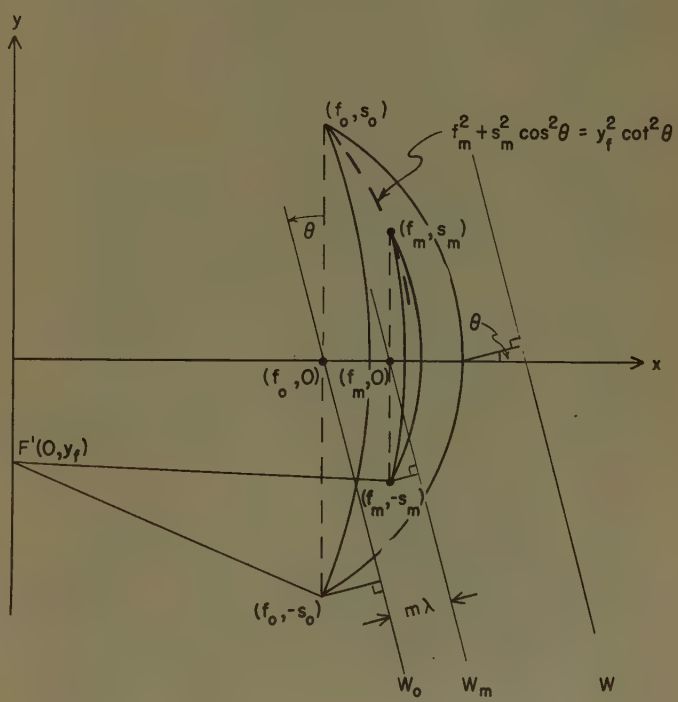

Fig. 6—Zoning procedure.

$$w_m = w_0. \tag{9}$$

As indicated in (8), the edge points of the interior lenses lie on an ellipse. The maximum number of interior lenses which may be fitted into the parent lens is

$$m_{\max} = \frac{w_0\cos\theta + f_0}{\lambda\sec\theta} \tag{10}$$

which follows from (7) and (8). Once f_m and s_m are computed (w_m, n, and θ are known), the interior lens desig-

nated by subscript m is designed in the same manner as was the parent lens.

In the final stepped version of the parent lens, the mth interior lens contributes the portion (mth zone) lying between ordinate values R_m and R_{m+1}. The quantities R_m and R_{m+1} are shown in Fig. 7 and selected by

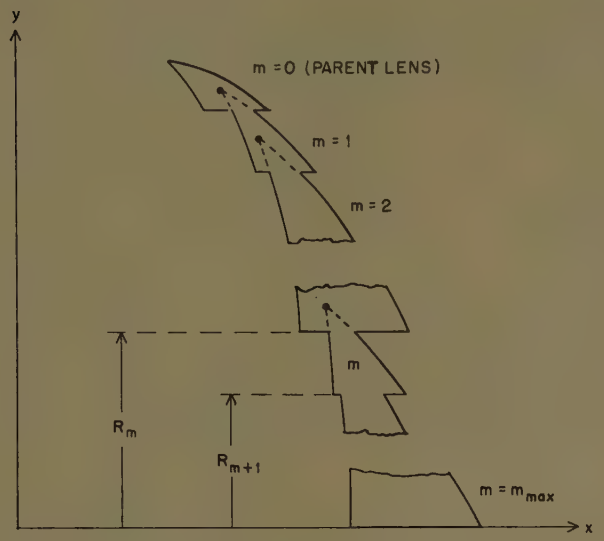

Fig. 7—Stepped lens showing overlap of edge points of interior zones.

the designer on the basis of mechanical as well as optical considerations. Because the points (f_m, $\pm s_m$) are overlapped by the $(m-1)$th zone it is not essential to go to an excessive number of approximations to determine the ray lattice which will adequately converge on (f_m, $\pm s_m$) and serve as the mth interior lens "skeleton." Once the acceptable ray lattice has been found for the mth lens, interpolating polynomials are fitted to only those lattice points which will lie between R_m and R_{m+1}, that is, which will lie on the zone surfaces ultimately to be used.

Interpolation

Usually there are many lattice points falling between R_m and R_{m+1}, permitting the use of very high order polynomials in the interpolation process. In the design of lenses of a few feet diameter, with $R_m - R_{m+1}$ of the order of several inches, it was found convenient to use five lattice points to fix the interpolating polynomial. The polynomials used were therefore of fourth order in y^2 (only even powers of y were required because of symmetry). Interpolation calculations were initially done on desk calculators, but with several lenses to be computed the many repetitions of similar numerical procedures made it economically expedient to accomplish most of this interpolation work on a high-speed automatic computer.[9] The numerical computations associated with the calculations of the ray lattices can also be programmed for high-speed calculators.[10] If a digital curve plotter were used in conjunction with a high-speed computer the approximating ray lattices could be automatically plotted as the points are computed and the characteristics of each ray lattice could be clearly and quickly observed.

Results

Theoretical

A three-dimensional rotationally-symmetric polystyrene X-band lens, designed by Sternberg,[3] was recomputed by our procedure and substantial agreement was found. This lens had $F/D = 0.5$, $D/\lambda \approx 15$, and $\theta \approx 4.5$ half-power beamwidths.

Several lenses have been designed by the procedures described above, and the calculations have been checked by ray tracing in the principal plane. To give an idea of the kind of design accuracy achievable with relative economy, we mention briefly a three-dimensional K-band lens obtained by rotating the cross section of a binormal cylindrical lens about its x axis. This lens was designed to have 4 zones, an $F/D < 0.48$, an aperture of 36 wavelengths, a beam offset of about 11 half-power beamwidths, and an index equal to that of polystyrene. A few rays for each zone were selected for ray-tracing on the basis that they would show the worst or largest deviations from the design angle θ. The maximum deviations of the emergent rays were $\approx 0.01\,\theta$ over the 3 outer zones and $0.08\,\theta$ over the innermost zone.

Experimental

The X-band lens was manufactured and tested and found to have very good two-dimensional scanning characteristics, despite the fact that it exhibited about two inches of astigmatism.[11] On the basis of this performance, we expect our K-band lens to exhibit correspondingly good performance, which we hope to be able to report in the future.

A small unzoned K-band lens of $F/D = 0.5$, $D/\lambda \approx 12$ designed for polystyrene and a beam offset of over 4 half-power beamwidths exhibited very good scanning characteristics in preliminary tests.

Acknowledgment

We wish to thank E. Wantuch of the Raytheon Manufacturing Company for several helpful comments and criticisms. We also wish to thank Misses Joan Sheehan and Dorothy Condon of Raytheon, and Miss Mary E. Lynch of AFCRC, Antenna Laboratory, for their invaluable assistance with computations.

[9] These interpolation calculations were performed on an IBM 701 by the Datamatic Corp. of Waltham, Mass.

[10] This has been done by R. M. Brown at the Naval Res. Lab. and reported on at the IRE meeting at New York, N. Y., March, 1956.

[11] Rotationally symmetric single element lenses necessarily exhibit astigmatism except on axis. The two inches mentioned in the text is an experimental determination of astigmatism at the design angle θ and refers to the difference in feed location for best azimuth pattern and for best elevation pattern at the design angle θ.

Circularly Polarized Slot Radiators*

ALAN J. SIMMONS†

Summary—A pair of narrow slots crossed at right angles and located at the proper point in the broad wall of a rectangular waveguide will radiate a circularly polarized wave. Some of the results of a study of the properties of such slots is presented. The study was undertaken with the aim of obtaining information useful in design of a circularly polarized linear array.

Some of the properties of the slot pairs are as follows:

1) They are inherently matched, independent of the slot length.
2) When the slot arms are made resonant, approximately 75 per cent of the incident power is radiated, with a vswr of 1.12.
3) When fed from one end of the waveguide, the slots radiate right-hand circular polarization; from the other end, left-hand.

In using these slots in linear arrays the power radiated is varied by changing slot length, since position and orientation are fixed by the requirements of circular polarization. The slots must be separated by a guide wavelength, so waveguide loading or other complicated schemes must be used to reduce the slot spacing.

Introduction

THE circularly polarized waveguide slot radiator is a novel microwave antenna, consisting of a circular hole or a pair of crossed slots cut into the broad wall of a rectangular waveguide at the proper spot to give circular polarization (Fig. 1). This kind of radiator was mentioned briefly by Watson[1] but has received little attention from those in the microwave antenna field. This report presents the results of a study of the properties of such slots and some possible applications.

To explain the fact that these slots radiate circular polarization, we note the equations for the transverse and longitudinal magnetic fields of the dominant (TE_{01}) mode in rectangular waveguide (Fig. 2, next page):

$$H_x = H_0\sqrt{1-\left(\frac{\lambda}{2a}\right)^2}\sin\frac{\pi x}{a},$$

$$H_z = -jH_0\left(\frac{\lambda}{2a}\right)\cos\frac{\pi x}{a},$$

where

H_x is the transverse magnetic-field intensity,
H_z is the longitudinal magnetic-field intensity,
H_0 is a constant,
λ is the free-space wavelength,
a is the waveguide width, and
x is the transverse coordinate.

Two values of x can be found for which $|H_x| = |H_z|$:

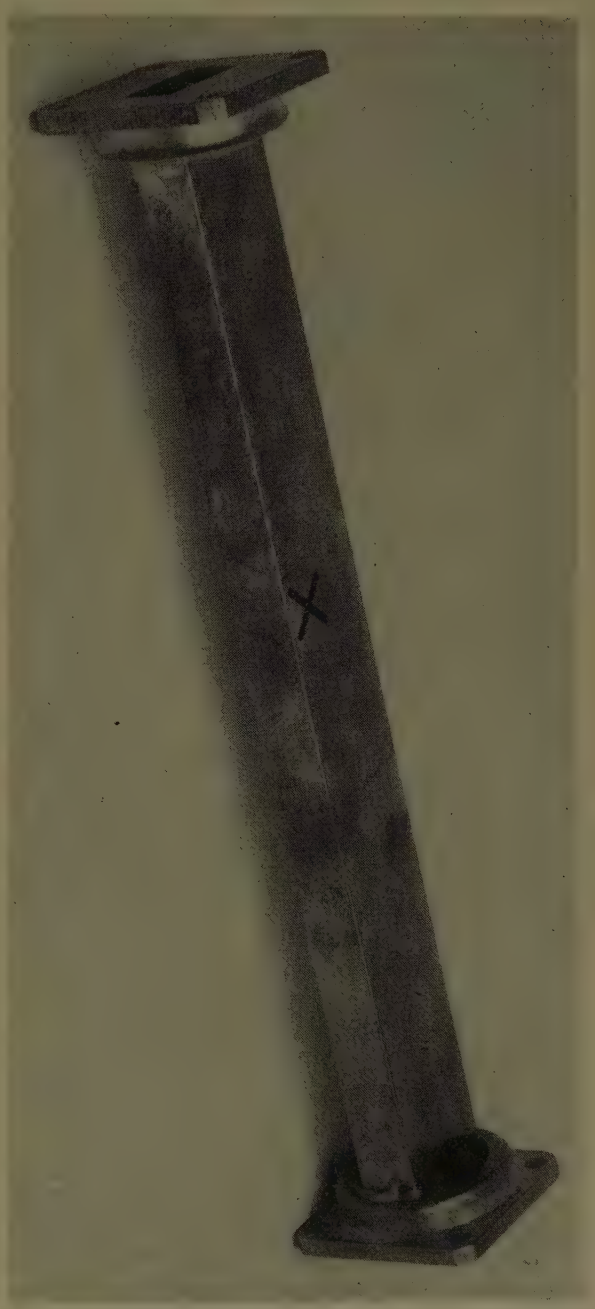

Fig. 1—A typical X-slot radiator.

These points are given by

$$x = \frac{a}{\pi}\operatorname{ctn}^{-1}\left[\pm\sqrt{\left(\frac{2a}{\lambda}\right)^2-1}\right]. \quad (1)$$

At points on the interior broad face of the waveguide for which (1) holds, the magnetic-field vector, $\vec{H}$, is

* Manuscript received by the PGAP, May 15, 1956.
† Microwave Antennas and Components Branch, Electronics Division, Naval Res. Lab., Washington, D. C.
[1] W. H. Watson, "The Physical Principles of Wave Guide Transmission and Antenna Systems," The Clarendon Press, Oxford, Eng., p. 103; 1947.

circularly polarized since the x and z components of this vector are equal in magnitude and in phase quadrature. From the boundary condition, $\vec{J}=n\times\vec{H}$, it follows that the vector-current distribution, $\vec{J}$, is likewise circularly polarized at these same points. A small circular hole cut through the wall at such a point will accordingly be excited by the circularly polarized current and radiate a circularly polarized wave, right-hand circular from one side of the waveguide and left-hand from the other, as shown in Fig. 2 for propagation in the $+z$ direction.

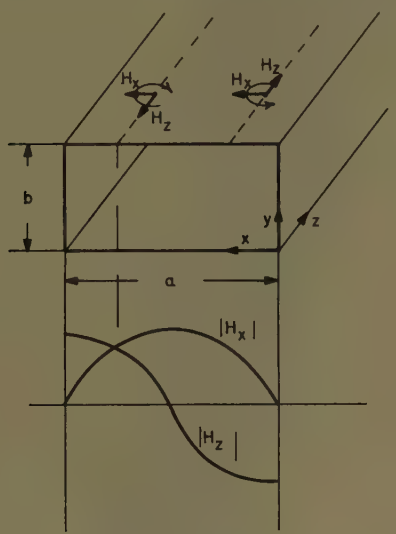

Fig. 2—Field configuration, TE_{01} mode.

For a wave propagating in the $-z$ direction, the direction of rotation is reversed and the slot which previously radiated right-hand circular polarization now radiates left-hand and vice versa.

Instead of a circular hole, a pair of narrow radiating slots at right angles to each other may be cut in the waveguide wall, the center of the pair being at the circularly polarized spot. The pair will then radiate circular or near-circular polarization. The orientation of the crossed-slot pair is arbitrary, but for convenience they have been cut at $\pm 45°$ to the z axis. This orientation permits slots of resonant length to be cut without running over the side wall. Fig. 3 shows the actual geometry which has been studied at X-band frequencies. The center of the slots is chosen halfway between side wall and center line of the waveguide, a value of $x=a/4$, which gives circular polarization at a frequency for which $\lambda/2a=1/\sqrt{2}$. (This frequency is 9273 mc.) As the frequency changes, the radiated polarization becomes slowly more elliptical, the axial ratio being simply

$$\sqrt{\left(\frac{2a}{\lambda}\right)^2-1}$$

or its reciprocal, whichever is greater than 1. This theoretical axial ratio is plotted in Fig. 4. As shown there, the polarization remains reasonably close to circular over a fairly large frequency band.

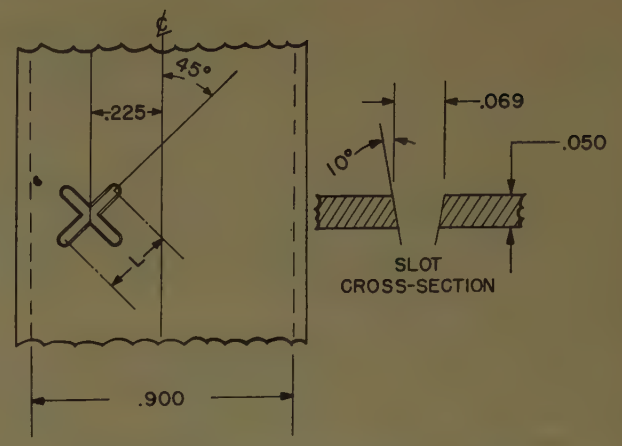

Fig. 3—X-slot geometry; dimensions in inches.

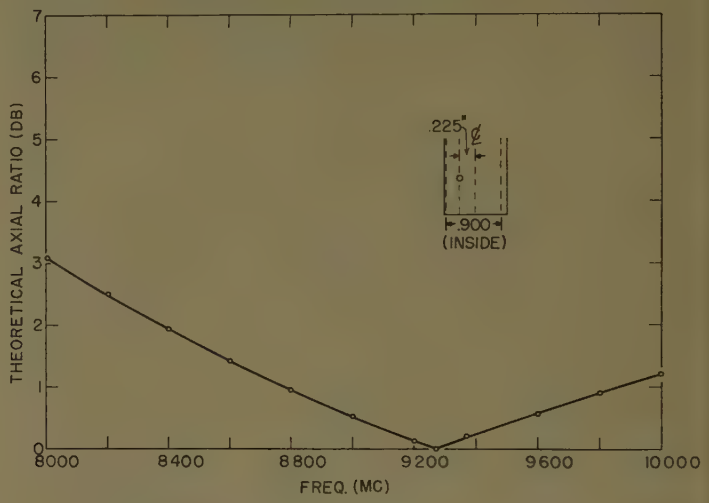

Fig. 4—Theoretical axial ratio for $x=a/4$; dimensions are in inches.

The slots are cut with a tapered cutter to facilitate accurate machining, giving a varying slot width (Fig. 3) which averages 1/16 inch. X slots were used instead of the simpler circular holes because it was possible to make the X slots resonant and thus radiate a large amount of power from a single slot.

Some Properties of X Slots

One of the most interesting properties of this kind of slot radiator is that of radiating one sense of circular polarization when excited by a wave traveling in one direction in the waveguide and the opposite sense for a wave traveling in the opposite direction. Alternatively, when used as a receiving antenna, an incident wave of right-hand circular polarization will generate a wave traveling toward one end of the waveguide, while an incident left-hand wave will give a wave traveling in the opposite direction toward the other end. (This directive property is made use of in waveguide directional couplers.[2]) Thus, the circularly polarized slot radiator

[2] M. Surdin, "Directive couplers in wave guides," *J.IEE*, vol. 93, pt. IIIA, p. 725; March-May, 1946.

may be used as a polarization detector, separating the two circularly polarized components of an incoming elliptically polarized wave.

Because of their directional properties, these slots have the property of being reflectionless—for if viewed as a scattering obstacle in the waveguide, a slot which is excited by a wave propagating in the $+z$ direction will be excited in that sense of circular polarization which causes it to reradiate energy only in the $+z$ direction, not in the $-z$ direction. This reflectionless property may also be predicted if one assumes that each of the two legs of the slots acts independently, that is, there is no coupling between the two legs. Then, on the basis of Stevenson's theory of slots in rectangular waveguide,[3] the reflection coefficients of the two legs taken individually are equal in magnitude but opposite in phase and so cancel. This holds true for any slot length, assuming slots whose width is much less than their length, and is borne out quite well in experiment.

Experimental Findings

Resonant Slots

Power Radiated: For use as a simple circularly polarized radiator, the x slot may be made of resonant length. Fig. 5 shows the power radiated as a function of frequency for a resonant X slot in a standard 1 by $\frac{1}{2}$ inch X-band waveguide. Note that at the resonant peak the power radiated is close to 80 per cent. (In comparison, the largest amount of power radiated from any circular slot which we measured was $9\frac{1}{2}$ per cent, obtained from a 0.437-inch-diameter slot.) The vswr for the X slot at resonance is only 1.12, in accordance with the reflectionless property mentioned previously. These measurements of power radiated were made by measuring the transmission coefficient of the slot as a lossy waveguide obstacle and calculating the power radiated as the apparent loss of the obstacle. This point is mentioned because there is some evidence that at resonance some power is lost in increased copper loss, causing a possible error of a few per cent in this curve.

Because of the virtually reflectionless character of the X slot, it is characterized most simply by its scattering matrix rather than by an impedance description. The only term of importance then is the transmission coefficient. The coefficients were measured by means of a movable short-circuit technique, using Deschamps construction.[4] This work was facilitated by use of a precision X-band automatic impedance recorder developed at the Naval Research Laboratory by William F. Gabriel.[5] This recorder automatically plots complex impedance on a Smith chart and thus reduces the amount of data taking and plotting necessary in the Deschamps method.

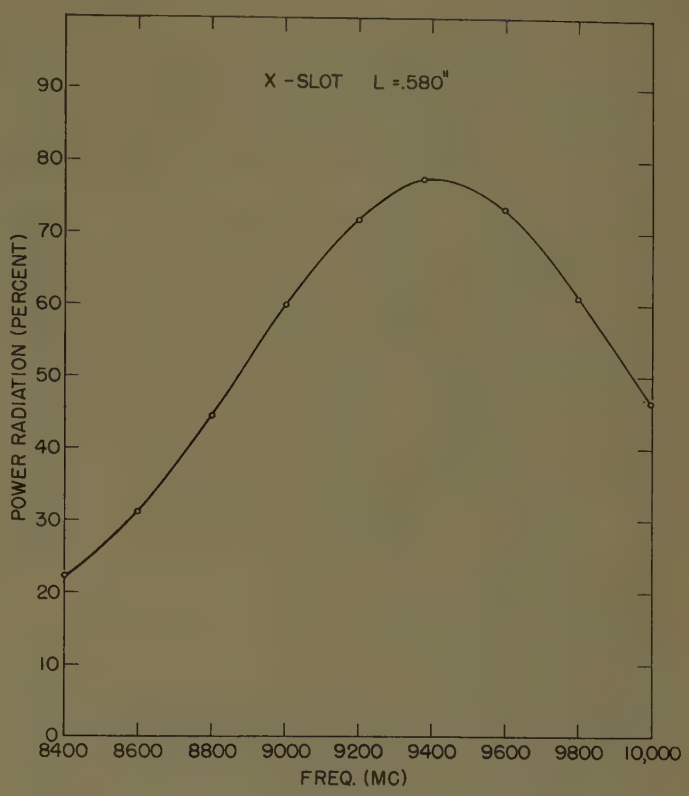

Fig. 5—Power radiated vs frequency, resonant slot.

The large amount of power radiated from the resonant slot can be predicted on the basis of Stevenson's theory[3] again assuming no coupling between the individual legs. In fact, by adjusting the waveguide height, b, each leg may be made to radiate 50 per cent of the incident power so that the total radiated power is in theory 100 per cent. To calculate the proper height b, the slot is treated as a scattering obstacle in the waveguide. Then the field beyond the slot in the $+z$ direction may be thought of as made up of three components: the initial field which would be there if there were no slot plus two components of scattered field due to reradiation down the waveguide from each of the two slot legs. The fundamental-mode components of the scattered field, which is all that concerns us, will be proportional to the original field, the constants of proportionality S_1 and S_2 (S_1 referring to one leg, S_2 to the other) depending on the slot geometry. The total field transmitted past the slot will then be $E_0(1+S_1+S_2)$ where E_0 is the original fundamental-mode field. Now for resonant slots centered at $x=a/4$ at an angle of $\pm 45°$ and with $\lambda=\sqrt{2}a$, we can calculate, following Stevenson, that

$$S_1 = S_2 = -\frac{1}{\left(\frac{2\pi}{\lambda}\right)\left(\frac{2\pi}{\lambda_g}\right)(ab)\left(\frac{73}{60\pi}\right)+1}$$

where λ_g=guide wavelength$=2a$ in this case. This theory assumes vanishingly thin slots cut in zero-thickness metal walls.

[3] A. F. Stevenson, "Theory of slots in rectangular wave guides," *J. Appl. Phys.*, vol. 19, pp. 24–38; January, 1948.

[4] G. A. Deschamps, "Determination of reflection coefficients and insertion loss of a wave guide junction," *J. Appl. Phys.*, vol. 24, p. 1046; August, 1953.

[5] W. F. Gabriel, "An automatic impedance recorder for X-band," NRL report 4204; August, 1953; Proc. IRE, vol. 42, pp. 1410–1421; September, 1954.

Since $S_1 = S_2$, the total fundamental-mode field in the waveguide beyond the resonant X slot is now $E_0(1+2S_1)$ and it is possible to adjust b so that S_1 equals $-\frac{1}{2}$. Then $E_0(1+2S_1)=0$ and no energy is transmitted past the slot. Since no energy is reflected, all the power must be radiated.

Setting $S_1 = -\frac{1}{2}$, we obtain an equation for b which, when solved, gives a height-to-width ratio of $b/a = 0.185$. For normal X-band waveguide of dimension $a = 0.900$ inch, this formula indicates a height of 0.167 inch to get total power radiated. Experiments with different height waveguides, however, indicated that this dimension is relatively uncritical, and so data were measured on a slot cut in a waveguide half-normal height ($b = 0.200$ inch). It was found that at resonance 90 per cent of the power is radiated and 3 per cent is reflected (vswr = 1.4). This represents fair agreement with the theory, based as it is on the questionable approximation of no coupling between the two slot legs.

Axial Ratio and Pattern: The axial ratio of the main beam radiated from a resonant slot in normal X-band waveguide is about 2 db when the waveguide is terminated in a matched load, indicating that the resonant slot perturbs the initially circularly polarized field to some extent. However, by a procedure exactly analogous to impedance matching, the axial ratio may be made unity by varying the reflection coefficient of the load. The load can be varied with a tuning screw so as to reflect back just enough signal to radiate opposite sense circular polarization and make the net radiation from the slot perfectly circularly polarized. Axial ratio as a function of frequency for slots with and without tuning screws and resonant at about 9375 mc is shown on Fig. 6. This slot was mounted at the center of a 7-inch ground plane in an attempt to eliminate the effect of the presence of the feeding waveguide. With the relatively small ground plane, the edge effect perturbs the pattern for one polarization more than for the other and so the axial ratio varies over the main beam of the slot pattern. Fig. 7 shows a typical antenna pattern for both horizontal and vertical polarization, with the axial ratio at various angles indicated by straight vertical lines.

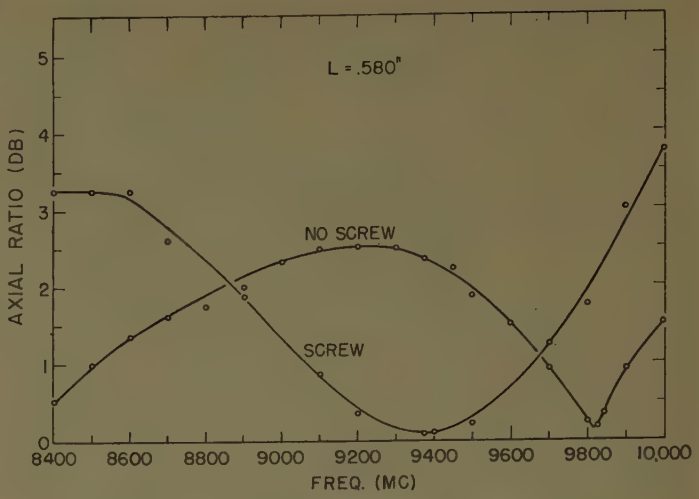

Fig. 6—Axial ratio vs frequency, resonant slot.

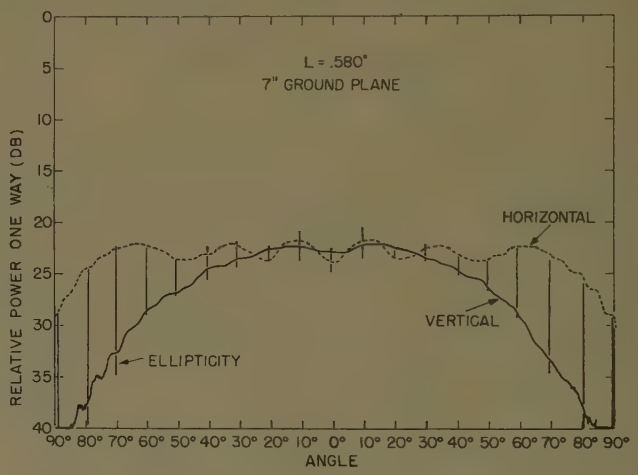

Fig. 7—Typical pattern, resonant slot on ground plane.

Nonresonant Slots

Power Radiated: For the design of a linear array of circularly polarized X slots it is necessary to be able to control the power radiated from each slot. The power radiated may not be varied by changing the orientation of the slot or its position, since these parameters are fixed by the requirement for circular polarization. Thus, the only remaining parameter is the length of the slot legs. By making the X slot nonresonant, the power radiated may be reduced. (Fortunately, the slot remains matched—the highest vswr occurs at resonance and decreases for the nonresonant slots.) Fig. 8 shows measured values of power radiated for slots of different length. All measurements were made by using the movable-short technique mentioned previously.

The nonresonant slot is somewhat more frequency-sensitive than the resonant as shown in Fig. 9 which gives the power radiated vs frequency for a typical nonresonant slot. Values for other length slots may be obtained approximately from this curve by scaling in terms of wavelength, though this is not quite accurate unless slot width is scaled too.

Axial Ratio: The axial ratio as a function of frequency for a 0.500-inch slot mounted on a 7-inch ground plane is shown in Fig. 10. The nonresonant slots give more nearly circular polarization at the design frequency than the resonant slots, probably because the perturbation theory which is used to predict their behavior is more nearly accurate.

Phase: With the nonresonant slots, phase shift becomes a problem. There are two sources of phase shift of concern. One is the phase angle ψ_{12} connected with the transmission coefficient. (This is the phase shift suffered by the wave passing by the slot.) Another phase shift, ψ_R, is that suffered by the radiated wave as it passes through the slot from the waveguide into space. If ψ_{12} and ψ_R differ from slot to slot a nonlinear phase front

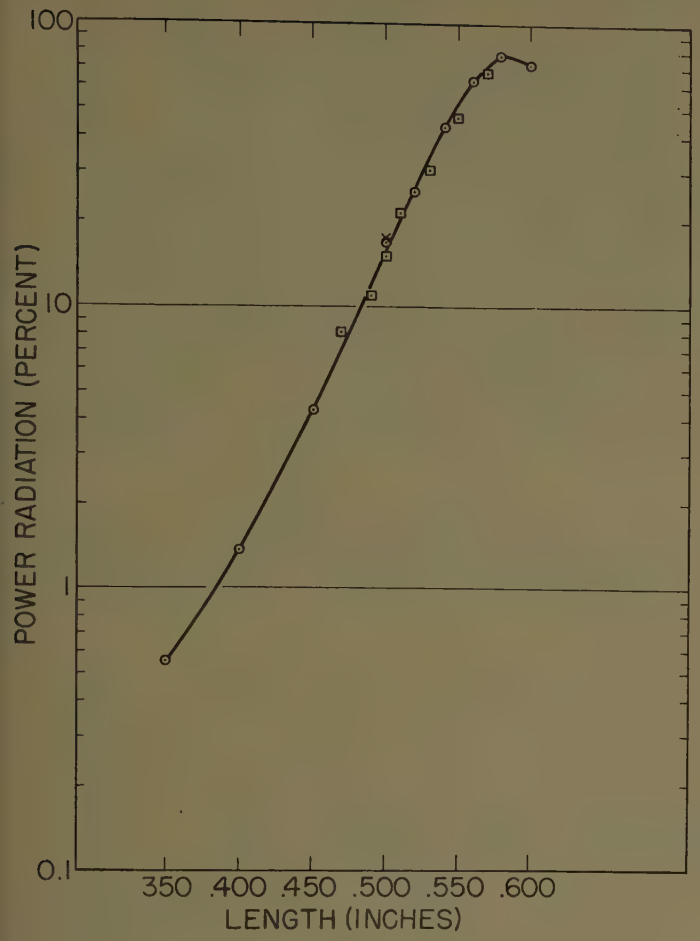

Fig. 8—Power radiated vs slot length. Length is measured as center-to-center distance of the rounded slot ends.

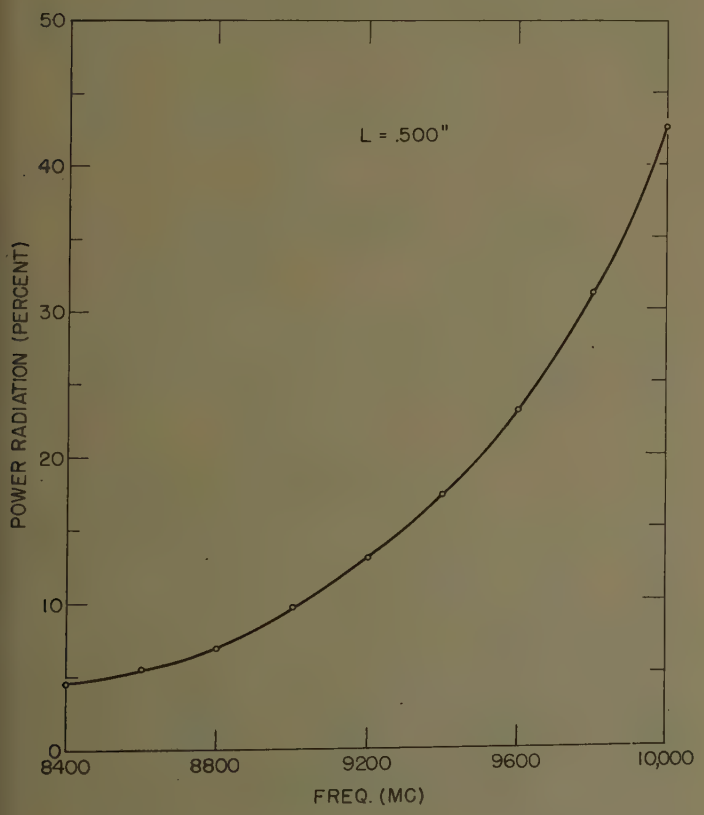

Fig. 9—Power radiated vs frequency, nonresonant slot.

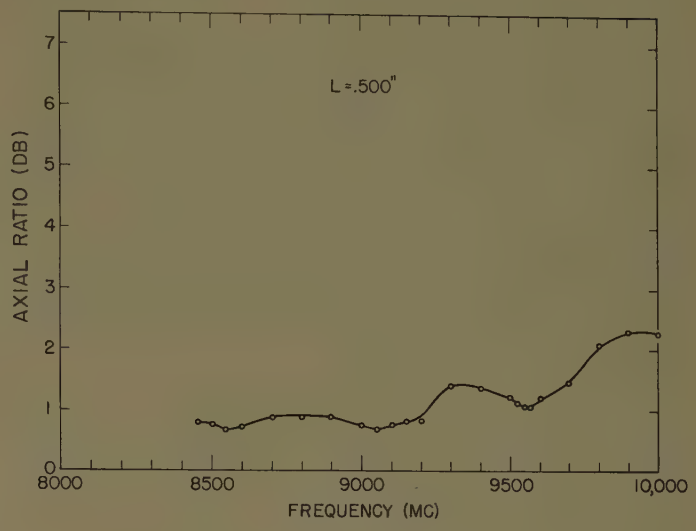

Fig. 10—Axial ratio vs frequency, nonresonant slot.

may arise, even if the slots in an array are uniformly spaced. Both of these phase shifts were measured, ψ_{12} by Deschamp's method and ψ_R by means of a microwave phase bridge incorporating a magic Tee and a calibrated phase shifter. The results are shown in Fig. 11 where the resonant slot is arbitrarily chosen as having a zero value of ψ_R and all other slots compared to it. The value of ψ_R plotted is the average for all polarizations.

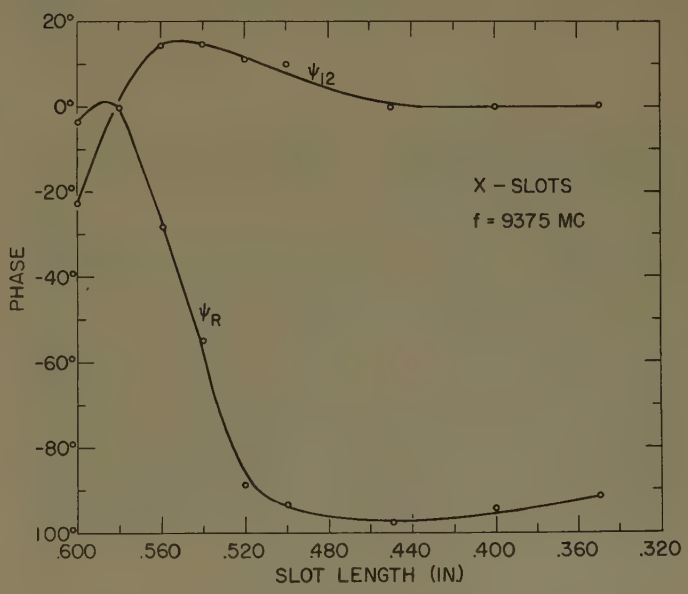

Fig. 11—Phase shift in radiation and in transmission vs slot length.

If the slots are made less than 0.520 inch in length, the phase shifts are small, and have been neglected in array design. Fortunately, a reasonably efficient array may usually be designed in which all slots are less than 0.520 inch.

Linear Array Design

The design of an array of X slots is straightforward and must be of the nonresonant type because of the re-

flectionless character of the slots. One serious difficulty remains: there is no way to reverse the phase of the slots as is usually done in order to reduce the slot-to-slot spacing to a half-guide wavelength. Thus, a spacing of a full-guide wavelength must be used for a broadside array, which gives rise to secondary maxima in the array pattern. These are equal in amplitude to the main beam. Several methods have been used to get around this difficulty, none entirely satisfactory. In one method two arrays are used, one on top of the other with the slots staggered to give an effective spacing of less than a free-space wavelength.

Another method of reducing interelement spacing is to load the waveguide so as to reduce the effective guide wavelength. Half-wavelength high-dielectric-constant slugs between each pair of slots were used for this purpose. Both of these methods gave antenna patterns with reasonably low side lobes and reasonable antenna gain.

Conclusion

In conclusion, we have shown that a pair of narrow slots crossed at right angles and located at the proper point in the broad wall of an ordinary rectangular waveguide will radiate a wave very nearly circularly polarized. Such X slots may be used as polarization detectors, being able to separate right-hand from left-hand circular polarization. They have unusual impedance properties, presenting a near match to the waveguide. They provide a means of obtaining a simple circularly polarized radiator, since they radiate up to 90 per cent of the incident power at resonance, as well as the possibility of designing a circularly polarized linear array.

Acknowledgment

The author would like to acknowledge the painstaking assistance of W. T. Slayton who made most of the measurements reported here.

The Effect of Mutual Impedance on the Spacing Error of an Eight-Element Adcock*

DOUGLAS N. TRAVERS†

Summary—**An eight-element Adcock array has the advantage of reduced spacing error as compared to four element arrays of the same size. If this error is calculated when the mutual impedances between elements are neglected, spacing error curves result which are poor approximations and may not be attainable in actual measurement. New relationships are derived for the two-phase eight-element array which include the effect of mutual impedance. Curves are plotted to show that earlier published values for the angular spacing between elements are probably too high to result in the best performance. It is shown that the value of $\rho = 27°15'$ which results when the mutual impedances are neglected may result in an appreciable spacing error. It is apparent that the selection of an antenna becomes quite important since the mutual impedance is determined thereby. Evaluation of the error in a particular case will depend on the antenna selected. It is also shown that, if the goniometer impedance is high, the spacing error will be reduced.**

List of Symbols

θ = minus azimuth of signal arrival.
S = diagonal spacing of elements.
$\phi = 2\pi S/\lambda$.
2ρ = angular separation of paired elements.
γ = phase of the emf induced in antenna 1.
α = phase of the emf induced in antenna 2.
δ = phase of the emf induced in antenna 3.
ζ = phase of the emf induced in antenna 4.
E_i = terminal voltage of ith antenna.
I_i = terminal current of ith antenna.
Z_{ik} = mutual impedances between antennas i and k.
Z_s = self impedance of any antenna.
Z_g = impedance looking into goniometer.
I_{ns} = current of the north-south group.
I_{ew} = current of the east-west group.
E_0 = amplitude of voltage in any antenna.
ϵ = observed bearing (counterclockwise).
λ = wavelength.
Δ = error in observed bearing.
A = determinant formed by the coefficients Z_{in}.
A_{ik} = cofactor of Z_{ik} determined by A.
E_{se} = goniometer search coil voltage.

Introduction

IN THE SEARCH for an Adcock direction finding antenna array having a low spacing error, considerable attention has been given to eight-element systems with paired elements.[1–3] This array, shown in

* Manuscript received by the PGAP, August 10, 1955; revised manuscript received, April 24, 1956.
† Southwest Res. Inst., San Antonio, Texas.

[1] P. G. Redgment, W. Struszynski, and G. J. Phillips, "An analysis of the performance of multi-aerial Adcock direction-finding systems," *J. IEE*, vol. 94, part IIIA, pp. 751–761; 1947.
[2] J. R. Wait and W. A. Pope, "Evaluation of errors in an eight-element Adcock antenna," IRE TRANS., vol. AP-2, pp. 159–162; October, 1954.
[3] D. N. Travers, "Spacing error analysis of the eight element two phase Adcock direction finder," IRE TRANS., vol. AP-3, pp. 63–65; April, 1955.

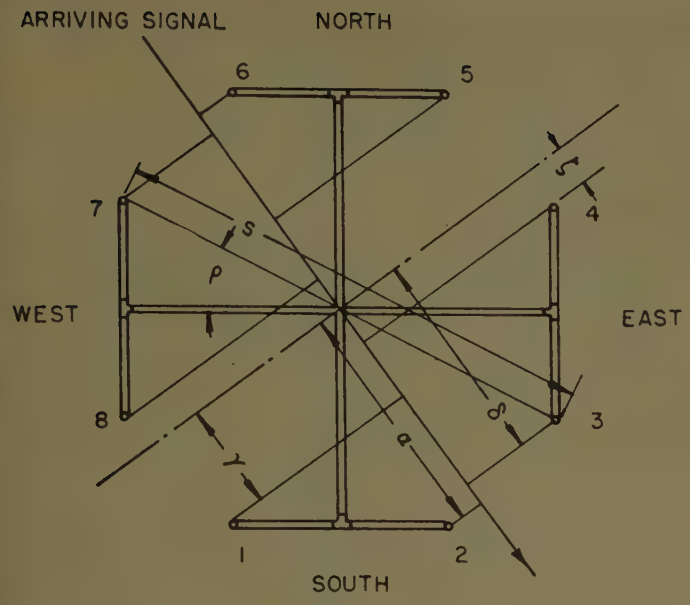

Fig. 1

the diagram of Fig. 1, uses eight antennas rather than four as in the more conventional Adcocks. The antennas are arranged in a circle and are fed by transmission lines which are shown by double lines. Four T connectors are employed to provide parallel connection of the two paired antennas of each quadrant. The array is thus fed with a conventional goniometer. Further details are given in the literature.

Earlier analyses of this array have resulted in the calculation of the spacing error without consideration of the mutual impedances between antennas. These results predicted that the angular spacing 2ρ should be about 54°. It is now evident that neglect of these mutual impedances does not lead to the optimum configuration for the array. This analysis includes the effect of the mutual impedances, and results suitable for calculation are derived.

The Spacing Error Equation

The array configuration is shown in Fig. 1. For convenience the notation used previously[3] is retained in this analysis, except for the numbering of the antennas. Counterclockwise rotation is used for both the antenna numbering and the positive direction of the azimuth angle θ. The array is excited by a vertically-polarized plane wave.

The antenna terminal voltages are related to the mutual impedances by (1) through (8):

$$E_i = \sum_{n=1}^{8} I_n Z_{in}, \tag{1}$$

where i has the value 1 through 8 and the impedances Z_{ii} include both the goniometer impedance Z_g and the antenna self impedance Z_s. Since the antennas are identical, the self impedances are equal and can all be designated Z_{11}. Simplification due to symmetry yields

$$Z_{12} = Z_{34} = Z_{56} = Z_{78}, \text{ etc.}, \tag{2}$$

and since

$$Z_{mn} = Z_{nm}, \tag{3}$$

all mutual impedances can be referred to the first antenna. Certain spacings between antennas are also equal giving further simplification, such as

$$Z_{13} = Z_{17}. \tag{4}$$

If A is the symmetrical determinant formed from the coefficients of (1), Z_{in}, then by use of (2)–(4)

$$A = \begin{vmatrix} Z_{11} & Z_{12} & Z_{13} & Z_{14} & Z_{15} & Z_{16} & Z_{13} & Z_{18} \\ Z_{12} & Z_{11} & Z_{18} & \cdot & \cdot & \cdot & \cdot & \cdot \\ Z_{13} & Z_{18} & Z_{11} & \cdot & \cdot & \cdot & \cdot & \cdot \\ Z_{14} & \cdot & \cdot & Z_{11} & \cdot & \cdot & \cdot & \cdot \\ Z_{15} & \cdot & \cdot & \cdot & Z_{11} & \cdot & \cdot & \cdot \\ Z_{16} & \cdot & \cdot & \cdot & \cdot & Z_{11} & \cdot & \cdot \\ Z_{13} & \cdot & \cdot & \cdot & \cdot & \cdot & Z_{11} & \cdot \\ Z_{18} & \cdot & \cdot & \cdot & \cdot & \cdot & \cdot & Z_{11} \end{vmatrix}. \tag{5}$$

The solutions for the currents are[4]

$$I_i = \frac{\sum_{n=1}^{8} A_{ni} E_n}{A} \tag{6}$$

where i has the value 1 through 8 and A_{ni} are the cofactors of A. From Fig. 1,

$$\begin{aligned} E_1 &= E_0 e^{i\gamma} & E_5 &= E_0 e^{-i\gamma} \\ E_2 &= E_0 e^{i\alpha} & E_6 &= E_0 e^{-i\alpha} \\ E_3 &= E_0 e^{i\delta} & E_7 &= E_0 e^{-i\delta} \\ E_4 &= E_0 e^{i\zeta} & E_8 &= E_0 e^{-i\zeta} \end{aligned} \tag{7}$$

where the phase angles are

$$\gamma = \frac{\phi}{2}\cos(\theta + \rho) \qquad \delta = \frac{\phi}{2}\sin(\theta + \rho)$$

$$\alpha = \frac{\phi}{2}\cos(\theta - \rho) \qquad \zeta = \frac{\phi}{2}\sin(\theta - \rho). \tag{8}$$

Because of the way in which the array is connected, the currents into the goniometer circuit are

$$\begin{aligned} I_{ns} &= I_1 + I_2 - (I_5 + I_6) \\ I_{ew} &= I_3 + I_4 - (I_7 + I_8). \end{aligned} \tag{9}$$

Substituting (6) into (9) yields

$$AI_{ns} = \sum_{n=1}^{8} E_n(A_{n1} + A_{n2} - A_{n5} - A_{n6})$$

$$AI_{ew} = \sum_{n=1}^{8} E_n(A_{n3} + A_{n4} - A_{n7} - A_{n8}). \tag{10}$$

[4] E. A. Guillemin, "The Mathematics of Circuit Analysis," John Wiley and Sons, Inc., New York, N. Y., ch. 1, "Determinants," pp. 1–29; 1949.

The goniometer search coil voltage is

$$E_{se} = Z_g I_{ns} \sin \epsilon - Z_g I_{ew} \cos \epsilon \tag{11}$$

$$= \frac{Z_g}{A}\left[\sum_{n=1}^{8} E_n(A_{n1} + A_{n2} - A_{n5} - A_{n6}) \sin \epsilon - \sum_{n=1}^{8} E_n(A_{n3} + A_{n4} - A_{n7} - A_{n8}) \cos \epsilon\right]. \tag{12}$$

Due to the complex form of (10), $|E_{se}|$ will, in general, have some minimum value at the observed bearing rather than the value zero. The position of the search coil at this minimum is found by taking the derivative of the magnitude of E with respect to ϵ and setting it to zero. When this is done, the following is obtained:

$$\tan 2\epsilon = \frac{2(ac + bd)}{(c^2 + d^2) - (a^2 + b^2)}, \tag{13}$$

where

$$a + jb = \sum_{n=1}^{8} E_n(A_{n1} + A_{n2} - A_{n5} - A_{n6})$$

$$c + jd = \sum_{n=1}^{8} E_n(A_{n3} + A_{n4} - A_{n7} - A_{n8}), \tag{14}$$

and the error is

$$\Delta = \epsilon - \theta. \tag{15}$$

In order to obtain results suitable for computation, it is necessary to reduce (13) to a simpler form. The greatest simplification occurs when it is assumed that all mutual impedances are zero and, therefore, that the antenna currents are determined by the impedances Z_{ii} only. In this case, (6) becomes

$$I_i = \frac{A_{ii} E_i}{A}, \tag{16}$$

and (13) reduces to

$$\tan \epsilon = \frac{\sin\left(\frac{\phi}{2} \sin\theta \cos\rho\right) \cos\left(\frac{\phi}{2} \cos\theta \sin\rho\right)}{\sin\left(\frac{\phi}{2} \cos\theta \cos\rho\right) \cos\left(\frac{\phi}{2} \sin\theta \sin\rho\right)}, \tag{17}$$

a result which has been published previously.[1-3]

The next order approximation assumes that the current in any one antenna is determined by the self impedance of that antenna, the goniometer input impedance, and the mutual impedances between that antenna and each of the others. It is assumed, therefore, that coupling between any two antennas does not affect the current in a third antenna. In this case, the cofactors A_{ik} are

$$A_{1k} = Z_{1k} A_{11} \quad \text{and} \quad A_{ik} = 0, \tag{18}$$

when

$$i \neq k, \qquad i \geqq 2, \quad \text{and} \quad k \geqq 2.$$

When these are used in (6), (9), and (12), the observed bearing (13) becomes

$$\tan 2\epsilon = \frac{2[AC + R(AD + CB) + (R^2 + X^2)BD]}{(A^2 - C^2) + 2R(AB - CD) + (R^2 + X^2)(B^2 - D^2)}, \tag{19}$$

where

$$A = \sin\left(\frac{\phi}{2} \cos\theta \cos\rho\right) \cos\left(\frac{\phi}{2} \sin\theta \sin\rho\right)$$

$$B = \cos\left(\frac{\phi}{2} \sin\theta \cos\rho\right) \sin\left(\frac{\phi}{2} \cos\theta \sin\rho\right)$$

$$C = \sin\left(\frac{\phi}{2} \sin\theta \cos\rho\right) \cos\left(\frac{\phi}{2} \cos\theta \sin\rho\right)$$

$$D = \cos\left(\frac{\phi}{2} \cos\theta \cos\rho\right) \sin\left(\frac{\phi}{2} \sin\theta \sin\rho\right) \tag{20}$$

$$R + jX = \frac{Z_{13} - Z_{14}}{Z_{11} + Z_{12} - Z_{15} - Z_{16}}. \tag{21}$$

When $R = 0$ and $X = 0$, (19) reduces to (17). When only $X = 0$, (19) reduces to

$$\tan \epsilon = \frac{C + RD}{A + RB}. \tag{22}$$

It is particularly important to note that the goniometer impedance can control the spacing error to some degree, since, when Z_g is sufficiently high, (21) reduces to a small quantity and (16) is approximated. Another special case of interest is the condition of $\rho = 22\frac{1}{2}°$, since, in this case, all eight antennas are equally spaced. When this is true

$$Z_{12} = Z_{18}$$
$$Z_{14} = Z_{16} \tag{23}$$

and with the approximation of (18),

$$A_{18} = A_{12}$$
$$A_{16} = A_{14},$$

so that (21) reduces to

$$R + jX = \frac{1}{1 + \left(\frac{Z_{11} - Z_{15}}{Z_{12} - Z_{14}}\right)}. \tag{24}$$

In Fig. 2, (19) has been plotted for four specific cases. A value of $\theta = 22°30'$ has been selected, since it is evident that (19) is an octantal error curve and the maximum error will occur near azimuths of 22°30', 67°30', etc. Since earlier work suggests $\rho = 27°15'$ as a value for element spacing, three curves are shown to illustrate the effect of R and X at this value. For comparison, the curve of $\theta = 22°30'$ and $\rho = 22°30'$ with $R = 0$ and $X = 0$ is also shown. It is evident that a substantial increase in error occurs as R increases to a value of 0.5. A further slight increase occurs when $R = 0.5$ and $X = 0.5$. It ap-

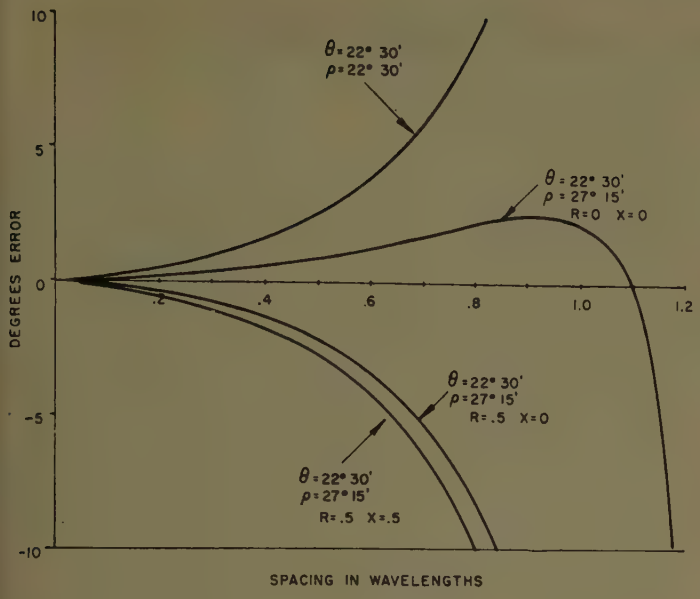

Fig. 2

pears that the effect of X is secondary to R, estimated from mutual impedance curves for the particular antenna in use. Error curves which resemble $\rho = 27°15'$, $R = 0$, $X = 0$ for cases when $R \neq 0$, $X \neq 0$ will be a compromise between ρ and R and to a lesser extent X.

Conclusion

Earlier analyses of the eight-element Adcock suggest values of angular spacing which are greater than are likely to be required in practice. The more accurate values for ρ can be determined with the aid of (13) or (19) and a knowledge of the mutual impedances between antennas. In practice, the exact value of ρ best suited to a particular antenna will depend on the antenna self and mutual impedance, and, therefore, the frequency and dimensions of the antenna. The error will also depend on the goniometer impedance, since $Z_{11} = Z_s + Z_g$. The manner in which the error depends on these factors is quite complicated, particularly if the antenna is other than a simple thin monopole. For this reason, it appears likely that the proper value for ρ can be determined most quickly by measurement of R and X at a particular value of ρ using the approximation of (18). The problem will be further complicated by the fact that, in general, R and X will not be constant with frequency. One estimate, made for thin monopoles at $\rho = 27°$ based on published mutual impedance curves[5] and calculations made from the general expression for mutual impedance between two dipoles,[6] indicated that these values of R and X will increase with frequency and may double in value over the operating frequency range of the array. The values of $R = 0.5$ and $X = 0.5$ are not intended to be representative of any particular antenna configuration, but it seems reasonable to expect values of R between 0 and $+1$, as is apparent from (24).

[5] E. A. Laport, "Radio Antenna Engineering," McGraw-Hill Book Co., Inc., New York, N. Y., pp. 533–536; 1952.
[6] J. D. Kraus, "Antennas," McGraw-Hill Book Co., Inc., New York, N. Y., ch. 10, sec. 10-5, "Mutual Impedance of Parallel Antennas Side by Side," pp. 265–268; 1950.

Correction

Benjamin Lax, chairman of the Combined Panel Session on Propagation in Doubly-Refracting Media and Future Directions for Research in Electromagnetic Wave Theory in Modern Physics, has requested that the following correction be made to the transcript of the discussion of papers, which appeared on pages 567–577 of the July, 1956 issue of IRE Transactions on Antennas and Propagation.

On page 568, in the first column, the comment by G. T. Rado should read as follows:

When I read Dr. Hogan's paper in the *Journal of Applied Physics*,[3] I noticed that he decreased the low frequency limit of some microwave ferrite devices by decreasing not only the saturation magnetization but also the anisotropy. The reason for having to decrease both of these parameters is that this low frequency limit is caused by the natural microwave resonance in ferrites. This microwave resonance, in turn, is determined not only by the saturation magnetization but also by the magnetocrystalline anisotropy, as we showed several years ago. One of the methods we used for demonstrating this role of the anisotropy consisted in adding to lithium ferrite such an amount of zinc that the saturation magnetization stayed roughly constant whereas the anisotropy decreased. We found experimentally that the microwave resonance did shift to lower frequencies after this particular amount of zinc was added. These studies showed that in order to decrease the microwave resonance frequency it is necessary to decrease the anistropy as well as the saturation magnetization. A significant aspect of Hogan's work is that he obtained not only a low anisotropy (and low saturation magnetization), but at the same time a nonlossy dielectric constant.

On the Synthesis of Line-Sources and Infinite Strip-Sources*

J. L. YEN†

Summary—**In this investigation Woodward's synthesis problem for line-sources and infinite strip-sources with arbitrarily spaced sample points is discussed on the basis of the well-known sampling theorem of bandwidth limited functions. Herein is described a method of synthesis based on the migration of zeros of the integral function $(\sin \pi u)/\pi u$ from which all possible solutions of the problem can be derived. Because of the nonuniqueness of the solution, a criterion is introduced, to derive a unique distribution function so that the integrated value of its squared magnitude is a minimum. It turns out that the solution under this criterion coincides with the one obtained by Woodward and Lawson. Examples are given to illustrate the different solutions obtainable for particular problems, and the significance of the least integrated squared magnitude criterion.**

Introduction

THE SPACE factor in the radiation patterns of both a line-source lying on the x axis between $x=\pm a$ and an infinite strip-source lying on the $y=0$ plane between $x=\pm a$ with edges parallel to the z axis as shown in Fig. 1 can be expressed as follows[1]

$$S(u) = \frac{2a}{\lambda}\int_{-\pi}^{\pi} g(p)\exp(ipu)dp. \qquad (1)$$

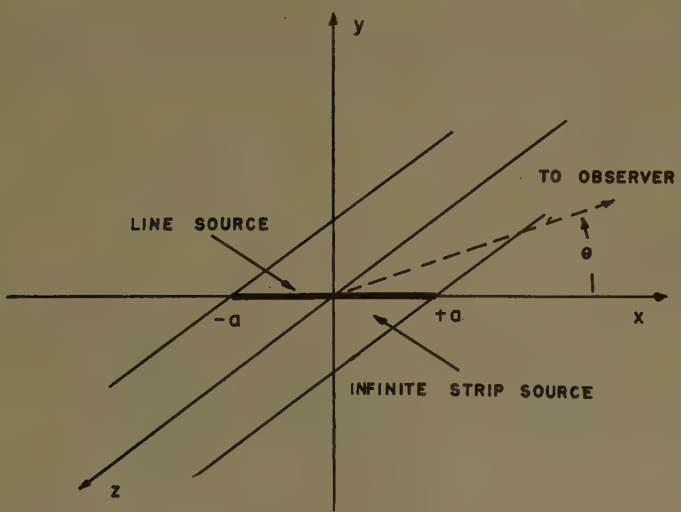

Fig. 1

Here, $u=2a/\lambda\cos\theta$, $p=\pi x/a$ and $g(p)$ is the distribution function describing the source distribution along the x axis. For the infinite strip-source, it is further assumed that the distribution is uniform along the z axis. The value of the space factor $S(u)$ for $|u|\leqq(2a/\lambda)$ belongs to the visible spectrum; *i.e.*, the radiation pattern. For $|u|>(2a/\lambda)$, the value of $S(u)$ belongs to the invisible spectrum and is associated with the energy storage in the near field. The properties of $S(u)$ have been discussed thoroughly by Taylor[2] with special emphasis on the position of zeros. The synthesis problem, namely that of finding a distribution function $g(p)$ which produces a space factor $S(u)$ satisfying certain prescribed conditions in the visible range, has been investigated by many authors. In particular, Woodward,[3] and Woodward and Lawson[4] considered the assignment of $S(u)$ at a finite number of sample points in the visible spectrum, and Knudsen[5] stressed the relation between this problem and the well-known sampling theorem of bandwidth limited functions.

In this investigation Woodward's problem for cases with arbitrarily distributed sample points is discussed on the basis of the sampling theorem. A method of synthesis, based on the migration of zeros of the integral function $(\sin \pi u)/\pi u$ from which all possible solutions of the problem can be derived is described. This method can be considered as a generalization of the sampling theorem for bandwidth limited functions to nonuniformly distributed sample points. Because of the nonuniqueness, a criterion is introduced, to derive a unique distribution function so that the integrated value of its squared magnitude is a minimum. It turns out that the solution under this criterion coincides with the one obtained by Woodward and Lawson. However, the method employed here offers a slight reduction in the numerical work involved. For problems that require the migration of outside zeros into the visible spectrum, the use of the above criterion results in the integrated values of the squared magnitude of the distribution functions being less than those obtained without invoking the criterion. Such problems belong to supergain situations. For cases which can be synthesized without migrating outside zeros into the visible spectrum, the improvement obtainable in using the criterion is less pronounced.

* Manuscript received by the PGAP, November 25, 1955; revised manuscript received, July 25, 1956. This work was supported by the Defense Res. Board of Canada, Grant DRB 5540-02.

† Univ. of Toronto, Toronto, Ont., Canada.

[1] H. J. Riblet, "Note on the maximum directivity of an antenna," PROC. IRE, vol. 36, pp. 620–623; May, 1948.

[2] T. T. Taylor, "Design of line-source antennas for narrow beamwidth and low side lobes," IRE TRANS., vol. AP-3, pp. 16–28; January, 1955.

[3] P. M. Woodward, "A method of calculating the field over a plane aperture required to produce a given polar diagram," *J.IEE*, vol. 93, pt. 3a, pp. 1554–1558; 1946.

[4] P. M. Woodward and J. D. Lawson, "The theoretical precision with which an arbitrary radiation pattern may be obtained from a source of finite size," *J.IEE*, vol. 95, pt. 3, pp. 363–370; September, 1948.

[5] H. L. Knudsen, "Shannons tidsopdelingssaetning og superforstaerkning hos antenner," *Sartryck ur Teknisk Tidskr.*, vol. 82, pp. 1–8; December 2, 1952.

Some Properties of the Space Factor $S(u)$

Before proceeding to a consideration of the synthesis problem, it is necessary to review some properties of the space factor $S(u)$, as given in (1), from a viewpoint based on the sampling theorem for bandwidth limited functions. When p is considered as the angular frequency, the space factor $S(u)$ becomes a "bandwidth limited" function, limited within the band $|p| \leqq \pi$. From the well-known sampling theorem[5,6] such a function is uniquely determined by its values at a series of sample points spaced at unit intervals extending towards infinity on both sides. In general, the members of a set of points spaced at unit intervals can be written as $u=c+n$, where $|c|<1$ and n is a positive or negative integer including zero. In order to avoid confusion, in later discussions such points will be called unit sample points. Let the value of $S(u)$ at the unit sample points be called unit sample values. Then the sampling theorem states that the unique reconstruction of the function from its unit sample values is

$$S(u) = \sum_{n=-\infty}^{\infty} S(c+n) \frac{(-1)^n \sin \pi(u-c)}{\pi(u-c-n)}. \tag{2}$$

The function $S(u)$ can be considered as composed from the unit sample values $S(c+n)$ by means of the composing function

$$\frac{(-1)^n \sin \pi(u-c)}{\pi(u-c-n)}. \tag{3}$$

This composing function is an integral function with zeros at $u=c+m$, $m \neq n$, and takes on the value unity at $u=c+n$. The associated distribution function $g(p)$ is proportional to the Fourier transform of (2)

$$g(p) = \begin{cases} \dfrac{\lambda}{4\pi a} \displaystyle\sum_{n=-\infty}^{\infty} S(c+n) \exp -i(c+n)p, & |p| \leqq \pi; \\ 0, & |p| > \pi. \end{cases} \tag{4}$$

A knowledge of all the unit sample values determines uniquely a space factor and the corresponding distribution function. However, in synthesis problems only a finite number of assignments are usually imposed. Moreover, the assignments may not be made at unit sample points. Thus, the sampling theorem must first be modified to take into account arbitrarily spaced assigned sample points. Secondly, the unassigned sample values can be manipulated to obtain different solutions of the synthesis problem. These aspects will be discussed in detail in the following sections.

[6] J. M. Whittaker, "Interpolatory Function Theory," Cambridge Tracts in Math. and Math. Phys., no. 33, ch. 4, Cambridge, Eng.; 1935.

Woodward's Problem and Synthesis by Migration of Zeros

Woodward's synthesis problem consists of finding a distribution function $g(p)$ that generates, according to (1), a space factor $S(u)$ whose values are prescribed at N assigned but arbitrarily located sample points in the visible spectrum, namely, $u=u_n$, $n=1, \cdots, N$, $|u_n| \leqq (2a/\lambda)$. Any function $S(u)$, which can be expressed in terms of a distribution function $g(p)$ in the form of (1), and which satisfies the prescribed conditions, is called an admissible space factor of the problem. Since there is more than one admissible space factor to Woodward's problem, its solution is nonunique. Without loss of generality, consider a simplified problem where the prescribed values at the N assigned sample points u_n are all zero except for one of them, say u_s, where the value is unity. Let $S_s(u)$ be an admissible space factor of the simplified problem and let the corresponding distribution function be $g_s(p)$. The conditions on $S_s(u)$ then become

$$S_s(u_n) = \delta_s{}^n, \qquad n = 1, \cdots, N. \tag{5}$$

The solution of the general synthesis problem can be regarded as a superposition of the solutions of these simplified problems; *i.e.*, $S(u)$ and $g(p)$ can be expressed as superpositions of $S_s(u)$ and $g_s(p)$ respectively, where s runs through the integers between 1 and N.

In order to solve the simplified problem, it is convenient to first find an admissible space factor, and then to derive the corresponding distribution function. Consider the expression of the space factor in terms of its unit sample values as given in (2). In general, the choice of the assigned sample points u_n is arbitrary as long as they are in the visible spectrum. By a suitable choice of the constant c, some of the N assigned sample point u_n can be made to coincide with some of the unit sample points $c+n$ as shown in Fig. 2(a). Let there be K points of coincidence denoted by $u=c+n_k$ where $k=1, \cdots, K$ and n_k belongs to a set of K integers, while the remaining $M=N-K$ assigned sample points be designated by $u=v_m$, $m=1, \cdots, M$. To reduce the numerical work involved in subsequent steps, the constant c should be chosen so that the number of coincidence K is as large as possible. For any choice of c there are two possibilities. Either the particular assigned sample point u_s at which the assigned sample value is unity does coincide with one of the unit sample points, say $u_s=c+n_t$ where n_t is one of the K integers n_k; or, it does not coincide with one of the unit sample points in which case it can be identified by $u_s=v_t$ where v_t is one of the M values v_m. Since the two cases lead to different results, they will be considered separately.

Consider first the case that $u_s=c+n_t$; *i.e.*, when the only nonvanishing assigned sample value occurs at a unit sample point. The prescribed constraints as given

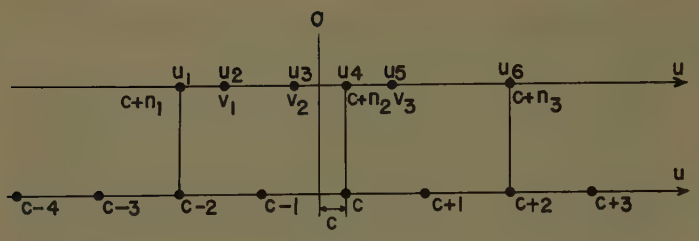

(a)

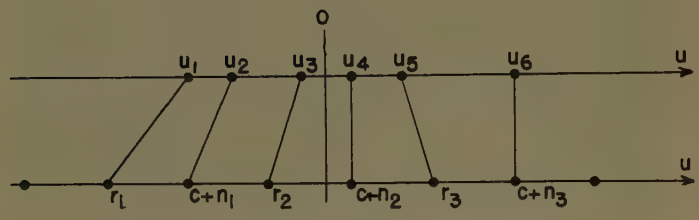

(b)

Fig. 2

in (5), when applied to expression (2) for the space factor, are reduced to

$$S_s(u) = \frac{(-1)^{n_t} \sin \pi(u-c)}{\pi(u-c-n_t)} + \sum_{n=-\infty, n\neq n_k}^{\infty} S(c+n) \frac{(-1)^n \sin \pi(u-c)}{\pi(u-c-n)}, \quad (6)$$

$$S_s(v_m) = 0, \qquad m = 1, \cdots, M. \quad (7)$$

For the well-known special case where all the assigned sample points coincide with unit sample points the constraints as given in (7) do not appear. This means that the unit sample values not corresponding to assigned sample points can be varied at will without affecting the admissibility of (6). In the usual solution all such unit sample values are taken to be zero thus resulting in an admissible space factor of the form (3) with n replaced by n_t.

In the general case the M constraints in (7) require that at least M of the unit sample values contained in the sum of (6) be nonvanishing. Let it be assumed that the allowed nonvanishing values occur at the M unit sample points $u=c+r_m$, where r_m for $m=1, \cdots, M$ indicates M integers not equal to n_k. These M unit sample values $S(c+r_m)$ are then adjusted to satisfy the constraints (7). The result is that the M zeros at $u=c+r_m$ of the integral function as given in (3) or in the first term of (6) are migrated to $u=v_m$ due to the sum in (6) as illustrated in Fig. 2(b). Thus, the effect of displacing some of the assigned sample points from unit sample points on the admissible space factor as given in (3) is to migrate the zeros from these unit sample points to the assigned sample points. Since only the zero pattern is of importance, the lines joining the zeros in the two zero patterns in Fig. 2(b) are arranged so that they do not cross each other. Such an admissible space factor is given by

$$S_s(u) = \frac{(-1)^{n_t} \sin \pi(u-c)}{\pi(u-c-n_t)} \frac{\prod_m (n_t - r_m)}{\prod_m (n_t + c - v_m)} \cdot \frac{\prod_m (u - v_m)}{\prod_m (u - c - r_m)}. \quad (8)$$

That (8) is of the same form as (6) can be seen from the partial fraction expansion of the last quotient. Also the M constraints (7) are satisfied due to the form of the numerator of the last quotient. The second factor is the normalization factor so that $S_s(c+n_t)=1$. The required distribution function is obtained by substituting the values of (8) for $u=c+n$ into (4).

If $u_s=v_t$; *i.e.*, when u_s does not coincide with one of the unit sample points, (8) can be replaced by

$$S_s(u) = \frac{\sin \pi(u-c)}{\sin \pi(v_t - c)} \frac{\prod_{m\neq t} (u - v_m)}{\prod_m (u - c - r_m)} \cdot \frac{\prod_m (v_t - c - r_m)}{\prod_{m\neq t} (v_t - v_m)}. \quad (9)$$

The general synthesis problem; *i.e.*, when $S(u_n)$ are arbitrarily assigned, can be treated as a linear combination of the above two types of solutions. Thus, in general

$$S(u) = \sum_{s=1}^{N} S(u_s) S_s(u). \quad (10)$$

The associated distribution function is therefore

$$g(p) = \begin{cases} \frac{\lambda}{4\pi a} \sum_{n=-\infty}^{\infty} \sum_{s=1}^{N} S(u_s) S_s(c+n) \exp -i(c+n)p, & |p| \leqq \pi; \\ 0, & |p| > \pi. \end{cases} \quad (11)$$

The space factors (8), (9), and (10) together with the corresponding distribution functions do not form the only solutions of the synthesis problem. By varying r_m; *i.e.*, by migrating some other zeros to v_m, different solutions are obtained. In addition, any linear combination of these is again a solution. The unique reconstruction of the space factor in terms of its unit samples is given in (2). By means of the above procedure all possible combinations of unit sample values, which produce admissible space factors, can be obtained. Hence, all possible solutions to the synthesis problem can be derived in the above manner.

Note that (8) and (9) can be considered as the composing functions for a generalized sampling theorem where M of the unit sample points located at $u=c+r_m$ are displaced to $u=v_m$. The function $S(u)$ limited within the band $|p| \leqq \pi$ can be reconstructed from its values at $u=c+n$, $n \neq v_m$, and $u=v_m$ by means of these generalized composing functions.

The Least Integrated Magnitude Squared Distribution Function

In view of the existence of the multitude of solutions, the question arises as to which particular one is to be used. For a line-source one may ask what distribution function gives a minimum value of ohmic loss. This implies that the integrated value of the squared magnitude of the distribution function $|g(p)|^2$ must be a minimum. Due to its simplicity, this criterion is applied in the following, yielding a result identical to the one obtained by Woodward and Lawson. In general, the criterion is related to a minimum energy storage in the near field and a minimum value for the supergain ratio as defined by Taylor.

Consider again the simplified problem, namely that of finding $S_s(u)$ and the associated $g(p)$ so that $S_s(u_s)=1$, $S_s(u_n)=0$ $n \neq s$. Now, however, a solution is sought for which the integrated value P of the squared magnitude of the distribution function $g(p)$ is a minimum. From Parseval's theorm, P can be expressed in terms of the uniformly spaced values $S_s(c+n)$ as follows

$$P = \int_{-\pi}^{\pi} |g(p)|^2 dp = \frac{1}{2\pi}\left(\frac{\lambda}{2a}\right)^2 \sum_{n=-\infty}^{\infty} |S_s(c+n)|^2. \quad (12)$$

Since the values of $S_s(c+n_k)$ are prescribed, the problem reduces to that of determining a set of values $S_s(c+n)$, $n \neq n_k$, which will minimize the quantity

$$\sum_{n=-\infty \neq n_k}^{\infty} |S_s(c+n)|^2, \quad (13)$$

under the M constraints

$$S_s(v_m) = \begin{Bmatrix} 0 \\ \delta_t{}^m \end{Bmatrix}. \quad (14)$$

Here, as well as in the following, the upper term in the braces is used for the case when $u_s=c+n_t$, whereas the lower term is valid for $u_s=v_t$.

In general $S_s(c+n)$ may be complex, hence let

$$S_s(c+n) = R_s(c+n) + iI_s(c+n), \quad n \neq n_k. \quad (15)$$

By the method of Lagrangian multipliers the following quantity is to be minimized

$$\sum_{n=-\infty \neq n_k}^{\infty} [R_s(c+n)^2 + I_s(c+n)^2] + \sum_{m=1}^{M} \mu_m \sum_{n=-\infty \neq n_k}^{\infty} \frac{(-1)^n I_s(c+n)}{v_m - c - n}$$

$$+ \sum_{m=1}^{M} \lambda_m \left[\begin{Bmatrix} \dfrac{(-1)^{n_t}}{v_m - c - n_t} \\ \delta_t{}^m \end{Bmatrix} + \sum_{n=-\infty \neq n_k}^{\infty} \frac{(-1)^n R_s(c+n)}{v_m - c - n} \right]. \quad (16)$$

Here, M_m and λ_m are $2M$ undetermined real Lagrangian multipliers.

On differentiating (16) with respect to $R_s(c+n)$ and $I_s(c+n)$, $n \neq n_k$, and equating to zero, one obtains

$$R_s(c+n) = -\frac{1}{2}\sum_{m=1}^{M} \lambda_m \frac{(-1)^n}{v_m - c - n},$$

$$I_s(c+n) = -\frac{1}{2}\sum_{m=1}^{M} \mu_m \frac{(-1)^n}{v_m - c - n}, \quad n \neq n_k. \quad (17)$$

Substituting the above values into (6) and remembering the "consistency" property[6] of the sampling theorem; *i.e.*,

$$\frac{\sin \pi(u - v_m)}{\pi(u - v_m)} = \sum_{n=-\infty}^{\infty} \frac{\sin \pi(v_m - c)}{\pi(v_m - c - n)} \frac{\sin \pi(u - c)}{\pi(u - c - n)}, \quad (18)$$

it follows that the space factor corresponding to the distribution function with the least integrated squared magnitude is

$$S_s(u) = \begin{Bmatrix} \dfrac{(-1)^{n_t} \sin \pi(u - c)}{\pi(u - c - n_t)} \\ 0 \end{Bmatrix} + \frac{1}{2}\sum_{m=1}^{M} (\lambda_m + i\mu_m) \times \left[\frac{\sin \pi(u - v_m)}{(u - v_m) \sin \pi(u - v_m)} + \sum_{k=1}^{K} \frac{\sin \pi(u - c)}{\pi(v_m - c - n_k)(u - c - n_k)} \right]. \quad (19)$$

In order to find the M multipliers λ_m, (19) is substituted into (14) resulting in the following set of M equations

$$\lambda_j - \frac{1}{\pi^2}\sin^2 \pi(v_j - c) \sum_{k=1}^{K}\sum_{m=1}^{M} \frac{\lambda_m}{(v_m - c - n_k)(v_j - c - n_k)} = \begin{Bmatrix} \dfrac{2(-1)^{n_t+1}}{\pi^2} & \dfrac{\sin^2 \pi(v_j - c)}{v_j - c - n_t} \\ \dfrac{2 \sin \pi(v_i - c)}{\pi} & \delta_t{}^i \end{Bmatrix}, \quad j = 1, \cdots M. \quad (20)$$

For the remaining M multipliers μ_m, a similar set of equations can be derived with λ_m replaced by μ_m and the right hand side replaced by zero. The solution of this set of $2M$ equations completely determines the space factor $S_s(u)$. For the most cases it can be assumed that the set of equations has a unique solution hence,

$\mu_m = 0$ and $I_s(c+n) = 0$. Thus, $S_s(c+n)$ is real and is equal to $R_s(c+n)$ as given by (17) with λ_m satisfying the set of (20).

In general, all the $S_s(c+n)$ for $n = \neq n_k$ as given in (17) are nonvanishing. Hence, the $S_s(u)$ thus derived can be considered as the result of migrating an infinite number of zeros of the integral function

$$\frac{\sin \pi(u - u_s)}{\pi(u - u_s)}.$$

This fact shows that the method described here is essentially a limiting form of that given in the last section.

Notice that (19) can be rearranged to read

$$S_s(u) = \sum_{n=1}^{N} a_n \frac{\sin \pi(u - u_n)}{\pi(u - u_n)}, \tag{21}$$

where the coefficients a_n can readily be obtained in terms of λ_m by means of term by term comparison. The corresponding distribution function is therefore

$$g(p) = \begin{cases} \dfrac{\lambda}{4\pi a} \displaystyle\sum_{n=1}^{N} a_n \exp(-iu_n p), & |p| \leqq \pi; \\ 0, & |p| > \pi. \end{cases} \tag{22}$$

The above result is nothing but the form adopted by Woodward and Lawson[4] from numerical experience in order "to avoid any tendency for the composite pattern to oscillate violently between the fixed points." In the present procedure the number of simultaneous equations to be solved, is M. By a proper choice of the constant c, M is always less than N, the number required in Woodward and Lawson's method. Hence, the use of (20) offers a slight reduction in the numerical work involved.

For the special case, when all assigned sample points coincide with unit sample points, it is obvious that (19) would reduce to a single term; *i.e.*, the space factor as given in (6) with all unit sample values in the summation equal to zero corresponds to the least integrated magnitude squared distribution function.

Since the M constraints given in (14) are linear in $S_s(c+n)$, the general synthesis problem can be treated in exactly the same manner. The result is again the superposition of the $S_s(u)$ derived in this section as given by (10) and (11).

The criterion adopted here can, in a rather loose manner, be put in terms of the supergain ratio γ as defined by Taylor[1]

$$\gamma = \frac{\dfrac{1}{2\pi}\displaystyle\int_{-\pi}^{\pi} |g(p)|^2 dp}{\left(\dfrac{\lambda}{4\pi a}\right)^2 \displaystyle\int_{-2a/\lambda}^{2a/\lambda} |S(u)|^2 du}.$$

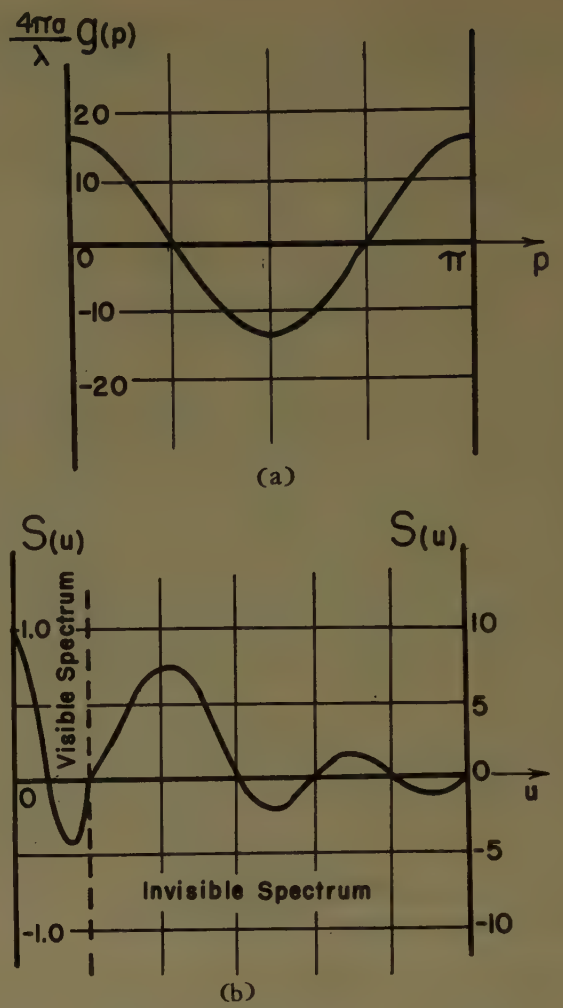

Fig. 3—Supergain example; $r_1 = 2$, $r_2 = -2$; $P = 18.06$.

For those $g(p)$'s which give nearly the same visible spectrum, the one with the least integrated value of the squared magnitude of $g(p)$ will also give a minimum value to the supergain ratio γ. Due to the large values of $g(p)$ in cases where zeros in the invisible spectrum have to be migrated into the visible spectrum, such cases are said to belong to the supergain situation with large values of γ.

Examples

Figs. 3–5 show the space factor $S(u)$ and the corresponding distribution function $g(p)$ for the following problem

u_n	-1	$-\frac{1}{2}$	0	$\frac{1}{2}$	1
$S(u_n)$	0	0	1	0	0.

The aperture width is $2a/\lambda = 1$. Obviously c can be chosen to be zero, and the solution of this problem requires the migration of the zeros of $(\sin \pi u)/\pi u$ into the visible spectrum from the invisible spectrum. Thus the problem corresponds to the "supergain" situation. Three sets

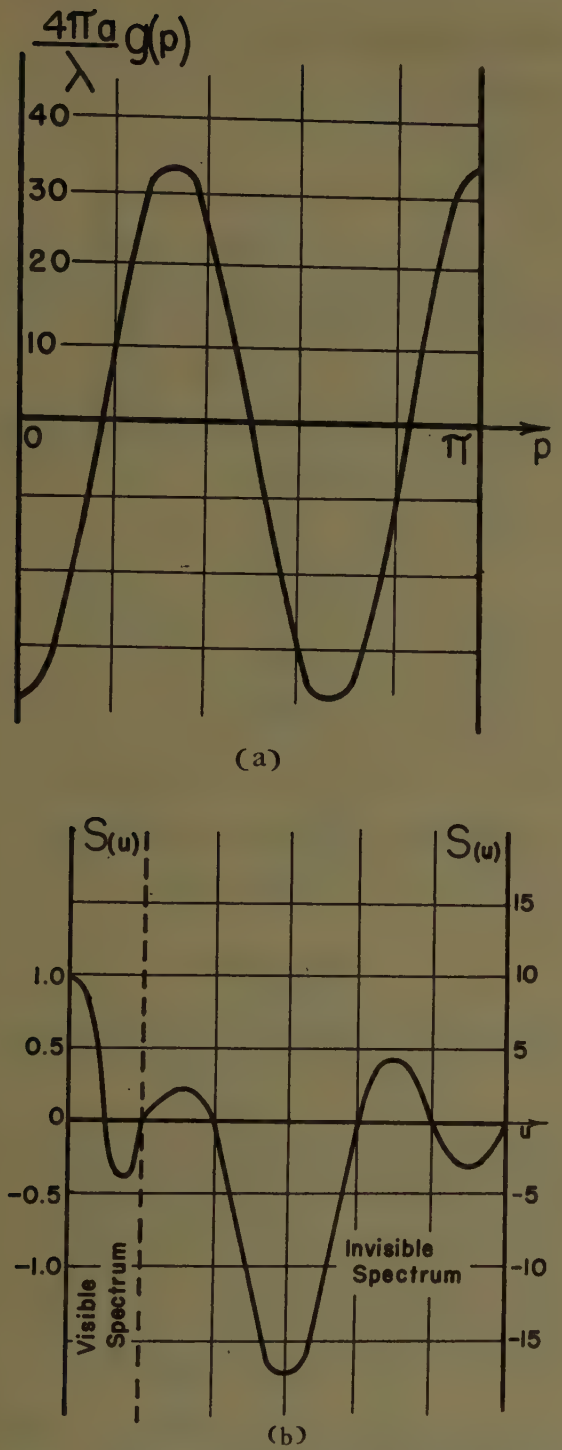

Fig. 4—Supergain example; $r_1=3$, $r_2=-3$; $P=97.64$.

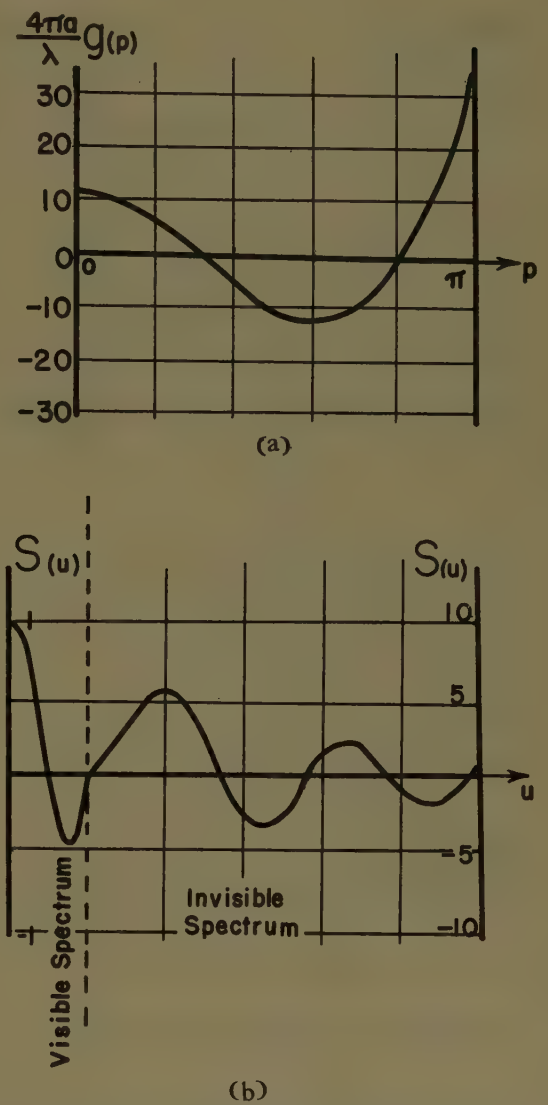

Fig. 5—Supergain example; least integrated squared magnitude distribution; $P=14.02$.

of solutions are plotted, one for migrating the zeros at $u=\pm 2$ to $u=\pm\frac{1}{2}$ (Fig. 3), one for migrating the zeros at $u=\pm 3$ to $u=\pm\frac{1}{2}$ (Fig. 4), and a third which gives the least integrated value P of the squared magnitude of the distribution function (Fig. 5). Since both $S(u)$ and $g(p)$ are even functions, only the values for $u\geqq 0$ and $p\geqq 0$ are shown. Notice that the scale used for $S(u)$ in the invisible spectrum is larger than that in the visible spectrum as a result of the supergain situation. From the corresponding values of P given in the figures, it is obvious that the last solution actually has a value of P less than the other two. Also, it can be seen that the visible spectrum remains essentially the same for all three solutions while the invisible spectrum has a lower magnitude for the last. This means that the last solution has a lower value of storage energy and a lower supergain ratio.

Figs. 6 and 7 show two solutions of the problem

u_n	−5	−4	−3	−2	−1	3/4	1	2	3	4	5
$S(u_n)$	0	0	0	0	0	1	3/4	3/8	1/4	3/16	3/20.

This visible spectrum corresponds to the well-known "cosecant" pattern. The width of the source is $2a/\lambda=5$. By choosing $c=0$, all the assigned sample points, except $u=\frac{3}{4}$, coincide with some of the unit sample points. A solution can be obtained by migrating the zero of

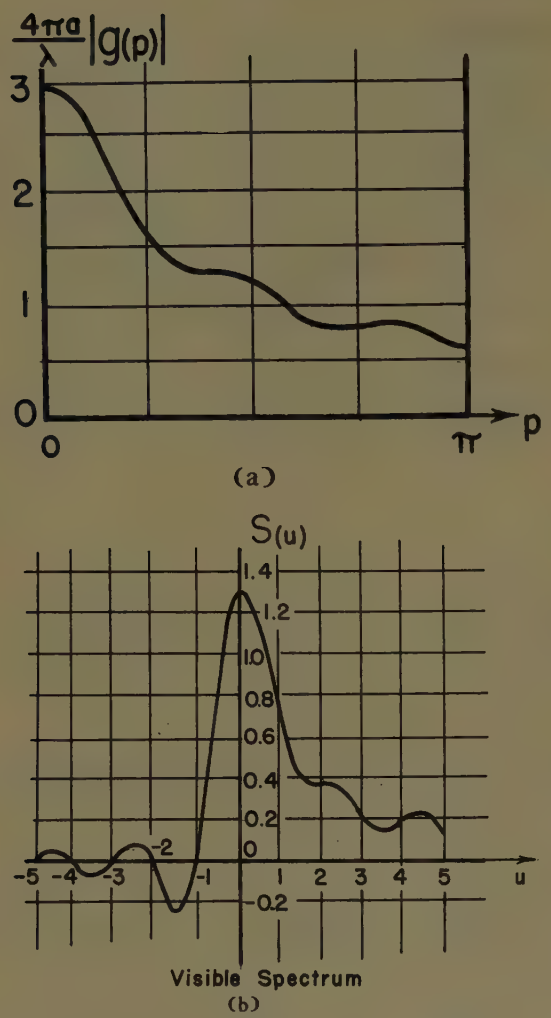

Fig. 6—Cosecant example; $r_1=0$; $P=0.01504$.

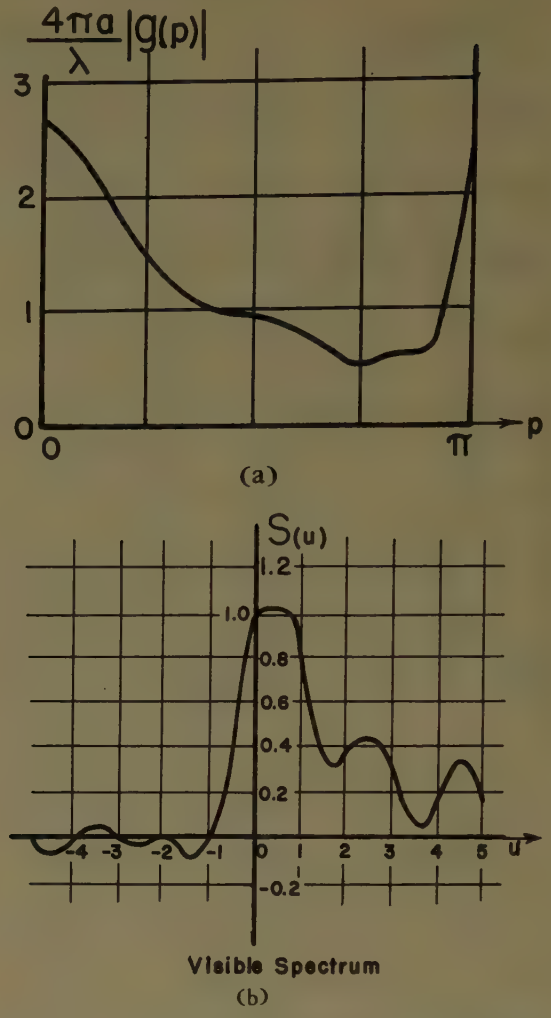

Fig. 7—Cosecant example; least integrated squared magnitude distribution; $P=0.01333$.

$$\frac{\sin \pi(u-n)}{\pi(u-n)} \text{ at } u=0 \text{ to } u=\frac{3}{4}.$$

Thus the synthesis can be carried out without the migrations of zeros from the invisible range into the visible spectrum. This solution is shown in Fig. 6. Another solution corresponding to the least integrated squared magnitude criterion is given in Fig. 7. Since the magnitude of the distribution function is an even function in p, only the values for $p>0$ are plotted. The phase of the distribution functions are omitted from the figures, because the main interest here is the values of P. By comparison, it is evident that the improvement of the second solution over the first, in regard to the value of P is rather small. Besides, this improvement is accomplished at the expense of larger variations in the visible spectrum between the assigned sample points. Thus, for cases where it is not necessary to migrate zeros into the visible spectrum from outside, the minimum P criterion does not seem to be very significant.

Acknowledgment

The author gratefully acknowledges the suggestions and criticism of Dr. George Sinclair. The work was supported by the Defense Research Board of Canada under Grant DRB 5540–02.

Radiation Characteristics with Power Gain for Slots on a Sphere*

Y. MUSHIAKE† AND R. E. WEBSTER‡

Summary—**Radiation patterns, impedances, and power gains of nonsymmetrically excited narrow slots on a sphere are considered. Numerical calculations of higher order ϕ-dependent modes of the radiation and admittance functions are discussed. These functions are applied to obtain the radiation characteristics of an equatorial slot backed by a radial transmission line and excited by feed points along the slot periphery. This geometry is treated directly as a boundary value problem, no assumption of aperture field distribution along the slot being made. Further application is shown for half wave slots on the sphere and for determining gains of uniformly excited zonal slots as a function of their location. Experimental results simulating the asymmetrically excited equatorial slot geometry are given.**

Introduction

RADIATION characteristics of a sphere have been discussed by a number of investigators in recent years. Perhaps the most notable contributions are those by Stratton and Chu,[1] Schelkunoff,[2] Bailin and Silver,[3] and C. T. Tai.[4] Rather extensive numerical calculations have been made of impedances for the symmetrically excited case,[5–8] and some vertical-plane radiation patterns have been obtained.[9] General expressions of the electromagnetic fields outside a sphere have also been given in terms of the tangential field distribution over the sphere.[10] There is, however, no discussion or formulation treated from boundary conditions for nonsymmetrical feed geometries,[11] and little quantitative data is available for such excitation. The work described in this paper is concerned with this aspect of the spherical antenna problem.

In the next section a conventional formulation is given for the fields of a spherical antenna in terms of the tangential electric field on the surface of the sphere. The problem of interest, however, is to obtain solutions for known feed systems without assuming aperture field distributions. The higher-mode radiation admittance $Y_m{}^e$ is then defined with this end in mind. The radiation function D_m is also defined, and expressions for the far field and power gain of narrow slots are obtained.

After evaluations of these functions for higher modes are obtained, their applications are discussed in a boundary value problem where the given conditions are certain distributions of feed currents. The basic geometry is a narrow equatorial slot backed by a radial transmission line. Radiation patterns and gains are computed, and corroborating experimental results are shown.

The functions $Y_m{}^e$ and D_m are also applied to the relatively simple problem of obtaining the radiation characteristics of slots with assumed aperture field distributions. The interesting resulting gains are shown for uniformly excited zonal slots as a function of their location and for half-wave equatorial slots.

The rationalized mks units system is used throughout.

Formulation for Spherical Antenna

Higher-Mode Radiation Admittance

Let us consider a perfectly conducting sphere with a narrow zonal slot as illustrated in Fig. 1, and let R, θ, ϕ, be the spherical coordinates, "a" the radius of the sphere, $\theta=\theta_1$ the position of the slot, and 2α the width of the slot with respect to the angle θ. Since a general electromagnetic field for a sphere can be constructed by a summation of various higher modes, we first discuss ϕ-dependent mth higher modes for which the distribution of the electric field over the sphere is given by the following function:

$$E_\theta{}^{me}(a,\theta,\phi) = \begin{cases} E_m \cos m\phi, & \theta_1-\alpha<\theta<\theta_1+\alpha \\ 0, & 0\leqq\theta<\theta_1-\alpha,\ \theta_1+\alpha<\theta\leqq\pi \end{cases} \quad (1)$$

and

$$E_\phi{}^{me}(a,\theta,\phi) = 0 \text{ (over all the sphere)}, \quad (2)$$

where E_m is an unknown constant to be determined later, and the common time factor $e^{j\omega t}$ is omitted in these equations.

Under this condition the exterior field of the sphere can easily be obtained in terms of E_m by applying the formulas already given by several other authors[10, 12], *i.e.*,

* Manuscript received by the PGAP, February 6, 1956.

† Tohoku Univ., Sendai, Japan. Formerly with the Antenna Lab., The Ohio State Univ. Res. Foundation, Columbus, Ohio.

†† Antenna Lab., The Ohio State Univ. Res. Found., Columbus, Ohio.

[1] J. A. Stratton and L. J. Chu, "Steady-state solutions of electromagnetic field problems," *J. Appl. Phys.*, vol. 12, pp. 230–248; March, 1941.

[2] S. A. Schelkunoff, "Principal and complementary waves in antennas," PROC. IRE, vol. 34, pp. 23P–32P; January, 1946.

[3] L. L. Bailin and S. Silver, "Exterior Electromagnetic Boundary Value Problems for Spheres and Cones," Tech. Memo. No. 305, Hughes Aircraft Co. Res. and Dev. Labs., Culver City, Calif.; July, 1953.

[4] C. T. Tai, "Some Electromagnetic Problems Involving a Sphere," Tech. Rep. No. 41, S. R. I. Project No. 591, Aircraft Radiation System Lab., Stanford Res. Inst., Stanford, Calif.; April, 1953.

[5] Stratton and Chu, *loc. cit.*

[6] P. D. P. Smith, "The conical dipole of wide angle," *J. Appl. Phys.*, vol. 19, pp. 11–23; January, 1948.

[7] C. H. Papas and R. King, "Input impedance of wide-angle conical antennas fed by a coaxial line," PROC. IRE, vol. 37, pp. 1269–1271; November, 1949.

[8] D. McCoy, "Numerical Calculations of Admittances for Narrow Zonal Slots in a Sphere," Tech. Rep. No. 522-8, Antenna Lab., The Ohio State Univ. Res. Foundation, prepared under Contract DA 36-039 sc 42548, U. S. Army, Signal Corps Eng. Labs., Fort Monmouth, N. J.; April, 1954.

[9] C. H. Papas and D. B. Brick, "Radiation of the Boss Antenna," Tech. Rep. No. 148, Cruft Lab., Harvard Univ., Cambridge, Mass.; April, 1952.

[10] Bailin and Silver, *loc. cit.*

[11] Geometries similar to those discussed here have been treated independently by R. C. Hansen at the Univ. of Illinois recently, but his results have not been published.

[12] Tai, *loc. cit.*

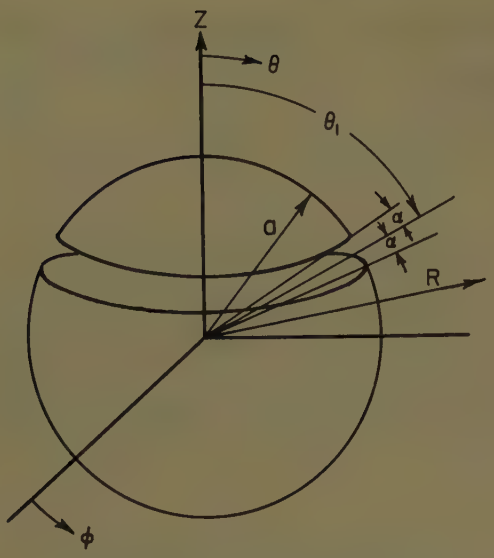

Fig. 1—Sphere with a narrow zonal slot.

and μ the electromagnetic constants of the medium outside the sphere and $k=\omega\sqrt{\mu\epsilon}$.

The total electromagnetic field for this antenna is obtained from a summation of these mth mode contributions, for example,

$$\left.\begin{aligned} E_\theta^e &= \sum_{m=0}^{\infty} E_\theta^{me} \\ H_\phi^e &= \sum_{m=0}^{\infty} H_\phi^{me} \end{aligned}\right\} \tag{7}$$

Now, let us define the amplitude of the gap voltage along the narrow slot by the following equation:

$$V_m = \int_{\theta_1-\alpha}^{\theta_1+\alpha} E_m a d\theta = 2a\alpha E_m. \tag{8}$$

$$\left.\begin{aligned} E_R^{me} &= -E_m \cos m\phi \sum_{n=m}^{\infty} B_n^m \frac{n(n+1)}{kR} \frac{kah_n^{(2)}(kR)}{[kah_n^{(2)}(ka)]'} P_n^m(\cos\theta) \\ E_\theta^{me} &= -E_m \cos m\phi \sum_{n=m}^{\infty} \left\{A_n^m \frac{h_n^{(2)}(kR)}{h_n^{(2)}(ka)} \frac{mP_n^m}{\sin\theta} + B_n^m \frac{a}{R} \frac{[kRh_n^{(2)}(kR)]'}{[kah_n^{(2)}(ka)]'} \frac{dP_n^m}{d\theta}\right\} \\ E_\phi^{me} &= E_m \sin m\phi \sum_{n=m}^{\infty} \left\{A_n^m \frac{h_n^{(2)}(kR)}{h_n^{(2)}(ka)} \frac{dP_n^m}{d\theta} + B_n^m \frac{a}{R} \frac{[kRh_n^{(2)}(kR)]'}{[kah_n^{(2)}(ka)]'} \frac{mP_n^m}{\sin\theta}\right\} \end{aligned}\right\} \tag{3}$$

$$\left.\begin{aligned} H_R^{me} &= -j\sqrt{\frac{\epsilon}{\mu}} E_m \sin m\phi \sum_{n=m}^{\infty} A_n^m \frac{n(n+1)}{kR} \frac{h_n^{(2)}(kR)}{h_n^{(2)}(ka)} P_n^m(\cos\theta) \\ H_\theta^{me} &= -j\sqrt{\frac{\epsilon}{\mu}} E_m \sin m\phi \sum_{n=m}^{\infty} \left\{A_n^m \frac{[kRh_n^{(2)}(kR)]'}{kRh_n^{(2)}(ka)} \frac{dP_n^m}{d\theta} - B_n^m \frac{kah_n^{(2)}(kR)}{[kah_n^{(2)}(ka)]'} \frac{mP_n^m}{\sin\theta}\right\} \\ H_\phi^{me} &= -j\sqrt{\frac{\epsilon}{\mu}} E_m \cos m\phi \sum_{n=m}^{\infty} \left\{A_n^m \frac{[kRh_n^{(2)}(kR)]'}{kRh_n^{(2)}(ka)} \frac{mP_n^m}{\sin\theta} - B_n^m \frac{kah_n^{(2)}(kR)}{[kah_n^{(2)}(ka)]'} \frac{dP_n^m}{d\theta}\right\} \end{aligned}\right\} \tag{4}$$

where

$$\left.\begin{aligned} A_n^m &= -\frac{2n+1}{2n(n+1)} \cdot \frac{(n-m)!}{(n+m)!} \int_{\theta_1-\alpha}^{\theta_1+\alpha} mP_n^m d\theta \\ B_n^m &= -\frac{2n+1}{2n(n+1)} \cdot \frac{(n-m!)}{(n+m)!} \int_{\theta_1-\alpha}^{\theta_1+\alpha} \frac{dP_n^m}{d\theta} \sin\theta d\theta \end{aligned}\right\} \tag{5}$$

$$[kRh_n^{(2)}(kR)]' = \frac{\partial}{\partial(kR)} [kRh_n^{(2)}(kR)] \tag{6}$$

and $P_n^m(\cos\theta)$ is the associated Legendre function, $h_n^{(2)}(x)$ the spherical Hankel function of second kind, ϵ

The mth mode radiation admittance Y_m^e can then be defined as the ratio of surface current to V_m such that Y_m^e is equal to actual input admittance for the $m=0$ mode. Using the expression for H_θ^{me} of (4) this admittance is given as follows:

$$Y_m^e = G_m^e + jB_m^e = -(1+\delta_m)(\sin\theta_1)\frac{\pi}{2}\sqrt{\frac{\epsilon}{\mu}} \sum_{n=m}^{\infty} \left\{\frac{A_n^m}{2\alpha} \frac{1}{M_n(ka)} m\left[\frac{P_n^m\{\cos(\theta_1-\alpha)\}}{\sin(\theta_1-\alpha)} + \frac{P_n^m\{\cos(\theta_1+\alpha)\}}{\sin(\theta_1+\alpha)}\right] + \frac{B_n^m}{2\alpha} M_n(ka)\left[\frac{dP_n^m\{\cos\theta_1-\alpha)\}}{d\theta} + \frac{dP_n^m\{\cos(\theta_1+\alpha)\}}{d\theta}\right]\right\} \tag{9}$$

where

$$M_n(ka) = -j\frac{kah_n^{(2)}(ka)}{[kah_n^{(2)}(ka)]'} \tag{10}$$

and $\delta_m = 1$ for $m = 0$ and $\delta_m = 0$ for $m \neq 0$.

Far-Zone Field and Power Gain

Introduction of the asymptotic expression of the spherical Hankel Function for large argument into (3) and (4) gives the far-zone field, *e.g.*,

$$E_R^{me} \cong 0$$

$$E_\theta^{me} \cong \frac{e^{-jkR}}{R}\frac{V_m}{ka}D_m \cos m\phi$$

$$E_\phi^{me} \cong \frac{e^{-jkR}}{R}\frac{V_m}{ka}\sin m\phi \sum_{n=m}^{\infty}(j)^n\left\{j\frac{A_n^m}{2\alpha}\frac{1}{h_n^{(2)}(ka)}\frac{dP_n^m}{d\theta} + \frac{B_n^m}{2\alpha}\frac{ka}{[kah_n^{(2)}(ka)]'}\frac{mP_n^m}{\sin\theta}\right\} \tag{11}$$

where

$$D_m = -\sum_{n=m}^{\infty}(j)^n\left\{j\frac{A_n^m}{2\alpha}\frac{1}{h_n^{(2)}(ka)}\frac{mP_n^m}{\sin\theta} - \frac{B_n^m}{2\alpha}\frac{ka}{[kah_n^{(2)}(ka)]'}\frac{dP_n^m}{d\theta}\right\}. \tag{12}$$

The total power W radiated from the sphere can be calculated by integrating the Poynting vector over the slot surface or over an infinitely large spherical surface. The actual expressions, as well as the resulting evaluation, of these two integrations are identical and may be reduced to the following form:

$$W = \sum_{m=0}^{\infty} G_m^r |V_m|^2 \tag{13}$$

where

$$G_m^r = -(1+\delta_m)\frac{\pi}{2}\sqrt{\frac{\epsilon}{\mu}}\sum_{n=m}^{\infty}\left\{\frac{A_n^m}{2\alpha^2}\operatorname{Re}\left(\frac{1}{M_n}\right)\int_{\theta_1-\alpha}^{\theta_1+\alpha} mP_n^m d\theta + \frac{B_n^m}{2\alpha^2}\operatorname{Re}(M_n)\int_{\theta_1-\alpha}^{\theta_1+\alpha}\frac{dP_n^m}{d\theta}\sin\theta d\theta\right\}. \tag{14}$$

G_m^r can be shown to coincide with G_m^e, the real part of the radiation admittance Y_m^e, for very narrow slots.[13]

$$G_m^r \cong G_m^e = \operatorname{Re}(Y_m^e), \quad \text{(for narrow slots)}. \tag{15}$$

[13] Y. Mushiake and R. E. Webster, "Radiation Characteristics with Power Gain for Slots on a Sphere," Tech. Rep. No. 522-15, Antenna Labs., The Ohio State Univ. Res. Foundation, prepared under Contract DA 36-039 sc 42548, U. S. Army, Signal Corps Eng. Labs., Fort Monmouth, N. J., presented at WESCON Convention, Los Angeles, Calif.; August 21–24, 1955.

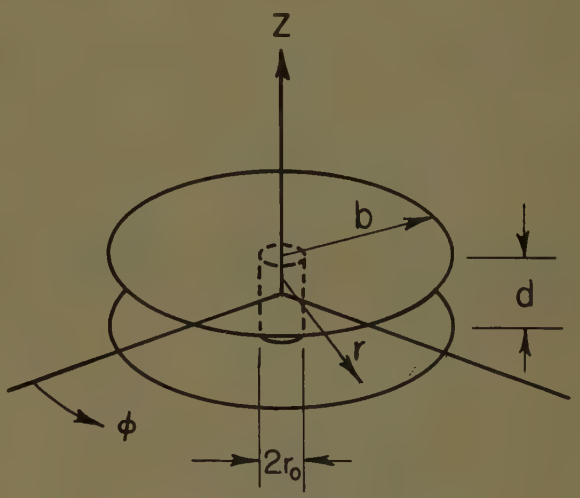

Fig. 2—Radial transmission line cavity.

From (7), (11), and (13) and the definition of power gain we obtain

$$G = \frac{73.13}{3600\,(ka)^2}\cdot\frac{\left|\sum_{m=0}^{\infty} V_m D_m \cos m\phi\right|^2}{\sum_{m=0}^{\infty} G_m^r |V_m|^2} \tag{16}$$

where G is the power gain of the sphere over that of a half-wave dipole for the E_θ^e component. In general $E_\phi^e \neq 0$, but in the equatorial plane for the equatorial slots we find that $E_\phi^e = 0$ from (3).

Zonal Slot Backed by Radial Transmission Line

Higher Mode Admittance of Radial Cavity

Consider the electromagnetic field between two perfectly conducting sheets terminated by a short circuit at $r = r_0$ (see Fig. 2), where the gap "d" is very small compared with the wavelength and the radius b, and the electric field, at the periphery is given by

$$E_z^{mi}(b, \phi, z) = \frac{V_m}{d}\cos m\phi, \tag{17}$$

$$E_\phi^{mi}(b, \phi, z) = 0 \tag{18}$$

corresponding to (1) and (2). This distribution is that of a ϕ-dependent TEM mode for which the ϕ component of the magnetic field is expressed as follows:

$$H_\phi^{mi} = -j\frac{V_m}{d}\sqrt{\frac{\epsilon}{\mu}}\frac{J_m'(kr)N_m(kr_0) - J_m(kr_0)N_m'(kr)}{J_m(kr)N_m(kr_0) - J_m(kr_0)N_m(kr)}\cdot\cos m\phi. \tag{19}$$

The existence of TE modes is possible, but their effects should be small for the boundary conditions considered here. The total electromagnetic field for this cavity is expressed as a summation of the mth mode contribu-

tions, *e.g.*,

$$\left.\begin{aligned} E_z^i &= \sum_{m=0}^{\infty} E_z^{mi} \\ H_\phi^i &= \sum_{m=0}^{\infty} H_\phi^{mi} \end{aligned}\right\}. \tag{20}$$

Corresponding to the radiation admittance Y_m^e defined by (9), the mth mode cavity admittance Y_m^i can be defined as follows:

$$Y_m^i = j(1+\delta_m)\frac{b\pi}{d}\sqrt{\frac{\epsilon}{\mu}} \cdot \frac{J_m'(kb)N_m(kr_0) - J_m(kr_0)N_m'(kb)}{J_m(kb)N_m(kr_0) - J_m(kr_0)N_m(kb)}. \tag{21}$$

Determination of Mode Amplitudes from the Boundary Conditions

In the preceding sections the electromagnetic fields outside the sphere and inside the slot were considered independently. Now we connect these fields at the slot surface by the given boundary conditions and determine the mode amplitude V_m.

Consider the general case of a given current source in the θ direction with arbitrary ϕ-dependent distribution connected across the two edges of the slot. This impressed current can be assumed to be a surface current, the density of which is expressed in the following form:[14]

$$K_\theta(\phi) = \sum_{m=0}^{\infty} K_m \cos m\phi \tag{22}$$

where K_m is determined by the Fourier expansion of $K_\theta(\phi)$, *i.e.*,

$$K_m = \frac{1}{(1+\delta_m)\pi}\int_{-\pi}^{\pi} K_\theta(\phi)\cos m\phi d\phi. \tag{23}$$

The boundary condition between such a surface current and the tangential magnetic fields H_ϕ^e and H_ϕ^i is given by

$$K_\theta(\phi) = \tfrac{1}{2}\left[H_\phi^e(a, \theta_1+\alpha, \phi) + H_\phi^e(a, \theta_1-\alpha, \phi) - H_\phi^i(b, \phi)\right] \tag{24}$$

where the impressed current is assumed to be of the symmetrical dipole type. Introducing the expressions of K_θ, H_ϕ^e and H_ϕ^i into (24) with (9) and (21) we can derive the following relation for each mth mode.

$$(1+\delta_m)\pi b K_m = (Y_m^i + Y_m^e)V_m \tag{25}$$

or

$$V_m = \frac{U_m}{Y_m^t} I \tag{26}$$

[14] Symmetrical distribution with respect to ϕ is considered.

where

$$Y_m^t = \frac{1}{Z_m^t} = G_m^t + jB_m^t = Y_m^e + Y_m^i = G_m^e + j(B_m^e + B_m^i) \tag{27}$$

$$I = 2\pi b K_0 = b\int_{-\pi}^{\pi} K_\theta(\phi)d\phi \tag{28}$$

$$U_m = \frac{1+\delta_m}{2}\cdot\frac{K_m}{K_0} = \frac{\int_{-\pi}^{\pi} K_\theta(\phi)\cos m\phi d\phi}{\int_{-\pi}^{\pi} K_\theta(\phi)d\phi}. \tag{29}$$

Thus the mode amplitude V_m is determined from a given arbitrary distribution of impressed current density $K_\theta(\phi)$. Substitution of this expression for V_m in (11) and (16) gives explicit formulas for the far-zone fields and power gain.

Single Feed Point

Theoretical Expressions and Numerical Results: As an idealized geometry of a single feed point on the slot, consider a small strip on which the impressed electric current is distributed uniformly as illustrated in Fig. 3, *i.e.*,

$$K_\theta(\phi) = \begin{cases} \text{constant}, & -\beta \leqq \phi \leqq \beta \\ 0, & -\pi \leqq \phi < -\beta, \beta < \phi \leqq \pi. \end{cases} \tag{30}$$

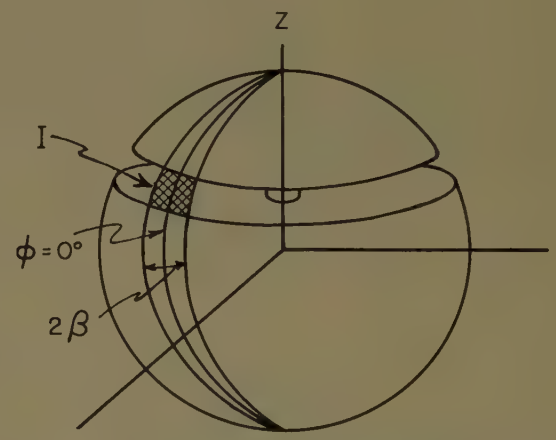

Fig. 3—Narrow zonal slot on a sphere backed with radial cavity and excited at one point.

For this feed system U_m can be calculated from (29), and if we assume $\beta \ll 0.1$ we find

$$U_m = \frac{\sin m\beta}{m\beta} \cong 1, \quad (\text{for } m \cong 10). \tag{31}$$

The input impedance Z_i can be defined for this feed system by the following equation:

$$Z_i = R_i + jX_i = \frac{V(0)}{I} \tag{32}$$

where $V(0)$ is the voltage at the feed point ($\phi=0$) obtained by summing the mode voltages

$$V_{(\phi)} = \sum_{m=0}^{\infty} V_m \cos m\phi. \tag{33}$$

Introduction of (26) and (33) into (32) gives

$$Z_i = \sum_{m=0}^{\infty} U_m Z_m{}^t. \tag{34}$$

Although the convergence of the imaginary part is not good,[15] the real part of this series converges rapidly. Accordingly, for the real part the approximation of (31) can be applied, and

$$R_i \cong \sum_{m=0}^{10} R_m{}^t, \quad (\text{for } ka \leqq 4). \tag{35}$$

Introducing (15), (26), (31), and (35) into (16), we obtain

$$G \cong \frac{73.13}{3600\,(ka)^2} \cdot \frac{\left| \sum_{m=0}^{10} Z_m{}^t D_m \cos m\phi \right|^2}{R_i}, \quad (\text{for } ka \leqq 4). \tag{36}$$

The numerical computations were carried out for

$$\begin{cases} \alpha = 1^\circ \\ \theta = \theta_1 = 90^\circ, \end{cases} \qquad \begin{cases} r_0/a = 0.1,\ 0.5 \\ ka = 1,\ 2,\ 3,\ 4. \end{cases}$$

The most difficult part of the computation was evaluation of the imaginary part of the series of $Y_m{}^e$ defined by (9) (because of poor convergence). To avoid this difficulty the series was approximated by a known series for large values of n.[16] The computed values of $Y_m{}^e$ and D_m are tabulated in Tables I and II. These results can be used to calculate radiation characteristics of other slots excited by arbitrarily ϕ-dependent feed systems. Evaluation of these functions for general zonal locations is straightforward but ponderous.

The relative horizontal plane field intensities with respect to ϕ computed from the numerator of (36) are plotted in Fig. 4 (next page). The values of maximum power gains over those of a half-wave dipole (calculated from the same equation) are also shown, and values of input resistance are indicated.

Experiment: To verify the theoretical calculations, radiation pattern measurements were made using a hemisphere over a ground plane. A sketch and the important dimensions of this apparatus are shown in Fig. 5. The radius r_0 of the short circuit for the cavity could be varied by using rings of different diameters. Although the diameter of the ground plane was comparatively large, it was not large enough to allow location of the

[15] It is possible to compute approximate value.
[16] Mushiake and Webster, *loc. cit.*

TABLE I*

RADIATION ADMITTANCES OF HIGHER MODES

m	$ka=1$		$ka=2$	
	$G_m{}^e\times1000$	$B_m{}^e\times1000$	$G_m{}^e=1000$	$B_m{}^e\times1000$
0	12.502	29.097	16.601	38.629
1	1.7322	1.515	8.9800	17.155
2	0.4036	−26.529	2.7751	2.540
3	0.2469	−66.793	0.7938	−19.758
4	0.0064	−116.43	0.1036	−46.541
5	0.00009	−174.18	0.0068	−67.378
6		−238.76	0.00027	−110.12
7		−309.48	0.00001	−145.73
8		−385.30		−184.68
m	$ka=3$		$ka=4$	
	$G_m{}^e\times1000$	$B_m{}^e\times1000$	$G_m{}^e\times1000$	$B_m{}^e\times1000$
0	29.255	55.199	33.423	64.433
1	11.391	23.791	17.773	31.345
2	10.194	17.284	13.282	25.413
3	3.6203	4.443	10.920	17.046
4	1.1336	−14.526	4.3248	3.386
5	0.2096	−34.604	1.4441	−15.069
6	0.0218	−62.580	0.3272	−34.618
7	0.0014	−87.607	0.0454	−54.829
8	0.00007	−114.07	0.0042	−75.703
9			0.0003	

($\theta_1=90^\circ$, $\alpha=1^\circ$)

* These values were computed from tabulated values of M_n and $P_n{}^m$ accurate to five decimal places and six significant figures respectively.

TABLE II*

NUMERICAL VALUE OF D_m

m	$ka=1$		$ka=2$	
	Re D_m	Im D_m	Re D_m	Im D_m
0	−0.6170	0.4052	−0.9933	0.8433
1	−0.0597	0.1501	−1.2495	−0.7115
2	−0.1609	−0.02992	−0.4145	−0.2412
3	0.00003	−0.04793	0.02285	−0.4756
4	0.00860	0.00000	0.20704	0.00070
5	−0.00000	0.00112	−0.00001	0.05855
6	−0.00011	−0.00000	−0.01256	−0.00000
7	0.00000	−0.00001	0.00000	−0.00219
8	0.00000	0.00000	0.00032	0.00000
9			−0.00000	0.00004
m	$ka=3$		$ka=4$	
	Re D_m	Im D_m	Re D_m	Im D_m
0	−0.5452	−1.7167	0.09219	−4.2575
1	−2.0777	−1.3542	1.3429	−1.8809
2	0.5542	−2.1619	1.4306	−3.3731
3	0.5158	−0.7507	3.0970	0.2492
4	0.87606	0.06689	1.1571	0.8641
5	−0.00368	0.45698	−0.1368	1.3396
6	−0.16235	−0.00009	−0.7798	−0.1082
7	0.00000	−0.04492	0.00043	−0.32014
8	0.01031	0.00000	0.10422	0.00000
9	−0.00000	0.00203	−0.00000	0.02853
10	−0.00035	0.00000	−0.00679	−0.00000
11			0.00000	−0.00144

($\theta=\theta_1=90^\circ$, $\alpha=1^\circ$)

* These values were computed from tabulated values of M_n and $P_n{}^m$ accurate to five decimal places and six significant figures respectively.

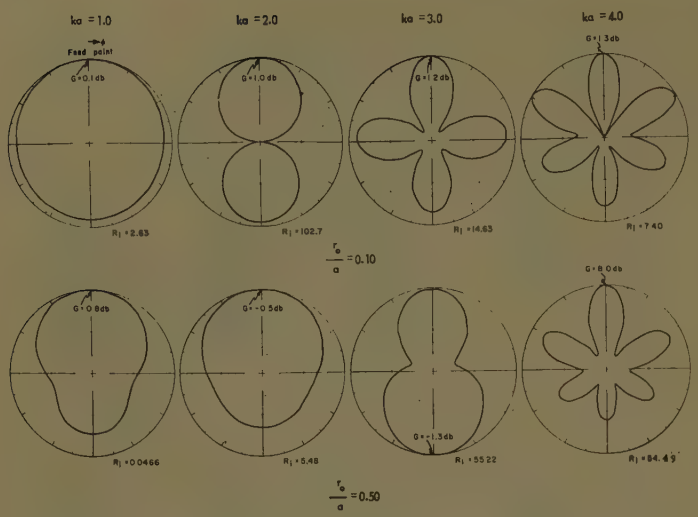

Fig. 4—Calculated electric field intensities of an equatorial slot with single feed point. Relative horizontal plane patterns with maximum gains and input resistances.

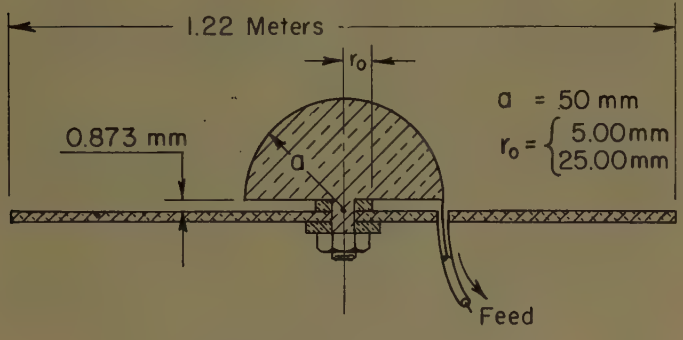

Fig. 5—Experimental apparatus.

transmitting antenna on it (the hemisphere and slot were used as the receiving antenna). The current distribution on the hemisphere, however, was considered to be almost the same as that on a complete sphere; therefore, the radiation intensity from the hemisphere in the equatorial plane beyond the ground sheet must be one-half of that of the complete sphere with the same current. This means that the relative radiation patterns in the equatorial plane are theoretically equal for the hemisphere and the whole sphere, although the absolute intensities are different. This relation does not hold, of course, for $\theta \neq 90°$. From these considerations it is inferable that there may be some error in the measured radiation patterns due to small irregularity of ground plane. In order to check this error, measurements were made at $\theta = 85°$, 90°, and 95° or at $\theta = 88°$, 90°, and 92°.

Fig. 6 (opposite) shows the results of the measurements at $\theta = 90°$ corrected according to the behavior of the patterns for adjacent angles of θ by averaging the three patterns. The frequency range was 955 mc to 4000 mc. Comparing these results with the theoretical ones, we find generally good agreement, except for some discrepancies in the relative magnitudes of lobes and the depth of the nodes for corresponding patterns.

Multiple Feed Points

Next consider a feed system with s feed points distributed around the slot at equal angles as in Fig. 7 (page 54). Assume the impressed current distribution is uniform over the strips of these feed points, *i.e.*,

$$K_\theta(\phi) = \begin{cases} \text{constant}, & \frac{2\pi}{s}u - \beta \leqq |\phi| \leqq \frac{2\pi}{s}u + \beta \\ 0, & \frac{2\pi}{s}u + \beta < |\phi| < \frac{2\pi}{s}(u+1) - \beta \end{cases}$$

$$(u = 0, 1, 2, \cdots \text{ and } u \leqq s/2). \quad (37)$$

Introducing this distribution into (29) and integrating we obtain

$$U_m = \begin{cases} \frac{\sin m\beta}{m\beta}, & m = sq,\ q = 0, 1, 2, \cdots \\ 0, & m = sq + u,\ u = 1, 2, \cdots, s-1. \end{cases} \quad (38)$$

The input impedance where all feed points are connected in parallel is given

$$Z_i = \frac{V(0)}{I} = \sum_{q=0}^{\infty} U_{sq} Z_{sq}{}^t, \quad (39)$$

hence an approximate expression similar to (35) can be obtained:

$$R = \simeq \sum_{q=0}^{q \leqq 10/s} R_{sq}{}^t, \quad (\text{for } \beta \ll 0.1,\ ka \leqq 4). \quad (40)$$

From these relations the power gain over that of a half-wave dipole is determined by

$$G \simeq \frac{73.13}{3600\,(ka)^2} \cdot \frac{\left| \sum_{q=0}^{q \leqq 10/s} Z_{sq}{}^t D_{sq} \cos(sq\phi) \right|^2}{R_i},$$

$$(\text{for } \beta \ll 0.1,\ ka \leqq 4). \quad (41)$$

The relative field intensity patterns with respect to the angle ϕ computed from the numerator of this equation are shown in Fig. 8. The maximum gain calculated from the same equation and the input resistance obtained from (40) are also shown. An inspection of Fig. 8 shows that almost omnidirectional radiation is obtainable by using six feed points around the slot on the sphere of $ka \leqq 4$.

Slots with Assumed Aperture Field Distribution

Uniformly Excited Zonal Slots

As a limiting case of multiple feed points where the number of excitations approaches infinity, uniformly excited zonal slots are considered. Although this type of

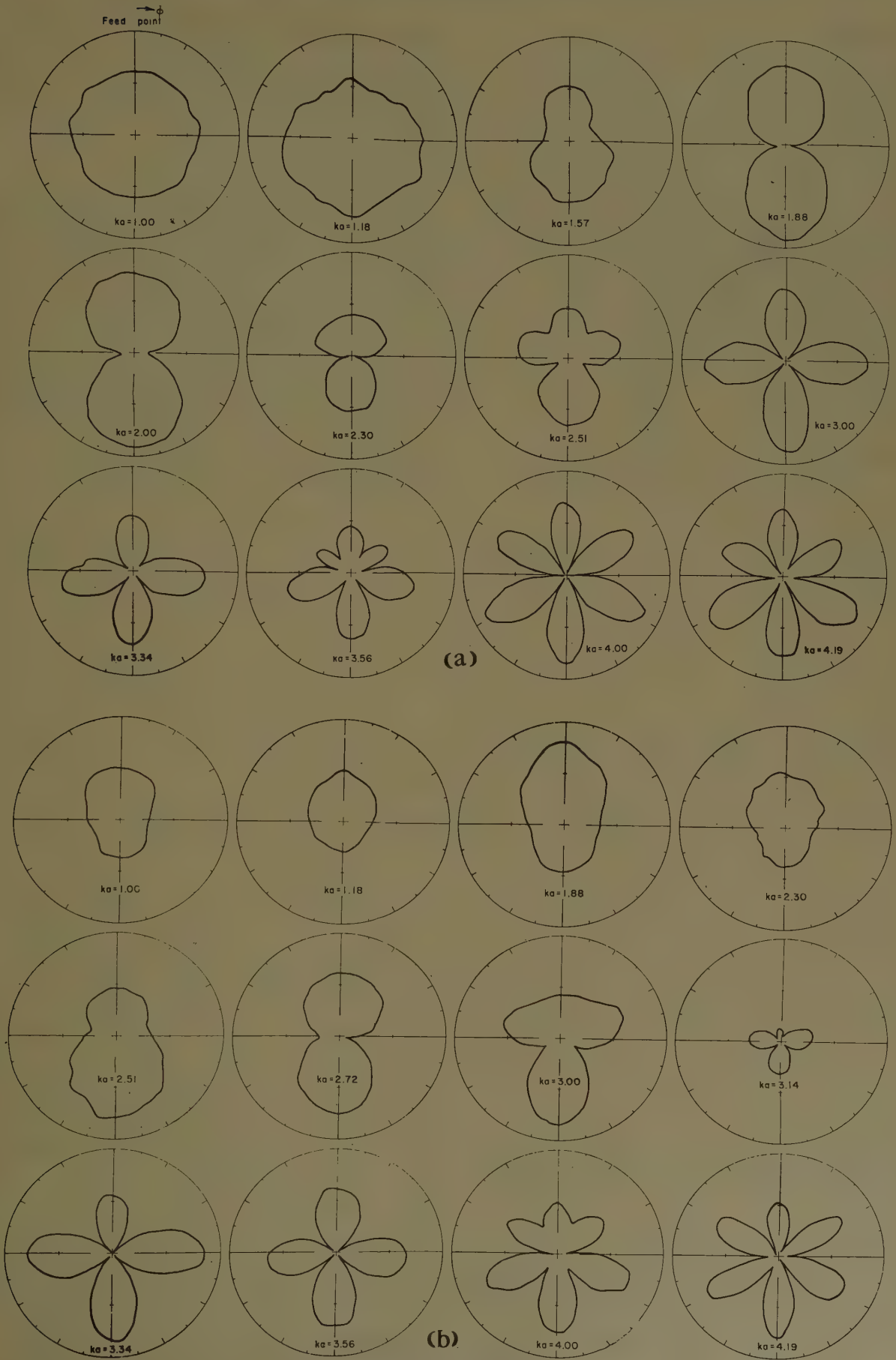

Fig. 6—(a) Measured electric field intensities of an equatorial slot with single feed point. Relative horizontal plane patterns. ($r/r_0=0.1$.) (b) Measured electric field intensities of an equatorial slot with single feed point. Relative horizontal plane patterns. ($r/r_0=0.5$.)

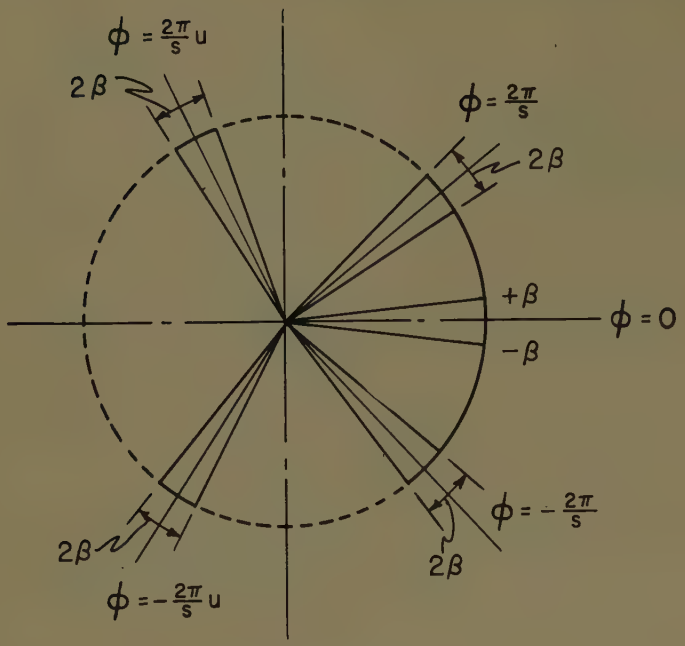

Fig. 7—Multiple feed points.

$$G = \frac{73.13}{3600\,(ka)^2} \cdot \frac{|D_0|^2}{G_0{}^r}. \tag{42}$$

Numerical values of G were computed for $\theta = 90°$ and $\theta_1 = 10°,\ 20°,\ \cdots,\ 90°$. These results are plotted in Fig. 9.

A Half-Wave Slot on a Sphere

A half-wave slot on a closed surface may be used as a gain standard, but the theoretical calculation for such slots is generally not simple. In the case of the slot on a sphere, however, if the aperture field distribution along the slot is assumed, the computations of power gain and radiation pattern are not difficult, because the required mode functions are already given in the preceding discussions. Furthermore, by a procedure similar to that of the section "Zonal Slot Backed by Radial Transmission Line," it is practicable to treat this geometry exactly, if desired, by prescribing the feed system and making no assumptions of the aperture field distribution.

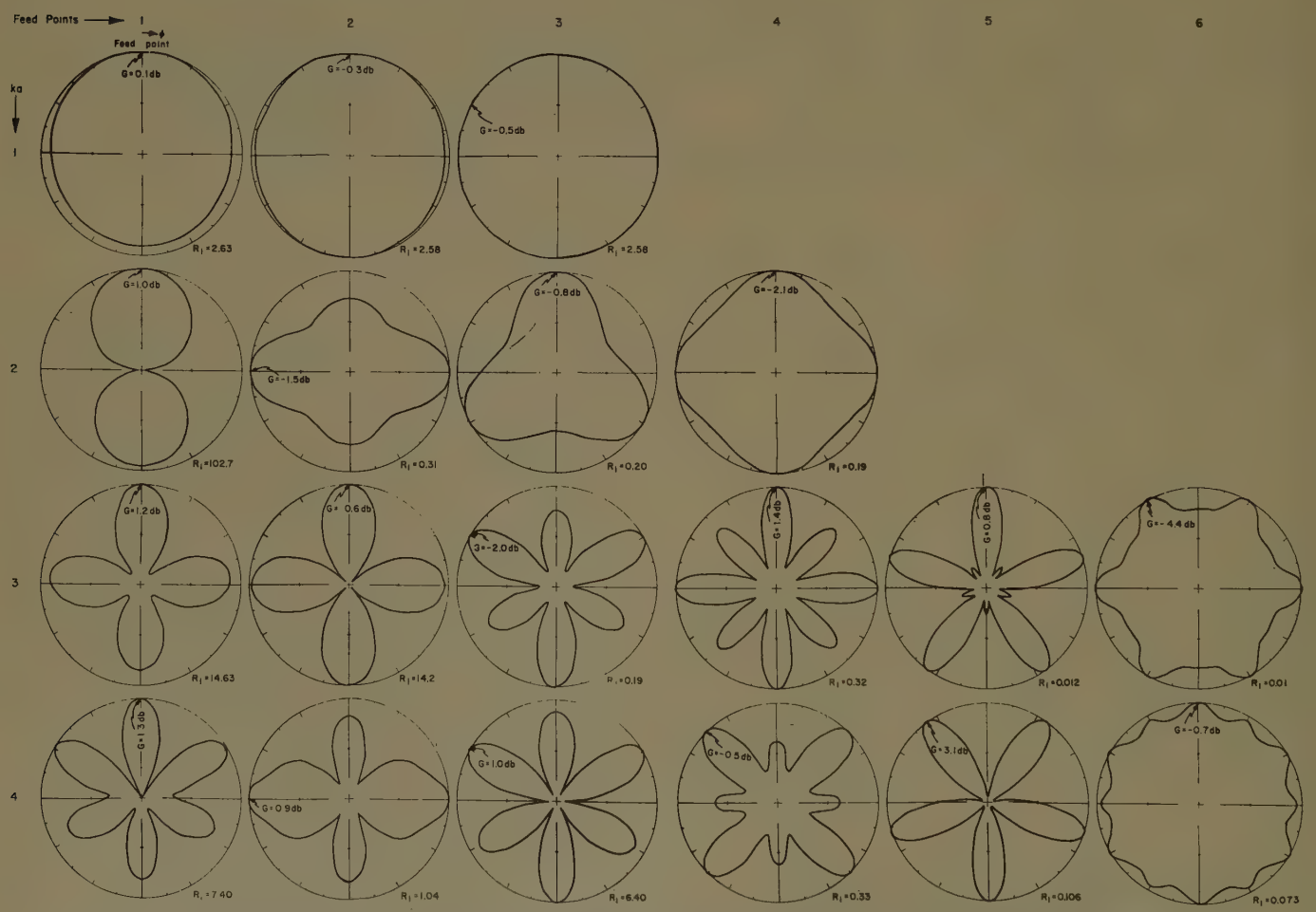

Fig. 8—Calculated electric field intensities of an equatorial slot with multiple feed points. Relative horizontal plane patterns with maximum gains and input resistances.

slot is already discussed by other authors, numerical values of power gains for this antenna have not yet been given. In the case of uniform excitation (16) reduces to

Here let us consider a center-driven slot near a half-wavelength long and located on the equator of the sphere as in Fig. 10. In this case a sinusoidal field distri-

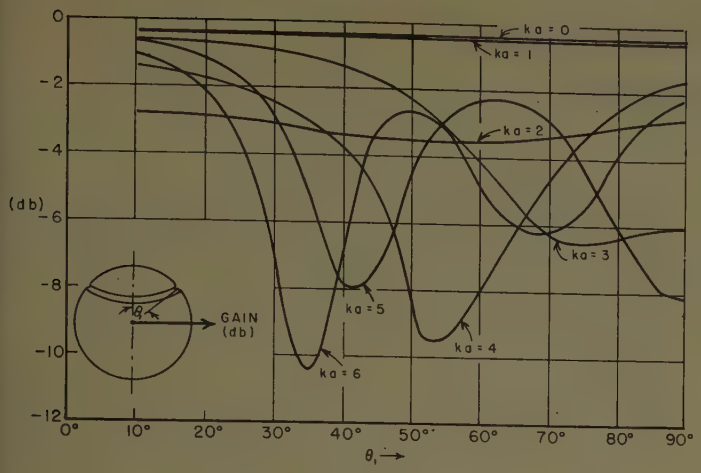

Fig. 9—Power gain of uniformly excited zonal slot over that of a half-wave dipole. Horizontal plane.

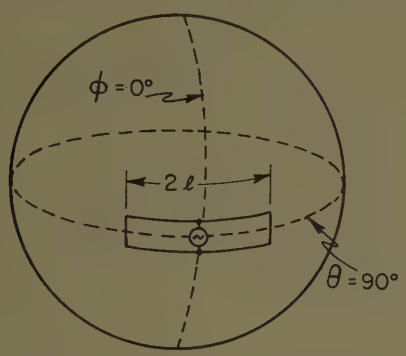

Fig. 10—Half-wave slot on a sphere.

bution expressed by the following equation is a reasonable assumption:

$$V(\phi) = \begin{cases} V \sin\left[\frac{2\pi}{\lambda}(l - a|\phi|)\right], & |a\phi| \leqq l \\ 0, & |a\phi| > l. \end{cases} \quad (43)$$

By Fourier expansion of (43) with respect to ϕ, V_m can be calculated as follows:

$$V_m = \frac{2V}{(1+\delta_m)\pi}\int_0^{l/a} \sin\left[\frac{2\pi}{\lambda}(l - a\phi)\right]\cos m\phi d\phi$$

$$= \begin{cases} \frac{V}{\pi ka}\cdot(1 - \cos kl), & m = 0 \\ \frac{V}{\pi}\cdot\frac{2ka}{(ka)^2 - m^2}\left[\cos\left(m\frac{l}{a}\right) - \cos kl\right], & m \neq ka \quad m \neq 0 \\ \text{and} & \\ \frac{V}{\pi}\cdot\frac{l}{a}\sin kl, & m = ka. \end{cases} \quad (44)$$

Introduction of these values of V_m into (16) gives the power gain over that of a half-wave dipole, and the relative radiation pattern of the slot. These numerical results are shown in Figs. 11 and 12.

As the limiting case where $ka \to \infty$ the radiation pattern and gain for a slot in an infinitely large conducting sheet radiating into half space are plotted in the same figures.

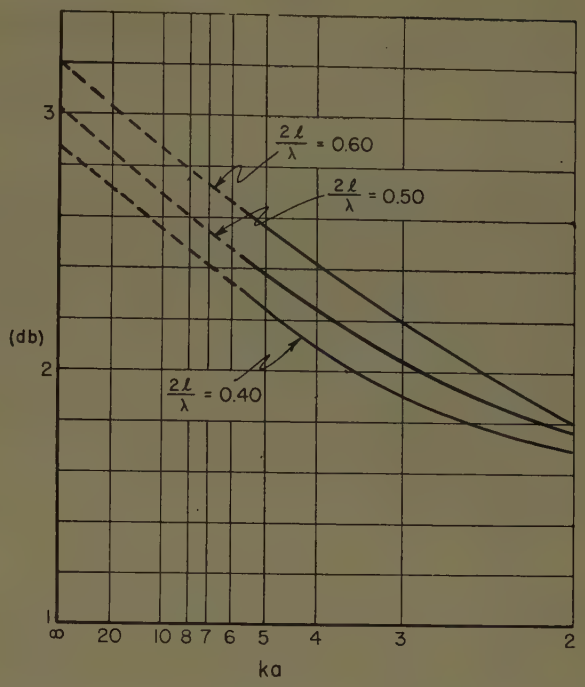

Fig. 11—Power gain of a half-wave slot on a sphere over that of a half-wave dipole (+2.15 db over isotropic source). $\phi = 0°$, $\theta = 90°$.

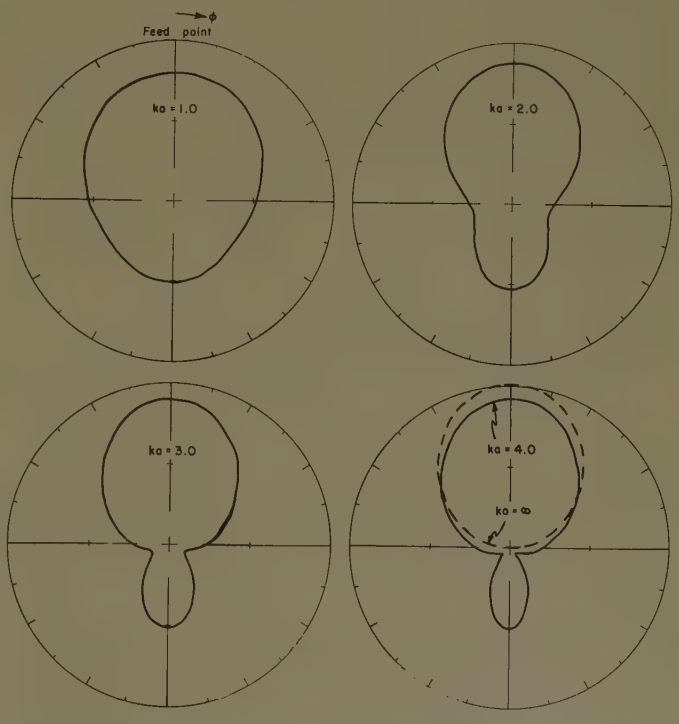

Fig. 12—Calculated electric field intensities of a half-wave slot on a sphere with 3-db power gain circle (over a half-wave dipole). $\theta = 90°$.

Acknowledgment

The work described in the present paper was performed under a contract between the Ohio State University Research Foundation and U. S. Army, Signal Corps Engineering Laboratories, Fort Monmouth, N. J. Acknowledgments are also due Prof. C. T. Tai for his comments concerning the work, and Mrs. Frances Phillips who performed numerical computations.

Cylindrical Radio Waves*

SAMUEL SENSIPER†

Summary—**The formulas required for simple accurate numerical evaluation of the radiation patterns from slots on large circular cylinders are derived. From the usual harmonic series, integral representations are obtained. These lead to either the residue series via the Watson transformation, or to the geometrical-optics representations via a saddle-point evaluation. Considerable attention is given to the calculation of the residue series constants so as to obtain sufficiently accurate numerical values for a wide range of circumference to wavelength ratios. Very good numerical agreement is shown between the representations derived here and results previously obtained from the harmonic series.**

The physical significance of the various representations is discussed and compared.

I. Introduction

MANY RADIATION, diffraction, and scattering problems in electromagnetic theory can often be formally solved in terms of harmonic series representations. However, the numerical handling of such solutions is at least tedious, even if tables of the functions involved are available, and may be practically impossible because of the slow convergence of such representations, if the dimension to wavelength ratio is large. A particular problem of this group, in which such a difficulty occurs, is the one concerning the radiation from slots on a conducting circular cylinder. In this paper, field solutions for this problem are given in terms of representations which are highly convergent, and consequently suitable for numerical computation, particularly when the circumference to wavelength ratio is large.

The development here takes the following course. In Section II, related work on both the sphere and cylinder problem is noted. This is followed by a review of the harmonic series representations in Section III, and by the derivation of the residue series representations and geometrical-optics representations in Sections IV and V, respectively. In Section VI, various expressions and series expansions are given for the residue series constants. Section VII contains a numerical comparison of the different representations, while the analysis of Section VIII shows how the slot-radiated and plane-wave scattered fields are related. In Section IX, the limiting case of a plane boundary is considered. Finally, Section X contains some discussion of the physical significance of the various representations, of the normal mode relationship, and of related problems.

* Manuscript received by the PGAP, May 15, 1956; revised manuscript received, August 24, 1956. This article is a summary of a report with an identical title given as reference 21 here. The work was sponsored by the Air Force Cambridge Research Center, Cambridge, Mass., under Contract AF 19(604)-262.

† Research Labs., Hughes Aircraft Co., Culver City, Calif.

II. Review of Related Work

The analogous sphere problem has been extensively investigated, and since the methods used in that case are intimately related to those used in the cylinder case here, the background of the sphere case is briefly reviewed first.

Many years ago Watson[1] showed how the harmonic series representations for the fields in the case of a source near a large sphere—*i.e.*, radio wave propagation over the earth—could be rigorously transformed via a contour integral into a highly convergent form suitable for use in the "shadow" region. Van der Pol and Bremmer[2] extended the application of this transformation procedure, which yields what they called the residue series. Further, they showed how the integral representations for the fields could also be evaluated by a saddle-point method, and that this latter procedure led to geometrical-optics representations suitable for the "illuminated" region. Eckersley and Millington[3] considered the large sphere problem using the phase integral method and exhibited the result as an eigenfunction solution.

Much of this work, by the above authors and many other investigators up to about 1949, was reviewed and extended in Bremmer's "Terrestrial Radio Waves,"[4] which treats the radio wave propagation problem in great detail and serves as a reference for the techniques available for handling this and related problems.

More recently, Marcuvitz[5] generalized the treatment of spherical diffraction problems via the theory of guided waves and demonstrated the equivalences among the various types of representations, while Friedman,[6] using the method of Watson in considering the large sphere problem, emphasized the eigen-value

[1] G. N. Watson, "The diffraction of radio waves by the earth," *Proc. Roy. Soc. London*, vol. A95, pp. 83–99; 1918; also vol. A95, pp. 546–563; 1919.

[2] B. Van der Pol and H. Bremmer, "The diffraction of electromagnetic waves from an electrical point source round a finitely conducting sphere, with applications to radiotelegraphy and the theory of the rainbow; the propagation of radio waves over a finitely conducting spherical earth"; *Phil. Mag.*, S. 7, vol. 24, pp. 141–176; July, 1937; S. 7, vol. 24, pp. 825–864; Suppl., November, 1937; S. 7, vol. 25, pp. 817–834; Suppl., June, 1938; S. 7, vol. 27, pp. 261–275; March, 1939.

[3] T. L. Eckersley and G. Millington, "Application of the phase integral method to the analysis of the diffraction and refraction of wireless waves round the earth," *Phil. Trans. Roy. Soc. London*, vol. A237, pp. 273–309; June, 1938.

[4] H. Bremmer, "Terrestrial Radio Waves," Elsevier Publishing Co., Inc., New York, N. Y.; 1949.

[5] N. Marcuvitz, "Field Representations in Spherically Stratified Regions," in "Theory of Electromagnetic Waves," Interscience Publishers, New York, N. Y., pp. 263–315; 1951.

[6] B. Friedman, "Propagation in a Non-Homogeneous Atmosphere," in "Theory of Electromagnetic Waves," Interscience Publishers, New York, N. Y., pp. 317–350; 1951.

nature of the highly convergent so-called residue series solution.

We now review some of the past work on the cylinder problem. Carter[7] considered various examples of dipole sources near a circular conducting cylinder and derived expressions for the fields in terms of harmonic series, *i.e.*, infinite series of integer order Bessel and Hankel functions. Recently, Lucke,[8] among others, showed similar results. The very analogous case of slots on circular cylinders was considered by Sinclair, Jordan, and Vaughn,[9] and also by Sinclair.[10] Silver and Saunders[11,12] considered both axial and circumferential slots and rigorously demonstrated that the equatorial plane patterns are independent of the axial extent of the slot on the cylinder. Papas[13] and Papas and King[14] also discussed the problem of radiation from slots on circular cylinders. In all these cases the representations for the solutions were in the form of harmonic series and, in nearly all where numerical work was shown, the circumference to wavelength ratio—which we shall designate as ka hereafter—was relatively small, that is, less than five. Taylor[15] (see also Sensiper, *et al.*[16]) showed radiation patterns in the equatorial plane from axial and circumferential slots for $ka=8$ and 12, and indicated that relatively simple empirically derived expressions represented to a good approximation the results obtained from extensive computation with the harmonic series. Also using the harmonic series, Bailin[17] determined the amplitude and phase of the radiation patterns from both axial and circumferential slots on a circular cylinder for $ka=8$ and 12, not only for the full azimuth angle, but also for a wide range of angles from the equatorial plane. Wait, Pope, and O'Grady,[18] using similar means, have shown the radiation patterns from axial slots on a circular cylinder for a wide range of values of ka up to $ka=21$.

As is often the case, several workers apparently realized almost simultaneously that the convergence limitations of the harmonic series representations for the cylinder case could be overcome by means already well known in the sphere problem. In a preliminary report, Sensiper[16] derived the residue series representation and noted the geometrical-optics representation. Based on earlier unpublished work, Franz and Depperman[19] showed the application of what they called a surface or "creeping wave" to the diffraction of an electromagnetic wave by a circular cylinder. The radiation and diffraction problem are of course intimately connected. Riblet,[20] considering the circular cylinder diffraction problem, also, indicated the application of normal mode expansions (equivalent to the residue series) and geometrical-optics approximations. In a report on which the present article is based, the residue series and the geometrical-optics representations for describing the radiation patterns of an axial and a circumferential slot were considered in detail.[21] Using similar means, Imai[22] analyzed the problem of the diffraction of an incident plane wave by a circular cylinder. He showed results very closely related to those obtained before,[21] and demonstrated the connection between the residue series waves and the "creeping waves" of Franz and Deppermann.[19] Proceeding in a similar manner, Franz[23] derived the representations for the Green's function for a circular cylinder. Friedlander[24] considered the scattering of a scalar wave pulse by a circular cylinder and obtained results related to those derived by the above-mentioned workers. In a recent report, Bailin and Spellmire[25] have extended previous work,[21] and demonstrated, in considerable detail, that extremely accurate numerical results for the radiation patterns from slots on large-

[7] P. S. Carter, "Antenna arrays around cylinders," PROC. IRE, vol. 31, pp. 671–693; December, 1943.

[8] W. S. Lucke, "Electric dipoles in the presence of elliptic and circular cylinders," *J. Appl. Phys.*, vol. 22, pp. 14–19; January, 1951.

[9] G. Sinclair, E. C. Jordan, and E. W. Vaughn, "Measurement of aircraft antenna patterns using models," PROC. IRE, vol. 35, pp. 1451–1462; December, 1947.

[10] G. Sinclair, "The patterns of slotted-cylinder antennas," PROC. IRE, vol. 36, pp. 1487–1492; December, 1948.

[11] S. Silver and W. K. Saunders, "The external field produced by a slot in an infinite circular cylinder," *J. Appl. Phys.*, vol. 21, pp. 153–158; February, 1950.

[12] S. Silver and W. K. Saunders, "The radiation from a transverse slot in a circular cylinder," *J. Appl. Phys.*, vol. 21, pp. 745–749; August, 1950.

[13] C. H. Papas, "Radiation from a transverse slot in an infinite cylinder," *J. Math. Phys.*, vol. 28, pp. 227–236; January, 1950.

[14] C. H. Papas and R. King, "Currents on the surface of an infinite cylinder excited by an axial slot," *Quar. Appl. Math.*, vol. 7, pp. 175–182; July, 1949.

[15] T. T. Taylor, "Design of Circular and Cylindrical Antennas," Hughes Aircraft Co., Res. and Dev. Labs., T.M. no. 280; January, 1952.

[16] S. Sensiper, W. G. Sterns, and T. T. Taylor, "A further study of the patterns of single slots on circular conducting cylinders," IRE TRANS., PGAP-3, pp. 240–250; August 1952; based on a paper presented at the Joint IRE-URSI Meeting, Washington, D. C.; April 21–24, 1952.

[17] L. L. Bailin, "The radiation field produced by a slot in a large circular cylinder," IRE TRANS., vol. AP-3, pp. 128–137; July, 1955; also, Hughes Aircraft Co., Res. and Dev. Labs., T.M. no. 309; June, 1953.

[18] J. R. Wait, W. A. Pope, and M. O'Grady, "Radiation Characteristics of Axial Slots on a Conducting Cylinder," Radio Phys. Lab., Def. Res. Telecommun. Estab., Ottawa, Can., PCC No. D-48-55-40-07; November, 1954.

[19] W. Franz and K. Deppermann, "Theory of diffraction by a cylinder as affected by the surface wave," *Ann. der Physik*, Ser. 6, vol. 10, pp. 361–373; 1952.

[20] H. J. Riblet, "Geometrical Optics Currents," Quarterly and Final Rep. on Contract No. AF 19(122)-167 for December, 1949 to December, 1952 from Microwave Dev. Labs., Inc., to Air Force Cambridge Res. Labs.

[21] S. Sensiper, "Cylindrical Radio Waves," Hughes Aircraft Co., Res. and Dev. Labs., T.M. no. 310; June, 1953.

[22] I. Imai, "The diffraction of electromagnetic waves by a circular cylinder," *Zeit. Physik*, vol. 137, pp. 31–48; 1954.

[23] W. Franz, "The Green's functions of cylinders and spheres," *Zeit. Naturforschung*, vol. 9a, pp. 705–716; September, 1954.

[24] F. G. Friedlander, "Diffraction of pulses by a cylinder," *Comm. on Pure and Applied Math.*, vol. 7, pp. 705–732; November, 1954.

[25] L. L. Bailin and R. J. Spellmire, "Convergent Representations for the Radiation Fields from Slots in Large Circular Cylinders," Hughes Aircraft Co., Res. and Dev. Labs., T.M. no. 386; July, 1955; also, paper presented at URSI Michigan Symposium on Electromagnetic Theory; June, 1955; to be submitted for publication.

diameter circular cylinders can be obtained by means of the residue series and geometrical-optics representations.

Work related to the above has been done by Lucke,[26] who, using the residue series obtained via the Watson transformation, computed the mutual admittance between slots on circular cylinders with large ka. Also, Jasik[27] used both residue series and geometrical-optics approximations to determine the diffraction caused by a transparent circular cylinder, in which the dielectric constant varied with radius so as to cause focusing, *i.e.*, the Luneberg lens. Very recently, Franz and Beckmann[28] extended previous work[19,23] to cylinders of finite conductivity.

Also, Keller[29] treated the scattering of a plane wave by an arbitrary convex cylinder and showed results similar in form to those available for the special case of a circular cylinder.

The above review is hardly comprehensive, but cannot be extended here. For a more complete review as of mid-1953 of work related to the present investigation, the interested reader is referred elsewhere.[21]

III. Harmonic Series Representations

Although the results in this section have been given elsewhere, they are briefly reviewed for ready reference and for the sake of continuity and definition. The configurations we are concerned with are shown in Fig. 1(a) and 1(b), and are called the infinite axial slot and the infinite circumferential slot, respectively. It is assumed that the source distributions over the slots on the cylinders are known. Cylindrical coordinates r, ϕ, and z are used, with a the radius of the perfectly conducting cylinders. The time variation of the fields is taken to be harmonic, that is, $e^{j\omega t}$, with ω the radian frequency, and the usual conventions are followed. The cylinder is taken to be immersed in free space with ϵ and μ, the permittivity and permeability of free space, respectively, so that

$$k^2 = \omega^2\mu\epsilon = \left(\frac{2\pi}{\lambda}\right)^2. \tag{1}$$

Further notation and additional definitions are introduced as they are required. It turns out that many of the field representations for finite slots are similar in form to those derived for infinite slots, so that the results given here are generally useful.[10–12] More is said of this later.

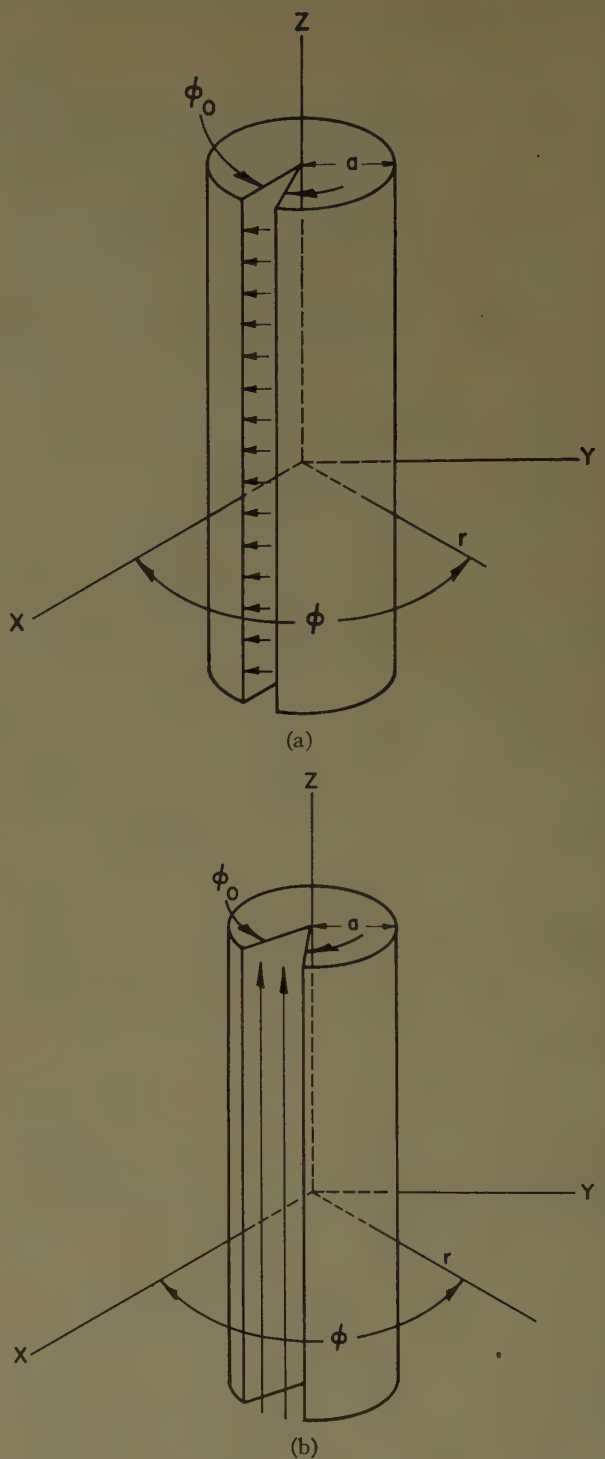

Fig. 1—(a) Infinite axial slot with only E_ϕ as the source component. (b) Infinite circumferential slot with only E_z as the source component.

A. The Axial Slot

With E_ϕ the only electric field component of the source and $\partial/\partial z = 0$ because of the two-dimensional character of the problem, $E_z = H_r = H_\phi = 0$. The remaining components can be derived from a magnetic Hertzian potential π_z*.[30]

[26] W. S. Lucke, "Mutual Admittance of Slots in Cylinders," Tech. Rep. no. 36, Project No. 591, Stanford Research Institute, Menlo Park, Calif.; February, 1953.

[27] H. Jasik, "The Electromagnetic Theory of the Luneberg Lens," D.E.E. thesis, Dept. of Elec. Eng., Polytechnic Institute of Brooklyn, Brooklyn, N. Y.; May, 1953.

[28] W. Franz and P. Beckmann, "Creeping waves for objects of finite conductivity," IRE Trans., vol. AP-4, pp. 203–208; July, 1956.

[29] J. B. Keller, "Diffraction by a convex cylinder," IRE Trans., vol. AP-4, pp. 312–321; July, 1956.

[30] J. A. Stratton, "Electromagnetic Theory," McGraw-Hill Book Co., Inc., New York, N. Y., pp. 28–32; 1951.

$$E_r = -j\frac{\omega\mu}{r}\frac{\partial \pi_z^*}{\partial \phi} \quad (2a); \qquad E_\phi = j\omega\mu\frac{\partial \pi_z^*}{\partial r} \quad (2b);$$

$$H_z = k^2\pi_z^*. \quad (2c)$$

π_z^*, of course, satisfies the cylindrical scalar wave equation, and one finds, on adding the complete orthogonal (in ϕ) set of elementary solutions, that

$$\pi_z^* = \sum_n A_n H_n^{(2)}(kr)e^{-jn\phi}. \quad (3)$$

$\sum_n$ means summation over all integer values of n including zero, and $H_n^{(2)}(kr)$ is the proper cylindrical function for the solution to have outgoing wave character for large r. Here we use the notation defined by Watson.[31] A_n in (3) is determined from a Fourier expansion of E_ϕ at $r=a$, E_ϕ being zero except over the slot, so that

$$\pi_z^* = \frac{V}{i2\pi a\omega\mu k}\sum_n f_n(\phi_0)\frac{H_n^{(2)}(kr)}{H_n^{(2)\prime}(ka)}e^{-jn\phi}. \quad (4)$$

The prime notation is used in (4) and in general here to designate differentiation with respect to the argument; that is, $f'(z)=df(z)/dz$. $f_n(\phi_0)$ depends on the assumed source distribution and one possible distribution is:

Type	*Distribution*	$f_n(\phi_0)$
constant field	$E_\phi(r=a)=\frac{V}{a\phi_0}, \quad \frac{\phi_0}{2}>\phi>\frac{-\phi_0}{2}$ $=0$, elsewhere.	$\frac{\sin\frac{n\phi_0}{2}}{\frac{n\phi_0}{2}}$

(5)

If the electric field across the gap becomes infinitely large as the gap width ϕ_0 becomes zero in such a manner that the voltage V,

$$V = \left|\int_{-\phi_0/2}^{\phi_0/2} E_\phi(r=a)d\phi\right|,$$

across the gap remains constant, the source becomes the usual delta source of magnitude V/a and $f_n(\phi_0)=1$. The fields can be derived from (4) through the use of (2). Incidentally, throughout this report it is assumed that the gap sources are centered at $\phi=0$; however, it should be clear that the potential and fields for other locations can be readily obtained through a simple rotation.

[31] G. N. Watson, "Theory of Bessel Functions," The Macmillan Co., New York, N. Y., 2nd ed., pp. 73–74; 1948.

B. The Circumferential Slot

Here, with E_z the only electric field component of the source and $\partial/\partial z=0$, $E_r=E_\phi=H_z=0$. The remaining components are derivable from an electric Hertzian potential π_z:

$$E_z = k^2\pi_z \quad (6a); \qquad H_r = \frac{j\omega\epsilon}{r}\frac{\partial \pi_z}{\partial \phi} \quad (6b);$$

$$H_\phi = -j\omega\epsilon\frac{\partial \pi_z}{\partial r}. \quad (6c)$$

Proceeding through the same arguments as before, one obtains

$$\pi_z = \frac{|E|}{2\pi k^2}\sum_n g_n(\phi_0)\frac{H_n^{(2)}(kr)}{H_n^{(2)}(ka)}e^{-jn\phi}. \quad (7)$$

$g_n(\phi_0)$ depends on the assumed source distribution, and one possible distribution is, in this case:

Type	*Distribution*	$g_n(\phi_0)$
cosine field	$E_z(r=a)=\lvert E\rvert\cos\frac{\pi}{\phi_0}\phi, \quad \frac{\phi_0}{2}>\phi>\frac{-\phi_0}{2}$ $=0$, elsewhere.	$\frac{2\pi}{\phi_0}\frac{\cos\frac{n\phi_0}{2}}{\left(\frac{\pi}{\phi_0}\right)^2-n^2}$

(8)

$|E|$ is the source maximum electric field strength. A sort of normalization is possible by requiring

$$\int_{-\phi_0/2}^{\phi_0/2} E_z(r=a)d\phi = 1;$$

with this, in (8), $|E|=\pi/2\phi_0$. Thus, with ϕ_0 becoming zero, the potential for a type of delta source results. The fields can be derived from (7) through the use of (6).

IV. Residue Series Representations

A. The Axial Slot

In order to derive the residue series, it is first necessary to recognize that an integral representation for π_z^* can be written as follows:

$$\pi_z^* = \frac{V}{j2\pi a\omega\mu k}\frac{1}{2j}\int_{C_1} f_\nu(\phi_0)\frac{H_\nu^{(2)}(kr)}{H_\nu^{(2)\prime}(ka)}e^{-j\nu\phi}\frac{e^{j\nu\pi}}{\sin\nu\pi}d\nu, \quad (9)$$

where ν is a complex variable. C_1 is a contour around the real ν axis as shown in Fig. 2, and is presumed to be closed across the real axis so as to avoid any poles of the integrand, with the abscissas across which the contour is closed approaching $\pm\infty$. Within C_1 the only poles of the integrand occur where $\sin\nu\pi=0$, that is, for real integer values of ν. The integral can be readily

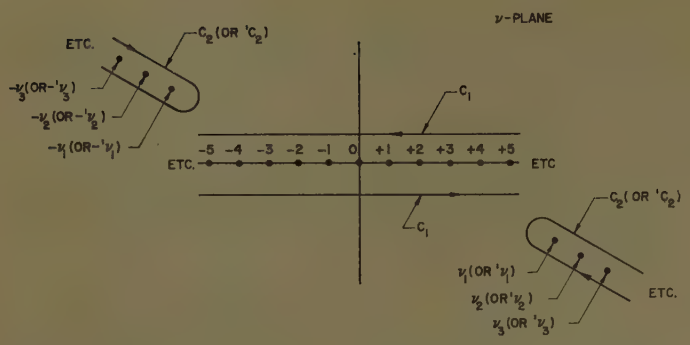

Fig. 2—ν plane showing contour C_1 around the real axis, contour C_2 around the complex ν_m roots where $H_{\nu_m}^{(2)}(z)=0$, and contour $'C_2$ around the complex $'\nu_m$ roots where $H'_{\nu_m}{}^{(2)'}(z)=0$.

evaluated by making use of the theory of residues, and the equivalence between the integral in (9) and the series in (4) is established.

In the limit, the contour C_1 is equivalent to two line integrals, one above and one below the real axis. In the usual way, the ends of the line integrals comprising C_1 are joined in the upper and lower half planes by large semicircles of radius R, drawn so as to avoid any singularities of the integrand. These contours can be closed, since the integrand contains no branch cuts but only simple poles. In general, the integrals along the semicircles approach zero as R approaches infinity, so that the line integrals can be deformed to enclose the poles of the integrand in the upper and lower half planes. These are the complex roots of $H_\nu^{(2)'}(ka)=0$ located as shown in Fig. 2. Therefore, the integral along C_1 can be deformed to one along $'C_2$, which is evaluated by the theory of residues.

Since

$$H_\nu^{(2)}(z) = e^{j\nu\pi}H_{-\nu}^{(2)}(z) = \frac{e^{j\nu\pi/2}}{j\sin\nu\pi}\left[e^{j(\nu\pi/2)}J_\nu(z) - e^{-j(\nu\pi/2)}J_{-\nu}(z)\right],^{31} \quad (10)$$

it is clear that if ν_m is a root of $H_\nu^{(2)}(z)=0$ then $-\nu_m$ is also. Obviously, this also applies to the ν roots of $H_\nu^{(2)'}(z)=0$, which are designated here by $'\nu_m$. We are using the convention that the roots are numbered $m=1, 2, 3, \cdots$, and that ν_m and $'\nu_m$ refer to those roots of $H_\nu^{(2)}(z)=0$ and $H_\nu^{(2)'}(z)=0$, respectively, whose real parts are greater than zero. On evaluation of the integral along $'C_2$, we obtain, after making use of (10), the characteristics of $'\nu_m$ roots, and the evenness of $f_\nu(\phi_0)$ in ν,

$$\pi_z{}^* = -\frac{V}{a\omega\mu k}\sum_{m=1}^{\infty} f_{'\nu_m}(\phi_0)\frac{H_{'\nu_m}^{(2)}(kr)}{e^{j'\nu_m\pi/2}}\frac{\cos{'\nu_m}(\pi-\phi)}{M_{|'\nu_m|}}, \quad (11a)$$

where

$$M_{|'\nu_m|} = \frac{j\sin{'\nu_m}\pi}{e^{j'\nu_m\pi/2}}\left[\frac{\partial H_\nu^{(2)'}(ka)}{\partial\nu}\right]_{\nu='\nu_m}. \quad (11b)$$

Similar expressions for the field components are readily obtained.

B. The Circumferential Slot

In this case the analysis proceeds in essentially the same fashion as for the axial slot. Consequently,

$$\pi_z = \frac{|E|}{2\pi k^2}\frac{1}{2j}\int_{C_1} g_\nu(\phi_0)\frac{H_\nu^{(2)}(kr)}{H_\nu^{(2)}(ka)}\frac{e^{j\nu(\pi-\phi)}}{\sin\nu\pi}\,d\nu. \quad (12)$$

Upon deforming C_1 into C_2 (see Fig. 2) we obtain, in an identical manner as before,

$$\pi_z = -j\frac{|E|}{k^2}\sum_{m=1}^{\infty} g_{\nu_m}(\phi_0)\frac{H_{\nu_m}^{(2)}(kr)}{e^{j\nu_m\pi/2}}\frac{\cos\nu_m(\pi-\phi)}{M_{|\nu_m|}}, \quad (13a)$$

where

$$M_{|\nu_m|} = \frac{j\sin\nu_m\pi}{e^{j\nu_m\pi/2}}\left[\frac{\partial H_\nu^{(2)}(ka)}{\partial\nu}\right]_{\nu=\nu_m}. \quad (13b)$$

and where ν_m has already been defined. Obviously, in this case also, similar expressions for the field components are readily obtained.

V. Geometrical-Optics Representations

Although the residue series derived above are highly convergent in the region near $\phi=\pi$, many terms are required near the illuminated region, and, in fact, the residue series are divergent in this latter region, *i.e.*, for $|\pi-\phi|>\pi/2$.[32] By handling the integral representations, (9) and (12)—or similar ones for the field components—in a different fashion, we can obtain representations more suitable for computation in the illuminated region. The procedure used below has been described in some detail and applied to the sphere case by Van der Pol and Bremmer.[2,4]

A. The Axial Slot

Since the contour C_1 is equivalent to two line integrals, one above and one below the real axis, from (9):

$$\pi_z{}^* = -\frac{V}{4\pi a\omega\mu k}\int_{C_1} f_\nu(\phi_0)\frac{H_\nu^{(2)}(kr)}{H_\nu^{(2)'}(ka)}\frac{e^{j\nu(\pi-\phi)}}{\sin\nu\pi}\,d\nu = -\frac{V}{4\pi a\omega\mu k}\left[\int_{\infty+j\epsilon}^{-\infty+j\epsilon}(\cdots)d\nu + \int_{-\infty-j\epsilon}^{\infty-j\epsilon}(\cdots)d\nu\right], \quad (14)$$

with ϵ positive, small, and real. Now,

$$\frac{1}{\sin\nu\pi} = \frac{\mp 2j}{e^{\mp j\nu\pi}}\frac{1}{1-e^{\pm j2\nu\pi}} = \mp 2j\sum_{m=0}^{\infty} e^{\pm j\nu(2m+1)\pi}, \quad (15)$$

where the upper and lower signs must be used in the upper and lower half planes, respectively. To put the

[32] This was shown by Franz, *op. cit.* and indicated by Friedlander, *op. cit.* The author had previously presumed (Sensiper, *op. cit.*) that the residue series are convergent for nearly all values of $\phi(\phi_0/2>\phi>-\phi_0/2$ possibly excepted), since the integrals over the infinite semicircles in the ν plane vanish, except, in some cases, for $\phi_0/2>\phi>-\phi_0/2$. However, in the illuminated region $|\pi-\phi|>\pi/2$, the terms in the residue series have exponential growth with m as $m\to\infty$. This can be shown by the use of the large order ν (or $'\nu$) representations noted, in fact, by the author himself as well as by Watson, *op. cit.*, and Franz, *op. cit.* and by the use of the large order residue and function values (Sensiper, *op. cit.*, and Watson, *op. cit.*).

integrands in such a form that for large ka the denominators do not have exponential character we multiply by $H_\nu^{(1)\prime}(ka)/H_\nu^{(1)\prime}(ka)$.[33] Also, to convert the integrals in (14) into the multidimensional integrals required to compute the geometrical-optics representation, the Hankel functions in the numerators are replaced by their Sommerfeld integral representations:

$$H_\nu^{(1)}(z) = -\frac{1}{\pi}\int_{\eta-j\infty}^{-\eta+j\infty} e^{jz\cos\tau_1+j\nu(\tau_1-\pi/2)}d\tau_1, \quad (16a)$$

$$H_\nu^{(2)}(z) = \frac{1}{\pi}\int_{-\pi+\eta-j\infty}^{\pi-\eta+j\infty} e^{-jz\cos\tau_2-j\nu(\tau_2-\pi/2)}d\tau_2, \quad (16b)$$

where $-\arg z<\eta<\pi-\arg z$.[34,35] Performing the identity multiplication noted above, and using (15) and (16), we obtain

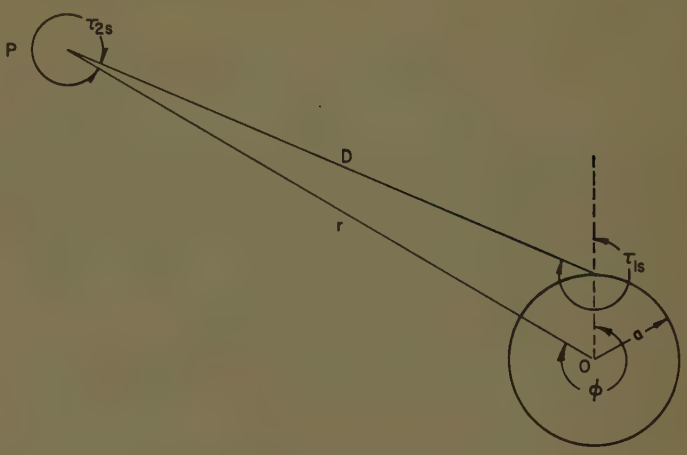

Fig. 3—Geometrical-optics parameters for $2\pi>\phi>(3\pi/2)$.

$$\pi_z^* = -\frac{V}{2\pi^3 a\omega\mu k}\sum_{m=0}^{\infty}\left\{\int_{-\infty+j\epsilon}^{\infty+j\epsilon}\frac{f_\nu(\phi_0)d\nu}{H_\nu^{(2)\prime}(ka)H_\nu^{(1)\prime}(ka)}\int_{\eta-j\infty}^{-\eta+j\infty}d\tau_1\int_{-\pi+\eta-j\infty}^{\pi-\eta+j\infty}d\tau_2\cos\tau_1 e^{jS_m^+}\right.$$
$$\left.+\int_{-\infty-j\epsilon}^{\infty-j\epsilon}\frac{f_\nu(\phi_0)d\nu}{H_\nu^{(2)\prime}(ka)H_\nu^{(1)\prime}(ka)}\int_{\eta-j\infty}^{-\eta+j\infty}d\tau_3\int_{-\pi+\eta-j\infty}^{\pi-\eta+j\infty}d\tau_4\cos\tau_3 e^{jS_m^-}\right\}, \quad (17)$$

where

$$S_m^+ = -kr\cos\tau_2 + ka\cos\tau_1 + \nu[2(m+1)\pi-\phi+\tau_1-\tau_2], \quad (18a)$$

and

$$S_m^- = -kr\cos\tau_4 + ka\cos\tau_3 + \nu[-2m\pi-\phi+\tau_3-\tau_4]. \quad (18b)$$

Eq. (17) is evaluated by means of a second-order saddle-point integration. If

$$I = \int_{-\infty}^{\infty}\cdots\int_{-\infty}^{\infty}A(z_1, z_2, \cdots, z_n)\cdot e^{f(z_1,z_2,\cdots,z_n)}dz_1dz_2,\cdots,dz_n, \quad (19a)$$

then the second-order approximation is given by

$$I_2 \sim \frac{(j\sqrt{2\pi})^n}{\sqrt{\Delta_s}}A(z_{1s}, z_{2s}, \cdots, z_{ns})e^{f(z_{1s},z_{2s},\cdots,z_{ns})}, \quad (19b)$$

where Δ_s is the nth-order determinant

$$\Delta_s = \left[\frac{\partial^2 f}{\partial z_p\partial z_q}\right]_s, \quad (19c)$$

and p and q take on all values from 1 to n.[36] The subscript s indicates that the quantities are evaluated at the saddle-point, that is, where

$$\frac{\partial f}{\partial z_1} = \frac{\partial f}{\partial z_2} = \cdots \frac{\partial f}{\partial z_n} = 0. \quad (19d)$$

From

$$\frac{\partial S_0^+}{\partial\tau_1} = \frac{\partial S_0^+}{\partial\tau_2} = \frac{\partial S_0^+}{\partial\nu} = 0,$$

we obtain

$$kr\sin\tau_{2s} = \nu_s^+, \quad (20a) \qquad ka\sin\tau_{1s} = \nu_s^+, \quad (20b)$$
$$\tau_{2s}-\tau_{1s} = 2\pi-\phi, \quad (20c)$$

where the + superscript is attached to ν_s^+ to distinguish it from a similar quantity obtained from S_0^-. From (20a) and (20b),

$$\frac{\sin\tau_{2s}}{\sin\tau_{1s}} = a/r. \quad (21)$$

Inspection shows that the position of this saddle point has the physical interpretation indicated in Fig. 3. It appears that the integral with the phase factor S_0^+ gives the fields resulting from rays reaching the observation point P, located as in Fig. 3, in the region of space where $2\pi>\phi>(3\pi/2)$ approximately. From

$$\frac{\partial S_0^-}{\partial\tau_3} = \frac{\partial S_0^-}{\partial\tau_4} = \frac{\partial S_0^-}{\partial\nu} = 0,$$

we obtain

$$kr\sin\tau_{4s} = \nu_s^-, \quad (22a) \qquad ka\sin\tau_{3s} = \nu_s^-, \quad (22b)$$
$$\tau_{3s}-\tau_{4s} = \phi. \quad (22c)$$

[33] Bremmer, *op. cit.*, p. 87.
[34] *Ibid.*, p. 37.
[35] A. Sommerfeld, "Partial Differential Equations in Physics," Academic Press, New York, N. Y., p. 89; 1949.
[36] Bremmer, *op. cit.*, p. 24.

Here

$$\frac{\sin \tau_{4s}}{\sin \tau_{3s}} = a/r, \tag{23}$$

and the position of this saddle point has the interpretation shown in Fig. 4. The integral with the phase factor S_0^- gives the fields resulting from rays reaching the observation point P located as in Fig. 4, in the region of space where $(\pi/2) > \phi > 0$, approximately. It now appears that, depending on the location of P, *i.e.*, the value of ϕ, π_z^* is given to this second-order approximation by one or the other of the multidimensional integrals in (17). This is evidently a result of the multivalued character of the ϕ coordinate in the circular coordinate system. As might be expected, upon evaluation to this approximation, both integrals with $m=0$ have precisely the same value and are even functions of ϕ. Further, the integrals for $m>0$ in (17) correspond to "rays" in the higher-order sheets of the Riemann surface defined by continuously increasing or decreasing ϕ.[24] Because of this interpretation, it is assumed that the contribution of these integrals is negligibly small.

Now

$$S_{0s}^- = -kr \cos \tau_{4s} + ka \cos \tau_{3s} = -kD, \tag{24}$$

and

$$\Delta_s = (j)^3(-kr \cos \tau_{4s} + ka \cos \tau_{3s}) = jkD, \tag{25}$$

where D is shown in Fig. 4. In the integrands in (17), $\cos \tau_1$ and $\cos \tau_3$ are slowly varying quantities compared to the exponentials, and correspond to the $A(z_1, z_2, \cdots, z_n)$ factor in (19a). Using (19b), (24), and (25), we find

$$\pi_z^* \sim \frac{V}{2\pi a \omega \mu k} \frac{2}{\pi} \frac{f_{\nu_s}^-(\phi_0) \cos \tau_{3s}}{H_{\nu_s}^{-(2)'}(ka) H_{\nu_s}^{-(1)'}(ka)} (2\pi)^{1/2} \cdot \frac{e^{-j(kD-(\pi/4))}}{(kD)^{1/2}}. \tag{26}$$

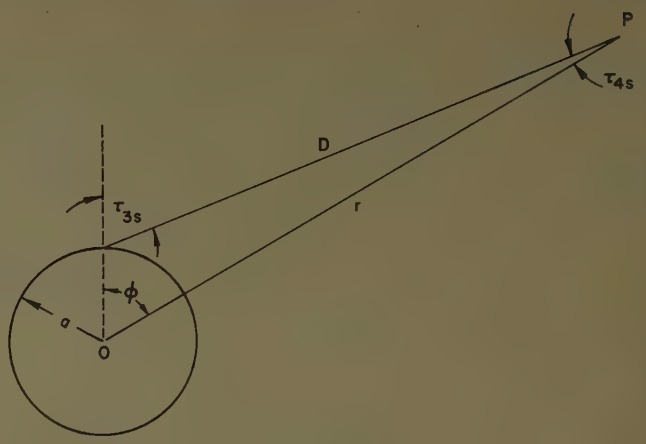

Fig. 4—Geometrical-optics parameters for $(\pi/2) > \phi > 0$.

and α not too near zero.[37,38] Using (22b), (27), and (28), we obtain

$$H_{\nu_s}^{-(2)'}(ka) H_{\nu_s}^{-(1)'}(ka) \sim \frac{2 \cos \tau_{3s}}{\pi ka}, \tag{29}$$

and

$$\pi_z^* \sim \frac{V}{\omega \mu} f_{ka \sin \tau_{3s}}(\phi_0) \frac{e^{-j(kD-\pi/4)}}{(2\pi kD)^{1/2}}. \tag{30}$$

The above procedure can easily be carried through for the contour integral representations for all the field components.[21] Only the value for E_ϕ, which is of major interest here, is shown; this is

$$E_\phi \sim \frac{V}{2\pi a} \pi ka f_{ka \sin \tau_{3s}}(\phi_0) \cos \tau_{4s} \left(\frac{2}{\pi kD}\right)^{1/2} e^{-j(kD-\pi/4)}. \tag{31}$$

B. The Circumferential Slot

The procedure here is essentially identical to the one just used. In this case from (12) and proceeding as before, we obtain

$$\pi_z = -\frac{|E|}{2\pi^3 k^2} \sum_{m=0}^{\infty} \left\{ \int_{-\infty+j\epsilon}^{\infty+j\epsilon} \frac{g_\nu(\phi_0) d\nu}{H_\nu^{(2)}(ka) H_\nu^{(1)}(ka)} \int_{\eta-j\infty}^{-\eta+j\infty} d\tau_1 \int_{-\pi+\eta-j\infty}^{\pi-\eta+j\infty} d\tau_2 e^{jS_m^+} + \int_{-\infty-j\epsilon}^{\infty-j\epsilon} \frac{g_\nu(\phi_0) d\nu}{H_\nu^{(2)}(ka) H_\nu^{(1)}(ka)} \int_{\eta-j\infty}^{-\eta+j\infty} d\tau_3 \int_{-\pi+\eta-j\infty}^{\pi-\eta+j\infty} d\tau_4 e^{jS_m^-} \right\}. \tag{32}$$

To second order

$$H_\nu^{(1),(2)'}(z) \sim \pm j \sqrt{\frac{2 \sin \alpha}{\pi z}} e^{\pm jz(\sin \alpha - \alpha \cos \alpha) \mp j\pi/4} \tag{27}$$

with

$$\nu = z \cos \alpha \tag{28}$$

The comments between (18) and (26) apply here also so that

$$\pi_z \sim \frac{|E|}{\pi^2 k^2} \frac{g_{\nu_s}^-(\phi_0)(2\pi)^{1/2}}{H_{\nu_s}^{-(2)}(ka) H_{\nu_s}^{-(1)}(ka)} \frac{e^{-j(kD-\pi/4)}}{(kD)^{1/2}}. \tag{33}$$

[37] Watson, *op. cit.*, p. 228.
[38] Summerfeld, *op. cit.*, pp. 118–119.

To second order

$$H_\nu^{(1),(2)}(z) \sim \sqrt{\frac{2}{\pi z \sin \alpha}}\, e^{\pm jz(\sin\alpha - \alpha\cos\alpha) \mp j\pi/4} \quad (34)$$

with the same restrictions as apply to (27). Thus,

$$H_{\nu_s}^{-(1)}(ka) H_{\nu_s}^{-(2)}(ka) \sim \frac{2}{\pi ka \cos \tau_{3s}}, \quad (35)$$

and

$$\pi_z \sim \frac{|E|}{k^2} g_{ka \sin \tau_{3s}}(\phi_0)\, ka \cos \tau_{3s} \frac{e^{-j(kD-\pi/4)}}{(2\pi kD)^{1/2}}. \quad (36)$$

The field component of major interest here is E_z, and for this we obtain

$$E_z \sim |E|\, g_{ka \sin \tau_{3s}}(\phi_0)\, ka \cos \tau_{3s} \frac{e^{-j(kD-\pi/4)}}{(2\pi kD)^{1/2}}. \quad (37)$$

VI. Residue Series Constants

Although the geometrical-optics field representations in the form of the second-order approximations—(30), (31), (36), (37), and associated expressions—are quite simple, so that numerical calculations are straightforward, no computational advantages accrue from the residue series unless useful expressions for

$$\nu_m,\ {}'\nu_m,\ \frac{\partial H_\nu^{(2)}(z)}{\partial \nu}\Big]_{\nu=\nu_m}, \quad \text{and} \quad \frac{\partial H_\nu^{(2)\prime}(z)}{\partial \nu}\Big]_{\nu={}'\nu_m} \quad \text{exist.}$$

Also, although the general characteristics, and even numerical values, of these quantities are well known because of work on the sphere problem, in that case values of $z=ka$ larger than 1000 are normally encountered so that certain approximations are permissible.[1–4] Here however, in the cylinder case, values of $z=ka$ from 10 to 1000 are of major interest, and a further consideration is required. In evaluating the precision obtained from the use of the residue series constants, one is faced with the somewhat embarrassing but desirable requirement that the numerical values calculated through the use of these constants agree closely with those obtained from the harmonic series. From computations with the harmonic series, quite accurate numerical results are available for the cylinder case for $ka=8$ and 12,[17] as well as, more recently, for a wider range of values, $21 \geqq ka \geqq 0.1$.[18] If good agreement can be obtained for $ka \approx 10$, then one is reasonably well assured that for larger ka the agreement will be even better, since the residue series constants are given by asymptotic series in powers of $1/ka$.

In order to simplify the following presentation, only the results of the analysis by which the formulas given below can be obtained are shown. The details, as well as higher order terms in many of the expansions, are given elsewhere.[21]

A. Tangent or Second-Order Approximations

From the second-order representations for the Hankel functions in terms of trigonometric functions, the residue series constants can be obtained. Although no tangent functions appear here, since the cylinder is assumed to be perfectly conducting, the terminology of the sphere case is retained to indicate the similarity.[2,4]

1. ν_m and $\dfrac{\partial H_\nu^{(2)}}{\partial \nu}\Big]_{\nu=\nu}$

The auxiliary parameter α_m appears and is given by

$$\alpha_m \sim \delta_m \left(1 + \frac{1}{30}\delta_m{}^2 + \frac{41}{12{,}600}\delta_m{}^4 + \frac{97}{226{,}800}\delta_m{}^6 + \cdots\right), \quad (38)$$

where

$$\delta_m = \left[\frac{3\pi}{4z}(4m-1)\right]^{1/3} e^{j\pi/3}. \quad (39)$$

$\nu_m = z\cos\alpha_m$ so that

$$\frac{\nu_m}{z} \sim 1 - \frac{1}{2}\delta_m{}^2 + \frac{1}{120}\delta_m{}^4 + \frac{1}{2800}\delta_m{}^6 + \frac{281}{9{,}072{,}000}\delta_m{}^8 + \cdots \quad (40)$$

$\dfrac{\partial H_\nu^{(2)}(z)}{\partial \nu}\Big]_{\nu=\nu_m}$ is given by

$$\frac{\partial H_\nu^{(2)}(z)}{\partial \nu}\Big]_{\nu=\nu_m} \sim j(-1)^m 2\sqrt{\frac{2}{\pi z}}\,\frac{\alpha_m}{\sqrt{\sin\alpha_m}}, \quad (41)$$

where from (38)

$$\frac{\alpha_m}{\sqrt{\sin\alpha_m}} = \sqrt{\delta_m}\left(1 + \frac{1}{10}\delta_m{}^2 + \frac{37}{2520}\delta_m{}^4 + \frac{563}{226{,}800}\delta_m{}^6 + \cdots\right). \quad (42)$$

2. ${}'\nu_m$ and $\dfrac{\partial H_\nu^{(2)\prime}(z)}{\partial \nu}\Big]_{\nu={}'\nu_m}$

In this case an auxiliary parameter ${}'\alpha_m$ appears and is given by (38), with α_m and δ_m there replaced by ${}'\alpha_m$ and ${}'\delta_m$, and with

$${}'\delta_m = \left[\frac{3\pi}{4z}(4m-3)\right]^{1/3} e^{j\pi/3}. \quad (43)$$

Similarly, ${}'\nu_m/z$ is given by (40) with ν_m and δ_m there replaced by ${}'\nu_m$ and ${}'\delta_m$. Also,

$$\left.\frac{\partial H_\nu^{(2)\prime}(z)}{\partial \nu}\right]_{\nu='\nu_m} \sim -j(-1)^m 2\sqrt{\frac{2}{\pi z}}\,'\alpha_m\sqrt{\sin\,'\alpha_m}, \quad (44)$$

where from (38)

$$'\alpha_m\sqrt{\sin\,'\alpha_m} = {}'\delta_m{}^{3/2}\left(1-\frac{1}{30}\,'\delta_m{}^2-\frac{47}{12{,}600}\,'\delta_m{}^4 - \frac{23}{42{,}000}\,'\delta_m{}^6+\cdots\right). \quad (45)$$

B. Hankel or Third-Order Approximations

For these approximations, one starts with the representations for the Hankel functions in terms of Hankel functions of order one-third or related functions.

1. ν_m and $\left.\dfrac{\partial H_\nu^{(2)}(z)}{\partial \nu}\right]_{\nu=\nu_m}$

from the Hankel-Langer representations.

Here, also, the auxiliary parameter α_m is useful, and is given again by (38), except that in this case

$$\delta_m = \left(\frac{3r_m}{z}\right)^{1/3} e^{i\pi/3}, \quad (46)$$

where r_m is the mth root (positive and real) starting with $m=1$ of

$$J_{1/3}(r) + J_{-1/3}(r) = 0. \quad (47)$$

$$H_{-2/3}^{(2)}(r_m e^{i\pi}) = \frac{2e^{i\pi/6}}{\sqrt{3}}\left[J_{2/3}(r_m) - J_{-2/3}(r_m)\right]. \quad (49)$$

2. $'\nu_m$ and $\left.\dfrac{\partial H_\nu^{(2)\prime}(z)}{\partial \nu}\right]_{\nu='\nu_m}$

from the Hankel-Langer representations.

Here, although a parameter $'\alpha_m$ is required in the development of the formulas, it does not appear explicitly in the final forms.

$'\nu_m/z$ is given by

$$\frac{'\nu_m}{z} \sim 1-\frac{1}{2}\,'\delta_m{}^2+\frac{1}{120}\left(1+\frac{8}{3'r_m{}^2}\right)'\delta_m{}^4 + \frac{1}{2800}\left(1+\frac{152}{9}\,\frac{1}{'r_m{}^2}+\frac{112}{81}\,\frac{1}{'r_m{}^4}\right)'\delta_m{}^6 + \frac{281}{9{,}072{,}000}\left(1+\frac{14{,}416}{281}\,\frac{1}{'r_m{}^2}-\frac{896}{843}\,\frac{1}{'r_m{}^4} + \frac{1792}{2529}\,\frac{1}{'r_m{}^6}\right)'\delta_m{}^8+\cdots \quad (50)$$

Now,

$$'\delta_m = \left(\frac{3'r_m}{z}\right)^{1/3} e^{i\pi/3}, \quad (51)$$

where $'r_m$ is the mth root (positive and real) starting with $m=1$ of

$$J_{2/3}('r) - J_{-2/3}('r) = 0. \quad (52)$$

$\left.\dfrac{\partial H_\nu^{(2)\prime}(z)}{\partial \nu}\right]_{\nu='\nu_m}$ is given by

$$\left.\frac{\partial H_\nu^{(2)\prime}(z)}{\partial \nu}\right]_{\nu='\nu_m} \sim \left(\frac{'r_m}{z}\right)^{1/2} e^{i\pi/3}\left\{\frac{\left[1-\left(\frac{'\nu_m}{z}\right)^2\right]^{3/4}\left(1+\frac{\epsilon_m}{'K_m}\right)^{1/2}}{\frac{d'\nu_m}{dz}}\left[H_{1/3}^{(2)}('K)\right]_{'\alpha='\alpha_m}\right\}. \quad (53)$$

At this point the reader should be cautioned that the same symbols are used for related quantities in the second-order and third-order approximations. A particular quantity should, of course, be used only in the appropriate approximation. Since $\nu_m = z\cos\alpha_m$, ν_m/z is given by (40) with δ_m by (46). For

$$\left.\frac{\partial H_\nu^{(2)}(z)}{\partial \nu}\right]_{\nu=\nu_m}$$

one obtains

$$\left.\frac{\partial H_\nu^{(2)}(z)}{\partial \nu}\right]_{\nu=\nu_m} \sim -\left(\frac{r_m}{z}\right)^{1/2} e^{i\pi/3}\,\frac{\alpha_m}{\left[1-\left(\frac{\nu_m}{z}\right)^2\right]^{1/4}}\,H_{-2/3}^{(2)}(r_m e^{i\pi}). \quad (48)$$

$H_{-2/3}^{(2)}(r_m e^{i\pi})$ can also be written as

For this

$$\frac{d'\nu_m}{dz} \sim 1-\frac{1}{6}\,'\delta_m{}^2-\frac{1}{360}\left(1+\frac{8}{3'r_m{}^2}\right)'\delta_m{}^4 - \frac{1}{2800}\left(1+\frac{152}{9}\,\frac{1}{'r_m{}^2}+\frac{112}{81}\,\frac{1}{'r_m{}^4}\right)'\delta_m{}^6 + \cdots, \quad (54)$$

and

$$\left(1+\frac{\epsilon_m}{'K_m}\right)^{1/2} = 1-\frac{1}{30'r_m{}^2}\,'\delta_m{}^2-\frac{1}{45'r_m{}^2}\left(\frac{16}{35}+\frac{1}{24}\,\frac{1}{'r_m{}^2}\right)'\delta_m{}^4 - \frac{1}{3375'r_m{}^2}\left(\frac{66}{7}+\frac{3}{14}\,\frac{1}{'r_m{}^2}+\frac{65}{432}\,\frac{1}{'r_m{}^4}\right)'\delta_m{}^6 + \cdots; \quad (55)$$

also,

$$[H_{1/3}^{(2)}('K)]_{'\alpha='\alpha_m} = H_{1/3}^{(2)}('r_m e^{i\pi})\left[1+\frac{1}{45'r_m^2}{}'\delta_m^2 + \frac{1}{1350'r_m^2}\left(\frac{43}{7}+\frac{5}{3}\frac{1}{'r_m^2}\right){}'\delta_m^4 + \frac{1}{2025'r_m^2}\left(\frac{36}{35}+\frac{43}{70}\frac{1}{'r_m^2}+\frac{1}{6}\frac{1}{'r_m^4}\right){}'\delta_m^6+\cdots\right] \quad (56)$$

$'K$, $'K_m$, ϵ_m, as well as $'\alpha$ and $'\alpha_m$ are parameters which appear in the course of the development, but which are not finally required. $H_{1/3}^{(2)}('r_m e^{i\pi})$ can also be written as

$$H_{1/3}^{(2)}('r_m e^{i\pi}) = \frac{2}{\sqrt{3}} e^{i\pi/6}[J_{1/3}('r_m) + J_{-1/3}('r_m)]. \quad (57)$$

3. Probably improved values for ν_m and $'\nu_m$ over those already exhibited can be obtained from the Hankel-Olver representations. In this case,

$$\frac{\nu_m}{z} \sim 1-\frac{1}{2}\delta_m^2+\frac{1}{120}\delta_m^4+\frac{1}{2800}\left(1-\frac{40}{9}\frac{1}{r_m^2}\right)\delta_m^6 + \frac{281}{9{,}072{,}000}\left(1-\frac{4640}{281}\frac{1}{r_m^2}\right)\delta_m^8+\cdots, \quad (58)$$

and

$$\frac{'\nu_m}{z} \sim 1-\frac{1}{2}{}'\delta_m^2+\frac{1}{120}\left(1+\frac{8}{3}\frac{1}{'r_m^2}\right){}'\delta_m^4 + \frac{1}{2800}\left(1+\frac{112}{9}\frac{1}{'r_m^2}+\frac{112}{81}\frac{1}{'r_m^4}\right){}'\delta_m^6 + \frac{281}{9{,}072{,}000}\left(1-\frac{80}{'r_m^2}-\frac{896}{843}\frac{1}{'r_m^4}+\frac{1792}{2529}\frac{1}{'r_m^6}\right){}'\delta_m^8 + \cdots \quad (59)$$

Here δ_m, $'\delta_m$, r_m, and $'r_m$ are given by (46), (51), and associated equations. ν_m/z and $'\nu_m/z$ given by (58) and (59) are believed to be correct at least to the order of the last term shown because they were derived from asymptotic expansions for the Hankel functions. Unfortunately, the corresponding values of

$$\left.\frac{\partial H_\nu^{(2)}(z)}{\partial\nu}\right]_{\nu=\nu_m} \text{ and } \left.\frac{\partial H_\nu^{(2)\prime}(z)}{\partial\nu}\right]_{\nu='\nu_m}$$

which can be derived from the Hankel-Olver forms have not yet been obtained. However, in a recent report,[39] in which asymptotic expansions of the Hankel functions were used to compute the residue series constants, representations of probably equivalent accuracy were shown.

[39] W. Franz and R. Galle, "Semiasymptotic series for the diffraction of a plane wave by a cylinder," *Zeit. Naturforschung*, vol. 10a, pp. 374–378; May, 1955.

C. Discussion

Although many of the formulas shown above are carried to a relatively large number of terms, with the exception of those derived from the Hankel-Olver representations, it should not be presumed that the latter terms in the series expressions are exactly correct. The essential reason for this is that except for (58) and (59) the formulas for the various residue series constants were derived from only single-term asymptotic representations for the Hankel functions. The order of the error can be estimated by comparing (40) with (58), and (50) with (59). It appears that for all practical values of $z=ka$ for which computations by the residue series are feasible, the third-order Hankel-Langer approximations are quite accurate; for not too small values of m, even the second-order approximations are adequate.[25]

In order to compute with the Hankel or third-order approximations, it is necessary to know or determine the values of r_m, $'r_m$, $H_{-2/3}^{(2)}(r_m e^{i\pi})$, and $H_{1/3}^{(2)}('r_m e^{i\pi})$. (Many of these have been shown in references 2, 4, 21–23, 25, 39, and additional sources of information are noted in reference 21.) In any case they can be computed from available tables.[40]

VII. Numerical Comparisons of the Different Representations

In order to determine how well the more convergent geometrical-optics and residue series representations agree with the harmonic series, direct numerical comparisons are of interest. Quite complete results obtained from the harmonic series representations are available for $ka=8$ and 12 for both axial and circumferential finite slots,[17] although for brevity only the $ka=12$ cases are considered here. Comparisons of the second-order geometrical-optics expressions with the harmonic series representations for $ka=8$ are given elsewhere.[21,25] Also given elsewhere are rather complete numerical comparisons of the harmonic series representations with both second- and third-order geometrical-optics expressions, as well as with the residue series representations for various values of ka.[25]

Since the radiation patterns of infinite slots are to be compared with those of finite slots, here, for simplicity, such comparisons are confined to the azimuthal plane. However, this is no essential restriction because the expressions in both cases are similar, with ka sin θ for the finite slots replacing ka for the infinite slots as the argument of the Hankel functions.[11,12,17] θ is the spherical polar angle measured from the axis of the cylinder, and $\theta=\pi/2$ defines the azimuthal plane. In the case of the simple finite circumferential slot, the harmonic series representation for the cross-polarized electric field component, which vanishes in the azimuthal plane, is similar to the expression for the principal electric field component for the finite and infinite axial

[40] "Tables of Bessel Functions of Fractional Order," vol. I, Columbia University Press, New York, N. Y.; 1948.

slots.[11,12,17] Consequently, it too can be transformed by the procedures described above into the more convergent forms.

In the following, the previous order of development is reversed and the geometrical-optics approximations are considered first.

A. Comparisons of the Second-Order Geometrical-Optics Approximations with the Harmonic Series Representations

1. The Axial Slot: In the far-field region, that is, for D and $r \gg a$ and both very large, it is evident from Fig. 4 that

$$\tau_{4s} = 0, \tag{60a}$$

$$\tau_{3s} \approx \phi, \tag{60b}$$

and

$$D \approx r - a\cos\phi. \tag{60c}$$

Using these in (31), and assuming $\phi_0 \to 0$ so that $f_{ka \sin \tau_{3s}}(\phi_0) = 1$, we obtain for the second-order geometrical-optics approximation,

$$E_\phi \approx \frac{V}{2\pi a}\pi ka\, e^{jka\cos\phi}\left(\frac{2}{\pi kr}\right)^{1/2} e^{-j(kr-\pi/4)}.$$
$$r \to \infty$$
$$\phi_0 \to 0 \tag{61}$$

On the other hand, from (2b) and (4), for $r \to \infty$ with $\phi_0 \to 0$, we find for the harmonic series representation,

$$E_\phi \sim \frac{V}{2\pi a}\left(\frac{2}{\pi kr}\right)^{1/2} e^{-j(kr-\pi/4)} e^{-j\pi/2} \sum_n \frac{e^{jn\pi/2}}{H_n^{(2)\prime}(ka)} e^{-jn\phi}.$$
$$r \to \infty$$
$$\phi_0 \to 0 \tag{62}$$

It is evident upon canceling common factors that we wish to know how closely does

$$\pi ka\, e^{jka\cos\phi} = e^{-j\pi/2} \sum_n \frac{e^{jn\pi/2}}{H_n^{(2)\prime}(ka)} e^{-jn\phi}\ ?. \tag{63}$$

The summation on the right side of (63) has been tabulated with the magnitude normalized to unity and the phase normalized to 0 degrees at $\phi = 0$ degrees; the normalization constant is

$$\sum_n \frac{e^{jn\pi/2}}{H_n^{(2)\prime}(ka)}\Bigg]_{ka=12} = 37.475\, e^{j1.045}.^{16} \tag{64}$$

Since the precise multiple of 2π radians in the phase is not defined in the summation and is, in fact, not significant, $(12\cos\phi - 4\pi)$ is used for the phase factor in the geometrical-optics approximation. Using the results noted above, we can make the comparison shown in Table I. Results are shown only for $90° \geqq \phi \geqq 0°$ since,

TABLE I

COMPARISON OF SECOND-ORDER GEOMETRICAL-OPTICS APPROXIMATION WITH HARMONIC SERIES REPRESENTATION FOR AXIAL SLOT FOR $ka = 12$

ϕ-Degrees	Magnitude		Phase-Degrees	
	Geometrical-Optics	Harmonic Series	Geometrical-Optics	Harmonic Series
0	37.699	37.475	−32.5	−30.1
10	37.699	37.475	−42.9	−40.5
20	37.699	37.363	−73.9	−71.2
30	37.699	37.138	−124.6	−121.5
40	37.699	36.688	−193.3	−189.4
50	37.699	35.939	−278.1	−273.5
60	37.699	34.477	−376.2	−370.8
70	37.699	32.491	−484.8	−478.8
80	37.699	29.568	−600.6	−595.7
90	37.699	25.633	−720.0	−718.0

as would be expected, the second-order geometrical-optics approximation rapidly deteriorates for $\phi > 90°$, that is, in the shadow region.

2. The Circumferential Slot: Using (60), and assuming the slot is a half-wave long in the circumferential direction so that $\phi_0 = \lambda/2a = \pi/ka$, we obtain from (37)

$$E_z \approx |E| \frac{\cos(\pi/2\sin\phi)}{\cos\phi} e^{jka\cos\phi}\left(\frac{2}{\pi kr}\right)^{1/2} e^{-j(kr-\pi/4)}.$$
$$r \to \infty$$
$$\phi_0 = \pi/ka \tag{65}$$

From (6a) and (7), for $r \to \infty$ with $\phi_0 = \lambda/2a = \pi/ka$, we find

$$E_z \sim |E| \frac{ka}{\pi}\left(\frac{2}{\pi kr}\right)^{1/2} e^{-j(kr-\pi/4)}$$
$$\cdot \sum_n e^{jn\pi/2} \frac{\cos\left(\frac{n}{2}\frac{\pi}{ka}\right)}{(ka)^2 - n^2} \frac{e^{-jn\phi}}{H_n^{(2)}(ka)}.$$
$$r \to \infty$$
$$\phi_0 = \pi/ka \tag{66}$$

After canceling common factors, we wish to know how closely does

$$\frac{\pi}{ka}\frac{\cos\left(\frac{\pi}{2}\sin\phi\right)}{\cos\phi} e^{jka\cos\phi}$$
$$= \sum_n e^{jn\pi/2} \frac{\cos\left(\frac{n}{2}\frac{\pi}{ka}\right)}{(ka)^2 - n^2} \frac{e^{-jn\phi}}{H_n^{(2)}(ka)}\ ?. \tag{67}$$

The right-hand side of (67) has also been tabulated in normalized form, where the normalization constant in this case is

$$\sum_n \frac{\cos\left(\frac{n}{2}\frac{\pi}{ka}\right)}{(ka)^2 - n^2} \frac{e^{jn\pi/2}}{H_n^{(2)}(ka)}\Bigg]_{ka=12} = 0.262\, e^{j5.656}. \quad [17] \quad (68)$$

Table II compares the left side of (68) with the right side. E_z here corresponds to E_θ of a finite slot with $\theta = \pi/2$, *i.e.*, in the azimuthal plane.[17] Again, for the same reason as before, only the range $90° \geqq \phi \geqq 0°$ is considered.

TABLE II

COMPARISON OF SECOND-ORDER GEOMETRICAL-OPTICS APPROXIMATION WITH HARMONIC SERIES REPRESENTATION FOR CIRCUMFERENTIAL SLOT FOR $ka = 12$

ϕ-Degrees	Magnitude		Phase-Degrees	
	Geometrical-Optics	Harmonic Series	Geometrical-Optics	Harmonic Series
0	0.262	0.262	−32.5	−35.9
10	0.256	0.256	−42.9	−46.3
20	0.239	0.240	−73.9	−77.4
30	0.214	0.215	−124.6	−128.1
40	0.182	0.185	−193.3	−197.3
50	0.147	0.152	−278.1	−283.0
60	0.110	0.119	−376.2	−383.0
70	0.0720	0.0891	−484.8	−495.1
80	0.0368	0.0631	−600.6	−616.9
90	0.0000	0.0427	−720.0	−746.1

B. Comparisons of the Residue Series Representations with the Harmonic Series Representations

Since very complete numerical comparisons of these representations are given elsewhere,[25] only the few points compared in the original report[21] are shown below. Since for ϕ near π only the $m = 1$ terms of the residue series are significant, it is possible to obtain ν_1 and $'\nu_1$ from the harmonic series data by a curve fitting process.[15,16] Comparing these values in Table III with the ones computed from the second- and third-order approximations given in Section VI, we obtain an indication of how closely the residue series agrees with the harmonic series.

TABLE III

COMPARISON OF $\nu_{1/z}$ AND $'\nu_{1/z}$ OBTAINED BY VARIOUS METHODS FOR $z = ka = 12$

	Harmonic Series Curve Fit	Tangent or Second-Order Approximation	Hankel-Langer Approximation
$\nu_{1/z}$	$1.181 - j0.310$	$1.174 - j0.308$	$1.175 - j0.310$
$'\nu_{1/z}$	$1.075 - j0.139$	$1.084 - j0.147$	$1.075 - j0.138$

A more exacting test than the one shown above is a point-by-point comparison of the residue series with the harmonic series. For example, at $\phi = \pi$ we have from the residue series with the use of (14a) and (2b) with $\phi_0 \to 0$ and $r \to \infty$,

$$E_\phi \sim -\frac{V}{2\pi a}\left(\frac{2}{\pi kr}\right)^{1/2} e^{-j(kr - \pi/4)} \frac{2\pi}{M_{|'\nu_1|}}$$
$$r \to \infty$$
$$\phi_0 \to 0$$
$$\phi = \pi. \quad (69)$$

On the other hand, for the same conditions, E_ϕ as given by the harmonic series can be obtained from (62). Thus, after canceling common factors, we wish to determine how closely does

$$-\frac{2\pi}{M_{|'\nu_1|}} = e^{-j\pi/2} \sum_n \frac{e^{-jn\pi/2}}{H_n^{(2)\prime}(ka)}?. \quad (70)$$

The right side of (70) can be computed with the use of (64) and available tables;[17] for $ka = 12$ its value is 5.02 $/\underline{-78.8°}$. The left-hand side for this case computed by the use of the Hankel-Langer representation is equal to 4.97 $/\underline{-79.2°}$, whereas from the tangent or second-order approximation it is equal to 3.82 $/\underline{-89.9°}$. The very close agreement obtained even for such a relatively small value of ka by the use of the Hankel-Langer representation is, of course, quite encouraging.[41] Equivalent, or better, agreement can be obtained for nearly all angles in the shadow region for both the axial and circumferential slots.[25]

VIII. Relationship to Scattered Fields

The far fields radiated by slots on a circular cylinder are closely related to the scattered fields which result when a plane wave is incident on the cylinder. It is of interest to specify this relationship exactly.

Assume a plane wave of unit amplitude polarized in the y direction and traveling in the negative x direction incident on a perfectly conducting circular cylinder. Then, in the usual way[42]

$$E_{y_i} = e^{jkx} = \sum_n e^{jn\pi/2} J_n(kr) e^{-jn\phi} \quad (71a)$$

and

$$H_{z_i} = -\sqrt{\frac{\epsilon}{\mu}}\, e^{jkx} \quad (71b)$$

are the components of the incident field. Matching the boundary conditions on the cylinder we find

$$H_{z_t}(r = a) = -J_\phi = j\sqrt{\frac{\epsilon}{\mu}}\,\frac{2}{\pi ka} \sum_n \frac{e^{jn\pi/2}}{H_n^{(2)\prime}(ka)} e^{-jn\phi}, \quad (72)$$

[41] The agreement is even better than indicated here. The retention of more significant figures, as well as several of the higher-order terms ($m > 1$) in the residue series, leads to a value of 5.01 $/\underline{-79.0°}$. (See Bailin and Spellmire, *op. cit.*)

[42] Stratton, *op. cit.*, pp. 372–374.

where $H_{z_t}(r=a)$ is the total axial magnetic field at the surface of the cylinder, and J_ϕ is the ϕ component of surface current density.[21,43] On the other hand, the far-field component of E_ϕ for a narrow infinite axial slot, $\phi_0 \to 0$, is given by (62). Note that the sum in (62) is identical to the one in (72).

In a similar manner, if a wave of unit amplitude polarized in the z direction and traveling in the negative x direction is incident on the cylinder,

$$E_{z_i} = e^{jkx} \quad (73a) \quad \text{and} \quad H_{y_i} = \sqrt{\frac{\epsilon}{\mu}}\, e^{jkx} \quad (73b)$$

are the components of the incident field. In this case,

$$H_{\phi_t}(r=a) = J_z = \sqrt{\frac{\epsilon}{\mu}}\,\frac{2}{\pi ka}\sum_n e^{jn\pi/2}\,\frac{e^{-jn\phi}}{H_n^{(2)}(ka)}, \quad (74)$$

where $H_{\phi_t}(r=a)$ is the total circumferential magnetic field at the surface of the cylinder, and J_z is the z component of surface current density. On the other hand, in this case, the far-field component of E_z for an infinite circumferential slot is given by (66). Here the comparison is complicated somewhat, since we have taken $\phi_0 = \lambda/2a$ in (66). However, if instead we take ϕ_0 to be very small, the

$$\cos\left(\frac{n}{2}\,\frac{\pi}{ka}\right) \Big/ \left[(ka)^2 - n^2\right]$$

factor, which comes from $g_n(\phi_0)$ in (8), becomes essentially a constant for significant values of n, and exerts no substantial influence on the value of the sum in (66). Consequently, for this case, the sum in (66) is equivalent to the one in (74).

Thus, aside from a generally unimportant constant multiplier, the dominant component of the far-field radiation pattern of a narrow infinite axial (circumferential) slot is equal to the $J_\phi(J_z)$ component of surface current density resulting from the scattering of a plane wave polarized perpendicular (parallel) to the axis of the cylinder. Clearly, the different representations available for the radiation fields from slots can also be used to determine the currents and scattered fields resulting from incident waves, or vice versa.

IX. Limiting Case of a Plane Boundary

If the radius of the circular cylinder is allowed to become infinite, it can be shown that the quite simple solutions for the resulting plane boundary result. This is demonstrated below only for the π_z^* component for the delta type infinite axial slot, $\phi_0 \to 0$ and $f_\nu(\phi_0) = 1$, since all the other cases follow in an essentially equivalent fashion.

[43] J. R. Mentzer, "Scattering and Diffraction of Radio Waves," Pergamon Press, London, England, pp. 60–63; 1955.

In order to approach the limit properly, the substitution $\nu = at$ is made, and a is allowed to become infinite while the quantities

$$\xi = r - a \text{ (height of observation point above surface)}, \quad (75a)$$

and

$$a\phi = \zeta \text{(horizontal distance between source and observation point)}, \quad (75b)$$

are kept constant. ζ and ξ are shown in Fig. 5. As $a \to \infty$,

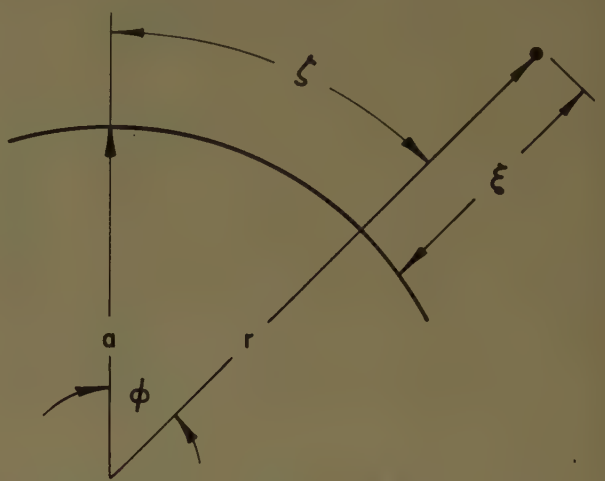

Fig. 5—Coordinates for equivalent plane boundary.

ζ and $\xi \to x$ and y, respectively, in a new coordinate system centered on the source line. Since

$$\frac{e^{j\nu(\pi-\phi)}}{\sin \nu\pi} = e^{-j\pi t}\,\frac{e^{jat\pi}}{\sin at\pi} = e^{-j\pi t}\,\frac{2j}{1 - e^{-j2at\pi}}, \quad (76)$$

and

$$\lim_{a\to\infty} \frac{1}{1 - e^{-j2at\pi}} = \begin{matrix} 0 \text{ in upper half-plane} \\ 1 \text{ in lower half-plane,} \end{matrix} \quad (77)$$

only the part of C_1 in the lower half-plane contributes. From approximations discussed elsewhere[21] with $\nu = at$, and $a \to \infty$, while $\xi = r - a$ remains constant, we find[44]

$$\lim_{a\to\infty} \frac{H_\nu^{(2)}(kr)}{H_\nu^{(2)\prime}(ka)} = -j\,\frac{k}{\sqrt{k^2 - t^2}}\, e^{j\xi\sqrt{k^2-t^2}}. \quad (78)$$

Substituting the results of the above in (9), we obtain

$$\lim_{a\to\infty} \pi_z^* = \pi_z^*{}_{\text{plane}}$$

$$= -\frac{V}{2\pi\omega\mu}\int_{-\infty-j\epsilon}^{\infty-j\epsilon} \frac{e^{j\xi\sqrt{k^2-t^2}}}{\sqrt{k^2 - t^2}}\, e^{-j\pi t}\,dt, \quad (79)$$

where ϵ is small, positive, and real. Putting

[44] Van der Pol and Bremmer, *op. cit.*, p. 153.

$$\zeta = r \cos \phi, \tag{80a}$$

$$\xi = r \sin \phi, \tag{80b}$$

(r and ϕ are now the polar coordinates in the new system) and then

$$t = k \cos \alpha, \tag{81}$$

and

$$u = \phi + \alpha, \tag{82}$$

there results

$$\pi_z^*{}_{\text{plane}} = \frac{V}{2\pi\omega\mu} \int_{-\pi+\phi+\Delta-j\infty}^{\phi+\Delta+j\infty} e^{-jkr \cos u} du, \tag{83}$$

where $\pi/2 > \Delta > 0$. But the integral is given by (16b), so

$$\pi_z^*{}_{\text{plane}} = \frac{V}{2\omega\mu} H_0^{(2)}(kr). \tag{84}$$

Eq. (84) and the field components resulting from the use of (2) are the values obtained from a line delta source of voltage V placed in a perfectly conducting plane, with the line source coinciding with the z axis.

X. Discussion

A. Physical Significance of Different Representations

For large r and $r \gg n$, the harmonic series representations can be written as a sum of terms like

$$e^{-jkr}(e^{jn\phi} + e^{-jn\phi}) = 2e^{-jkr} \cos n\phi,$$

where only the exponential variation is considered. The wave system of the individual elementary waves appears as an undamped, outward radial traveling cylindrical wave in its r variation, if we neglect the slow $1/\sqrt{r}$ variation, and as an undamped angular standing wave, or two oppositely directed undamped angular traveling waves, in its ϕ variation. Or, the elementary wave system can be considered as made up of two undamped traveling waves, one going as $e^{-j(kr-n\phi)}$, the other as $e^{-j(kr+n\phi)}$.[45] Thus, in the harmonic series representation, the total radiation appears as a resultant of the sum of the various order multipole cylindrical line sources located at the axis of the cylinder.

In the residue series representations, for large r and $|{}'\nu_m/ka|$ (or $|\nu_m/ka|$) of order unity, *i.e.*, low-order roots, a typical term appears as

$$e^{-jkr} \cos {}'\nu_m(\pi - \phi) = \tfrac{1}{2}e^{-jkr}[e^{j'\nu m(\pi-\phi)} + e^{-j'\nu_m(\pi-\phi)}]$$

where only the exponential variation is considered. ${}'\nu_m$ has a positive real part and a negative imaginary part, so that $e^{j'\nu m(\pi-\phi)}$ represents a damped wave traveling in the increasing ϕ direction, whereas $e^{-j'\nu_m(\pi-\phi)}$ represents a damped wave traveling in the decreasing ϕ direction. This wave system corresponds to an undamped outward radial traveling wave, and an angular standing wave, which results from the interference of two damped angular traveling waves. On the other hand, for the higher-order roots, particularly for $Im\ {}'\nu_m$ (or ν_m) very large, the variation in r can be shown to approach the form $\cos(kr - \pi/4)$ (or $\sin(kr - \pi/4)$) for $r \to \infty$. For these parts of the solution, the r variation appears as an essentially undamped radial standing wave resulting from the interference of inward and outward radial traveling waves.

A view of the residue series representation related to the one noted first above results from the use of (15) for the lower half plane in (11a), for example, so as to obtain

$$\pi_z^* = \sum_{n=0}^{\infty} \pi_{zn}^*, \tag{85a}$$

where

$$\pi_{zn}^* = -\frac{V}{a\omega\mu k} \sum_{m=1}^{\infty} f_{'\nu_m}(\phi_0) \frac{H_{'\nu_m}^{(2)}(kr)}{\left[\dfrac{\partial H_\nu^{(2)\prime}(ka)}{\partial \nu}\right]_{\nu='\nu_m}} \cdot \{e^{j'\nu_m[\phi - 2(n+1)\pi]} + e^{-j'\nu_m[2n\pi+\phi]}\}. \tag{85b}$$

It will be clear on examination that the first term in the braces in (85b) represents a wave which has traveled n times around the cylinder in the decreasing ϕ direction, whereas the second term represents a wave which has traveled n times around the cylinder in the increasing ϕ direction.

The significance of the geometrical-optics representation, particularly for the single-term, second-order, saddle-point approximation, seems quite clear. Note, for example from (31) or (37), that the radiation field appears as if it originated solely from the source on the cylinder, *i.e.*, as a simple cylindrical wave radiating from this source modified only by some amplitude factor. Of interest in connection with the half-wave circumferential slot is the

$$\frac{\cos(\pi/2 \sin \phi)}{\cos \phi}$$

factor in (65); this is the well-known element factor for a linear half-wave slot.

B. Residue Series and Normal Modes

Although we have used the Watson transformation procedure to go from the harmonic series to the residue series, it should be noted that the latter can be derived without the aid of the contour deformation technique. The terms in the appropriate residue series are, in fact, the normal modes in the cylindrical geometry considered. Thus, if use is made of the orthogonality of the $H_\nu^{(2)}(z)/\sqrt{z}$ functions for $\nu = \nu_m$ or ${}'\nu_m$ in the domain

[45] Bremmer, *op. cit.*, pp. 23–26, for a fuller discussion of this point of view in the related sphere case.

$z=kr$, with $r=a$ to ∞, an expansion identical to the residue series results. This development can not be expanded here, but it appears clear that this approach, which already has been demonstrated for the sphere case, can be applied to the circular cylinder problem also. Indeed, as noted in Section II, Riblet[20] indicated the use of the normal mode procedure for the circular cylinder problem. With regard to the normal mode point of view in the sphere case, the initial work of Eckersley and Millington,[3] and the recent work of Bremmer[46] and Sommerfeld[47] among others, applies. Particularly noteworthy is the investigation by Marcuvitz.[5]

C. Related Problems

The specific problem considered here is a rather special one of a general class. What is meant can be best understood by considering Fig. 6. Here is shown a

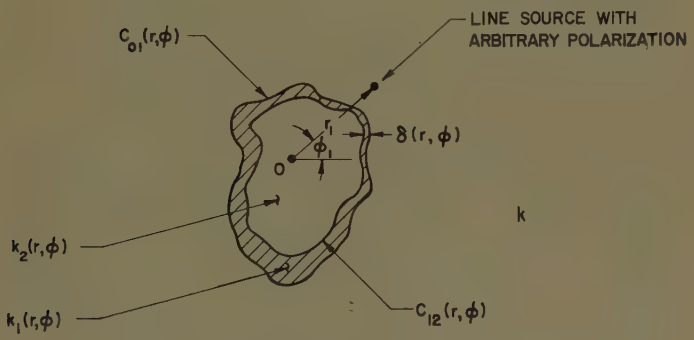

Fig. 6—Generalized scattering cylinder and source.

cylinder of cross section—curve $C_{12}(r, \phi)$—enclosing a medium whose propagation characteristics are specified by $k_2(r, \phi)$. Surrounding this at a distance $\delta(r, \phi)$ is another cylinder—curve $C_{01}(r, \phi)$—and between $C_{12}(r, \phi)$ and $C_{01}(r, \phi)$ is a medium which is characterized by $k_1(r, \phi)$. For simplicity (!), the external medium is taken as free space, characterized by k. Although shown external, the source might be between $C_{12}(r, \phi)$ and $C_{01}(r, \phi)$, or inside $C_{12}(r, \phi)$. Instead of a dielectric coating on $C_{12}(r, \phi)$, a corrugated surface, or some surface specified by an impedance $Z(r, \phi)$, might be assumed.

The solution of this generalized problem would seem hopeless, and possibly useless, in such generality. Nevertheless, it is thought that the point of view represented is quite useful. For example, here we have considered some examples of the case for $C_{12}(r, \phi)=a$, $k_2=\infty$, $k_1=k$ or $\delta=0$, $\phi_1=0$ and $r_1=a$. Reference to the work of other investigators on some aspects of the circular cylinder problem has already been made in Section II. But also in this class are the following: the corrugated surface and dielectric-clad circular cylinder problem,[48] the elliptic cylinder problem,[49] the parabolic cylinder problem where the cylinder is either of classical shape[50,51] or distorted,[52] and many others obtained as the surfaces are distorted into full planes, half planes, wedges, etc.

In some of the cases where exact formal solutions are possible, the geometrical-optics approach and residue series or normal mode approach has already led to significant improvement in one's ability to obtain *numerical* results.[53] It seems clear that an extension of these methods to other such problems would yield results which are not only interesting in themselves, but also useful for the information they would yield by extrapolation about the more intractable problems.

XI. Conclusion

The problem of radiation from a slot on a circular cylinder has been considered, particularly from the aspect of obtaining expressions which are useful for computation when the circumference to wavelength ratio is large. Rather good agreement was shown between the numerical values obtained from the geometrical-optics and residue series representations derived here, and the results previously obtained from the harmonic series representations. The relationship of the problem discussed here to the scattering problem has been shown, and the limiting case of a plane boundary was noted. The physical significance of the various types of representations was discussed, and the relationship of the residue series representation to the normal mode solution was described briefly. Finally, a point of view was described, whereby the problem considered here is one of a general class, in which the solutions exhibit the so-called cylindrical radio waves.

XII. Acknowledgment

The author would like to thank T. T. Taylor, L. L. Bailin, and other colleagues for their suggestions and advice.

[46] *Ibid.*, pp. 202–207, pp. 207–213; shown here is the relationship which exists between the complete geometrical-optics series and the residue (or normal mode) series for the sphere case. It appears clear that a similar relationship exists for the circular cylinder case.

[47] Sommerfeld, *op. cit.*, pp. 214–224.

[48] R. S. Elliott, "Azimuthal surface waves on circular cylinders," *J. Appl. Phys.*, vol. 26, pp. 368–376; April, 1955.

[49] J. R. Wait, "Field produced by an arbitrary slot on an elliptic cylinder," *J. Appl. Phys.*, vol. 26, pp. 458–463; April, 1955.

[50] S. O. Rice, "Diffraction of plane radio waves by a parabolic cylinder," *Bell. Sys. Tech. J.*, vol. 33, pp. 417–504; March, 1954.

[51] J. B. Keller, R. M. Lewis, and B. D. Seckler, "Asymptotic Solution of Some Diffraction Problems," N.Y.U. Inst. of Math. Sci., Div. of Elec. Res., Res. Rep. no. EM-81; June, 1955.

[52] S. Silver, "Microwave Antenna Theory and Design," McGraw-Hill Book Co., Inc., New York, N. Y.; pp. 151–155, 500–502; 1949.

[53] Two recent articles of interest related to this subject are: J. R. Wait, "Currents excited on a conducting surface of large radius of curvature," IRE Trans., vol. MTT-4, pp. 143–145; July, 1956. Also, S. I. Rubinow and T. T. Wu, "First correction to the geometric-optics scattering cross section from cylinders and spheres," *J. Appl. Phys.*, vol. 27, pp. 1032–1039; September, 1956.

A Study of Radar Elevation-Angle Errors Due to Atmospheric Refraction*

B. M. FANNIN† AND K. H. JEHN†

Summary—**Refractive-index variations in the atmosphere cause errors in radar measurements. This paper presents the results of a theoretical study of the elevation-angle error due to the refraction of electromagnetic waves in the troposphere. The study is based upon ray theory, using standard meteorological data reported by the United States Weather Bureau for the surface and the standard pressure levels. Computed errors are tabulated for thirty-four monthly mean refractive-index profiles selected as being representative of various type air masses for different seasons and latitudes. In order to get an indication of the spread in propagation errors to be expected during a particular season for fixed locations, computations have been carried out based on the 0300Z soundings for the odd days of January (1950–1954) and July (1950–1953) for nine U. S. locations. The diurnal influence is investigated by analyzing the variations in surface refractive index for January and July, 1953, and also for nine U. S. locations.**

Introduction

REFRACTIVE-INDEX variations at microwave frequencies in the atmosphere cause errors in radar position-in-space measurements. Even though the refractive-index values generally lie between unity and 1.0004, present-day radar systems are refined to the point where errors due to atmospheric effects can be a significant portion of the over-all system inaccuracies. This paper is concerned with the error introduced into elevation-angle measurements by refraction of the radar wave as it propagates through the atmosphere. The major variation of refractive index is that of a general decrease toward unity with height as the air density decreases; the assumption being made in this study that the atmosphere is horizontally stratified. In general, variations in a horizontal plane do exist but, except for unusual cases, these variations will not materially alter elevation-angle errors. The effect of ground-reflected energy is not included in this study.

A specific refractive-index profile is influenced by local conditions but depends to a large extent on such factors as the type of air mass involved, the season, and the latitude. Therefore the first phase of this study has been directed toward average conditions representative of various type air masses for different seasons and latitudes. The second phase is concerned with the spread in propagation errors to be expected during a particular season for a given time of day for fixed locations while the third phase is concerned with the influence of diurnal variations in surface refractive index.

* Manuscript received by the PGAP, February 23, 1956; revised manuscript received April 15, 1956. The research reported in this paper has been sponsored by the St. Louis Ordnance District under Contract DA 23-072-ORD-763.

† Electrical Eng. Res. Lab., The Univ. of Texas, Austin, Texas.

Computational Techniques

The physics of the problem is thus that of a spherical earth surrounded by a spherically symmetrical atmosphere. In this study the elevation angle is restricted to 3° or greater. This allows ray theory methods to be used throughout, since the rays of interest are well above those that become trapped by surface ducts, and also permits the use of more approximate computational procedures than are valid for extremely small elevation angles. The electromagnetic energy is considered as traveling along rays that obey Snell's law and Fermat's principle. The rays do not travel in a straight line but are curved as indicated in Fig. 1. In this figure O and P denote the radar location and the point under observation, respectively, while A denotes the apparent position of P. Two ray paths between O and P are shown, one being straight as would be the case if there were no atmosphere. The elevation-angle error, $\Delta\alpha$, as well as the parameters α, d, r_0, and h are indicated in Fig. 1. Zero and unity subscripts denote quantities at O and P, respectively, while primes denote quantities associated with a reference atmospheric condition.

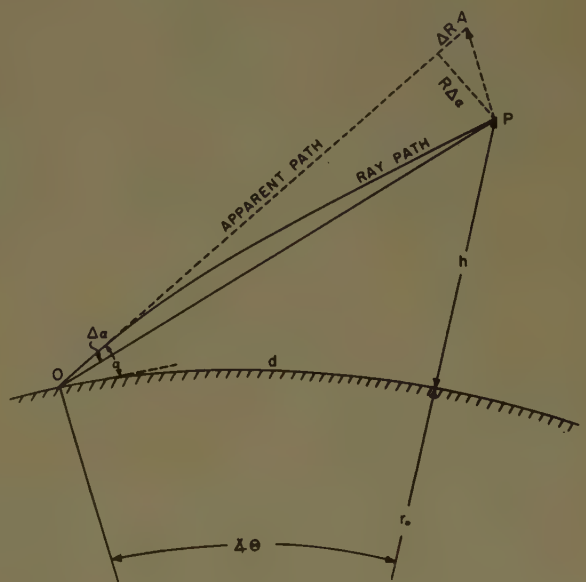

Fig. 1—Problem geometry.

Using Snell's law, considering ray paths for the actual refractive-index distribution and for a reference profile for the ray that passes through O and P, and neglecting some higher order terms, the following expression was derived for computing the elevation-angle errors

TABLE I

GENERAL INFORMATION PERTAINING TO THE MONTHLY MEAN REFRACTIVE-INDEX PROFILES STUDIED

Profile No.	Station	General Location	Station Elevation, Feet	Mean Surface Index, N-Units	Latitude-Longitude	Predominant Air Mass	Month (1951)
1	Norman Wells, NWT	North America	290	322.9	65N-127W	*cP*	Jan.
2	Swan Island	North America	35	375.0	17N-84W	*mT*	Jan.
3	Tatoosh Is., Wash.	North America	86	314.5	48N-125W	*mP*	Jan.
4	Edmonton, Alberta	North America	2219	288.5	54N-113W	*cP*	Jan.
5	Miami, Fla.	North America	12	374.5	26N-80W	*mT*	July
6	Anchorage, Alaska	North America	132	332.0	61N-150W	*mP*	July
7	Fort Smith, NWT	North America	665	316.5	60N-112W	*cP*	July
8	El Paso, Texas	North America	3916	278.6	32N-106W	*cT*	July
9	Heard Island	Pacific Ocean	—	312	53S-73E	*mP*	Jan.
10	Canton Island	Pacific Ocean	5	397	03S-172W	*mT*	Jan.
11	St. Paul Island	Pacific Ocean	20	309	57N-170W	*mP*	Jan.
12	Heard Island	Pacific Ocean	—	308	53S-73E	*mP*	July
13	Canton Island	Pacific Ocean	5	380	3S-172W	*mT*	July
14	Ship I	Atlantic Ocean	—	308	59N-19W	*mP*	Jan.
15	Maderia, Portugal	Atlantic Ocean	184	326	33N-17W	*mT*	Jan.
16	Ship I	Atlantic Ocean	—	328	59N-19W	*mP*	July
17	Maderia, Portugal	Atlantic Ocean	184	343	33N-17W	*mT*	July
18	Madra, India	Asia	52	351	13N-80E	*mT*	Jan.
19	Aden, Arabia	Asia	3	362	13N-45E	*cT* or *mT*	Jan.
20	Akita, Japan	Asia	32	311	40N-140E	*mP*	Jan.
21	Jodhpur, India	Asia	735	291.5	26N-73E	*cP*	Jan.
22	Hong Kong, China	Asia	—	393	22N-114E	*mT*	July
23	Habbaniya, Iraq	Asia	144	301	33N-44E	*cT*	July
24	Lerwick Obs., England	Europe	272	303	60N-01W	*mP*	Jan.
25	Bordeaux, France	Europe	157	320	45N-01W	*mT*	Jan.
26	Munchen, Germany	Europe	1726	295	48N-12E	*mP* or *cP*	Jan.
27	Lerwick Obs., England	Europe	272	321.4	60N-01W	*mP*	July
28	Bordeaux, France	Europe	157	338	45N-01W	*mT*	July
29	Aoulef, Algeria	Africa	902	285.4	30N-02W	*cT*	Jan.
30	Pretoria, Union of S.A.	Africa	4487	296	26S-28E	*mT*	Jan.
31	Aoulef, Algeria	Africa	902	271.2	30N-02W	*cT*	July
32	Dakar, Senegal	Africa	62	388	15N-17W	*mT*	July
33	Alice Springs	Australia	1795	287.5	24S-134E	*cT*	Jan.
34	Cloncurry	Australia	618	293	21S-140E	*cT*	July

$$\Delta\alpha' = \cot\alpha\left[(n_0 - n_0') - \frac{1}{z_1}\int_0^{z_1}(n - n')dz\right] \quad (1)$$

in which $\Delta\alpha' = (\alpha - \alpha')$ and

$$z = \left\{1 - \sin\alpha\left[\sin^2\alpha + (r/r_0)^2 - 1\right]^{-1/2}\right\}.$$

For a given α, z is a function of h only so that the integral in (1) is equal to the area under a $(n-n')$ vs h curve, the h scale being nonlinear. This integral was evaluated graphically.

The reference profile employed did not differ greatly from the average of those being considered and, in addition, was represented by a simple analytic function[1] so that the elevation-angle error for the reference case could be calculated accurately by analytical methods. Using (1) the values of the α's relative to this reference case were computed, this procedure considerably increasing the computational accuracy over using the no-atmosphere case as a reference. Though the computational accuracy for the values of $(\Delta\alpha \tan\alpha)$ for the profiles considered is better than one part in $(10)^6$, the values given do not carry this degree of significance since the profiles were based on values at the standard pressure levels only.

[1] The reference profile employed was

$$N = 542.9 + 4.854h - 100.86\sqrt{h + 3.919}$$

for $0 \leqq h \leqq 103.9$ where h is in thousands of feet and N is in N-units. Above $h = 103.9$, N is taken to remain zero.

STUDIES OF MEAN REFRACTIVE-INDEX PROFILES

The first order correction for refraction errors would be based upon a world-wide, all-year average profile. However, considerable improvement over this would be obtained by employing a mean profile based upon the location and season involved.

Data Employed

In order to get results of maximum usefulness for planning purposes in connection with radar guidance systems the best basis for selecting mean profiles is in association with air mass types rather than purely geographical considerations. Thus each profile selected is intended to be representative of the vertical refractive-index distribution for a given air mass and season. Reference was made to a standard source[2] of world-wide air mass distributions in order to choose stations for the month in question as near the geographical center of the source region as possible. The profiles selected are listed in Table I along with the name, general location, elevation, and latitude-longitude of the station and the associated air mass and month.

Use was made of the reported monthly mean upper air data published in U. S. Weather Bureau Monthly Climatic Data for the World. Refractive index computed on the basis of the dry air density as defined by

[2] B. Haurwitz and J. M. Austin, "Climatology," McGraw-Hill Book Co. Inc., New York, N. Y.; 1944 (map inserts).

TABLE II

VALUES OF ($\Delta\alpha$ TAN α) FOR THE MONTHLY MEAN REFRACTIVE-INDEX PROFILES LISTED IN TABLE I

$\Delta\alpha$ = elevation-angle error in $(10)^{-6}$ radians
Height in Thousands of Feet (Relative to Radar Level)

Profile No.	$\alpha=3°$			$\alpha=5°$				$\alpha=8°$				$\alpha=12°$			$\alpha=20°$				$\alpha=90°$			
	Height			Height				Height				Height			Height				Height			
	10	30	50	10	30	50	70	30	50	70	100	30	70	130	30	70	130	200	30	70	130	200
1	65	118	146	69	133	171	194	138	182	208	232	139	213	252	140	216	257	276	140	220	264	285
2	80	150	180	84	166	206	232	173	218	248	275	176	254	299	177	258	305	325	178	262	312	334
3	51	104	131	54	119	156	180	125	167	195	220	127	201	243	127	204	248	267	129	208	255	276
4	49	93	119	52	108	143	164	113	153	178	202	115	184	222	115	187	227	244	116	191	234	252
5	72	141	173	76	158	200	226	166	213	244	271	168	250	296	169	253	302	323	170	258	310	334
6	58	114	142	62	130	168	193	136	180	208	234	138	214	258	139	217	263	283	140	221	270	292
7	48	103	131	52	119	156	179	125	167	195	220	127	200	243	128	204	249	268	129	208	256	277
8	37	84	109	40	99	133	155	104	143	169	192	106	175	213	107	178	218	235	107	182	225	243
9	49	103	130	53	118	155	178	123	165	193	218	125	199	240	126	202	246	265	128	206	253	274
10	95	167	198	99	185	226	251	192	238	268	295	195	274	319	196	277	326	346	197	282	333	355
11	49	101	128	53	115	152	175	121	163	190	214	123	196	238	124	199	243	262	125	203	250	270
12	49	97	127	52	112	152	175	117	162	190	215	119	196	237	120	199	243	261	121	204	250	270
13	76	149	180	80	166	207	233	174	220	250	277	176	256	302	177	260	308	329	179	264	315	338
14	49	101	129	53	116	154	176	121	164	191	215	123	195	238	124	200	243	261	126	204	250	270
15	58	112	140	62	128	165	188	133	176	203	229	136	209	252	137	212	258	277	138	216	265	286
16	57	114	142	61	122	168	191	135	178	206	231	137	212	255	138	215	260	280	140	219	267	289
17	60	122	151	62	138	177	201	145	189	217	243	147	223	267	148	226	273	293	149	231	280	302
18	70	128	159	74	144	185	209	150	196	225	251	152	231	275	153	235	281	301	155	239	288	310
19	78	144	172	82	160	198	221	167	209	237	263	169	243	287	170	246	293	312	172	251	300	322
20	47	99	129	50	114	154	176	120	165	191	217	122	197	240	123	200	245	263	124	204	252	273
21	42	87	114	46	101	138	161	106	148	175	199	108	181	221	109	184	227	245	110	188	234	254
22	82	156	188	86	174	217	243	182	230	260	288	184	267	313	185	270	320	341	187	275	327	350
23	54	101	124	58	115	148	169	120	157	183	207	122	188	230	123	191	235	254	124	195	242	263
24	47	96	125	50	110	150	173	116	160	187	211	119	193	234	120	197	239	258	121	201	246	267
25	54	108	136	57	123	161	185	128	172	200	225	130	206	248	131	209	253	272	133	214	260	281
26	48	96	122	52	110	146	168	116	156	183	205	118	188	227	119	191	233	250	120	195	239	259
27	53	108	137	56	123	162	186	129	173	201	226	131	207	249	132	210	255	274	134	215	262	283
28	62	120	149	66	136	174	198	142	185	214	240	146	220	263	146	223	269	289	147	227	276	298
29	44	86	111	47	100	134	156	105	144	170	194	107	175	216	108	179	221	239	109	183	228	248
30	55	104	128	58	119	152	173	125	162	187	210	127	192	231	128	195	236	253	129	199	242	261
31	27	70	94	30	84	117	140	89	127	153	178	91	159	200	92	162	206	224	93	166	212	233
32	86	155	186	90	172	214	240	179	226	257	284	181	263	309	182	267	315	336	184	272	322	345
33	41	87	112	44	102	136	158	107	146	172	196	109	178	218	110	181	223	241	111	185	230	250
34	40	87	113	43	101	136	159	107	147	173	198	109	179	221	110	182	226	245	111	186	233	254

the NACA standard atmosphere was used to represent conditions in the higher levels.

The months of January and July were selected as representative of winter and summer conditions, respectively. The single best set of data at hand was for the year 1951 so these data were used throughout this phase of the study.

Elevation-Angle Errors

Elevation-angle errors for the profiles mentioned in the last paragraph are presented in Table II for a number of elevation angles and heights above the radar level. The quantity actually recorded in this table is ($\Delta\alpha$ tan α), this quantity varying less widely than $\Delta\alpha$ and being nearly independent of the elevation angle (for a given height) for $\alpha > 30°$.

Fig. 2 is a plot of the information contained in Table II for profile no. 1. The curves in this figure would all coincide with the one for $\alpha = 90°$ if it were not for the curvature of the earth and to a lesser extent for the curvature of the rays.[3] Similar plots as in Fig. 2 but for different mean profiles would have the same general appearance and characteristics but the amount of error

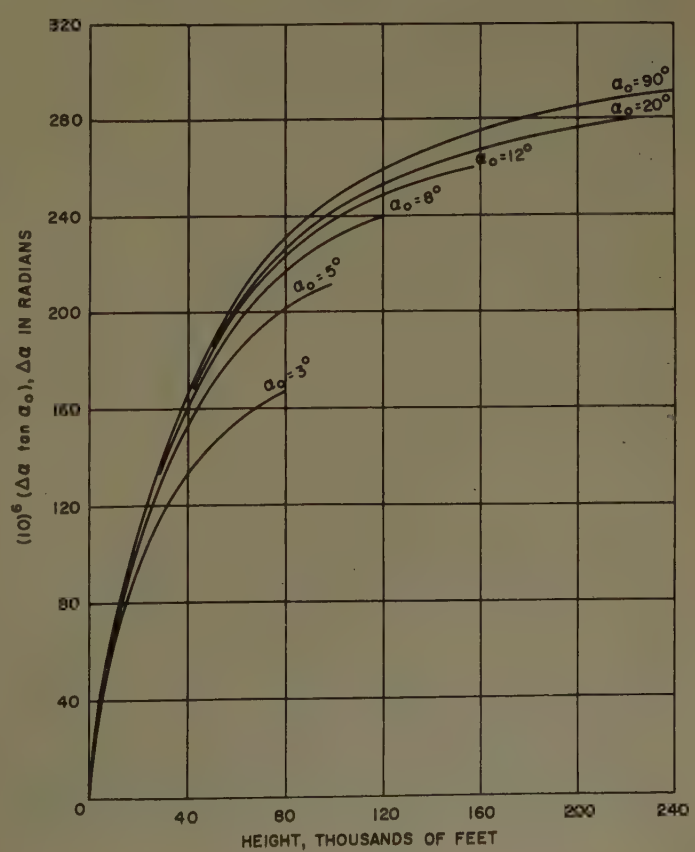

Fig. 2—Elevation angle errors for mean profile no. 1.

[3] The $\alpha = 90°$ case is a trivial one since tan α and $\Delta\alpha$ have the values ∞ and 0, respectively. However, the product ($\Delta\alpha$ tan α) remains finite as $\alpha \to 90°$, the limiting value being the maximum for this product in practical cases.

for each target position would vary considerably from case to case.

From a study of either (1) or the errors for the different profiles it is seen that the value of refractive index at the radar level has a more severe effect upon the elevation-angle error than variations at any other level, especially for high targets. Also, the refractive index near the surface in general varies more widely from time to time and place to place than the refractive index at higher levels. Thus, a rough indication of the amount of refraction for a given atmospheric condition is contained in the surface value of refractive index.

Naturally the surface refractive index (and consequently the refraction) at sites several thousand feet above mean sea level is normally less than for low stations. This effect is evident in a comparison of the errors for profiles 4 and 30 with those for profiles 1 and 17, respectively.

An examination of the errors for the monthly mean profiles reveals that the refraction is, in general, least for cT air, intermediate for cP and mP air, and greatest for mT air. This observation is as expected since the refractive index of air at a given pressure level increases with increasing moisture content and decreasing temperature, the moisture content being the more important factor at the surface. In a cT air mass the air is hot and dry, both factors leading to a low value of refractive index. In polar air masses the low temperature and low water content result in an intermediate refractive-index value, cP air generally being drier but also colder than mP air. The moisture content in mT air is normally sufficiently great to cause the refractive index to be relatively quite high. The results for profiles 1, 10, and 23 give a good comparison of dependence upon air mass type since the station elevation in each of these cases is quite low.

The season and latitude are found to be less dominant factors in refraction based on mean profiles representative of air masses in their source regions.

For $\alpha = 12°$ and $h = 100{,}000$ feet, the elevation-angle errors for the 34 mean profiles in Table II vary between the extremes of 0.87 and 1.43 milliradians. The percentage variation would not be greatly different for the other columns in the table (except possibly for $h = 10{,}000$ feet). Thus the mean conditions for different locations have a considerable spread about a world-wide average.

Day-to-Day Variations

From the results of the last section it is seen that corrections for propagation errors in radar guidance systems based upon a mean profile for the location and season would be a considerable improvement over basing the corrections on a world wide mean. Though in some locations a particular type air mass may remain relatively "pure" throughout a given season, at many places, particularly in middle latitudes, several different air mass types may influence the climatological situation during a single month. Thus the radar errors due to propagation at some locations may change only slightly over an extended period of time, while at other places the spread in the errors may be relatively large. The results of an investigation of the day-to-day variations in propagation conditions at some selected U. S. stations are contained in this section.

Data Employed

Theoretical elevation-angle errors have been computed for a large number of refractive-index profiles for the nine stations indicated in Fig. 3. These locations were selected as being representative of widely different climatological situations.

The meteorological data have been obtained from standard U. S. Weather Bureau information, values being taken from Daily Upper Air Bulletins for the standard pressure levels. For each station the 0300Z soundings for the odd days of the month were employed for 1950–1954 for January and 1950–1953 for July.

Elevation-Angle Error Distributions

The main results of this phase of the investigation are presented in Fig. 3 in the form of distribution-of-error curves for each location and month for $\alpha = 90°$ and $h = 200{,}000$ feet and for $\alpha = 3°$ and $h = 10{,}000$ feet. Points for the distribution curves were obtained by dividing the $(\Delta\alpha \tan \alpha)(10)^6$ scale into intervals of two units each, counting the number of cases that fell into each of these intervals, and smoothing these points by obtaining running averages using weighting factors in the ratios 1:2:3:2:1. These points were used as a guide for drawing the distribution curves but a little additional smoothing was incorporated.

The error distribution curves for the different locations exhibit the characteristics that would be expected qualitatively from known general meteorological conditions. For example, the error distribution curves for Tatoosh Island are relatively narrow for both January and July because of the maritime influence, in which variations in both moisture and temperature are small through the year. On the other hand, most of the errors for Lake Charles are closely bunched for July but are widely scattered for January. This results from a predominant Gulf breeze during the summer, intrusions of polar air being rare, while in the winter cold fronts more frequently pass through Lake Charles so that the meteorological conditions range all the way from warm and moist due to winds from the Gulf to cold and dry associated with cP air following a front. The situation for Columbia is the reverse of that for Lake Charles, the air mass type being more consistently continental polar during the winter while in the summer air from the Gulf frequently covers the area in addition to the polar air. Similar qualitative explanations apply for the remaining stations. It is felt, therefore, that the results presented here can be applied at least qualitatively to numerous other locations with similar climatological environments.

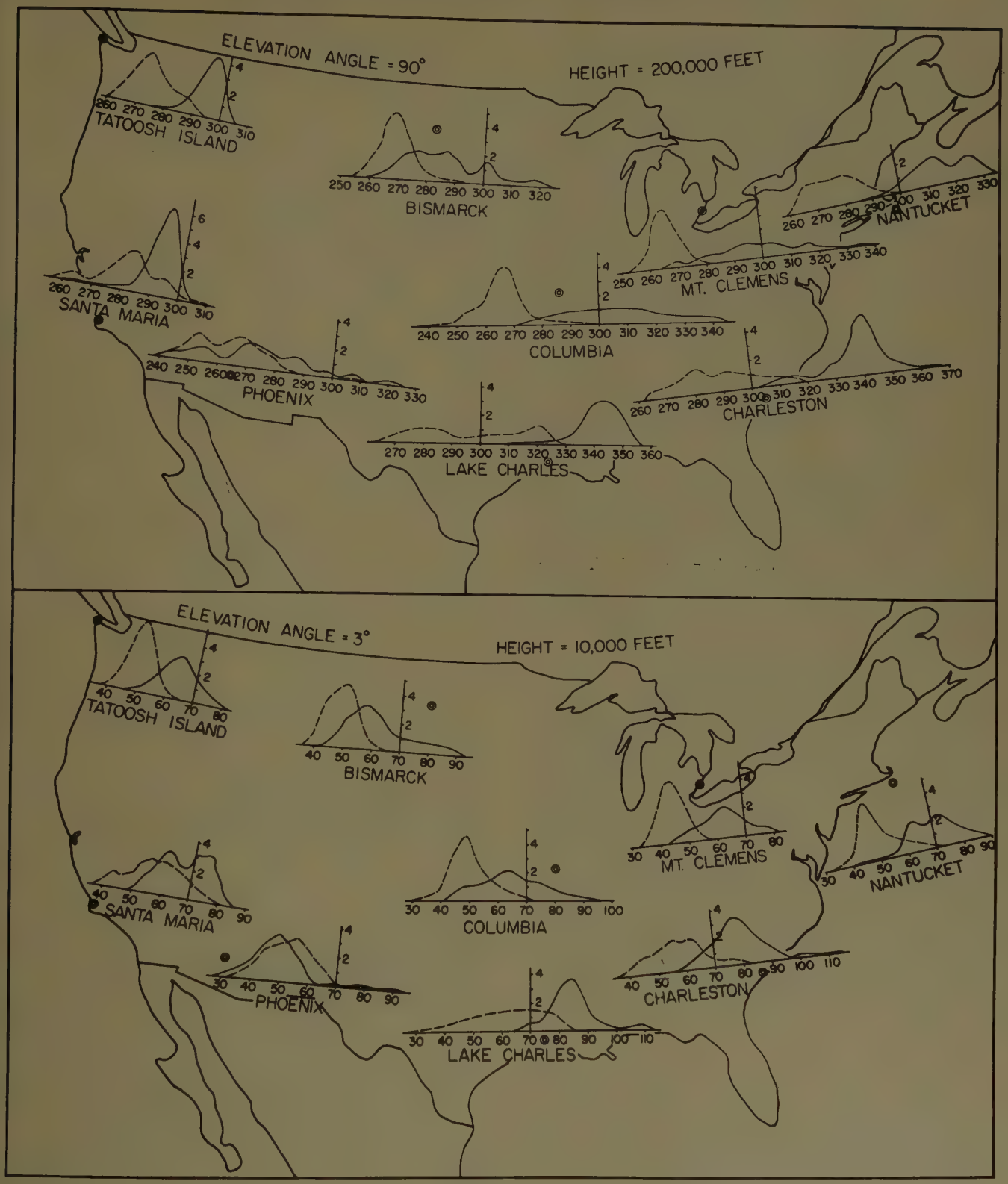

Fig. 3—Error distribution curves for nine U. S. locations—abscissas are $(\Delta\alpha \tan \alpha)\ (10)^4$, $\Delta\alpha$ in radians. Ordinates are number of cases per unit of abscissa. January data: dashed curve - - - ; July data: solid curve———.

For the error distribution curves in Fig. 3 and others for different heights and elevation angles not included here, it is observed that, in general, the shape and width of the error distribution curves vary only slightly with height (for $h > 10{,}000$ ft) and elevation angle for a given location and season even though the average value of $(\Delta\alpha \tan \alpha)$ increases considerably with increasing height. The error factor $(\Delta\alpha \tan \alpha)$, for a given profile and height, would be independent of elevation angle if it were not for the curvature of the earth and of the ray,

the effects of both of which are relatively small for $\alpha > 3°$. Since the quantity ($\Delta\alpha \tan \alpha$) is almost directly proportional to n_0 for great heights and to the average value of $(n_0 - n)$ over the height interval between the radar and target levels for low targets, the above noted observational fact implies that the percentage variation in the average gradient of refractive index for low heights is much greater than the percentage variation of n_0.

The separate values of the error factor ($\Delta\alpha \tan \alpha$) for Lake Charles for January and Columbia for July are plotted vs the surface refractive index in Fig. 4. A distinction has been made between tropical and polar air masses. These scatter plots show the error to be almost directly proportional to the surface refractive index for a given elevation angle for great heights. The error factor ($\Delta\alpha \tan \alpha$) and surface refractive index are seen to have about the same distributions for low heights even though there is quite a scatter to the points. At Lake Charles in January it is seen that in general the larger errors are associated with tropical air and the smaller values correspond to polar air masses. Thus, for this case, the spread of the errors would be considerably reduced if a distinction were made between the two air mass types. The same is not true for the case of Columbia for July, air mass contrasts being much less pronounced.

Diurnal Variations

There is frequently a pronounced diurnal variation of the temperature and humidity in the lower atmosphere. Since the diurnal variations are primarily the result of radiative heating and cooling of the surface, significant changes in the refractive index generally occur in only the first few hundred feet of the atmosphere. On the basis of this concept of the situation, the correlation between the errors and the surface refractive-index values should be considerably better for diurnal type variations than that indicated by Fig. 4 for low heights. Thus, in order to get an indication of the amount of diurnal variation to be expected in propagation errors, an analysis has been carried out on the surface refractive-index values for nine U. S. locations.

Data Employed

For this phase of the study, stations were selected to correspond as closely as possible with those employed in the day-to-day variations study. A number of replacements were necessary, however, because some of the surface data were not readily available. The pressure (MSL), temperature, and humidity data were obtained from standard U. S. Weather Bureau information, values being taken from the hourly Airways Weather reports. The months of January and July, 1953, were again selected and the surface refractive-index values computed at three-hour intervals.

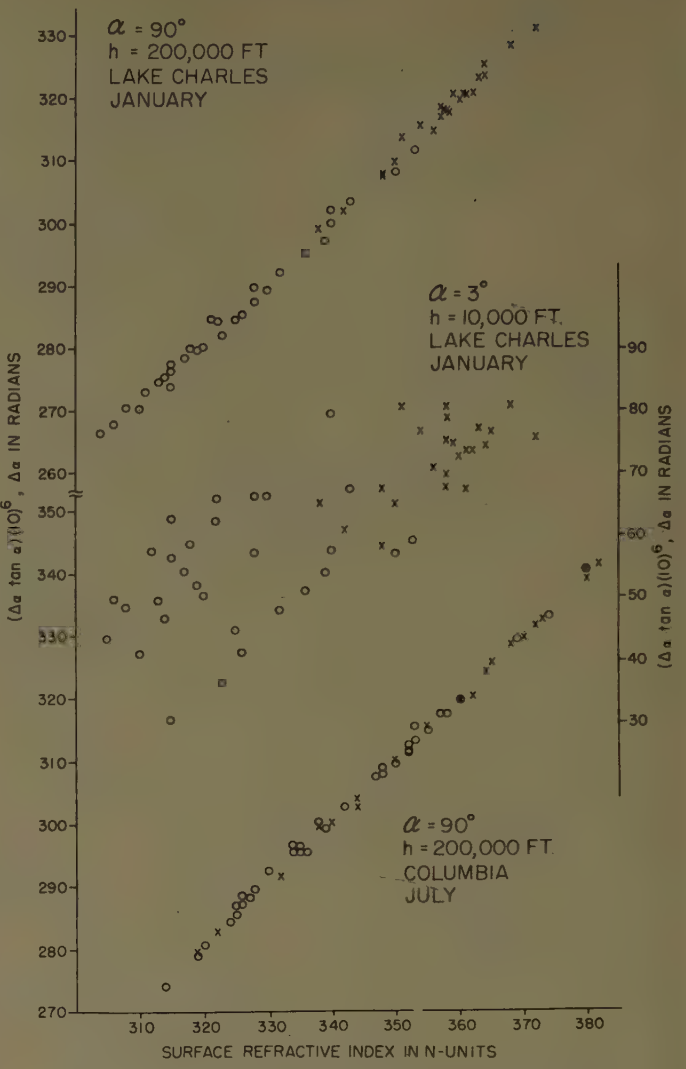

Fig. 4—Elevation-angle error vs surface refractive index for Columbia (July) and Lake Charles (January).

Results

The mean and standard deviation of the surface refractive index were computed for each location and month for each hour of the day considered. The pressure values used in the computations were not the actual surface values but ones modified to correspond to a mean sea-level value so that absolute values of computed index are considerably modified for stations with appreciable elevations. However, this modification will have negligible effect upon relative magnitudes.

Figs. 5 and 6 show the diurnal variations in the mean and standard deviation of surface refractive index for four of the stations studied. The curves shown for Bismarck, N. D., are found to pretty well represent the conditions for Columbia, Mo.; Boston, Mass.; and Grand Rapids, Mich., while the values for Lake Charles, La., correspond closely to those for Miami, Fla. Also, curves for Denver, Colo., are similar to the ones for

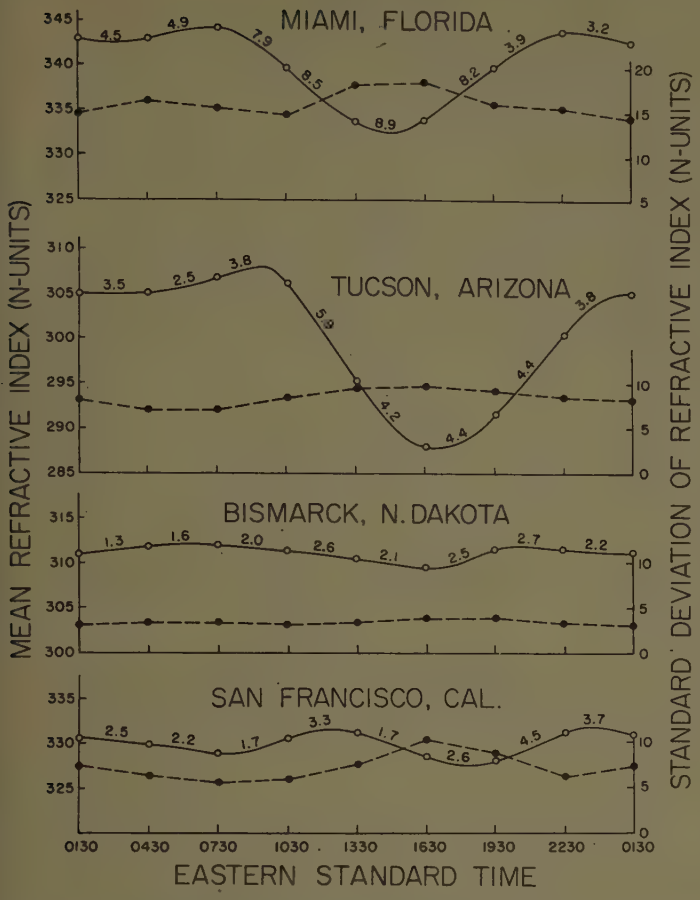

Fig. 5—Diurnal variation of mean surface refractive index for January. Solid curves = mean refractive index. Dashed curves = variance of the daily values of refractive index.

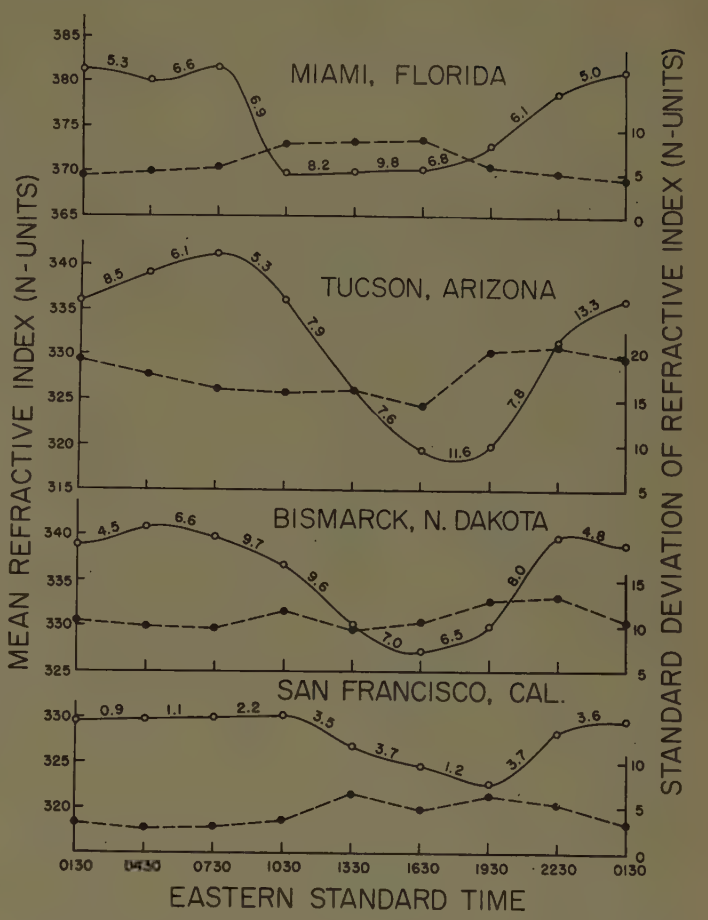

Fig. 6—Diurnal variation of mean surface refractive index for July. Solid curves = mean refractive index. Dashed curves = variance of the daily values of refractive index.

Tucson, Ariz., except that the diurnal variation in mean refractive index is not quite as pronounced for Denver.

As an indication of the relative variability in refractive index between two successive times, the standard deviation of the *difference* in refractive index between successive observations was computed for each station and season.

These values are entered as small numerals on the mean index curves between the times involved. These "difference-sigmas" reflect the degree of fluctuation in the daily changes in surface refractive index during the period involved. The effects of differing meteorological situations are evident in Figs. 5 and 6. Since the mean surface refractive index is closely associated with the mean value of $(\Delta\alpha \tan \alpha)$ and the standard deviation of the surface refractive index is indicative of the spread in error distribution curves of the type shown in Fig. 3, the results of this phase of the study furnish pertinent data concerning the diurnal and interdiurnal variations in propagation errors.

Solar Flares and Atmospheric Noise*

E. I. KING† AND A. W. SULLIVAN†

Summary—**In this paper, the effects of solar flares on low-frequency atmospheric noise are examined. Relations between the rise of noise, and the area of the flare, its intensity, location on the sun, and time of day are studied. Noise levels preceding flares are also examined to determine whether there are any phenomena which may be used for the prediction of high-frequency fade-outs.**

Introduction

SUDDEN IONOSPHERIC disturbances (SID's) have a severe disrupting effect on radio communications. These disturbances are generally defined as any anomalous condition in the ionosphere which alters the propagation of electromagnetic energy. Included are fade-outs (Dellinger fades), sudden phase anomalies (SPA), sudden enhancements of atmospherics (SEA), and also sudden cosmic absorption (SCA). There has also been some speculation as to whether solar flares might be identified by some radio means utilizing the effects of SID's. Solar flares could thus be "observed" under adverse visual conditions.

Bureau[1] was one of the first scientists to note a relationship between SEA's and solar flares. In 1937 he observed atmospheric noise on various frequencies from 12 to 46 kc. During some flares he noted that the noise increased. This enhancement was most pronounced between 22.2 and 30 kc, with a maximum at 27 kc. Below 22.2 kc and above 30 kc, the effect was less noticeable. He also observed that the increase in noise did not always occur, and concluded that the association depended on the magnitude of the flare.

Sullivan[2] examined a sample of atmospheric noise recorded during a flare, and observed that the most pronounced increase occurred at 189 kc, compared with a slight increase at 100 kc, and no noticeable effect at both 52 and 530 kc. A 100-kc signal was also recorded. These curves of Fig. 1 are typical of both the noise enhancements and the variation of signal strengths during a flare.

Kimpara[3] has noted an increase in noise levels at 27 kc during a flare. This flare was rather intense and produced other effects, including fade-outs and a geomagnetic disturbance. The SEA exhibited an interesting characteristic, however, as it began to increase about one hour before the onset of the flare. As the flare erupted, the noise enhancement became more pronounced. Kimpara suggested that if this increase were to occur regularly, the fade-outs which followed could be predicted.

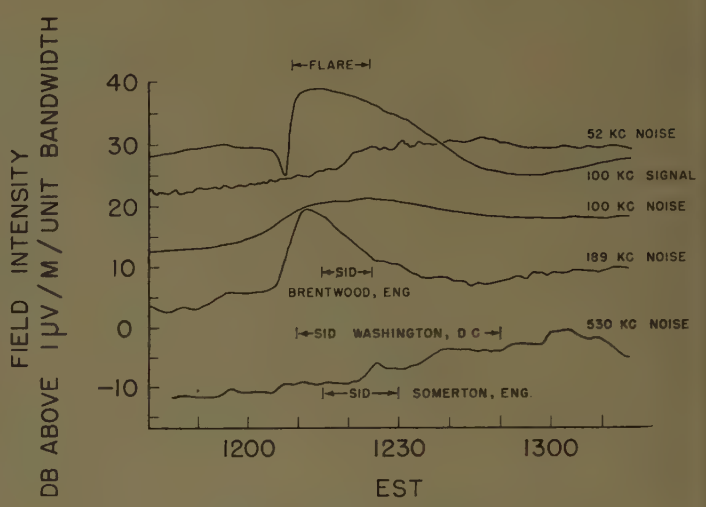

Fig. 1—Solar flare occurring on September 19, 1950.

Warwick[4] studied the association of flares with both SEA's and SID's. Although she notes a greater association of SEA's with larger and brighter flares, she states that SEA's may be associated with very small, faint flares. Furthermore, she sees no association of SEA's with the position of the flare, *i.e.*, as to whether the flare is east or west of the sun's central meridian; neither does she see any relationship between the increase of noise and the distance of the flare from the center of the solar disk.

Ellison[5] has studied the increase of noise as a function of the width of the H_α line of the flare emission. He believes this to be the simplest indication of the energy output of the flare, and hence of its effect on the ionosphere. By determining the per cent association of the noise with the different classes of flares, at different time intervals, he concludes that all flares of classes 2 and 3 may be identified between 0900 and sunset, local time. Thus with a small number of receivers properly placed in longitude, he feels that all flares of classes 2 and 3 may be identified, regardless of visual conditions.

Procedure

The noise records obtained at Gainesville, Fla., for the first five months of 1951 were examined to investigate the relationship between flares and SEA's at frequencies of 15, 52, 100, 189, and 530 kc. The average value of the noise envelope at the output of a diode detector with a 40-second time constant was measured with a 70-foot vertical antenna feeding a narrow-band

* Manuscript received by the PGAP, September 6, 1955; revised manuscript received, September 11, 1956.

† Eng. and Ind. Experiment Station, Univ. of Florida, Gainesville, Fla.

[1] R. Bureau, "Ionospheric disturbances of sudden beginning and their effect on long waves," *C. R. Acad. Sci., Paris*, vol. 206, p. 361; 1938.

[2] A. W. Sullivan, H. M. VanValkenburg, and J. M. Barney, "Low frequency atmospheric radio noise in Florida," *Trans. Amer. Geophys. Union*, vol. 33, pp. 650–656; October, 1952.

[3] A. Kimpara, "The sudden ionospheric disturbances on 22 November 1952," *Proc. Res. Inst. Atmos. Nagoya Univ.*, vol. 2, pp. 40–52; January, 1954.

[4] C. S. Warwick, "Some Characteristics of Solar Flares," Sci. Rep. No. 14, Harvard Univ., Cambridge, Mass.; January, 1954.

[5] M. A. Ellison, "The H_α radiation from solar flares in relation to sudden enhancements of atmospherics near 27 kc/s," *J. Atmos. Terr. Phys.*, vol. 4, pp. 226–239; December, 1953.

receiver. Flare data obtained from CRPL[6] publications were time of occurrence, area, intensity, and location on solar disk.

Due to various reasons, noise data were not available for all five frequencies during every flare. Thus, in those analyses in which frequency was not a factor, an SEA was indicated when the noise increased on any one frequency.

Per cent association (PA) is used as an indication of the relationship between the flares and SEA's. Mathematically,

$$\text{PA} = \frac{X}{X+Y}$$

where

X = number of flares with SEA's

Y = number of flares with no SEA's

$X+Y$ = total number of flares.

The probable accuracy of each point is a function of both the value of PA, and the total number of flares in the sample. If the calculated PA is assumed to be correct, the standard deviation[7] from this value, is $\sigma = PQ/N$, where P = PA, $Q = 100 - \text{PA}$, N = number of flares in the sample.

Results

The first characteristic of the flares examined for its effects on SEA's was the flare intensity. The data were divided into three groups according to the intensity of the flares, and the PA was calculated for each frequency individually, and for the frequencies as a group (assuming an SEA to occur if any frequency showed an increase during a flare).

Referring to Fig. 2 there appears to be a relationship between the intensity of the flare and the per cent association of SEA's. That is, the greater the intensity of a flare, the greater the probability of an SEA.

In the event that both the intensity and the amount of radiation would be related to the PA of SEA's, the relationship between SEA's and the area of the flare is presented in Fig. 3. There is evidence of a trend, but owing to the small number of samples, it is quite possible that this trend is due to chance.

If the ultraviolet radiation from a solar flare were to show any directional characteristic, the per cent association might show a relationship to the location of the flare on the solar disk. A plot of the relationship between PA and the angle that the radius vector to the flare made with the line of sight to the earth is shown in Fig. 4 (next page). Although there seems to be a greater PA for flares near the solar limb, the σ is again large enough to make this slight correlation almost meaningless. Thus it is assumed that the flare radiation causing SEA's is

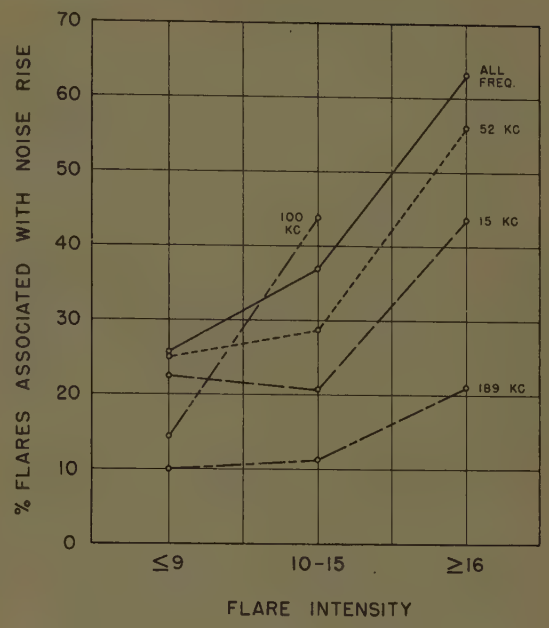

Fig. 2—Per cent association of noise rise during flares as a function of flare intensity.

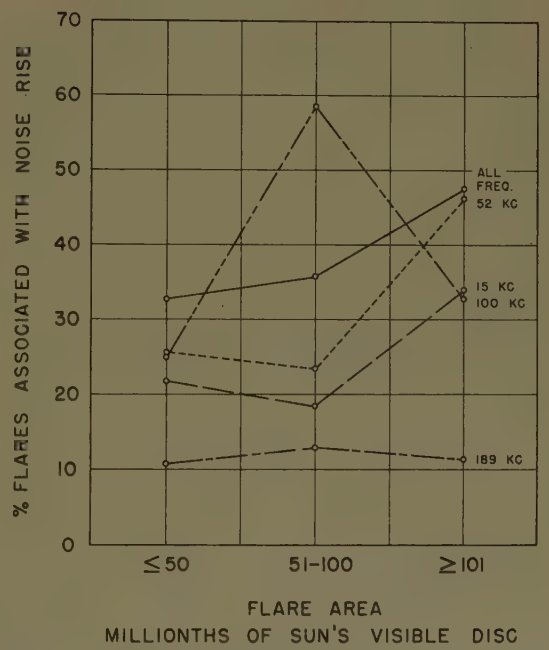

Fig. 3—Per cent association of noise rise during flares as a function of flare area.

either nondirectional, or only slightly so. Other investigators have concluded that the radiation from flares is nondirectional.

Considering the diurnal variation of various characteristics of the ionosphere, a diurnal variation of PA was expected. The results of the analysis for all frequencies as shown in Fig. 5 indicate that PA was greatest from 1200–1800^h EST (PA = 45.0), and descended to a minimum from 1800–2400^h (PA = 30). It is interesting to note that SEA's do occur at night when this side of the earth is in darkness.

Per cent association as a function of frequency without regard to the various flare parameters is indicated

[6] U. S. Dept. of Commerce, "Ionospheric Data," Central Radio Propagation Lab., Boulder, Colo.; 1951.

[7] C. H. Richardson, "An Introduction to Statistical Analysis," rev. ed., Harcourt, Brace and Co., Inc., New York, N. Y., p. 425; 1944.

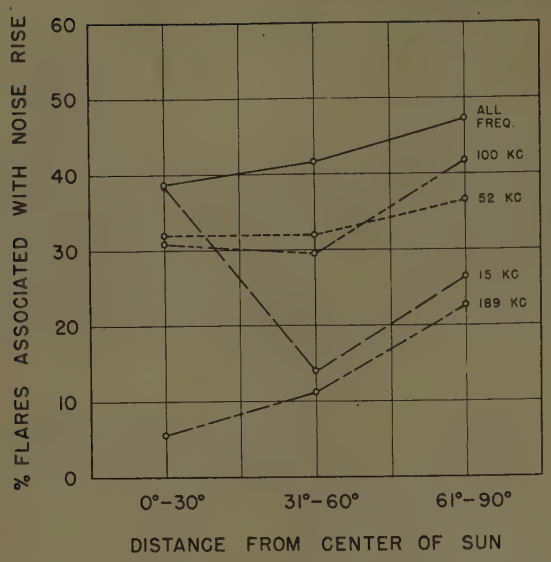

Fig. 4—Per cent association of noise rise during flares as a function of distance of the flare from the center of the sun.

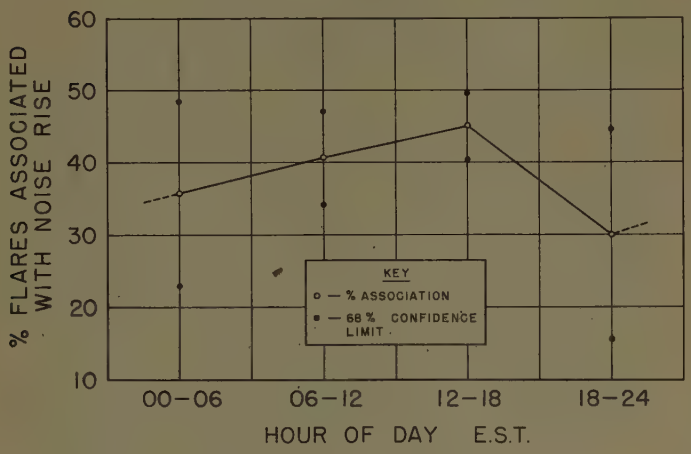

Fig. 5—Per cent association of noise rise during flares as a function of time of day.

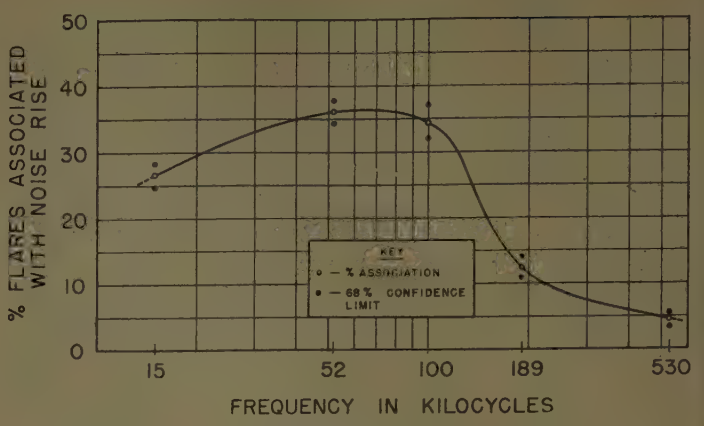

Fig. 6—Per cent association of noise rise during flares as a function of frequency.

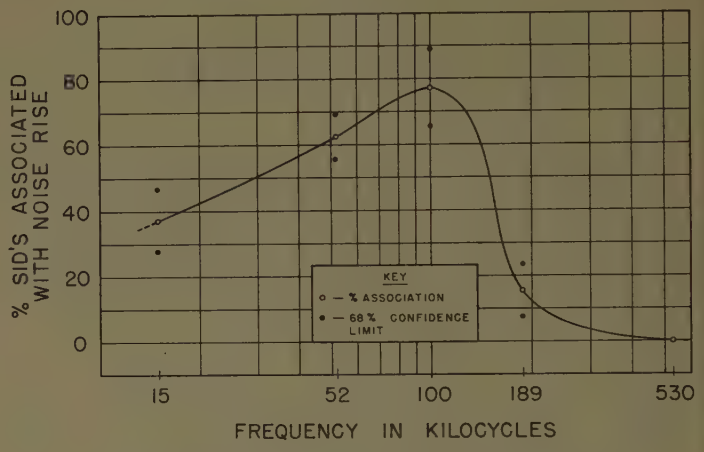

Fig. 7—Per cent association of noise rise during SID's as a function of frequency.

in Fig. 6. Although it is realized that there is a significant gap between 15 and 50 kc, the maximum per cent association of approximately 37 per cent occurs between 65 and 70 kc. This is the frequency band in which atmospheric noise levels are most likely to rise during the occurrence of a flare. However, if the flare were accompanied by an SID the maximum association (PA = 77.0 per cent) occurs at about 100 kc, as shown in Fig. 7.

It should be noted that per cent association does not give the relative effect of a flare on noise, but rather the probability that the flare will affect the noise. It may be reasonably assumed, however, that the classes of flares which show a greater PA will also have a greater effect on the noise rise. That is, the greater the probability for an SEA, the more pronounced will that SEA be, when, and if, it occurs.

Conclusion

Bureau's results indicated that the noise increase was most pronounced between 22.2 and 30 kc, falling off below 22.2 and above 30 kc. Although there is a gap in Fig. 6 from 15–52 kc, it seems unlikely that there could be a maximum between 22.2 and 30 kc. However, it is quite likely that both results are correct and the variation is due to geographic location of the receivers relative to the noise sources. Bureau's observation that an SEA did not always occur during a flare was substantiated. It seems evident that SEA's cannot be used to detect the occurrence of flares with a high degree of accuracy from a single receiving site, even though a relatively wide band of frequencies are monitored.

One of the more useful applications of SEA's would have been in predicting SID's. Kimpara's observations of an increase in the noise approximately one hour before a flare was an indication of a possibility of predicting SID's. Unfortunately this effect was never noted in the noise recorded at Gainesville, Fla.

Warwick's conclusion noting a greater association of SEA's with larger and brighter flares is well substantiated, although the relationship with flare intensity is much more pronounced than with area. With respect to the flare position on the sun, both studies seem to indicate no relationship.

Acknowledgment

The research reported in this paper was made possible through support and sponsorship extended by the Air Force Cambridge Research Center, Cambridge, Mass., under Contract No. AF 19(604)-876.

On Scattering and Reflection of Electromagnetic Waves by Rough Surfaces*

VICTOR TWERSKY†

Summary—**Simple approximations for the reflection coefficients and differential scattering cross sections per unit area of a random distribution of arbitrary protuberances on a ground plane are given in terms of the scattering amplitude of an isolated protuberance, their average number in unit area, and the given incident wave. These functions take into account multiple coherent scattering, and are mutually consistent in fulfilling the energy principle. It is shown, in general, that if the horizon angle approaches zero, then the reflection coefficients approach unity linearly, and the horizontal/vertical back scattering vanishes like the fourth/second power of the angle. General results are then specialized to arbitrary hemispheres and circular semicylinders, and applied to limiting cases of perfect conductors with radii very small or very large compared to wavelength.**

Introduction

WE CONSIDER a simple model for the scattering and reflection of waves from rough surfaces: a plane electromagnetic wave incident on a uniformly random distribution of relatively arbitary bosses (protuberances) on a ground plane. It seems to take account of the essential physics of the problem, and is at the same time simple enough to be analyzed in some detail.

Our approach is essentially an extension of Rayleigh's treatment of a single circular semicylinder,[1] and of our previous single scattering treatment of distributions of circular semicylinders and hemispheres.[2] The present material applies to relatively arbitrary bosses, and although the treatment is approximate it includes the effects of multiple coherent scattering.

We obtain the reflection coefficients

$$R_{\pm}(k_0, k_i) = \left| \pm \frac{1 + Z_{\pm}}{1 - Z_{\pm}} \right|^2, \qquad Z_{\pm} = \frac{\pi \rho f_{\pm}(k_0, k_i) \cdot \mathbf{e}}{k^2 \mathbf{i} \cdot \mathbf{e}},$$

and the corresponding differential scattering cross sections per unit area

$$\sigma_{\pm}(\mathbf{s}, k_i) = \frac{\rho}{k^2} \left| \frac{f_{\pm}(\mathbf{s}, k_i)}{1 - Z_{\pm}} \right|^2.$$

Here $+$, $-$ indicate incident "vertical," "horizontal" polarization with respect to the ground plane; ρ is the average number of scatterers in unit area, and $k = 2\pi/\lambda$. The unit vectors k_i, k_0, and $\mathbf{s}$ are the directions of incidence, specular reflection (with respect to ground), and observation; $\mathbf{e}$ is the direction normal to the plane of incidence (*i.e.*, the direction of the incident $\boldsymbol{H}_+$ and $\boldsymbol{E}_-$), and $\boldsymbol{i}$ is the normal of the ground plane. $f_{\pm}(\mathbf{s}, k_i)$ is the scattering amplitude of an isolated boss (*i.e.*, the far field angular function), subject primarily to the restriction that $\mathbf{f}(k_0, k_i) = f(k_0, k_i)\mathbf{e}$. For the two-dimensional problem of a "striated" surface (such that the plane of incidence and observation is normal to the axes of the cylindrical scatterers) we divide Z by π/k, and σ by $\pi/2k$; also ρ is to be multiplied by unit length.

The above R and σ (and their extensions to distributions in boss size, shape, etc. we discuss in the text) are mutually consistent in fulfilling the energy principle. They are simple enough in form so that certain general consequences can be deduced directly for relatively arbitrary bosses, *e.g.*, that the reflection coefficients approach unity linearly as the horizon angle vanishes. They depend essentially on the scattering amplitude of an isolated boss, which may in turn be expressed in terms of the amplitude of the symmetrical scatterer consisting of the boss and its reflection in the ground plane. Thus we may apply the above directly to half circular cylinders, spheres, and ellipsoids, making use of the known functional forms, tabulated values, or experimental data for the "full" scatterers. For a more complicated scatterer, we may use a static approximation at one frequency limit and a current distribution approximation at the other, or make direct measurements on the single object. To illustrate such applications, we later specialize R and σ to circular semicylinders and to hemispheres, and treat the case of perfect conductors with radius very small and very large compared to wavelength in some detail.

In order to facilitate application of the results (*e.g.*, to propagation over rough terrain and seas, to the effects of surface roughness on large microwave components or other approximately smooth scatterers, etc.), our present derivation is essentially intuitive; we use far field forms, a selfconsistent argument, and the energy principle. An analytical treatment[3] would begin with

* Manuscript received by the PGAP, January 20, 1956; revised manuscript received, April 28, 1956. This work was supported in part by contracts DA-36-039-sc-31435 at the Electronic Defense Lab., Mountain View, Calif., and AF-19(122)-42 at the Institute of Mathematical Sciences, Division of Electromagnetic Research, New York Univ., New York, N. Y.

† Electronic Defense Lab., Sylvania Elec. Prod., Inc., Mountain View, Calif.

[1] Lord Rayleigh, "On the light dispersed from fine lines ruled upon reflecting surfaces or transmitted by very narrow slits," *Phil. Mag.*, vol. 14, pp. 350–359; September, 1907; Rayleigh regarded the scattered part of the solution as specifying the incoherent scattering of a striated surface. Plots of the scattered intensity will be found in C. T. Tai, "Reflection of Plane Electromagnetic Waves from a Perfectly Conducting Grounded Half-Cylinder," TR No. 40, Cruft Lab., Harvard Univ., Cambridge, Mass.; 1948.

[2] V. Twersky, "Reflection coefficients for certain rough surfaces," *J. Appl. Phys.*, vol. 24, pp. 659–660; May, 1953.

[3] See V. Twersky, "On Multiple Scattering and Reflection of Waves by Rough Surfaces," rep. no. EDL-E9, Sylvania Electronic Def. Lab., 1955, for an analytical treatment of the analogous scalar problem; this report treats the electromagnetic and acoustic cases in parallel. The analytical material and acoustic applications of this report will be published in *J. Acoust. Soc., Amer.*, vol. 29, January, 1957. The present paper overlaps the applications section of the one on acoustics (see footnote 8); we rephrase certain material here in electromagnetic terms in order to facilitate application and comparison with experiment.

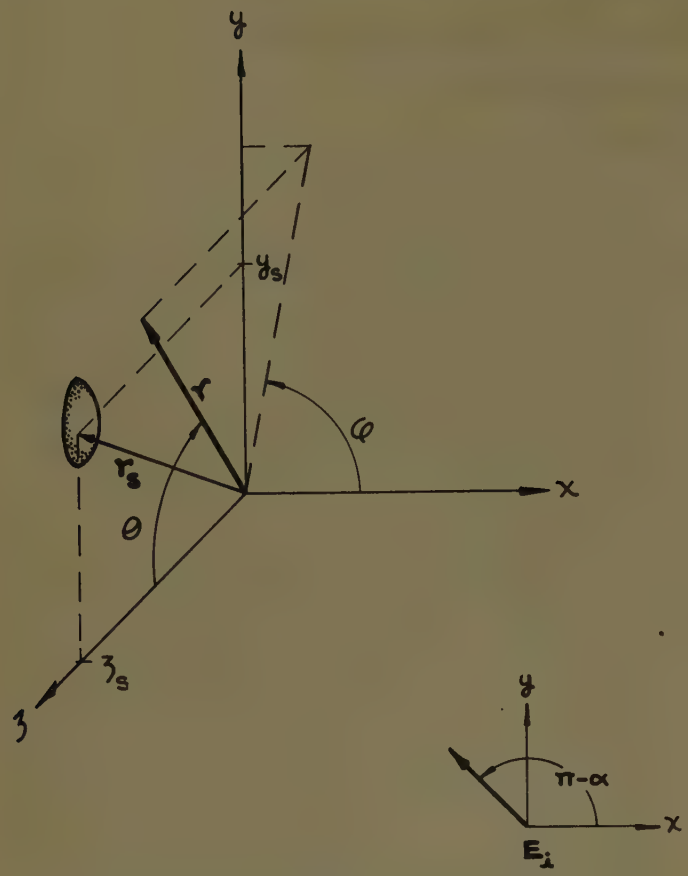

Fig. 1—Scattering of a plane wave by an arbitrary boss on a perfectly conducting plane.

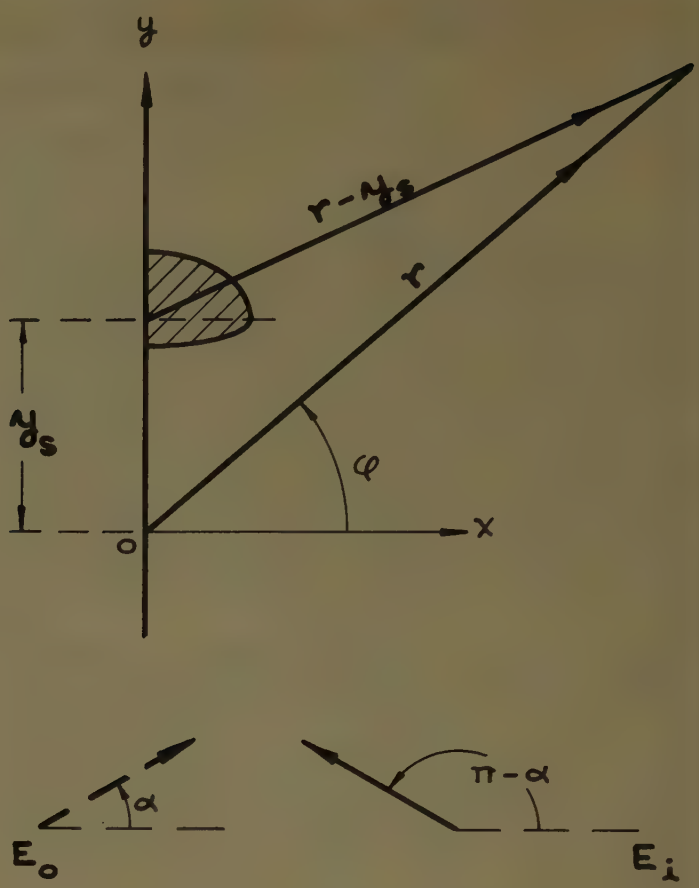

Fig. 2—Scattering of a plane wave by an arbitrary cylindrical boss on a perfectly conducting plane.

a Green's function representation for the boundary value problem of a single configuration of bosses, and seek to average the corresponding energy flux over an ensemble of such configurations. Our forms of R and σ would then be obtained by approximating averages with two variables held fixed by averages with one fixed, and neglecting the excitation of a scatterer arising from the fluctuations of the average radiation scattered by the others. Thus, through either derivation, the range of validity of our forms is to be determined by quantitative experiments. Their qualitative accord with certain existing measurements is discussed in the text.

In distinction to other models,[4] the present emphasizes the elementary scattering processes which may be involved in a variety of reflection phenomena. The results are limited in applicability primarily by the simplicity of the assumed "statistics," *i.e.*, here the average separation of scatterers is considered large compared to their width.

General Results

The Single Boss

We use the geometries of Figs. 1 and 2, restricting discussion to the right-hand half-spaces; the ground plane is $x=0$, and the plane of incidence is $z=0$. The two cases of incident E parallel and perpendicular to the plane of incidence, *i.e.*, "vertical" and "horizontal" polarizations, are distinguished by subscripts $+$ and $-$ respectively. The incident fields for the two cases are specified by

$$H_+^i = e \exp(ik\mathbf{r}\cdot k_i) = e\psi_i, \qquad E_-^i = -e\psi_i, \tag{1}$$

where the time factor $\exp(-i\omega t)$ is suppressed; $\mathbf{e}$ is a unit vector normal to the plane of incidence, and $k_i = -i\cos\alpha + j\sin\alpha$ is a unit vector in the incident direction of propagation. Corresponding fields reflected by the ground plane in the absence of bosses are

$$H_+^0, E_-^0 = e \exp(ik\mathbf{r}\cdot k_0) = e\psi_0, \tag{2}$$

where $k_0 = i\cos\alpha + j\sin\alpha$ is a unit vector in the direction of specular reflection. Here all units are suppressed since our final concern is only with certain dimensionless ratios in free space.

The solution of Maxwell's equations for scattering of a plane wave by a single, essentially arbitrary, boss at the origin of coordinates on the ground plane may be specified by

$$L = L^i + L^0 + L^s, \tag{3}$$

where $L^{i,0}$ represents $H_+^{i,0}$ or $E_-^{i,0}$, and where L^s indicates the corresponding scattered components. The re-

[4] See Appendix of footnote 3 for a representative bibliography.

maining field terms, and the boundary conditions at the boss, follow from Maxwell's equations. At large distances from the boss, $\boldsymbol{L}^s$ has the form

$$\boldsymbol{L}^s \sim h_0(kr)\boldsymbol{f}(\mathbf{s}, \mathbf{k}_i), \quad h_0(kr) = \frac{e^{ikr}}{ikr}, \quad \mathbf{s} = \mathbf{r}/r \tag{4}$$

in three dimensions, and

$$\boldsymbol{L}^s \sim H(kr)\boldsymbol{f}(\mathbf{s}, \mathbf{k}_i),$$

$$H(kr) = \left(\frac{2}{i\pi kr}\right)^{1/2} e^{ikr},$$

$$\boldsymbol{f}(\mathbf{s}, \mathbf{k}_i) = \mathbf{e}f(\phi, \pi - \alpha) \tag{4a}$$

in two. The scattering amplitude $\boldsymbol{f}$ indicates the far-field response in the direction $\mathbf{s}$ to plane wave excitation of direction $\mathbf{k}_i$ and "polarization" $+$ or $-$; f_+ is in units of $\boldsymbol{H}$, and f_- is in units of $\boldsymbol{E}$, *i.e.*, f_- and $f_+ \times \mathbf{s}$ give the scattered polarization.

Using an image technique due to Rayleigh,[1] we have in general

$$f_\pm(\mathbf{s}, \mathbf{k}_i) = g_\pm(\mathbf{r}, \mathbf{k}_0) \pm g_\pm(\mathbf{s}, \mathbf{k}_i), \tag{5}$$

where the $\boldsymbol{g}$'s are the scattering amplitudes of the symmetrical scatterer consisting of the boss and its reflection in the ground plane; $\pm\boldsymbol{g}_\pm(\mathbf{s}, \mathbf{k}_i)$ is the response of the scatterer to a wave of (1), and $\boldsymbol{g}_\pm(\mathbf{s}, \mathbf{k}_0)$ is the response to its image of (2). Equivalently f_+ is twice the symmetric component of $\boldsymbol{g}_+(\mathbf{s}, \mathbf{k}_0)$ with respect to reflection of the direction of incidence, and f_- is twice the antisymmetric component of $\boldsymbol{g}_-(\mathbf{s}, \mathbf{k}_0)$; useful alternative forms of the right side of (5) follow from the symmetry of the scatterer, and from the reciprocity theorem.

In the following we regard $\boldsymbol{f}$ essentially as a "parameter" of the problem of scattering by a distribution of bosses. If $\boldsymbol{g}$ is known explicitly, as for a sphere, then $\boldsymbol{f}$ for a hemisphere follows by superposition. More generally, approximations for $\boldsymbol{g}$ are to be obtained from the boundary value problem of an isolated scatterer excited by a plane wave, or from direct measurements.

By applying the vector analog of Green's theorem to $\boldsymbol{L}$ and $\boldsymbol{L}^*$ in the region external to the scatterer, and using a surface integral representation of the amplitude, we find that in the specular direction

$$-\mathrm{Re}\ \mathbf{e}\cdot\boldsymbol{f}(\mathbf{k}_0, \mathbf{k}_i) = (k^2/4\pi)p, \qquad p = p_a + p_s;$$

$$p_s = \frac{1}{k^2}\int_{1/2} |\boldsymbol{f}(\mathbf{s}, \mathbf{k}_i)|^2 d\Omega = \int_{1/2} q(\mathbf{s}, \mathbf{k}_i) d\Omega. \tag{6}$$

The function p is the total energy cross section of the boss (the time-averaged power it derives from the incident wave and dissipates as heat and as scattered radiation divided by the time-averaged incident power density), and p_a and p_s are the absorption and scattering cross sections. The $\frac{1}{2}$ on the integral indicates integration over the angular half-space containing the boss, and q is the differential scattering cross section.[5] Similarly in two dimensions we replace $k^2/4\pi$ in (6) by $k/4$, and $1/k^2$ by $2/\pi k$.

In addition to (6), which holds for both f_+ and f_-, there are other general restrictions on the amplitudes arising from reciprocity and symmetry (of the $\boldsymbol{g}$'s) which distinguish the behavior for the two polarizations. Thus it is clear physically that they differ near grazing incidence, since the plane wave excitation (*i.e.*, the sum of the two waves occurring in the image problem) approaches zero for f_- and doubles for f_+. In terms of the angles of incidence $(\pi-\alpha)$ and observation (ϕ) measured from the ground normal in the plane of incidence, it may be shown[6] that f_- vanishes like $\cos\alpha$, $\cos\phi$ as $|\alpha| \to (\pi/2)$, $|\phi| \to (\pi/2)(\theta = \pi/2)$ and that f_+ is nonvanishing (*i.e.*, that for these values f_- behaves essentially like $\boldsymbol{E}_-{}^i + \boldsymbol{E}_-{}^0$ and vanishes like $\cos\alpha\cos\phi$, while f_+ behaves like $\boldsymbol{H}_+{}^i + \boldsymbol{H}_+{}^0$). In terms of the "horizon angle" $\beta \to 0$, we have in the plane of incidence $(\theta = \pi/2)$

$$f_-\left(\phi, \frac{\pi}{2} + \beta\right), \quad f_-\left(\left|\frac{\pi}{2} - \beta\right|, \pi - \alpha\right) \to O(\beta);$$

$$f_-\left(\left|\frac{\pi}{2} - \beta\right|, \frac{\pi}{2} + \beta\right) \to O(\beta^2); \quad f_+ \nrightarrow O. \tag{7}$$

For simplicity, we restrict discussion to bosses whose amplitudes evaluated in the specular direction with respect to ground fulfill

$$\boldsymbol{f}(\mathbf{k}_0, \mathbf{k}_i) = \mathbf{e}f(\mathbf{k}_0, \mathbf{k}_i) = \mathbf{e}f. \tag{8}$$

This requires that $\boldsymbol{g}(\mathbf{k}_0, \mathbf{k}_0)$ and $\boldsymbol{g}(\mathbf{k}_0, \mathbf{k}_i)$ are both of the form $\mathbf{e}g$, *i.e.*, that for the symmetrical scatterer, the far field in the plane normal to $\mathbf{e}$ preserves the incident polarization (in the sense that it remains parallel or perpendicular) with respect to that plane.

Distribution of Bosses

Proceeding heuristically, we now extend the above to a random distribution of identical bosses covering the plane $x = 0$. The picture is essentially that of a two-dimensional ideal gas, the average separation of scatterers being assumed large compared to their size. We

[5] See V. Twersky, "Certain transmission and reflection theorems," *J. Appl. Phys.*, vol. 25, pp. 859–862; July, 1954 for the two-dimensional case; the extension to three is straightforward. Eq. (6) applies the usual "forward-amplitude scattering theorem" to an object on a plane by introducing a symmetry requirement. (Similarly for an object inside a "corner reflector" consisting of three right angled planes, an analogous theorem relates the amplitude in the back scattered direction to the total energy cross section.) Our normalization of the amplitude has been chosen so that for a bounded lossless object we obtain $-\mathrm{Re}\ \mathbf{e}\cdot\boldsymbol{g}(\mathbf{k}_0, \mathbf{k}_0) = (4\pi)^{-1}\int|\boldsymbol{g}(\mathbf{s}, \mathbf{k}_0)|^2 d\Omega$, *i.e.*, so that the right side is the average of $|\boldsymbol{g}|^2$ over all angles of observation; similarly for two dimensions, we have 2π instead of 4π.

[6] The dependence on α follows from applying the reciprocity theorem to rewrite (5) as $\boldsymbol{g}_\pm(-\mathbf{k}_0, -\mathbf{s}) \pm \boldsymbol{g}_\pm(-\mathbf{k}_i, -\mathbf{s})$, and then using the appropriate integral representations of the $\boldsymbol{g}$'s; *e.g.*, for a perfect conductor $\boldsymbol{g}_-(\mathbf{s}, \mathbf{k}_0) \propto \int e^{-ik\mathbf{s}\cdot\mathbf{r}'}(\mathbf{e} - \mathbf{ss})\cdot\boldsymbol{K}(\mathbf{r}', \mathbf{k}_0) dS'$ where $\mathbf{e}$ is the unit dyadic, and $\boldsymbol{K}$ the surface current. The dependence on ϕ follows from using the symmetry of the scatterer (the boss plus its reflection) to rewrite (5) as $\boldsymbol{g}_\pm(\mathbf{s}, \mathbf{k}_0) \pm \boldsymbol{g}_\pm(\mathbf{s}', \mathbf{k}_0)$, where (for $\theta = \pi/2$), $\mathbf{s}, \mathbf{s}' = \pm\mathbf{i}\cos\phi + \mathbf{j}\sin\phi$.

write the contribution at a field point $\boldsymbol{r}$ arising from a boss located at $\boldsymbol{r}_s$ (see Fig. 1) as

$$h_0(k|\boldsymbol{r}-\boldsymbol{r}_s|)\boldsymbol{F}(\mathbf{s},\boldsymbol{k}_i)\exp(i\boldsymbol{k}\boldsymbol{k}_i\cdot\boldsymbol{r}_s),$$
$$\mathbf{s}=(\boldsymbol{r}-\boldsymbol{r}_s)/|\boldsymbol{r}-\boldsymbol{r}_s|, \tag{9}$$

where $\boldsymbol{F}$ is the multiple scattered analog of $\boldsymbol{f}$, and where $\exp(i\boldsymbol{k}\boldsymbol{k}_i\cdot\boldsymbol{r}_s)$ is the phase difference at $\boldsymbol{r}_s$ introduced by the incident wave. Multiplying (9) by ρ, the average number of bosses in unit area, and using the method of stationary phase to integrate the result over the plane $x=0$, gives the average "coherent" scattered wave

$$\langle\boldsymbol{L}\rangle = 2C\boldsymbol{F}(\boldsymbol{k}_0,\boldsymbol{k}_i)\psi_0 \tag{10}$$

where $C=\pi\rho/k^2\boldsymbol{i}\cdot\boldsymbol{k}_0$; similarly in two dimensions we obtain (10) with $C=\rho/k\boldsymbol{i}\cdot\boldsymbol{k}_0$ and ρ as the number in unit length.

We obtain $\boldsymbol{F}$ from the selfconsistent assumption that the multiple scattered amplitude equals the response of an isolated boss to the incident plane wave plus its response to half the coherent plane wave arising from the distribution.[7] This assumption, restriction (7), and the fact that $f(\boldsymbol{k}_0,\boldsymbol{k}_i)=f(\boldsymbol{k}_i,\boldsymbol{k}_0)$, gives

$$\boldsymbol{F}(\boldsymbol{k}_0,\boldsymbol{k}_i)=\boldsymbol{F}(\boldsymbol{k}_0,\boldsymbol{k}_i)\mathbf{e}=\boldsymbol{F}\mathbf{e},\quad \boldsymbol{F}=f(1+C\boldsymbol{F})=f/(1-Cf). \tag{11}$$

Note that $\boldsymbol{F}$ cannot become infinite, since $C>0$ and $\mathrm{Re}\ f<0$ [from (6)]; if $|Cf|<1$, then $\boldsymbol{F}=f[1+Cf+(Cf)^2+\cdots]$ may be interpreted in terms of "orders of scattering."

The sum of the coherent scattered wave (10) plus the wave reflected from the ground plane (2) gives the total coherent reflected wave

$$\langle\boldsymbol{L}_r\rangle = (1+2C\boldsymbol{F})\psi_0\mathbf{e}=\frac{1+Z}{1-Z}\psi_0\mathbf{e},$$
$$Z=Cf=C\mathbf{e}\cdot\boldsymbol{f}(\boldsymbol{k}_0,\boldsymbol{k}_i), \tag{12}$$

where $C=\pi\rho/k^2\cos\alpha$, $\rho/k\cos\alpha$ for three, two dimensions. Since the first Fresnel zone has the area $\pi r\lambda/\cos\alpha$, or the width $2(\lambda r)^{1,2}/\cos\alpha$ in two dimensions (provided that $\lambda\ll\gamma\cos^2\alpha$), the coherent scattering of (10) is proportional to the average wave scattered in the specular direction by an element at the center of the zone times the number of elements in the zone; from this viewpoint, we may use (12) for practical purposes when the "illuminated region" includes the first Fresnel zone.

From (12) and (1) we obtain the "reflection amplitudes," and the power reflection coefficients

$$A_\pm=\pm\frac{1+Z_\pm}{1+Z_\pm},\qquad R=\left|\frac{1+Z_\pm}{1-Z_\pm}\right|^2. \tag{13}$$

[7] The factor 1/2 may be interpreted (except for normal incidence) as the sum of contributions from scatterers lying between a boss and the source; however, it is a consequence of the definitions of the amplitudes. The analogous procedure for a "random screen" (see footnote 3) uses the incident wave and the mean of the coherent reflected and forward scattered waves.

The phase change of the coherently reflected wave introduced by the scatterers is given by

$$\tan^{-1}[2ImZ/(1-|Z|^2)];$$

here π is to be added to the horizontal polarization to obtain the total phase change on reflection. The functions $Z_-\sec\alpha$ and $Z_+\cos\alpha$ are the normalized surface impedances for the coherent wave, *i.e.*, the ratio of $E_{\tan}$ to $H_{\tan}$ on the ground plane divided by the impedance of the external medium.

Having obtained the average coherent field, we now use the energy principle to obtain a corresponding value of the "incoherent," (*i.e.*, fluctuation) scattering from unit area of distribution. Thus since the normalized time-averaged power in unit area of incident wave must equal the power coherently reflected, incoherently scattered, and absorbed by that portion of the "surface" it illuminates, we require

$$1=R+\rho P/\boldsymbol{i}\cdot\boldsymbol{k}_0,\qquad P=P_a+P_s,$$
$$\rho P_s=\int_{1/2}\sigma(\mathbf{s},\boldsymbol{k}_i)d\Omega, \tag{14}$$

where P, the analog of p of (6), is the total cross section of a boss in the distribution, and σ is the differential scattering cross section per unit area. Applying (14) to R of (13) and then using (6) gives $P=p/|1-Z|^2$, and consequently $\int_{1/2}\sigma d\Omega=\rho|1-Z|^{-2}\int_{1/2}qd\Omega$; hence, on equating within the integral sign, we obtain

$$\sigma(\mathbf{s},\boldsymbol{k}_i)=\frac{\rho q(\mathbf{s},\boldsymbol{k}_i)}{|1-Z|^2}=\frac{\rho|\boldsymbol{f}(\mathbf{s},\boldsymbol{k}_i)|^2}{k^2|1-Z|^2}; \tag{15}$$

for two dimensions, we divide σ by $\pi/2k$.

We use these forms of R and σ (which neglect primarily the incoherent multiple scattering) in all that follows. For either polarization, R gives the coherently reflected power density, and $\sigma(\mathbf{s},\boldsymbol{k}_i)$ gives the incoherent power scattered into unit solid angle around $\mathbf{s}$ by unit area of "surface" (or into a wedge of unit plane angle and unit height, for two dimensions); these are time-averaged (over one period) and ensemble averaged, and have been normalized by division by the time-averaged incident power density. The total average reflected (Poynting) power for a distribution in the plane $x=0$ is

$$\langle\boldsymbol{S}\rangle=R(\boldsymbol{k}_0,\boldsymbol{k}_i)\boldsymbol{k}_0+\iint\frac{\sigma(\mathbf{s},\boldsymbol{k}_i)}{|\boldsymbol{r}-\boldsymbol{r}_s|^2}\mathbf{s}dy_sdz_s,$$
$$r_s^2=y_s^2+z_s^2, \tag{16}$$

where $\mathbf{s}$ is a unit vector from a point on the plane of the distribution $\boldsymbol{r}_s$ to the observation point $\boldsymbol{r}$; see Fig. 1. Antenna factors, etc., may be introduced to obtain practical forms, the origin of $\boldsymbol{r}$ and $\boldsymbol{r}_s$ being taken as the center of the illuminated region; for narrow beams, only

the k_0 term need be retained near the specular angle, and only the **s** term at other angles. In two dimensions, for a distribution along the y axis, we drop the integration over z_s (the direction **e** of the axes of the infinite cylinders), and replace $|\boldsymbol{r}-\boldsymbol{r}_s|^2$ by $|\boldsymbol{r}-\boldsymbol{r}_s|$; see Fig. 2. The reflection problem is thus determined by R and σ, and these are specified in (13) and (15) essentially by the known, or measurable, scattering amplitude of an isolated boss.

Our results are to be compared with: 1) the averages of measurements over a large number of appropriate, fixed configurations of scatterers; 2) with time-averaged measurements over a moving collection of scatterers (here the motion must be slow enough so that each wavelength "sees" effectively a fixed configuration, and the measurement interval long enough to include a large number of configurations).

The above may be generalized directly to more than one kind of scatterer. Thus if we rewrite the amplitude of (12) in the selfconsistent form $B=(1+Z)/(1-Z)=(1+Z)+BZ$, this indicates that for a discrete distribution of several types of scatterers we replace Z in R by

$$Z = \Sigma_n Z_n = \Sigma_n \frac{\pi \rho_n f_n}{k^2 \cos \alpha}, \tag{17}$$

where ρ_n is the number of type n scatterers in unit area. [The different types of scatterers are in "series"; that all "coupling" between them is included may be seen from expanding $(1+\Sigma Z_n)/(1-\Sigma Z_n)$]. The corresponding differential scattering cross section per unit area is again obtained from the energy theorems (14) and (6):

$$\sigma(\mathbf{s}, \boldsymbol{k}_i) = \Sigma \sigma_n = \Sigma \frac{\rho_n |\, f_n(\mathbf{s}, \boldsymbol{k}_i)\,|^2}{k^2 |\, 1 - \Sigma Z_m\,|^2}. \tag{18}$$

Similarly for a continuous distribution in size, shape, physical properties, or orientation of the scatterers, we replace the sums in (17) and (18) by integrations over the appropriate parameter, ρ again playing the role of the distribution function.

Note that the analogous results for a "random screen" may be obtained directly from the above. Thus the transmission and reflection amplitudes corresponding to either of the fields of (2) are $A_{t,r}=\frac{1}{2}(A_+ \mp A_-)$, where $A_\pm$ is given in (13) with $Z_\pm=(\pi\rho/k^2 \cos \alpha)[\boldsymbol{g}(\boldsymbol{k}_0, \boldsymbol{k}_0) \pm \boldsymbol{g}(\boldsymbol{k}_0, \boldsymbol{k}_i)]\cdot\boldsymbol{e}$. The corresponding differential cross section per unit area is $\sigma(\mathbf{s}, \boldsymbol{k}_0)=(\rho/k^2)|\boldsymbol{f}_1(1-Z_+)^{-1} + \boldsymbol{f}_2(1-Z_-)^{-1}|^2$, where $\boldsymbol{f}_{1,2}=\boldsymbol{g}(\mathbf{s}, \boldsymbol{k}_0) \pm \boldsymbol{g}(\mathbf{s}, \boldsymbol{k}_i)$. Here, in distinction to (5), the central $\pm$ is not correlated with the type of $\boldsymbol{g}$ (*i.e.*, with incident polarization).

General Deductions

Before applying R and σ to specific scatterers, we deduce certain general consequences. Thus from (12) and (7) we see that as the horizon angle β approaches zero, the Z's reduce to

$$Z_- \to O(\beta) \to 0, \qquad Z_+ \to O(\beta - 1) \to \infty \tag{19}$$

(however, the surface impedances become independent of β). The reflection amplitudes $\pm(1+Z_\pm)/(1-Z_\pm)$ thus approach -1 for either case, both polarizations having undergone phase changes of π on reflection. Thus the model acts like a perfect reflector as grazing incidence is approached, and this behavior of rough surfaces is well known experimentally. In addition, the phase change of both polarization components on reflection is in accord with interference experiments for even highly conducting surfaces. The phase change of the vertical component in such experiments is usually interpreted on the basis of a nonvanishing ratio of dielectric constant to conductivity (*i.e.*, a perfect conductor, as in (1) and (2), indicates a phase change of π only for the horizontal); however, we see that it may also be accounted for by scattering from surface roughness. (Of course, scattering is the significant mechanism in either interpretation, since the macroscopic parameters of a "uniform medium" must ultimately be derived by considering elementary scattering processes.)

The reflection coefficient near grazing, for either polarization, is thus

$$R = 1 + \frac{4 \operatorname{Re} Z}{|\, 1 - Z\,|^2} \to 1 - O(\beta), \tag{20}$$

so that R approaches unity linearly as the horizon angle vanishes. Also if the angle of observation is arbitrary but the angle of incidence approaches grazing, then, from (7) and (15) [or (18)], we see that σ_- and σ_+ vanish like β^2; if the angle of observation is near grazing in the plane of incidence, and the angle of incidence is arbitrary, then σ_- vanishes like β^2, and σ_+ is nonvanishing; if both angles are near grazing in the plane of incidence, *i.e.*, forward or back scattering near grazing, then

$$\sigma_- \to O(\beta^4), \qquad \sigma_+ \to O(\beta^2), \tag{21}$$

the back scattering being much larger for the vertical.

We are also led to other general results. Thus if $|f|$ is small (*e.g.*, small scatterers), and if the angle of incidence is not near grazing, then Z is small and we may approximate R and σ by their single scattered values:

$$R \to R^1 = 1 + 4 \operatorname{Re} Z = 1 - \rho p / i \cdot k_0, \quad \sigma \to \sigma^1 = \rho q(\mathbf{s}, \boldsymbol{k}_i),$$

$$\rho p_s = \int_{1/2} \sigma^1 d\Omega. \tag{22}$$

These forms also hold near grazing incidence for horizontal polarization (and arbitrary bosses), inasmuch as the original plane wave excitation becomes small for this case. They break down near grazing for vertical polarization because of multiple scattering; *i.e.*, there all secondary waves from scatterers between the source and a particular boss are in phase and reinforce, the phase differences introduced by the source at the various scatterers being annulled by their path differences.

Special Cases

In the following we specialize the above to circular semicylinders, and to hemispheres. We give explicit forms for perfect conductors with radius small and large compared to wavelength.[8]

Circular Semicylinders

For the two-dimensional problem as in Fig. 2, we have

$$\mathbf{f}(\mathbf{s}, \mathbf{k}_i) = f(\phi, \pi - \alpha)\mathbf{e}, \quad Z = \frac{\rho f(\alpha, \pi - \alpha)}{k \cos \alpha},$$

$$R = \left|\frac{1+Z}{1-Z}\right|^2, \qquad \sigma = \frac{2\rho}{\pi k}\left|\frac{f(\phi, \pi - \alpha)}{1-Z}\right|^2. \quad (23)$$

For a circular semicylinder we superpose the known results for the circular cylinder, and write

$$f_\pm(\phi, \pi - \alpha) = g_\pm(\phi, \alpha) \pm g_\pm(\phi, \pi - \alpha)$$

$$= \sum_{n=-\infty}^{\infty} A_{n\pm} e^{in\phi}[e^{-in\alpha} \pm e^{-in(\pi-\alpha)}], \quad (24)$$

where the A's are known. Thus for a perfect conductor of radius a (to which we restrict the following), we have $A_{n-} = -J_n(ka)/H_n(ka)$ in terms of Bessel functions and Hankel functions of the first kind; similarly for A_{n+}, we replace these functions by their ka derivatives.

If $a \ll \lambda$, then an expansion in powers of ka yields to lowest order

$$f_\mp(\phi, \pi - \alpha) = -\frac{i\pi(ka)^2}{2}\begin{Bmatrix} 2\cos\phi\cos\alpha \\ 1 - 2\sin\phi\sin\alpha \end{Bmatrix},$$

$$\mathrm{Re}\, f_\mp(\alpha, \pi - \alpha) = -\frac{\pi^2(ka)^4}{4}\begin{Bmatrix} \cos^2\alpha \\ (1 + 2\sin^2\alpha)/2 \end{Bmatrix}. \quad (25)$$

Thus to the order of $(ka)^4$ we have

$$|1 - Z_\mp|^2 = 1 + \frac{\pi^2(ka)^4}{4}\left[\frac{\rho}{k\cos\alpha}\begin{Bmatrix} 2\cos^2\alpha \\ 1 + 2\sin^2\alpha \end{Bmatrix} + \left(\frac{\rho}{k\cos\alpha}\right)^2\begin{Bmatrix} (2\cos^2\alpha)^2 \\ (1 - 2\sin^2\alpha)^2 \end{Bmatrix}\right]. \quad (25a)$$

Hence except near grazing incidence we may use[9]

$$R_\mp \approx R_\mp^1 = 1 - \frac{\pi^2\rho a(ka)^3}{2\cos\alpha}\begin{Bmatrix} 2\cos^2\alpha \\ 1 + 2\sin^2\alpha \end{Bmatrix},$$

$$\sigma_\mp \approx \sigma_\mp^1 = \frac{\pi\rho a(ka)^3}{2}\begin{Bmatrix} (2\cos\phi\cos\alpha)^2 \\ (1 - 2\sin\phi\sin\alpha)^2 \end{Bmatrix}. \quad (26)$$

The scattering is thus proportional to λ^{-3}, and consequently the longer wavelengths are better reflected. We have $R_+ \lesseqgtr R_-$ when $\alpha \gtrless 30°$; similarly for back scattering, $\sigma_+ \gtrless \sigma_-$ when $\alpha \gtrless 30°$; if $\alpha = 0$, and $\phi < 60°$, then the horizontal scattering is greater; if $\alpha = \phi = 0$, then $\sigma_- = 4\sigma_+$. On the other hand, if $\beta = (\pi/2) - \alpha = (\pi/2) - |\phi| \to 0$ then R and σ (back) reduce to

$$R_- \to 1 - \pi^2(ka)^3\rho a\beta, \qquad R_+ \to 1 - 6(k/\rho)\beta;$$

$$\sigma_- \to 2\pi(ka)^3\rho a\beta^4, \qquad \sigma_+ \to (18k/\pi\rho)\beta^2. \quad (27)$$

If $a \gg \lambda$, then[10] we may either evaluate (24) asymptotically, or else use an equivalent current distribution approximation for the cylinder, and superpose cylinder results to treat the boss. For a large cylinder excited by either of the waves of (2), we have[11]

$$g_\pm(\phi, \alpha) = \pm g_1(\phi, \alpha) + g_2(\phi, \alpha);$$

$$g_1 = \tfrac{1}{2}(ka\pi i\,|\sin\Phi|\,)^{1/2}e^{-i2ka|\sin\Phi|},$$

$$g_2 = -\tfrac{1}{2}\cot\Phi\sin(ka\sin 2\Phi); \quad \Phi = \frac{\phi - \alpha}{2}. \quad (28)$$

This form of g_1 is not valid near the forward direction; there we use

$$g_1 \to ka\,\Phi^2(1 - i\pi ka/2) \to 0,$$

$$g_2 \to -ka[1 - \Phi^2(1 + 2k^2a^2/3)] \to -ka;$$

$$2ka\,|\sin\Phi\,| \to 0. \quad (28a)$$

In the above, g_1 of (28) is essentially the "geometrically reflected" term, and g_2 the "shadow forming" term; however, near the forward scattered region, g_1 [as indicated by (28a)] falls off much more rapidly with angle than the geometrical form of (28). The forward amplitude theorem gives the total scattering cross section per unit length as $-\mathrm{Re}(4/k)g(\alpha, \alpha) = 4a$, *i.e.*, twice the projected area, as expected physically for $\lambda \to 0$.

[8] Note that for the two-dimensional problem our values of R and σ for a perfectly conducting rough surface for horizontal, vertical polarization are identical to these of the acoustic problem of small amplitude sound waves reflected from free (−), rigid (+) rough surfaces (*e.g.*, as approximated by reflection at the sea surface from below and above respectively). In addition, this correspondence also exists in the plane of incidence for the large hemispheres. More generally R and σ apply for arbitrary bosses on free, rigid ground planes provided that $\mathbf{f}\cdot\mathbf{e}$ is taken as the appropriate scalar amplitude.

[9] σ^1 was given originally by Rayleigh, *op. cit.*, and R^1 by Twersky, *op. cit.* Note also that S. O. Rice ("Comment on the Reflection of Microwaves from the Surface of the Ocean," rep. no. C4-NDRC-119, October 29, 1942) gave a single scattering treatment of parallel "wedge edges" randomly distributed in angle and height about a mean plane. His ratio of horizontal to vertical back scattering equals that of (26), *i.e.*, the result for a single semicylinder.

[10] This reflection problem was treated in V. Twersky, "Reflection from Semicylindrical Mirrors on a Plane," rep. no. DA-18-10, Nuclear Development Associates, Inc., N. Y., 1953. Work performed at NDA under Purchase Order Number 34895 with the Applied Physics Lab. The Johns Hopkins Univ., Baltimore, Md.

[11] Eq. (28) is given in P. M. Morse and H. Feshbach, "Methods of Theoretical Physics," (M.I.T. Notes, 1946), p. 352 ff.; see also their text (McGraw-Hill Book Co., Inc., N. Y., 1953), p. 1551 ff., for the acoustic problem of the sphere. We write $\mathbf{g}$ as a surface integral in terms of the tangential components of the scattered fields, say $\mathbf{E}^s$ and $\mathbf{H}^s$; we use the boundary condition $\mathbf{E}^s = -\mathbf{E}_{\tan}{}^0$, and the jump condition $\mathbf{H}^s = \pm\mathbf{H}_{\tan}{}^0$ on the lit, dark sides to get $\mathbf{g}_1$, $\mathbf{g}_2$; then $\mathbf{g}_1$ of (28) is obtained by stationary phase, and $\mathbf{g}_1$ of (28a), $\mathbf{g}_2$ by exact evaluation of these approximate integrals.

Using the above value for g we obtain

$$2f_{\pm}(\phi, \pi-\alpha) = (ka\pi i)^{1/2}\left[\pm\left|\sin\Phi_0\right|^{1/2}e^{-i2ka|\sin\Phi_0|} + \left|\cos\Phi_i\right|^{1/2}e^{-i2ka|\cos\Phi_i|}\right] - \cot\Phi_0 \sin(ka\sin 2\Phi_0) \mp \tan\Phi_i \sin(ka\sin 2\Phi_i);$$

$$\Phi_0 = \frac{\phi-\alpha}{2}, \qquad \Phi_i = \frac{\phi+\alpha}{2}. \tag{29}$$

The first term of (29) is to be replaced by $\pm 2g_1$ of (28a) if $\phi\to\alpha$; thus

$$Z_{\pm} = -\frac{\rho a}{\cos\alpha}\left[1 \pm \frac{\tan\alpha\sin(ka\sin 2\alpha)}{2ka} - \frac{1}{2}\left(\frac{\pi i\cos\alpha}{ka}\right)^{1/2} e^{-i2ka\cos\alpha}\right]. \tag{30}$$

The first term of Z (the shadow forming term arising from the image wave) is the largest; the second (the shadow term of the incident wave) is negligible except near $\alpha\to\pi/2$. The third term (the incident wave reflected at cylindrical surfaces) indicates specular reflection at the plane $x=a$, the tangent plane of all bosses; this last term, which is negligible compared to the first, is significant in R when ρa sec $\alpha\to 1$; if 2 ka cos $\alpha\to 0$, then the part of this term within the brackets is to be replaced by $-\cos^2\alpha(1-i\pi ka/2)$.

For small α we keep only the first term of Z, and use

$$R \approx R^1 = 1 - 4\rho a\sec\alpha; \tag{31}$$

here R contains only the image wave and its single scattered shadow term; thus a single boss prevents a width $2a$ sec α of plane from acting as a flat mirror, and $1-2\rho a$ sec α is the effective plane mirror length of unit length of distribution. For larger α, we use the multiple scattered form of these terms, *i.e.*,

$$R \approx \left|\frac{1-\rho a\sec\alpha}{1+\rho a\sec\alpha}\right|^2; \tag{31a}$$

in either case, the result also equals the transmission coefficient of the analogous "random screen." (See Twersky[3] for a discussion of "multiple shadowing.") If ρa sec $\alpha\to 1$, then the third term of Z is also required; at the limit, the image of the incident wave is suppressed by its shadow forming term, so that

$$R \approx \rho^2\lambda a/2^5\cos\alpha, \qquad \rho a\sec\alpha = 1, \tag{32}$$

which is proportional to the single scattered reflection coefficient of a random screen of cylinders. As α increases, all terms of Z are required; the R's show polarization dependence. Finally as $2ka$ cos $\alpha\to 0$ we use the first two terms of (30) and the alternate form of the last term:

$$R_- \to 1 - \beta\rho a(ka)^2 8/3, \qquad R_+ \to 1 - 2\beta/\rho a; \tag{33}$$

compare with (27). Note that the use of (33) depends on $2ka$ cos α, whose smallness is the criterion both for the significance of the shadow term of the incident wave, and for the rapidly vanishing form of the cylindrical reflection. In both cases, the criterion is essentially that for replacing sin x by x, and this introduces roughly a ten per cent error when $x=\pi/4$. The value $2ka$ cos $\alpha<\pi/4$ is also "Rayleigh's criterion" (see Kerr[12]) $2ka$ cos α is the path difference between the waves reflected from the top of the "roughness" and from the ground plane, so that its magnitude measures departure from a smooth plane.

The incoherent scattering is proportional to the square of (29). If $\phi\neq\alpha$, and $|\alpha|$, $|\phi|\nleftrightarrow(\pi/2)$, then we may use

$$\sigma \approx \frac{\rho a}{2(1+\rho a\sec\alpha)^2}\left\{\left|\sin\frac{\phi-\alpha}{2}\right| + \left|\cos\frac{\phi+\alpha}{2}\right|\right\}, \tag{34}$$

which is independent of wavelength and polarization; the oscillating cross term was neglected, since it is not significant when integrated over a portion of the distribution or over a small range of ka. At $\phi=\alpha$, using $f(\alpha, \pi-\alpha)$ of (30), we replace the function in braces by $4ka/\pi$. If $-\phi=(\pi/2)-\beta\to(\pi/2)$ then we restore the oscillating term in (34) to obtain

$$\sigma_{\mp}\left(\frac{\pi}{2}-\beta, \pi-\alpha\right)\to\frac{2\rho a}{(1+\rho a\sec\alpha)^2}\cos\left(\frac{\alpha}{2}-\frac{\pi}{4}\right)\cdot\begin{matrix}\sin^2\\ \cos^2\end{matrix}\left\{ka\beta\cos\left(\frac{\alpha}{2}+\frac{\pi}{4}\right)\right\}, \tag{35}$$

while for $\phi=(\pi/2)-\beta$, the signs on $\pi/4$ are to be reversed. A polar plot of σ as a function of ϕ is thus roughly semicircular except for a peak at $\phi=\alpha$; in addition $\sigma_-\to 0$ as $|\phi|\to(\pi/2)$. On the other hand, if $\alpha=(\pi/2)-\beta\to(\pi/2)$, and $\phi\nleftrightarrow(\pi/2)$, then the complete forms of σ give

$$\sigma_- \to 2\rho a(ka\beta)^2\cos\left(\frac{\pi}{4}+\frac{\phi}{2}\right)\cos^2\left(\frac{\pi}{4}-\frac{\phi}{2}\right),$$

$$\sigma_+ \to (\beta^2/2\rho a)\cos\left(\frac{\pi}{4}+\frac{\phi}{2}\right), \tag{36}$$

both vanishing like β^2. In the specular direction, $\sigma_-\to 8\rho a(ka)^5\beta^4/9\pi$, $\sigma_+\to 2k\beta^2/\rho$; in the back scattered direction [compare with (27)] we have

$$\sigma_- \to \rho a(ka)^2\beta^4/2, \qquad \sigma_+ \to \beta^2/2\rho a. \tag{37}$$

From (27), (33), and (37) we see that at low angles our model indicates relatively little difference in behavior between large and small bosses, and this may be of interest for the sea surface: for the sea, the "bosses"

[12] D. E. Kerr, "Propagation of Short Ratio Waves," McGraw-Hill Book Co., Inc., New York, N. Y.; 1951, pp. 411, 423 ff., and H. Goldstein, "A Primer of Sea Echo," rep. no. 157, U. S. Navy Electronics Lab., San Diego, Calif., p. 481 ff.; 1950.

consist more generally of the waves which are large compared to wavelength and the ripples which are small, so that the agreement between the present results and certain experimental data in Kerr[12] and Goldstein[12] (on low angel measurements of reflection coefficients and back scattering cross sections) need not be fortuitous. Thus in general our reflection coefficients approach unity linearly as the horizon angle β vanishes, and the horizontal coefficient for either large or small scatterers is more sensitive to scatterer size and wavelength than the vertical. In general, our horizontal back scattering vanishes like β^4, and the vertical like β^2; the dependence on wavelength for large, small scatterers is given by λ^{-3}, λ^{-2} for horizontal, and λ^{-1}, λ^0 for vertical. Also, since $\sigma_-/\sigma_+ \propto (1-R_-)\beta^2/(1-R_+) \propto (\rho ka\beta)^2$ for both small and large radii, the vertical scattering will be the larger, particularly if the scatterers are small and few (*i.e.*, a calm sea); if $ka\beta$ is not small (*e.g.*, large scatterers as for a rough sea), then from (34), the back scattering is independent of polarization. These findings are in qualitative agreement with the data in Kerr[12] and Goldstein.[12] (Our results also allow for a fairly comprehensive interpretation of the optical experiments described by Rayleigh[1] and Tai.[1]

Hemispheres

For the three-dimensional problem as in Fig. 1, we have

$$Z = \frac{\rho \boldsymbol{f}(k_0, k_i)\cdot \mathbf{e}}{k^2 \cos\alpha}, \quad R = \left|\frac{1+Z}{1-Z}\right|^2, \quad \sigma = \frac{\rho}{k^2}\left|\frac{\boldsymbol{f}(\mathbf{s}, k_i)}{1-Z}\right|^2. \tag{38}$$

For a hemisphere on a ground plane $x=0$ excited by a wave traveling in the plane $z=0$, we superpose the known results for a sphere and write

$$\boldsymbol{f}_\pm = \sum_{n=1}^{\infty} \frac{2n+1}{n(n+1)}\left[a_{n\pm}\left(\boldsymbol{\theta}\frac{\partial_\phi}{\sin\theta} - \boldsymbol{\phi}\partial_\theta\right)\partial_\phi(P_{n_0} \pm P_{n_i}) + a_{n\mp}\left(\boldsymbol{\theta}\partial_\theta + \boldsymbol{\phi}\frac{\partial_\phi}{\sin\theta}\right)\cos\theta\,(P_{n_0}' \pm P_{n_i}')\right], \tag{39}$$

where $\boldsymbol{\theta}$ and $\boldsymbol{\phi}$ are unit vectors in the coordinates of Fig. 1, and where

$$P_{n_0} = P_n(\mathbf{s}\cdot k_0) = P_n(\sin\theta\cos(\phi-\alpha)),$$
$$P_{n_i} = P_n(\mathbf{s}\cdot k_i) = P_n(\sin\theta\cos(\phi-\pi+\alpha)) \tag{40}$$

are Legendre polynomials; the primes on P represent differentiation with respect to argument. As previously, $\boldsymbol{f}_-$ is in units of $\boldsymbol{E}$, and $\boldsymbol{f}_+$ in units of $\boldsymbol{H}$, *i.e.*, $\boldsymbol{f}_-$ and $\boldsymbol{f}_+ \times \mathbf{s}$ give the scattered polarization; polarization is thus preserved with respect to the plane of incidence, provided that $\mathbf{s}$ is in this plane. The a_n are known; in particular, for a perfect conductor (to which we restrict the following) we have $a_{n-} = -j_n(ka)/h_n(ka)$ in terms of spherical Bessel functions and Hankel functions of the first kind, and $a_{n+} = -[kaj_n(ka)]'/[kah_n(ka)]'$, where the primes represent ka derivatives.

If $a \gg \lambda$, then corresponding to (24), (25), and (26) we obtain

$$\boldsymbol{f}_\mp(\mathbf{s}, k_i) = i(ka)^3\begin{Bmatrix}\boldsymbol{\theta}\cos\alpha\cos\phi - \boldsymbol{\Phi}\cos\theta\cos\alpha\sin\phi \\ \boldsymbol{\theta}(\sin\theta - 2\sin\alpha\sin\phi) - \boldsymbol{\Phi}2\cos\theta\sin\alpha\cos\phi\end{Bmatrix}, \quad \mathrm{Re}\,\boldsymbol{f}_\mp(k_0, k_i)\cdot\mathbf{e} = -\frac{(ka)^6}{3}\begin{Bmatrix}\cos^2\alpha \\ 1+4\sin^2\alpha\end{Bmatrix}, \tag{41}$$

$$|1 - Z_\mp|^2 = 1 + (ka)^6\left[\frac{\pi\rho}{k^2\cos\alpha}\frac{2}{3}\begin{Bmatrix}\cos^2\alpha \\ 1+4\sin^2\alpha\end{Bmatrix} + \left(\frac{\pi\rho}{k^2\cos\alpha}\right)^2\begin{Bmatrix}\cos^4\alpha \\ \cos^2 2\alpha\end{Bmatrix}\right], \tag{42}$$

$$R_\mp \approx 1 - \frac{4\pi\rho a^2(ka)^4}{3\cos\alpha}\begin{Bmatrix}\cos^2\alpha \\ 1+4\sin^2\alpha\end{Bmatrix}, \quad \sigma_\mp \approx \rho a^2(ka)^4\begin{Bmatrix}|\boldsymbol{\theta}\cos\alpha\cos\phi - \boldsymbol{\phi}\cos\theta\cos\alpha\sin\phi|^2 \\ |\boldsymbol{\theta}(\sin\theta - 2\sin\alpha\sin\phi) - \boldsymbol{\phi}2\cos\theta\sin\alpha\cos\phi|^2\end{Bmatrix}, \tag{43}$$

the scattering being proportional to λ^{-4}, *i.e.*, essentially Rayleigh scattering. Except for normal incidence, the horizontal polarization is better reflected; correspondingly, the vertical back scattering is the greater. On the other hand, if $\beta = (\pi/2) - \alpha = (\pi/2) - |\phi| \to 0$, then R and σ (back) reduce to

$$R_- \to 1 - \frac{4}{3}\pi\rho a^2(ka)^4\beta, \quad R_+ \to 1 - \left(\frac{20}{3}\right)\frac{k^2\beta}{\pi\rho};$$
$$\sigma_- \to \rho a^2(ka)^4\beta^4, \qquad \sigma_+ \to \frac{9k^2}{\pi^2\rho}\beta^2. \tag{44}$$

In the range between (43) and (44) [as well as between (26) and (27)], the horizontal reflection coefficient increases smoothly to unity, and the corresponding back scattering cross section drops smoothly to zero. On the other hand, the vertical reflection coefficient decreases initially to a minimum value (at an angle more or less analogous to the "pseudo Brewster" angle in optics), and then rises steeply to unity; the corresponding back scattering increases to a maximum, and then drops sharply to zero. The phases of the coherent waves relative to the incident wave may be obtained from (13) and (41) or (25); the horizontal starts at π minus a small quantity and increases to π; the vertical starts at a small negative value and increases to π.

If $a \gg \lambda$, then corresponding to (28) and (28a) we obtain (for incident $\boldsymbol{E}^0$)

$$\boldsymbol{g} = \boldsymbol{g}_1 + \boldsymbol{g}_2, \qquad \boldsymbol{g}_{1,2} = g_{1,2}(\boldsymbol{\gamma}\cos\mu \pm \boldsymbol{\mu}\sin\mu),$$
$$g_1 = \frac{ika}{2}e^{-i2ka|\sin\Gamma|}, \quad g_2 = -\frac{ka}{2}\cot\Gamma J_1(ka\sin 2\Gamma);$$

$$\Gamma = \frac{1}{2}\cos^{-1}(\mathbf{s}\cdot\mathbf{k}_0) = \frac{\gamma}{2}. \tag{45}$$

$$g_1 \to (ka\Gamma)^2(1 - ika4/3),$$

$$g_2 \to -(ka)^2[1 - \Gamma^2(1 + k^2a^2/2)]/2;\ 2ka\sin\Gamma \to 0. \tag{45a}$$

Here γ is the polar angle from $\mathbf{k}_0$ to $\mathbf{s}$, and μ is the azimuthal angle measured from $\mathbf{e}$ in the plane normal to $\mathbf{k}_0$; $\boldsymbol{\gamma}$ and $\boldsymbol{\mu}$ are unit vectors. Thus the "geometrically reflected" term g_1 is not isotropic as indicated by (45); but has a sharp cusp in the forward direction. The forward amplitude theorem gives the expected total cross section $-(4\pi/k^2)\ \mathrm{Re}\ \mathbf{g}(\mathbf{k}_0, \mathbf{k}_0)\cdot\mathbf{e} = 2\pi a^2$.

Superposing $\mathbf{g}$'s corresponding to the waves of (1) and (2), we obtain

$$\mathbf{f}_\pm(\mathbf{s}, \mathbf{k}_i) = \pm g_1(\mathbf{s}, \mathbf{k}_0)\mathbf{b}_+ + g_2(\mathbf{s}, \mathbf{k}_0)\mathbf{d}_+ + g_1(\mathbf{s}, \mathbf{k}_i)\mathbf{b}_- \pm g_2(\mathbf{s}, \mathbf{k}_i)\mathbf{d}_-;$$

$$\mathbf{b}_\pm = \frac{\boldsymbol{\theta}[\pm\cos(\alpha\mp\phi) - \sin\theta] + \boldsymbol{\phi}\cos\theta\sin(\alpha\mp\phi)}{1 \mp \sin\theta\cos(\alpha\mp\phi)},$$

$$\mathbf{d}_\pm = -\frac{\boldsymbol{\theta}[\pm\cos(\alpha\mp\phi) + \sin\theta] + \boldsymbol{\phi}\cos\theta\sin(\alpha\mp\phi)}{1 \pm \sin\theta\cos(\alpha\mp\phi)}. \tag{46}$$

In the plane of incidence, $\theta = \pi/2$, we have $\mathbf{b}_\pm = \mathbf{d}_\pm = -\boldsymbol{\theta} = \mathbf{e}$, and consequently

$$\mathbf{f}_\pm\left(\frac{\pi}{2}, \phi; \frac{\pi}{2}, \pi - \alpha\right)\cdot\mathbf{e} = \frac{ka}{2}\left[\pm ie^{-i2ka|\sin\Phi_0|} + ie^{-i2ka|\cos\Phi_i|} - \cot\Phi_0 J_1(ka\sin 2\Phi_0) \mp \tan\Phi_i J_1(ka\sin 2\Phi_i)\right];$$

$$\Phi_0 = \frac{\phi - \alpha}{2}, \qquad \Phi_i = \frac{\phi + \alpha}{2}. \tag{47}$$

where the first term is to be replaced by $\pm g_1$ of (45a) if $\phi \to \alpha$. Consequently corresponding to (30), (31a), (32) and (33), we obtain

$$Z_\pm = -\frac{\pi\rho a^2}{2\cos\alpha}\left[1 \pm \frac{\tan\alpha J_1(ka\sin 2\alpha)}{ka} - \frac{i}{ka}e^{-i2ka\cos\alpha}\right] \tag{48}$$

$$R \approx \left|\frac{1 - \pi\rho a^2/2\cos\alpha}{1 + \pi\rho a^2/2\cos\alpha}\right|^2. \tag{49}$$

$$R \approx \frac{\rho^2a^2\lambda^2}{2^6\cos^2\alpha}, \qquad \frac{\pi\rho a^2}{2\cos\alpha} = 1. \tag{50}$$

$$R_- \to 1 - \pi\rho a^2(ka)^2\beta, \quad R_+ \to 1 - (4/\pi\rho a^2)\beta. \tag{51}$$

Here $1 - \pi\rho a^2\sec\alpha$ is the effective plane mirror area of unit area of distribution.

The incoherent scattering, except near the specular direction and except for α near grazing, is given approximately by

$$\sigma_\pm \approx \left[\frac{\rho a^2}{2(1 + \pi\rho a^2/2\cos\alpha)^2}\right]\frac{1}{2}\left|\pm\mathbf{b}_+e^{-i2ka|\sin\Gamma_i|} + \mathbf{b}_-e^{-i2ka|\sin\Gamma_0|}\right|^2$$

$$= \sigma_0[1 \pm \mathbf{b}_+\cdot\mathbf{b}_-\cos\{\sqrt{2}ka([1 + \sin\theta\cos(\phi + \alpha)]^{1/2} - [1 - \sin\theta\cos(\phi - \alpha)]^{1/2})\}];$$

$$\Gamma_{i,0} = \tfrac{1}{2}\cos(\mathbf{s}\cdot\mathbf{k}_{i,0}). \tag{52}$$

Except for $|\phi| \to \pi/2$, we ignore the oscillating term, and use

$$\sigma_\pm \approx \sigma_0 = \frac{\rho a^2}{2(1 + \pi\rho a^2/2\cos\alpha)^2}. \tag{53}$$

At the specular angle we use (48) to obtain $\sigma_\mp = \sigma_0(ka)^2/2$. In the plane of incidence, $\theta = \pi/2$, the function in braces in (52) reduces to

$$ka\left[\left|\sin\frac{\phi - \alpha}{2}\right| + \left|\cos\frac{\phi + \alpha}{2}\right|\right];$$

then, if $-\phi = (\pi/2) - \beta \to (\pi/2)$, we obtain

$$\sigma_\mp \to 2\sigma_0\begin{matrix}\sin^2\\ \cos^2\end{matrix}\left\{ka\beta\cos\left(\frac{\alpha}{2} + \frac{\pi}{4}\right)\right\}; \tag{54}$$

similarly in the forward direction, $\phi = (\pi/2) - \beta$, we change the sign of $\pi/4$. On the other hand if $\theta \to 0$, then (52) gives

$$\sigma_\mp \to 2\sigma_0\{1 \pm [\cos 2\alpha + 2\theta\sin\alpha\sin\phi(1 + \cos 2\alpha)]\}. \tag{55}$$

Thus except near the specular and grazing directions, σ is independent of s. This also holds approximately for the two-dimensional case; *i.e.*, (34) is roughly independent of ϕ.

For $\alpha = (\pi/2) - \beta \to (\pi/2)$, we replace $\pi\rho a^2/2\cos\alpha$ in (52) by $-Z_\pm$ of (48). For $\theta = \pi/2$, $|\phi| \to (\pi/2)$,

$$\sigma_- \to \rho a^2(ka\beta)^2\cos^2\left(\frac{\pi}{4} - \frac{\phi}{2}\right), \quad \sigma_+ \to \beta^2/\pi^2\rho a^2, \tag{56}$$

both vanishing like β^2. In the specular direction, $\sigma_- \to \rho a^2(ka)^6\beta^4/2^4$, $\sigma_+ \to k^2\beta^2/\pi^2\rho$. In the back scattered direction [compare with (44)] we have

$$\sigma_- \to \rho a^2(ka)^2\beta^4/4, \qquad \sigma_+ \to \beta^2/\pi^2\rho a^2. \tag{57}$$

Summary of Low Angle Results

Here we collect some of the specific results obtained near grazing incidence. For arbitrary scatterers, the reflection coefficients approach unity linearly as the horizon angle β vanishes,

$$(1 - R) \to O(\beta) \to 0, \tag{58}$$

and the horizontal $(-)$, vertical $(+)$ back scattering vanish like

$$\sigma_- \to O(\beta^4), \qquad \sigma_+ \to O(\beta^2). \tag{59}$$

The frequency dependence for perfectly conducting scatterers with radius very small (case S), and very large (case L) compared to wavelength is

$$\sigma \propto (1 - R) \propto \lambda^{-n}; \tag{60}$$

for hemispheres,

$$n = 4(S_-), 2(L_-), 2(S_+), 0(L_+), \tag{61}$$

where S_- indicates horizontal polarization and small radius, etc.; for semicylinders,

$$n = 3(S_-), 2(L_-), 1(S_+), 0(L_+). \tag{62}$$

The ratios of the horizontal to vertical back scattering for large or small scatterers fulfill

$$(\sigma_-/\sigma_+) \propto (1 - R_-)\beta^2/(1 - R_+) \propto (Mka\beta)^2;$$

$$M = \rho\pi a^2, \rho 2a, \tag{63}$$

where M is the fraction of the "average cell" taken up by a scatterer. Also

$$\sigma_\pm(\text{small})/\sigma_\pm(\text{large}) \propto (a/\lambda)^n, \tag{64}$$

where $n = 2$ for hemispheres, and 1 for semicylinders.

We may also apply our results to parallel cylindrical bosses of finite length l (long compared to wavelength) by neglecting their end contributions. In particular, for incidence and observation in the plane normal to their axes, we use the three-dimensional formalism with $f = f_\infty(kl/\pi)$, where f_∞ is the amplitude of the infinitely long boss. Hence we may use our two dimensional results for R and σ, provided that we replace their ρ by ρl, and multiply σ by l/λ, *i.e.*, essentially, the reflection coefficients are unaltered and only the frequency dependence of the incoherent scattering is changed. Thus the frequency dependence of $1-R$ near grazing is as in (62), while that of the back scattering becomes

$$4(S_-), 3(L_-), 2(S_+), 1(L_+). \tag{62a}$$

ACKNOWLEDGMENT

We are grateful to Prof. J. B. Keller and Dr. H. Goldstein for fruitful discussions.

Radio Communications by Means of Very Short Electric Waves*

GUGLIELMO MARCONI

DURING the last 12 months, a good deal of attention, both scientific and popular, has been directed to the published accounts, of varying degrees of accuracy, of my recent researches regarding the use and potentialities of very short electric waves for radio communication over relatively long distances. My object tonight is to give you facts about the results obtained and the observations made by myself and my assistants, and to furnish some description of the apparatus used and of the methods employed.

The study of what may be termed "very short" waves dates from the discovery of electric waves themselves, *i.e.*, from the time of the classical experiments of Hertz and his contemporaries some 42 years ago. In many of these experiments Hertz used very short electric waves, and conclusively proved that these waves followed the same laws as waves of light as regards speed of propagation, reflection, refraction, and diffraction.

The problem of utilization of very short waves for wireless communication is not a new one to me, for I have devoted to it much thought and labor since the time of my earliest wireless experiments 38 years ago. In 1896 I was able to demonstrate to the Engineers of the Post Office that waves of the order of 30 centimeters, corresponding to a frequency of approximately one million kilocycles, and now sometimes termed microwaves, could be successfully used for telegraphic communication over a distance of $1\frac{3}{4}$ miles by employing suitable reflectors. Later this distance was increased to $2\frac{1}{2}$ miles. These early results were described by the late Sir William Preece at a meeting of the British Association in September, 1896, and at subsequent lectures, and were referred to in greater detail in a paper which I read before the Institution of Electrical Engineers on March 3, 1899. At that lecture I demonstrated how it was possible, by means of "very short" waves, for reflectors to concentrate transmission in a given direction instead of allowing the waves to spread in all directions.

At that time, however, the use of these very short waves did not appear very promising, and for many years my investigations, like those of my contemporaries, were directed to the use of progressively longer waves which reached the length of ten thousand meters.

In 1916, war requirements called for methods of radio communication more secret than those which were then in use, and reopened the interest of the directive properties inherent in the very short waves, and I again turned

* Reprinted from *Proceedings of the Royal Institution of Great Britain*, vol. 22, pp. 509–544; 1933.

my attention and investigations to the generation and reception of very short waves. I am indebted to the valuable assistance which I received then from C. S. Franklin, of the Marconi Company.

At that time, using special spark transmitters and a 2-meter wavelength, 6 miles of reliable communication were secured; and later tests with the same wavelength, carried out at Carnarvon, gave good signals at a distance of over 20 miles, with the indication that a greater range would have been possible.

The remarkable results which I obtained during the period 1919–1924 with the use of wavelengths from 100 to 6 meters, which led to the collapse of the long wave Imperial scheme and its substitution by high-speed short-wave Beam Marconi Stations, and in fact brought about the present radio revolution of short-wave long-distance radio telegraph and telephone services, again distracted my attention from the study of microwaves.[1]

Electromagnetic waves under 1 meter in length are usually referred to as quasi-optical waves, the general belief being that with them communication is possible only when the two ends of the radio circuit are within visual range of one another; and that consequently their usefulness is defined by that condition.

Long experience has, however, taught me not always to believe in the limitations indicated by purely theoretical considerations or even by calculations, for these, as we well know, are often based on insufficient knowledge of all the relevant factors, but, in spite of adverse forecasts, to try out new lines of research, however unpromising they may seem at first sight.

It was about 18 months ago that I decided again to take up the systematic investigation of the properties and characteristics of these very short waves, in view of the palpable advantages which they seemed to offer, *i.e.*, the small dimensions of the radiators, receivers, and reflectors necessary for radiating and receiving a considerable amount of electrical energy, and in view also of the fact that they do not suffer interference from natural electrical disturbances such as atmospherics.

It was, of course, obvious to me that these investigations would be facilitated if it were possible efficiently to utilize considerably more power in the transmitters, and employ more reliable and practical receivers than those that were then available. I also decided to resume these researches in Italy where, as President of the National Research Council, I enjoyed special facilities. I may also add that I was afforded every possible assistance and encouragement by the Italian Government.

Most of the research necessary for the construction of the new apparatus employed on these tests has been carried out by my personal assistant, G. A. Mathieu. His work, aided by suggestions and observations of my own, has resulted in the possibility of generating and radiating very short waves of greater power than hitherto, and in the elaboration and construction of practical and easily adjustable receivers. I am also indebted to G. A. Isted, of the Marconi Company, for much valuable work.

At the beginning of our work a choice had to be made between two alternative ways of attacking the problem —by the magnetron, or the electron oscillator. As a powerful transmitter was the principal aim, the magnetron road was a very tempting one; but the necessity of employing rather high potentials, of producing an auxiliary field, and doubts of being able to ensure good modulation, made us prefer the Barkhausen-Kurz effect.

Not less important was the choice of the wavelength to be employed. Since it appeared improbable that there would be any great difference in the propagation properties of waves of say 80 to 20 cm, we decided first to concentrate our efforts on the generation and efficient radiation of what may be termed a medium wavelength on the microwave scale—that is a wavelength of the order of half a meter, *i.e.*, 600,000 kc.

The first circuit tried was of the well-known Barkhausen and Gill Morell plate grid Lecher wire type, which has been used in nearly all recent experiments. In that circuit we tried, with varying success, all the new and obsolete receiving and amplifying valves of the cylindrical plate type that were available; but as soon as any was pressed for power, its life proved to be only a matter of minutes.

Our efforts were, therefore, directed towards the production of a more suitable valve; and after a time a valve with a 4-ampere tungsten filament and a molybdenum grid, supported by electrical welding on molybdenum, was produced, which led to a great improvement so far as the power obtainable and the life of the valve were concerned.

However, the inadequacy of the plate grid Lecher circuit was soon apparent; and a new symmetrical two-valve circuit was thought out, and tried after two special valves, the mirror images of one another, had been constructed for it.

The development of this new circuit has led to the present new transmitting circuit and is shown in Fig. 1.

This new electronic oscillator is characterized by three definite tuned circuits, namely, an inside and outside filament-tuning, and a plate-tuning circuit, and also by the use of a feeder-impedance-transformer, the purpose of the latter being to match the internal resistance of the valves with that of an efficient dipole aerial.

[1] "Radio Telegraphy," paper read at American Institute o fElectrical Engineers, June 20, 1922—Proc. IRE, vol. 10, pp. 215–238; August, 1922.
"Results obtained over very long distances by short waves and directional wireless telegraphy," *J. Roy. Soc. Arts.*, vol. 72, p. 607; 1924.
"Radio communications," *id.*, vol. 73, p. 121.
"Radio Communications," paper read before Institute of Civil Engineers, October 26, 1926—vol. 222. Session 1925–1926, part 2.
"Le radiocommunicazioni a fascio," *Nuova Antologia*, Rome; November 16, 1926.
"Radio Communications," paper read before American Institute of Electrical Engineers and the Institute of Radio Engineers, New York, N. Y.; October 17, 1927.

These various circuits are indicated in Fig. 1.

The small disks at the end of the dipole aerial are acting as end capacities and our experience has definitely indicated that their use secures more radiated power and renders easier the adjustment of the feeder-impedance-transformer than is otherwise possible.

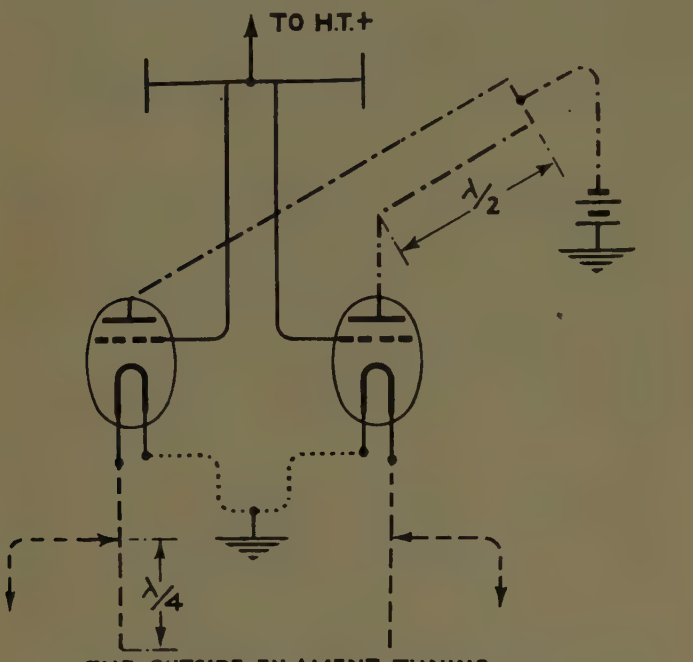

Fig. 1.

The plate-tuning and the inside filament-tuning are the most important of all, in fact they are the controlling factors of the wavelength at which the transmitter can be made to oscillate with efficiency; all the other adjustments being dependent upon them.

It is necessary to point out that the correct length of conductor required to connect the two plates together to secure plate tuning is very small—it is only about 5 cm for a wavelength of the order of 50 cm—and the explanation of the fairly long kind of Lecher wire, shown in Fig. 1, is that it has been found possible and also desirable to add to that short conductor another conductor one wavelength long, bent back on itself to avoid loss by radiation.

The action of the plate-tuning is easily followed. It controls the frequency of the oscillations in a manner analogous to a straight steel bar vibrating with its middle point fixed.

This is really the case, since by connecting a thermocouple in the middle of the tuning-plate conductor and leaving the other connections free, the two plates and the conductors behave like a dipole aerial terminated by large end capacities.

The inside and outside filament-tuning might at first appear to be acting only as effective chokes, but in fact both are necessary to ensure the correct distribution of potentials along and between the elements of the new circuit.

The correct distribution of the potential along the plate and filament circuits, obtained by these tunings, is shown in Fig. 2.

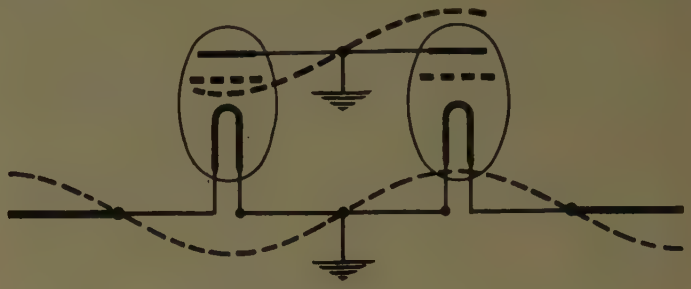

Fig. 2—Distribution of potential along filament and filament-tuning and plate-tuning circuit.

It is interesting to note that the circuit still oscillates very well—but at about half the power if the filament of one of the valves be switched out—but that the set cannot be made to oscillate at all if one of the plates is disconnected, thus confirming again the controlling action of the plate-tuning circuit.

Of course, it is not sufficient to tune correctly all the external portions of the new circuit, it is necessary also to adjust the electrical supplies to the valves employed to generate electronic oscillations between their electrodes to a frequency corresponding as closely as possible to that to which the external circuit is tuned.

There is a definite pulling effect of the oscillation into the frequency controlled by the circuit adjustments, and the closer the correspondence of the electrical adjustments to that frequency the more powerful and the more stable is the transmitter.

The degree of filament heating is another important factor upon which the efficiency of the transmitter depends. Starting with cold filaments, the oscillations will start as soon as the saturation of the grid current is reached, when the radiated energy will go on rapidly increasing as the filaments reach a further degree of brilliancy until it passes through a sharp maximum; after which a further increase in the heating of the filament will bring about a rapid decrease in the efficiency, and finally the cessation, of the oscillations.

Naturally, the development of the valves has proceeded parallel with that of the circuit.

The filament thickness of the valves, the diameter and pitch of their grids, and the length of their plates and grids were successively varied, until the best results were obtained. The method of supporting the electrodes was also investigated and found to be a matter of importance. I regret, however, that I have no time to go further into this tonight.

The radiated energy of one standard unit transmitter has been measured by placing the whole apparatus, except the aerial and feeder, in a calorimeter and taking temperature curves first with the transmitter in oscillation, and then in nonoscillating condition, all the electric currents being kept constant.

Consistent results were obtained by this method indicating an average radiation power of 3.5 watts.

The power absorbed by the filament is approximately 30 w, that by the grid approximately 25 w, the over-all efficiency being, therefore, about 6 per cent, increasing to 14 per cent, if the grid power only be taken into account.

The possibility of substantially increasing the radiating power of a transmitter was successfully realized by running several of these unit transmitters in parallel with their aerials all in line and spaced so as to secure the maximum directive effect.

The keeping of these unit transmitters electrically in step has been rendered possible by linking up, two by two, the outside filament-tuning of adjacent transmitters by means of phasing links $1\frac{1}{2}$ wavelengths long.

Fig. 3 shows the schematic diagram of the arrangement for parallel working. It will be noticed that condensers are placed at the maximum current points, in order to permit of the independent regulation of the filament heating current of each valve; the same principle applying in the case of four transmitters.

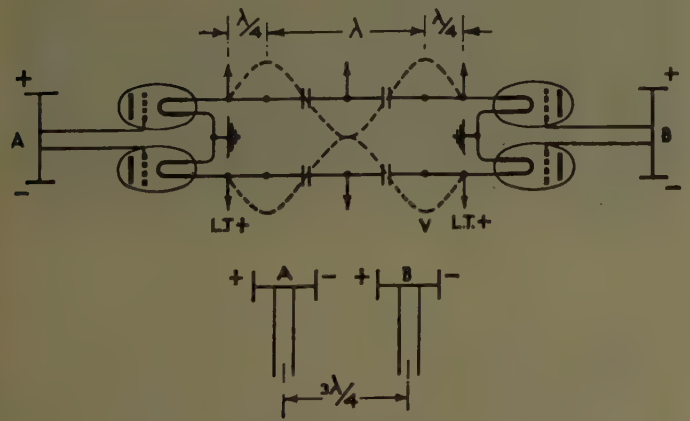

Fig. 3—Illustrating method of keeping in step two-unit transmitter spaced $3\lambda/4$.

There are several ways of modulating the new transmitter. The principal methods are to superimpose the modulation on the grid high tension positive dc supply, or on the plate steady bias negative potential. But there are many other ways such as push-pull action on the plate or the grid, or even push-pull between two transmitting units. All these methods were tried and their peculiar characteristics ascertained, but the plate modulation was adopted, at least for the time being, on account of its simplicity.

In the case of several transmitting units working in step, all the plate circuits are connected in parallel and are consequently modulated simultaneously.

The plate filament impedance of a unit transmitter at 1000 cycles has been measured and found to be of the order of 2500 ohms. This value has been successfully used for designing the modulating transformer.

During these investigations the problem of wavemeter and frequency had, of course, to be taken into careful consideration.

At an early stage in our work, when the plate-grid Lecher wire circuit was used, the coupling of a Lecher wire wavemeter to the transmitter was found fairly satisfactory, and measurements made by observing the pulling effect exercised by its coupling on the electrical supplies; but this proved quite useless as soon as more power was available.

Sensitive, but necessarily also high resistance, thermo-junctions were used at the center of a dipole constituted by two straight rods fixed into the terminals of the thermo-couple, but the tuning was very flat and indefinite.

With the comparatively large amount of energy radiated from the new transmitter, it was then found possible to use the thermo-couple of a stand 0 to 125 milliamperes Weston Ammeter, the low internal resistance of which had already enabled us to secure a much sharper tuning.

Our present standard wavemeter and radiation indicator was then developed by placing the thermo-couple of that instrument in the center of a dipole aerial provided with large end capacities taking the form of large disks. Naturally, the total length of the arrangement securing tuning is substantially shorter than with the usual straight rod dipole arrangement. It is only 8 cm instead of 28 cm in the case of 60-cm wavelength, and the arrangement secures a marked improvement in sensitiveness and selectivity.

With this type of wavemeter it is possible to measure wavelengths to a millimeter, by coupling to the wavemeter a Lecher wire which, when in tune, pulls the oscillation induced in the wavemeter down to practically zero. Such an arrangement permits the calibration of the standard instrument which, in the system developed, is used as a radiation indicator to adjust both the transmission and the modulation.

Having ascertained the mechanism of working of the new circuit, it was then possible to investigate if it could readily be used for the production of shorter wavelengths, say, of the order of 40, 30, or 20 cm.

The first thing observed was that by varying proportionally all the dimensions of the external circuits and readjusting the electrical supplies, the standard valves were capable of generating at practically constant efficiency all wavelengths with a perfect continuous range from 80 cm to 50 cm.

Below 50 cm the tuning of the plate circuit became very indefinite and the efficiency fell off rapidly.

It looked, therefore, as if with the normal type of valves the plate circuit at this shorter wavelength was behaving as one of our standard disk wavemeters would, if the end capacities were disproportionate to the length of the connecting rod.

With a view to checking this conclusion, a set of valves was constructed having smaller and shorter electrodes, and with them a continuous range from 55 to 35 centimeter wavelength was obtained with an efficiency as satisfactory as with the other type.

It is interesting to point out here that while with each type of valve the grid high potential and plate negative potential had to be increased as the wavelength was decreased, the same wavelength of say 55 cm could be produced at its maximum power with either of the valves, but with a grid potential in the case of the smaller valves, smaller than in that of the standard 60-cm type.

The idea of utilizing a system of unit reflectors followed logically on that of the system of unit transmitters just described.

The advantages inherent in the possibility of placing side by side several transmitter units working in phase with each other for the purpose of increasing the power of a transmitting station would, in fact, have been partly lost if the same method could not have been extended to the reflector.

Considering the type of multiunit transmitter developed we decided to adopt, at least for the time being, the ordinary well-known cylindrical parabolic reflector.

Of this type of reflector we already possessed a considerable amount of experience and data, and its design was a fairly straightforward proposition.

However, the high efficiency observed by experimenting with these very short waves with free and reflector rods in place of wires or rods supported at each end by insulators, leads to a peculiar type of construction where each reflector rod is supported at its middle point by a copper tube bent into a true parabolic curve.

Fig. 4 will convey a good idea of this kind of herringbone reflector construction, and the manner in which these units can be mounted side by side to build up a multiple unit reflector.

This reflector system is economical in construction and offers the important advantage of a small wind resistance.

The aperture of the reflector was fixed to three wavelengths, because we knew from experience that with this type of reflector very little was to be gained by exceeding this figure.

The focal length of the reflector has been made equal to $\frac{1}{4}$ of the wavelength used.

The distance between the reflector rods has been determined by the desirability of placing the unit transmitter and the unit reflector at a distance securing the maximum directive effect without producing unduly large and detrimental side beams. This critical distance is $\frac{3}{4}$ of a wavelength.

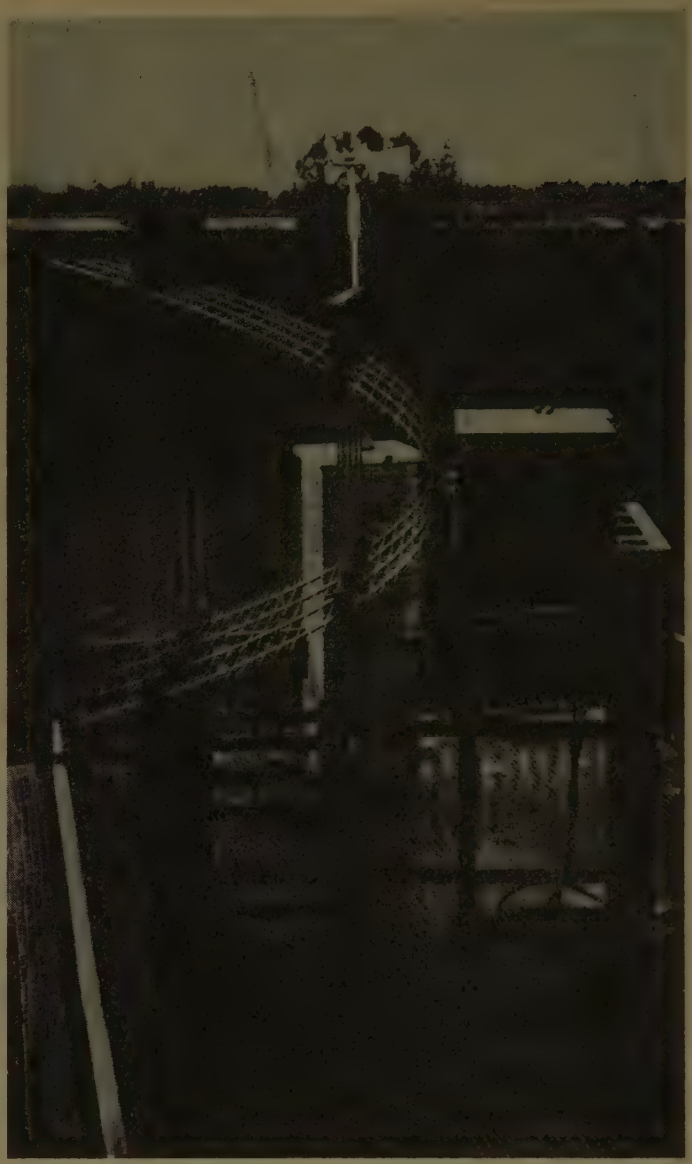

Fig. 4—Transmitter and receiver installed in the Vatican.

The fixing of this distance by the above considerations, and the necessity of preventing the reflector and rods from touching one another, determined the maximum length of the reflector rods and consequently their spacing distance, since these two factors are interdependent.

While the addition of two unit reflectors on each side of the directly excited reflector unit by one transmitting unit secured no appreciable advantage, a very marked improvement in the radiation power was observed by placing the transmitting dipole no longer at the center of one of the reflector units, but on the focal line between two adjacent reflector units.

In the case of several unit transmitters, this method of exciting, say, three unit reflectors by two unit trans-

mitters, thus securing the simultaneous excitation of the center unit reflector by two unit transmitters, offers a new method of keeping the oscillation of several transmitters in phase.

With this mode of keeping several transmitters in phase, the tuning of the outside filament plays an important role, and their adjustment is critical.

With this system of unit transmitters and unit reflectors, many different arrangements are possible, each corresponding to a different power of radiation which can be made variable over wide limits.

Fig. 5 shows some of these alternative arrangements.

Fig. 5(a) shows the simplest and most economical case of one unit transmitter working in the center of one unit reflector.

Fig. 5(b) is the next more powerful arrangement; one-unit transmitter exciting two reflector units.

Fig. 5(c), which is our present normal arrangement, consists of two transmitting units exciting three reflector units, and so on.

Fig. 5(e) shows the arrangement of our four transmitter units, five-reflector unit transmitter, described hereafter.

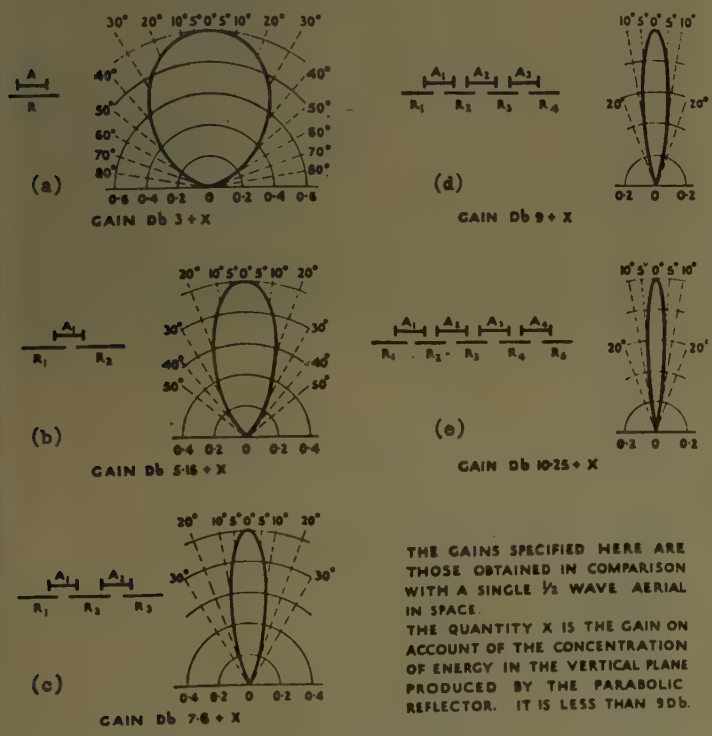

Fig. 5—Energy polar diagrams.

On the right side of each of these alternatives has been drawn the horizontal polar diagram obtainable by each, and the values indicated in decibels are the gain due to the directive properties secured by the adequate spacing of the unit transmitters. To this gain must be added the gain secured by the parabolic reflector itself, which is of the order of 8 decibels.

The first short distance receiving tests carried out indicated that as in the case of the transmitter, electron oscillator receiving circuits based on a plate grid Lecher wire principle were inadequate. The time spent in investigating the possibilities of this type of circuit was by no means wasted, however, for, in addition to the experience gained in the novel practice of tuning a receiver by means of resistance adjustment and by milliammeter and voltmeter readings, the preliminary experiments brought to our knowledge the following valuable information.

It was clearly indicated that the successful newly developed transmitting valves were very inefficient when used in the receiver, thus rather upsetting the more or less generally accepted idea that with the Barkhausen oscillating circuits the same valves were suitable for both purposes. In contrast with what was observed in the case of the transmitter, it was found that the plates of the valves were the active electrodes, and should, therefore, be connected to the aerial instead of to the grids. Further, it was made clear that tuning was best secured by varying grid, filament, and plate potentials more or less simultaneously; and that no design would be useful commercially unless all circuits were provided with current-measuring instruments.

I will now show you our last type of receiving valve mounted on special antivibrating sockets.

In view of the results obtained, the plate grid Lecher wire circuit was therefore definitely discarded, and a receiver was constructed on the same lines as the new transmitting circuit comprising a plate, grid, and inside and outside filament-tuning.

The results obtained with this new receiver were most satisfactory. It was not at first appreciated, however, that too tight a coupling existed between the plate and the grid circuit and that, therefore, the big advantage of plate and inner filament-tuning was not being realized. Consequently, all the first types of receiver used in earlier demonstrations were not provided with either grid or inner filament-tuning.

The electrical adjustments of the receiver are critical, but this disadvantage has been largely overcome by designing special resistances giving only small resistance variation for relatively large movements of their controlling handles.

Fig. 6 gives the schematic diagram of our latest receiving circuit which is in present use.

Numerous distance tests, and a few official demonstrations have been given from time to time, and each has gone to prove the availability and practicability of these very short waves for the purposes of radio communication.

The first demonstration was given to representatives of the Italian Ministry of Communications early in October, 1931, between Santa Margherita and Sestri

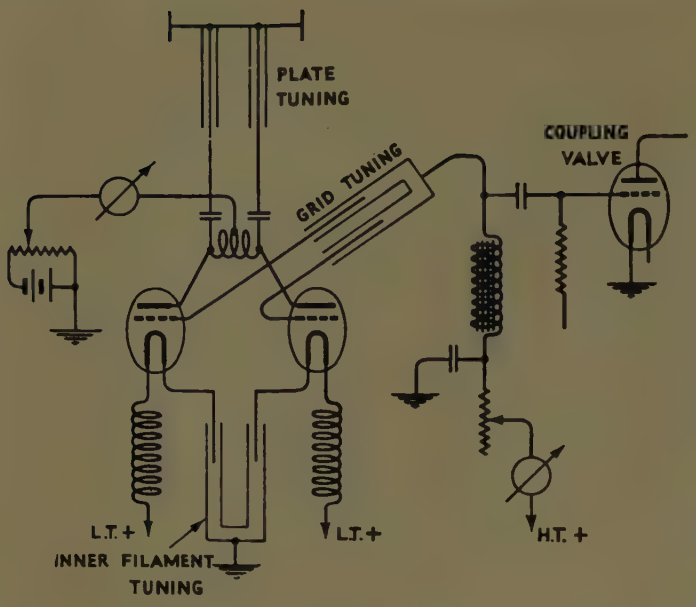

Fig. 6.

Levanta, near Genoa, a distance of 11 miles over sea.

The transmitter, consisting of two radiating units working into four reflector units, was installed at Santa Margherita on the balcony of a private villa, at a height of 50 meters above sea level.

The receiver, which was of our first type, without plate or inner filament-tuning and without supersonic variable plate bias, was installed on the top of a small signal station tower at Sestri Levante, at a height of 70 meters above sea level.

The elevation of the two instruments was capable of giving a direct line of vision over a distance of 24 miles, that is to say, slightly more than twice the actual distance at which the test was carried out.

On October 29, 1931, a second demonstration was given to the same experts and between the same places, with an improved receiver, fitted with variable supersonic plate bias; moreover, at that demonstration the commercial possibility of a carrier suppressor-voice-operated device, developed for the transmitter, was also shown.

The third demonstration took place on November 19, 1931, between the same transmitting experimental station at Santa Margherita and Levanto, a distance this time of 22 miles, mostly over sea.

The receiver at Levanto was installed on the balcony of a private villa, at a height above sea level of 110 meters.

The sum of the heights of the two stations was 160 meters, which is sufficient for a direct vision over 27.5 statute miles, or 20 per cent in excess of the distance covered. This demonstration was given to representatives of the Italian Government and the Press.

It is very interesting, I think, to mention that, although the apparatus used was the same as that for the previous demonstration between Santa Margherita and Sestri Levante, the increase of the distance from 11 to 23 miles made very little difference to the strength of the signals received.

The next was a duplex demonstration, which took place on April 6, 1932, again between Santa Margherita and Sestri Levante. Its purpose was to show the advanced model incorporating two-wire telephone terminal apparatus, and to demonstrate the practicability and the resulting advantages of working both transmitter and receiver in the same reflector.

That demonstration was given to experts of the Italian Government and representatives from the Universities and Technical Colleges.

All the new apparatus was explained and demonstrated, and excellent two-way communication was maintained on two wires for several hours.

Soon after the duplex demonstration of Santa Margherita to Sestri Levante, the Vatican authorities decided to adopt the new system for telephonic communication between the Vatican City and the Palace of His Holiness the Pope at Castel Gandolfo, near Rome.

This application is of great interest as the distance between the two points, a matter of 20 km, is entirely over land, and also because there is no actual clear vision between the two places, on account of the intervening trees in the Vatican Garden, and those of the Avenue built over the Gianiculum Hill, situated at about 4 miles from the Vatican.

Having at the time no experience of such working conditions, it was decided to check beforehand the possibility of successfully operating such a circuit.

For that purpose, a small experimental single transmitter reflector unit was placed at the Vatican City and a standard receiver with a single unit reflector was installed first at the College of Mondragone, east of Castel Gandolfo, from which a direct vision of the transmitter was possible, and afterwards at Castel Gandolfo.

These interesting tests took place towards the end of April, 1932, and were entirely successful, the signals being received with great strength at Mondragone and afterwards only slightly weaker at Castel Gandolfo, leaving no doubt as to the possibility of successfully linking together the two places, notwithstanding what would generally have been considered unfavorable conditions.

It is also interesting to mention that to reach Mondragone, the waves had to pass through the masts and aerials of the high power Radio Station of the Italo Radio Company at Terranuova.

On April 26, 1932, a demonstration of the apparatus was given to His Holiness the Pope.

At the end of last month, the apparatus for that first commercial link on a wavelength below 1 meter was

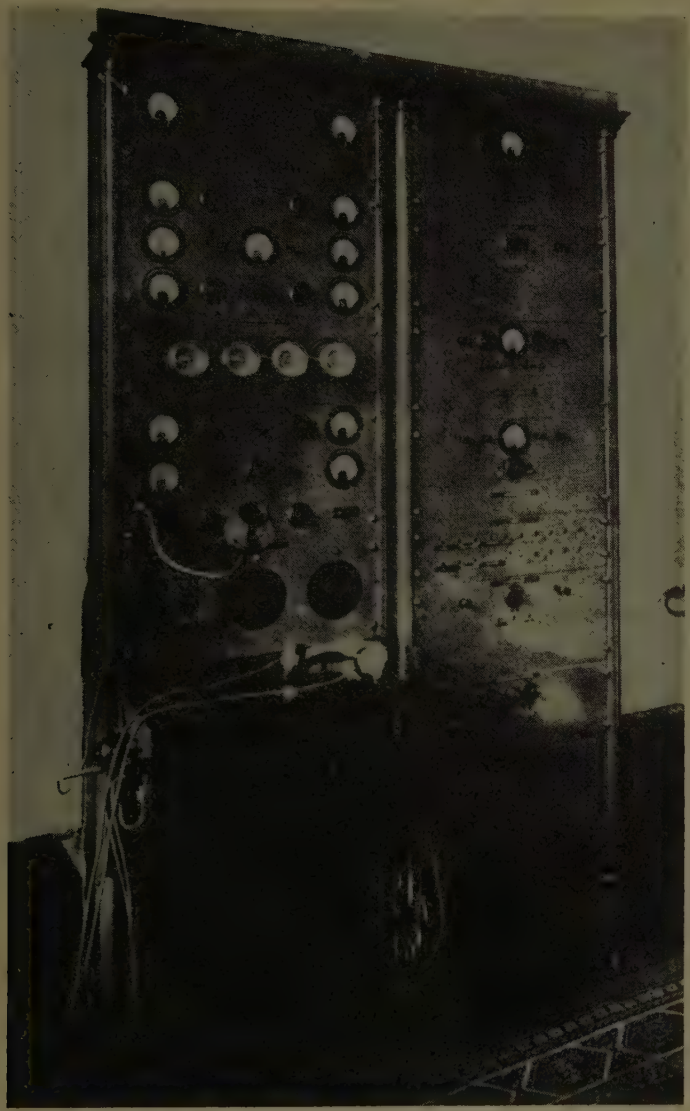

Fig. 7—Remote control equipment of Vatican transmitter.

Fig. 8—Back view of remote control equipment of Vatican transmitter.

installed and tested, and although the official inauguration will not take place until next month, the circuit is already in operation and working satisfactorily.

Fig. 4 shows the transmitter and receiver which are working in the same reflector, recently installed on the roof of the Annex of the main Vatican Wireless Station.

Fig. 7 shows the remote control of this transmitter and receiver as well as the telephone terminal equipment which permits the extension of the radio circuit to any ordinary Vatican or outside telephone line.

Fig. 8 gives the back view of the same apparatus.

Figs. 4, 7, and 8 illustrate the new very short-wave system as the practical outcome of our recent tests and researches.

With the object of carrying out long distance tests, a five-unit reflector, four-unit transmitter was constructed, which constitutes what I believe to be the most powerful short-wave transmitter yet produced.

This transmitter induced 30 milliamperes in the standard wavemeter at a distance of 12 meters, representing 21 wavelengths from the aperture of the reflector.

Fig. 9 (next page) is a photograph of this experimental transmitter, while Fig. 10 illustrates the four-unit transmitters, working in phase side by side, mounted inside the screened box, behind the reflectors.

In July of this year, one of our standard receivers with single reflector unit was installed astern of the main deck of the yacht "Elettra," and preliminary tests were carried out with the new powerful transmitting station installed at Santa Margherita.

These tests demonstrated that although the optical distance corresponding to the small height of the Santa Margherita Station and the yacht "Elettra" was only 14.6 nautical miles, the signals were still perceivable at a distance of 28 miles, consequently well beyond the optical range and notwithstanding the intervening curvature of the earth. These signals began to lose

Fig. 9—Experimental transmitter.

Fig. 10—Four-unit transmitter.

strength noticeably at about 11 miles from Santa Margherita, that is, before reaching the optical limit, but after passing that position they were observed to decrease in strength only gradually, until no longer perceptible. Above a distance of 22 miles the signals were suffering from a kind of deep fading causing them to disappear completely from time to time.

At a distance of 18 miles the speech was still 90 per cent intelligible, but from 20 miles until the signals could no longer be heard, tone Morse signals only could be clearly identified.

At the end of July, 1932, the equipment of the Santa Margherita Station was transported to the obsolete Seismographic Observatory of Rocca di Papa which is situated about 12 miles south of Rome, at a height of 750 meters above sea level and about 15 miles inland.

On August 2, good duplex communication was established between the new experimental station and the yacht anchored in front of Ostia, a distance of about 18 miles, 57-cm waves being used from Rocca di Papa to the yacht "Elettra," and 26-meter waves in the reverse direction.

On the 3rd, the yacht was forced to leave for Civitavecchia Harbor on account of bad weather, but the journey was utilized for a propagation test.

During this test, and with the view of keeping the beam directed on the yacht, the reflector at Rocca di Papa was turned east of Ostia, 5° every half hour.

Very good signals were received on the yacht up to a distance of 85 km. At that distance the signal strength decreased considerably, but remained perfectly audible in spite of the intervening hills masking completely the position of the transmitting station.

The signals were only lost at a distance of 90 km, when, having to enter Civitavecchia Harbor, the receiving reflector could no longer be kept directed on Rocca di Papa.

On August 6, the yacht with representatives of the Italian Government on board, moved on to the line Rocca di Papa-Golfo Aranci, Sardinia, for the purpose of carrying out a long distance investigation on the propagation of these waves.

The tests started when the yacht was 34 miles from Rocca di Papa with excellent duplex telephonic communication, very strong signals being heard at both ends of the circuit.

At 58 miles good duplex communication was still possible; that is to say, already 6 miles in excess of the optical range; but shortly afterwards the signals lost their strength rapidly, became erratic and suffered from slow and very deep fading until, at a distance of 80 miles, they could only be perceived at times.

Listening, of course, continued, in spite of these poor conditions, when on reaching 87 miles, the average strength of the signal suddenly increased and soon reached practically the same strength as was observed at 46 miles.

This return to good signal strength conditions lasted until the distance of 100 miles was reached, when the signals faded away again very rapidly, assuming a slow and deep fading characteristic. They were finally perceived for the last time at a distance of 110 miles.

On August 10, this important long-distance test was repeated.

Over the first 70 miles the results repeated themselves very well, but from that distance onwards they varied in regard to the following points.

First, the signals, instead of fading away rapidly to nearly complete inaudibility, at the distance of 72 miles assumed a character of very slow and deep fading but maintained an average intensity of signals nearly constant up to 110 miles from Rocca di Papa.

Secondly, at that distance, instead of losing the signals altogether, they kept that slow, deep, fading characteristic with a progressive decrease of average strength until they became inaudible from time to time, and were heard for the last time on the yacht at a distance of 125 nautical miles from Rocca di Papa.

The yacht arrived the same night at Golfo Aranci, Sardinia, and next morning the receiving apparatus was disembarked and installed on the tower of the signal station of Cape Figari, 340 meters above sea level.

Rocca di Papa station had been requested to start transmission again at 4 P.M., and we had the great satisfaction of being able to pick up its signals almost immediately.

The tests lasted until midnight, the signals, however, assuming the same slow, deep fading already observed on the yacht, excellent 100 per cent intelligible speech being received during the strong periods of the signals, but reaching practically inaudibility during the weak periods.

The average signal strength appeared also better before sunset than after.

The distance between Rocca di Papa and Cape Figari is 168 statute miles while the optical distance taking account of the height of the two places is only 72 statute miles.

It is interesting to add that at Cape Figari the angle of reception was investigated several times by tilting the reflector and it was found that the waves from the distant station reached the receiving experimental station from a horizontal direction.

In conclusion, I feel that I may say that some of the practical possibilities of a hitherto unexplored range of electrical waves have been investigated, and a new technique, which is bound to extend very considerably the already vast field of the applications of electric waves to radio communications, developed.

The permanent and practical use of microwaves, on the Vatican Castel Gandolfo link, provides the first example of what will be, in my opinion, a new and economical means of reliable radio communication, free from electrical disturbances, eminently suitable for use between islands, and to and from islands and the mainland, and also between other places separated by moderate distances.

The new system is unaffected by fog, and offers a high degree of secrecy, by virtue, principally, of its sharp directive qualities.

Its strategic uses in wartime are obvious, no less than its practical value to navies and aircraft, in so far as the communications can be confined to any desired direction.

The fact, however, that the distance of propagation of these waves appears to be limited, suggests other advantages in wartime, besides greatly reducing the possibility of mutual interference between distant stations.

In regard to the limited range of propagation of these microwaves, the last word has not yet been said. It has already been shown that they can travel round a portion of the earth's curvature, to distances greater than had been expected, and I cannot help reminding you that at the very time when I first succeeded in proving that electric waves could be sent and received across the Atlantic Ocean in 1901, distinguished mathematicians were of the opinion that the distance of communications, by means of electric waves, would be limited to a distance of only about 165 miles.[2]

In any case, the new system is now available for advantageously replacing optical or light signalling in all its long-distance applications, as for example, between signaling stations along coasts, or between forts constructed along a frontier, and in general will be found advantageous in many cases where the erection and maintenance of an ordinary short-distance telephone or cable circuit is difficult, or too expensive.

Other applications such as broadcasting and television are already under consideration, and the study of the new fields of application for these so far unutilized electric waves will, I feel sure, soon bring about the design of greatly improved methods and apparatus.

[2] H. M. Poincaré, "Notice sur la télégraphie sans fil," Annuaire pour l'an 1902 du bureau des longitudes, Paris.

Diffraction of Surface Waves by a Semi-Infinite Dielectric Slab*

CARLOS M. ANGULO†

Summary—**The discontinuity at the end of the slab is regarded as the junction of an open dielectric-filled waveguide and a free-space waveguide.**

A variational expression is set up for the terminal impedance representing the effect of the discontinuity on the surface wave. Close upper and lower bounds for the impedance are obtained.

A variational expression is also set up for the transfer impedance between the surface wave and one of the modes of the continuous mode spectrum associated with the free-space waveguide. The transfer impedances yield the modal amplitudes of the fields. The synthesis of all the modal components gives the electromagnetic field scattered by the end of the slab. The synthesis is carried out for the far field by the method of steepest descents.

Terminal impedances and forward radiation patterns are plotted as functions of the thickness for several permittivities $\epsilon_r=2.49$; 10; 100. The approximation obtained by the variational expression is excellent for small values of ϵ_r and begins to be bad for $\epsilon_r>10$. For very large values of ϵ_r it is possible to obtain a rough estimate of the impedance, immediately, from the values for $\epsilon_r=10$.

Introduction

IT IS WELL KNOWN that surface waves can propagate along dielectric slabs. In this paper, the effect produced by the abrupt termination of the slab is studied. Certain familiarity with surface waves is assumed and the reader is referred to Barlow and Cullen,[1] Kiely,[2] and Zucker,[3] for a survey on the subject. The diffraction problem is attacked by modal analysis and synthesis, considering the dielectric slab as an open waveguide. On the use of the waveguide concepts, as applied to open diffraction problems, and on the use of one-dimensional representation theory, the reader is referred to Marcuvitz.[4,5]

We will consider only surface waves with $H_y=H_z=E_x=0$ (see Fig. 1). The symmetry of the structure with respect to the plane $y=-d$ suggests immediately that the surface waves can be classified as H_x even about the plane $y=-d$ and H_x odd about $y=-d$. H_x symmetry means $\vec{E}\cdot\vec{z_0}=0$ at this plane and the fields will not be disturbed by the insertion of an electric wall at the plane of symmetry ($\vec{z_0}$ is the unit vector in the OZ direction). H_x antisymmetry with respect to the plane $y=-d$ means $\vec{H}\cdot\vec{z_0}=0$ at this plane and the fields would not be disturbed if we insert a magnetic wall at $y=-d$.

In view of the above remarks we will not consider the semi-infinite dielectric slab as in Fig. 1 but only half-space as in Fig. 2. Furthermore, the only difference between one-half of the slab with symmetrical excitation and one-half of the slab with antisymmetrical excitation is that the reflection coefficient at $y=-d$, looking toward $y=-\infty$, is:

$\Gamma=-1$ for symmetrical excitation
$\Gamma=1$ for antisymmetrical excitation.

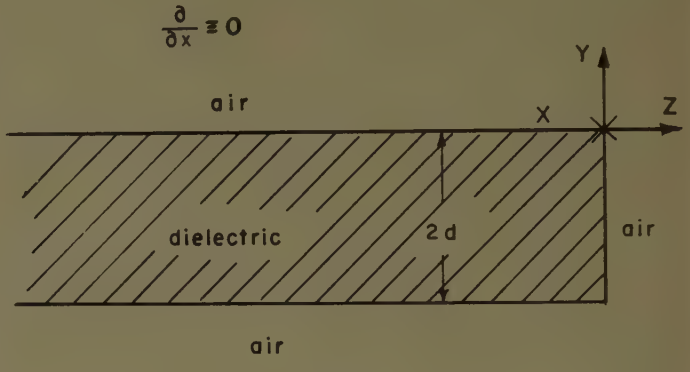

Fig. 1

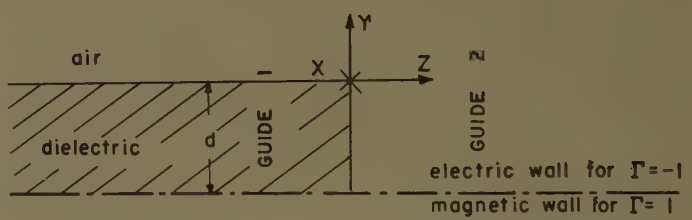

Fig. 2

We will carry out all derivations simultaneously for the symmetrical and the antisymmetrical excitation with Γ having the meaning just explained.

The mks rationalized system of units is the only one used throughout the paper.

The time variation is taken as $e^{+j\omega t}$.

II. Representation of the Field in the Dielectric Waveguide and in the Air Waveguide

Representation of the Electromagnetic Field in the Dielectric Slab (Fig. 2)

The projections of $\vec{E}$ or $\vec{H}$ on a plane $z=$constant yield the other component of the field. We will concern ourselves, therefore, only with the components of the fields transversal to the direction of propagation z.

Maxwell's equations for the components transversal to z are (if $H_y=E_x=/\partial x\equiv 0$)

* Original manuscript received by the PGAP, December 22, 1955; revised manuscript received, April 23, 1956. Presented at Symposium on Electromagnetic Wave Theory, Univ. of Michigan, Ann Arbor, Mich., June, 1955.

† Brown University, Providence, R. I.

[1] H. M. Barlow and A. L. Cullen, "Surface waves," *J. Elect. Engrg.*, vol. 100, pp. 329–341; November, 1953.

[2] D. G. Kiely, "Dielectric Aerials," John Wiley and Sons, Inc., New York, N. Y.; 1952.

[3] F. Zucker, "Theory and applications of surface waves," *Muono Cimento*, vol. 9, pp. 450–473; June, 1952.

[4] N. Marcuvitz, "Guided Wave Concept in Electromagnetic Theory," Microwave Res. Inst., Polytechnic Inst. Blyn. Res. Rep. R-269-52, PIB-208; 1952.

[5] N. Marcuvitz, New York Univ. Res. Rep. No. En-29; 1951. (Field representations in spherically-stratified regions.)

$$\frac{\partial E_y}{\partial z} = j\omega\mu\mu_0 H_x + \frac{1}{j\omega\epsilon_0}\frac{\partial}{\partial y}\frac{1}{\epsilon}\frac{\partial}{\partial y}H_x \quad (1a)$$

$$\frac{\partial H_x}{\partial z} = j\omega\epsilon\epsilon_0 E_y \quad (1b)$$

where ϵ and μ are the relative permittivity and permeability of homogeneous and isotropic media, $\epsilon_0 = 1/36\pi 10^9$, $\mu_0 = 4\pi 10^{-7}$. In the dielectric slab (Fig. 2)

$$\epsilon = \epsilon(y) = \begin{cases} 1 & 0 < y < \infty \\ \epsilon & -d < y < 0. \end{cases}$$

Any field distribution with $H_y = E_x = 0$ in the dielectric slab can be represented as a superposition of all its characteristic modes with $H_y = E_x = 0$. As we will see later, the mode spectrum is, in this case, partially continuous and partially discrete (the surface waves). The representation of the fields will be

$$E_y(y, z) = \sum_1^N V_n(z)e_n(y) + \int_{-\infty}^{\infty} V(\eta, z)e(\eta, y)d\eta \quad (2a)$$

$$H_x(y, z) = \sum_1^N I_n(z)h_n(y) + \int_{-\infty}^{\infty} I(\eta, z)h(\eta, y)d\eta, \quad (2b)$$

where η is the propagation wave-number in the OY direction for a mode of the continuous part of the spectrum.

The mode amplitudes V and I carry the dependence of the fields on the z coordinate (direction of propagation) and are independent of the boundary conditions in the cross section.

The mode functions h and e embody the variation of the fields in the cross section of the guide and are independent of the boundary conditions along OZ.

The fields represented by (2) are solutions of (1) if

$$\frac{\partial V}{\partial z} + j\zeta ZI = 0 \quad (3a)$$

$$\frac{\partial I}{\partial z} + j\zeta YV = 0 \quad (3b)$$

$$e = -\frac{h}{\epsilon(y)} \quad (4a)$$

$$\left[\epsilon(y)\frac{\partial}{\partial y}\frac{1}{\epsilon(y)}\frac{\partial}{\partial y} + \eta^2(y)\right]h = 0 \quad (4b)$$

plus the boundary conditions along OY. We have defined

$$\frac{1}{Y} = Z = \frac{\sqrt{K_0^2\epsilon(y) - \eta^2(y)}}{\omega\epsilon_0} = \frac{\zeta}{\omega\epsilon_0} \quad (5)$$

and

$$K_0^2 = \omega^2\mu_0\epsilon_0. \quad (6)$$

Note that (3) and (4) apply to each mode of the spectrum. The functions V, I, e, h in (3) and (4) stand for $V_n(z)$, $I_n(z)$, $e_n(y)$, $h_n(y)$ if we apply the equations to mode n of the discrete spectrum; and they stand for $V(\eta, z)$, $I(\eta, z)$, $e(\eta, y)$, $h(\eta, y)$ if we apply them to one mode of the continuous part of the spectrum.

The propagation wave-number in the OZ direction (ζ) is a constant independent of y for each mode. The propagation wave-number in the OY direction (η) is a function of ϵ (y)

$$\eta^2(y) = K_0^2\epsilon(y) - \zeta^2. \quad (7)$$

The complete set of modes used in (2) is defined by (4). The orthogonality relations are

$$\int_{-d}^{\infty} e_n(y)h_m(y) = -\delta_{nm} \quad (8a)$$

$$\int_{-d}^{\infty} e(\eta, y)h(\eta', y)dy = -\delta(\eta - \eta'). \quad (8b)$$

These modes have been found by the characteristic Green's Function method. The reader is referred to Marcuvitz,[5] for the general outline of the method, and Angulo,[6] for its application to our problem.

The modes of the discrete part of the spectrum (surface waves) are given by

$$h_n(y) = \frac{1}{N_n}\left[\frac{1 - \Gamma e^{-j(y+d)\eta_{dn}}}{1 - \Gamma e^{-2j\eta_{dn}d}}e^{j\eta_{dn}y}u_{-1}(-y) + e^{j\eta_{an}y}u_{-1}(y)\right] \quad (9)$$

for

$$-d < y < \infty$$

where $u_{-1}(y)$ stands for the Heaviside's step function.

η_{dn} and η_{an} represent the propagation wave-number in the dielectric and in the air respectively; they are solutions of the resonance equation

$$\eta_{an} - \frac{\eta_{dn}}{\epsilon}\frac{1 + \Gamma e^{-2j\eta_{dn}d}}{1 - \Gamma e^{-2j\eta_{dn}d}} = 0 \quad (10a)$$

$$\eta_{dn}^2 - \eta_{an}^2 = K_0^2(\epsilon - 1). \quad (10b)$$

The normalization constant N_n is given by

$$2K_0N_n^2 = \frac{\epsilon - 1}{\epsilon}\frac{\epsilon - j\eta_{an}d + j\dfrac{\eta_{an}^2}{K_0^2}\eta_{an}(\epsilon - 1)d}{-j\dfrac{\eta_{an}}{K_0}\dfrac{\eta_{dn}^2}{K_0^2}}. \quad (11)$$

In most cases one is interested in having only one mode propagating along the structures. The frequency will be chosen with that purpose in mind, and the structure will have only the lowest surface wave as the discrete mode spectrum.

[6] C. M. Angulo, Scientific Rep. AF 1391/1, Div. Eng., Brown Univ., 1955. (Diffraction of surface waves by a semi-infinite dielectric slab.)

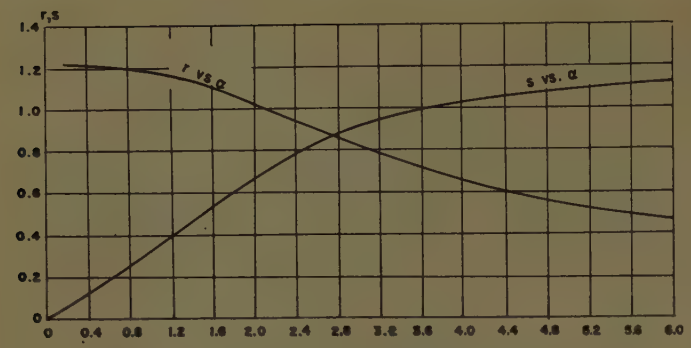

Fig. 3—r and s vs α for symmetrical excitation ($\Gamma=-1$) and $\epsilon=2.49$.

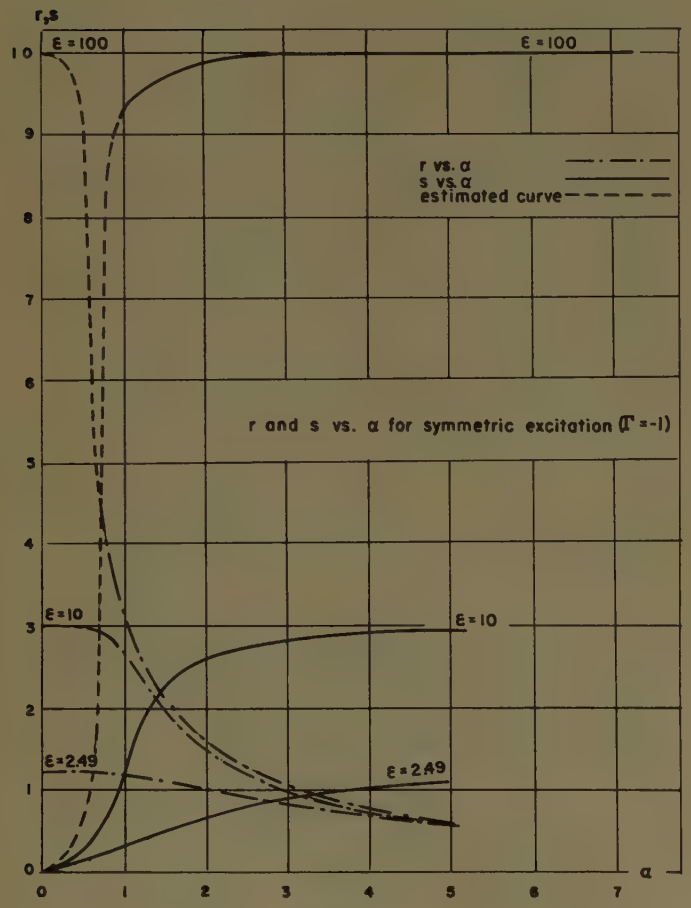

Fig. 4

The first solution of (10) (lowest surface wave) has been obtained for $\epsilon=2.49$, 10, 100. In Figs. 3 and 4 we have the plot of

$$s=-j\frac{\eta_{a1}}{K_0}=\frac{|\eta_{a1}|}{K_0} \quad \text{and} \quad r=\frac{\eta_{d1}}{K_0} \quad \text{vs} \quad \alpha=2K_0d$$

for a dielectric slab with symmetrical excitation ($\Gamma=-1$). s represents the normalized absolute value of the wave-number in the OY direction, in the air, for the lowest symmetrical surface wave. r represents the normalized wave-number in the OY direction, in the dielectric, for the lowest symmetrical surface wave.

As we see from the plots

$$0<\alpha<\infty$$
$$\sqrt{\epsilon-1}>r>0$$
$$0<s<\sqrt{\epsilon-1}.$$

The lowest symmetrical mode is always present in the discrete spectrum no matter how small we make the frequency K_0 or the thickness of the slab $2d$.

For

$$0<\alpha<\frac{2\pi}{\sqrt{\epsilon-1}}$$

only this mode is in the discrete spectrum.

In Figs. 5 and 6 we have r and s vs α for the lowest antisymmetrical ($\Gamma=1$) surface wave.

The modes of the continuous part of the spectrum are

$$h(y,\eta)=\frac{1}{\sqrt{-j\pi\dfrac{X}{\eta}}}\cdot\left[\cos\eta y+\frac{1}{\epsilon}\frac{\eta d}{\eta}j\frac{1+\Gamma e^{-2j\eta_d d}}{1-\Gamma e^{-2j\eta_d d}}\sin\eta y\right] \tag{12a}$$

for

$$0<y<\infty$$

and

$$h(y,\eta)=\frac{1}{\sqrt{-\pi j\dfrac{X}{\eta}}}\frac{1-\Gamma e^{-2j\eta_d(y+d)}}{1-\Gamma e^{-2j\eta_d d}}e^{j\eta_d y} \tag{12b}$$

for

$$-d<y<0$$

with

$$X=j\eta-j\frac{\eta_d}{\epsilon}\frac{1+\Gamma e^{-2j\eta_d d}}{1-\Gamma e^{-2j\eta_d d}}. \tag{12c}$$

η and η_d are the propagation wave-number in the OY direction in the air and in the dielectric respectively for the same mode; they are related by

$$\eta_d=\sqrt{K_0^2(\epsilon-1)+\eta^2}. \tag{12d}$$

Representation of the Fields in the Half Free-Space (Fig. 2)

This is a special case of the previous paragraph where $\epsilon(y)=1$ for all values of y. The spectrum is continuous only and V and I become the Fourier transforms of the fields.

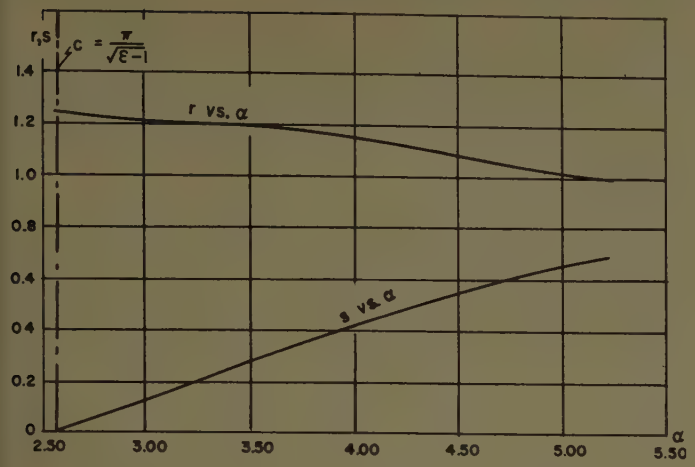

Fig. 5—r and s vs α for antisymmetrical excitation ($\Gamma=1$) and $\epsilon=2.49$.

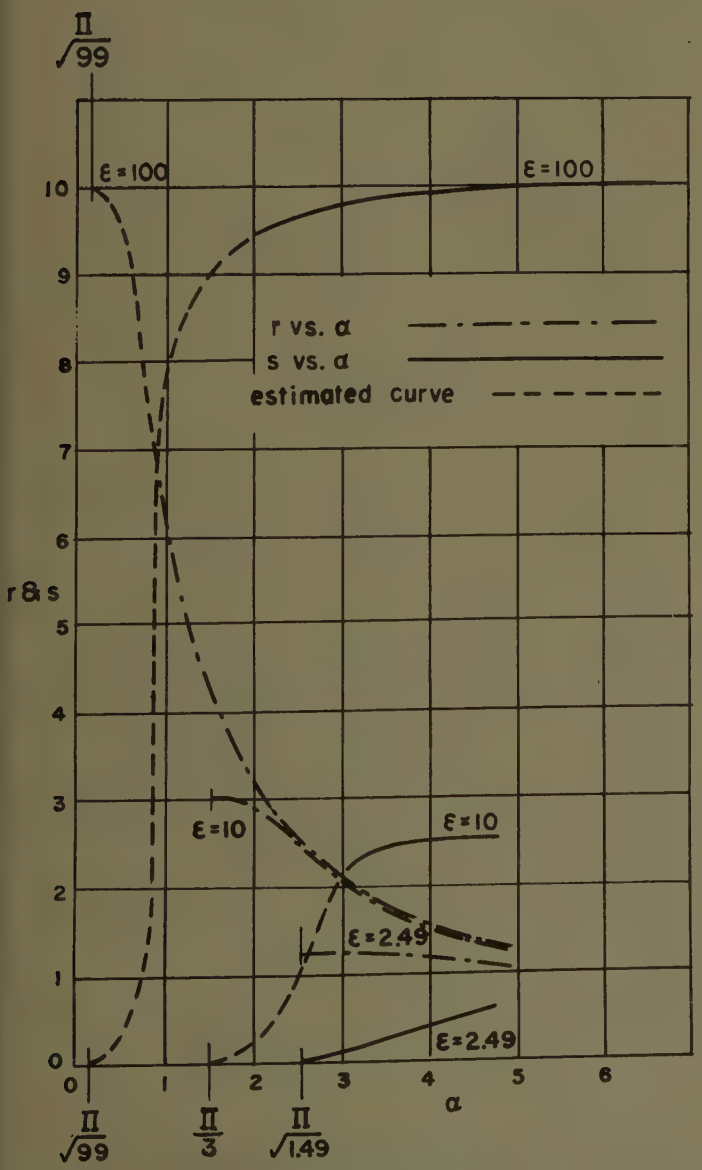

Fig. 6—r and s vs α for antisymmetric excitation ($\Gamma=+1$).

$$h(y,\eta)=\frac{1-\Gamma-j(1+\Gamma)}{4\sqrt{\pi}}\left[e^{j\eta(y+d)}-\Gamma e^{-j\eta(y+d)}\right] \quad (13)$$

for

$$-d<y<\infty.$$

We recognize that this is the Fourier cosine or the Fourier sine representation for the half-space $-d<y<\infty$ depending on Γ being either -1 or $+1$.

III. Variational Expressions for the Terminal Impedance and the Transfer Impedance Equivalent to the Discontinuity at the End of a Semi-Infinite Dielectric Slab (Upper and Lower Bounds)

The Integral Equation for E_y and the Variational Expressions for the Admittance Parameters (Upper Bound of the Admittance)

We look at the end of a semi-infinite dielectric slab (Fig. 2) as the junction of the two waveguides. The problem of finding the transverse variation of the fields has been solved in Section II. The problem of finding the variation along OZ has been reduced to the solution of (3).

Let us assume that the structure of Fig. 2 is excited by the lowest surface wave in the slab incident from $z=-\infty$, and by a plane wave of amplitude I_{inc} from $z=+\infty$.

We can represent H_x at $z=0_-$ in terms of the characteristic modes of guide 1 [upper index (1)]

$$H_x(y,0_-)=I_1^{(1)}(0)h_1^{(1)}(y)-\sum_2^N Y_n^{(1)}V_n^{(1)}(0)h_n^{(1)}(y)$$

$$-\int_{-\infty}^{\infty}Y^{(1)}(\eta)V^{(1)}(\eta,0)h^{(1)}(\eta,y)d\eta. \quad (14)$$

And at $z=0_+$ in terms of the modes of guide 2 [upper index (2)]

$$H_x(y,0_+)=-2I_{\text{inc}}^{(2)}h^{(2)}(\eta',y)$$

$$+\int_{-\infty}^{\infty}Y^{(2)}(\eta)V^{(2)}(\eta,0)h^{(2)}(\eta,y)d\eta. \quad (15)$$

The summation in (14) is extended to all the surface waves, and the integral must be carried out through a path such that $I_{\text{mag}}\zeta<0$ consistently with the time dependence $e^{+j\omega t}$.

The continuity of H_x at $z=0$ requires that (14) and (15) be equal, therefore

$$I_1^{(1)}(0)h_1^{(1)}(y)+2I_{\text{inc}}^{(2)}h^{(2)}(\eta',y)$$

$$=-\int_{-d}^{\infty}\mathcal{Y}(\eta,y,y')E_y(y',0)dy' \quad (16)$$

where

$$\mathcal{Y}(\eta, y, y') = \sum_{2}^{N} Y_n^{(1)} h_n^{(1)}(y) h_n^{(1)}(y') + \int_{-\infty}^{\infty} Y^{(1)}(\eta) h^{(1)}(\eta, y) h^{(1)}(\eta, y') d\eta + \int_{-\infty}^{\infty} Y^{(2)}(\eta) h^{(2)}(\eta, y) h^{(2)}(\eta, y') d\eta. \quad (17)$$

Eq. (16) is the integral equation for the unknown field $E_y(y, 0)$. Despite our inability to solve it we can obtain a great deal of information by variational methods.

In view of the linearity of Maxwell's equations we can write that the electric field at the plane of the discontinuity must be the addition of two terms, each one proportional to one of the excitations, that is

$$E_y(y, 0) = -I_1^{(1)}(0)\mathcal{E}_1(y) - 2I_{\text{inc}}^{(2)}\mathcal{E}_2(y). \quad (18)$$

The contributions of this field (voltages) to the two exciting modes are

$$V_1^{(1)}(0) = I_1^{(1)}(0) \int_{-d}^{\infty} h_1^{(1)}(y)\mathcal{E}_1(y)dy + 2I_{\text{inc}}^{(2)} \int_{-d}^{\infty} h_1^{(1)}(y)\mathcal{E}_2(y)dy \quad (19a)$$

$$V^{(2)}(\eta', 0) = I_1^{(1)}(0) \int_{-d}^{\infty} h^{(2)}(\eta', y)\mathcal{E}_1(y)dy + 2I_{\text{inc}}^{(2)} \int_{-d}^{\infty} h^{(2)}(\eta', y)\mathcal{E}_2(y)dy. \quad (19b)$$

Combined with the integral equation we obtain

$$V_1^{(1)}(0) = I_1^{(1)}(0) \int_{-d}^{\infty}\int_{-d}^{\infty} \mathcal{Y}(\eta, y, y')\mathcal{E}_1(y)\mathcal{E}_2(y')dydy' + 2I_{\text{inc}}^{(2)} \int_{-d}^{\infty}\int_{-d}^{\infty} \mathcal{Y}(\eta, y, y')\mathcal{E}_1(y)\mathcal{E}_2(y')dydy' \quad (20a)$$

$$V^{(2)}(\eta', 0) = I_1^{(1)}(0) \int_{-d}^{\infty}\int_{-d}^{\infty} \mathcal{Y}(\eta, y, y')\mathcal{E}_1(y')\mathcal{E}_2(y)dydy' + 2I_{\text{inc}}^{(2)} \int_{-d}^{\infty}\int_{-d}^{\infty} \mathcal{Y}(\eta, y, y')\mathcal{E}_2(y)\mathcal{E}_2(y')dydy'. \quad (20b)$$

Eqs. (19) and (20) are exact and provide the link between the surface wave in guide 1 and mode η' in guide 2. If we assume that the structure is excited *only* by the surface wave ($I_{\text{inc}}^{(2)} = 0$), (19) and (20) become

$$V_1^{(1)}(0) = I_1^{(1)}(0) \int_{-d}^{\infty} h_1^{(1)}(y)\mathcal{E}_1(y)dy \quad (21a)$$

$$V^{(2)}(\eta, 0) = I_1^{(1)}(0) \int_{-d}^{\infty} h^{(2)}(\eta', y)\mathcal{E}_1(y)dy \quad (12b)$$

and

$$V_1^{(1)}(0) = I_1^{(1)}(0) \int_{-d}^{\infty}\int_{-d}^{\infty} \mathcal{Y}(\eta, y, y')\mathcal{E}_1(y)\mathcal{E}_1(y')dydy' \quad (22a)$$

$$V^{(2)}(\eta', 0) = I_1^{(1)}(0) \int_{-d}^{\infty}\int_{-d}^{\infty} \mathcal{Y}(\eta, y, y')\mathcal{E}_1(y')\mathcal{E}_2(y)dydy'. \quad (22b)$$

Either set defines the terminal admittance of the slab presented to the surface wave and the transfer impedance coupling the surface wave to mode η' in guide 2.

$$Y_{11}V_1^{(1)}(0) = I_1^{(1)}(0) \quad (23a)$$

$$Y_{21}V^{(2)}(\eta', 0) = I_1^{(1)}(0). \quad (23b)$$

We cannot calculate the exact values of the admittances because we do not know the functions $\mathcal{E}_1(y)$ and $\mathcal{E}_2(y)$ to be inserted above. However, we can write the variational expressions for the parameters

$$Y_{11} = \frac{\int_{-d}^{\infty}\int_{-d}^{\infty} \mathcal{Y}(\eta, y, y')\mathcal{E}_1(y)\mathcal{E}_1(y')dydy'}{\left[\int_{-d}^{\infty} h_1^{(1)}(y)\mathcal{E}_1(y)dy\right]^2} \quad (24a)$$

$$Y_{21} = \frac{\int_{-d}^{\infty}\int_{-d}^{\infty} \mathcal{Y}(\eta, y, y')\mathcal{E}_1(y')\mathcal{E}_2(y)dydy'}{\int_{-d}^{\infty} h_1^{(1)}(y)\mathcal{E}_2(y)dy \int_{-d}^{\infty} h^{(2)}(\eta, y')\mathcal{E}_1(y')dy'}. \quad (24b)$$

If we take $\mathcal{E}_1 = \mathcal{E}_2$, (24b) becomes

$$Y_{21} = Y_{11} \frac{\int_{-d}^{\infty} h_1^{(1)}(y)\mathcal{E}_1(y)dy}{\int_{-d}^{\infty} h^{(2)}(\eta, y)\mathcal{E}_1(y)dy}. \quad (24c)$$

We will use (24a) and (24c).

The expressions (24a) and (24b) are variational and independent of the amplitudes of $\mathcal{E}_1(y)$ and $\mathcal{E}_2(y)$. If we insert a trial field the error in the admittance would be of higher order than the error in the field.

A reasonable approximation for the field at $z = 0$ is the incident surface mode, that is, the field that we would have at $z = 0$ if the dielectric were not discontinued.

After the necessary integrations the approximation yields

$$\frac{K_0 N_1^2}{\sqrt{1+s^2}} \frac{Y_{11}}{Y_1^{(1)}} = C_1(\alpha, \epsilon) + C_2(\alpha, \epsilon) \int_0^{\alpha} \cos rx H_0^{(2)}(x)dx + C_3(\alpha, \epsilon) \int_0^{\alpha} \sin rx H_0^{(2)}(x)dx + C_4(\alpha, \epsilon) \int_{\alpha}^{\infty} e^{-xs} H_0^{(2)}(x)dx. \quad (25)$$

Eq. (25) gives the lower bound of the terminal admittance of the slab, normalized with respect to the characteristic admittance of the surface wave.

The coefficients of (25) are

$$C_1(\alpha,\epsilon)=\frac{\frac{s^2}{\epsilon}+\frac{1}{2}}{s\sqrt{1+s^2}}+j\,\frac{1}{\pi}\left[\frac{\frac{s^2}{\epsilon}+\frac{1}{2}}{s\sqrt{1+s^2}}\,2\ln\left(\sqrt{1+s^2}+s\right)+\frac{1}{2}\,\frac{\frac{1}{\epsilon^2}+\frac{s^2}{r^2}}{1-r^2}\right]$$

$$-\Gamma\left[\frac{s}{1+s^2}+\frac{\frac{s}{\epsilon}}{1-r^2}\right]\frac{\alpha}{2}H_0^{(2)}(\alpha)+\Gamma\left[\frac{1}{1+s^2}+\frac{1}{2}\,\frac{\frac{1}{\epsilon^2}+\frac{s^2}{r^2}}{1-r^2}\right]\frac{\alpha}{2}H_1^{(2)}(\alpha) \tag{26a}$$

$$2C_2(\alpha,\epsilon)=\frac{\alpha}{2}\left(\frac{1}{\epsilon^2}+\frac{s^2}{r^2}\right)-\frac{s}{\epsilon}\left(2-\frac{1}{r^2}\right) \tag{26b}$$

$$C_3(\alpha,\epsilon)=\frac{1+s^2}{r\epsilon}+\frac{s^2}{2r^3}+\frac{\frac{1}{\epsilon^2}+\frac{s^2}{r^2}}{4r(r^2-1)} \tag{26c}$$

$$C_4(\alpha,\epsilon)=-\Gamma\left[\frac{s}{2(1+s^2)}+\frac{s}{\epsilon}\,\frac{\epsilon+1}{\epsilon-1}-\frac{\alpha}{2}\right]e^{\alpha s} \tag{26d}$$

where ϵ is the relative dielectric constant of the slab, $H_0^{(2)}$, $H_1^{(2)}$ are the Hankel's functions of second kind and zero and first order respectively. The constants N_1, s, α, r, are defined in the first paragraph of Section II. Notice that, although the coefficients C are written in terms of r, s, ϵ, and α, they are functions only of two variables, since the other two are determined through (10).

Eq. (25) cannot be simplified further. Information and tabulation for the incomplete Fourier transforms of the Hankel's function can be found in Schwartz.[7] However, the tabulation given does not cover the range of interest to us.

An asymptotic expression for (25) can be obtained using the method of steepest descents; but, unfortunately, the approximation is good only for $\alpha>5$ and in our problem we are also interested in $\alpha<5$. We have, therefore, carried numerical integrations where necessary.

If $\alpha\to 0$ only the lowest symmetrical mode remains as a possible natural mode of the structure. Making $\Gamma=-1$ we obtain as $\alpha\to 0$

$$\operatorname{Re}\frac{Y_{11}}{Y_1^{(1)}}\to 1+\frac{(\epsilon-1)(3-\epsilon)}{4\epsilon^2}\,\alpha^2 \tag{26e}$$

$$\operatorname{Imag}\frac{Y_{11}}{Y_1^{(1)}}\to\frac{1}{2\pi}\left(\frac{\epsilon-1}{\epsilon}\right)^2\alpha^2\ln\frac{2}{\alpha}\,. \tag{26f}$$

As we should expect, there is no discontinuity at the end of the slab when $\alpha\to 0$ and the real part of the admittance is an even function of α around $\alpha\to 0$. The imaginary part of the admittance has the expected singularity at $\alpha=0$ and is always greater than zero (our discontinuity is capacitive).

If $\alpha\to\infty$

$$\operatorname{Re}\frac{Y_{11}}{Y_1^{(1)}}\to\frac{1}{\sqrt{\epsilon}}-2\Gamma\sqrt{\frac{\epsilon}{\pi\alpha}}\sin\alpha \tag{27a}$$

$$\operatorname{Imag}\frac{Y_{11}}{Y_1^{(1)}}\to-\frac{2}{\sqrt{\epsilon}}\,\frac{1}{\alpha}\,. \tag{27b}$$

This is the result to be expected, as the thickness goes to infinity we approach normal incidence inside the dielectric and the end of the slab represents a jump in characteristic impedance.

The Integral Equation for H_x and the Variational Expressions for the Impedance Parameters (Lower Bound of the Admittance)

One can derive expressions for the impedance parameters of the discontinuity which are stationary with respect to the magnetic field at the discontinuity. The procedure is similar to the one in the previous section, and we will write only the final results.

$$Z_{11}=\frac{\int_{-d}^{\infty}\int_{-d}^{\infty}\mathcal{Z}(\eta,y,y')\mathcal{H}_1(y)\mathcal{H}_1(y')\,dy\,dy'}{\left[\int_{-d}^{\infty}e_1^{(1)}(y)\mathcal{H}_1(y)\,dy\right]^2} \tag{28a}$$

[7] L. Von Schwartz, "Untersuchung einiger mit den zylinderfunktionen nullter ordnung verwandten funktionen," *Luftfahrtforschung*, vol. 20, pp. 341–351; February, 1944.

and

$$Z_{21} = \frac{\int_{-d}^{\infty}\int_{-d}^{\infty} \mathcal{Z}(\eta, y, y')\mathcal{H}_1(y)\mathcal{H}_2(y')dydy'}{\int_{-d}^{\infty} e_1^{(1)}(y)\mathcal{H}_2(y)dy \int_{-d}^{\infty} e^{(2)}(\eta, y')\mathcal{H}_1(y')dy'} \quad (28b)$$

or, with the approximation $\mathcal{H}_1 = \mathcal{H}_2$

$$Z_{21} = Z_{11} = \frac{\int_{-d}^{\infty} e_1^{(1)}(y)\mathcal{H}_1(y)dy}{\int_{-d}^{\infty} e^{(2)}(\eta, y)\mathcal{H}_1(y)dy}. \quad (28c)$$

The expressions (28a) and (28b) are minimum for the exact field $\mathcal{H}_1(y)$. Any approximate value of (28a) provides a lower bound for the admittance.

The approximation made early in this section yields now

$$\begin{aligned} \Upsilon_0 N_1^2 \sqrt{1+s^2}\,\frac{Z_{11}}{Z_1^{(1)}} &= \gamma_1(\alpha, \epsilon) + \gamma_2(\alpha, \epsilon)\int_0^{\alpha} \cos rx H_0^{(2)}(x)dx \\ &+ \gamma_3(\alpha, \epsilon)\int_0^{\alpha} \sin rx H_0^{(2)}(x)dx \\ &+ \gamma_4(\alpha, \epsilon)\int_{\alpha}^{\infty} e^{-xs} H_0^{(2)}(x)dx \end{aligned} \quad (29)$$

for the lower bound of the admittance of the slab normalized with respect to the characteristic admittance of the surface mode.

The coefficients of (29) are

$$\begin{aligned} \gamma_1(\alpha, \epsilon) = {} & \frac{1+2s^2}{2s}\sqrt{1+s^2} + j\frac{1}{\pi}\left[\frac{1+\frac{s^2\epsilon^2}{r^2}}{2}\right. \\ & \left. + 2\frac{1+2s^2}{s}\sqrt{1+s^2}\ln\left(\sqrt{1+s^2}+s\right)\right] \\ & + \Gamma\frac{\alpha}{2}\left[\frac{3}{2} - \frac{1}{2}\frac{s^2\epsilon^2}{r^2}\right]H_1^{(2)}(\alpha) \\ & - \frac{\alpha s}{2}(\epsilon+1)\Gamma H_0^{(2)}(\alpha) \end{aligned} \quad (30a)$$

$$\gamma_2(\alpha, \epsilon) = \frac{1-r^2}{2}\left[\alpha\frac{1+\frac{s^2\epsilon^2}{r^2}}{2} - 2s + \frac{s\epsilon}{r^2}\right] \quad (30b)$$

$$\gamma_3(\alpha, \epsilon) = \frac{1}{2r}\left[\frac{1+\frac{s^2\epsilon^2}{r^2}}{2} + (1-r^2)(1+2s^2)\right] \quad (30c)$$

$$\gamma_4(\alpha, \epsilon) = \Gamma(1+s^2)\left[\frac{s}{2(1+s^2)} - s\frac{\epsilon+1}{\epsilon-1} + \frac{\alpha}{2}\right]e^{\alpha s}. \quad (30d)$$

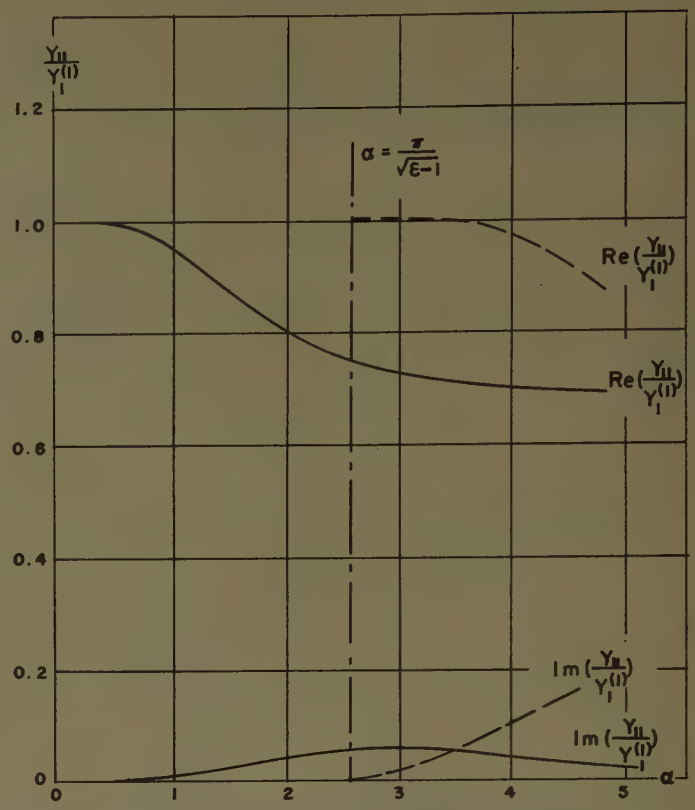

Fig. 7— ——— $(Y_{11}/Y_1^{(1)})$ vs α for symmetrical excitation $(\Gamma = -1)$ and $\epsilon = 2.49$. – – – $(Y_{11}/Y_1^{(1)})$ vs α for antisymmetrical excitation $(\Gamma = +1)$ and $\epsilon = 2.49$.

Plot of $Y_{11}/Y_1^{(1)}$ vs α

The terminal admittance of the slab has been computed numerically for $\epsilon = 2.49$ (polystyrene), $\epsilon = 10$, and $\epsilon = 100$.

For $\epsilon = 2.49$ the two bounds of the admittance are closer to each other than the possible error in the computation. The agreement is better than 5 per cent. Therefore we have plotted only one curve; instead of plotting the two bounds, Fig. 7 plots $Y_{11}/Y_1^{(1)}$ vs α for symmetrical and antisymmetrical excitation. We can see that the imaginary part is much smaller than the real one.

For $\epsilon = 10$ the bounds are no longer so close. (See Figs. 8 and 9.) For larger values of ϵ the difference between the two bounds is greater; $\epsilon = 10$ seems to be the larger value of ϵ for which our expressions for the admittance give reasonably accurate results, and that only for the real part.

For $\epsilon = 100$ the admittance is too small to be plotted. The real part of $Y_{11}/Y_1^{(1)}$ drops extremely fast from $+1$ to zero as α increases. The imaginary part is extremely small.

IV. Forward Radiation Pattern

Eqs. (23b) and (24c), with $\mathcal{E}_1(y) = e_1^{(1)}(y)$ yield

$$V^{(2)}(\eta, z) = \frac{I_1^{(1)}(0)}{Y_{11}} e^{-i\sqrt{K_0^2-\eta^2}z} dy' \int_{-d}^{\infty} -h(\eta, y)e_1^{(1)}(y)dy. \quad (31)$$

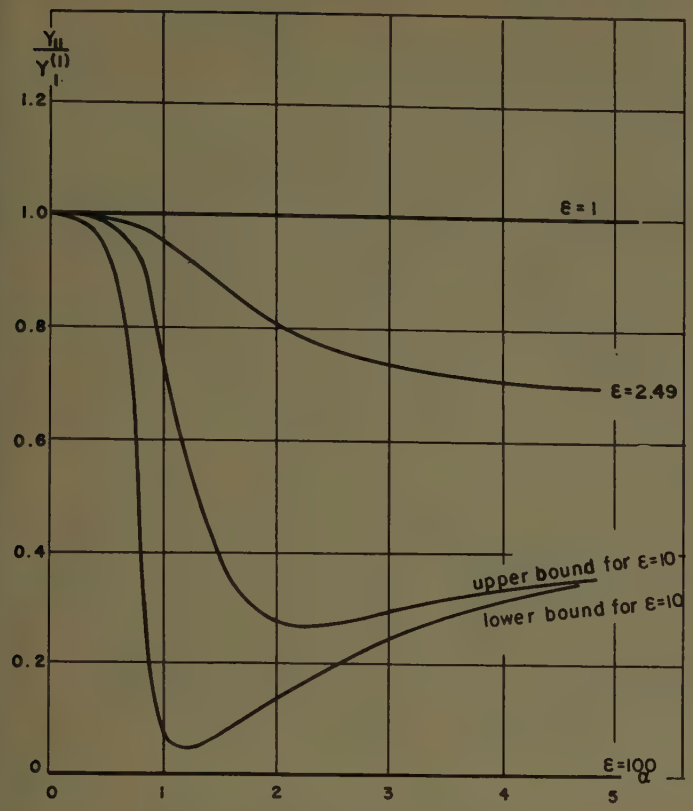

Fig. 8—Re($Y_{11}/Y_1^{(1)}$) vs α for symmetrical excitation ($\Gamma=-1$).

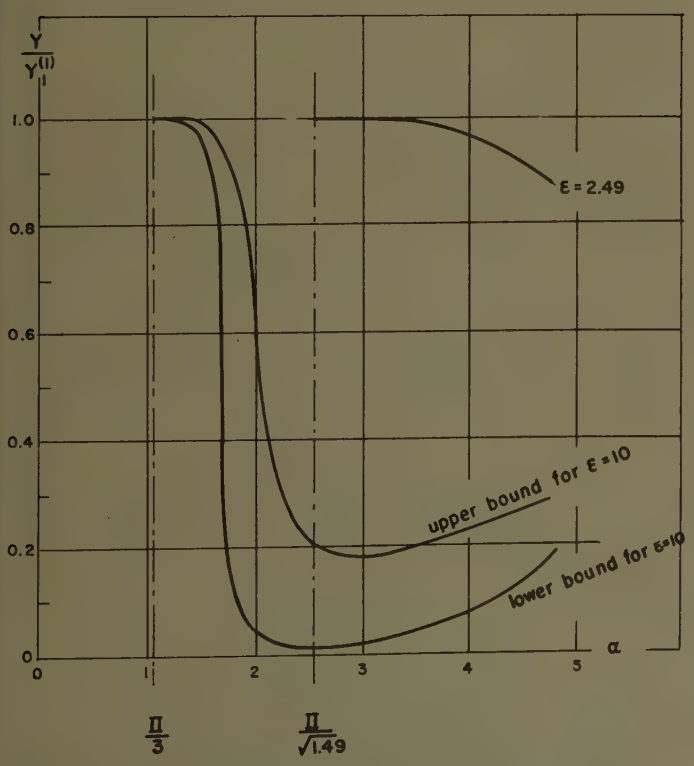

Fig. 9—Re($Y_{11}/Y_1^{(1)}$) vs α for antisymmetrical excitation ($\Gamma=+1$).

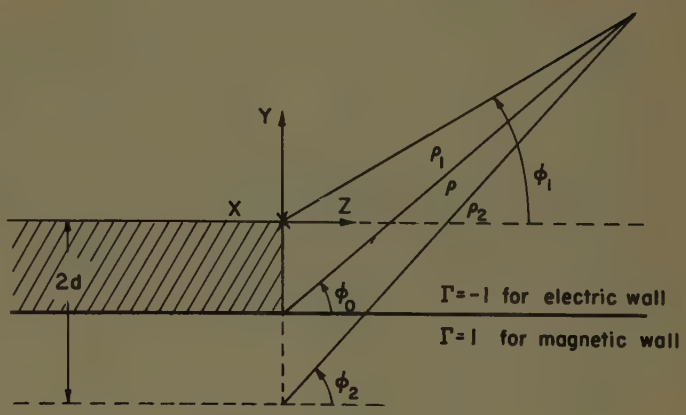

Fig. 10

The synthesis of the modal voltages gives

$$E_y(y, z) = Z_{11}I_1^{(1)}(0)\int_{-\infty}^{\infty}d\eta\int_{-d}^{\infty} - h(\eta, y')e(\eta, y)$$
$$\cdot e_1^{(1)}(y')e^{-j\sqrt{K_0^2-\eta^2}z}dy'. \tag{32}$$

As before the paths of integration in the η plane is chosen that $I_{\text{mag}}\sqrt{K_0^2-\eta^2}<0$. The mode functions have been given in Section II.

If the proper substitutions are made and the integration in y' carried out we obtain

$$E(\rho, \phi_0) =$$
$$A\int_p \frac{\sin^2\phi + js\sin\phi - \epsilon}{(\sin^2\phi - r^2)(\sin\phi + js)}$$
$$\cdot\cos\phi\,[e^{-jK\rho_2\cos(\phi+\phi_2)} - e^{-jK\rho_1\cos(\phi-\phi_1)}]d\phi \tag{33}$$

where

$$A = -j\frac{Z_{11}I_1^{(1)}(0)}{2\pi N_1\Gamma}\quad\frac{\epsilon-1}{\epsilon}. \tag{34}$$

The meaning of the new coordinates is shown in Fig. 10.

The path of integration is indicated in Fig. 11(a). Sufficiently far away $\phi_1\approx\phi_2\approx\phi_0$. The first integral has a saddle point at $\phi=-\phi_2\approx-\phi_0$ and the second at $\phi=\phi_1\approx\phi_0$. If we deform the path in each case into the corresponding steepest descent path indicated in Fig. 11(b) we can write

$$E_y(\rho, \phi_0)$$
$$= A\int_{p_2}\frac{\sin^2\phi + js\sin\phi - \epsilon}{(\sin^2\phi - r^2)(\sin\phi + js)}\cos\phi e^{-jK\rho_2\cos(\phi+\phi_0)}d\phi$$
$$-\Gamma A\int_{p_1}\frac{\sin^2\phi + js\sin\phi - \epsilon}{(\sin^2\phi - r^2)(\sin\phi + js)}\cos\phi e^{-jK\rho_1\cos(\phi-\phi_0)}d\phi$$
$$+2\pi jA\frac{\Gamma\epsilon}{\epsilon-1}e^{-K\rho_1 s\sin\phi_0}e^{-jK\rho_1\sqrt{1+s^2}}\cos\phi_0. \tag{35}$$

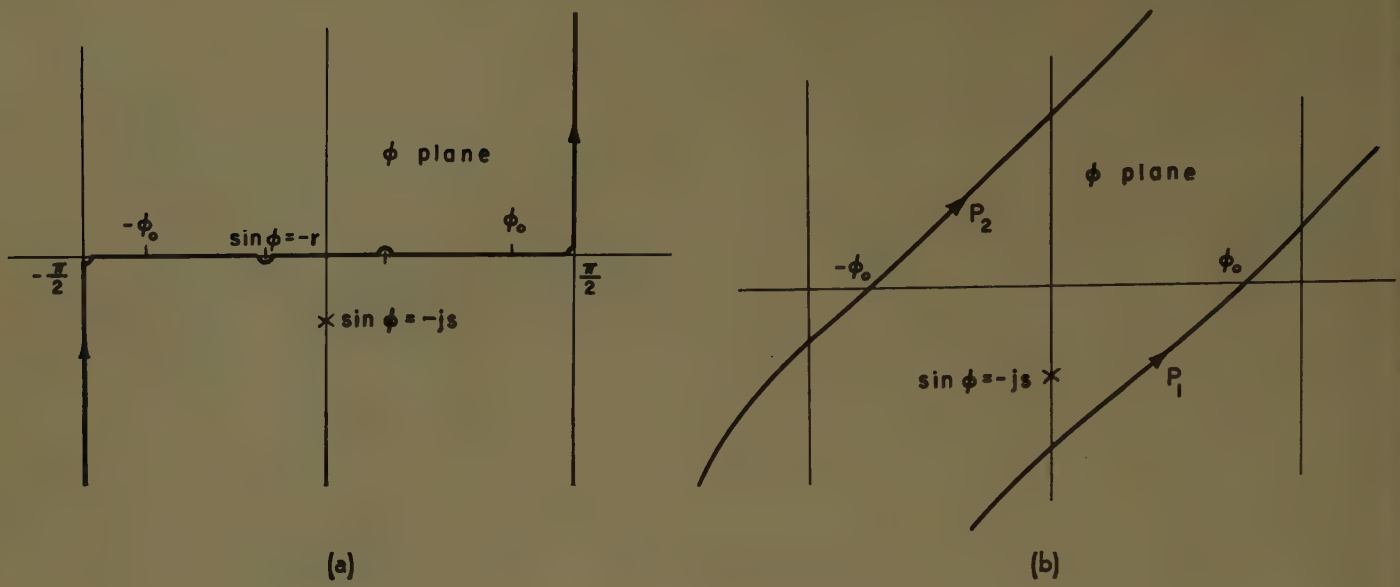

Fig. 11

$$E_y(\rho,\phi_0)=\frac{Z_{11}I_1^{(1)}(0)}{N_1\sqrt{2\pi}}\,\frac{\epsilon-1}{\epsilon}\,e^{j3(\pi/4)}\,\frac{e^{-jK\rho}}{\sqrt{K\rho}}\,\frac{\cos\phi_0}{\sin^2\phi_0-r^2}\left[\Gamma(\sin\phi_0-\frac{\epsilon}{\sin\phi_0-js})e^{-jKd\sin\phi_0}+\left(\sin\phi_0-\frac{\epsilon}{\sin\phi_0+js}\right)e^{jKd\sin\phi_0}\right]. \tag{36}$$

In cases like the one in Figs. 11(a) and 11(b) where the observation angle is large enough

$$|\sin\phi_0|>r$$

we must add to (35) the integrals around the poles at $\sin\phi=\pm r$. However, the two contributions cancel each other, and we can ignore the two poles at $\sin\phi=\pm r$ in all cases.

The third term in (35) is the contribution to the second integral due to the pole at $\phi=\arcsin(-js)$. This contribution is present only if the saddle point $\phi=\phi_0$ is sufficiently close to $\pi/2$ as to make the steepest descent path P_1, intersect the imaginary axis below the pole as in the case in Fig. 11(b). The physical meaning is obvious in Fig. 10, as the observation angle increases we come so close to the plane of discontinuity that we have the surface wave added to the radiated field. However, the contribution is negligible compared with the radiated field, since its amplitude decreases as a negative real exponential for large ρ.

The integration of (35) by the methods of steepest descents yields, finally, as a first approximation for the far field (the third term of (35) being neglected)

Following similar steps we would obtain for the first approximation of H_x

$$H_x(\rho,\phi_0)=-\frac{E_y(\rho,\phi_0)}{Z_0\cos\phi_0}. \tag{37}$$

And, from the knowledge of the fields

$$\frac{P}{P_{inc}}=\frac{8}{\pi}\left(\frac{\epsilon-1}{\epsilon}\right)^2\frac{\sqrt{1+s^2}}{\left|1+\frac{Y_{11}}{Y_1^{(1)}}\right|^2}\,\frac{\cos^2\phi_0}{K_0N_1^2}\left[\frac{\left((\sin^2\phi_0+s^2-\epsilon)\sin\phi_0\sin\left(\frac{\alpha}{2}\sin\phi_0\right)+s\epsilon\cos\left(\frac{\alpha}{2}\sin\phi_0\right)\right]^2}{(\sin^2\phi_0-r^2)(\sin^2\phi_0+s^2)}\right]. \tag{38}$$

If $\Gamma=1$ (antisymmetrical excitation)

$$\frac{P}{P_{inc}}=\frac{8}{\pi}\left(\frac{\epsilon-1}{\epsilon}\right)^2\frac{\sqrt{1+s^2}}{\left|1+\frac{Y_{11}}{Y_1^{(1)}}\right|^2}\,\frac{\cos^2\phi_0}{K_0N_1^2}\left[\frac{\left((\sin^2\phi_0+s^2-\epsilon)\sin\phi_0\cos\left(\frac{\alpha}{2}\sin\phi_0\right)-s\epsilon\sin\left(\frac{\alpha}{2}\sin\phi_0\right)\right]^2}{(\sin^2\phi_0-r^2)(\sin^2\phi_0+s^2)}\right]. \tag{39}$$

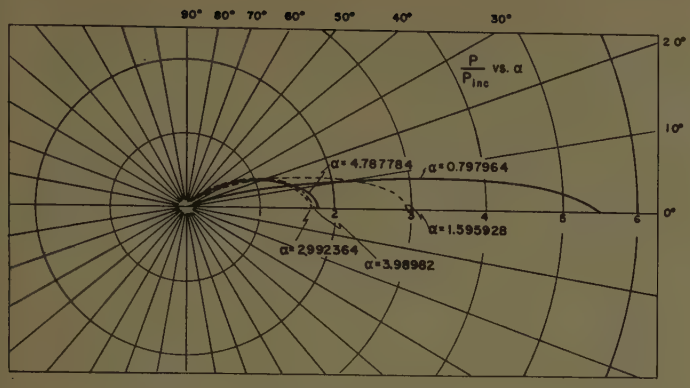

Fig. 12—Radiation pattern for symmetrical excitation. $\epsilon = 2.49$.

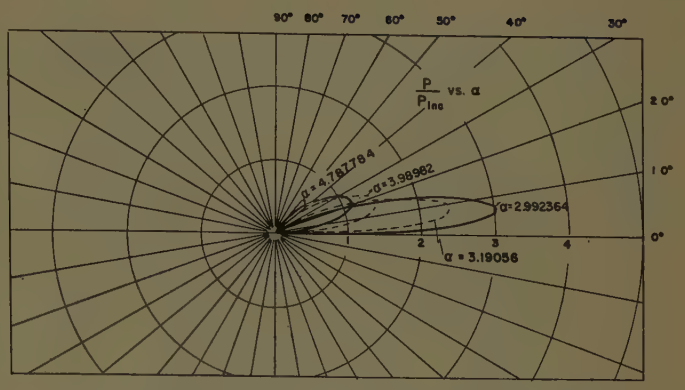

Fig. 13—Radiation pattern for antisymmetrical excitation. ($\Gamma = +1$) and $\epsilon = 2.49$.

The right-hand members of (38) and (39) represent the power radiated at an angle ϕ_0, per unit width of dielectric slab, per unit angle, and per unit incident power in the lowest surface wave per unit width of dielectric slab.

The relative power is plotted in Figs. 12 and 13 for several values of α for half of the dielectric slab and $\epsilon = 2.49$.

Acknowledgment

The work in this paper was in partial fulfillment of the D.E.E. degree at the Polytechnic Institute of Brooklyn. The advice of Prof. N. Marcuvitz is greatly appreciated. Additional work was made possible by the Cambridge AF Research Center Contract AF19(604)1391 with Brown University.[6] The help of W. Chang in the computations is also gratefully acknowledged.

Alternative Field Representations in Regions Bounded by Spheres, Cones, and Planes*

LEOPOLD B. FELSEN†

Summary—**Alternative representations are obtained directly by the method of characteristic Green's functions for the fields radiated by arbitrarily placed scalar and vector (electromagnetic) point sources in regions bounded by surfaces which are describable in terms of single coordinates in a spherical coordinate system. Such surfaces are spheres, cones, and planes, or a combination of these. The representations are distinguished from one another by different convergence properties for various ranges of values of the location of source and observation points and of the boundary surface geometry. Considered in particular are the diffraction by a sphere, a wedge, and a wedge with a spherical dome for both the scalar and vector cases.**

I. Introduction

THE DESCRIPTION of acoustic and electromagnetic phenomena in regions bounded, respectively, by rigid and perfectly conducting surfaces which are describable in terms of a single coordinate in a spherical coordinate system is well known. Such surfaces are spheres, cones, and planes, and the region may be bounded by any combination of these. Diffraction problems in such regions are usually solved by expressing the desired field solution in terms of modes (eigenfunctions) orthogonal over the spherical cross section, and in terms of modal coefficients which depend on the radial coordinate and take into account the sources in the field.

The formal solutions so obtained are often inconvenient because of the slow convergence of this angular mode (radial transmission) representation for certain ranges of values of the obstacle parameters and of the locations of the source and observation points. It is desirable, therefore, to have available a scheme whereby the solutions for three-dimensional scalar and vector boundary value problems in such regions can be constructed *directly* in various *alternative* forms which exhibit different convergence properties.

The construction of alternative representations for scalar, two-dimensional, azimuthally symmetric Green's functions in spherical regions has been carried out by

* Original manuscript received by the PGAP, September 28, 1955; revised manuscript received, May 28, 1956. A portion of this paper has been presented at Symposium on Electromagnetic Wave Theory, Univ. of Michigan, Ann Arbor, Mich., June, 1955.

† Microwave Res. Inst., Polytechnic Inst. of Brooklyn, N. Y.

Marcuvitz[1] by the method of characteristic Green's functions. From this viewpoint, the two one-dimensional problems characteristic of the given two-dimensional operator are analyzed separately to yield each a one-dimensional "characteristic" Green's function and its associated complete set of orthonormal eigenfunctions. These characteristic solutions can be combined directly in various forms, thus giving rise to alternative representations for the desired two-dimensional Green's function. For example, the latter can be represented either in terms of the angular modes and the radial characteristic Green's function (this is the usual formulation alluded to above), or in terms of the radial modes and the angular characteristic Green's function. By virtue of this formalism, the function-theoretic considerations, which are necessary to convert one representation into the other, also become particularly clear.

The principal purpose of this paper is the application of the characteristic Green's function method to the formulation of vector diffraction problems in the above-described spherical regions. The solution for the vector fields and eventually for the dyadic Green's functions is found from spherical transmission line theory[2–5] whereby propagation is assumed to take place in the radial direction and the transverse (to r) dependence is described in terms of orthogonal vector modes (see Section II-B).[6] This solution is expressed in terms of scalar functions which are related to the radial Hertzian potentials and which resemble closely the three-dimensional Green's functions for associated scalar problems. Thus, the dyadic Green's functions can be represented directly in various forms if alternative representations have been found for the appropriate scalar Green's functions. The construction of alternative solutions for three-dimensional scalar Green's functions (which is of interest by itself) is carried out in Section II-A of this paper as a directed extension of the two-dimensional formalism discussed by Marcuvitz, by treating separately the three one-dimensional problems characteristic of the three-dimensional operator. The desirability of constructing various solutions for scalar and vector diffraction problems has also been recognized by Tilston,[7] who obtains three alternative representations by applying Green's theorem or the Lorentz reciprocity theorem to suitably chosen functions in regions bounded by various single-coordinate surfaces. However, with Tilston's method, each representation requires essentially the solution of a new problem; his formulation does not highlight the underlying connection between the various representations, which is brought out very clearly by the characteristic Green's function approach.

In order to apply the formalism discussed above to the representations of various Green's functions, it is necessary to have at one's disposal the characteristic (Green's function and eigenfunction) solutions for the different specified domains. Such solutions have been obtained elsewhere[8,9] and are not listed here except when required for the discussion of special problems. As regards the characteristic Green's function formulations, stress is placed on "perturbation" type representations in which the characteristic Green's functions are separated into two parts, one of which describes an unperturbed solution while the other takes into account the effect of the specified boundary. For example, an angular characteristic Green's function for a single, infinite cone can be separated into a "free space" portion (with the cone absent), and an additional term which accounts for the presence of the cone. Thus, the associated three-dimensional Green's function separates directly into a free-space solution and a perturbation term which represents the scattering from the obstacle.

The above-described technique has been applied to the solution of a number of diffraction problems. Diffraction by a sphere, a wedge, and a wedge with a spherical dome, are treated in this paper (Section III), while the diffraction by a cone, and a cone with a spherical tip form the subject of a companion paper.[10] Both scalar and vector problems are treated. For the sphere, the Green's function formulation is carried out in terms of angular modes (radial transmission), and radial modes (angular transmission). As is well known, the angular mode representation is convenient for the determination of the scattering from a small sphere. The angular transmission representation is useful in connection with some problems for a large sphere;[11] in particular, it yields a very rapidly convergent expression for the current induced in the shadow region on a perfectly conducting sphere when a plane wave is incident.

The diffraction of the radiation from arbitrarily oriented scalar and vector dipole sources by a wedge is formulated as a radial transmission problem. This representation is rapidly convergent if either the source point

[1] N. Marcuvitz, "Field representations in spherically-stratified regions," *Comm. Pure & Appl. Math.*, vol. 4, pp. 263–315, sec. 5; August, 1951.

[2] *Cf.* S. A. Schelkunoff, "Electromagnetic Waves," D. Van Nostrand Co., New York, N. Y., chs. 10, 11; 1943.

[3] Marcuvitz, *op. cit.*, (sec. 2b).

[4] L. B. Felsen, "Spherical Transmission Line Theory," Rep. R-253-51, PIB-194, Microwave Res. Inst., Polytechnic Inst. Bklyn.; January, 1952.

[5] L. B. Felsen and N. Marcuvitz, "Slot coupling of rectangular and spherical waveguides," *J. Appl. Phys.*, vol. 24, pp. 755–770, (see appendix); June, 1953.

[6] L. L. Bailin and S. Silver, "Exterior electromagnetic boundary value problems for spheres and cones," IRE TRANS., vol. AP-4, pp. 5–15; January, 1956. An alternative approach, based on the Lorentz reciprocity theorem, is presented here.

[7] W. V. Tilston, "Contributions to the Theory of Antennas," Dept of Elect. Eng., Univ. of Toronto, Toronto, Ont., Can.; October, 1952. (Grant from the Defence Research Board of Canada.)

[8] Marcuvitz, *op. cit.* (sec. 4).

[9] L. B. Felsen, "Alternative Field Representations in Regions Bounded by Spheres, Cones, and Planes," Rep. R-359-54, PIB-293, Microwave Res. Inst., Polytechnic Inst. of Bklyn.; January, 1954.

[10] Felsen, p. 121, this issue.

[11] *Cf.* A. Sommerfeld, "Partial Differential Equations in Physics," Academic Press, New York, N. Y., ch. 5 (appendix 2), ch. 6 (appendix); 1949.

or the observation point is located near the wedge apex, and permits the direct investigation of the field behavior near the edge. For the special case of plane wave incidence at an arbitrary angle with respect to the apex (*i.e.*, source point at infinity), the scalar Green's function solution obtained here in terms of spherical wave functions is compared, and shown to agree, with the cylindrical wave solution which is arrived at by a generalization of Sommerfeld's method of images.[12] If a spherical dome centered on the apex is superposed on the wedge, the radial transmission formulation yields a representation consisting of the simple wedge solution and a perturbation term accounting for the effect of the sphere. The latter is rapidly convergent for small sphere radius.

II. Alternative Representations for Formal Solutions

A. Scalar Diffraction Problems

The Green's function problem to be solved in the region τ is

$$(\nabla^2 + k^2)\mathcal{G}(\boldsymbol{r}, \boldsymbol{r}') = -\delta(\boldsymbol{r} - \boldsymbol{r}'), \quad k \text{ real}, \tag{1a}$$

where the operator ∇^2 is given in spherical coordinates by

$$\nabla^2 = \frac{1}{r^2}\frac{\partial}{\partial r}r^2\frac{\partial}{\partial r} + \frac{1}{r^2\sin\theta}\frac{\partial}{\partial\theta}\sin\theta\frac{\partial}{\partial\theta} + \frac{1}{r^2\sin^2\theta}\frac{\partial^2}{\partial\Phi^2}. \tag{1b}$$

The delta function source term is defined in the usual manner by

$$\delta(\boldsymbol{r} - \boldsymbol{r}') = 0, \ \boldsymbol{r} \neq \boldsymbol{r}'; \quad \int_\tau \delta(\boldsymbol{r} - \boldsymbol{r}')d\tau' = 1, \ \boldsymbol{r} \text{ in } \tau. \tag{2}$$

The surface or surfaces bounding the region τ are to be describable in terms of single coordinates in a spherical coordinate system (Fig. 1). This restricts the bounding surfaces to be of the following type:

$$\begin{aligned} &\text{radial domain, } r_1 \leqq r \leqq r_2\text{: spheres at } r = r_1, r_2\\ &\theta - \text{domain, } \theta_1 \leqq \theta \leqq \theta_2\text{: cones at } \theta = \theta_1, \theta_2\\ &\Phi - \text{domain, } \Phi_1 \leqq \Phi \leqq \Phi_2\text{: planes at } \Phi = \Phi_1, \Phi_2. \end{aligned} \tag{3}$$

The end points of the domains may include $r_1 = 0$ and/or $r_2 = \infty$, $\theta_1 = 0$ and/or $\theta_2 = \pi$, periodicity in Φ. The boundary conditions on $\mathcal{G}$ defined in (1) are to be of the following types over any single-coordinate surface:

$$\partial\mathcal{G}/\partial n = 0 \tag{4a}$$

$$\partial(r\mathcal{G})/\partial n = 0 \tag{4b}$$

$$\mathcal{G} = 0. \tag{4c}$$

n is the direction normal to the surface. These conditions are modified to require finiteness if the domain includes the singular points $r = 0$, and/or $\theta = 0, \pi$, and to require the radiation condition at infinity if the radial domain is unbounded. The Green's function satisfying condition (4a) on all boundaries is proportional to the acoustic pressure due to a vibrating point source at $\boldsymbol{r} = \boldsymbol{r}'$. A Green's function satisfying (4b) on the radial boundaries and (4c) over the remaining boundaries is proportional to the electromagnetic Hertz potential for an oscillating radial electric dipole at $\boldsymbol{r} = \boldsymbol{r}'$, while a Green's function satisfying (4c) in the radial domain and (4b) in the angular domains is proportional to the Hertz potential for a radial magnetic dipole [see (16) and (22)]. For the acoustical case, the boundaries are perfectly rigid, while for the electromagnetic cases they are perfectly conducting.

Eq. (1a) may be rewritten in the form

$$\left(\frac{\partial^2}{\partial r^2} + \frac{1}{r^2\sin\theta}\frac{\partial}{\partial\theta}\sin\theta\frac{\partial}{\partial\theta} + \frac{1}{r^2\sin^2\theta}\frac{\partial^2}{\partial\phi^2} + k^2\right)r\mathcal{G}(\boldsymbol{r}, \boldsymbol{r}') = -\frac{\delta(r - r')\delta(\theta - \theta')\delta(\phi - \phi')}{r'\sin\theta'}. \tag{5}$$

In view of the separability of (5) [with (4)] with respect to r, θ, and ϕ, the solution of the three-dimensional problem may be represented in terms of those of the three one-dimensional problems characteristic of the three-dimensional operator. A typical one-dimensional "characteristic" Green's function problem is formulated below. The complete set of orthonormal functions characteristic of the one-dimensional operator in the given domain is obtained by an integration about the singularities of the characteristic Green's function in the complex plane.[13] The completeness relation is expressed as a representation of the identity operator (delta function).

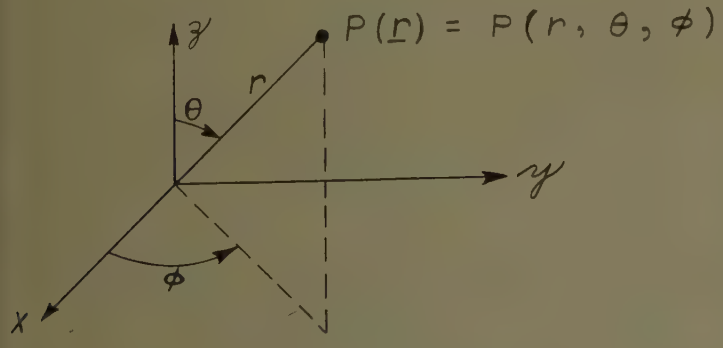

Fig. 1—Spherical coordinate system.

[12] H. Carslaw, "Diffraction by a wedge of any angle," *Proc. London Math. Soc.*, vol. 19, 1919.
H. M. MacDonald, *Proc. London Math. Soc.*, vol. 14, 1914.

[13] Marcuvitz, *op. cit.* (sec. 3).

Typical One-Dimensional Problem:

Eigenvalue problem:

$$\left[\frac{d}{dx}p(x)\frac{d}{dx}+\xi q(x)+\lambda_{xi}w(x)\right]X_i(x,\xi)=0. \tag{6}$$

Characteristic Green's function problem:

$$\left[\frac{d}{dx}p(x)\frac{d}{dx}+\xi q(x)+\lambda_x w(x)\right]G_x(x,x';\xi;\lambda_x) = -\delta(x-x'). \tag{7}$$

Completeness relation:

$$\frac{\delta(x-x')}{w(x')}=\sum_i X_i(x,\xi)X_i(x',\xi) = -\frac{1}{2\pi i}\oint_C G_x(x,x';\xi;\lambda_x)d\lambda_x. \tag{8}$$

The variable x stands for either r, θ, or ϕ, and the boundary conditions on the eigenfunctions X_i and the characteristic Green's function G_x are identical with those ln ($r\mathcal{G}$) in the r, θ, ϕ domains, respectively (for a discrete spectrum). ξ is a fixed parameter, while λ_x is a complex variable whose domain is restricted so as to assure a unique solution for G_x. The spectral representation of the delta function is given either in terms of the contour integral of the characteristic Green's function (C encircles all singularities of G_x in the complex λ_x plane in the positive sense) or by the symmetric representation in series form in terms of the eigenfunctions. The latter representation is obtained from the former by evaluating the residues at the singularities of G_x which are located at the eigenvalues $\lambda_x=\lambda_{xi}$. [For a continuous spectrum the series is replaced by an integral and the discrete summation index by a continuous index. Also a bi-orthogonal representation for the delta function is frequently more useful than the symmetric one in (8).[14]] For the characteristic problem in the r domain, $x\equiv r$, $p=1=q$, $\xi=k_2$, $w=-1/r^2$, $X=R$. For the ϕ domain, $x\equiv\phi$, $p=1=w$, $q=0$, $X=\Phi$. For the θ domain, $x\equiv\theta$, $p=w=-1/q=\sin\theta$, $X=\Theta$ and ξ, like λ, is a separation parameter. Two eigenvalue problems are possible in this case: a) ξ fixed, $\lambda_i\rightarrow$eigenvalue; b) λ fixed, $\xi\rightarrow$eigenvalue. The solutions of these two eigenvalue problems are discussed in a previous report.[9]

The solutions of the three one-dimensional characteristic problems can be employed directly to yield alternative representations for the three-dimensional Green's function defined in (5). It can be verified by direct substitution into (5), interchange of order of summation or integration and differentiation, and recourse to the appropriate form of (6)–(8) that the solution for $\mathcal{G}$ can be represented in the following alternative forms (see Appendix):

$$rr'\mathcal{G}(r,r') = \sum_i \Phi_i(\phi)\Phi_i(\phi')\sum_l \Theta_l(\theta,\lambda_j)\Theta_l(\theta',\lambda_j)G_r(r,r';\lambda_l) \tag{9}$$

$$= -\frac{1}{2\pi i}\sum_j \Phi_j(\phi)\Phi_j(\phi')\oint_C d\lambda G_\theta(\theta,\theta';\lambda_j;\lambda)G_r(r,r';\lambda) \tag{10}$$

$$= \sum_j \Phi_j(\phi)\Phi_j(\phi')\sum_i R_i(r)R_i(r')G_\theta(\theta,\theta';\lambda_j;\lambda_i). \tag{11}$$

In the notation of (9)–(11) the parameter ξ has been omitted in R and Φ, and has been replaced by λ_j in Θ. The indices i,j,l denote quantities associated with the eigenvalue problems in r, ϕ, and θ, respectively. The contour C in the complex λ plane encloses the singularities of G_θ in the positive sense and no others (Fig. 2).

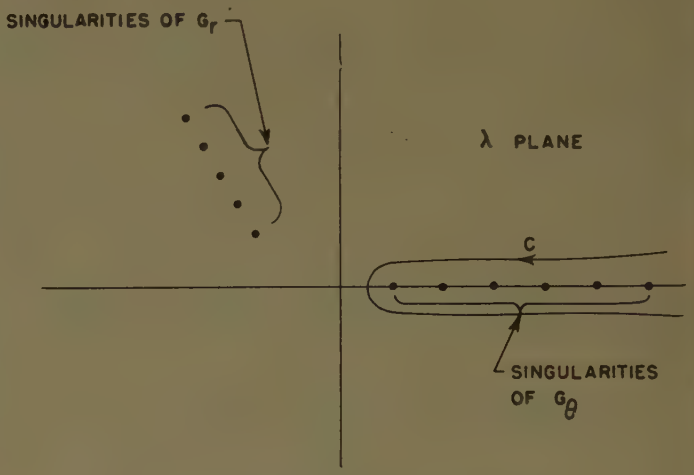

Fig. 2—Contours of integration and singularities in complex λ plane.

One readily verifies the validity of (9)–(11) by function-theoretic means. Thus, the transition from (10) to (9) follows directly from (8) with $x\equiv\theta$, *etc.*, upon evaluating the residues at the singularities of G_θ. Eq. (11) may be obtained from (10) by deforming C to enclose the singularities of G_r and applying (8) with $x\equiv r$, *etc.* The path deformation is possible since G_r and G_θ are defined so as to have no singularities at infinity in the λ plane. A great many additional representations are possible as well but are not included here;[9] the expressions chosen above are employed in the evaluation of the problems in Section III. They are to be considered as formal, and their applicability in any particular given situation as regards convergence, etc., must be examined. The representations in (9) and (11) correspond to a transmission-line analysis of the diffraction problem in which transmission takes place along the r and θ directions, respectively. The characteristic Green's functions in these cases take on the role of transmission line voltages or currents.

B. Vector Diffraction Problems

The problem to be considered here is the determination of the electromagnetic fields radiated by an arbitrarily located and oriented electric or magnetic dipole

[14] *Ibid.* (For a detailed discussion of characteristic Green's function problems, the reader is referred to secs. 3 and 4.)

source in a region bounded by perfectly conducting surfaces which are describable in terms of single spherical coordinates (3). The solution of the dipole problems furnishes the dyadic Green's functions in terms of which the fields due to a distributed source may be represented; thus the dipole problem is basic for the consideration of any physical radiation problem. As has been pointed out previously, the vector problem posed above is solved directly by means of spherical transmission line theory which regards the region as a spherical waveguide in which propagation takes place in the radial direction. The approach to be taken here is to express the spherical transmission line solution in terms of scalar functions which have properties analogous to those of the scalar Green's functions described in Subsection A so that the alternative representations obtained there may be utilized for the vector case as well.

The first problem to be considered is that of the electric dipole. The electromagnetic fields must satisfy the Maxwell equations with a delta function driving term

$$\nabla \times \boldsymbol{E} = -j\omega\mu\boldsymbol{H}; \qquad \omega(\mu\epsilon)^{1/2} = k = 2\pi/\lambda$$
$$\nabla \times \boldsymbol{H} = j\omega\epsilon\boldsymbol{E} + \mathbf{J}; \qquad \mathbf{J} = \mathcal{J}\delta(\boldsymbol{r} - \boldsymbol{r}'). \quad (12)$$

The constant vector $\mathcal{J}$ denotes the strength of the electric current source. In conformity with engineering practice, a time dependence $\exp(+j\omega t)$ is assumed in (12). ω is the angular frequency, k is the wavenumber in the medium, λ is the wavelength, and μ and ϵ are the (constant) permeability and dielectric constant of the medium, respectively. As is well known, the electromagnetic fields can be expressed in terms of scalar radial (Hertz) potential functions as follows:

$$\boldsymbol{E}(\boldsymbol{r}, \boldsymbol{r}') = \boldsymbol{E}'(\boldsymbol{r}, \boldsymbol{r}') + \boldsymbol{E}''(\boldsymbol{r}, \boldsymbol{r}'); \quad \boldsymbol{H} = \boldsymbol{H}' + \boldsymbol{H}'' \quad (13a)$$
$$\boldsymbol{E}'(\boldsymbol{r}, \boldsymbol{r}') = \nabla \times \nabla \times [\boldsymbol{r}\Pi'(\boldsymbol{r}, \boldsymbol{r}')]$$
$$\boldsymbol{E}''(\boldsymbol{r}, \boldsymbol{r}') = -j\omega\mu\nabla \times [\boldsymbol{r}\Pi''(\boldsymbol{r}, \boldsymbol{r}')] \quad (13b)$$
$$\boldsymbol{H}'(\boldsymbol{r}, \boldsymbol{r}') = j\omega\epsilon\nabla \times [\boldsymbol{r}\Pi'(\boldsymbol{r}, \boldsymbol{r}')]$$
$$\boldsymbol{H}''(\boldsymbol{r}, \boldsymbol{r}') = \nabla \times \nabla \times [\boldsymbol{r}\Pi''(\boldsymbol{r}, \boldsymbol{r}')]. \quad (13c)$$

The single and double primes denote E-mode ($H_r' \equiv 0$) and H-mode ($E_r'' \equiv 0$) quantities, respectively. The scalar potential functions Π' and Π'' satisfy the homogeneous scalar wave equation (1a) where $\boldsymbol{r} \neq \boldsymbol{r}'$, and are expressible in terms of the scalar transverse mode functions and the transmission line voltages and currents as follows:[15,16]

$$j\omega\epsilon r\Pi'(\boldsymbol{r}, \boldsymbol{r}') = \sum_i I_i'(r, \boldsymbol{r}')\phi_i(\varphi), \quad \varphi = (\theta, \phi), \quad (14a)$$

$$j\omega\mu r\Pi''(\boldsymbol{r}, \boldsymbol{r}') = \sum_i V_i''(r, \boldsymbol{r}')\psi_i(\varphi). \quad (14b)$$

i is a double summation index (different for E and H-modes). The two-dimensional scalar mode functions ϕ_i and ψ_i are solutions of transverse eigenvalue problems of the Dirichlet and Neumann type, respectively, which are described in the "Waveguide Handbook."[17] V_i and I_i are spherical mode voltages and currents which satisfy inhomogeneous spherical transmission-like equations.[18] The source defined in (12) gives rise to equivalent voltage and current generator excitations at $r = r'$ in each modal transmission line, and the terminations of the transmission lines are determined by the boundary conditions in the radial domain. The two coupled first-order transmission-line equations in V_i and I_i can be reduced to second-order differential equations involving only V_i or I_i, which resemble the equation for the radial characteristic Green's function G_r defined in Subsection A in connection with the scalar Green's function problems [see (7), with appropriate substitutions for the radial domain]. Thus, I_i' and V_i'' in (14) can be represented in terms of radial characteristic Green's functions; the result is found to be the following (for $r \neq r'$):

$$I_i'(r, \boldsymbol{r}') = \left[\mathcal{J}_t \cdot {}_t\nabla' \frac{\partial}{\partial r'} + \mathcal{J}_r \frac{\lambda_i'}{r'^2}\right] \cdot [\phi_i(\theta', \phi')G_{rI}(r, r'; \lambda_i')] \quad (15a)$$

$$V_i''(r, \boldsymbol{r}') = [-j\omega\mu\mathcal{J}_t \times \boldsymbol{r}_0 \cdot {}_t\nabla'] \cdot [\psi_i(\theta', \phi')G_{rV}(r, r'; \lambda_i'')] \quad (15b)$$

where

$${}_t\nabla = \boldsymbol{\theta}_0 \frac{1}{r}\frac{\partial}{\partial\theta} + \boldsymbol{\phi}_0 \frac{1}{r\sin\theta}\frac{\partial}{\partial\phi} \quad (15c)$$

$$\mathcal{J}_t = \mathcal{J} - \boldsymbol{r}_0\mathcal{J}_r. \quad (15d)$$

The prime on ${}_t\nabla'$ denotes the replacement of r, θ, ϕ in ${}_t\nabla$ by r', θ', ϕ'. The characteristic Green's functions G_{rI} and G_{rV} satisfy at the end-points of the radial domain the same boundary conditions as I_i' and V_i'', respectively.

Upon substitution of (15) into (14) and interchanging of the order of differentiation and summation, one obtains series whose summands comprise a radial characteristic Green's function and a modal representation in the transverse $\theta\phi$ domain. These series resemble the scalar Green's function representation in (9). In relating the transverse scalar mode functions ϕ_i and ψ_i for the vector problem to those defined for the scalar problem, cognizance must be taken of the different normalizations of the modal sets. In the notation employed here (same as in footnote 17), the vector mode functions $\nabla_t\phi_i$ and $\nabla_t\psi_i$ are normalized to unity. It is readily shown from an application of Green's theorem and the defining equations for ϕ_i and ψ_i that this specification implies the orthonormality of the functions $(\phi_i k_{ci}')$ and $(\psi_i k_{ci}'')$, where $k_{ci}' = (\lambda_i')^{1/2}$ and $k_{ci}'' = (\lambda_i'')^{1/2}$ are the appropriate

[15] Felsen, footnote 4 (sec. II E).
[16] Marcuvitz, *op. cit.*, (sec. 2b).
[17] N. Marcuvitz, "Waveguide Handbook," MIT Radiation Lab. Ser., McGraw Hill Book Co., Inc., New York, N. Y., vol. 10, sec. 1.8; 1951.
[18] Felsen and Marcuvitz, *op. cit.* [eqs. (2.14) and (A1)].

eigenvalues, and $\lambda_i \neq 0$.[19] On the other hand, the mode functions Φ_j and Θ_l in (9) are each normalized to unity [see (8)] so that the two-dimensional mode set in the $\theta\phi$ domain is orthonormal as well. Upon employing the *orthonormal* mode functions, one therefore expresses the potential functions in (14) as follows ($r \neq r'$)

$$j\omega\epsilon r\Pi'(\boldsymbol{r}, \boldsymbol{r}') = \mathcal{J}_t \cdot {}_t\nabla' \frac{\partial}{\partial r'} S_1'(\boldsymbol{r}, \boldsymbol{r}') + \frac{\mathcal{J}_r}{r'^2} S_2'(\boldsymbol{r}, \boldsymbol{r}'), \quad (16a)$$

$$r\Pi''(\boldsymbol{r}, \boldsymbol{r}') = -\mathcal{J}_t \times \boldsymbol{r}_0 \cdot {}_t\nabla' S_1''(\boldsymbol{r}, \boldsymbol{r}'), \quad (16b)$$

where

$$S_1'(\boldsymbol{r}, \boldsymbol{r}') = \sum_j \sum_l \Phi_j^{(1)}(\phi)\Phi_j^{(1)}(\phi')\Theta_l^{(1)}(\theta, \lambda_j)\Theta_l^{(1)}(\theta', \lambda_j) \frac{G_{rI}(r, r'; \lambda_l)}{\lambda_l}, \quad (17a)$$

$$S_2'(\boldsymbol{r}, \boldsymbol{r}') = \sum_j \sum_l \Phi_j^{(1)}(\phi)\Phi_j^{(1)}(\phi')\Theta_l^{(1)}(\theta, \lambda_j)\Theta_l^{(1)}(\theta', \lambda_j) G_{rI}(r, r'; \lambda_l) \quad (17b)$$

$$= rr' \mathcal{G}_I(\boldsymbol{r}, \boldsymbol{r}') = -r^2 \nabla_t \cdot {}_t\nabla S_1'(\boldsymbol{r}, \boldsymbol{r}'), \quad (17c)$$

$$S_1''(\boldsymbol{r}, \boldsymbol{r}') = \sum_j \sum_l \Phi_j^{(2)}(\phi)\Phi_j^{(2)}(\phi')\Theta_l^{(2)}(\theta, \lambda_j)\Theta_l^{(2)}(\theta', \lambda_j) \frac{G_{rV}(r, r'; \lambda_l)}{\lambda_l}. \quad (17d)$$

The transverse mode functions satisfy the following boundary conditions:

$$\Phi_j^{(1)} = 0, \quad \text{when} \quad \phi = \phi_1, \phi_2;$$
$$\Theta_l^{(1)} = 0, \quad \text{when} \quad \theta = \theta_1, \theta_2, \quad (18a)$$

for the E modes, and

$$\frac{d}{d\phi}\Phi_j^{(2)} = 0, \quad \text{when} \quad \phi = \phi_1, \phi_2;$$
$$\frac{d}{d\theta}\Theta_l^{(2)} = 0, \quad \text{when} \quad \theta = \theta_1, \theta_2, \quad (18b)$$

for the H modes. On perfectly-conducting boundaries at $r = r_1, r_2$, $V_i = 0, dI_i/dr = 0$, so that the radial characteristic Green's functions satisfy the conditions

$$\frac{d}{dr} G_{rI} = 0, \quad G_{rV} = 0, \quad \text{when} \quad r = r_1, r_2. \quad (18c)$$

The remarks following (3) and (4) apply here as well. It is seen from (17b) and (9) that S_2' represents directly a three-dimensional scalar Green's function with appropriately specified boundary conditions. Thus, as is well known, the problem of diffraction by a radial dipole source (*i.e.*, $\mathcal{J}_t \equiv 0$) is directly reducible to a single equivalent scalar problem. The alternative representations discussed in Subsection A are therefore directly applicable to this case. For a transverse dipole, on the other hand, the functions S_1' and S_1'' resemble the scalar Green's functions, but differ by the additional $(1/\lambda_l)$ factor in the summand. The infinite series in l can be converted into a contour integral enclosing only the singularities of the appropriate $G_\theta(\theta, \theta'; \lambda_j; \lambda)$ in the complex λ plane [see (10)]. Since $\lambda_l \to \lambda$ in this transformation it is seen that a possible additional pole is located at the origin in the λ plane; in any contour deformation this pole must be taken into account. The $(1/\lambda)$ factor does not affect adversely the behavior of the integrand at $|\lambda| \to \infty$. If a contour deformation through an infinite semicircle in the λ plane is possible for the scalar problems in sec. A, it is certainly possible for the present case containing the pole at $\lambda = 0$. Therefore, the alternative representations for $\mathcal{G}$ in (9)–(11) may be applied directly to S_1' and S_1'' defined in (17a) and (17d), provided that the additional $(1/\lambda)$ factor is included, and the possible pole at $\lambda = 0$ is properly taken into account. In (17a) and (17d), $\lambda_l \neq 0$. The case $\lambda_l = 0$ arises only in biconical regions and must be taken into account separately.

From a knowledge of the potential functions Π' and Π'', the total electromagnetic fields may be computed from (13). After some manipulation the result can be written in the following form.

$$\boldsymbol{E}(\boldsymbol{r}, \boldsymbol{r}') = -z(\boldsymbol{r}, \boldsymbol{r}') \cdot \mathcal{J}, \quad (19)$$

where

$$-j\omega\epsilon z(\boldsymbol{r}, \boldsymbol{r}') = (\nabla \times \nabla \times \boldsymbol{r}_0)(\nabla' \times \nabla' \times \boldsymbol{r}_0) S_1'(\boldsymbol{r}, \boldsymbol{r}') + k^2 (\nabla \times \boldsymbol{r}_0)(\nabla' \times \boldsymbol{r}_0) S_1''(\boldsymbol{r}, \boldsymbol{r}'). \quad (19a)$$

$z(\boldsymbol{r}, \boldsymbol{r}')$ in (19a) represents the dyadic spatial impedance (for $r \neq r'$). In employing the representation in (19) it is understood that the dot product post-multiplication is to be carried out first. The magnetic field is given in terms of the potential functions Π' and Π'' by (13).

It should be stressed that (19) and (19a) simplify considerably for the special case of a radial dipole (*i.e.*, $\mathcal{J}_t \equiv 0$). From these equations, or directly from (16), (13a), and (13b) one finds for this instance:

$$\boldsymbol{E}(\boldsymbol{r}, \boldsymbol{r}') = \frac{1}{j\omega\epsilon} (\nabla \times \nabla \times \boldsymbol{r}_0) \left[\frac{S_2'(\boldsymbol{r}, \boldsymbol{r}')}{r'^2} \boldsymbol{r}_0 \cdot \mathcal{J} \right], \quad (20a)$$

$$\boldsymbol{H}(\boldsymbol{r}, \boldsymbol{r}') = (\nabla \times \boldsymbol{r}_0) \left[\frac{S_2'(\boldsymbol{r}, \boldsymbol{r}')}{r'^2} \boldsymbol{r}_0 \cdot \mathcal{J} \right]. \quad (20b)$$

[19] The case $\lambda_t' = 0$ gives rise to the TEM mode which can exist only in biconical regions and must be taken into account separately.

The problem of the magnetic dipole is analyzed in direct analogy to the above. The field equations in this case are:

$$\nabla \times \boldsymbol{E} = -j\omega\mu\boldsymbol{H} - \boldsymbol{M}; \quad \boldsymbol{M} = \boldsymbol{m}\delta(\boldsymbol{r} - \boldsymbol{r}'),$$
$$\nabla \times \boldsymbol{H} = j\omega\epsilon\boldsymbol{E}. \tag{21}$$

The constant vector $\boldsymbol{m}$ denotes the strength of the magnetic current source. The electromagnetic fields are expressed in terms of the scalar potential functions Π' and Π'' as in (13); the spherical mode representation for the latter is given in (14). Upon following a procedure directly analogous to that employed for the electric dipole, one obtains the following representation for the potential functions ($r \gtrless r'$):

$$r\Pi'(\boldsymbol{r}, \boldsymbol{r}') = \boldsymbol{m}_t \times \boldsymbol{r}_0 \cdot {}_t\nabla' S_1'(\boldsymbol{r}, \boldsymbol{r}'), \tag{22a}$$

$$j\omega\mu r\Pi''(\boldsymbol{r}, \boldsymbol{r}') = \boldsymbol{m}_t \cdot {}_t\nabla' \frac{\partial}{\partial r'} S_1''(\boldsymbol{r}, \boldsymbol{r}') + \frac{m_r}{r'^2} S_2''(\boldsymbol{r}, \boldsymbol{r}'), \tag{22b}$$

where

$$S_2''(\boldsymbol{r}, \boldsymbol{r}') = \sum_j \sum_l \Phi_j^{(2)}(\phi)\Phi_j^{(2)}(\phi')\Theta_l^{(2)}(\theta, \lambda_j)\Theta_l^{(2)}(\theta', \lambda_j) \cdot G_{rV}(r, r'; \lambda_l) \tag{23a}$$

$$= rr'\mathcal{G}_V(\boldsymbol{r}, \boldsymbol{r}') = -r^2\nabla_t \cdot {}_t\nabla S_1''(\boldsymbol{r}, \boldsymbol{r}'), \tag{23b}$$

and S_1' and S_1'' are given in (17a) and (17d) respectively. The dyadic spatial admittance y defined by:

$$\boldsymbol{H}(\boldsymbol{r}, \boldsymbol{r}') = -y(\boldsymbol{r}, \boldsymbol{r}') \cdot \boldsymbol{m} \tag{24}$$

is obtained in analogy with (19a) in the following form:

$$-j\omega\mu y(\boldsymbol{r}, \boldsymbol{r}') = (\nabla \times \nabla \times \boldsymbol{r}_0)(\nabla' \times \nabla' \times \boldsymbol{r}_0)S_1''(\boldsymbol{r}, \boldsymbol{r}') + k^2(\nabla \times \boldsymbol{r}_0)(\nabla' \times \boldsymbol{r}_0)S_1'(\boldsymbol{r}, \boldsymbol{r}'). \tag{25}$$

For a radial magnetic dipole, simplifications analogous to those in (20a) and (20b) occur.

III. Application to Various Scalar and Vector Diffraction Problems

In this section the formal theory presented in Section II is applied to obtain suitable representations for several scalar and vector diffraction problems. As is customary in mathematical physics, a time dependence $\exp(-i\omega t)$ is implied henceforth. The appropriate one-dimensional characteristic solutions are merely stated, and stress is placed on the direct formulation of convenient representations.[20]

A. The Sphere

The geometry of the configuration is shown in Fig. 3.

[20] For a more detailed discussion, see footnotes 8 and 9.

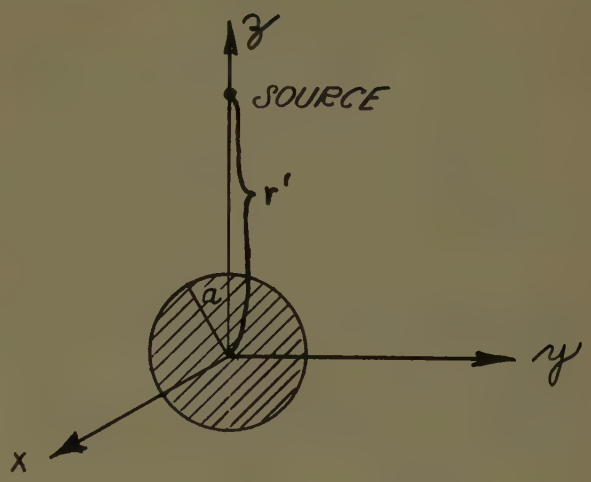

Fig. 3—Sphere in free space.

The origin of coordinates is located at the center of the sphere whose radius is "a." In view of the symmetry of the obstacle, the source may be located on the polar (z) axis without loss of generality. The boundary conditions in both the ϕ and θ domains are those of periodicity of the Green's function and its derivative. The corresponding angular characteristic Green's functions and eigenfunctions are listed below [See (6)–(8) for their formulation.]

ϕ-domain

$$G_\phi^0(\phi, \phi'; \lambda) = -\frac{\cos\mu(\pi - |\phi - \phi'|)}{2\mu \sin\mu\pi}, \quad \lambda = \mu^2. \tag{26}$$

Singularities: simple poles at $\lambda = m^2$, $m = 0, 1, 2 \ldots$

$$\delta(\phi - \phi') = \frac{1}{\pi}\sum_{m=0}^{\infty} \epsilon_m \cos m(\phi - \phi'), \qquad \epsilon_m = \begin{cases} 1/2, & m = 0 \\ 1, & m \neq 0. \end{cases} \tag{27}$$

The superscript ^{0} on G_ϕ^0 denotes the periodic Green's function.

θ-domain

$$G_\theta^0(\theta, \theta'; \lambda_1; \lambda_2) = -\frac{\pi}{2}\frac{\Gamma(\nu + \mu + 1)}{\Gamma(\nu - \mu + 1)\sin(\nu - \mu)\pi} \cdot P_\nu^{-\mu}(\cos\theta_<) P_\nu^{-\mu}(-\cos\theta_>), \tag{28a}$$

$$\lambda_1 = \mu^2, \quad \lambda_2 = \nu(\nu + 1), \quad \mathrm{Re}\,\mu > 0. \tag{28b}$$

$P_\nu^\mu(x)$ is the associated Legendre function of order μ, degree ν, argument x. $\theta_<$ stands for θ when $\theta < \theta'$, and for θ' when $\theta > \theta'$; the converse applies to $\theta_>$. Consider $\mu = \mu_r \geqq 0$, μ_r real and fixed. Then the singularities are simple poles at $\lambda_2 = (\mu + n)(\mu + n + 1)$, $n = 0, 1, 2, \cdots$, and

$$\frac{\delta(\theta-\theta')}{\sin\theta'}=\frac{1}{2}\sum_{n=0}^{\infty}[2(n+\mu)+1]\frac{\Gamma(\eta+2\mu+1)}{n!}P_{n+\mu}^{-\mu}(\cos\theta)P_{n+\mu}^{-\mu}(\cos\theta') \tag{29a}$$

$$=\frac{1}{2}\sum_{n=m}^{\infty}(2n+1)\frac{(n-m)!}{(n+m)!}P_n^m(\cos\theta)P_n^m(\cos\theta'),\qquad \mu=m=\text{integer}. \tag{29b}$$

The boundary conditions on the radial characteristic problem comprise the radiation condition at infinity and the following at $r=a$:

a) $(d/dr)(G_r/r)=0$ for the acoustical case (perfectly rigid sphere),

b) $G_r=0$ for the vertical magnetic dipole (perfectly conducting sphere),

c) $(d/dr)\,G_r=0$ for the vertical electric dipole (perfectly conducting sphere).

Cases a) and b) are discussed in footnote 9; case c) is described in footnote 8. The result for case c) is, for example:

$$G_r(r,r';\lambda)=\frac{i}{k}j_\nu(kr_<)h_\nu^{(1)}(kr_>)-\frac{i}{k}h_\nu^{(1)}(kr)h_\nu^{(1)}(kr')\frac{j_\nu'(ka)}{h_\nu'^{(1)}(ka)}, \tag{30}$$

where

$\lambda=\nu(\nu+1)$.

The spherical Bessel functions $z_\nu(x)$ are defined as

$$z_\nu(x)=(\pi x/2)^{1/2}Z_{\nu+1/2}(x), \tag{32}$$

where Z_ν is a cylindrical Bessel function. The prime on a Bessel function denotes the derivative with respect to the argument. The first expression on the right-hand side of (30) is the radial characteristic Green's function G_r^0 appropriate to a radial domain $0<r<\infty$ (*i.e.*, with the sphere absent),[21] while the second term represents the disturbing effect of the sphere. Thus, the representation for G_r in (30) is of the "perturbation" type alluded to in the Introduction.

1. *Scalar Problem*: The scalar Green's function $\mathcal{G}$, which is defined in (1a), satisfies the radiation condition at infinity, and has a vanishing derivative on the sphere surface, is written down directly in the following alternative forms [see (9), (11), (27)–(32); also footnote 1, sec. 5]:

$$\mathcal{G}(\boldsymbol{r},\boldsymbol{r}')=\frac{i}{4\pi krr'}\sum_{n=0}^{\infty}(2n+1)P_n(\cos\theta)j_n(kr_<)h_n^{(1)}(kr_>)-\frac{i}{4\pi krr'}\sum_{n=0}^{\infty}(2n+1)P_n(\cos\theta)h_n^{(1)}(kr)h_n^{(1)}(kr')\frac{j_n'(ka)}{h_n'^{(1)}(ka)} \tag{33}$$

$$=\frac{i}{4krr'}\sum_{\xi}\frac{(2\xi+1)j_\xi'(ka)}{\sin\xi\pi\dfrac{\partial}{\partial\xi}h_\xi'^{(1)}(ka)}P_\xi(-\cos\theta)h_\xi^{(1)}(kr)h_\xi^{(1)}(kr'). \tag{34}$$

The singularities are simple poles at the zeros $\nu=\xi$ of $h_\nu'^{(1)}(ka)$.

Thus,

$$r'^2\delta(r-r')=\sum_{\xi}(2\xi+1)\frac{h_\xi^{(1)}(kr)h_\xi^{(1)}(kr')j_\xi'(ka)}{ik(\partial/\partial\xi)h_\xi'^{(1)}(ka)}, \tag{31a}$$

where

$$(\partial/\partial\xi)h_\xi'^{(1)}(ka)\equiv[(\partial/\partial\nu)h_\nu'^{(1)}(ka)]_{\nu=\xi}. \tag{31b}$$

In view of the location of the source at $\theta'=\phi'=0$, $\mathcal{G}$ has no ϕ dependence and only the $m=0$ term in (27) contributes. Since the radial characteristic Green's function representation in (30) is of the perturbation type, the radial transmission representation for the total Green's function in (33) separates naturally into two parts, the first of which is the free-space result $[\exp(iku)]/4\pi u$,

[21] Marcuvitz, "Field representations in spherically-stratified regions," *op. cit.* [see (4.34)].

$u=|\mathbf{r}-\mathbf{r}'|$, while the second is the scattered portion due to the sphere. When $ka=2\pi(a/\lambda)$ is small, the series for the scattered portion is rapidly convergent, due to the damping behavior of $(j_n'/h_n'^{(1)})$ when $n\gg ka$. When $ka\gg 1$, the expression in (33) is poorly convergent, while the angular transmission representation in (34) is rapidly convergent for certain ranges of location of source and observation points. Also, the contour integral representation in (10) is convenient for the evaluation of the ray-optical scattering as $k\to\infty$. The scalar problem posed here has been studied in great detail by a number of investigators[22–24] in connection with the propagation of radio waves over a spherical earth. The result for the other Green's functions can be written down directly in a similar manner. In this connection, the recent work of Franz[24] on evaluations of Green's functions for cylinders and spheres should be mentioned explicitly.

2. *Vector Problem*: Considered next is the (vector) problem of an arbitrarily, oriented, electric dipole. Such a source can be decomposed into a radial and a transverse current source, and only the latter need be treated since the vertical source has been discussed above. In view of the symmetry of the configuration, the transverse source can be placed on the z axis and oriented in the $\mathbf{x}_0$ direction without loss of generality. Thus, $\theta'=\phi'=0$, and $\mathcal{J}=\boldsymbol{\theta}_0\mathcal{J}=\mathbf{x}_0\mathcal{J}$. The first step is the evaluation of the functions S_1' and S_1'' defined in (17a) and (17d), respectively. From (27), (29b), and (30), one can write down directly the following representation for S_1':

$$S_1'=\frac{i}{2\pi k}\sum_{m=0}^{\infty}\epsilon_m\cos m(\phi-\phi')\sum_{n=m;n\neq 0}^{\infty}(2n+1)\frac{(n-m)!}{(n+m)!}\frac{P_n^m(\cos\theta)P_n^m(\cos\theta')}{n(n+1)}$$
$$\cdot\left[j_n(kr_<)h_n^{(1)}(kr_>)-h_n^{(1)}(kr)h_n^{(1)}(kr')\frac{j_n'(ka)}{h_n'^{(1)}(ka)}\right]. \tag{35}$$

In (35) the time dependence $\exp(-i\omega t)$ has been adhered to. To transform (16), (20), *etc.*, into this scheme, $j=(-1)^{1/2}$ is replaced everywhere by $-i$. Thus, from (16a)

$$-i\omega\epsilon\Pi'(\mathbf{r},\mathbf{r}')=\mathcal{J}\frac{\partial^2}{r'\partial\theta'\partial r'}S_1'(r,r'). \tag{36}$$

Since

$$\frac{\partial}{\partial\theta'}P_n^m(\cos\theta')\Big]_{\theta'=0}=\begin{cases}0, & m\neq 1\\ -n(n+1)/2, & m=1\end{cases}, \tag{37}$$

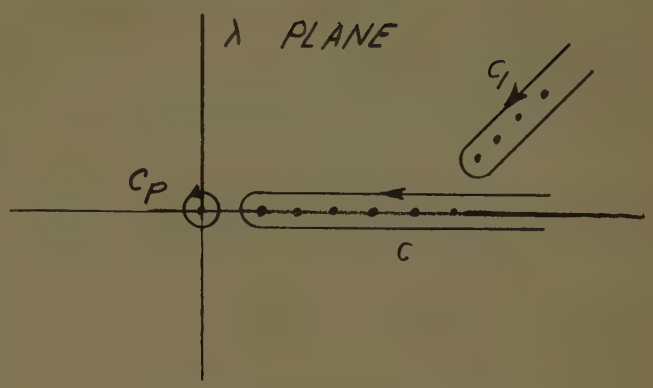

Fig. 4—Contours and singularities in complex λ plane (sphere problem).

only the $m=1$ term in S_1' contributes to Π'. Therefore, no other terms in m need be retained. It is apparent from (9) and (10) that the following contour integral representation for S_1' applies:

$$S_1'\Big]_{m=1}=-\frac{1}{2\pi i}\frac{1}{\pi}\cos(\phi-\phi')\cdot\oint_C G_\theta^0(\theta,\theta';1;\lambda)G_r(r,r';\lambda)\frac{d\lambda}{\lambda}. \tag{38}$$

The contour C (enclosing the singularities of G_θ^0) and other singularities of the integrand in the λ plane appear in Fig. 4, above. If the behavior of G_θ^0 and G_r at infinity in the λ plane assures that there is no contribution to the integral in (38) over a path at infinity it is seen that

$$\oint_C=-\oint_{C_1}-\oint_{C_p}. \tag{39}$$

The contour C_1 encloses the singularities of G_r, and the contour C_p encloses the pole at $\lambda=0$. The evaluation of the integral over the contour C_1 in terms of the residues at the poles which are enclosed yields the representation given in (11) save for the additional $(1/\lambda)$ factor. Thus,

$$S_1'\Big]_{m=1}=\frac{\cos\phi}{\pi}\sum_{\xi}G_\theta^0(\theta,\theta';1;\xi(\xi+1))\cdot\frac{(2\xi+1)h_\xi^{(1)}(kr)h_\xi^{(1)}(kr')j_\xi'(ka)}{ik\xi(\xi+1)(\partial/\partial\xi)h_\xi'^{(1)}(ka)}+\frac{\cos\phi}{\pi}[G_rG_\theta^0]_{\lambda=0}. \tag{40}$$

[22] G. N. Watson, *Proc. Roy. Soc. London*, vol. 95, p. 63; 1918.
[23] H. Bremmer, "Terrestrial Radio Waves," Elsevier Publishing Co., New York, N. Y.; 1949. (See Part I.)
[24] W. Franz, "On the Green's functions for the cylinder and sphere," *Z. Naturf.*, vol. 9a, pp. 705–716; 1954.

Upon substituting for G_r and G_θ^0 from (30) and (28), respectively, and recognizing that

$$h_0^{(1)}(x) = j_0(x) + in_0(x)$$
$$= \sin x - i\cos x = -ie^{ix}, \quad (41)$$

one obtains

$$S_1'\Big]_{m=1} = \frac{\cos\phi}{2ik}\sum_\xi \frac{(2\xi+1)h_\xi^{(1)}(kr)h_\xi^{(1)}(kr')j_\xi'(ka)}{\sin\xi\pi(\partial/\partial\xi)h_\xi'^{(1)}(ka)} \cdot P_\xi^{-1}(\cos\theta')P_\xi^{-1}(-\cos\theta) + \frac{i}{4\pi k}\cos\phi\tan\frac{\theta'}{2}\cot\frac{\theta}{2}\left[e^{ik|r-r'|} + e^{ik(r+r'-2a)}\right]. \quad (42)$$

The convergence properties of S_1' as given by (35) and (42) are analogous to those of $\mathcal{G}$ as represented by (33) and (34), respectively.

The function S_1'' in (17d) differs from S_1' only in that G_{rI} in S_1' is replaced by G_{rV}. The radial mode representation of S_1'' is found to be (only the $m=1$ term contributes)

$$S_1''\Big]_{m=1} = \frac{1}{2ik}\cos(\phi-\phi')\left\{\sum_\xi \frac{(2\eta+1)h_\eta^{(1)}(kr)h_\eta^{(1)}(kr')j_\eta(ka)}{\sin\eta\pi(\partial/\partial\eta)h_\eta^{(1)}(ka)}P_\eta^{-1}(\cos\theta')P_\eta^{-1}(-\cos\theta) - \frac{1}{2\pi}\tan\frac{\theta'}{2}\cot\frac{\theta}{2}\left[e^{ik|r-r'|} - e^{ik(r-r'-2a)}\right]\right\}, \quad (43a)$$

where

$$h_\eta^{(1)}(ka) = 0. \quad (43b)$$

The radial mode representation is very convenient, for example, for the evaluation of the currents induced by an incident plane wave on the shadow side of a large conducting sphere. For plane-wave incidence, one employs the asymptotic formula

$$h_\xi^{(1)}(kr') \sim e^{ikr'-i(\xi+1)\pi/2}, \quad r'\to\infty. \quad (44)$$

In addition, the factor A, where

$$A = \mathcal{J}(\mu/\epsilon)^{1/2}ik[\exp(ikr')]/4\pi r' = \mathcal{J}F, \quad (45)$$

is set equal to unity to normalize the result to an incident wave of unit intensity,[25] *i.e.*,

$$E_{inc} = x_0\exp(-ikz). \quad (46)$$

Upon substituting (42) and (43) into (16) and (13) it is found that the incident wave in (46) excites the following tangential magnetic field on the sphere's back side.

$$H_\phi = -\sqrt{\frac{\epsilon}{\mu}}\frac{\pi}{ka}\cos\phi\left\{i\sum_\xi \frac{(2\xi+1)\exp(-i\xi\pi/2)}{\sin\xi\pi(\partial/\partial\xi)h_\xi'^{(1)}(ka)}\frac{d}{d\theta}P_\xi^{-1}(-\cos\theta) + \sum_\eta \frac{(2\eta+1)\exp(-i\eta\pi/2)}{\sin\eta\pi(\partial/\partial\eta)h_\eta^{(1)}(ka)}\frac{P_\eta^{-1}(-\cos\theta)}{\sin\theta}\right\}, \quad (47a)$$

$$H_\theta = -\sqrt{\frac{\epsilon}{\mu}}\frac{\pi}{ka}\sin\phi\left\{i\sum_\xi \frac{(2\xi+1)\exp(-i\xi\pi/2)}{\sin\xi\pi(\partial/\partial\xi)h_\xi'^{(1)}(ka)}\frac{P_\xi^{-1}(-\cos\theta)}{\sin\theta} + \sum_\eta \frac{(2\eta+1)\exp(-i\eta\pi/2)}{\sin\eta\pi(\partial/\partial\eta)h_\eta^{(1)}(ka)}\frac{d}{d\theta}P_\eta^{-1}(-\cos\theta)\right\}. \quad (47b)$$

The series in (47) are rapidly convergent for $ka\gg1$, $\theta>\pi/2$, *i.e.*, in the shadow region. The terms in the series contain a damping factor $\exp[-|\operatorname{Im}\nu|(\theta-\pi/2)]$ for $\theta>\pi/2$, where ν stands for ξ or η, and $\operatorname{Im}\nu$ is large. Thus, the induced currents in the shadow region decay exponentially away from the shadow boundary. Approximate solutions for ξ and η, as well as for the functions occurring in (47), have been obtained by Sommerfeld in his analysis of the scalar diffraction problems[10] (see also Bremmer[23] and Franz[24]).

If a vertical electric dipole is situated at the surface of a large sphere, the far field for $\theta>\pi/2$ is also readily computed from the radial mode representation. The same applies to a tangential magnetic dipole source on the sphere surface, and, therefore, to the gain pattern in back of the sphere radiated by a a small slot in front of the sphere and fed from the interior.

B. The Wedge

The configuration is shown in Fig. 5. The wedge is formed by two semi-infinite planes intersecting along the z axis and located at $\phi=0$ and $\phi=\alpha$, respectively. The radial domain in this case is $0<r<\infty$, the θ-domain is $0\leqq\theta\leqq\pi$ and the ϕ-domain is $0\leqq\phi\leqq\alpha$.[26] The character-

[25] L. B. Felsen, "Back-scattering from wide-angle and narrow-angle cones," *J. Appl. Phys.*, vol. 26, pp. 138–151; February, 1955. (See Appendix B.)

[26] MacDonald, *op. cit.*, Tilston, *op. cit.* An analysis of the wedge problem in terms of spherical coordinates has also been carried out here.

istic problem in the θ-domain is identical with that expressed in (28a) and (29a). The radial characteristic Green's function G_r^0 is given by the first term on the right-hand side of (30). In the ϕ-domain, the delta function representations in terms of the eigenfunctions $\Phi^{(1)}$ and $\Phi^{(2)}$ in (18a) and (18b), respectively, are the following:

$$\text{a) } \Phi_j^{(1)} = 0 \quad \text{at} \quad \phi = 0, \alpha$$

$$\delta(\phi - \phi') = \frac{2}{\alpha} \sum_{m=1}^{\infty} \sin p\phi \sin p\phi',$$

$$p = \frac{m\pi}{\alpha}. \tag{48}$$

$$\text{b) } d\Phi_j^{(2)}/d\phi = 0 \quad \text{at} \quad \phi = 0, \alpha$$

$$\delta(\phi - \phi') = \frac{2}{\alpha} \sum_{m=0}^{\infty} \epsilon_m \cos p\phi \cos p\phi'. \tag{49}$$

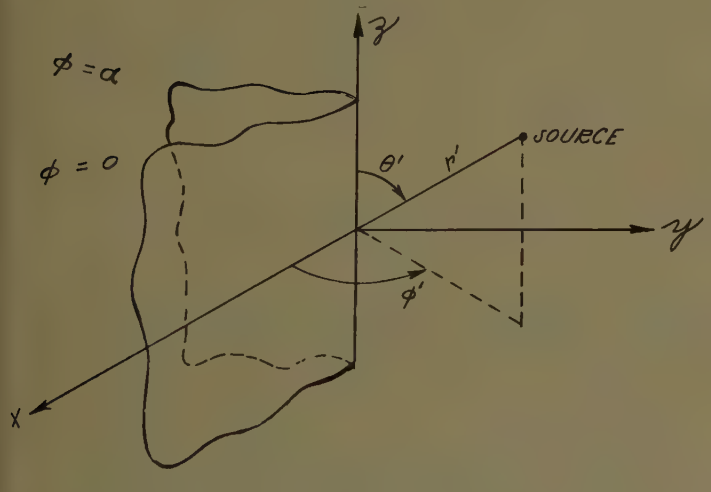

Fig. 5—Infinite wedge.

1. *Scalar Problem*: Consider the acoustic Green's function $\mathcal{G}$ satisfying the boundary condition $\partial\mathcal{G}/\partial\phi = 0$ at $\phi = 0$, α. The radial transmission representation in (9) is obtained directly as follows:

$$rr'\mathcal{G}(r, r') = \frac{i}{k\alpha} \sum_{m=0}^{\infty} \epsilon_m \cos p\phi \cos p\phi' \sum_{n=0}^{\infty} [2(n+p)+1] \frac{\Gamma(n+2p+1)}{n!} \cdot P_{n+p}^{-p}(\cos\theta) P_{n+p}^{-p}(\cos\theta') j_{n+p}(kr_<) h_{n+p}^{(1)}(kr_>). \tag{50}$$

For plane wave incidence ($r' \to \infty$) the Hankel functions are replaced by their asymptotic value in (44). To normalize the result to an incident wave of unit intensity [exp (ikr')]$/4\pi r'$ is set equal to unity and one obtains

$$\mathcal{G}(r; \infty\ \theta', \phi',) = \frac{4\pi}{\alpha} \sum_{m=0}^{\infty} \epsilon_m \cos p\phi \cos p\phi' e^{-ip\pi/2} f_p(r; \theta, \theta'), \tag{51a}$$

where

$$f_p(r; \theta, \theta') = \sum_{n=0}^{\infty} [2(n+p)+1] \frac{\Gamma(n+2p+1)}{n!} \cdot P_{n+p}^{-p}(\cos\theta) P_{n+p}^{-p}(\cos\theta') \frac{j_{n+p}(kr)}{kr} e^{-in\pi/2} \tag{51b}$$

$$= J_p(k\rho \sin\theta') e^{-ikr\cos\theta\cos\theta'}, \quad \rho = r\sin\theta. \tag{51c}$$

The identity of the spherical wave representation in (51b) and the cylindrical wave representation in (51c) is established upon use of the Gegenbauer addition theorem.[27]

The representation in (50) is rapidly convergent when either the source point or the observation point is located near the origin. (For a given location of the source, the origin is selected to yield the desired angle of incidence, θ'.) In particular, one readily obtains the behavior of $\mathcal{G}$ near the edge. Upon employing the series representation for the spherical Bessel functions, one obtains for $r \ll r'$, $kr \ll 1$

$$\mathcal{G} = \frac{i}{2\alpha r'} \left[h_0^{(1)}(kr') + 2\cos q\phi \cos q\phi' \cdot \left(\frac{k\rho}{2}\right)^q h_q^{(1)}(kr') \frac{\sin^q\theta'}{\Gamma(1+q)} \right] + 0(r), \tag{52}$$

where $q = \pi/\alpha < 1$, *i.e.*, we have assumed $\alpha > \pi$.

For plane-wave incidence observed far from the wedge apex (*i.e.*, $kr' \to \infty$, $kr \gg 1$), (51a), with (51b), may be transformed via the Sommerfeld integral representation of the spherical Bessel function into a representation which permits a direct asymptotic evaluation in closed form. The details of this evaluation have been discussed elsewhere[28] and are not reported here because of space limitations.[29]

2. *Vector Problem:* For the electromagnetic problem consider a transverse (to $\mathbf{r}'$) electric dipole to be situated at $\mathbf{r} = \mathbf{r}'$ in Fig. 5. The scalar functions S_1' and S_1'' in (17a) and (17d) are written down in direct analogy with (50), and substitution into (16) and (13), or directly into (20), yields the electromagnetic fields. If the transverse current source is represented as

$$\mathcal{J} = \boldsymbol{\theta}_0 \mathcal{J}_\theta + \boldsymbol{\Phi}_0 \mathcal{J}_\phi, \tag{53}$$

the electromagnetic fields near the edge of the wedge are found to be the following ($q = \pi/\alpha < 1$):

[27] G. N. Watson, "Theory of Bessel Functions," Cambridge Univ. Press, Cambridge, Eng., p. 370 [see (9)]; 1922.

[28] L. B. Felsen, "Radiation and Diffraction Problems Involving Wedges and Cones," paper presented at IRE-WESCON meeting; August, 1956.

[29] See also, F. Oberhettinger, "On asymptotic series for functions occurring in the theory of diffraction of waves by wedges," *J. Math. and Phys.*, vol. 34, January, 1956.

$$\boldsymbol{E} = F\frac{2qi}{\Gamma(q)}\left(\frac{k\rho}{2}\right)^{q-1}(\sin\theta')^{q-1}e^{-iq\pi/2}(\mathcal{J}_\theta\cos\theta'\sin q\phi' + \mathcal{J}_\phi\cos q\phi')(\boldsymbol{\varrho}_0\sin q\phi + \boldsymbol{\Phi}_0\cos q\phi) + O(r^{2q-1}), \quad (54a)$$

$$\boldsymbol{H} = F\left(\frac{\epsilon}{\mu}\right)^{1/2}\left[-2q\mathcal{J}_\phi\sin\theta'\boldsymbol{z}_0 + \frac{2qi}{\Gamma(q)}\left(\frac{k\rho}{2}\right)^{q-1}(\sin\theta')^{q-1}e^{-iq\pi/2}\right.$$

$$\left.\cdot(\mathcal{J}_\theta\sin q\phi' + \mathcal{J}_\phi\cos\theta'\cos q\phi')(\boldsymbol{\varrho}_0\cos q\phi - \boldsymbol{\Phi}_0\sin q\phi)\right] + O(r^{2q-1}), \quad (54b)$$

where F is defined in (45). Again it has been found convenient to introduce the cylindrical coordinate ρ as in (51c). Also the vector field itself has been represented in terms of cylindrical coordinates, where the unit vectors $\boldsymbol{\varrho}_0$ and $\boldsymbol{z}_0$ are given by

$$\boldsymbol{\varrho}_0 = \boldsymbol{r}_0\sin\theta + \boldsymbol{\theta}\cos\theta, \quad \boldsymbol{z}_0 = \boldsymbol{r}_0\cos\theta - \boldsymbol{\theta}_0\sin\theta. \quad (55)$$

It is of interest to investigate (54) for the special cases of a plane-wave incident at an angle (θ', ϕ') and polarized so that either the electric or the magnetic vector field is perpendicular to the edge. The former case obtains when $\mathcal{J}_\theta \equiv 0$. In order to normalize to an incident wave of unit intensity, $\mathcal{J}_\phi F$ is set equal to unity. The resulting (54) yield a behavior near the edge which agrees at $\theta' = \pi/2$ (normal incidence) with that obtained from the known two-dimensional solution. For $\theta' \neq \pi/2$, the field components normal to the edge differ by a factor $(\sin\theta')^{q-1}$ from their value at normal incidence.—The case $\mathcal{J}_\phi \equiv 0$ leads to analogous results.

C. The Wedge with a Spherical Dome

The physical configuration in this case, shown in Fig. 6 is the same as in Fig. 5 except that a sphere of radius "a," centered at the origin, is superimposed on the wedge. If the radial transmission representation is employed, the results for this problem differ from those in the preceding section only in that the radial characteristic Green's function G_r^0 is replaced by the Green's function G_r appropriate to the sphere. Since the characteristic Green's function for the sphere separates into two portions, of which one represents the unperturbed (no sphere) solution and the other the effect of the sphere, the three-dimensional scalar Green's function appropriate to the case of a radial electric dipole, for example, can be represented as follows:

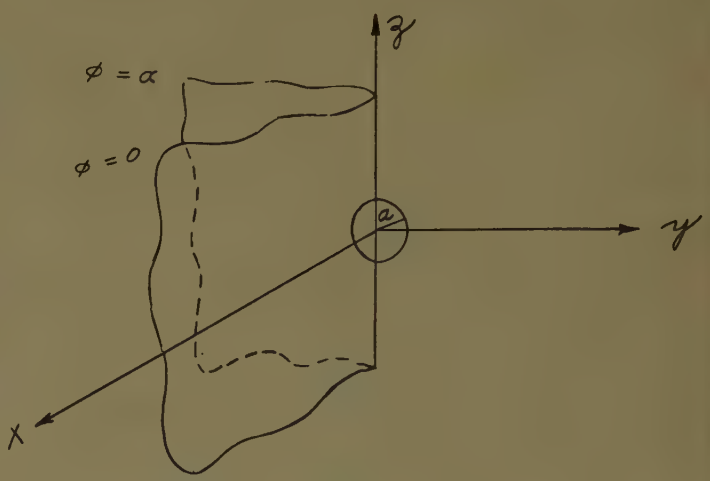

Fig. 6—Wedge with spherical dome.

$$\mathcal{G} = \mathcal{G}_{\text{wedge}} - \frac{i}{ka\,rr'}\sum_{m=1}^{\infty}\sin p\phi\sin p\phi'\sum_{n=0}^{\infty}[2(n+p)+1]\frac{\Gamma(n+2p+1)}{n!}P_{n+p}^{-p}(\cos\theta)P_{n+p}^{-p}(\cos\theta')$$

$$\cdot\frac{h_{n+p}^{(1)}(kr)\,h_{n+p}^{(1)}(kr')}{h_{n+p}'^{(1)}(ka)/j_{n+p}'(ka)}. \quad (56)$$

The first term on the right-hand side of (56) is the solution for the wedge alone as given in (50), except that $(\epsilon_m\cos p\phi\cos p\phi')$ is replaced by $(\sin p\phi\sin p\phi')$. The remaining double series represents the perturbation due to the sphere and is rapidly convergent when (ka) is small. The representation chosen for $\mathcal{G}_{\text{wedge}}$ need not be that employed in (50) but may be taken in any other convenient form. For example, for plane-wave incidence the solution in cylindrical coordinates is the most convenient [see (51a)]. The far scattering $(kr \gg 1)$ in this case is obtained by an asymptotic evaluation of the wedge result,[28,29] and the termwise summation of the series in (56), if (ka) is small.

The electromagnetic vector problem is solved in a manner directly analogous to the above.

D. The Cone

The problems of diffraction by a cone and a cone with a spherical tip are treated in a companion paper.

Appendix

Formal Verification of (10)

Upon substituting the Green's function representation from (10) into the left-hand side of (5) and interchanging the order of differentiation and summation and integration, one obtains

$$\left(\frac{\partial}{\partial r^2}+\frac{1}{r^2\sin\theta}\frac{\partial}{\partial\theta}\sin\theta\frac{\partial}{\partial\theta}+\frac{1}{r^2\sin^2\theta}\frac{\partial^2}{\partial\phi^2}+k^2\right)rr'\mathcal{G}(\boldsymbol{r},\boldsymbol{r}')$$
$$=-\frac{1}{2\pi i}\sum_j\Phi_j(\phi')\oint_C d\lambda\left\{\Phi_j(\phi)G_\theta\left(\frac{d^2}{dr^2}+k^2\right)G_r\right.$$
$$+\Phi_j(\phi)G_r\frac{1}{r^2\sin\theta}\frac{d}{d\theta}\sin\theta\frac{d}{d\theta}G_\theta$$
$$\left.+\frac{G_rG_\theta}{r^2\sin^2\theta}\frac{d^2}{d\phi^2}\Phi_j(\phi)\right\}. \tag{57}$$

In view of the differential equations satisfied by G_r, G_θ, $\Phi_j(\phi)$ [see (6)–(8), with the appropriate definitions listed at the end of the paragraph following (8)], one may rewrite the right-hand side of (57) as

$$-\frac{1}{2\pi i}\sum_j\Phi_j(\phi')\oint_C d\lambda\left\{-\delta(r-r')G_\theta\Phi_j(\phi)\right.$$
$$\left.-\frac{\delta(\theta-\theta')}{r^2\sin\theta}G_r\Phi_j(\phi)\right\} \tag{58}$$
$$=\delta(\phi-\phi')\delta(r-r')\frac{1}{2\pi i}\oint_C d\lambda G_\theta$$
$$=-\frac{\delta(\phi-\phi')\delta(r-r')\delta(\theta-\theta')}{\sin\theta'}. \tag{59}$$

The second term in (58) does not contribute since G_r has no singularities inside the contour C (see Fig. 2) so that $\oint_C G_r d\lambda=0$. From (59) it is seen that the representation in (10) satisfies the differential equation (5). The boundary conditions on $\mathcal{G}$ are satisfied as well by the appropriate choice of boundary conditions on G_r, G_θ, and G_ϕ.

Acknowledgment

The research described in this paper was conducted under Contract No. AF–19(604)–890 sponsored by the Air Force Cambridge Research Center.

The author wishes to express his appreciation to Prof. N. Marcuvitz for stimulating discussions on the topic of this paper.

Plane-Wave Scattering by Small-Angle Cones*

LEOPOLD B. FELSEN†

Summary—**Rigorous expressions alternative to the familiar formulas in terms of spherical harmonic series are developed for the scattering of acoustic (and electromagnetic) waves by the tip of a perfectly rigid (or perfectly conducting) semi-infinite cone. For plane wave incidence the expressions are valid for observation points lying in a region excluding the rays which are reflected from the sides of the cone according to the laws of geometrical optics. Approximate closed-form results are obtained for on-axis or off-axis incidence and observation for cones with small apex angle for the acoustical plane wave scattering, and for electromagnetic scattering of incident waves whose electric vector is directed perpendicular to the cone axis. The results are correct to $0(\phi^2)$, where ϕ is the cone apex angle, and agree, for the special case of plane wave back-scattering along the cone axis, with those obtained previously by a different method.**

The case of diffraction by a spherically tipped cone is also treated.

Introduction

THE GENERAL problem of the construction of alternative representations for the fields radiated by arbitrarily placed scalar and vector point sources in regions bounded by spheres, cones, and planes has been discussed in the preceding paper.[1] In this paper the formalism is applied to yield solutions for the scattering by a semi-infinite cone and by a spherically tipped cone.

A radial transmission analysis of the former problem has been carried out previously,[2,3] and approximate closed form results have been obtained for the plane wave back-scattering along the cone axis for cones with large and small apex angle. The radial transmission approach leads to a *total field* representation in terms of a very slowly convergent series which has been summed approximately to yield the above-mentioned special solutions.

In this paper an angular transmission formulation is examined which has the virtue of yielding *explicitly* the desired expressions for the *scattering* by the cone tip outside the domain containing the rays reflected from

* Manuscript received by the PGAP, September 28, 1955; revised manuscript received, May 28, 1956. Presented at Symposium on Electromagnetic Wave Theory, Univ. of Michigan, Ann Arbor, Mich., June, 1955. The research described in this paper was sponsored by the AF Cambridge Res. Center, under Contract No. AF-19(604)-890.

† Microwave Res. Inst., Polytechnic Inst. of Brooklyn, N. Y.

[1] Felsen, p. 109, this issue.

[2] K. M. Siegel, *et al.*, "Electromagnetic and acoustical scattering from a semi-infinite cone," *J. Appl. Phys.*, vol. 26, pp. 309–313; March, 1955.

[3] L. B. Felsen, "Back-scattering from wide-angle and narrow-angle cones," *J. Appl. Phys.*, vol. 26, pp. 138–151; February, 1955.

the sides of the cone according to the laws of geometrical optics (the solution inside the latter region may be determined in first approximation from ray-optical considerations). This (contour-integral) representation for the scattering by the cone tip is rapidly convergent for small cone apex angles and is evaluated here to first order for plane wave incidence and observation either on or off the cone axis. The solutions so obtained agree with those derived from the radial transmission analysis for the special case of plane wave back-scattering along the cone axis. It is of interest to note, in addition, that the rigorous off-axis differential scattering cross section for an electromagnetic plane wave incident along the axis obtained here agrees with the expression derived by K. M. Siegel, *et al.*, via physical optics,[4] even though physical optics considerations cannot properly be applied to surfaces containing a vertex, such as a cone.

If the cone is tipped with a sphere, the radial transmission representation is suitable for the evaluation of the plane wave scattering when the sphere radius is small, while the angular transmission representation is useful for some problems involving a large sphere.

The Cone

Scalar Diffraction Problems

$\partial\mathcal{G}'/\partial\theta = 0$ *on Cone Surface:* We wish to find the Green's function $\mathcal{G}'$ which satisfies the three-dimensional inhomogeneous wave equation

$$(\nabla^2 + k^2)\mathcal{G}'(\boldsymbol{r}, \boldsymbol{r}') = -\delta(\boldsymbol{r} - \boldsymbol{r}'), \tag{1}$$

and the following boundary conditions:

$$\mathcal{G}' \text{ is finite at } r = 0; \quad r\left(\frac{\partial \mathcal{G}'}{\partial r} - ik\mathcal{G}'\right) \to 0 \text{ at } r \to \infty \tag{2a}$$

$$\partial\mathcal{G}'/\partial\theta = 0 \text{ at } \theta = \theta_0. \tag{2b}$$

The geometry of the configuration and the spherical coordinate system are shown in Fig. 1. The Green's function $\mathcal{G}'$ so defined is proportional to the excess acoustic pressure caused by a point source in the presence of a perfectly rigid cone, and to the electromagnetic Hertz potential due to a radially directed magnetic dipole source outside a perfectly conducting cone. From the preceding paper[5] and Appendix I it is seen that the solution for $\mathcal{G}'$ can be written formally in alternative forms as follows:

$$rr'\mathcal{G}'(\boldsymbol{r}, \boldsymbol{r}') = \frac{i}{4\pi k}\csc^2\left(\frac{\theta_0}{2}\right) j_0(kr_<)h_0^{(1)}(kr_>)$$
$$- \frac{i}{2k}\sum_{m=0}^{\infty}\epsilon_m \cos m(\Phi - \Phi') \sum_q (2q+1)\frac{\Gamma(q+m+1)(d/d\theta_0)P_q^{-m}(-\cos\theta_0)P_q^{-m}(\cos\theta)P_q^{-m}(\cos\theta')}{\Gamma(q-m+1)\sin(q-m)\pi\left[\dfrac{\partial^2}{\partial q\partial\theta_0}P_q^{-m}(\cos\theta_0)\right]}$$
$$\cdot j_q(kr_<)h_q^{(1)}(kr_>) \tag{3}$$
$$= \frac{-1}{2\pi^2 k}\sum_{m=0}^{\infty}\epsilon_m \cos m(\Phi - \Phi')\oint_c d\lambda j_\nu(kr_<)h_\nu^{(1)}(kr_>)G_\theta'(\theta, \theta' m^2; \lambda) \tag{4}$$

where

$$\epsilon_0 = \tfrac{1}{2}; \quad \epsilon_m = 1, \quad m \neq 0 \tag{5a}$$
$$\lambda = \nu(\nu+1) = (\nu + \tfrac{1}{2})^2 - \tfrac{1}{4} \tag{5b}$$
$$\frac{d}{d\theta_0}P_q^{-m}(\cos\theta_0) \equiv \frac{d}{d\theta}P_q^{-m}(\cos\theta)\Big]_{\theta=\theta_0} = 0 \tag{5c}$$

j_ν and $h_\nu^{(1)}$ are spherical Bessel and Hankel functions, respectively, and are defined in terms of cylindrical Bessel functions as:

$$z_\nu(x) = \sqrt{\frac{\pi x}{2}}Z_{\nu+1/2}(x), \tag{6}$$

where Z_ν and z_ν stand for J_ν, $H_\nu^{(1)}$ and j_ν, $h_\nu^{(1)}$, respectively. $r<$ stands for r when $r<r'$, and for r' when

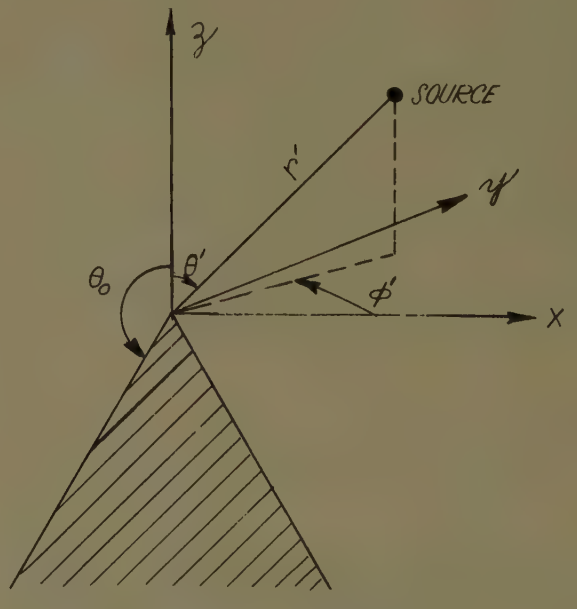

Fig. 1—Point source and semi-infinite cone.

[4] K. M. Siegel, *et al.*, "Bistatic radar cross sections for surfaces of revolution," *J. Appl. Phys.*, vol. 26, pp. 297–305; March, 1955. [See (3–8).]

[5] Felsen, reference 1 (9) and (10).

$r>r'$; the converse is true for $r>$. The angular characteristic Green's function G_θ' is given in (56). The contour of integration in the λ plane, as well as the singularities of the integrand in (4), are shown in Fig. 2. The singularities of G_θ' are simple poles on the positive real axis, while those of $j_\nu h_\nu^{(1)}$ are a branch point at $\lambda=-\frac{1}{4}$. The branch cut has been drawn so as to assure regularity in the λ plane for all values of r, *i.e.*, Re $(\nu+\frac{1}{2})>0$. It is readily verified by a residue evaluation that (3) and (4) are equivalent. The solutions given in (3) and (4) were first obtained by Carslaw by a different approach.[6] Eq. (3) is a representation for $\mathcal{G}'$ in terms of transmission (propagation) in the radial direction, and is rapidly convergent when either the source point or the observation point is located near the cone tip. It is not convenient for computation when both r and r' are very large; nevertheless, the slowly convergent series in (3) has been summed approximately for the special case of plane wave back-scattering along the cone axis, *i.e.*, $\theta=\theta'=0$.[2,3]

The first term on the right-hand side of (56) represents the "free space" portion of G_θ', in absence of the cone.[7] Therefore, if the free space portion only is employed in (3) or (4), the result for $\mathcal{G}'$ is the response to a point source in free space which is known to be equal to $[\exp(ik|\mathbf{r}-\mathbf{r}'|)]/4\pi|\mathbf{r}-\mathbf{r}'|$. The second term in (56), $G_{\theta s}'$, represents directly the effect of the cone, and its substitution into (4) yields the scattered portion of $\mathcal{G}'$, to be denoted by $\mathcal{G}_s'$. Since the free-space portion of $\mathcal{G}'$ is known, only the evaluation of $\mathcal{G}_s'$ need concern us here. In order to obtain a representation for $\mathcal{G}_s'$ in terms of transmission along the θ coordinate we deform the contour C into the contour C' enclosing the branch cut. It can be shown that there is no contribution to the integral from the infinite circle in the λ plane when $(\theta+\theta')<(2\theta_0-\pi)$, so that the integrals over the paths C and C' are equal. The restriction on $(\theta+\theta')$ excludes from the range of applicability that domain which contains the rays reflected from the sides of the cone according to the laws of geometrical optics (see Fig. 3). The expression is valid, however, in the remaining region where the diffraction due to the cone tip is most noticeable.

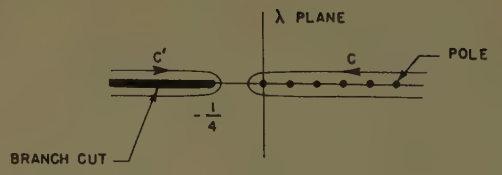

Fig. 2—Contours of integration and singularities in λ plane (scalar problem).

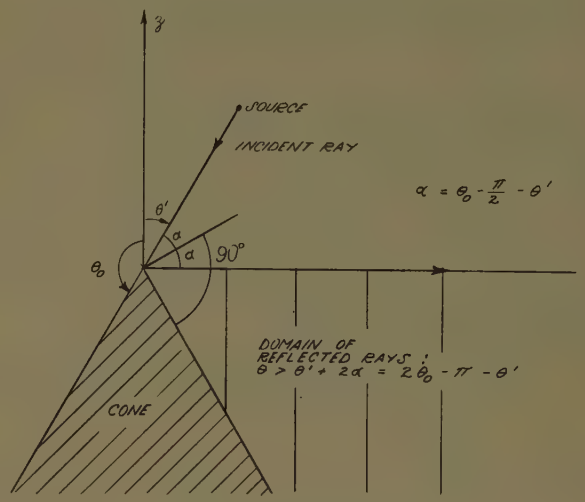

Fig. 3—Ray-optical domains.

Since

$$j_\nu(kr_<)h_\nu^{(1)}(kr_>) = \tfrac{1}{2}h_\nu^{(1)}(kr)h_\nu^{(1)}(kr') + \tfrac{1}{2}h_\nu^{(2)}(kr_<)h_\nu^{(1)}(kr_>), \quad (7)$$

and since $h_\nu^{(1)}(x)h_\nu^{(2)}(y)$ as well as $G\theta_s'$ is an even function of $(\nu+\frac{1}{2})$,[8] the portion of the integrand containing $h_\nu^{(1)}h_\nu^{(2)}G\theta_s'$ is continuous across the branch cut in the λ plane [see (5b)] so that it makes no contribution to the integral over the path C'. Therefore, the scattering due to the cone tip is given by:

$$rr'\mathcal{G}_s'(\mathbf{r},\mathbf{r}') = \frac{1}{8\pi k}\sum_{m=0}^{\infty}\epsilon_m\cos m(\Phi-\Phi')\int_{-1/2-i\infty}^{-1/2+i\infty}d\nu(2\nu+1)h_\nu^{(1)}(kr)h_\nu^{(1)}(kr')\cdot\frac{P_\nu^{-m}(\cos\theta)P_\nu^{-m}(\cos\theta')\Gamma(\nu+m+1)\dfrac{d}{d\theta_0}P_\nu^{-m}(-\cos\theta_0)}{\sin(\nu-m)\pi\,\Gamma(\nu-m+1)\dfrac{d}{d\theta_0}P_\nu^{-m}(\cos\theta_0)}, \quad (8)$$

where $(\theta+\theta')<(2\theta_0-\pi)$. The transition to the ν plane is carried out via (5b). It is seen that the representation in (8) contains only outgoing waves, in view of the $h_\nu^{(1)}(kr)$ factor. This conforms with the physical requirements on the behavior of the scattered radiation. The θ transmission representation for $\mathcal{G}'$ could formally have been written down directly.[9] However, the above approach was chosen in order to avoid convergence difficulties encountered in a radial mode representation of the free-space Green's function.

For the evaluation of $\mathcal{G}_s'$ in the limit of vanishing cone apex angle, use is made of the following approximate expressions for the ratio of the derivatives of the

[6] H. S. Carslaw, "The scattering of sound waves by a cone," *Math. Annalen*, vol. 75, pp. 133–147; 1914. [See (18).]
[7] Felsen, reference 1 (28).
[8] W. Magnus and F. Oberhettinger, "Special Functions of Mathematical Physics," Chelsea Publishing Co., New York, N. Y., pp. 17, 1, and 62; 1949.
[9] Felsen, reference 1 (11), and Appendix.

Legendre functions to $0[(\pi-\theta_0)^2]$:

$$\frac{\dfrac{d}{d\theta_0}P_\nu^{-m}(-\cos\theta_0)}{\dfrac{d}{d\theta_0}P_\nu^{-m}(\cos\theta_0)} \approx \frac{(-1)^m\pi\Gamma(1+\nu+m)}{\Gamma(m)\Gamma(m+1)\Gamma(1+\nu-m)\sin\nu\pi}\left(\frac{\pi-\theta_0}{2}\right)^{2m}, \quad m \geqq 1,\ \theta_0 \to \pi \tag{9a}$$

$$\approx -\frac{\pi\nu(\nu+1)}{\sin\nu\pi}\left(\frac{\pi-\theta_0}{2}\right)^2, \quad m=0,\ \theta_0\to\pi. \tag{9b}$$

Also, for plane wave incidence, the asymptotic formula

$$h_\nu^{(1)}(kr') \sim e^{ikr'-i(\nu+1)\pi/2}, \qquad kr' \to \infty \tag{10}$$

is employed. If (9) and (10) are substituted into (8), use is made of the relation

$$P_\nu^m(\cos\phi) = (-1)^m\frac{\Gamma(\nu+m+1)}{\Gamma(\nu-m+1)}P_\nu^{-m}(\cos\phi), \tag{11}$$

and the change of variable

$$\nu = -\tfrac{1}{2}+ix,\ x \text{ real}, \tag{12}$$

is introduced, one obtains, to $0[(\pi-\theta_0)^2]$:

$$rr'\mathcal{G}_s'(\mathbf{r},\mathbf{r}') \approx -\frac{\pi}{4}\sqrt{\frac{r}{2\pi k}}\left(\frac{\pi-\theta_0}{2}\right)^2 e^{i(kr'-\pi/4)} \cdot[\tfrac{1}{2}I_0+\cos(\Phi-\Phi')I_1], \tag{13}$$

where

$$I_0 = \int_{-\infty}^{\infty}dx\,x\,\frac{e^{x\pi/2}}{\cosh^2\pi x}H_{ix}^{(1)}(kr)\cdot(\tfrac{1}{4}+x^2)K_x(\cos\theta)K_x(\cos\theta') \tag{14}$$

$$I_1 = \int_{-\infty}^{\infty}dx\,x\,\frac{e^{x\pi/2}}{\cosh^2\pi x}H_{ix}^{(1)}(kr)K_x^{\,1}(\cos\theta)K_x^{\,1}(\cos\theta'). \tag{15}$$

Neumann's notation

$$K_x^{\,m}(\cos\theta) = P_{-(1/2)+ix}^{\,m}(\cos\theta) \tag{16}$$

for the conical functions of Mehler has been introduced above.

If the scattering is to be observed far from the cone tip, *i.e.*, $kr\gg1$, the asymptotic formula in (10) may also be employed for $H_{ix}^{(1)}(kr)$ in (14) and (15). Actually, (10) applies only for values of $x\leqq N$, $N\ll kr$; however, it can be shown that the error introduced by applying this asymptotic expression for all x in (14) and (15) is $0[N^2\exp(-\alpha N)]$, where $\alpha=\pi-\delta-(\theta+\theta')$, $\delta=0(1/N)$, $1\ll N\ll kr$. Thus, if for a given angle of incidence θ', the observation angle θ is not near the geometric optical boundary of the rays reflected from the sides of the cone, the above approximation is justified. Upon writing

$$e^{x\pi} = \cosh x\pi + \sinh x\pi \tag{17}$$

and remembering that $K_x^{\,m}(\cos\phi)$ is an even function of x, it is seen that the $(\cosh\pi x)$ term in (17) does not contribute to the integrals in (14) and (15) so that

$$I_0 = 2\sqrt{\frac{2}{\pi kr}}\,e^{i(kr-\pi/4)}I_0', \tag{18}$$

$$I_1 = 2\sqrt{\frac{2}{\pi kr}}\,e^{i(kr-\pi/4)}I_1', \tag{19}$$

where

$$I_0' = \int_0^\infty dx\,x\,\frac{\tanh\pi x}{\cosh\pi x}\left(\frac{1}{4}+x^2\right)K_x(\cos\theta)K_x(\cos\theta'), \tag{20}$$

$$I_1' = \int_0^\infty dx\,x\,\frac{\tanh\pi x}{\cosh\pi x}K_x^{\,1}(\cos\theta)K_x^{\,1}(\cos\theta'). \tag{21}$$

The integrals I_0' and I_1' are evaluated in terms of an integral given by Mehler:[10]

$$I_0' = \frac{2}{\pi}\,\frac{1+\cos\theta\cos\theta'}{(\cos\theta+\cos\theta')^3}, \tag{22}$$

$$I_1' = \frac{2}{\pi}\,\frac{\sin\theta\sin\theta'}{(\cos\theta+\cos\theta')^3}. \tag{23}$$

Thus, the plane wave scattering observed far from the tip of a narrow-angle cone is given to $0[(\pi-\theta_0)^2]$ by:

$$\mathcal{G}_s'(\mathbf{r},\mathbf{r}') \approx i\frac{e^{ikr}}{kr}\left(\frac{\pi-\theta_0}{2}\right)^2\frac{2}{(\cos\theta+\cos\theta')^3}\cdot[1+\cos\theta\cos\theta'+2\sin\theta\sin\theta'\cos(\Phi-\Phi')] \tag{24}$$

where $kr\gg1$, $\theta_0\approx\pi$, $(\theta+\theta')<(2\theta_0-\pi)$, and the factor $[\exp(ikr')]/4\pi r'$ has been set equal to unity to normalize the result to an incident wave of unit intensity. When the wave is incident along the cone axis, $\theta'=0$, and

$$\mathcal{G}_s'(\mathbf{r},\mathbf{r}')]_{\theta'=0} \approx \frac{i}{2}\,\frac{e^{ikr}}{kr}\left(\frac{\pi-\theta_0}{2}\right)^2\sec^4\frac{\theta}{2}, \quad \theta<(2\theta_0-\pi). \tag{25}$$

For back-scattering, $\theta=\theta'$, $\Phi=\Phi'$, so that (24) becomes:

$$\mathcal{G}_s'(r,\theta',\Phi';\infty,\theta',\Phi') \approx i\frac{e^{ikr}}{4kr}\left(\frac{\pi-\theta_0}{2}\right)^2\sec^3\theta'[2+\sin^2\theta'], \quad \theta'<\left(\theta_0-\frac{\pi}{2}\right). \tag{26}$$

The special result for back-scattering along the cone axis, *i.e.*, $\theta=\theta'=0$, agrees with that obtained previously by an evaluation of the slowly convergent series representation in (3).[11]

$\mathcal{G}=0$ *on cone surface:* The determination of the Green's function $\mathcal{G}$ which satisfies the differential equation (1), the boundary condition (2a) and

[10] L. B. Felsen, "Some definite integrals involving conical functions," *J. Math. and Phys.*, vol. 35, pp. 177–178; July, 1956.
[11] Felsen, reference 3 (2-27).

$$\mathcal{G} = 0 \text{ at } \theta = \theta_0 \tag{27}$$

is carried out as in the beginning of the second section. This Green's function is proportional to the electromagnetic Hertz potential for a radially directed electric dipole source outside a perfectly conducting cone. In particular, $\mathcal{G}$ can be represented as in (4) except that G_{θ}' is replaced by G_{θ}. G_{θ} is given by (57) provided that the replacement

$$\frac{(d/d\theta_0)P_{\nu}^{-m}(-\cos\theta_0)}{(d/d\theta_0)P_{\nu}^{-m}(\cos\theta_0)} \rightarrow \frac{P_{\nu}^{-m}(-\cos\theta_0)}{P_{\nu}^{-m}(\cos\theta_0)} \tag{28}$$

is made.[12] Upon contour deformation, the scattered portion, $\mathcal{G}_s$, of $\mathcal{G}$ is given by the expression in (8), subject to the replacement in (28). For a narrow-angle cone ($\theta_0 \approx \pi$) one obtains, for the $m=0$ term:

$$\frac{P_{\nu}(-\cos\theta_0)}{P_{\nu}(\cos\theta_0)} \approx \frac{\pi}{2\ln\left(\frac{\pi-\theta_0}{2}\right)} \frac{1}{\sin\nu\pi}, \quad \theta_0 \rightarrow \pi. \tag{29}$$

Since the $m=1$ term does not contribute to this order of magnitude of $(\pi-\theta_0)$ [see (9b) and (40)] only the $m=0$ term need be considered here. For plane wave incidence observed far from the cone tip an evaluation as previously shown leads to the result (to $0\{1/\ln[2/(\pi-\theta_0)]\}$):

$$\mathcal{G}_s(\boldsymbol{r},\boldsymbol{r}') \approx -i\frac{e^{ikr}}{kr} \frac{1}{2\ln\left(\frac{2}{\pi-\theta_0}\right)} \frac{1}{\cos\theta+\cos\theta'}, \tag{30}$$

where $kr \gg 1$, $\theta_0 \approx \pi$, $\theta+\theta' < (2\theta_0-\pi)$. In obtaining (30) use has been made of the relation:[10]

$$\int_0^{\infty} dx\, x \frac{\tanh\pi x}{\cosh\pi x} K_{ix}(\cos\theta)K_{ix}(\cos\theta') = \frac{1}{\pi}\frac{1}{\cos\theta+\cos\theta'}. \tag{31}$$

For the special case where $\theta=\theta'=0$, the result in (30) agrees with that previously obtained by summing a slowly convergent series representation similar to that in (3).[13]

Vector Diffraction Problems

Consider an electric dipole of vector strength $\mathcal{J}$ situated at the point $\boldsymbol{r}=\boldsymbol{r}'$ outside a perfectly conducting cone defined by the surface $\theta=\theta_0$ (geometry as in Fig. 1). The components of $\mathcal{J}$ in the r, θ, Φ directions are $\mathcal{J}_r$, $\mathcal{J}_{\theta}$, and $\mathcal{J}_{\Phi}$, respectively. The total field can be regarded as a superposition of the separate responses due to $\mathcal{J}_r$, $\mathcal{J}_{\theta}$, and $\mathcal{J}_{\Phi}$. The response to a radial electric dipole source may be obtained from the scalar Green's function $\mathcal{G}$ discussed in the last part of second section. The electric field due to a transverse dipole source of vector strength $\mathcal{J}_t$ can be represented in terms of the scalar functions S_1' and S_1'' as follows:[14]

$$\begin{aligned}\boldsymbol{E} = {} & \boldsymbol{r}_0\left(\frac{\partial^2}{\partial r^2}+k^2\right)(\mathcal{J}_t\cdot{}_t\nabla')\frac{\partial}{\partial r'}\left(\frac{S_1'}{-i\omega\epsilon}\right) \\ & + \boldsymbol{\theta}_0\left[\frac{-1}{i\omega\epsilon r}\frac{\partial^2}{\partial r\partial\theta}(\mathcal{J}_t\cdot{}_t\nabla')\frac{\partial S_1'}{\partial r'} - \frac{i\omega\mu}{r(\sin\theta)}\frac{\partial}{\partial\Phi}(\mathcal{J}_t\times\boldsymbol{r}_0\cdot{}_t\nabla'S_1'')\right] \\ & + \boldsymbol{\Phi}_0\left[\frac{-1}{i\omega\epsilon r(\sin\theta)}\frac{\partial^2}{\partial r\partial\Phi}(\mathcal{J}_t\cdot{}_t\nabla')\frac{\partial S_1'}{\partial r'} + \frac{i\omega\mu}{r}\frac{\partial}{\partial\theta}(\mathcal{J}_t\times\boldsymbol{r}_0\cdot{}_t\nabla'S_1'')\right]\end{aligned} \tag{32a}$$

where

$$\mathcal{J}_t\cdot{}_t\nabla' = \frac{\mathcal{J}_{\theta}}{r'}\frac{\partial}{\partial\theta'}+\frac{\mathcal{J}_{\Phi}}{r'\sin\theta'}\frac{\partial}{\partial\Phi'}, \tag{32b}$$

$$\mathcal{J}_t\times\boldsymbol{r}_0\cdot{}_t\nabla' = \frac{\mathcal{J}_{\Phi}}{r'}\frac{\partial}{\partial\theta'}-\frac{\mathcal{J}_{\theta}}{r'\sin\theta'}\frac{\partial}{\partial\Phi'}. \tag{32c}$$

An analogous expression can be written down for the magnetic field.

A suitable representation for the scalar function S_1'' is given by the right-hand side of (4)[15] provided that the integrand is multiplied by $(1/\lambda)$ and the path C in Fig. 2 is drawn so as to exclude the pole at $\lambda=0$. The scalar function S_1' can be similarly represented except that G_{θ}' is replaced by G_{θ}. The paths of integration C in the λ planes are as shown in Fig. 4. When applied to S_1', the

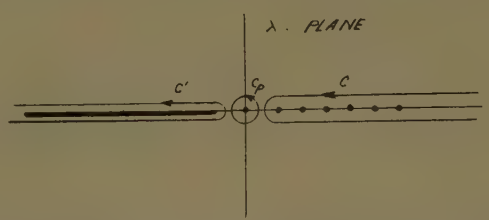

Fig. 4—Contours of integration and singularities in λ plane (vector problem).

poles in Fig. 4 represent the singularities of G_{θ}, and when applied to S_1'', the poles represent the singularities of G_{θ}'. Thus,

$$S_1' = -\frac{1}{2\pi^2 k}\sum_{m=0}^{\infty}\epsilon_m\cos m(\Phi-\Phi')\cdot\oint_C\frac{d\lambda}{\lambda}j_{\nu}(kr_<)h_{\nu}^{(1)}(kr_>)G_{\theta}(\theta,\theta';m^2;\lambda), \tag{33a}$$

$$S_1'' = -\frac{1}{2\pi^2 k}\sum_{m=0}^{\infty}\epsilon_m\cos m(\Phi-\Phi')\cdot\oint_C\frac{d\lambda}{\lambda}j_{\nu}(kr_<)h_{\nu}^{(1)}(kr_>)G_{\theta}'(\theta,\theta';m^2;\lambda). \tag{33b}$$

[12] See Appendix.
[13] Felsen, reference 3 (2-35c).
[14] Felsen, reference 1 (19)–(20).
[15] *Ibid.*, (17d) and (10).

Since the angular characteristic Green's functions G_θ and G_θ' decompose into a "free-space" portion and a perturbation term accounting for the effect of the cone [see (57)], the scattered electric field $\boldsymbol{E}_s$ is given directly by (32a), (32b), and (32c) with G_θ and G_θ' in (33a) and (33b) replaced by the perturbation terms $G_{\theta s}$ and $G_{\theta s}'$, respectively. In order to obtain, as in the scalar case, a representation which is rapidly convergent for plane wave scattering from narrow-angle cones, the contour C in the λ plane in Fig. 4 is deformed into the contours C enclosing the pole at $\lambda=0$ and C' enclosing the branch cut. Since

$$\oint_C = -\oint_{C_p} - \oint_{C'}, \tag{34}$$

it follows that

$$S_{1s}' = \frac{1}{2\pi^2 k}\sum_{m=0}^{\infty}\epsilon_m \cos m(\Phi-\Phi')\,[2\pi i(\text{Residue at } \lambda=0)] + \frac{1}{8\pi k}\sum_{m=0}^{\infty}\epsilon_m\cos m(\Phi-\Phi')\int_{-1/2-i\infty}^{-1/2+i\infty} d\nu(2\nu+1)\frac{h_\nu^{(1)}(kr)h_\nu^{(1)}(kr')}{\nu(\nu+1)} \cdot \frac{P_\nu^{-m}(\cos\theta)P_\nu^{-m}(\cos\theta')\Gamma(\nu+m+1)P_\nu^{-m}(-\cos\theta_0)}{\sin(\nu-m)\pi\Gamma(\nu-m+1)P_\nu^{-m}(\cos\theta_0)} \tag{35a}$$

$$S_{1s}'' = \frac{1}{2\pi^2 k}\sum_{m=0}^{\infty}\epsilon_m \cos m(\Phi-\Phi')\,[2\pi i\ (\text{Residue at } \lambda=0)] + \frac{1}{8\pi k}\sum_{m=0}^{\infty}\epsilon_m\cos m(\Phi-\Phi')\int_{-1/2-i\infty}^{-1/2+i\infty} d\nu(2\nu+1)\frac{h_\nu^{(1)}(kr)h_\nu^{(1)}(kr')}{\nu(\nu+1)} \cdot \frac{P_\nu^{-m}(\cos\theta)P_\nu^{-m}(\cos\theta')\Gamma(\nu+m+1)(d/d\theta_0)P_\nu^{-m}(-\cos\theta_0)}{\sin(\nu-m)\pi\Gamma(\nu-m+1)(d/d\theta_0)P_\nu^{-m}(\cos\theta_0)}. \tag{35b}$$

S_{1s}' and S_{1s}'' denote the scattered portions of S_1' and S_1''. The transition from the expressions in (33a) and (33b) to those in (35a) and (35b) is carried out as in the scalar case, and the same restrictions on θ and θ' apply.

In the evaluation of the residue of the integrals in (33a) and (33b) at $\lambda=0$ it is convenient to separate the $m=0$ terms from the others. Since[16]

$$P_\nu^{-m}(\cos\theta) = \frac{1}{\Gamma(1+m)}\cdot\tan^m\left(\frac{\theta}{2}\right)F\left(-\nu,\nu+1;1+m;\sin^2\frac{\theta}{2}\right), \tag{36}$$

where F is the hypergeometric function, and [17]

$$\Gamma[1-(m-\nu)]\sin(m-\nu)\pi = \pi/\Gamma(m-\nu), \tag{37}$$

it is readily shown that the expressions in (57), with (28), reduce to

$$G_{\theta s}(\theta,\theta';m^2;0) = -G_{\theta s}'(\theta,\theta';m^2;0) = -\frac{1}{2m}\tan^m\left(\frac{\theta}{2}\right)\tan^m\left(\frac{\theta'}{2}\right)\tan^{2m}\left(\frac{\pi-\theta_0}{2}\right) \qquad m \geqq 1. \tag{38}$$

Thus, for $m\geqq 1$, $G_{\theta s}$ and $G_{\theta s}'$ are finite at $\lambda=0$ so that the integrands in (33a) and (33b) have a simple pole at $\lambda=0$. Let S_{1sr}' and S_{1sr}'' denote the contribution to S_{1s}' and S_{1s}'' from the terms $m\geqq 1$ in the series containing the residues in (35a) and (35b), respectively. Then

$$S_{1sr}' = -S_{1sr}'' = \frac{-i}{2\pi k}j_0(kr<)h_0^{(1)}(kr>)\sum_{m=1}^{\infty}\frac{\cos m(\Phi-\Phi')}{m}\left[\tan\frac{\theta}{2}\tan\frac{\theta'}{2}\tan^2\left(\frac{\pi-\theta_0}{2}\right)\right]^m. \tag{39}$$

When $m=0$, G_θ and G_θ' have a simple pole at $\lambda=0$ [see (57)] so that the integrands in (33a) and (33b) contain a double pole at $\lambda=0$. The $m=0$ term need not be evaluated, however, since it does not contribute to the electric field as given in (32a), (32b) and (32c). Since the $m=0$ term is independent of Φ and Φ', there is no contribution to terms containing $(\partial/\partial\Phi)$ or $(\partial/\partial\Phi')$ in (32a), (32b), and (32c). The remaining terms in the $\boldsymbol{\theta}_0$ and $\boldsymbol{\Phi}_0$ components of $\boldsymbol{E}$ involve $(\partial^2/\partial\theta\partial\theta')S_1'$ and $(\partial^2/\partial\theta\partial\theta')S_1''$. If this partial differentiation is carried out on the $m=0$ term in S_1' and S_1'' as given in (33a) and (33b), it is found that this integrand does not contain a pole at $\lambda=0$, in view of the relationship:[18]

$$\frac{d}{d\theta}P_\nu(\cos\theta) = -\nu(\nu+1)P_\nu^{-1}(\cos\theta) = P_\nu^1(\cos\theta). \tag{40}$$

Similarly, in the $\boldsymbol{r}_0$ component of $\boldsymbol{E}$ (for $r\neq r'$), the $m=0$ term in the expression $[(\partial^2/\partial r^2)+k^2](\partial/\partial\theta')S_1'$

[16] Magnus and Oberhettinger, *op. cit.*, p. 60.
[17] *Ibid.*, p. 1.
[18] *Ibid.*, p. 63.

does not contain a pole at $\lambda=0$, in view of (40) and the differential equation satisfied by the spherical Bessel functions:

$$\left[\frac{d^2}{dr^2}+k^2-\frac{\nu(\nu+1)}{r^2}\right]z_\nu(kr)=0. \tag{41}$$

In view of (41) it is also seen that S_{1s}' does not contribute to the radial component of the electric field. Since S_{1s}' and S_{1s}'' as given in (35a) and (35b) yield the scattered portion of $\boldsymbol{E}$ when substituted into (32a), (32b), and (32c), one expects from physical considerations that the solution comprises only outgoing waves. It appears that this demand is not met by the residue contribution in (39) in view of the presence of the j_0 (standing wave) term. However, it is found upon substitution into (32a), (32b), and (32c) that (for $r\neq r'$) the contribution of S_{1sr}' and S_{1sr}'' to the electric field arises solely from the outgoing part of j_0 so that the significant portion of $j_0(kr<)h_0^{(1)}(kr>)$ is $h_0^{(1)}(kr)h_0^{(1)}(kr')/2$, in conformity with the physical requirement.

The evaluation of the plane wave scattering from a narrow-angle cone can be carried out approximately as in the scalar problems. Consider the case where

$$\mathcal{J}_\theta\equiv 0, \text{ i.e. } \mathcal{J}_t=\Phi_0\mathcal{J}_\phi. \tag{42}$$

Upon moving this source to infinity one obtains an incident plane wave whose electric vector is directed perpendicular to the cone axis. If $kr\gg 1$, the r_0 component does not contribute to $0(1/kr)$ [see (41)], so that the far field is transverse (to r). Since S_{1s}' is operated on by $(\partial/\partial\Phi')$ in (32a), (32b), and (32c), the $m=0$ terms in (35a) do not contribute to the field. For $\theta_0\approx\pi$, only the $m=\pm 1$ terms in (35a) contribute to $0(\pi-\theta_0)^2$ [see (38), (40), and (9b)]. Upon employing (10) for the Hankel functions in the integral in (35a), changing variables as in (12) and employing (40) and (9b), one obtains for the integral (when $m=1$):

$$\int_{-1/2-i\infty}^{-1/2+i\infty}\approx 4ie^{ik(r+r')}\left(\frac{\pi-\theta_0}{2}\right)^2\frac{\tan\left(\frac{\theta}{2}\right)\tan\left(\frac{\theta'}{2}\right)}{\cos\theta+\cos\theta'}, \tag{43}$$

in view of (16) of Felsen.[10] Thus, the contributing portion of S_{1s}' in (35a) to the electric field is as follows (to $0[(\pi-\theta_0)^2]$):

$$S_{1s}'\Big]_{m=1}\approx\frac{i}{4\pi k}e^{ik(r+r')}\cos(\Phi-\Phi')\left(\frac{\pi-\theta_0}{2}\right)^2\cdot\tan\frac{\theta}{2}\tan\frac{\theta'}{2}\left[1+\frac{2}{\cos\theta+\cos\theta'}\right]. \tag{44}$$

In the evaluation of S_{1s}'' to $0[(\pi-\theta_0)^2]$, both the $m=0$ and $m=1$ terms are required. The contribution from the $m=0$ term in (35b) is as follows (only the integral contributes to the field):

$$S_{1s}''\Big]_{m=0}\approx\frac{i}{4\pi k}e^{ik(r+r')}\left(\frac{\pi-\theta_0}{2}\right)^2\frac{1}{\cos\theta+\cos\theta'}, \tag{45}$$

where use has been made of (9b) and (31). When $m=1$, the residue contribution is given in (39); the integral in (35b) is found to yield the same expression as (43) except for a minus sign. Thus, the contributing portion of S_{1s}'' is given to $0[(\pi-\theta_0)^2]$ by:

$$S_{1s}''\Big]_{m=0,1}\approx S_{1s}''\Big]_{m=0}-S_{1s}'\Big]_{m=1}. \tag{46}$$

The far scattered electric field is found upon substituting (44) and (46) into (32a), (32b), and (32c). In order to normalize the result to an incident plane wave of unit intensity, the factor

$$F=\mathcal{J}_\Phi\sqrt{\frac{\mu}{\epsilon}}\,ik\frac{e^{ikr'}}{4\pi r'} \tag{47}$$

is set equal to unity.[19] The following result is obtained (to $0(\pi-\theta_0)^2$):

$$E_{\theta s}(r;\infty,\theta',\Phi')\approx\frac{e^{ikr}}{ikr}\sin(\Phi-\Phi')\left(\frac{\pi-\theta_0}{2}\right)^2\left[\frac{\sec^2\left(\frac{\theta}{2}\right)+\sec^2\left(\frac{\theta'}{2}\right)}{\cos\theta+\cos\theta'}+\frac{\sin^2\theta+\sin^2\theta'}{2\cos^2\frac{\theta}{2}\cos^2\left(\frac{\theta'}{2}\right)(\cos\theta+\cos\theta')^2}\right], \tag{48a}$$

$$E_{\Phi s}(r;\infty,\theta',\Phi')\approx\frac{e^{ikr}}{ikr}\left(\frac{\pi-\theta_0}{2}\right)^2\left\{\frac{-2\sin\theta\sin\theta'}{(\cos\theta+\cos\theta')^3}+\cos(\Phi-\Phi')\left[\frac{\sec^2\left(\frac{\theta}{2}\right)+\sec^2\left(\frac{\theta'}{2}\right)}{\cos\theta+\cos\theta'}+\frac{\sin^2\theta+\sin^2\theta'}{\left[2\cos^2\frac{\theta}{2}\right]\cos^2\left(\frac{\theta'}{2}\right)(\cos\theta+\cos\theta')^2}+\frac{16\sin^2\frac{\theta}{2}\sin^2\frac{\theta'}{2}}{(\cos\theta+\cos\theta')^3}\right]\right\}, \tag{48b}$$

where $kr\gg 1$, $\theta_0\approx\pi$, $(\theta+\theta')<(2\theta_0-\pi)$. In view of the azimuthal symmetry of the conical obstacle, the co-

[19] Felsen, reference 3, Appendix B.

ordinate system may be rotated about the z axis so that $\Phi' = -\pi/2$, without loss of generality (see Fig. 1). The electric field in the incident wave which gives rise to the scattered field in (48a) and (48b) is then given by:

$$E_{\text{inc}}(r) = x_0 e^{ik\cdot r} = x_0 e^{-ikr(\cos\theta\cos\theta' - \sin\theta\sin s'\sin\Phi)} \quad (49)$$

x_0 is a unit vector in the x direction in Fig. 1.

If the wave is incident along the cone axis, *i.e.*, $\theta' = 0$, (48a) and (48b) yield (with $\Phi' = -\pi/2$):

$$E_s(r;\ \infty,\ 0,\ -\pi/2)$$

$$\approx (\theta_0 \cos\Phi - \Phi_0 \sin\Phi)\frac{e^{ikr}}{ikr}\left(\frac{\pi - \theta_0}{2}\right)^2 \sec^4\frac{\theta}{2}. \quad (50)$$

For back-scattering in the direction of incidence, $\theta = \theta'$, $\Phi = \Phi'$, so that (48a) and (48b) become:

$$E_s(r,\ \theta',\ \Phi';\ \infty,\ \theta',\ \Phi')$$

$$\approx x_0 \frac{e^{ikr}}{ikr}\left(\frac{\pi - \theta_0}{2}\right)^2 \frac{\sin^4\left(\frac{\theta}{2}\right) + \cos\theta\cos^2\left(\frac{\theta}{2}\right)}{\cos^3\theta}. \quad (51)$$

The results in (50) and (51), for $\theta = 0$, reduce to the expressions for the back-scattering on the cone axis obtained previously by summing a slowly convergent series representation analogous to that in (3).[20] It is of interest to note that the differential back-scattering cross section $|rE_s|^2$ obtained from (50) also agrees with that obtained by Siegel, *et al.*,[4] from physical optics, although physical optics considerations can basically not be justified for surfaces containing a vertex, such as a cone.

The Cone with a Spherical Tip

The geometry of the configuration is shown in Fig. 5. A cone defined by the surface $\theta = \theta_0$ is tipped with a sphere of radius a centered at its apex. This problem differs from the preceding one only in its radial aspect, and the radial characteristic problem is selected in conformity with the boundary conditions on the sphere surface. For the case of a radial electric dipole, for example, the solution of the characteristic problem is that stated in (30) and (31) of Felsen.[1] If a radial transmission representation is selected, the three-dimensional Green's function $\mathcal{G}'$ which satisfies the condition $(\partial/\partial_n)(r\mathcal{G}') = 0$ on the boundary, for example, is given as in (3), except that G_r^0 from (53) is replaced by G_r from (30) of Felsen.[1] Since G_r exhibits an "unperturbed" (no sphere) portion and a perturbation term accounting for the sphere, the radial transmission formulation leads to a result which contains the Green's function for an untipped cone (see first part of second section) plus a perturbation term. The perturbation term is rapidly convergent when (ka) is small, and when either the source or observation point is located far from the sphere and near the cone axis.

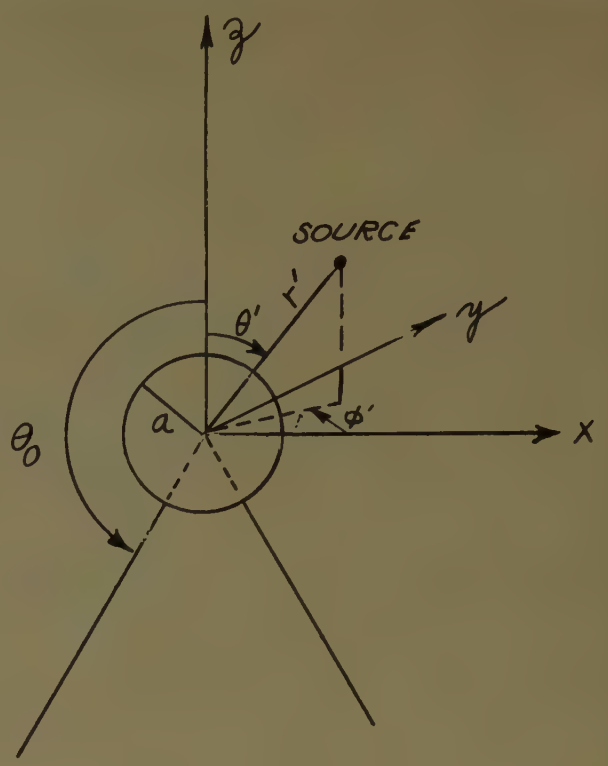

Fig. 5—Cone with spherical tip.

If the θ-transmission formulation is employed [see (11) of Felsen[1]] the three-dimensional Green's function contains a term which is equal to the Green's function for a sphere and a perturbation term which accounts for the presence of the cone, in view of the separation exhibited by (57). For example, if the source is located on the cone axis, the Green's function $\mathcal{G}'$ can be written down directly as:

$$rr'\mathcal{G}' = [rr'\mathcal{G}']_{\text{sphere}} - \frac{i}{4\kappa}\sum_{\xi}\frac{(2\xi+1)j_\xi'(ka)}{\sin\xi\pi\dfrac{\partial}{\partial\xi}h_\xi'^{(1)}(ka)}h_\xi^{(1)}(kr)h_\xi^{(1)}(kr')\frac{P_\xi(\cos\theta)(d/d\theta_0)P_\xi(-\cos\theta_0)}{(d/d\theta_0)P_\xi(\cos\theta_0)} \quad (52)$$

The Green's function for the sphere is given in (33) and (34) of Felsen,[1] or any other convenient form. When (ka) is large, and $r' \to \infty$, $kr \gg 1$ (*i.e.*, for plane wave incidence observed far from the sphere), the perturbation series in (52) is rapidly convergent if $\theta < 2\theta_0 - \pi$, *i.e.*, in the diffraction domain outside of the region containing the rays reflected from the sides of the cone according to geometrical optics. The effect of the cone decreases exponentially away from the boundary surface $\theta = 2\theta_0 - \pi$ of the domain of reflected rays.

[20] Felsen, reference 3 (3-14c).

The Green's function solutions for other types of source configurations and boundary conditions are obtained in direct analogy with the above.

Appendix

One-Dimensional Characteristic Problems for the Cone

r domain: $0<r<\infty$

φ domain: $0\leqq\phi\leqq 2\pi$

This problem has been listed in Felsen,[1] (26) and (27).

θ domain: $0\leqq\theta\leqq\theta_0$

a) $dG_0'/d\theta=0$ at $\theta=\theta_0$

$$G_\theta'(\theta,\theta';\mu;\lambda_2)=\frac{\pi P_\nu^{-\mu}(\cos\theta_<)\left[P_\nu^{-\mu}(\cos\theta_>)(d/d\theta_0)P_\nu^{-\mu}(-\cos\theta_0)-P_\nu^{-\mu}(-\cos\theta_>)(d/d\theta_0)P_\nu^{-\mu}(\cos\theta_0)\right]}{2\left[\Gamma(\nu-\mu+1)/\Gamma(\nu+\mu+1)\right]\sin(\nu-\mu)\pi(d/d\theta_0)P_\nu^{-\mu}(\cos\theta_0)},\tag{56}$$

$$=G_\theta^0(\theta,\theta';\mu;\lambda_4)+\frac{\pi}{2}\frac{P_\nu^{-\mu}(\cos\theta)P_\nu^{-\mu}(\cos\theta')(d/d\theta_0)P_\nu^{-\mu}(-\cos\theta_0)}{\left[\Gamma(\nu-\mu+1)/\Gamma(\nu+\mu+1)\right]\sin(\nu-\mu)\pi(d/d\theta_0)P_\nu^{-\mu}(\cos\theta_0)},\tag{57}$$

Characteristic Green's function:

$$G_r^0(r,r';\lambda_1)=\frac{i}{k}j_\nu(kr_<)h_\nu^{(1)}(kr_>),$$

$$\lambda_1=\nu(\nu+1),\qquad \mathrm{Re}\,(\nu+\tfrac{1}{2})>0.\tag{53}$$

Singularities of G_r: branch point at $\lambda_1=-\frac{1}{4}$. The branch cut in the λ_1 plane is drawn along the negative real λ_1 axis.

where $\lambda_2=\nu(\nu+1)$, and $\mu\geqq 0$ and fixed. G_θ^0 is the characteristic Green's function appropriate to the "unperturbed" domain $0\leqq\theta\leqq 2\pi$ [see Felsen,[1] (28)] so that the second term on the right-hand side of (57) represents the effect of the conical obstacle. Thus, G_θ' as given in (57) is a perturbation type Green's function.

Singularities: simple poles at $\lambda_2=q(q+1)\geqq 0$, where $(d/d\theta_0)P_q^{-\mu}(\cos\theta_0)=0$.

$$\frac{\delta(\theta-\theta')}{\sin\theta'}=-\frac{1}{2\pi i}\oint_{C_2}G_\theta'(\theta,\theta';\mu;\lambda_2)d\lambda_2$$

$$=\frac{1}{2}\csc^2\frac{\theta_0}{2}\delta_{\mu 0}-\frac{\pi}{2}\sum_q(2q+1)\frac{\Gamma(q+\mu+1)(d/d\theta_0)P_q^{-\mu}(-\cos\theta_0)}{\Gamma(q-\mu+1)\sin(q-\mu)\pi(\partial^2/(\partial q\partial\theta_0)P_q^{-\mu}(\cos\theta_0)}P_q^{-\mu}(\cos\theta)P_q^{-\mu}(\cos\theta'),\tag{58}$$

Delta function representation:

$$r'^2\delta(r-r')=\frac{1}{2\pi i}\oint_{C_1}G_r(r,r';\lambda_1)d\lambda_1\tag{54}$$

$$=\frac{1}{2\pi k}\int_{-1/2-i\infty}^{-1/2+i\infty}d\nu(2\nu+1)j_\nu(kr)h_\nu^{(1)}(kr').\tag{55}$$

The contour C_1 in the λ_1 plane encircles the branch cut in the positive sense. r and r' in (55) can be interchanged.

where $\delta_{\mu 0}=1$, $\mu=0$; $\delta_{\mu 0}=0$, $\mu\neq 0$; $q>0$. C_2 encircles the positive real λ_2 axis in the positive sense.

b) $G_\theta=0$ at $\theta=\theta_0$

$G_\theta(\theta,\theta';\mu;\lambda_2)$ is given as in (57) except that the replacement

$$\frac{(d/d\theta_0)P_\nu^{-\mu}(-\cos\theta_0)}{(d/d\theta_0)P_\nu^{-\mu}(\cos\theta_0)}\to\frac{P_\nu^{-\mu}(-\cos\theta_0)}{P_\nu^{-\mu}(\cos\theta_0)}\tag{59}$$

is made.

Singularities: simple poles at $\lambda_2=p(p+1)>0$, where $P_p^{-\mu}(\cos\theta_0)=0$.

$$\frac{\delta(\theta-\theta')}{\sin\theta'}=-\frac{\pi}{2}\sum_p(2p+1)\frac{\Gamma(p+\mu+1)P_p^{-\mu}(-\cos\theta_0)}{\Gamma(p-\mu+1)\sin(p-\mu)\pi(\partial/\partial_p)P_p^{-\mu}(\cos\theta_0)}P_p^{-\mu}(\cos\theta)P_p^{-\mu}(\cos\theta').\tag{60}$$

Theory of the Scintillation Fading of Microwaves*

OSAMU TUKIZI†

Summary—**A theory is presented indicating that the scintillation fading may be attributed to the incoherent scattering of microwaves by atmospheric irregularities in mass motion at an average velocity.**

By use of the perturbation theory, the resultant of scattered fields at the receiver is calculated which, on account of the interference with the direct wave, gives rise to the received field oscillating rapidly with small amplitudes around a mean level. Account is taken of the directivity of transmitting and receiving antennas which facilitates the calculation of received field, and also of the Doppler effect due to the translational mass motion of turbulent eddies.

Agreement with experimental results is satisfactory.

Introduction

THE SCINTILLATION is a type of fading apparently specific to the waves at hyperfrequencies and is characterized by its almost regular oscillation with small amplitudes and short periods in contrast to the roller, *i.e.*, the kind of fading that is of more or less irregularly fluctuating nature.

It is known that the scintillation is closely related to the meteorological condition and, in fact, a steady scintillation is likely to occur when the atmosphere is fairly calm around the path of propagation.

Basing on experimental records, Durkee[1] has classified the microwave fading into four types, two of which belong to our scintillation. Their specific features are summarized as follows: one is quite common in winter sometimes lasting for several days at a time. It is comparatively rare in summer and, when it occurs, it seldom continues for more than a few hours. The other, on the contrary, is almost nonexistent in winter and fairly common in summer, being superposed on a steady average value or a slow irregular variation.

The first type in Durkee's classification might be termed the winter type and the second the summer type; the difference between these two types of scintillation is possibly attributed to the seasonal variation in atmospheric condition or more precisely to the difference in nature of turbulent eddies.

It is the aim of the present paper to indicate that the scintillation fading can be interpreted as a phenomenon arising from interference between the direct and the scattered waves. Small turbulent eddies are assumed to behave as moving scatterers which in mass give rise to a slight shift in the frequency of the resultant of scattered waves.

Effect of the earth will be disregarded because the scintillation is known to appear even when no reflection at the earth surface is believed taking place, provided that the transmitter and the receiver elevated sufficiently are both equipped with antennas of good directivity.

The Scattered Radiation[2]

Consider a nonconducting medium with inductive capacity ϵ which may be written

$$\epsilon(\boldsymbol{r}, t) = \epsilon_0 + \epsilon_1(\boldsymbol{r}, t), \tag{1}$$

where ϵ_0 is a constant to be stated later and $\epsilon_1(\boldsymbol{r}, t)$ is the fluctuating part assumed to be of very small magnitude in comparison with ϵ_0. It is known that the Hertz vector $\boldsymbol{\Pi}(\boldsymbol{r}, t)$ satisfies the following:

$$\nabla^2\boldsymbol{\Pi} + \frac{\epsilon_1}{\epsilon_0}\nabla(\nabla\cdot\boldsymbol{\Pi}) - (\epsilon_0 + \epsilon_1)\mu\frac{\partial^2\boldsymbol{\Pi}}{\partial t^2} = -\frac{1}{\epsilon_0}\boldsymbol{P}, \tag{2}$$

which reduces, for a homogeneous medium, $\epsilon_1 = 0$, to the well-known wave equation. With $\epsilon_1 \neq 0$, the equation may be solved by perturbation theory where it is assumed that $\boldsymbol{\Pi}$ may be written

$$\boldsymbol{\Pi} = \boldsymbol{\Pi}_0 + \boldsymbol{\Pi}_1. \tag{3}$$

Substituting this into (2) and neglecting the terms higher than the second order, we obtain the following two equations for $\boldsymbol{\Pi}_0$ and $\boldsymbol{\Pi}_1$:

$$\nabla^2\boldsymbol{\Pi}_0 - \epsilon_0\mu\frac{\partial^2\boldsymbol{\Pi}_0}{\partial t^2} = -\frac{1}{\epsilon_0}\boldsymbol{P}, \tag{4}$$

$$\nabla^2\boldsymbol{\Pi}_1 - \epsilon_0\mu\frac{\partial^2\boldsymbol{\Pi}_1}{\partial t^2} = -\frac{\epsilon_1}{\epsilon_0}\boldsymbol{E}_0, \tag{5}$$

where

$$\boldsymbol{E}_0 = \nabla(\nabla\cdot\boldsymbol{\Pi}_0) - \epsilon_0\mu(\partial^2\boldsymbol{\Pi}_0/\partial t^2). \tag{6}$$

Eq. (4) is the wave equation for a homogeneous atmosphere and has the solution

$$\boldsymbol{\Pi}_0(\boldsymbol{R}, t) = \frac{1}{4\pi\epsilon_0}\int_{v_0}\frac{\boldsymbol{P}(\boldsymbol{r}_0, t - |\boldsymbol{R} - \boldsymbol{r}_0|/c)}{|\boldsymbol{R} - \boldsymbol{r}_0|}dv_0, \tag{7}$$

where c is the velocity of light in a medium with capacitivity ϵ_0 and the integral extends over all of space. If we assume a harmonic oscillator, $\boldsymbol{p}(t) = \boldsymbol{p}_0 e^{-i\omega t}$, at the origin and neglect the near fields, (7) reduces to

$$\boldsymbol{\Pi}_0(\boldsymbol{R}, t) = \frac{1}{4\pi\epsilon_0}\frac{\boldsymbol{p}(t - |\boldsymbol{R}|/c)}{|\boldsymbol{R}|}. \tag{8}$$

Eq. (5), on the other hand, is the inhomogeneous wave equation whose solution is

* Manuscript received by the PGAP, February 1, 1956.

† Elect. Commun. Lab., Musasino-si, Tokyo, Japan.

[1] A. L. Durkee, "Results of microwave propagation tests on a 40-mile overland path," Proc. IRE, vol. 36, pp. 197–205; February, 1948.

[2] The procedure in this section is after H. Staras, "Scattering of electromagnetic energy in a randomly inhomogeneous atmosphere," *J. Appl. Phys.*, vol. 23, pp. 1152–1156; October, 1952.

$$\boldsymbol{\Pi}_1(\boldsymbol{R}, t) = \frac{1}{4\pi\epsilon_0}\int_v \frac{\epsilon_1(\boldsymbol{r}, t - |\boldsymbol{R}-\boldsymbol{r}|/c)}{|\boldsymbol{R}-\boldsymbol{r}|} \cdot \boldsymbol{E}_0\left(\boldsymbol{r}, t - \frac{|\boldsymbol{R}-\boldsymbol{r}|}{c}\right) dv, \tag{9}$$

the integral extending over all of space. Since $\boldsymbol{E}_0$ is the primary incident field, we see that the scattered field results from the elementary dipoles induced by $\boldsymbol{E}_0$ within the elementary volume dv which we shall hereafter call the scatterer. From (6) and (8), we obtain, to a first approximation, the Hertz vector for the scattered field,

$$\boldsymbol{\Pi}_1(\boldsymbol{R}, t) = -\left(\frac{k}{4\pi\epsilon_0}\right)^2 \int_v \frac{\epsilon_1\left(\boldsymbol{r}, t - \dfrac{|\boldsymbol{R}-\boldsymbol{r}|}{c}\right)}{|\boldsymbol{R}-\boldsymbol{r}| \cdot |\boldsymbol{r}|} \cdot \hat{\boldsymbol{r}} \times [\hat{\boldsymbol{r}} \times \boldsymbol{p}(t^*)]\, dv, \tag{10}$$

where $k = \omega/c$ is the propagation factor for the homogeneous medium and $t^* = t - (|\boldsymbol{R}-\boldsymbol{r}| + |\boldsymbol{r}|)/c$. A circumflex has been used for denoting a unit vector.

Now, we divide $\epsilon_1(\boldsymbol{r}, t)$ into two parts and write

$$\epsilon_1(\boldsymbol{r}, t) = \langle\epsilon_1\rangle + \Delta\epsilon(\boldsymbol{r}, t), \tag{11}$$

where $\langle\epsilon_1\rangle$ is the spatial average of ϵ_1 and $\Delta\epsilon$ the part fluctuating randomly with time and position around the average value. If we choose ϵ_0 of (1) such that $\langle\epsilon_1\rangle$ is equal to the average of the amplitude of fluctuation, then by virtue of (1) and (11)

$$\epsilon(\boldsymbol{r}, t) = \epsilon_0 + \langle|\Delta\epsilon|\rangle + \Delta\epsilon(\boldsymbol{r}, t), \tag{12}$$

where $\langle|\Delta\epsilon|\rangle = \langle\epsilon\rangle - \epsilon_0$ is the average amplitude of fluctuation, $\langle\epsilon\rangle$ being the spatial average of $\epsilon(\boldsymbol{r}, t)$. Hence, we get from (10) and (11)

$$\boldsymbol{\Pi}_1(\boldsymbol{R}, t) = -\left(\frac{k}{4\pi\epsilon_0}\right)^2 \langle|\Delta\epsilon|\rangle \int_v \frac{\hat{\boldsymbol{r}} \times [\hat{\boldsymbol{r}} \times \boldsymbol{p}(t^*)]}{|\boldsymbol{R}-\boldsymbol{r}| \cdot |\boldsymbol{r}|} dv, \tag{13}$$

the term multiplied by $\Delta\epsilon(\boldsymbol{r}, t)$ vanishing because of the random property of the latter.

Fig. 1(a) illustrates schematically the variation of $\epsilon(\boldsymbol{r}, t)$ where the part $\Delta\epsilon(\boldsymbol{r}, t)$ fluctuates around the constant average value $\langle\epsilon\rangle$. There sometimes appears, however, another component, $\Delta\epsilon'(\boldsymbol{r}, t)$ say, that oscillates about a constant value with a longer quasi-period and larger amplitudes accompanying the former type of fluctuations, as shown in Fig. 1(b). It will be readily seen that $\langle|\Delta\epsilon|\rangle$ in (13) is to be replaced, then, simply by

$$\langle|\Delta\epsilon|\rangle \to \langle|\Delta\epsilon|\rangle + \langle|\Delta\epsilon'|\rangle. \tag{14}$$

This case of two-component fluctuations will be referred to in Appendix II.

Calculation of the Integral

In what follows we shall neglect effects of the earth, since the scintillation is known to appear even when the reflected ray is totally masked out, for example, by an intervening hill. Let the transmitter be at the origin of a rectangular coordinate system, the dipole $\boldsymbol{p}_0$ being oriented along the x axis, and the receiver on the z axis at a distance R from the transmitter.

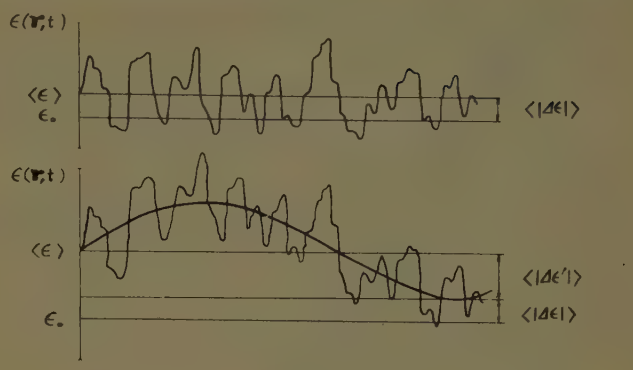

Fig. 1—Schematic illustrations defining ϵ_0.

We define first the antenna pattern function by

$$\phi(\theta) = \exp\left(-\frac{g}{2}\sin^2\frac{\theta}{2}\right), \tag{15}$$

where g is the gain and θ the angle which the positive z axis subtends with the radius vector $r(r)$ drawn from the origin. If g_1 and g are the gains of transmitting and receiving antennas, respectively, the field at the receiver coming from a scatterer at the point (r, θ) will be characterized by the effective pattern function defined by

$$\Psi(r, \theta) = \phi(\theta)\phi(\theta') = \exp\left[-\frac{g}{4}\zeta(r)(1-\cos\theta)\right], \tag{16}$$

with

$$\zeta(r) = \nu + r^2(R-r)^{-2}, \qquad \nu = \frac{g_1}{g}. \tag{17}$$

It can be shown that (16) is a fairly good approximation except in the immediate neighborhood of the receiver. (See Fig. 2.)

The integral in (13) is obviously a vector parallel to $-\boldsymbol{p}_0$ so that only the x component of integrand needs to be considered. Hence, if we introduce the antenna directivity defined by (16), which is axially symmetric about the z axis, we get from (13) the resultant scattered field at the receiver

$$\boldsymbol{\Pi}_1(\boldsymbol{R}, t) = -\frac{1}{4\pi\epsilon_0}\left\langle\left|\frac{\Delta\epsilon}{\epsilon_0}\right|\right\rangle \frac{1}{2}\boldsymbol{p}_0 F(k), \tag{18}$$

where

$$F(k) = \int_0^{R'} dr \int_0^{\pi} k^4 e^{-i\omega t}\Psi(r, \theta) h_0^{(1)}(kr) h_0^{(1)}(kr_1) r^2 \cos\theta \sin\theta d\theta, \tag{19}$$

$h_0^{(1)}(kr)$ being the spherical Hankel function of the first kind and $r = |\boldsymbol{r}|$, $r_1 = |\boldsymbol{R}-\boldsymbol{r}| = (R^2 + r^2 - 2rR\cos\theta)^{1/2}$.

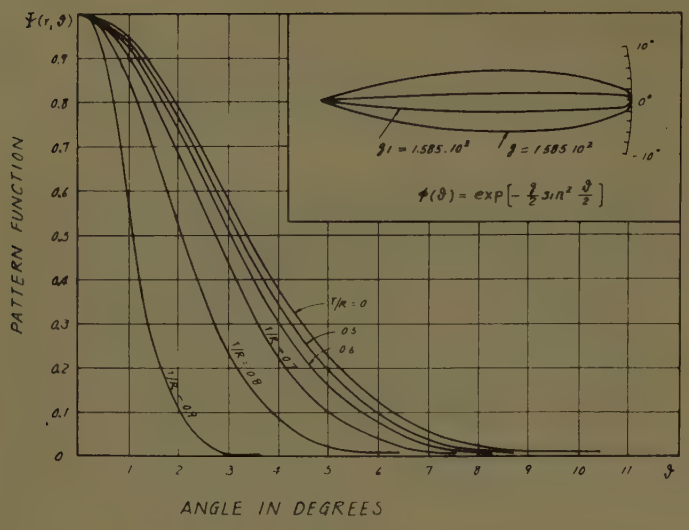

Fig. 2—Pattern functions $\Psi(r, \theta)$ and $\phi(\theta)$.

For simplicity $\cos\theta$ has been substituted for $1-\frac{1}{2}\sin^2\theta$ approximately, since, as the function $\Psi(r, \theta)$ indicates, integration is effective only for small values of θ if antennas are of sufficiently high gain. Use of the pattern function also allows integration to extend over the sphere centered at the origin and of radius R' which we take smaller than R for the moment.

We shall now take into account the mass motion of scatterers which may be regarded analogous to a wind blow in the space of propagation. If a scatterer is in motion at a constant velocity v, the wave that the scatterer reradiates will have a frequency ω slightly different from that of the incident wave ω_0. This is the well-known Doppler effect.

Since $|v| \ll c$, the frequency shift may be written

$$\Delta\omega \equiv \omega - \omega_0 = k_0 v \cdot \left[\frac{R-r}{|R-r|} - \frac{r}{|r|}\right], \tag{20}$$

where $k_0 = \omega_0/c$ is the propagation factor for the homogeneous medium with capacitivity ϵ_0 and $\boldsymbol{r}$ and $\boldsymbol{R}$ the position vectors, as before, of the scatterer and the receiver, respectively, both in reference to the transmitter.

Let be denoted by $L(k)$ the product of all the factors that depend on $k(=\omega/c)$ under the integral sign of (19):

$$L(k) = k^4 \exp(-ickt) h_0^{(1)}(kr) h_0^{(1)}(kr_1). \tag{21}$$

We write $k = k_0 + \Delta k$ where the variation Δk is of a very small magnitude compared to k_0 and notice that Δk has rather a random nature around an average value, $\langle\Delta k\rangle$ say, depending on the velocity of scatterer which will as much be different in sense as in magnitude from place to place. We may then replace $L(k)$ in (19) by the spatial average

$$\langle L\rangle = L(k_0) \exp\left[i\langle\Delta k\rangle(R - ct)\right], \tag{22}$$

where R is the distance between terminals substituted for simplicity in place of $r + r_1$. The average $\langle\Delta k\rangle$ is, as shown in Appendix I, given by

$$\langle\Delta k\rangle = \frac{2k_0 9(\nu)}{g_1 + g} \frac{V}{c} \cos\Theta, \tag{23}$$

where g_1 and g are the gains of transmitting and receiving antennas, $q(\nu)$ a function of ν alone and $V\cos\Theta$ the component of the average wind speed along the line joining terminals.

Inserting these expressions for the product defined by (21), we get from (19)

$$F(k) = G(k_0) \exp\left[-i\omega_0 t - i\langle\Delta k\rangle(ct - R)\right], \tag{24}$$

where

$$G(k_0) = k_0^4 \int_0^{R'} dr \int_0^{\pi} \Psi(r, \theta) h_0^{(1)}(k_0 r) h_0^{(1)}(k_0 r_1) \cdot r^2 \cos\theta \sin\theta d\theta. \tag{25}$$

Now, we expand $h_0^{(1)}(k_0 r_1)$ in spherical harmonics and integrate term by term with respect to θ, by use of the formula[3]

$$\int_0^{\pi} e^{z\cos\theta} P_n(\cos\theta) \cos\theta \sin\theta d\theta = 2i_n'(z), \tag{26}$$

where

$$i_n'(z) \equiv \left(\frac{\pi}{2}\right)^{1/2} \frac{d}{dz}\left\{I_{n+1/2}(z)/z^{1/2}\right\}. \tag{27}$$

Then, we get from (25)

$$G(k_0) = 2k_0^4 \int_0^{R'} e^{-(g/4)\zeta r^2} h_0^{(1)}(k_0 r) \cdot \sum_{n=0}^{\infty} (2n+1) j_n(k_0 r) h_n^{(1)}(k_0 R) i_n'\left(\frac{g}{4}\zeta\right) dr. \tag{28}$$

It can be shown that the most predominant terms of the series are those with values of n around $n_0 = e/4(k_0 r \cdot g\zeta)^{1/2}$ and this makes it permissible to use for $h_n^{(1)}(k_0 R)$ its asymptotic form $(-i)^n h_0^{(1)}(k_0 R)$ provided that $k_0 R \gg g\zeta$. Hence, by use of the formula

$$j_1(x + iy) = i \sum_{n=0}^{\infty} (2n+1)(-i)^n j_n(x) i_n'(y), \tag{29}$$

which may be derived from the Gegenbauer addition formula for $j_1(x+iy)$[4] by differentiating both sides with respect to y, it follows at once that

$$G(k_0) = -2ik_0^4 h_0^{(1)}(k_0 R) \cdot \int_0^{R'} e^{-(g/4)\zeta} j_1\left(k_0 r + i\frac{g}{4}\zeta\right) h_0^{(1)}(k_0 r) r^2 dr. \tag{30}$$

[3] G. N. Watson, "Theory of Bessel Functions," Cambridge Univ. Press, Cambridge, Eng., p. 369; 1922.
[4] *Ibid.*, p. 366.

If $k_0R \gg g \gg 1$ which is usually the case, the integration can readily be performed, *e.g.*, by the method of stationary phase, and yields, at the limit that R' tends to R

$$G(k_0) = -2\pi i k_0 \exp(ik_0R). \tag{31}$$

By virtue of (18) and (24), this gives ultimately the Hertz vector for the resultant scattered radiation at the receiver

$$\mathbf{\Pi}_1(\boldsymbol{R}, t) = \frac{1}{4\pi\epsilon_0} \frac{p\left(t - \frac{|\boldsymbol{R}|}{c}\right)_{\omega_0}}{|\boldsymbol{R}|} i\pi\left(\left|\frac{\Delta\epsilon}{\epsilon_0}\right|\right) k_0R \cdot \exp\left[i\langle\Delta k\rangle(R - ct)\right], \tag{32}$$

with

$$p\left(t - \frac{|\boldsymbol{R}|}{c}\right)_{\omega_0} = p_0 \exp\left[-i\omega_0\left(t - \frac{|\boldsymbol{R}|}{c}\right)\right]. \tag{33}$$

We see from (8) and (32) that the resultant scattered field is proportional to the primary field whose frequency is ω_0 unaffected by the motion of scatterers. Adding these together we obtain, by (3), the total field at the receiver:

$$\mathbf{\Pi} = \mathbf{\Pi}_0 + \mathbf{\Pi}_1 = \mathbf{\Pi}_0\left\{1 - i\pi\left(\left|\frac{\Delta\epsilon}{\epsilon_0}\right|\right) k_0R \cdot \exp\left[i\frac{2k_0g}{g_1 + g}\left(t - \frac{R}{c}\right)V\cos\Theta\right]\right\}. \tag{34}$$

Comparison with Experiment

It can be shown that the received field referred to the free space is, by (34),

$$(E/E_0)^2 = 1 + (2\pi k_0R \cdot \Delta N)^2 + 4\pi k_0R \cdot \Delta N \sin\left[\frac{2k_0}{g_1 + g} qV\cos\Theta \cdot \left(t - \frac{R}{c}\right)\right], \tag{35}$$

where average has been taken over one cycle of the carrier oscillation during which the third term is considered nearly constant in time. The average fluctuation of refractive index ΔN has been introduced in place of $\frac{1}{2}\langle|\Delta\epsilon/\epsilon_0|\rangle$ where ϵ_0 differs slightly in magnitude from the permittivity for free space.

If $1 \gg (2\pi k_0R \cdot \Delta N)^2$, it follows from (35), expressed in decibels, that

$$E/E_0 = \bar{A}\sin(\tilde{\nu}t - \delta), \tag{36}$$

with

$$\begin{cases} \nu = (4\pi q(\nu)/\lambda)(g_1 + g)^{-1}V\cos\Theta, & (37) \\ \bar{A} = 20(\log_{10} e)(2\pi)^2 \dfrac{R}{\lambda}\Delta N \text{ in } dB. & (38) \end{cases}$$

We see that, to the degree of approximation used, the received field manifests a simple oscillating nature as a consequence of the interference between the direct and the scattered waves.

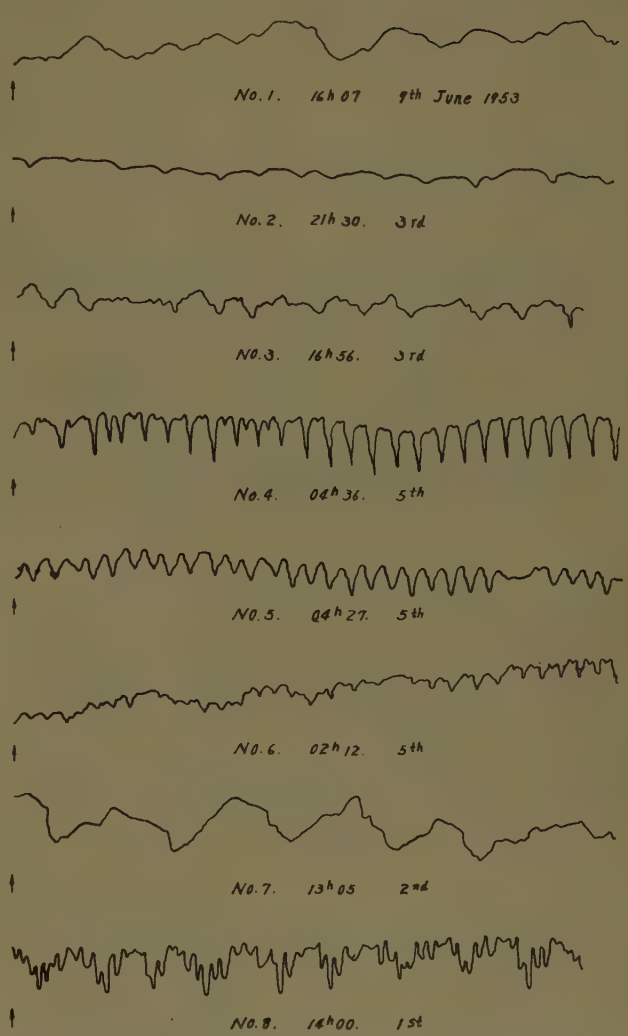

Fig. 3—Typical samples of scintillation in rapid recording. The full scale for about one minute beginning at the time indicated.

In Fig. 3 are illustrated typical examples of scintillation taken from records of the propagation test which the *Electrical Communication Laboratory* carried out in June, 1953, at a wavelength of 7.5 cm. Records were taken at a speed of 12 cm/min, the figure showing the duration of about one minute from the time indicated.

We see that periodicity in records is remarkable and that at least two oscillations of different periods appear to exist in superposition. The existence of longer period oscillations might be ascribed to the different scales of turbulence which play effective rôles in tropospheric radio scattering.[5]

Eq. (37) shows that the scintillation frequency $\tilde{\nu}$ is proportional to the average wind-speed component $V\cos\Theta$ along the line joining terminals. To check this,

[5] H. G. Booker and W. E. Gordon, "A theory of radio scattering in the troposphere," PROC. IRE, vol. 38, pp. 401–412; April, 1950. (See also Appendix II.)

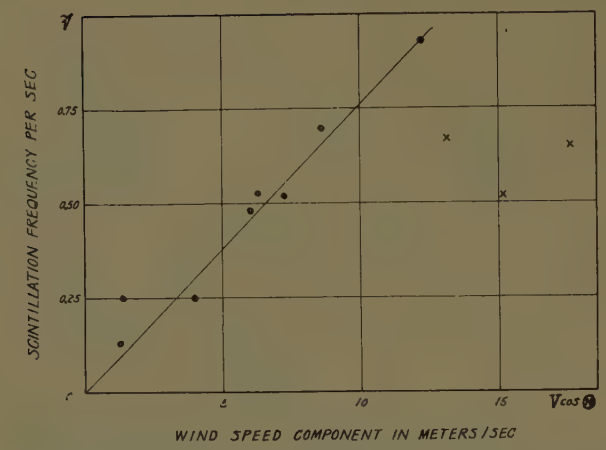

Fig. 4—Relation between the frequency of scintillation and the average wind-speed component along the line joining terminals. Slope of the straight line: 0.076, calculated from (37) and (45) with values of $g_1 = 1.585 \cdot 10^3$ (32 db) and $g = 1.585 \cdot 10^2$ (22 db).

values of the frequency read from records of Fig. 3 are plotted in Fig. 4 against the wind-speed component observed at the summit of Mt. Tukuba where the transmitter was located. The wind-speed is the average taken from anemographic records over a 10-minute interval centered at the corresponding time indicated in Fig. 3. Corrections have been made of the values for specific wind-directions by use of the calibration curve supplied by Tukuba Meteorological Station.

A theoretical straight line is also shown in Fig. 4, drawn from the origin with the slope calculated from (37). The value of $g_1 + g$ has been taken as $1.744 \cdot 10^3$ and that of ν as 10, the gains of the transmitting and receiving antennas being of 32 and 22 db respectively.

Out of all 11 records taken during the period of experiment, 3 are in disagreement with the theoretical prediction. Their waveforms are similar to those of Nos. 2, 5, and 6 of Fig. 3, and yet the corresponding values of wind-speed are appreciably dispersing as indicated with crosses in Fig. 4. The discrepancy might be accounted for strong local wind-blow which was occasional at the point of observation and was not representative of the average to be taken over the entire space of propagation.

Eq. (38) indicates that the amplitude of scintillation $\tilde{A}$ is inversely proportional to the wavelength λ and proportional to the distance R between the transmitter and the receiver. Figs. 5 and 6 show the results of analysis based on the data of August 1, 1954, which were selected from records of a three-path propagation test undertaken by the Laboratory.

The test was carried out for about two weeks between Tukuba and Hutago, 149 km apart, at frequencies of 1.5 and 4 gc/s,[6] and simultaneously between Mitaka and Tukuba at 4 gc/s. The relative locations were such that the Laboratory (at Mitaka) was situated just amid and

[6] 1 gigacycle = 10^9 cycles.

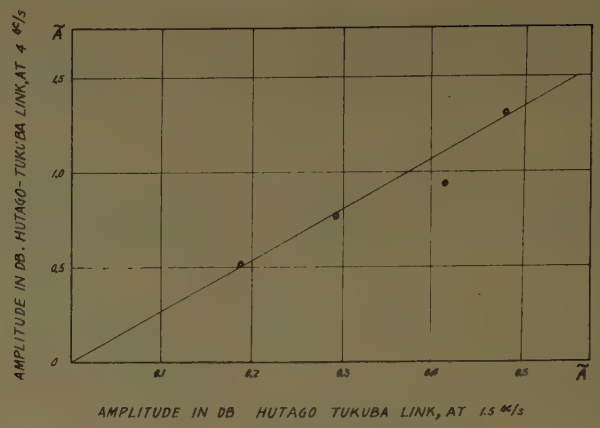

Fig. 5—Dependence of the scintillation amplitude on the frequency of waves. Slope of the straight line, taken equal to the frequency ratio.

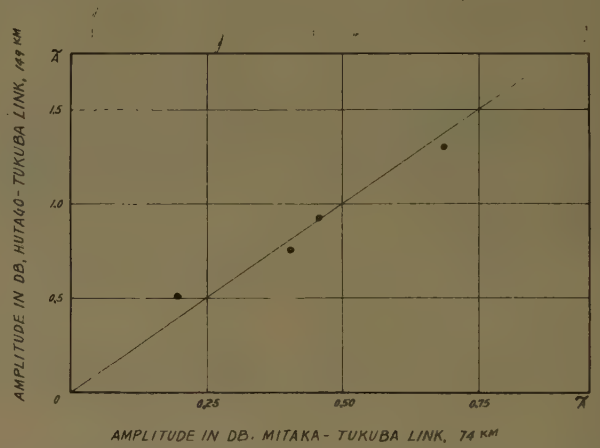

Fig. 6—Dependence of the scintillation amplitude on the intertermi-nal distance. Slope of the straight line, taken equal to the distance ratio.

on the Tukuba-Hutago path. Since no rapid recording was effected at this experiment, analysis was made of the data read from the chart records which were taken at a conventional speed of 12 cm/hour.

In Fig. 5 are compared the average values of the scintillation amplitudes $\bar{A}$ for the two Tukuba-Hutago paths at different frequencies, 1.5 and 4 gc/s, and, in Fig. 6, for two links of different distances, 74 and 149 km, at nearly the same frequency. Averages have been taken for each of three paths over a ten-minute interval around 6, 8, 11, and 15 hours of the local time. These illustrations appear to support the theoretical prediction, if it is legitimate to assume that the average fluctuation of refractive index ΔN is the same over the entire space that contains two different links.

The values of ΔN estimated from Figs. 5 and 6 with (38) are plotted in Fig. 7 as a function of local mean time. It appears that the average fluctuation exhibits a diurnal variation analogous to that of the atmospheric temperature. This agrees with the known fact that the scintillation has in general a smaller amplitude in winter than in summer.

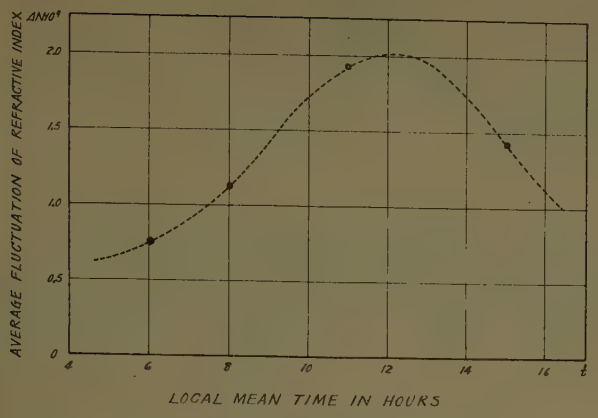

Fig. 7—Diurnal variation of refractive-index fluctuation.

We see that the average fluctuation of refractive index is of the order of 10^{-9}. This order of magnitude is not in contradiction with the observation by Bussy and Birnbaum[7] who report that "fluctuations that occurred in distances of from 0.5 to 5 m had an amplitude less than $0.04 \cdot 10^{-6}$ in n." It would be plausible to obtain more appropriate values if the measurement could have been made for distances of the order of a wavelength.

Appendix I

The Average Frequency-Shift

Let $v(V,\Theta,\Phi)$ be a wind velocity whose angular coordinates are specified with respect to the fixed reference system used in the text.

The frequency-shift is, by (20),

$$\Delta\omega = c\Delta k = k_0 V\left[\left\{\frac{R}{r_1} - \left(1+\frac{r}{r_1}\right)\cos\theta\right\}\cos\tilde{H} - \left(1+\frac{r}{r_1}\right)\sin\theta\sin\tilde{H}\cos(\phi-\Phi)\right]. \tag{39}$$

where $r_1=(R^2+r^2-2rR\cos\theta)^{1/2}$ as before. By taking average over the whole space of propagation, we consider $v(V,\Theta,\Phi)$ constant throughout the region.

Introducing again the antenna pattern function $\Psi(r,\theta)$ of (16) and (17), we define the average $\langle\Delta k\rangle$ by

$$\langle\Delta k\rangle = \frac{1}{\tilde{D}}\int_0^{R'} dr\int_0^{\pi} d\theta\int_0^{2\pi}\Psi^2(r,\theta)(\Delta k)r^2\sin\theta\,d\phi \equiv \frac{\tilde{N}}{\tilde{D}}, \tag{40}$$

with

$$\tilde{D} = \int_0^{R'} dr\int_0^{\pi} d\theta\int_0^{2\pi}\Psi^2(r,\theta)r^2\sin\theta\,d\phi$$

$$= 2\pi\int_0^{R'} e^{-\mu}\left(\frac{2\pi}{\mu}\right)^{1/2} I_{1/2}(\mu)r^2dr,$$

and

$$\mu = 2\cdot\frac{g}{4}\zeta(r) = \frac{g}{2}[\nu + r^2(R-r)^{-2}]. \tag{41}$$

Eq. (40) implies that contribution to the average is considered to depend on the fraction of power that arrives at the receiver after being re-radiated by a scatterer to which the shift Δk is prescribed.

If we insert (39) into (40) and integrate with respect to ϕ, we have

$$\tilde{N} = 2\pi k_0\frac{V}{c}\cos\Theta\int_0^{R'} dr\int_0^{\pi} e^{-\mu(1-\cos\theta)}\cdot\left\{\frac{R-r\cos\theta}{r_1} - \cos\theta\right\} r^2\sin\theta\,d\theta. \tag{42}$$

The integral that comes from the second term in (39) has vanished because of the axial symmetry of the pattern function.

Now we expand $1/r_1$ in zonal harmonics and interchange the order of summation and integration which is permissible obviously. It follows that

$$\int_0^{\pi} e^{\mu\cos\theta}\frac{R}{r_1}\sin\theta\,d\theta = \sum_{n=0}^{\infty}\left(\frac{r}{R}\right)^n\int_0^{\pi} e^{\mu\cos\theta}P_n(\cos\theta)\sin\theta\,d\theta = \left(\frac{2\pi}{\mu}\right)^{1/2}\left\{I_{1/2}(\mu) + \sum_{n=0}^{\infty}\left(\frac{r}{R}\right)^{n+1} I_{n+3/2}(\mu)\right\}$$

$$\int_0^{\pi} e^{\mu\cos\theta}\frac{r}{r_1}\cos\theta\sin\theta\,d\theta = \frac{r}{R}\frac{\partial}{\partial\mu}\int_0^{\pi} e^{\mu\cos\theta}\frac{R}{r_1}\sin\theta\,d\theta = \left(\frac{2\pi}{\mu}\right)^{1/2}\sum_{n=0}^{\infty}\left(\frac{r}{R}\right)^{n+1} I_{n+3/2}(\mu)$$

and also

$$\int_0^{\pi} e^{\mu\cos\theta}\cos\theta\sin\theta\,d\theta = \left(\frac{2\pi}{\mu}\right)^{1/2} I_{3/2}(\mu).$$

If we introduce these relations, (42) reduces to

$$\tilde{N} = 2\pi k_0\frac{V}{c}\cos\Theta\int_0^{R'} e^{-\mu}\left(\frac{2\pi}{\mu}\right)^{1/2}\{I_{1/2}(\mu) - I_{3/2}(\mu)\}r^2dr,$$

whence, μ being large compared to $\pi/2$,

$$\langle\Delta k\rangle = \tilde{N}/\tilde{D} = k_0\frac{V}{c}\cos\Theta\left[\int_0^{R'}\frac{r^2}{\mu^2}dr \Big/ \int_0^{R'}\frac{r^2}{\mu}dr\right].$$

[7] H. E. Bussy and G. Birnbaum, "Measurement of variations in atmospheric refractive index with an airborne microwave refractometer," *J. Res. NBS*, vol. 51, pp. 171–178; October, 1953.

By virtue of (41), this may be rewritten

$$\langle \Delta k \rangle = k_0 \frac{V}{c} \cos\Theta \cdot \frac{2}{g} \frac{\partial}{\partial \nu} [-\log p(\nu)], \qquad (43)$$

where

$$p(\nu) = \lim_{R' \to R} \int_0^{R'} \frac{r^2 dr}{\nu + \left(\frac{r}{R-r}\right)^2} \cdot$$

The integration can be effected in a straightforward manner and it is readily shown that

$$-\frac{\partial}{\partial \nu} \log p(\nu) = \frac{1}{1+\nu} q(\nu) \qquad (44)$$

with

$$q(\nu) = \frac{\frac{\pi}{4\sqrt{\nu}}(35\nu^2 - 3\nu^3 - 25\nu + 1) + \frac{\nu+1}{3}(\nu^2 - 28\nu + 19) + 2(2\nu^2 - 5\nu + 1)\log \nu}{\frac{\pi}{2}\sqrt{\nu}(6\nu - \nu^2 - 1) + \frac{\nu+1}{3}(\nu^2 - 10\nu + 1) + 2\nu(\nu - 1)\log \nu} \cdot \qquad (45)$$

From (43)–(45) it follows that

$$\langle \Delta k \rangle = \frac{2}{g_1 + g} q(\nu) \frac{k_0 V}{c} \cos\Theta.$$

Appendix II

Two-Component Fluctuations

Consider an inhomogeneous medium containing in unit volume a large number of eddies whose dimensions are of or less than the order of wavelength.

If the density of these small eddies varies with position and time, the atmospheric index of refraction will be of the two-component fluctuations as in Fig. 1(b). Such a density fluctuation of eddies may arise from a larger-scale turbulence whose translational motion will in general be slower than that of component eddies.

By use of primes to indicate quantities that concern subsidiary turbulence, we obtain, instead of (35),

$$(E/E_0)^2 = 1 + (2\pi k_0 R)^2 [\Delta N^2 + \Delta N'^2 + 2\Delta N \cdot \Delta N' \cos \left\{ \frac{2k_0}{g_1 + g} q(\nu)(V - V') \cdot \left(t - \frac{R}{c}\right) \cos\Theta \right\}]$$
$$+ 4\pi k_0 R \left[\Delta N \sin \left\{ \frac{2k_0}{g_1 + g} q(\nu) V \cos\Theta \cdot \left(t - \frac{R}{c}\right) \right\} + \Delta N' \sin \left\{ \frac{2k_0}{g_1 + g} q(\nu) V' \cos\Theta \cdot \left(t - \frac{R}{c}\right) \right\} \right].$$

Neglecting the second term, smaller than others, we have in decibels

$$E/E_0 = \tilde{A} \sin(\tilde{\nu} t - \delta) + \tilde{A}' \sin(\tilde{\nu}' t - \delta'), \qquad (46)$$

with

$$\left.\begin{aligned} \tilde{\nu} &= (4\pi/\lambda) q(\nu)(g_1 + g)^{-1} V \cos\Theta \\ \tilde{\nu}' &= (4\pi/\lambda) q(\nu)(g_1 + g)^{-1} V' \cos\Theta \end{aligned}\right\} \qquad (47)$$

and

$$\left.\begin{aligned} \tilde{A} &= 20(\log_{10} e)(2\pi)^2 \frac{R}{\lambda} \Delta N \\ \tilde{A}' &= 20(\log_{10} e)(2\pi)^2 \frac{R}{\lambda} \Delta N' \end{aligned}\right\}. \qquad (48)$$

It is seen that the scintillation has two components of oscillations as observed, *e.g.*, in record No. 8 of Fig. 3.

The frequency ratio $\tilde{\nu}/\tilde{\nu}'$, estimated from the record, is of about 6.2 and the ratio in amplitude $\tilde{A}/\tilde{A}'$ is of about 1/2.2. These values appear, as (47) and (48) suggest, to be of reasonable orders of magnitude for the ratios V'/V and $\Delta N/\Delta N'$ respectively, although the corroboration is left to future investigations.

Ray Theory vs Normal Mode Theory in Wave Propagation Problems*

LESLIE G. McCRACKEN†

Summary—**The Euler-Maclaurin expansion, as a possible tool for summing mode series in wave propagation problems, is examined for the problem of a dipole radiating monochromatic energy between two parallel plates. When the expansion is applied to this problem, it is found that the expansion formula transforms the mode series into the known ray theory solution.**

Introduction

CALCULATIONS of the field in tropospheric wave propagation problems lead to the use of series expansions based on ray and normal mode theories. In using these expansions, one finds that when a few terms of the ray theory solution approximate the field reasonably well, many, many terms of the normal mode solution would be required to achieve the same order of approximation, and *vice versa*. The ray solution usually suffices at ranges close to the transmitter; the normal mode solution is used for distances far from the transmitter. At intermediate ranges, neither of the two expansions is satisfactory for practical calculations.

Previous studies of C. L. Pekeris have been aimed at finding ways to calculate the field in the intermediate region[1,2] and at discovering the connection between ray and mode theories. In Pekeris' recent paper,[3] he found that the two expansions are related by a Fourier cosine transform[4] and suggested that it might be possible to use the Euler-Maclaurin expansion[5] to sum either the ray or the normal mode solution. This suggestion of Pekeris forms the basis of the present paper.

The Problem

To show the power of the Poisson formula

$$\sqrt{\beta}\left[\frac{1}{2}F_c(0)+\sum_{n=1}^{\infty}F_c(n\beta)\right]=\sqrt{\alpha}\left[\frac{1}{2}f(0)+\sum_{n=1}^{\infty}f(n\alpha)\right] \quad (1)$$

where

$$\beta\alpha = 2\pi$$

$$F_c(u)=\sqrt{\frac{2}{\pi}}\int_0^{\infty}f(x)\cos uxdx$$

$f(x)$ of bounded variation on $[0, \infty]$

$f(x)\searrow 0$ as $x\to\infty$.

Pekeris addressed himself to the problem of a point-source radiating monochromatic energy between two perfectly conducting, parallel plates of separation distance H. For this problem, he expressed the ray and normal mode solutions as follows in (2) and (3).

$$\begin{aligned}\Psi = &\{g[r^2+(h-z)^2]-g[r^2+(h+z)^2]\}\\&+\sum_{n=0}^{\infty}\{g[r^2+(h-z+2nH)^2]\\&+g[r^2+(z-h+2nH)^2]\\&-g[r^2+(z+h+2nH)^2]\\&-g[r^2+(-z-h+2nH)^2]\}\end{aligned} \quad (2)$$

where

$$g(R^2)\equiv\frac{e^{-ik_0R}}{R}$$

h = height of dipole above lower plate located at $z=0$,

(r, z) = cylindrical coordinates,

H = separation distance of plates.

$$\Psi=-\left(\frac{2\pi i}{H}\right)\sum_{n=1}^{\infty}H_0^{(2)}(k_nr)\sin\left(\frac{n\pi h}{H}\right)\sin\left(\frac{n\pi z}{H}\right)$$

where

$$\begin{cases}k_n=\left[k_0^2-\dfrac{n^2\pi^2}{H^2}\right]^{1/2}, & k_0>n\pi/H\\ k_n=-i\left[\dfrac{n^2\pi^2}{H^2}-k_0^2\right]^{1/2}, & k_0<n\pi/H.\end{cases} \quad (3)$$

Using the mode solution (3) and the Poisson formula (1) Pekeris succeeded in generating the ray solution (2). Thus, he clearly showed that the terms of the two expansions are related by Fourier cosine transforms. Using the same example treated by Pekeris, we shall establish another connection between ray theory and mode theory using the Euler-Maclaurin expansion.

* Manuscript received by the PGAP, October 7, 1955.
† Dept. of Elec. Eng., Lehigh Univ., Bethlehem, Pa.

[1] C. L. Pekeris, "The field of a microwave dipole antenna in the vicinity of the horizon," *J. Appl. Phys.*, vol. 18, pp. 667–680; July, 1947.

[2] C. L. Pekeris, "The field of a microwave dipole antenna in the vicinity of the horizon, II," *J. Appl. Phys.*, vol. 18, pp. 1025–1027; November, 1947.

[3] C. L. Pekeris, "Ray theory vs normal mode theory in wave propagation problems," *Proc. Symp. Appl. Math.*, vol. 2, pp. 71–75; Amer. Math. Soc., 1950.

[4] E. C. Titchmarsh, "Introduction to the Theory of Fourier Integrals," Oxford Univ. Press, New York, N. Y., p. 61; 1937.

[5] E. T. Whittaker and G. N. Watson, "Modern Analysis," Cambridge Univ. Press, Cambridge, Eng., p. 127; 1935.

The Euler-Maclaurin Expansion

The Euler-Maclaurin sum formula reads[6]

$$(z-a)f'(a) = f(z) - f(a) - \frac{z-a}{2}\{f'(z) - f'(a)\} + \sum_{m=1}^{n-1}(-1)^{m-1}\frac{B_m(z-a)^{2m}}{(2m)!}\{f^{(2m)}(z) - f^{(2m)}(a)\} - \frac{(z-a)^{2n+1}}{(2n)!}\int_0^1 \phi_{2n}(t) f^{(2n+1)}\{a+(z-a)t\}\,dt. \quad (4)$$

Here $\phi_n(t)$ is the nth Bernoulli polynomial, $\{B_n\}$ are the Bernoullian numbers, and $f(z)$ is analytic on $[a,z]$. By integrating (4) from a to $a+r\omega$, Whittaker and Watson show

$$\int_a^{a+r\omega} F(x)\,dx = \omega\left\{\frac{1}{2}F(a) + \sum_{n=1}^{r-1}F(a+n\omega) + \frac{1}{2}F(a+r\omega)\right\} + \sum_{m=1}^{n-1}(-1)^m\frac{B_m\omega^{2m}}{(2m)!}\{F^{(2m-1}(a+r\omega) - F^{(2m-1)}(a)\} + R_m \quad (5)$$

where

$$R_n \equiv \frac{\omega^{2n+1}}{(2n)!}\int_0^1 \phi_{2n}(t)\left\{\sum_{m=0}^{r-1}F^{(2n)}(a+m\omega+\omega t)\right\}dt.$$

Making the transitions given below

$$\begin{cases} a \to 0 \\ r \to \infty \\ \omega \to 1 \end{cases} \quad (6)$$

we arrive at the following sum formula

$$\sum_{\nu=0}^{\infty} f(\nu) = \frac{1}{2}f(0) + \int_0^\infty f(x)\,dx - \sum_{m=1}^{n-1}\frac{(-1)^m B_m}{(2m)!}\{f^{(2m-1)}(\infty) - f^{(2m-1)}(a)\} - R_n$$

$$R_n = \frac{1}{(2n)!}\int_0^1 \phi_{2n}(t)\left\{\sum_{m=0}^{\infty} f^{(2n)}(m+t)\right\}dt. \quad (7)$$

The Connection

Starting from the mode solution where

$$f(n) = -\left(\frac{2\pi i}{H}\right)H_0^{(2)}\left[r\left(k_0^2 - \frac{n^2\pi^2}{H^2}\right)^{1/2}\right]\cdot\sin\left(\frac{n\pi z}{H}\right)\sin\left(\frac{n\pi h}{H}\right) \quad (8)$$

we use (7) and obtain the sum. Let $x \equiv (n\pi/H)$ and

$$f(n) \overset{T}{\to} f_1(x),$$

then

$$\sum = \frac{1}{2}f_1(0) - 2i\int_0^\infty H_0^{(2)}[r\sqrt{k_0^2 - x^2}]\sin zx\sin hx\,dx - \sum_{m=1}^{n-1}\frac{(-1)^m B_m}{(2m)!}\left(\frac{\pi}{H}\right)^{2m-1}\cdot\{f_1^{(2m-1)}(\infty) - f_1^{(2m-1)}(0)\} - R_n. \quad (9)$$

The factor $(\pi/H)^{2m-1}$ in (9) arises from differentiation, and the remainder term R_{in} corresponds to the one in (7). But $f_1(0)=0$, $f_1^{(n)}(\infty)=0$, so

$$\sum = -2i\int_0^\infty H_0^{(2)}[r\sqrt{k_0^2 - x^2}]\sin zx\sin hx\,dx + \sum_{m=1}^{n-1}\frac{(-1)^m B_m}{(2m)!}\left(\frac{\pi}{H}\right)^{2m-1} f_1^{(2m-1)}(0) - R_n. \quad (10)$$

The integral in (10) has been evaluated by Pekeris, hence the sum can be written as

$$\sum = \{g[r^2 + (h-z)^2] - g[r^2 + (h+z)^2]\} + \sum_{m=1}^{n+1}\frac{(-1)^m B_m}{(2m)!}\left(\frac{\pi}{H}\right)^{2m-1} f_1^{(2m-1)}(0) - R_n. \quad (11)$$

The first two terms of (11) agree with the corresponding terms of the ray solution, (2); these take care of the direct ray and the ray reflected from the plane $z=0$. The summation and the remainder R_{in} require some attention to show that they can be used to generate the remaining terms of the ray solution. We now go into the problem of calculating the derivatives and completing the summation in (11). First, the derivatives.

We have

$$f_1^{(2m-1)}(0) = -\left(\frac{2\pi i}{H}\right)\frac{d^{2m-1}}{dx^{2m-1}}\cdot[H_0^{(2)}[r\sqrt{k_0^2 - x^2}]\sin zx\sin hx]_{x\to 0}. \quad (12)$$

The differentiation can be done easily, after an integral representation of the Hankel function is inserted in (12). The one chosen is

$$H_0^{(2)}[r\sqrt{k_2 - x^2}] = \frac{i}{\pi}\int_{C_2}\frac{e^{-ik\sqrt{r^2+\omega^2}}}{\sqrt{r^2+\omega^2}}e^{i\omega x}d\omega \quad (13)$$

where the contour C_2 is shown[7] in Fig. 1. The result of

[6] *Ibid.*, p. 128.

[7] This integral representation is based on Weyrich's formula; *cf.*, W. Magnus and F. Oberhettinger, "Special Functions of Mathematical Physics," Chelsea Publishing Co., New York, N. Y., p. 34; 1949. The phase sense of the contour was established by integrating (13) for small arguments and comparing the resulting logarithmic singularity with the one well known for the Hankel function of the second kind. Gene Corum's interest in this regard is gratefully acknowledged.

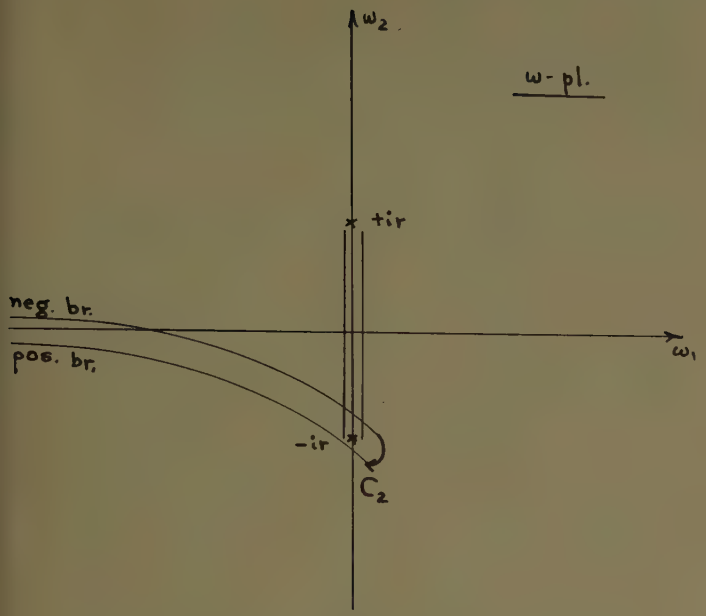

Fig. 1.

differentiation and allowing $x \to 0$ is given by

$$f_1^{(2m-1)}(0) = \frac{1}{2H}\int_{C_2} g[r^2+\omega^2]\{[i(\omega-h+z)]^{2m-1} + [i(\omega-z+h)]^{2m-1} - [i(\omega+h+z)]^{2m-1} - [i(\omega-h-z)]^{2m-1}\}d\omega. \quad (14)$$

The summation in (11) can now be carried out. Calling the result S_n, we have

$$S_n = \sum_{j=1}^{4} \sqrt{2}\sin(j\pi/2 - \pi/4)T_j \quad (15)$$

where

$$T_j \equiv \sum_{m=1}^{n-1} \frac{(-1)^m B_m}{(2m)!}\left(\frac{\pi}{H}\right)^{2m-1} \cdot \frac{1}{2H}\int_{C_2} g[r^2+\omega^2][i(\omega-\omega_j)]^{2m-1}d\omega \quad (16)$$

and where

$$\omega_1 \equiv h - z;\ \omega_2 \equiv z - h;\ \omega_3 = -h - z;\ \omega_4 \equiv h + z. \quad (17)$$

Now the generating function for the Bernoullian numbers is known to be

$$\frac{t}{e^t - 1} = 1 - \frac{t}{2} + \sum_{m=1}^{\infty} \frac{(-1)^{m-1}B_m}{(2m)!}t^{2m} \quad (18)$$

hence the sum for T_j can be found if we let $n \to \infty$. The result is

$$T_j = \frac{1}{2\pi i}\int_{C_2} g(r^2+\omega^2)\left\{\frac{1}{\omega-\omega_j} - \frac{\pi i}{H} - \frac{\pi i/H}{e^{i\pi/H(\omega-\omega_j)} - 1}\right\}d\omega \quad (19)$$

When this is substituted in (15), the middle terms

$$\left(-\frac{\pi i}{2H}, -\frac{\pi i}{2H}, \frac{\pi i}{2H}, \frac{\pi i}{2H}\right)$$

drop out and we are left with

$$S_\infty = \sum_{j=1}^{4} \sqrt{2}\sin(j\pi/2 - \pi/4)\frac{1}{2\pi i}\int_{C_2} g(r^2+\omega^2) \cdot \left\{\frac{1}{\omega-\omega_j} - \frac{\pi i/H}{e^{i\pi/H(\omega-\omega_j)} - 1}\right\}d\omega. \quad (20)$$

The second term in the integrand of (20) has simple poles at $\omega = 2nH + \omega_j$, $n = 0, \pm 1, \pm 2, \pm 3, \cdots$, and the residue at the poles is unity. As a consequence of Mittag-Leffler's theorem,[8] (20) can be written as

$$S_\infty = \sqrt{2}\sum_{j=1}^{4}\sin(j\pi/2 - \pi/4)\frac{1}{2\pi i}\int_{C_2}\frac{e^{-ik\sqrt{r^2+\omega^2}}}{\sqrt{r^2+\omega^2}} \cdot \sum_{-\infty}^{\infty}{}'\frac{1}{\omega - (2nH+\omega_j)}d\omega \quad (21)$$

and the integral is readily evaluated when the contour C_2 is closed properly and when the poles it contains are specified. The contour C_2 can be closed by the point at infinity when the one-valuedness of the integrand of (21) is established and when the conditions for convergence are laid out. Single-valuedness of the integrand can be retained by noting a second branch cut[8] from $\omega = +ir$ to $\omega = \infty$. Convergence of the integral is established by considering the behavior of $e^{-ik\sqrt{r^2+\omega^2}}$ as $|\omega| \to \infty$. These considerations lead to the selection of a contour as shown in Fig. 2 below. The second branch cut is drawn

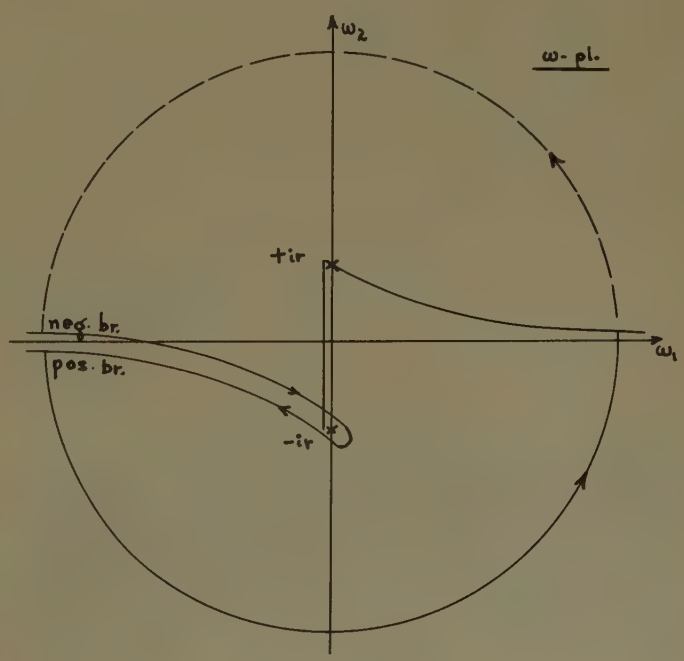

Fig. 2.

[8] K. Knopp, "Theory of Functions, Part II," Dover Publishing Co., New York, N. Y., pp. 34–57, 112–118; 1947.

asymptotic to an axis separating the half-planes of convergence and nonconvergence; on each sheet of the two sheeted Riemann surface, the integral is convergent in only *one* half-plane. The orientation of these half-planes is determined by the value of k. In the problem at hand, k has been assumed to be real; so that the axis of separation corresponds to the real axis.

Now that the contour is closed, the integral can be evaluated. Around the point at infinity (taken in the proper half-planes), no contribution is realized as a consequence of Jordan's Lemma,[9] hence the value of the integral is $2\pi i$ times the sum of the residues of the poles enclosed by the contour.

The result is easily shown to be given by

$$S_\infty = \sum_{n=1}^{\infty} g[r^2 + (2nH + h - z)^2] + \sum_{n=1}^{\infty} g[r^2 + (2nH + z - h)^2] - \sum_{n=1}^{\infty} g[r^2 + (2nH - z - h)^2] - \sum_{n=1}^{\infty} g[r^2 + (2nH + h + z)^2]. \quad (22)$$

Consideration of the remainder term is the last point in the analysis. According to (7), the remainder term is

$$R_n = \frac{1}{(2n)!} \int_0^1 \phi_{2n}(t) \left\{ \sum_{m=0}^{\infty} f^{(2n)}(m + t) \right\} dt. \quad (23)$$

Whittaker and Watson, *op. cit.*, p. 115.

Since each of the integrals $\int \phi_{2n}(t) f^{(2n)}(m+t)dt$ is bounded, passage to the limit $n \to \infty$ yields a zero remainder. The final result of the analysis is thus

$$\Psi = \{g[r^2 + (h - z)^2] - g[r^2 + (h + z)^2] + \sum_{n=1}^{\infty} g[r^2 + (2nH + z - h)^2] + \sum_{n=1}^{\infty} g[r^2 + (2nH + h - z)^2] - \sum_{n-1}^{\infty} g[r^2 + (2nH - h - z)^2] - \sum_{n=1}^{\infty} g[r^2 + (2nH + h + z)^2]. \quad (24)$$

The connection between the mode theory and ray theory solutions has now been clearly established.

Conclusion

Starting out from the mode solution to the parallel-plate boundary-value problem, the ray theory solution has been generated through the use of the Euler-Maclaurin expansion.

The analysis has shown that the success of the transformation method depends on one's ability to find suitable Fourier transforms for the radial and height-functions of the mode solution. The analysis also shows that the method is not as direct as that based on the Poisson summation formula.

Universal Curves for the Vertical Polarization Reflection Coefficient*

GUNNAR P. OHMAN†

Summary—**A set of universal curves is presented by which the approximate magnitude and phase of the reflection coefficient for vertical polarization can be determined at any grazing angle with relatively little computation. The approximation, which is almost always sufficiently accurate for engineering purposes, is excellent if the relative impedance of the reflecting medium is high and still quite good even if the impedance ratio is only moderately greater than unity.**

* Manuscript received by the PGAP, January 24, 1956; revised manuscript recevied July 30, 1956.

† Naval Research Lab., Washington, D. C.

Description of the Universal Curves

THE VOLTAGE reflection coefficient for vertical polarization at a plane interface between two mediums is given by[1]

$$R_v/\phi_v = \frac{\eta^2 \sin\psi - \sqrt{\eta^2 - \cos^2\psi}}{\eta^2 \sin\psi + \sqrt{\eta^2 - \cos^2\psi}}, \quad (1)$$

[1] See, for example, H. R. Reed and C. M. Russell, "UHF Propagation," John Wiley and Sons, Inc., New York, N. Y., p. 90; 1953.

where ψ is the grazing angle, and η is the ratio of the intrinsic impedances of the two mediums, and is given by,[2]

$$\eta^2 = \epsilon_r - jX = \frac{(\epsilon_2 - j\sigma_2/\omega)\mu_1}{(\epsilon_1 - j\sigma_1/\omega)\mu_2}. \tag{2}$$

For the important case of reflection of a ray in air by the earth's surface, ϵ_r is merely the dielectric constant of the earth (air taken as unity), and $X = 60\sigma_2\lambda$ (rationalized mks units).

The calculation of the reflection coefficient by (1) is fairly laborious especially when η^2 is a complex number. It is the purpose of this article to present a set of universal curves by which the reflection coefficient can be found with relatively little computation, although at the expense of some, usually negligibly small, theoretical inaccuracy. The derivation of these curves is based on an approximation which sets the quantity, $\sqrt{\eta^2 - \cos^2\psi}$, equal to the constant, $\sqrt{\eta^2 - \cos^2\psi_{90}}$, where ψ_{90} is the grazing angle at which the phase of the reflection coefficient is $-90°$. With this approximation the magnitude and phase of the reflection coefficient are given respectively by

$$R_v \doteq \sqrt{\frac{(1-\rho)^2 + R_{90}^2(1+\rho)^2}{(1+\rho)^2 + R_{90}^2(1-\rho)^2}}, \tag{3}$$

and

$$\phi_v \doteq \tan^{-1}\frac{-4\rho R_{90}}{(\rho^2 - 1)(1 + R_{90}^2)}, \tag{4}$$

where R_{90} is the magnitude of the reflection coefficient when $\psi = \psi_{90}$, and $\rho = \sin\psi/\sin\psi_{90}$, a dimensionless parameter. Eqs. (3) and (4) are plotted as families of curves in Figs. 1(b) and 1(c) (next page) respectively.

Before these curves can be used to find the reflection coefficient, both ψ_{90} and R_{90} must be determined. Formulas for these quantities, which can be derived by setting the real part of (1) equal to zero, are

$$\psi_{90} = \cos^{-1}\sqrt{\frac{|\eta|^8 - \epsilon_r - \sqrt{(|\eta|^8 - \epsilon_r)^2 - (|\eta|^8 - 1)(|\eta|^8 - |\eta|^4)}}{|\eta|^8 - 1}}, \tag{5}$$

and

$$R_{90} = \tan\frac{1}{4}\left(2\tan^{-1}\frac{X}{\epsilon_r} - \tan^{-1}\frac{X}{\epsilon_r - \cos^2\psi_{90}}\right). \tag{6}$$

In order to permit graphical determination, curves of constant ψ_{90} and R_{90} are plotted vs ϵ_r and X in Fig. 1(a). When η^2 lies outside of the range of Fig. 1(a), the following simple, approximate formulas may be used; *i.e.*, when $|\eta|^2 \gg 1$,

$$\psi_{90} \doteq \cot^{-1}\sqrt{\epsilon_r^2 + X^2} \tag{7}$$

$$R_{90} \doteq \tan\left(\frac{1}{4}\tan^{-1}\frac{X}{\epsilon_r + 1}\right). \tag{8}$$

Use of the Curves

When the parameters ϵ_r and X are known, Figs. 1(a), 1(b), and 1(c) may be used to determine the approximate magnitude and phase of the reflection coefficient at any grazing angle. The procedure is as follows:

1) Read R_{90} and ψ_{90} vs ϵ_r and X on Fig. 1(a).
2) Calculate $\rho = \sin\psi/\sin\psi_{90}$ or the reciprocal if greater than 1.
3) On Figs. 1(b) and 1(c) read the magnitude and phase of the reflection coefficient corresponding to the value of R_{90} found on Fig. 1(a) and the calculated value of ρ or its reciprocal.

As numerical examples the reflection coefficient will be found at $\psi = 14.48°$ and $\psi = 33.8°$ for the specific case of $\epsilon_r = 2$ and $X = 3$ by the procedure outlined.

1) R_{90} is read as 0.200, and ψ_{90} as 30.00° on Fig. 1(a).
2) For $\psi = 14.48°$ $\rho = \sin 14.48°/\sin 30.00° = 0.500$, and for $\psi = 33.8°$ $\rho = \sin 33.8°/\sin 30.00° = 1.111$, and $1/\rho = 0.900$.
3) Using the curves marked $R_{90} = 0.200$ on Figs. 1(b) and 1(c), the reflection coefficient at $\psi = 14.48°$ ($\rho = 0.500$) is found to be $0.388/\underline{-152.85°}$, and at $\psi = 33.8°$ ($1/\rho = 0.900$), $0.207/\underline{-74.65°}$.

Although not required in these examples, interpolation between curves will generally be necessary.

Accuracy

To illustrate the accuracy possible with the universal curves, the reflection coefficient has been calculated exactly (1) for three different values of η^2 and the results are compared with those obtained using the approximate formulas (3) and (4) on which the universal curves are based. These values are $\eta^2 = 2 - j3$ ($R_{90} = 0.200$, $\psi_{90} = 30.00°$), $8 - j1.849$ ($R_{90} = 0.050$, $\psi_{90} = 19.27°$), and $32 - j13.92$, ($R_{90} = 0.100$, $\psi_{90} = 9.61°$), and the results are compared in Fig. 2. The phase calculations are compared only for the first case because the difference is too small to be shown conveniently in the last two.

Fig. 2 shows that the over-all accuracy of the universal curves improves as η^2 is taken larger, and that the maximum error occurs at $\psi = 90°$ in each case. It will be found that the error here is largely one of magnitude, being too high, if ϵ_r is much larger than X, and in phase, phase lag being too small, if the opposite is true. At $\psi = 0$ and $\psi = \psi_{90}$ the error is zero, and, unless η^2 is very small,

[2] *Ibid.*, p. 86.

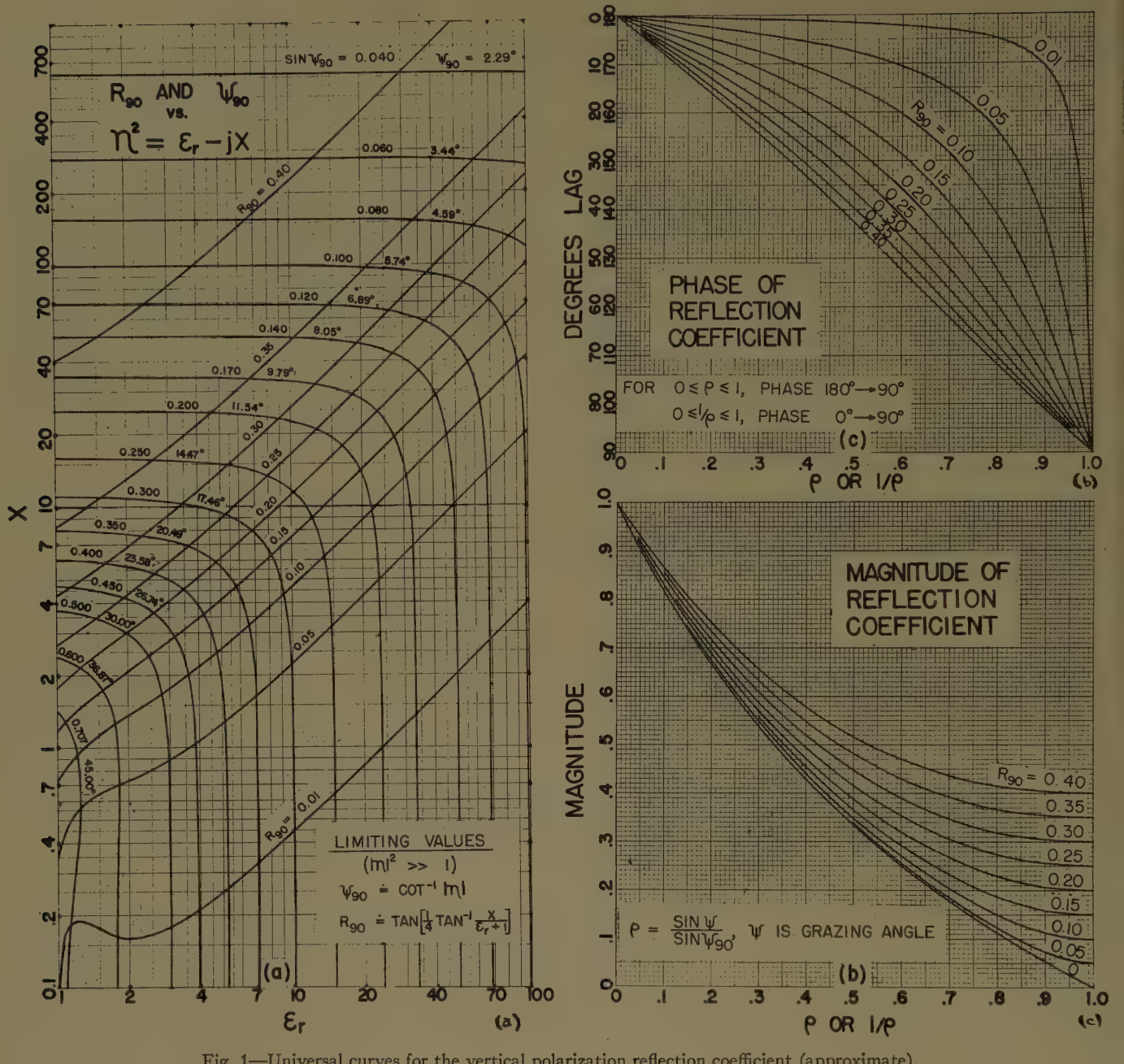

Fig. 1—Universal curves for the vertical polarization reflection coefficient (approximate).

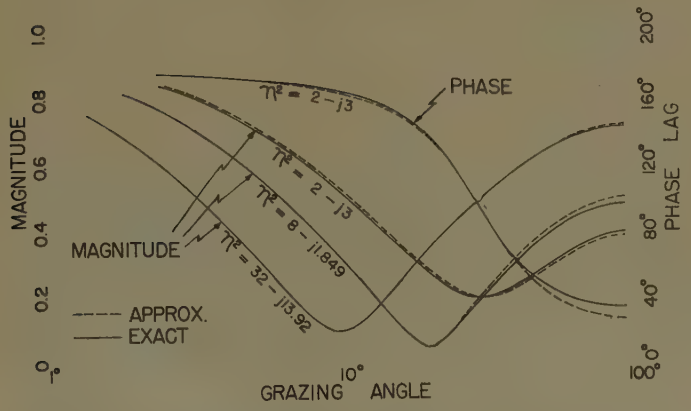

Fig. 2—Reflection coefficient calculated by the exact and approximate formulas.

the error at intermediate grazing angles should be completely negligible. The approximation made in deriving these curves insures high accuracy in the vicinity of the grazing angle corresponding to the magnitude minimum since it is known that this occurs very close to ψ_{90}, especially if η^2 is large.

In general these universal curves will furnish a good over-all approximation to the reflection coefficient for vertical polarization whenever sin ψ_{90} is less than 0.5, and an excellent one if it is less than 0.3, provided that ϵ_r is at least 2 in both cases. If X is very large, the restriction on ϵ_r may be relaxed some. Rarely are ϵ_r and X known with sufficient certainty to justify a more accurate computation.

communications

Aircraft Telemetry Antenna*

FRANK E. BUTTERFIELD†

AN ALTERNATIVE to the Angle of Attack Indicator Antenna of Anderson, Dorrenbacher, Krausz, and Margerum[1] should not go unmentioned. The directivity in the aft direction, illustrated in the lefthand portion of their Fig. 2, is, of course, a consequence of the traveling wave or quadrature portion of the currents flowing on the aircraft fuselage. These currents become important for large diameter conductors. Consider the continuity of current required at the quarter-wave stub feed point, as illustrated in Fig. 1.

I_a, antenna current, must equal I_f, fuselage current. I_a is a maximum at the feed point for stub length $l=\lambda/4$. I_a, and hence, I_f, can be reduced by making $l=\lambda/2$ as shown in Fig. 2. This technique has been used with precisely the result illustrated in Fig. 2 of Anderson, *et al.*

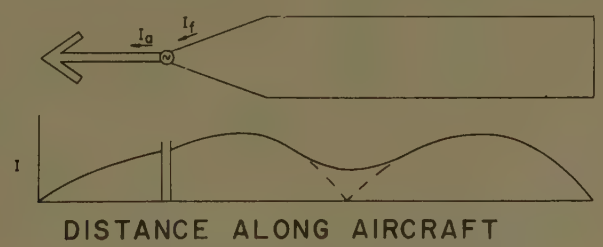

Fig. 1—Currents on antenna and fuselage for quarter-wave radiator.

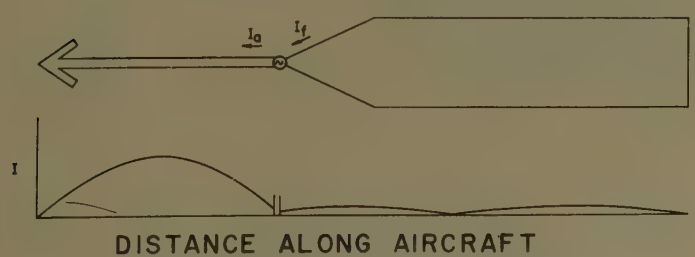

Fig. 2—Currents on antenna and fuselage for half-wave radiator.

Furthermore, the half-wave radiator may be shunt fed, providing a solid metallic path from fuselage to radiator requiring no isolating chokes for instrument wiring.

* Received by the PGAP, May 27, 1956.
† Sylvania Elec. Products, Inc., Mountain View, Calif.
[1] R. E. Anderson, C. J. Dorrenbacher, R. Krausz, and D. L. Margerum, "A multiple telemetering antenna system for supersonic aircraft," IRE TRANS., vol. AP-3, pp. 173–176; October, 1955.

The Optimum Aperture Function in a Long Array*

GLENDON C. McCORMICK†

A UNIFORM amplitude distribution over an aperture, assuming phase constancy, produces the maximum gain. This familiar fact is slightly modified in a very long linear array where ohmic losses are significant. In a linear array fed from a transmission line carrying a traveling wave; *e.g.*, in the slotted waveguide array, let the power radiated by the rth slot be e_r. It can usually be justified physically that

$$e_r = kf_r^2 \tag{1}$$

where f_r is the magnitude of the amplitude function and k is a constant. Then the total power radiated, P, is given by

$$P = k \sum_1^N f_r^2. \tag{2}$$

It is readily shown that

$$k = \frac{1 - P_L \exp\left[(N-1)\beta\right]}{\sum_1^N f_r^2 \exp\left[(r-1)\beta\right]} \tag{3}$$

where P_L is the fractional power left over, N the total number of elements, $\beta = 0.230\,\alpha d$, where d is the spacing between elements, and α the attenuation in the line in decibels per unit length.

The power gain of the array is proportional to NP. Replacing the summations by the equivalent integrals

$$NP = \frac{N\left\{1 - P_L \exp\left[(N-1)\beta\right]\right\} \int_{-1}^{1} f^2(x)\,dx}{\exp\left[(N/2-1)\beta\right] \int_{-1}^{1} f^2(x) \exp\left(\frac{Nx\beta}{2}\right) dx}. \tag{4}$$

For given P_L and f there is an optimum value of N to produce the maximum gain, obtained by differentiating the above expression. It follows that optimum N is obtained from the solution of the equation

$$1/t - \coth(a - t) = \frac{\int_{-1}^{1} xf^2 \exp(tx)\,dx}{\int_{-1}^{1} f^2 \exp(tx)\,dx} \tag{5}$$

where $t = \beta N/2$, $a = \frac{1}{2}(\beta - \log_e P_L)$.

A similar result for a uniform aperture distribution has been obtained by Gruenberg.[1]

A related problem is to find the optimum function f_r for maximum gain for a given N and P_L. If the aperture phase varies linearly, the gain will be a maximum, subject to (3), for

$$\sum_1^N f_r = \text{maximum}. \tag{6}$$

Applying Lagrange's method of undetermined multipliers

$$\sum_1^N \delta f_r = 0$$

$$\sum_1^N f_r \exp(r\beta)\delta f_r = 0$$

from which

$$f_r \exp(r\beta) = \lambda$$

$$f_r = \lambda \exp(-r\beta) \tag{7a}$$

and for the corresponding continuous distribution

$$f(x) = \lambda' \exp(-tx). \tag{7b}$$

The maximum signal is proportional to

$$k^{1/2} \sum_1^N f_r.$$

Therefore, the gain of the optimum distribution in comparison with that of a uniform distribution is given by

$$\frac{G_{\text{opt}}}{G_{\text{unif}}} = \frac{k_{\text{opt}}}{k_{\text{unif}}} \left\{ \sum_1^N \exp(-r\beta) \right\}^2 \Big/ N^2$$

and it follows readily that

$$\frac{G_{\text{opt}}}{G_{\text{unif}}} = \left(\frac{\sinh t}{t}\right)^2. \tag{8}$$

The solution of (5) for the optimum function gives

$$t_{\text{opt}} = a/2 \tag{9}$$

or since $t = 1/20 \log_e 10\,\alpha l$, where l is the total length of the array,

$$l_{\text{opt}} \approx -\frac{5}{\alpha} \log_{10} P_L. \tag{10}$$

* Received by the PGAP, April 3, 1956.
† Radio and Elec. Eng. Div., Natl. Res. Council, Ottawa, Canada.

[1] H. Gruenberg, "A waveguide array for solar noise studies," IRE TRANS., vol. AP-3, pp. 147–152; October, 1954.

Taking $P_L=0.05$ and substituting the values of α for standard waveguide, l_{opt} has the following values:

S band (brass)	540 feet
X band (aluminum)	145 feet
K band (silver)	54 feet.

These lengths can be regarded as the limit beyond which no increase in gain is possible. It is obvious that they are only of interest in radio astronomy.

Since $t_{opt}=0.75$ for $P_L=0.05$, it is evident from (8) that the distribution, (7), could result in a significant improvement of gain for a very long array, but the effect is negligible for arrays the length of which is not extraordinary. The asymmetrical distribution causes an increase in side-lobe level, as shown in Fig. 1.

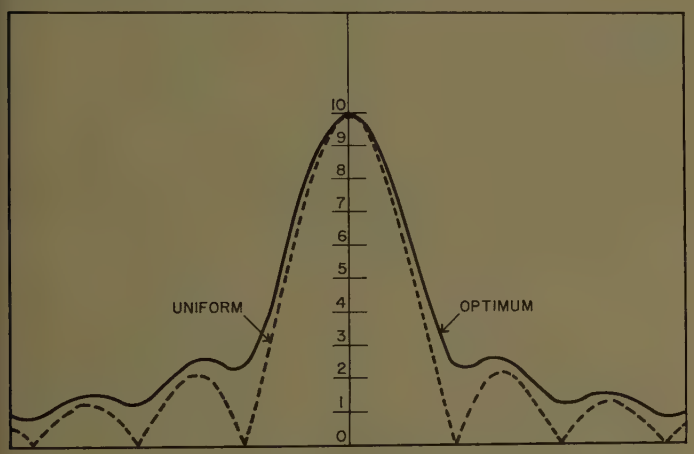

Fig. 1—Amplitude pattern of optimum aperture function, $P_L=0.05$. Pattern of uniform distribution (- - - -) shown for comparison.

If it is required that the optimum aperture function be symmetrical, an additional restraint is imposed. The same procedure as before leads to

$$f_r = \lambda \operatorname{sech}\left(\frac{N\beta}{2} - r\beta\right) \tag{11a}$$

or

$$f(x) = \lambda' \operatorname{sech} tx. \tag{11b}$$

Eq. (11a), when substituted in (5), gives

$$\coth (a - t) = \frac{\operatorname{sech} t}{gd\, t} \tag{12}$$

where $gd\, t = 2 \tan^{-1} \exp(t) - \pi/2$, while the corresponding equation for the uniform distribution is

$$\coth (a - t) = 2/t - \coth t. \tag{13}$$

The solutions of (9), (12), and (13) are plotted as a function of a in Fig. 2.

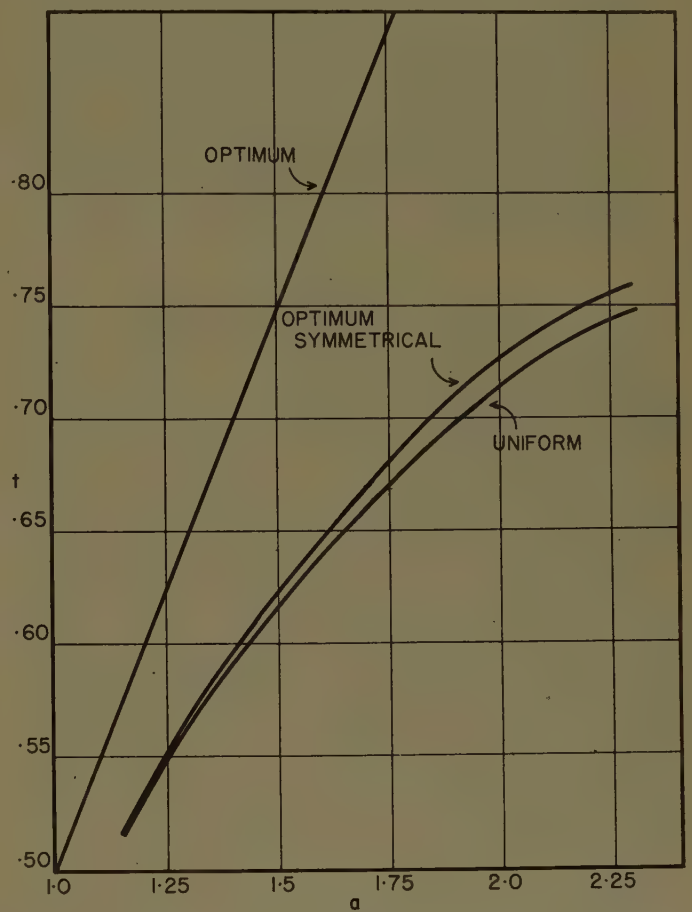

Fig. 2—Curves for the determination of optimum length for particular aperture functions, $t=0.115\, l_{opt}$; $a \approx -\frac{1}{2} \log_e P_L$.

The symmetrical distribution, (11), produces a negligible improvement in gain, even at $t=0.7$ (0.2 per cent), while the side-lobe level of the pattern is slightly reduced, to about 18 per cent.

The writer is indebted to Dr. H. Gruenberg for pointing out two errors in the original manuscript, and for several interesting discussions thereof.

Variational Principles for Electromagnetic Resonators and Waveguides*

VICTOR H. RUMSEY†

I READ THE above paper[1] by A. D. Berk with interest and appreciation, but I think I should point out that the reaction concept does give "variational" formulas when applied to the general anisotropic problem. Indeed, variational solutions to all of the problems considered by Dr. Berk are represented by the general equation[1]

$$\langle aa \rangle = 0 \tag{1}$$

which, in addition, applies to the general lossy case.

Since the familiar reciprocity theorem does not apply to an arbitrary anisotropic medium, it is natural to assume that the reaction concept is restricted to isotropic media. This is not so, as I pointed out in the original articles,[2] but since I have met several people who are under this impression, it may be worthwhile to demonstrate as an example the variational properties of (1) for the cavity resonance problem considered by Dr. Berk. The reader is referred to Berk[1] for a description of the problem and the notation.

We note that the self reaction $\langle aa \rangle$ is a function of frequency ω and the approximate frequency at resonance is the particular value of ω for which $\langle aa \rangle$ vanishes. Let a and b represent two different assumed distributions and let ω_a and ω_b represent the approximate frequencies at resonance calculated from a and b by using (1). Let the subscript ω_a or ω_b denote the frequency at which a typical reaction is evaluated. Thus

$$\langle aa \rangle_{\omega_a} = 0 \tag{2}$$

$$\langle bb \rangle_{\omega_b} = 0. \tag{3}$$

Now suppose that b differs slightly from a, *i.e.*, b is a slight variation of a. Then ω_b will differ slightly from ω_a, (assuming $\langle aa \rangle$ to be a continuous function of ω). Thus

$$0 = \langle bb \rangle_{\omega_b} = \langle bb \rangle_{\omega_a} + (\omega_b - \omega_a) \frac{\partial}{\partial \omega} \langle bb \rangle \Big|_{\omega=\omega_a} + \text{higher terms} \tag{4}$$

and

$$\begin{aligned} \langle bb \rangle_{\omega_a} &= \langle aa \rangle_{\omega_a} + \langle (b-a), a \rangle_{\omega_a} + \langle a, (b-a) \rangle_{\omega_a} \\ &\quad + \langle (b-a), (b-a) \rangle_{\omega_a} \\ &= \langle a, (b-a) \rangle_{\omega_a} + \langle (b-a), a \rangle_{\omega_a} + \text{higher terms.} \end{aligned} \tag{5}$$

Now let a represent the correct distribution, so that ω_a is the correct frequency at resonance. Then since the correct solution at resonance is source-free

$$\langle ax \rangle_{\omega_a} = 0 \quad \text{and} \quad \langle xa \rangle_{\omega_a} = 0 \tag{6}$$

for any test source x. It follows from (5) that $\langle bb \rangle_{\omega_a} = 0$ and therefore, from (4), $(\omega_b - \omega_a)$ is of the second order provided $(\partial/\partial\omega)\langle bb \rangle|_{\omega=\omega_a}$ is not zero. This proof applies to anisotropic media because we have preserved the order of the two symbols xy in the typical reaction $\langle xy \rangle$, *i.e.*, we have not assumed $\langle xy \rangle = \langle yx \rangle$. Indeed, it might appear to the uninitiated that the proof rests simply on a baffling notation, without depending on Maxwell's equations or any electromagnetic theory. Actually (6) implicitly depends on the generalized reciprocity theorem for anisotropic media,[2] and consequently the proof hinges on this theorem.

Having made my point let me say that its significance might well be questioned because, in practice, we usually have no assurance that the assumed distribution is close to correct. As Dr. Berk emphasizes, the practical success of the formulas depends overwhelmingly on the assumed distribution.

* Received by the PGAP, June 22, 1956.
† University of Illinois, Urbana, Ill.
[1] IRE TRANS., vol. AP-4, pp. 104–111; April, 1956.
[2] V. H. Rumsey, "Reaction concept in electromagnetic theory," *Phys. Rev.*, vol. 94, pp. 1483–1491; June, 1954; and vol. 95, p. 1705; September, 1954.

Symposium on Present and Future Uses of Refractive Index Data for Radio Propagation Purposes*

L. J. ANDERSON†

ON SEPTEMBER 6 and 7, 1956, a symposium was convened at Lexington, Mass., on "Present and Future Uses of Refractive Index Data for Radio Propagation Purposes." The symposium was sponsored by Commission II of URSI, and the host agencies were the Air Force Cambridge Research Center and the Lincoln Laboratories of Massachusetts Institute of Technology. The objectives of these meetings were:

1) To acquaint the numerous groups using routine weather and refractometer data for propagation purposes with the progress made by the other groups in the field;
2) to outline the areas in which weather data has been reduced to refractive index;
3) to specify the limitations of refractive index data as imposed by measuring and processing techniques;
4) to acquaint the data users and data suppliers with each other's needs and problems.

The agencies represented were:

Air Force Cambridge Research Center
Lincoln Laboratories, M.I.T.
Air Weather Service
Army Electronic Proving Ground
Bell Telephone Laboratories
Central Radio Propagation Laboratory
Cornell University
Ent Air Force Base
Evans Signal Laboratory, SCEL
Fourth Weather Group, Air Research and Development Command, Baltimore
Johns Hopkins University
National Weather Records Center
Radio Meteorological Section, SCEL
Rome Air Development Center
Signal Corps Radio Propagation Agency
Smyth Research Associates
University of Texas, EERL
U. S. Navy Electronics Laboratory
Wright Air Development Center.

The first day's sessions were held at AFCRC, with Dr. Philip Newman acting as Chairman. They were devoted to the presentation of descriptive papers on tropospheric refraction, ducting, scattering, and radio meteorology. The second day's sessions were held at the Lincoln Laboratories and were moderated by J. H. Chisholm. The data-supplying agencies described the nature and extent of their data and its limitations. Service representatives then described their future requirements in the field of propagation predictions. The afternoon session was an informal discussion concerned with the coordination and implementation of the future programs. One topic of considerable interest was the establishment of a central repository for refractometer data, which are being collected in increasing volume. The University of Texas group offered to serve in this capacity and suggested the form in which such data should be forwarded to their file. The purpose of such an agency would be to serve as a source of refractometer data for any one having a need for it. The data would be supplied for the cost of reproduction and would be in unanalyzed form.

It was felt by all attendees that the meetings were very worthwhile and adequately fulfilled the objectives set up. Both host agencies are to be commended on the arrangements and the facilities provided.

* Manuscript received by the PGAP, November 15, 1956.
† Smyth Research Associates, San Diego, Calif.

Abstracts of Papers From the IRE-URSI Symposium Held April 30, May 1-3, 1956—Washington, D. C.

Applications of the Reaction Concept—V. H. Rumsey, *University of Illinois**—This paper is an extension of the author's article in *Physical Review*, vol. 94, pp. 1483–91, June, 1954 which included applications to calculations of impedance, scattering coefficients, etc. The first aim of this paper is to show in a more general manner how the reaction concept provides a simple technique for analyzing any practical measurement of the effects associated with electromagnetic waves. The second aim is to present a new class of applications which gives approximate formulas for the parameters of antennas, waveguides, etc., based on assumed distributions, as hitherto, but requiring less algebraic and computational labor.

Five Years of 21 CM Research—Bart J. Bok, *Harvard Observatory*—On March 25, 1951, Ewen and Purcell succeeded for the first time in the detection of 21 cm radiation from interstellar neutral atomic hydrogen. In the brief interval of five years that has elapsed since that discovery, 21 cm research has become one of the most effective approaches to the study of our galaxy.

The most spectacular advances have been made in the search for the spiral structure of our galaxy. In this area the Dutch and Australian groups have made a major contribution and detailed studies of the G. R. Agassiz Station of Harvard Observatory and at the Department of Terrestrial Magnetism of the Carnegie Institution are rounding out the preliminary picture. The analysis of the profiles is beset with difficulties since no clear-cut direct distance criteria are available, but, by judicious blending of the analyses in galactic longitude and latitude, the description of the spiral features of our entire galaxy lies within reach. The need must be stressed for related optical studies of associations of blue-white stars of spectral types *O* and *B* and of continued emphasis on optical and radio studies of the distribution function of circular velocity in our galaxy and of peculiar motions in the interstellar neutral atomic hydrogen.

A second important area for 21 cm research is that of astrophysical studies of the interstellar medium. The group at the Naval Research Laboratory has pioneered in the detection and study of absorption features and through this research they are contributing effectively to our knowledge of the cloud structure of the interstellar medium and to the distance measurement of various sources of strong continuous radio radiations. At the G. R. Agassiz Station, astrophysical research in the 21 cm field is being developed along these broad lines.

Firstly, the study of the association of interstellar gas and dust has shown that in most interstellar clouds and complexes neutral atomic hydrogen has a density roughly equal to one hundred times that of the cosmic dust. Secondly, a comprehensive study of the Orion region indicates that neutral atomic hydrogen enevlops most of the spectacular optical features in this section and that this neutral atomic hydrogen plays a critical part in the evolutionary development of these features. Thirdly, we are learning much about the fine structure of the interstellar medium from related radio studies for closely-spaced networks of positions in the sky; notably are we finding out about the extent and masses of the hydrogen clouds.

Finally, we mention briefly the area of extra galactic studies of 21 cm research. Here there is still a great paucity of concrete results, but the field appears critical for the future. The Australian discovery of the 21 cm radiation associated with the Magellanic Clouds was the first major contribution in this area and the recent Naval Research Laboratory observations of an absorption feature originating in the very remote Cygnus source represents another major discovery in this field.

For future 21 cm research we require first of all steerable precision paraboloid antennas with surfaces accurate to within half an inch or so and with the largest attainable apertures. Second, we need a variety of stable electronic equipment, some with very narrow bandwidth—at least to 5 kc/sec—for use in the study of the fine structure of the galactic interstellar medium, others with broad bandwidth adapted especially to the study of weak extragalactic features.

The Great Solar Regions of February 9–24, 1956, and Their Terrestrial Effects—A. H. Shapley, *National Bureau of Standards* and W. O. Roberts, *High Altitude Observatory*—The history of the most active solar regions of the new cycle, which began in 1954, will be presented. Worldwide reports from the cosmic data network have been collated by the joint National Bureau of Standards-High Altitude Observatory group that works together on sun-earth relationships. The biggest spurt of solar activity since the peak of the last solar cycle occurred in an extensive group of active centers 20 degrees north of the solar equator, which passed the east limb between February 9 and February 14. These regions were the source of major activity, including several large solar flares with associated outbursts of solar radio noise. The fastest-moving solar prominence ever detected occurred above this area, at the east solar limb. Sudden ionospheric disturbances of all types and peculiar geomagnetic disturbances were recorded while the regions traversed the solar disk. The largest cosmic ray increase ever recorded was also reported in association with west limb passage of these groups.

The Earth Satellite Program.

1) **Satellites in the IGY**—Lloyd V. Berkner, *Associated Universities, Inc.*

2) **The International Geophysical Year Earth Satellite Program**—Homer E. Newell Jr., *Naval Research Laboratory.*—Present VANGUARD plans call for a sphere at least 20 inches in diameter and weighing 21.5 pounds. The satellites will be launched by means of a three stage rocket from Cape Canaveral, at the Patrick Air Force Base, Florida. It is hoped that an orbit of inclination between 35° and 45° can be achieved, with perigee no less than 200 miles. The VANGUARD satellites will be tracked both optically, and by radio using the Naval Research Laboratory Minitrack system. There are plans to organize the amateur astronomers to aid in the optical tracking program, and to encourage the radio amateurs to participate in the radio tracking of the satellite. Telemetering of measurements will go via the Minitrack rf link. Computing centers will be set up to compute the orbit being followed by the satellite and to analyze the tracking information for geodetic studies and to determine upper air densities. The ephemerides of the satellite will be widely disseminated to permit the various observers around the world to acquire the satellite. The Technical Panel on the Earth Satellite Program, of the U. S. National Committee for IGY, is now considering various proposals and suggestions for experiments, and will select those to be done in the IGY satellites. Typical among those being considered are geodetic studies; determination of upper air densities; measurements of dust and micrometeors in space and their erosive effects upon the surface of a satellite; observation and measurement of the sun's radiation in the ultraviolet and X ray wavelengths, especially in the Lyman alpha region at 1216 A; determination of the amount of hydrogen in interplanetary space by means of the Lyman alpha observations; measurements of the earth's albedo; magnetic field measurement; ionospheric studies; and cosmic ray observations.

Accuracy of Standard Radio Frequencies Received at a Distant Point—Warren C. Stickler, *National Bureau of Standards*—The National Bureau of Standards operates two standard-frequency broadcasting stations. One is located at Beltsville, Maryland, and the other on the island of Maui in the Hawaiian Islands. The frequencies as transmitted are guaranteed accurate to within plus or minus one part in ten to the eighth. However, largely because of the vertical motion of the ionosphere, the accuracy of the received frequencies can not be stipulated, but only estimated. A radio receiving station was established near Boulder, Colorado, for the purpose of evaluating the frequency changes which are introduced between transmitting and receiving point. Limited frequency recording was commenced in November, 1954. Among others, sixteen months of frequency recordings are now available from the WWV 10 mc signal,

* This work was partially supported by Contract AF33(616)-3220.

and some interesting information can be determined from these records. A brief discussion of the station, the circuitry in use, and equipment in operation to date will be presented. Specific examples of frequency records will be shown and discussed. Plans for the future will be mentioned briefly.

A New Method of Measuring Microwave Pulse Power—Harold A. Thomas, *National Bureau of Standards*—The theory and preliminary results of a proposed new method of measuring microwave pulse power will be discussed. An electron beam is passed through a waveguide parallel to the E field produced by the microwave power flowing in the fundamental mode. The dc accelerating potential of the beam is adjusted so that the transit time of the electrons crossing the guide is n half cycles of the microwave frequency where n is an odd integer. Electrons entering in the favorable phase gain an amount of energy proportional to the field intensity and involving only other easily determined quantities. A retarding potential method is used to measure the increase in energy of the electrons and thus the field intensity in the guide is determined by means of a dc potential measurement. The power flowing in the guide can then be calculated from the field intensity by means of the Poynting vector. Some of the accuracy limitations and uncertainties will be discussed and also mention will be made of other applications of this principle to coaxial power and vhf potential measurements.

Method for Accurate Measurement of Antenna Gains—H. V. Cottony, *National Bureau of Standards*—Critical examination and comparison of antenna gains encountered in technical literature sometimes reveals discrepancies and suspected inaccuracies of the order of several decibels. Experimentation with scaled model antennas for vhf scatter propagation led to the adoption of techniques which resulted in consistent and reproduceable measurements of gain in the frequency band of 300–400 mc. The practices include the use of a transfer reference antenna, half-wave dipole as a standard for calibration of the reference antenna, and a technique for correcting for reflections from terrain irregularities. The equipment used is briefly described. A standard antenna with a computed gain of 9.36 decibels was measured at various times with the average discrepancy of approximately 0.06 decibels. Construction of balun transformer is discussed. A comparison is made with the gains obtained by alternate methods.

Advances in the Design and Application of the Radio-Frequency Permeameter—Alvin L. Rasmussen, Albert W. Enfield, and Alfred E. Hess, *National Bureau of Standards*—Improvements are described for increasing the frequency coverage, accuracy, and ease of application of the radio-frequency permeameter developed at the National Bureau of Standards to measure initial complex permeability of toroidally shaped ferromagnetic materials of low conductivity. The rf permeameter is an impedance transformer, the primary of which is wound on a powdered iron toroid. The secondary is a shorting enclosure or section of coaxial line which envelops both the primary and the toroidal test sample. Removable primaries have several inductances so that they are usable for measuring a wide range of permeabilities from 0.05 to 50 megacycles. A miniature oven is inserted in the secondary for temperature dependence measurements. A dc field applied parallel to the rf field in the secondary is used in measuring parallel reversible premeability. Calibration is accomplished through the use of a transfer permeability standard.

The Impedance of a Coil Near a Conductor—D. L. Waidelich and C. J. Renken, Jr., *University of Missouri**—The results are given of experiments undertaken to determine the manner in which the apparent inductance and resistance of an alternating current coil changes when it is brought near a plate of nonferrous metal. An approximate theoretical analysis of the situation is included which gives good results when the distance between the metal and coil is more than ten per cent of the coil diameter. Most of the results are given graphically and give the change of coil inductance and resistance as functions of distance from coil to metal, frequency, metal conductivity, and a combination of two dissimilar metals, one upon the other. Suggestions as to possible uses of this information in the instrumentation field are included.

A Theory of Ionosphere Forward Scatter Scaling Laws—A. D. Wheelon, *Ramo-Wooldridge Corporation*—The weak and fluctuating field strengths observed over very long distances at vhf are here attributed to scattering from E region turbulence. An earlier phenomenological model used to explain qualitatively the frequency and scattering angle dependence of this propagation† is refined by extending the hydrodynamical theory of homogenous turbulence proposed by Villars and Weisskopf. One finds that the propagation constants $q=4\pi/\lambda \sin(\theta/2)$ corresponding to the experimental band 30 to 108 mc just straddle the "smallest blob" cutoff $K_s=2\pi/l_s \approx$ (2 meters)$^{-1}$ of the E region. Numerical integration of the turbulence theory is used to determine the correlation of dielectric fluctuations at small separations and from it, the scattering cross section, which is found to change its *character* rapidly within the above band. Refractive corrections to the scattering are included and give interesting modifications to the scattering when the transmitter frequency ($\omega > 28$ mc) is not too far above the maximum usable frequency for the path. Corresponding power ratios amongst the 28, 49, and 108 mc transmissions exhibit frequency dependences in excellent agreement with the measurements of Bailey, Bateman, and Kirby‡ at NBS, if one chooses the single arbitrary constant $K_s \approx 1/2m$. The variation of signal level with scattering angle θ is calculated for 49 mc and also found to be in accord with NBS data. Explanations for the diurnal and seasonal variations of the exponents which occur in these scaling laws are given.

Oblique Incidence Radio Observations of Meteor Trails—G. R. Sugar, *National Bureau of Standards*—An experiment was performed at 49.8 mc over two 1240 km paths to examine some of the characteristics of radio reflections from meteor trails. The experiment, utilizing the highly directive antennas and other apparatus set up for the Carysbrook investigations,* compared the numbers and durations of meteor trail reflections observed at two receiving locations during the same time interval. These locations were chosen such that the transmitting and receiving antenna beams for the first receiver intersected over the midpoint of the great circle path from transmitter to receiver whereas for the second receiver the antenna beams intersected at a point seven degrees off the great circle path. The system sensitivity was such that the meteor trails observed had minimum electron line densities of 10^{12} electrons per meter.

It was found that the number of trails observed at the second location was 3.5 times that observed at the first location. The average duration of the reflections observed at the second location was 0.5 times that observed at the first location. The results appear to be, in general, consistent with those which would be predicted from the theory of meteor trail reflections described by Eshleman and Manning.†

Some Comments on the Specular Meteoric Theory of Ionospheric Scatter-Transmission‡—H. G. Booker, *School of Electrical Engineering, Cornell University*—Two theories have been proposed to explain the experiments of Bailey *et alia*§ on 50 mc between Cedar Rapids (Iowa) and Sterling (Virginia):

1) According to Bailey *et alia*[1] the transmission is due to scattering by irregularities in electron-density caused by atmospheric turbulence. The ionization rendered irregular in this way could be produced by ultra violet light, by protons, by meteors, or in any other way.

2) According to Eshleman and Manning‖ the transmission is entirely due to specular reflection from meteor trails that have not been affected by atmospheric turbulence, and no other source of ionization is involved.

McKinley** has drawn attention to the importance of assessing the contribution of meteoric ionization to scatter-transmission by converting radar data concerning meteors. There is a Martyn's type theorem for this problem according to which scattering at frequency f at an angle θ to the forward direction is related to backscattering at frequency $f \sin \theta/2$. From this theorem it follows that scatter-transmission at 50 mc from Cedar Rapids to Sterling is to be deduced from radar observations at about 10 mc. McKinley did not have radar data available at this frequency, but presented

* This work was completed under Contract No. ANL-31-109-38-575 with the Argonne Nat. Lab.

† A. D. Wheelon, "Note on scatter propagation with a modified exponential correlation," PROC. IRE, vol. 43, pp. 1381–1383; October, 1955.

‡ D. K. Bailey, R. Bateman, and R. C. Kirby, "Radio transmission at vhf by scattering and other processes in the lower ionosphere," PROC. IRE, vol. 43, pp. 1220–1221; October, 1955.

* A. D. Wheelon, "Note on scatter propagation with a modified exponential correlation," PROC. IRE, vol. 43, pp. 1381–1383; October, 1955.

† V. R. Eshleman and L. A. Manning, "Radio communication by scattering from meteoric ionization," PROC. IRE, vol. 42, pp. 530–536; March, 1954.

‡ This research was supported by U. S. Signal Corps Contract DA36-039-sc-56748.

§ Bailey, Bateman, Berkner, Booker, Montgomery, Purcell, Salisbury and Weisner, *Phys. Rev.*, vol. 86, p. 141; 1952.

‖ V. R. Eshleman and L. A. Manning, "Radio communication by scattering from meteoric ionization," PROC. IRE, vol. 42, pp. 530–536; March, 1954.

** McKinley, *Can. J. Phys.*, vol. 32, p. 450; 1954.

data for the vhf band from which a reasonable extrapolation to 10 mc is possible. Operating in this way on McKinley's Table VIII, it follows that the background signal of scatter-transmission cannot be explained in terms of short-duration meteor-echoes having no irregular fading but might be explained in terms of long-duration meteor-echoes lasting more than a second. The latter however are the irregularly fading meteor-echoes that have to be explained by the effect on the trail produced by atmospheric turbulence as explained in another paper.* It follows therefore from McKinley's data that if meteoric ionization makes a substantial contribution to the background signal in scatter-transmission, as it probably does at night, it does so via the long-duration category of meteor-reflections whose effect has to be calculated by a theory of type 1) and not by one of type 2).

Ionospheric Motions Observed on High-Frequency Backscatter Soundings—L. H. Tveten, *National Bureau of Standards*—Range-time records of F_2 propagated backscatter signals often show a pattern of well-defined, regularly-spaced striations representing the effect of focusing regions, which change their range as a function of time. In a study of many of these records it appeared that the observed pattern was usually a result of motions in the reflecting F_2 region.

A simple expression for the speed of motion is given as a function of the time rate of change of the range of the striations, which can be scaled directly from the records. Wavelengths of ionospheric ripples can also be deduced from scaled data. In general, only components of velocity and wavelength can be scaled, using a single antenna orientation. Measurements in more than one direction or from more than one point should yield enough information to enable values of velocity and wavelength to be obtained.

Components of ionospheric motion were measured along azimuth 150° from Sterling, Virginia. The mean component thus measured for December, 1952 agreed approximately with that observed during the same month, in the same quadrant, in a vertical-incidence experiment near Harvard University.

The records showed few periods of apparently little or no motion. Some records were characterized by striations suggesting motion in more than one direction at the same time and others by fixed-range striations.

Some Direction-Finding Observations on Traveling Ripples in the Ionosphere—W. J. Ross, *Ionosphere Research Laboratory, Pennsylvania State University*†—An account is given of some continuous wave direction-finding measurements made in New Zealand in the high frequency range over a 2600 kilometer East-West path using a new type of direction-finder. Several records taken show a distinct periodic variation in azimuth of the incoming wave direction, of quasi-triangular form with period about two minutes and amplitude a few degrees. These fluctuations have been interpreted as arising from traveling ripples in the ionosphere. The calculated wavelengths and amplitudes of these ripples are found to agree fairly well with the values found by other workers, but the periodicities are smaller and the calculated velocities (about 100 km/min) much larger than have been found elsewhere. These results and a tentative identification of the ripples as compressional waves in region F are discussed briefly.

Methods of Analyzing Fading Records From Spaced Receivers*—G. S. Sales, *Ionosphere Research Laboratory, Pennsylvania State University*—This paper is based on a report by Dr. R. B. Banerji of the above laboratory.

An examination is made of methods of analysis of drift records at three spaced receivers. The interrelation between various methods of drift measurement is discussed, and a comparison made of the amounts of data and computation required. The effectiveness of the methods in taking into account random motions superposed on steady drifts, and anisotrophy, is also dealt with. The Putter† method is extended to include the case of random motion.

Some experimental results on the fading of 75 kc waves are summarized briefly.

Fading of Low Frequencies and the Double Gaussian Correlogram‡—S. A. Bowhill, *Ionosphere Reesarch Laboratory, Pennsylvania State University*—The fading of radio waves can be studied in two ways: by its structure in time or in space. The temporal and spatial correlograms for a randomly fading signal are frequently found to be Gaussian in form, and it is possible to define a structure size and a fading time as the characteristic widths of these correlograms.

At low frequencies (below 200 kc), the fading often contains two components with markedly different fading times. These give a correlogram which is no longer Gaussian in form but can be represented by the sum of two Gaussian curves of different widths and amplitudes. A simple method of analysis is described which enables these two components to be resolved for any experimental curve. The application of the method to the study of low frequency fading signals is dealt with in some detail.

On Meteor Echoes from Underdense Trails at Very High Frequencies§—Morton Loewenthal, *Lincoln Laboratory, Massachusetts Institute of Technology*—The cylindrical model for a weakly ionized meteor trail leads to a (wavelength)^3 dependence in the reflected power and a (wavelength)^2 in the duration of the echo. In the frequency ranges which have been investigated most extensively (25–100 mc), both these laws agree with the experimental evidence. It is apparent, however, that such agreement cannot continue with increasing frequency since the derivations of the frequency dependence ignore the trail formation process; that is, they assume that the time for the meteor to produce the reflecting trail is small compared to the duration of the echo. It is the purpose of this paper to analyze the behavior of the echo in the frequency range where the time of trail formation is important. As a result, it is found that the duration and amplitude of the echoes are considerably smaller than those predicted by the lower frequency relations. The theory involves the properties of Fresnel integrals or error functions of complex arguments. These were programmed on the Whirlwind II Computer and from these computations it is possible to determine the effect of diffusion on the echo amplitude. The problem of expressing this relationship by closed form approximations in terms of elementary functions is considered. Applications of these results to meteor problems are desired.

The Harvard Radio Meteor Program—Gerald S. Hawkins, Curtis L. Hemenway, and Fred L. Whipple, *Harvard College Observatory*—Harvard College Observatory, in conjunction with the Lincoln Laboratory of M.I.T., is embarking on an extensive program for the study of meteors by radar methods. A megawatt transmitter and six receiving stations are being set up in southern Massachusetts, each site having a dipole array of approximately 100 elements. The experiment will give information on the heights, velocities, and orbits of individual meteors down to 12th magnitude. In addition the ionization will be determined at six different points along the trail giving a direct measure of the length of the electron column produced by the meteor. These facts are vital in assessing the influence of meteors on the ionosphere and their role in forward propagation.

Galactic and Solar Radio Emission as Limiting Background Noise in Systems Using Ionospheric and Tropospheric Scattering—Vernon H. Goerke, *National Bureau of Standards*—An important factor which must be considered in estimating the requirements for ionospheric and tropospheric scatter propagation circuits is the background radio noise due to galactic and solar radio emission. An evaluation of the maximum and minimum radio noise received by large aperture antennas is made over a frequency range of 25–10,000 mc.

The reported noise levels have been derived from published radio astronomy measurements, from solar radio astronomy measurements at the National Bureau of Standards and from measurements made with antennas used in the investigation of ionospheric scattering at vhf.

The expected fluctuations in solar radio noise emission is discussed.

A Compound Interferometer for Radio-Astronomy with a Single-Lobed Radiation Pattern—A. E. Covington and N. W. Broten, *National Research Council of Canada*

* Booker, see elsewhere in abstracts of papers.

† The research reported here was carried out under a Research Grant from the University of New Zealand and the author was supported by a University of New Zealand Research Fund Fellowship. The preparation of this paper has been sponsored by the Geophysical Research Directorate of the Air Force Cambridge Research Center, Air Research and Development Command under Contract AF19(604)-1304.

* The research reported here was carried out under a Research Grant from the University of New Zealand and the author was supported by a University of New Zealand Research Fund Fellowship. The preparation of this paper has been sponsored by the Geophysical Research Directorate of the Air Force Cambridge Research Center, Air Research and Development Command under Contract AF19(604)-1304.

† P. S. Putter, Report of the Physical Society Conference on the Physics of the Ionosphere, Physical Society, 1955.

‡ The preparation of this paper has been sponsored by the Geophysics Research Directorate of the Air Force Cambridge Research Center, Air Research and Development Command, under Contract AF19(604)-1304.

§ The research in this document was supported jointly by the Army, Navy, and Air Force under contract with the Massachusetts Institute of Technology.

—The 150-foot slotted waveguide antenna for operation on a wavelength of ten centimeters at the National Research Council, Ottawa, Canada, is now in operation as one element of an interferometer. The other element is a simple interferometer with element separation equal to that of the long array and offset to one side of the long array. A rotary phase-shifter is in the arm connection between array and simple interferometer and, after Ryle, is used with a phase-sensitive detector. The resultant pattern consists of the product of the three terms: 1) the single lobe pattern of the long array; 2) the interference pattern of the simple interferometer, and 3) the interference pattern between the simple interferometer and array. The presence of two interference patterns suggests the name, "compound interferometer," and the new antenna produces a fan-shaped beam 2′ E-W×2° N-S. The instrument is now being used to obtain daily drift-curves of the sun.

Limitations in the Determination of the Position of a Radio Star—S. Matt, *General Electric Company*—In the determination of the position of a radio star the accuracy limitations can be divided into two classes, those external to measuring equipment and those which can be attributed to the measuring equipment.

Of the limitations external to the measuring equipment the superposition of two radio sources, such as Cygnus A superimposed upon a galactic background is given major consideration here. In such a case it is the unsymmetrical component of the background with respect to the "point" source which shifts the position of the source. The total background contributes to the signal power received increasing the minimum resolvable power level. The use of an antenna array as an inphase array or as an interferometer are compared.

Some of the limitations caused by the measuring equipment are considered such as the integration error and the minimum resolvable power deviation.

Systematic Errors Caused by the Scanning of Antenna Arrays: Phase Shifters in the Main Feed Line*—J. L. Spradley and W. J. Odlum, *Hughes Aircraft Company*—If it is assumed that the mutual coupling between elements in an antenna array is the same for all elements for a given interelement phase shift, but is a function of phase shift, a useful equivalent circuit representation of the entire system is possible. The equivalent circuit consists of a main transmission line periodically loaded by branch transmission lines which are terminated by identical impedances. The impedances represent the radiating elements and are functions of phase shift. If the array is scanned by placing phase shifters in the main line between branch line junctions, these phase shifters can be mathematically treated as variable lengths of transmission lines.

The problem thus is reduced to circuit theory. Expressions for the radiating currents as functions of phase shift and equivalent element impedances are deduced from which the radiation pattern is obtained in the form of an infinite series. The first term of the series is the desired pattern and the remainder has been defined as the systematic error. The analysis indicates that the pattern will not be deteriorated by the systematic error and is relatively insensitive to the amount of mutual coupling present. Experimental results show a good correlation with the theory.

Closely Spaced Transverse Slots in Rectangular Waveguides*—Richard F. Hyneman, *University of Illinois*—A structure consisting of closely and periodically spaced transverse slots cut in the broad face of a rectangular waveguide imbedded in an infinite ground plane is considered. By employing the Reaction Concept an approximate expression for the complex propagation constant of the dominant traveling wave is obtained. Solutions to this equation for various waveguide and slot dimensions and for slot spacings up to about one-quarter wavelength are presented. It is found that considerable control over the rate of attenuation is exercised by the slot spacing to slot width ratio and by the depth or narrow dimension of the waveguide. In addition to the dominant wave, an unattenuated slow wave similar to that observed with corrugated surfaces is shown to exist under certain conditions. Experimental measurements show good agreement with the theory.

Approximate Reflection Computations Using a Variational Principle†—Stephen J. Fricker, *Lincoln Laboratory, Massachusetts Institute of Technology*—A method is given for the approximate determination of the reflection produced when a plane wave is incident upon a region of variable dielectric constant (variable in the direction of propagation). The method is similar in principle to the "steepest descents" method of solving sets of simultaneous equations, where an error function is set up, the magnitude of which is then reduced in steps in the most direct manner. The reflection problem is set up in the form of an integral equation, and a variational formulation then gives a function which is stationary with respect to the correct solution. This function is used as the error function to be minimized. An initial trial solution is used in the minimization procedure, which then yields a correction term for the initial solution. In principle, this corrected solution is then itself corrected, etc., in prcatice the rapidly increasing algebraic complexity discourages higher order corrections. Examples for some simple cases are given, with the initial trial function taken as the unperturbed incident wave (the "Born" approximation). The first term corrections give solutions which are quite close to the exact solutions, and more accurate than those obtained through use of the "Born" approximation alone.

A Constant Beamwidth Radiator—K. S. Kelleher and C. Goatley, *Melpar, Inc.*—For particular applications in the field of direction-finding, it would be desirable to utilize an antenna having a radiation beam which is essentially of constant angular width over a wide frequency range. One type of radiator which approaches the fulfillment of this desired characteristic is a circular arc source along which all points are radiating in phase and with equal amplitude.

Analytical investigations of this radiator show that if the radius of the arc, R, is sufficiently long (viz R/λ becomes large enough), the radiation pattern tends to take the form of a sector of a circle. Concurrently, the beamwidth becomes less dependent on frequency and approaches a value equal to the angle subtended by the arc.

Experimental investigation has verified the predicted appearance of the radiation pattern. The experimental radiator consists of a waveguide horn flared in the E plane and approximately 21 wavelengths in radius at 12.5 kmc. Radiation patterns of the antenna are shown and the radiation pattern analysis is discussed.

A Perturbation Method for the Analysis of Leaky Wave Antennas—L. O. Goldstone and A. A. Oliner, *Polytechnic Institute of Brooklyn*—A perturbation method, based on a transverse resonance, is presented for the analysis of "leaky" wave antennas. The method yields approximate results which are in simple and practical form. Application is made to a number of practical structures for which experimental data are available for comparison. These include slotted rectangular and cylindrical waveguides carrying various modes. Satisfactory agreement is obtained between measurement and theory.

Shaped Beams from Microwave Lenses—C. W. Morrow, P. L. Bachman, and H. T. Ward, *Melpar, Inc.*—Microwave lens-type antennas which produce specified radiation patterns will be discussed. Design equations, based on geometrical-optics approximations, are derived. The theory is similar to Chu's theory of shaped beams from reflectors.

A two-surface symmetrical lens between parallel-plates has been constructed and evaluated. The lens surface nearest the horn feed has the shape to give the desired pattern. The second surface is designed to coincide with a line of constant phase. Consequently, no refraction occurs at the second surface, and its influence is thereby obviated. The desired pattern was a 60° flat-top beam; the measured pattern agreed with the specified one to within ±1 db and had 20 db sidelobes. The modification of the pattern as the size of the lens is changed from its original value (20λ aperture) and the variation in diffraction effects are noted in data taken over a 2 to 1 frequency band.

A second, two-dimensional, asymmetrical lens has been designed to give a 30° flat-top beam. One lens surface has been eliminated by totally immersing the feed in the dielectric material and extending it back into the waveguide. This simplifies the design and construction, and gives increased gain, since reflections at one interface are eliminated. The measured pattern agreed with the specified one to within ±2 db and had 13 db sidelobes. The measured diffraction effects on the specified pattern are correlated to theoretical patterns obtained by simple diffraction theory.

The Theoretical Loss of Antenna Gain Resulting from a Random Aperture Distribution—W. C. Hoffman, *Rand Corporation*—A quantitative treatment is given of

* The work described in this paper was done under contract No. AF19(604)-1317 with the Air Force Cambridge Research Center.

* This work was sponsored by Wright Air Development Center under contract No. AF33(616)-310.

† The research in this document was supported jointly by the Army, Navy, and Air Force under contract with the Massachusetts Institute of Technology.

the nonrealization of the theoretical gain of an antenna with a random aperture distribution. The method developed can be applied to forward-scatter reception by appealing to reciprocity and specifying the covariance function of the aperture distribution.

The Fresnel-zone form of the diffraction integral is employed with appropriate modifications, in particular the introduction of the aperture distribution $F(\epsilon, \mu) = A_0 \exp\{-j\psi(\epsilon, \mu)\}$, where $\psi(\epsilon, \mu) = S(\epsilon, \mu) + j \ln A(\epsilon, \mu)/A_0$, and S and A are, respectively, the phase and amplitude distributions across the aperture and A_0 is the constant amplitude characteristic of a homogenous medium. The modified phase function $\psi(\epsilon, \mu)$ is assumed to be a complex Gaussian process, so that forming the expression for the average power gives rise to appearance of the exponential form of the Gaussian characteristic function under the integral sign. One thus obtains an explicit expression for the average antenna gain function in terms of an integral involving the covariance of the phase differences across the aperture.

A variational approach then leads to an integral equation for the form of the (plane) aperture which is optimum from the standpoint of maximizing value of the diffraction integral in the direction of the beam axis for a preassigned covariance function of the complex phase $\psi(\epsilon, \mu)$.

Reduction of Doppler Contribution to Total Spectral Line Bandwidth by a Method Utilizing Spontaneous Coherent Emission—L. E. Norton, *RCA Laboratories*—In frequency stabilization of a conventional oscillator, using as reference a standard frequency defined by a microwave spectral line, the precision ultimately obtainable is limited largely by the Doppler effect associated with thermal motion of the absorbing particles. A method* for reducing the Doppler contribution to total spectral line bandwidth is described. The signal was usually obtained as a self-induced coherent microwave emission (frequently termed spontaneous coherent emission), excited by coherently pulsed resonance excitation. In view of the present interest in coherent spontaneous emission, and its relation to molecular and atomic oscillators and amplifiers, it appears desirable to describe these early experiments which have not been published. Experimental results are shown and described.

Amplitude Stabilization of a Microwave Signal Source—G. F. Engen, *National Bureau of Standards*—The recent and continuing advances in the microwave measurements art are placing ever increasing demands on the stability of the microwave oscillator. The problem of amplitude or power stability has, in general, received less attention than the companion problem of frequency stability. An amplitude stabilizer has been developed at the NBS Boulder Laboratories, employing a recently developed self balancing dc bolometer bridge and a commercially available electrically controlled ferrite attenuator, which achieves power stabilities of a few parts in 10^4 per hour.

Use of a high directivity directional coupler permits stabilization of the forward traveling component of the signal, thus providing the equivalent of a matched, stable generator. In practice, a broadband source match of vswr less than 1.07 is achieved, and this figure may be further improved, at a given frequency by suitable tuning.

The device also has applications as a precision calibrated attenuator, since known changes in power level may be achieved by switching certain of the associated dc components.

Performance of Three-Millimeter Harmonic Generators and Crystal Detectors—John M. Richardson and Russell B. Riley, *National Bureau of Standards*—Because of the growing applications of millimeter wave measurements, a fairly thorough investigation of what could be expected from sources and detectors in the 3 mm region was made. The sources consisted of fourth-harmonic generators from a 1.25 cm fundamental. A type of crystal holder for both harmonic generators and detectors in which a small crystal wafer is positioned in the broad wall of the millimeter waveguide, being contacted by a whisker passing across the waveguide (the flush-crystal type) was found to be superior in general to units using crystal cartridges or modifications thereof. Factors affecting the performance of these units have been investigated statistically. These factors were principally the type of silicon used, the condition of the whisker point, and surface cleaning of the silicon. It was also found that the short-circuit current sensitivity in micro-amperes per microwatt of a good crystal detector of the type described above is not greatly less than the value for crystals at lower microwave frequencies, so that the minimum detectable signal is about the same. The factor limiting the dynamic range of a measurement is the maximum 3 mm power that can be produced, which in this report was 50 μw. As an additional result, evidence for an important effect in which the harmonic generation process degrades the signal-to-noise ratio of the source is presented and discussed.

Novel Circuit for a Crystal Controlled Variable Frequency Oscillator—D. Makow, *National Research Council, Ottawa Canada*—In the past quartz crystals have been used extensively to control single frequencies. This paper describes a circuit where a crystal exercises considerable control over a continuously variable frequency spectrum.

The circuit is characterized by multiloop feedback, which enables oscillation to be maintained at three frequencies, f_1, f_2, and f_3, and $f_1+f_2=f_3$, with the corresponding voltages confined to certain branches of the circuit and coupled to each other through three mixers. The frequency f_3 is restricted by a quartz crystal resonator, whereas the frequencies f_1 and f_2 are tunable in such a manner, that as f_1 increases, f_2 decreases and vice versa. The L-C resonators which control f_1 and f_2 drift in the same direction when the ambient conditions change. Such a drift cannot influence f_1 and f_2, since the latter can change only when the L-C resonators shift in the opposite direction. The presence of a crystal in the feedback loop also improves the phase stability of the circuit Since two L-C and one crystal resonator determine two frequencies only, high frequency resetability is possible.

An experimental model has been tested, and shows a thirty to hundredfold reduction of the frequency drift with temperature, excellent short and long term stability and a remarkably small initial frequency drift with switching on.

The Phase of the Low Radio Frequency Ground Wave—J. R. Johler, *National Bureau of Standards*—The phase of the low frequency ground wave is implicit in its theoretical development. Most computations in the past have considered only the amplitude. But, in recent years, the importance of a precise evaluation of the phase has increased, especially in connection with the use of various systems of low frequency radio navigation. The phase of the propagated ground wave is also an important consideration in the solution of the more general problem of the propagation of a transient in a radio communication system.

This paper is concerned with the computation of the phase of the low frequency ground wave from the mathematical model developed by Sommerfeld, Watson, Bremmer, Van der Pol, Norton, and others. The effect on the ground wave of frequency, disturbing influence of the source, finite conductivity of the earth, altitude above the surface of the earth, and vertical lapse of the permittivity of the earth's atmosphere are demonstrated. The special theoretical considerations pertinent to the evaluation of the phase and the physical significance of the phase are discussed.

Back-Scattering Characteristics of the Sea in the Region from 10 to 50 KMC—J. C. Wiltse, S. P. Schlesinger, C. M. Johnson, *The Johns Hopkins University*—Measurements of back scattering from the ocean have been made over the frequency range from 10 to 50 kmc by means of several cw doppler microwave systems operating simultaneously. The systems were mounted on the bow of a ship and various antenna depression angles from 0° (horizontal) to 90° were used. Data were obtained for vertical, horizontal, and circular polarization, and for the cross-polarized component of vertically polarized radiation. Horn antennas of 20 db gain were used at each frequency of operation, and, in addition, higher and lower gain antennas were used at certain selected frequencies. Signals recorded from a variety of sea conditions have been used to calculate the back-scattering cross section per unit area, $\sigma°$. These calculations indicate that $\sigma°$ is nearly constant with microwave frequency and increases as the antenna depression angle is increased. The doppler frequency characteristics of the returned signals have also been obtained from the measurements. A comparison is made between the results obtained and those predicted theoretically from simple scattering mechanisms.

Propagation Through the Troposphere and Ionosphere—Virgil A. Counter, *Lockheed Aircraft Corporation*—There are various applications in radio astronomy as in other fields in which knowledge of character and amount of deviation from free space propagation is desired for transmission through the troposphere and ionosphere.

* Reports No. 1–No. 10 Investigation of Practical Utilization of Molecular Absorption Phenomena for Frequency Control. Contract No. DA36-039-sc-15525 placed by U. S. Army, Signal Corps Engineering Laboratories, Fort Monmouth, N. J.

Frequencies are considered which are large compared to the critical frequency. Approximate methods are presented for the direct evaluation of the ray integrals in a stratified atmosphere for finite source distances at all elevation angles. Values of range deviation and elevation angle deviation are presented for normal and extreme atmospheric conditions.

Approximate formulas for the total attenuation of a clear troposphere are discussed. Formulas and values for the rotation of the polarization vector and attenuation of the wave during passage through the ionosphere are also presented.

Ray-Caustics Method for Anomalous-Refraction Propagation—Ming S. Wong, *Wright Air Development Center*—Simple ray tracing explains the radio holes, antiholes, ducts, and dense signal fadings observed in airborne propagation at 250–10,000 mc. Ray-theoretical angles of arrival, phases, and range corrections for multipath signals are in line with experiments. Ray densities, however, become infinite at caustics (which are numerous and widespread in case of dense fadings).

In place of a rigorous solution for refraction in 3-dimensionally variable air (studied by mathematicians several ways), classical theory of caustics can be adapted to obtain good-enough approximations showing all essentials of the observed radio field-intensity variations. Results by Keller, Kay, *et al.* (NYU) on caustics are used with rays traced for any spatial variations of the atmospheric refractive index.

Amplitude Fluctuations on Line-of-Sight Transmission Paths—R. B. Muchmore and A. D. Wheelon, *Ramo-Woolridge Corp.*—Phase fluctuations on line-of-sight paths have previously been discussed by the authors.* This paper treats amplitude fluctuations on such transmission paths theoretically. Expressions for the amplitude fluctuations induced by antenna-to-medium coupling are derived and compared with the amplitude variations induced in the medium itself. It is shown that, for even very large receiving antennas, the antenna-to-medium coupling is unimportant in producing signal strength variations. This leaves the medium itself as the important agent in production of amplitude fluctuations. It is shown that these fluctuations are, under the proper conditions, very simply related to the phase variations.

Propagation of 8.6 Millimeter Radio Waves at 14,000 Feet Elevation—C. W. Tolbert and A. W. Straiton, *The University of Texas*—Radio propagation measurements between Pikes Peak and Mount Evans were made during August, 1955 using a frequency of 35,000 megacycles per second. Attenuation due to water vapor and oxygen absorption appeared to be small in the absence of precipitation. Simultaneous comparisons made with 10,000 megacycle signals showed that when precipitation produces as much as three decibels attenuation at the lower frequency, the 35,000-megacycle signal was attenuated into the noise level twenty-two decibels below the free space signal level.

* "Line-of-sight propagation phenomena—I. ray treatment; II. scattered components," URSI Spring meeting 1955, also PROC. IRE, vol. 43, pp. 1437–1458; October, 1955.

The Effect of Superrefractive Layers on 50–5,000 MC Non-Optical Fields—E. E. Gossard, *U. S. Navy Electronics Laboratory* and L. J. Anderson, *Smyth Research Associates*—Field strength data on a 94-mile overwater link are correlated with refractive layer parameters as derived from radiosonde data. Regression coefficients are obtained for describing fields at 52, 100, 550, 3300, and 5000 mc. These coefficients are used to compute empirical attenuation coefficients over the frequency range as a function of duct height and intensity. The procedures for performing the analysis were chosen such that the derived attenuation coefficients form the basis of an objective method of predicting nonoptical fields at ranges up to 200 miles.

Twilight Region Propagation of Microwaves Beamed over Great and Small Circle Paths*—Thomas J. Carroll and Rose M. Ring, *Lincoln Laboratory, Massachusetts Institute of Technology*—From the viewpoint of mode theory with an air layer, tropospheric propagation into the twilight region occurs because the tropospheric air layer partially suppresses the upward leakage of energy which gives rise to the large db/mi attenuation rates just beyond the horizon in conventional airless 4/3 earth theory, which treats only the earth curvature effect on the diffraction of radio waves beyond the horizon. These large airless earth attenuation rates are experimentally observed for only a few tens of miles beyond the horizon until the twilight region is reached where it is essential to consider the full effect of the leaky waveguide action of the air layer.

Of all planes which may be passed through two terminals T and R on the earth's surface, the plane through the center of the earth cuts the surface in a great circle of largest radius. As the plane through T and R is rotated, it cuts sea level in a small circle whose radius decreases as the plane departs more from the plane of the great circle. If the axes of two sharp-beamed antennas be swung equal amounts off-azimuth so as to point along a particular small circle joining T and R, the profile to be surmounted in the plane of the swung beam axes constitutes a greater obstruction than does the profile of the great circle path which would obstruct propagation between antennas oriented on-azimuth.

However, the large antenna pattern losses imposed on propagation in the great circle plane by sharp beams at the terminals swung off-azimuth may allow larger twilight region fields to be propagated in the vicinity of the plane of the small circle determined by the swung beams. The sharp swung beams may thus discriminate too much against the great circle profile to which thinking about the earth profile as an obstacle is usually limited.

The extra loss for small circle propagation of a single mode compared to great circle propagation for antennas oriented on azimuth has been calculated from air layer mode theory for a linearly or curvilinearly tapered air layer, in good agreement with the synchronously swung beam experiments of Chisholm *et al.*, over the 188 mile, 2 degree path, in 1953–54, with 0.6 degree beam antennas. The calculation involves merely substitution of the small circle radius, the index of refraction variation, and the air layer thickness appropriate to the plane of the swung beams in the mode attenuation formula applied formerly only to great circle profiles.

Thus experiments on the swinging of sharp beams in twilight region propagation can be interpreted very simply in terms of earth and beam geometry and an idealized air layer, without other ad hoc assumptions, as can most other features of normal high power tropospheric propagation well beyond the horizon.

Plausible seasonal changes of surface index and gradient cause the single mode calculation to behave qualitatively as do the experiments, both as regards swung-beam pattern shape and the absolute level of the signal.

* The research in this document was supported jointly by the Army, Navy, and Air Force under contract with the Massachusetts Institute of Technology.

Long Distance High Power Radio Propagation at Frequencies Exceeding the MUF*—W. G. Abel and M. L. Philips, *Lincoln Laboratory, Massachusetts Institute of Technology*—Usable median signal levels on 22 mc were recorded continuously during two five-day periods in June and July, 1955 at distances of 1540 and 1800 miles from a 500 kilowatt cw transmitter. Except for an hour or so on several of the days, the frequency of the transmitted signal exceeded the muf for the path, at times by as much as 10 mc. Diurnal variations of the median signal level in excess of 90 decibels were recorded during a single 24-hour period. Maximum signal levels were obtained about noon and shortly before midnight local time; minimum levels at approximately 0700 and 1800. Minimum median signal to noise ratio was about 10 decibels.

Comparison with vertical incidence ionospheric data taken near the midpoint of the transmission path indicates roughly a linear variation of signal intensity in decibels above a reference level with the logarithm of the F_2-layer muf, the slope decreasing with prevalence of high fE_s. For a given muf, high signal level seems generally associated with low fE_s, suggesting possible obscuring of F_2-layer scatter by the underlying layer.

Radioteletype Transmission Above the MUF—H. A. Schulke, Jr., *Signal Corps Eng. Labs.*—As part of the continuous effort to find more efficient means of spectrum utilization for long range radio communication circuits, a series of three tests were conducted by the Long Range Equipment Section of the Signal Corps Engineering Laboratories and Lincoln Laboratory to investigate the feasibility of maintaining continuously usable signal levels on a single frequency at ranges of 1800 to 2000 miles using a 500 kw hf transmitter. The results of the first two tests indicated the possibility of transmitting radioteletype information over the Dallas, Texas, to Caribou, Maine, test circuit. The third test was conducted on 21.57 mc from July 25 to 30, 1955, using standard 850 cycle shift fsk teletype, and the test results indicated that using a broad-

* The research in this document was supported jointly by the Army, Navy, and Air Force under contract with the Massachusetts Institute of Technology.

band fsk converter 86.1 per cent of the transmitted lines of copy were received without error, and that using an experimental narrow-band fsk converter 91 per cent of all transmitted lines were received without error. The third test also pointed out that extreme multipath conditions occur daily for periods up to eight hours with signal delays of as much as 36 milliseconds.

The Communication Possibilities of a New Type of Ionospheric Scatter*—Allen M. Peterson, O. G. Villard, Jr., Ray L. Leadabrand, and Philip B. Gallagher, *Stanford University*—A new class of radio echoes from the ionosphere has recently been identified at Stanford University.† These echoes originate within the *E* and *F* layers, under conditions where the line of sight from a radar meets a line of the earth's magnetic field at perpendicular incidence. This appears to be the first direct evidence of a potentially useful ionospheric scatter occurring at *F* layer height.

The echoes are seen primarily at night, and are readily detectable with low power radars operating in the 6 to 30 mc frequency range. They are observable for several hours at a time on a large percentage of the nights. Although their exact cause is unknown, it is reasonable to suppose that they are a manifestation of low-latitude, low-intensity auroral activity in view of their night-time occurrence, and their aspect-sensitivity with respect to the earth's magnetic field. On the other hand they have been seen regularly as far south as New Mexico and are not directly associated with geomagnetic disturbances.

The field-aligned ionization may be used for communication purposes in much the same manner as auroral ionization, that is, by pointing the antennas at both locations wishing to communicate, generally towards the north.

The geometry of reflection from the field aligned ionization is investigated, outlining the area of "useful" ionization and the "region of communication" for both the *E* and *F* layer heights of reflection. The probability of obtaining communication from a transmitter located at Stanford to a receiver at any location within the region of communication is determined.

The Geometry of Auroral Communications—Ray L. Leadabrand and Irving Yabroff, *Stanford University*—Auroral ionization was found by radio amateurs to be useful for communication purposes as early as 1939. Such ionization makes hf and vhf propagation possible over paths as great as several hundred km when other more normal propagation modes do not exist. The geometry of reflection is investigated for a variety of transmitter locations based upon the assumption of specular reflection from columnar ionization aligned with the earth's magnetic field lines. The results of the investigations outline the areas of useful auroral ionization and the regions of propagation. The probability of obtaining propagation from a particular transmitter location to any receiver location within the region of propagation has been determined. These geometrical studies allow the communicator to predict the most useful transmitter and receiver locations in utilizing auroral ionization for communication purposes. It also makes possible the minimization of the effects of auroral propagation when it is considered a detrimental propagating mode —resulting in undesirable multipath effects, etc.

Methods of Measuring Ionospheric Reflection Coefficient Using Sweep Frequency Equipment*—H. Myron Swarm, *University of Washington*, and R. A. Helliwell, *Stanford University*—Two methods for the measurement of ionospheric reflection are described. They make use of sweep frequency equipment and are designed to provide information on the variation of the reflection coefficient of the Sporadic-*E* layer as a function of frequency.

The first method is based on the measurement of the highest frequency at which each multiple-hop trace can be observed. For each frequency a value of the layer reflection coefficient can be computed when certain equipment parameters and the ground reflection coefficient are known. Information regarding absorption and focussing can be obtained by studying the lowest frequency of each multiple-hop trace.

In the second method the relative amplitude of each multiple-hop echo is recorded. From the ratios of the amplitudes averaged over several fading periods both the reflection coefficient and the over-all system sensitivity can be estimated. The method can thus be extended to layers producing only single-hop reflections.

Examples of the application of these two methods are shown.

Interference Measurement of Small Multipath Delay Changes—De Forest L. Trautman, Jr., *Hughes Aircraft Company*—Oblique incidence ionospheric-sounding studies heretofore have been made with short pulses, ideally shorter than the minimum delay differences between the propagation components, but limited by the greater bandwidth and peak power required to shorten the pulses.

Precision of delay difference measurement is limited by the pulse length used. This technique has been extended by transmitting alternately short and long pulses; the long pulses being sharply rectangular with as rapid rise and decay as the short pulses. Typical pulse widths have been 20 and 1000 microseconds.

At the receiver, a *C*-scope display shows both the multiple short pulses from the individual propagation components as with prior sounding techniques plus the successive superposition of the long pulse components. The relative magnitudes of the individual components is measured by the height of their short pulses while the magnitudes to which they combine in the received long pulse depends also upon their relative instantaneous phase.

Study of cine recordings yields these interference fading cycles, which establish the rate of change of phase or delay between propagation components except for sense or sign, which generally can be established from prolonged observation of the short pulses.

The complexity of the long pulse shapes increases with the number of multipath components present and interpretation of delay change rates becomes difficult when more than three components overlap. Overlapping can be controlled, however, by suitably shortening the pulse when many multipath components are arriving.

Short and long pulse transmissions from Dayton, Ohio, have been recorded in Los Angeles (3080 kilometers) and Honolulu (7120 kilometers). Typical recordings and their analyses will be shown. This extension of oblique incidence sounding technique provides greatly improved sensitivity of delay changes and should facilitate study of ionospheric layer mobility and similar phenomena.

Corner Reflector Antenna with Arbitrary Dipole Orientation and Apex Angle—R. W. Klopfenstein, *RCA Laboratories*—It has recently been pointed out that for certain dipole orientations, a corner reflector antenna serves as a circularly polarized radiator of moderate gain and bandwidth characteristics.* This has led to renewed interest in corner reflector characteristics for arbitrary dipole orientation and apex angle.

This paper is concerned with the determination of corner reflector characteristics for reflectors of arbitrary apex angle excited by any infinitesimal dipole source which is tangent to a circular cylinder having the reflector axis as its axis. Use is made of the dyadic Green's functions for the perfectly conducting wedge recently given by C. T. Tai,† and the results are obtained as infinite series of Bessel functions.

The quantities of interest are the relative phase and magnitude of vertical and horizontal components of electric field, the directive gain of the antenna, and the radiation resistance of the dipole source. These have been computed for a continuous range of apex angles from 30° to 180° for dipole-axis spacings up to about a wavelength.

The results of this general analysis are useful not only for the determination of reflector characteristics for apex angles not subject to image analysis, but also for the obtaining of certain limiting forms for small apex angles which are not readily apparent from the image analyses.

A Circularly Polarized Corner Reflector Antenna—O. M. Woodward, Jr., *RCA Laboratories*—Unidirectional, circularly polarized radiation may be obtained by tilting a dipole in a corner reflector. Inherent advantages of this antenna are the simplicity of both the construction and adjustment.

The theory of images is employed to develop the basic theory of the antenna for the cases of greatest practical interest. An experimental investigation has been made on the radiation characteristics of a practical-sized antenna as a function of its geometric parameters. From this data, an

* This research was supported jointly by the U. S. Army, the Navy, and the Air Force under contract Nonr 251(07) with Stanford University.

† A. M. Peterson, O. G. Villard, Jr., R. L. Leadabrand, and P. B. Gallagher, "Regularly-observable aspect-sensitive radio reflections from ionization aligned with the earth's magnetic field and located within the ionospheric layers at middle latitudes," *J. Geophys. Res.*; December, 1955.

* This research was sponsored by the Electronics Research Directorate of the Air Force Cambridge Research Center.

* O. M. Woodward, Jr., "A circularly polarized corner reflector antenna," submitted for presentation at the URSI Spring Meetings, 1956.

† C. T. Tai, "A glossary of dyadic Green's functions," Tech. Rep. No. 46, Stanford Res. Inst., Stanford, Calif., July, 1954.

antenna producing unidirectional, circularly polarized radiation has been designed and constructed.

A demonstration of the adjustment and operation of the antenna will be presented.

Measurement of Scattering Cross Sections of Figures of Revolution*—J. Honda, S. Silver, and F. Clapp, *University of California*—Interest in scattering cross sections is motivated by many fundamental and practical considerations. Work on echo cross section (back scattering) has been particularly intensive because of radar applications. One of the striking features of echo cross section measurements is the divergence between results obtained by independent investigators. This paper is a report of developments of the program on scattering measurements in our laboratory. We have employed the half-space technique which is applicable to obtaining the differential cross section for figures of revolution in the principal planes. The considerations underlying cross section measurements are discussed and the particular measurement techniques which we have developed are presented. Data on echo cross sections of spheroids and cones are given to illustrate the problems and methods.

Scattering from Finite Cones—K. M. Siegel, *Engineering Research Institute, The University of Michigan*—For the small wavelength approximation, the radar cross section of a finite cone is in agreement with physical optics approximations. It is reasoned that the main contributors to the nose-on cross section are the ring singularity in the rear and the point up front. It becomes clear that in the small wavelength approximation, the ring singularity contribution dominates. An upper bound to the nose-on cross section for a finite cone is given by the nose-on result for the loop. As one approaches the resonance region from the small wavelength side, one finds that the cross section of the cone starts approaching the loop answer and at the first major maximum one finds the results are in agreement. This indicates that the cone near or on the first resonant maximum has the same behavior as a resonant loop. Many other cone results are discussed.

The author wishes to acknowledge contributions to this paper from Professor S. Silver, J. Honda, and F. Clapp of the University of California, and Dr. S. Chapman of Cornell Aeronautical Laboratory, Inc., and Dr. M. J. Ehrlich of Microwave Radiation Company, Inc.

Evaluation of the Field Produced by Slots on a Wedge—C. E. Schensted and A. L. Maffett, *Engineering Research Institute, The University of Michigan*—An expression for the field produced by two symmetrically located and excited slots on a wedge can be derived by the usual separation of variables technique. The ϕ component of the electric field is given by

$$\frac{E_\phi}{2i} = \frac{\partial}{\partial r}\frac{\pi V_0}{2\phi_0}\sum_{n=0}^{\infty}(-)^n H^{(1)}(n+\tfrac{1}{2})\frac{\pi}{\phi_0}(kr)\,J \cdot (n+\tfrac{1}{2})\frac{\pi}{\phi_0}(ka)\sin(n+\tfrac{1}{2})\frac{\pi\phi}{\phi_0}$$

where V_0 is the voltage impressed across the slots which are at a distance a from the tip of the wedge whose faces are given by $\phi=\phi_0$. For $r\to\infty$ this approaches the asymptotic value

$$\frac{E_\phi}{2i} = \frac{V_0}{\phi_0}e^{ikr} + \frac{\pi i}{4}\sqrt{\frac{\pi k}{2r}}\sum_{n=0}^{\infty}(-)^n e^{-i(n+1/2)\pi^2/2\phi_0}\,J \cdot (n+\tfrac{1}{2})\frac{\pi}{\phi_0}(ka)\sin(n+\tfrac{1}{2})\frac{\pi\phi}{\phi_0}.$$

This series can be related to scattering of a plane wave by a wedge. After the geometric optics terms for the plane wave scattering have been subtracted off, the remaining series can be summed for large ka. The first terms of the asymptotic series for large ka are

$$E_\phi = \frac{V_0}{2\pi}e^{ikr} + \frac{\pi i}{4}\sqrt{\frac{\pi k}{2r}}\Big[e^{-ika\cos(\phi-\phi_0)}U(\phi+\pi-\phi_0) - e^{-ika\cos(\phi-\phi_0)}U(\pi-\phi-\phi_0)\Big] + \frac{iV_0 e^{ik(r+a)}}{8\phi_0\sqrt{ar}}\left[\frac{1}{\cos\dfrac{\pi(\pi+\phi)}{2\phi_0}} - \frac{1}{\cos\dfrac{\pi(\pi-\phi)}{2\phi_0}}\right],$$

$$\text{where } U(x)=\begin{cases}0 & (x<0)\\ 1 & (x>0).\end{cases}$$

Second Order Beams of Two-Dimensional Slot Arrays—L. A. Kurtz, J. S. Yee, *Hughes Aircraft Co.*—Second order, or "forked" beams are found to exist in the radiation patterns of many two-dimensional slot arrays. These beams appear at large angles relative to the main beam, and their magnitudes vary as the main beam is scanned away from broadside. These beams arise because the slots usually do not have the same element factors. Successive slots may have either opposite angles of inclination or opposite displacement from the centerline of the waveguide. In such cases, they have slightly different polarizations and consequently different element factors.

In the analysis of the second order beams, two successive slots are considered as one element of the array so that all the elements are similar. These slot pairs are spaced more than a wavelength apart, thus giving rise to three principal maxima in the radiation patterns. The relative magnitudes of these maxima are determined by the element factor of the slot pair.

The analysis has been applied to calculate the magnitudes and positions of the second order beams of two-dimensional arrays of both series and shunt slots. For many conventional designs, the forked lobes are seriously high and prevent the achievement of the desired sidelobe level. Methods of preventing this are discussed, and experimental results are presented to substantiate the analysis.

New Method of Antenna Coupling to a Balanced Two-Wire Line—Carlyle J. Sletten, *Air Force, Cambridge Research Center*—A very simple method has been discovered whereby one can control the radiation from a two-wire line by properly orienting a dipole radiator with respect to this line. A relative conductance from 0 to 0.3 g/G_0 can be obtained by rotating the dipole through an angle of 20°. A brief treatment is given of the electromagnetic coupling principle employed. Experimental curves of impedance characteristics as function of adjustable parameters are presented along with antenna patterns made with arrays of these elements. Cross polarization, line unbalance, frequency response, resonant element length, H-plane patterns and other effects related to this new method of feeding electric dipoles are described. Antenna performance with this feeding principle is very satisfactory and applicable to many problems of array design.

A Variable Polarization Microwave Transducer—W. A. Snyder, *Hughes Aircraft Co.*—A microwave transducer which converts a linearly polarized input signal to an arbitrary elliptically polarized output is described. With a plane polarized input to the device, an output having the same or the orthogonal plane polarization, or an elliptical polarization of any axial ratio, including circular polarization, can be electronically selected. Both right and left handed senses of circular or elliptical polarization are equally obtainable.

The device consists of a ferrite rotator in conjunction with a quarter wave plate (*i.e*, a 90-degree differential phase shifter) in a waveguide of circular cross section. The ferrite rotator is actuated by a solenoid.

By controlling the solenoid current, and hence the magnetic field in the ferrite material, a given linearly polarized input wave can be rotated so as to be incident on the quarter wave plate in such a plane as to produce the desired output polarization. In particular, a linearly polarized incident wave lying in either of the symmetry planes of the quarter wave plate passes through unaffected. Incident waves lying in planes at 45 degrees or −45 degrees with the phase shifter symmetry planes result in either right handed or left handed circularly polarized outputs. For other planes of incident polarization, elliptically polarized outputs result.

An important characteristic of the polarization transducer is nonreciprocal operation. The transducer has the properties of a four port circulator, the two senses of circularly polarized output modes and the two independent plane polarized input modes corresponding to the four terminal pairs.

The polarization transducer can be switched electronically with a speed which is limited only by the electromagnet and the associated circuits.

A Theory of Long-Duration Meteor-Echoes Based on Atmospheric Turbulence*—H. G. Booker, *School of Electrical Engineering, Cornell University*—The theory of atmospheric turbulence has been applied to meteor trails and the following deductions have been made, relevant to the 90 km level in the atmosphere:

1) The general circulation supplies turbulent energy at a rate of about 20 watts per kilogram of atmosphere. The formula for this quantity depends only on quantities directly measured by radio meteoric technique.

* Work supported by Office of Naval Research (Contract N7-ONR-29529).

* This research was supported by U. S. Signal Corps Contract DA36-039-sc-56748 and by the National Science Foundation.

2) The smallest eddies permitted by viscosity to exist have a size of about 1 meter and a turbulence velocity of about 2 meters/second. The size of the smallest eddies is therefore about 60 molecular mean free paths.

3) The largest eddies present have a size of about 1 kilometer and a turbulence velocity of about 300 meters/second.

4) The time required for the smallest eddies to mix the trail is about 0.4 second and that for the largest eddies about 40 seconds.

5) Diffusion of the trail is only controlled by molecular diffusion during about the first 0.4 second. After this, eddy diffusion takes over and the coefficient of diffusion increases proportional to the square of the time elapsed since the formation of the trail. After about 40 seconds have elapsed, eddy diffusion is controlled by the largest eddies and the coefficient of diffusion thereafter remains constant at a value of the order of ten thousand times the molecular value.

6) Calculation of the radar echo from a meteor trail must be made in two parts:

(a) The coherent contribution calculated by the theories of Lovell and Clegg* and of Kaiser and Closs,† modified by the above statement concerning the diffusion coefficient.

(b) The incoherent contribution calculated by theories such as those of Booker and Gordon,‡ Villars and Weisskopf,§ Gallet,‖ Batchelor,** and Silverman,†† due allowance being made for the existence of a minimum eddy-size as described in 2).

The upshot is that the coherent contribution can exceed the incoherent contribution for only about half a second. After half a second behavior of the echo is controlled by the incoherent contribution. Thus the theory of Kaiser and Closs† does not give the predominant contribution to the echo after about half a second and so cannot constitute an explanation of long-duration meteor-echoes.

7) At times large compared with half a second the echo decreases in amplitude inversely proportional to the cube of the time elapsed since the formation of the trail. After about 40 seconds the amplitude decrease becomes inversely proportional to only the first power of time elapsed since formation of the trail, but a correction for recombination is then necessary. The decrease in the amplitude of the echo after about half a second is controlled by the incoherent contribution to the echo and is very slow compared with the decrease of the coherent contribution. It is the slow decrease of the incoherent contribution arising from the effect of atmospheric turbulence on the trail that is the true explanation of long-duration meteor-echoes. This explanation does not require the enormously high trail-densities postulated by Kaiser and Closs.

8) The wavelength-dependence of long-duration meteor-echoes is closely related to the spectrum of turbulence, which is therefore capable of more or less direct measurement by radar technique. The part of the spectrum that can conveniently be measured in this way is the part vitally affected by viscosity and not well understood at the present time.

9) Meteor echoes that show little or no coherent contribution (such as the *F* type echoes of McKinley and Millman*) arise from trails for which the foot of the perpendicular from the radar is not sufficiently near to the point of maximum trail-density. This diminishes the coherent echo but leaves the incoherent echo unaffected.

10) During the course of eddy-diffusion of a meteor trail the irregularities of electron-density are likely to become somewhat elongated along the earth's magnetic field. It may be therefore that long-duration meteor-echoes are more easily detected in the vhf band if viewed perpendicular to the earth's magnetic field.

An Experimental Study of Atmospheric Turbulence in the Lower *E*-Region Using Meteor Echoes of Long Duration†—R. Cohen, *School of Electrical Engineering, Cornell University*—A theory of long duration meteor echoes has been presented by Booker,‡ based upon the idea that, a few seconds following formation of the trail, incoherent scattering caused by atmospheric turbulence controls the behavior of the radio echo. With a view toward confirming this theory experiments have been undertaken using meteoric ionization to study ionospheric turbulence. CW transmitters and receivers having identical dipole antenna systems at frequencies of about 17, 30, and 50 mc/sec were installed at sites separated by 31 km of hilly terrain, so as to suppress the ground wave. High speed recordings on dual-channel paper tape were taken simultaneously for pairs among the three frequencies, both during the winter meteor showers of November and December, 1955, and at times thereafter when only sporadic meteors were present.

Results of an analysis of the meteor events of interest show that, on all frequencies, the decrease in the amplitude of long duration echoes after they begin to decay is in accordance with the Booker theory, field-strength being inversely proportional to the third power of the time subsequent to trail formation. The wavelength dependence of the irregularly fading echoes is also investigated, and some information is derived concerning the spectrum of atmospheric turbulence in the viscosity range.

An associated experiment was attempted earlier to obtain echoes from the ambient ionization irregularities produced by atmospheric turbulence. A powerful radar system was employed, using a paraboloidal antenna one-hundred feet in diameter beaming vertically upward at a frequency of 27.85 mc/sec in conjunction with a 200 kw pulse transmitter. No echoes of this sort were obtained during repeated attempts in 1954, nor in early 1955, when, with the collaboration of K. L. Bowles, a 30 db improvement in signal to noise ratio was achieved by use of post-detector integration techniques.

The Formation of Sporadic *E* Ionization and the Recently Discovered Low Latitude Aspect Sensitive Ionization Aligned with the Earth's Magnetic Field Lines*—R. L. Leadabrand, A. M. Peterson, and O. G. Villard, Jr., *Stanford University;* H. M. Swarm, *University of Washington*—Radio echoes due to reflection from aspect sensitive ionization aligned with the earth's magnetic field lines are consistently observed at Stanford University.† The echoes, corresponding to oblique reflection from the *E*- and *F*-regions of the ionosphere, have many characteristics similar to auroral echoes, although their occurrence is not associated with magnetic disturbances. The appearance of the *E*-region aspect sensitive, oblique echoes, has been found to be correlated with the appearance of night time sporadic-*E* ionization at middle latitudes. The nature of the field aligned ionization is such that it suggests a production mechanism of charged particle bombardment, thus offering a possible explanation for the production of night time sporadic-*E* ionization.

Study and Interpretation of Low Angle Fluctuations from the Radio Star Cassiopeia as Observed at Ithaca, N. Y.—B. Dueño, *College of Agriculture and Mechanic Arts, University of Puerto Rico*—Low angle fluctuation data of the radio-star Cassiopeia for the period comprised between September, 1954 to August, 1955 have been compared with ionospheric sounder data from Ottawa, Canada. A remarkable relation between the incidence of fluctuations and sporadic-*E* has been observed for the month of December, 1954. The coincidence of *Es* and fluctuations was found, in general, to be very good during the midwinter period and poor afterwards. The pierce-thru region for inospheric layers at a height of 400 km comes out approximately 1500 km north of Ithaca. In this region the normal sun controlled forms of ionization should be a minimum during the midwinter period. It is reasonable to expect that layers at the 120 km level should be most influential in causing fluctuations during this period. Several fluctuationless days were recorded during this midwinter period and practically none at other times. One notable feature of fluctuations at lower transit is a tendency for fluctuations to exhibit peaks of amplitude reaching, on certain occasions, values from two to four times to value of the undisturbed signal from the star. The months in which this condition was most prevalent were April, May, and June.

* Lovell and Clegg, *Proc. Phys. Soc. Lond.*, vol. 60, p. 491; 1948.

† Kaiser and Closs, *Phil. Mag.*, vol. 43, p. 1; 1952.

‡ H. G. Booker and W. E. Gordon, "A theory of radio scattering in the troposphere," Proc. IRE, vol. 38, pp. 401–412; April, 1950.

§ F. Villars and V. F. Weisskopf, "On the scattering of radio waves by turbulent fluctuations of the atmosphere," Proc. IRE, vol. 43, pp. 1232–1239; October, 1955.

‖ R. M. Gallet, "Aerodynamical mechanisms producing electronic density fluctuations in turbulent ionized layers," Proc. IRE, vol. 43, pp. 1240–1252; October, 1955.

** Batchelor, Cornell Univ. Tech. Rep. No. 26, 1955.

†† Silverman, *J. Appl. Phys.*, submitted for publication.

* D. W. R. McKinley and P. M. Millman, "A phenomenological theory of radar echoes from meteors," Proc. IRE, vol. 37, pp. 364–375; April, 1949.

† This research was supported by a U. S. Signal Corps grant under Contract DA36-039-sc-56748 and by the National Science Foundation.

‡ H. G. Booker, see elsewhere in abstracts of papers.

* This research was supported jointly by the U. S. Army, the Navy, and the Air Force under Contract Nonr 251(07) with Stanford University

† A. M. Peterson, O. G. Villard, Jr., R. L. Leadabrand, and P. B. Gallagher, "Regularly-observable aspect-sensitive radio reflections from ionization aligned with the earth's magnetic field and located within the ionospheric layers at middle latitudes," *J. Geophys. Res.*; December, 1955.

On the Origin of Nocturnal *E* Ionization—M. Dubin, *Air Force Cambridge Research Center*—Recent upper atmosphere rocket experiments have produced new evidence of importance in understanding the mechanisms responsible for the existence of the night-time *E* layer. An Aerobee rocket fired by the navy after midnight on July 8, 1955 obtained mass spectra of the ion content of the atmosphere in the range of altitudes from 98 to 120 km; only positive ions of molecular nitrogen were detected. These results are contrary to an hypothesis proposed by Nicolet for nocturnal *E* ionization and are quite difficult to explain on the basis of the physical reactions expected for the *E* region.

An ionization process resulting from direct collisions of meteoric particles with atmospheric gases is suggested as a possible mechanism for explaining this anomaly.

Such a process is of fundamental importance in meteor physics. Its plausibility is discussed.

A second Aerobee rocket, fired by the Air Force at twilight on October 12, 1955, released a quantity of atomic sodium over a range of altitudes from 85 to 113 km. The failure to detect an increase in the intensity of emission of sodium *D* lines during the night is consistent with the hypothesis of nocturnal *E* ionization produced by collisions of meteoric particles.

Evidence of a Relationship Between Back-Scatter from Field-Aligned Ionization in the *F*-Layer, and Fluctuations in the 5577A [OI] Airglow*—O. G. Villard, Jr. and Sidney Stein, *Stanford University*—It has been found that radar echoes may be obtained from ionization lying within the *E* and *F* layers of the ionosphere, and behaving as if it consisted of scattering columns aligned with the earth's magnetic field.†

The echoes, while generally strongest in the hours around midnight, fluctuate considerably in intensity from time-to-time and from night-to-night. The strongest reflection is obtained when the line-of-sight from a transmitter meets a field line at perpendicular incidence at an altitude roughly corresponding to the ion density maxima of the *E* and *F* layers.

Although this requirement restricts considerably the area from which echoes may be received at any given geographical location, it is nevertheless possible—in the case of the *F*-layer—to determine whether activity exists within a sector of roughly ±30 degrees centered on geomagnetic north. This sector is considerably wider in the case of *E*-layer echoes.

In an effort to determine whether a relationship exists between these echoes and fluctuations in the 5577A [OI] airglow, a scatter-sounder has been operated at the Upper Air Research Observatory, Sacramento Peak, New Mexico, in conjunction with the light measurements of E. A. Manring and H. B. Pettit. Several nights, during which simultaneous records were made, have been examined in detail.

A reasonable agreement between *F*-layer radio echoes and light fluctuations was found, suggesting a strong connection between the two effects. Certain of the diurnal features of the green airglow emission and the *F*-region backscatter were found to be similar.*

H. F. Radar Echoes with Unusual Characteristics†—G. C. Rumi, *School of Electrical Engineering, Cornell University*—Using a high power 27.85 mc/sec radar many echoes were observed at Ithaca, New York, during the fall of 1955.

In addition to echoes which have characteristics normally associated with echoes from aurora or meteor trails, there were many with unusual characteristics.

These characteristics of the echoes are:

1) They are discrete and generally have durations less than 0.5 second.

2) They show no preferred range. The maximum range observed was around 1000 km.

3) They rise from noise level to maximum value in two repetition periods of the radar or 40 milliseconds. Calculations of the velocity required to produce the first Fresnel Zone of a column of ionization (deduced from the rise time of the echo and its range) give values in some cases greater than 100 km/sec.

4) They decay very rapidly, in some cases dropping from maximum amplitude (at least five times noise level) to less than the noise level in 40 milliseconds.

5) They generally occurred for two hours around midnight, but did not occur every night. During the months of September, October, and November they occurred on over half the nights. Very few were observed during December. As many as four hundred echoes in one hour were seen. No correlation with known meteor showers was observed.

It does not appear that these echoes can be explained on the basis of present theories of echoes from meteor trails. It is possible that they may be reflections from atmospheric discharges.

A feature of the experimental program was the continuous recording of the A scope presentation on magnetic tape. This method of recording made it possible to measure at a later time the details of those very short echoes.

The Propagation of Long Waves Near 100 KC/S Over Distances of the Order 800 KM‡—E. R. Schmerling, *Ionosphere Research Laboratory, Pennsylvania State University*—Observations made by recording the cw signals radiated from four transmitters of the Danish Decca Navigator chain at frequencies near 100 kc and distances of the order 800 km reveal that the summer records on the three lower frequencies may be consistently interpreted in terms of a simple mirror model for the ionospheric reflecting region. Quasi-cylcic amplitude changes near sunrise and sunset appear to be produced by interference between the ground and once-reflected sky waves. The times and amplitudes of these features enable the reflection heights and reflection coefficients to be determined.

The results are best fitted by a phase change of 180 degrees on reflection, and heights in the range 60–75 km. At the lowest frequency, 71 kc, the morning and evening reflection coefficients decrease steadily from about 0.5 at night to 0.05 during the day. At 85 kc and 114 kc the reflection coefficients go through a pronounced minimum immediately before ground sunrise, but increase steadily after sunset. The sky-wave behavior shows a progressive change with increasing frequency, culminating in the highly irregular behavior observed at 128 kc, which is not susceptible to interpretation by this model. Polarization measurements were not satisfactory, but reveal that the sky-wave is neither closely circularly nor linearly polarized near sunrise and sunset.

The author acknowledges the receipt of a maintenance award from the Department of Scientific and Industrial Research in England during the period covered by the above work. The research was conducted in the Radio Group of the Cavendish Laboratory, Cambridge University, Cambridge, England.

Characteristics of Ionospherically Reflected, Vertically Incident Radio Waves at 75 KC/S*—R. E. Houston, Jr., *Ionosphere Research Laboratory, Pennsylvania State University*—Using a pulsed one quarter megawatt 75 kc transmitter, measurements of group height, change in phase height, absorption, and polarization are being made. Some preliminary results of these measurements are presented and compared with similar observations on 150 kc.

For the winter months, group height records show an average height of around 95 km at night with a mean diurnal variation of about 5 km.

The phase height data are mainly concerned with diurnal variations, which, during the winter months, are of the order of 11 km. Tentative conclusions from the general shape of the envelope of winter months "averages" are drawn. The characteristic rapid drop near ground sunrise and sharp rise about ground sunset is evident.

The absorption measurements are also primarily concerned with diurnal variations. A mean value of $-\log \rho$ for the winter months indicates a value of about 2.7 nepers at noon and one neper at midnight.

Observed parameters for the polarization are given. These are compared with theoretical deductions presented in another paper at these meetings.

The Polarization of Vertically Incident Radio Waves at 75 KC/S†—J. J. Gibbons, G. S. Levy, and S. R. Butler, *Ionosphere Research Laboratory, Pennsylvania State University*—The polarization of 75 kc radio waves reflected at vertical incidence from the ionosphere has been computed using the

* This work was supported jointly by the Army, Navy, and the Air Force under contract with Stanford University.

† A. M. Peterson *et al.*, *J. Geophys. Res.*, vol. 60, p. 497; 1955.

* M. Nicolet, *Phys. Rev.*, vol. 93, p. 633; 1954.

† The research reported in this paper was supported by U. S. Signal Corps Contract DA36-039-sc-56748 and by the National Science Foundation.

‡ The preparation of this paper has been sponsored by the Geophysics Research Directorate of the Air Force Cambridge Research Center, Air Research and Development Command under Contract AF19(604)-1304.

* The preparation of this paper has been sponsored by the Geophysics Research Directorate of the Air Force Cambridge Research Center, Air Research and Development Command under Contract AF19(604)-1304.

† The preparation of this paper has been sponsored by the Geophysics Research Directorate of the Air Force Cambridge Research Center, Air Research and Development Command under Contract AF19(604)-1304.

midnight model deduced by Parkinson.* This model was obtained by applying the Mitra† recombination coefficient to a sunset model based on various experimental data.

The computations are carried out, treating the coupling as a perturbation, by the method of variation of parameters. The results are compared with the 75 kc experimental data so far available at this laboratory.

No echo has been consistently observed which would correspond to what was interpreted at 150 kc[1] as a coupling echo. The computed results are in agreement with this observation.

Some Features of VLF Propagation Deduced from Aircraft Flight Data—J. L. Heritage and S. Weisbrod, *Smyth Research Associates*, and J. E. Bickel, *U. S. Navy Electronics Laboratory*—Some general properties of long distance daytime and night-time vlf signal vs distance curves are considered. In some cases, the influence of changing distance can be distinguished from the effects of ionospheric reflection properties changing with time. On certain flights, several frequencies were recorded simultaneously. A daytime and night-time set of such multifrequency signal vs distance curves are analyzed for apparent height of reflection. The steep incidence daytime reflection height differs considerably at the extremes of the frequencies studied (16.6 kc and 40 kc). The night-time apparent reflection height appears to be frequency sensitive as well as being sensitive to time and incidence angle variation at a single frequency.

Measurement of Atmospheric Radio Noise Moments—Forrest F. Fulton, Jr. and William H. Ahlbeck, *National Bureau of Standards*—Direct measurements of the first, second, and logarithmic moments of atmospheric radio noise envelope voltages at a number of frequencies will be presented. The relationship between measurement of the moments and measurement of the cumulative probability distribution will be discussed.

Variations in the Statistical Character of Atmospheric Noise—A. D. Watt, *National Bureau of Standards*—Measured amplitude-and-time distributions of the envelope of atmospheric noise for various frequencies, bandwidths, times, and geographic locations will be presented. The manner in which these various factors effect the resulting distributions will be discussed, and examples of the effects of variations in these factors will be shown.

Audio Frequency Atmospheric 10–900 Cycles Per Second—Jules Aarons, *Air Force Cambridge Research Center*—The audio frequency electromagnetic spectrum in the range 10–900 cps was surveyed over a two month period, Summer 1955. A loop and vertical antenna were alternately switched to a narrow band analyzer (2 to 6 cps). The site chosen, Mescalero, New Mexico, was relatively free of man-made interference but local storms were recorded.

Results indicate the energy in the band is centered in the region 40–120 cps. Heavy attenuation of signals in the region 450–900 cps takes place during the day. Sunset raises the signal level of this high frequency portion of the spectrum to that of the lower frequency range. Large numbers of pulses are also seen during the night. The peak intensity level at all frequencies occurs around local midnight. Local storms have a spectrum similar to daytime levels.

The data indicates that the night-time levels at all frequencies come from great distances. The daytime energy is concentrated in the 40–120 cycle band and this portion of the band appears to come from distant atmospherics but the 450–900 cycle energy is relatively local in origin.

During one period of several hours a large increase of narrow band energy was seen at 33 cycles per second. The possibilities of this being radiation at the gyro frequency of the sodium ion is discussed.

The Sferic Characteristics of Thunderstorms—Herbert L. Jones, *Oklahoma A. & M. College*—In order to obtain a more precise location of a given thunderstorm center it is considered necessary to substantially increase the present knowledge of the sferic nature of thunderstorms. Consequently the research program for the tornado season of 1956 at the Oklahoma A. & M. Tornado Laboratory has been designed to provide a substantial increase in the recorded data for all types of thunderstorms, including those that may contain tornadoes.

The number of strokes per second coming from a thunderstorm center varies over a wide range from one second to another. The data from a number of storms of various types are correlated in an attempt to demonstrate that individual storm centers do exist, although each storm center may be a part of an over-all group. Comparisons are made between the data obtained from moving film and the data as recorded by the automatic stroke counter.

The Resonant Properties of Ring Circuits—F. J. Tischer, *Huntsville, Ala.*—The ring circuit* is a new type of resonant circuit for microwave frequencies. It consists of a waveguide section with the ends connected to form a ring and a coupling element by which the ring guide is coupled to a main guide.

Three different wave modes can be excited in the ring guide: unidirectional waves, bidirectional waves of equal amplitude, and bidirectional waves of unequal amplitude. The type of the excited mode depends on the coupling element. The corresponding coupling conditions are directional, nondirectional, and semidirectional coupling. Introduction of discontinuities in the directionally coupled ring guide causes a wave pattern similar to that obtained for semidirectional coupling.

The circuit data and relations for the frequency response are presented for the different wave modes. The Q values of the ring guide in general and for rectangular cross section are derived and discussed.

The Transfer Matrix in Microwave Circuits, with Particular Reference to Resonant Cavities†—Leo Young, *Westinghouse Electric Corp.*—A wave picture is set up for microwave circuits. The circuit parameters are the elements of transfer matrices. It is demonstrated how the behavior of a cavity can be predicted in terms of directly measurable parameters. Such an analysis can describe resonant cavities in the way that circuit theory describes tuned circuits containing L, C, and R. It is believed that many of the results obtained are new, and some were perhaps unsuspected. It is hoped that this approach will prove helpful and will make for a clearer understanding of the subject.

Exact expressions for the Q and logarithmic decrement σ of a transmission line cavity are derived in terms of these measurable parameters. Expressions are also obtained for resonance amplification; bandwidth; and resonant length or frequency pulling by a mismatched load.

Certain basic differences between a cavity and an L-C-R circuit are pointed out.

Exact Synthesis of Waveguide Bandpass Filters Based on Prescribed Insertion Loss Functions—Henry J. Riblet, *Microwave Development Labs., Inc.*—This paper gives a synthesis procedure for the design of waveguide filters of arbitrary bandwidth consisting of a cascade of equal length impedance transformers. It is shown that necessary conditions on the insertion loss function of such a filter are sufficient for its physical realizability as a cascade of impedance transformations. Optimum insertion loss functions are proven to imply symmetrical filter configurations. This theory provides a theoretically exact prototype for the design of broadband direct coupled waveguide filters consisting of a cascade of suitable spaced inductive loads in a uniform waveguide. Other applications are noted.

Aperture-Coupled Filters—F. Shnurer and J. B. Travis, *General Electric Company, Advanced Electronics Center at Cornell University*—Rigid requirements for a bandpass filter having low insertion loss together with a very high off-band attenuation has led to a novel method of coupling filter sections. Using this technique, it has been possible to design a four-section filter having a bandwidth of 20 mc at K band with an insertion loss less than 0.3 db.

A discussion of the method of design is presented together with its relation to conventional filter design found in the literature. Experimental results obtained with several designs are given. Also suggestions for improving performance and extending results to other frequency bands are included.

Microwave Multiplexers in Strip-Line—Howard C. Turnage and Robert B. Wilds, *Melpar, Inc.*—Size, weight, flexibility, and ease of fabrication have made strip transmission line particularly adaptable for realization of multiplexer systems in the uhf range. Methods and results of the use of strip-line in coupling adjacent broadband filters are described in this paper.

The problem of passively coupling two or more adjacent filters of direct coupled cavity type to a single source is investigated. The driving point impedance of this type filter is examined both theoretically and experimentally, and the effect on passive coupling considered. A coupling procedure

* R. W. Parkinson, *J. Atmos. Terr. Phys.*, vol. 7, p. 203; 1955.
† A. Mitra, Scientific Rep. No. 68, Ionosphere Res. Lab., Penn. State Univ., University Park, Pa.; September 1, 1954.

* F. J. Tischer, Swedish Patent No. 152,491; August 26, 1952.
† This paper was part of a thesis submitted for the M.S. degree at the Johns Hopkins University, Baltimore, Md.

is described which, without the use of padding or of lossy elements, permits the loss at the crossover point between adjacent coupled filters to be held between three and five decibels above the points of minimum passband insertion loss. Experimental results with coupled stripline filters are used to verify this procedure.

On the Analysis of Symmetrical Waveguide Junctions—Raymond S. Potter, *Naval Research Laboratory*—The theory of finite groups, when applied to the group of symmetry field matrices which characterize the propagating modes and structure of a particular waveguide junction, has been shown by Dicke, Kerns, and Auld to be a valuable technique for determining the optimum matching conditions together with the location of the impedance matching elements which effect the optimum matching conditions.

It will be shown that the technique is particularly useful in establishing the physical realizability and optimum performance of a three or more port junction. It will also be shown that the analytical details of the technique can be more easily applied by the microwave engineer if the following implications of the original papers are highlighted:

1) The evenness or oddness of the modal symmetry can be determined from either the electric or the magnetic field components but is most easily determined from a component which is either always parallel or always normal to the particular structural symmetry plane.

2) The symmetrical interchange of terminals of a waveguide junction requires that the junction be lossless and that the distance from the geometrical center to the terminals of identical cross section waveguide be $n\lambda_g/2$ wavelengths where n is any positive integer.

3) The determination of a set of normal modes of a waveguide junction is dependent upon the multiplicity of the roots of the generator matrix characteristic equation.

4) The normal modes of a waveguide junction are not unique but the junction's optimum impedance matching conditions are unique.

The Dynamo Currents in the Ionosphere Obtained with Spherical Harmonic Analysis and with the Principle of Balance of Power*—W. Pfister and T. J. Keneshea, *Air Force Cambridge Research Center*—Dynamo currents in the ionosphere have been computed by Maeda, by Fejer, and by Baker for simple idealized models of the ionosphere. The method presented here permits the removal of many of the restrictive assumptions and can deal, for example, with any kind of electron distribution around the globe. The unknown dynamo current distribution is written as a series of spherical harmonic functions with unknown coefficients. For each of these harmonics the primary induced power has to be balanced by the outgoing and used-up power expressed as the product of two current densities and the tensor resistivity. This leads to a system of linear equations. The method has been used to compute the S_q current system from the tidal winds. The result is in close agreement with the experimentally observed current system as given by Bartels if an amplification factor of 50 and nearly the same phase for the wind at the level of the ionosphere is assumed.

* Supported by the Geophysics Research Directorate, Air Force Cambridge Research Center, Air Research and Development Command, under contract AF19(604)-969.

Lunar and Unusual Solar Effects on the Ionosphere*—S. Matsushita, *High Altitude Observatory, University of Colorado; and guest worker at the National Bureau of Standards, Boulder, Colorado. (On leave from Kyoto University, Japan)*—In the equatorial region, *Es* reflection is abnormally intense in the daytime. This equatorial *Es* occasionally shows sudden disappearance in the early afternoon. We conclude from the study of ionograms during the period from 1952 to 1955, that this phenomenon occurs in the vicinity of the full and the new moons. We also find, supplementing previous results of others for Huancayo, that lunar stratification of F_2 is evident on ionograms made at Talara, Guam and other stations in the equatorial region. We suggest a mechanism to explain these lunar effects on *Es* and F_2.

Ionospheric variations that result from increased solar activity are discussed, using ionograms obtained at 10 stations. Magnetic variations accompanying these ionospheric variations are also considered.

Solar Control of the Ionosphere—H. Friedman, *U. S. Naval Research Laboratory*—X ray and far ultraviolet detectors have been carried to heights as great as 185 kms in a series of ten rocket experiments covering the past seven years. On the basis of these tests it is possible to attribute *D*-region ionization to solar Lyman alpha at 1216A and most of *E*-region to X rays from 10A to 100A. Longer wavelength X rays and ultraviolet between 100A and 1000A ionize the *F* region. In the Schumann region from 1300A to 1750A the solar intensity falls far below that to be expected from a 6000 deg K black body. As a result there is no sharp transition region from O_2 to O and the dissociation of molecular oxygen progresses rather slowly with altitude. The O_2 concentration in F_2 region remains high enough to control the recombination coefficient by means of charge exchange with atomic oxygen ions.

A clear correlation has been observed between the intensity of ionizing radiations from the sun and the activity of the solar corona. Small rocket techniques are now available which permit firings coincident with solar flares and radio fadeout. A series of such firings will be initiated this summer with the purpose of identifying the flare radiations leading to Sudden Ionospheric Disturbances.

The *D* and Lower *E*-Region—J. C. Seddon, *Naval Research Laboratory*—A re-examination of old rocket data records has revealed the fact that the peculiar but regular variations in the ellipticity of the radiation received from the V-2 rocket can readily be explained if the rocket is in uncharged regions. In September, 1949 flight, these regular variations ended abruptly at 75 km, whereupon the variations were irregular up to 90 km. Sudden changes can be correlated with the beat frequencies observed in the usual manner for altitudes above 84 km. No differential absorption is observed between the ordinary and extraordinary components up to 90 km, and the total absorption is not particularly noticeable. Above 92 km, however, the differential absorption is very evident, and at 98 km the total absorption becomes high. Additional data were obtained from two other rocket flights. On one of these flights some ionization was detected beginning at 68 km. The conclusions reached are that the *D* region begins abruptly in the neighborhood of 70 km, but that absorption at 4 mc does not become severe until the rocket is in the lower edge of the *E* region where the electron density is about 10^5 per cc.

This study has resulted in a proposed method for measuring *D*-layer densities and absorption using rockets. The method is briefly discussed.

* Supported by the Geophysics Research Directorate, Air Force Cambridge Research Center, Air Research and Development Command, under contract AF19(604)-969.

The Electron-Density-Height Profiles in Region *F* of the Ionosphere*—E. R. Schmerling, *Ionosphere Research Laboratory, Pennsylvania State University*—Methods for reducing standard *h'–f* records to electron-density-height profiles are briefly discussed. A method due to Kelso† has been used at the Cavendish Laboratory in England to obtain these profiles from a large number of records chosen from several observatories at summer, equinox, and winter months for various phases of the sunspot cycle. This is more fully discussed by Schmerling and Thomas.‡ The information thus made available enables the electron production and loss processes in the ionosphere to be determined as a function of height, and theories of the formation and behavior of the F_1 and F_2 layers to be examined in terms of the observed facts.

Analysis of the night time behavior in such a way that the effects of movements are minimized show that the loss coefficient decreases approximately exponentially with height. Both quadratic (recombination) and linear (attachment) laws can fit these results, with some bias in favor of the latter. It is shown how this can lead to the formation of both F_1 and F_2 from the same ionizing agency, in accord with the hypothesis of Bradbury.§ The day time behavior is examined in terms of such a model, and seen to give consistent values of loss coefficient if the linear decay law is taken. Detailed considerations show qualitative agreement with the charge transfer mechanism proposed on theoretical grounds by Bates and Massey.‖ The scale heights for electron production and loss are about 35 km, and the datum level for $z=0$ in the production term is about 200 km.

Calculation of the Distribution of the Electron Density in the Ionosphere—J. M. Kelso, *Ramo-Wooldridge Corp.*—A method

* This research program was supported by a grant from the Department of Scientific and Industrial Research in England and was conducted in the Radio Group of the Cavendish Laboratory, Cambridge University, Cambridge, England.

† J. M. Kelso, *J. Geophys. Res.*, vol. 57, p. 3; 1952.

‡ E. R. Schmerling and J. O. Thomas, *Phil. Trans. Roy. Soc.*, in press.

§ N. E. Bradbury, *J. Terr. Mag. Atmos. Elect.*, vol. 43, p. 55; 1938.

‖ D. R. Bates and H. S. W. Massey, *Proc. Roy. Soc., A.*, vol. 192, p. 1; 1948.

is given for calculating the vertical distribution of electrons in an ionosphere in the presence of the earth's magnetic field. The data required are obtained from experimental records of group height as a function of frequency. As in all past work of this type, only layers for which the electron distribution is a monotonic function of height can be treated directly.

This procedure is intended for the use of workers who do not have an electronic calculator at their disposal. The results are obtained by comparing the observed group heights with those obtained from approximate distributions. Various examples obtained from theoretical distributions are used to show the abilities and limitations of the method.

Antenna Smoothing in Two Dimensions—R. N. Bracewell, *Stanford University*—The discussion of antenna smoothing (Bracewell and Roberts, *Australian Journal of Physics*, vol. 7, p. 615, 1954) has been extended to two dimensions. When the antenna has a fan beam, interesting phenomena arise from the fact that extra information is obtainable in each celestial direction by spinning the beam through all position angles. The problem of reconstructing the true distribution from the observations means overcoming not only the blurring effect of averaging over the immediate neighborhood, but the further effect of confusion with distant parts of the distribution which happen to lie in the fan beam.

Analysis of data taken with fan, or strip, beams is likely to remain of lasting importance in radio astronomy since the largest pencil beams will be susceptible of incorporation as elements in linear arrays.

Flux Measurements of Discrete Radio Sources at Frequencies Below 30 Megacycles—H. W. Wells, *Department of Terrestrial Magnetism, Carnegie Institution of Washington*—Following the preliminary observations of discrete radio sources at 12.5 and 15.5 mc reported at Dublin in 1955, efforts have been made to measure the flux of certain radio sources in "absolute" terms at frequencies below 30 mc.

Principal sources of error in such measurements are: 1) effective antenna area, 2) measurement of equivalent antenna temperature. Steps taken to minimize the probable errors will be described. These include the use of simple dipoles, the measurement of antenna efficiency, the intercomparison of noise diodes with thermal sources, and the elimination of "saturation" or "non-linearity" effects in the receiver.

Measurements of Virgo and Taurus A at 26.75 mc show intensities approximately equal at 53×10^{-24} w. m^{-2} (c/s)$^{-1}$. At 18.5 mc the intensity of Virgo is 150×10^{-24} w. m^{-2} (c/s) .

The instrumental improvements strongly indicate that values reported for Cassiopeia A at Dublin (1955) for 12.5 and 15.5 mc (220 and 240×10^{-24} w. m^{-2} (c/s)$^{-1}$ respectively) should be nearly doubled but must await experimental verification during the summer of 1956. It is also anticipated that relative amplitudes of Cygnus A and Cassiopeia A at frequencies below 20 mc may be resolved at the same time.

A Model for Non-Thermal Radio Source Spectra—N. G. Roman and F. T. Haddock, *Naval Research Laboratory*—A model is presented to explain the observed radio spectrum of Cassiopeia A on the assumption that the underlying non-thermal emission process has an intrinsic spectrum which follows the law, $S(\nu)\propto\nu^{-\alpha}$. With only minor adjustments the same model can explain several rather different source spectra.

Depolarization of Solar Radio Bursts—M. H. Cohen, *Cornell University*—T. Hatanaka has given a theory for the depolarization of radio waves in an ionized magnetized medium.* The depolarization is a result of a dispersion in ellipse orientation angles because of differential Faraday rotation within the receiver pass band. Polarization measurements then give an upper limit to the integral of longitudinal magnetic field times electron density along the ray path. It is shown that Hatanaka's measurements of solar bursts are not inconsistent with the assumption of dipole-type magnetic fields in the corona, with a field strength of one gauss at the pole. Possible measurements to determine dispersion are discussed.

Radio Observation of the Lunar Occultation of M1—B. F. Burke and K. L. Franklin, *Department of Terrestrial Magnetism, Carnegie Institution of Washington*—The February 21, 1956 occultation of the crab nebula, M1, was observed at a frequency of 22.2 mc. A simple phase-switching interferometer was used, composed of two eight-dipole arrays, at a spacing of 20 wavelengths. While the interferometer pattern was such that brightness measurements could not be made continuously, it was hoped that information could be obtained about both the radio brightness distribution of the crab nebula and the possible existence of a lunar ionosphere. Severe scintillations prevented quantitative measurements of the source brightness, but the records obtained yield data providing a sensitive test for the presence of an ionosphere. Strong refractive effects would be noticed at a low frequency such as 22 mc, if appreciable ionization existed. The observations showed no appreciable refractive effects, the crab nebula returning to greater than half intensity no more than three minutes after reappearance from behind the sunlit limb, with no observable initial enhancement. The upper limit of electron density thus established depends upon the model used, but making use of Link's calculation† an upper limit of 10^3 el. cm^{-3} is indicated. This upper limit is 100 times less than the previous limit of Elsmore and Whitfield‡ from their measurement of the occultation of IC443.

Radio Observations of Jupiter—K. L. Franklin and B. F. Burke, *Department of Terrestrial Magnetism, Carnegie Institution of Washington*—Progress in observing Jupiter is reported, including the active cooperation of the BAA, Lowell Observatory and R. S. Richardson at Mount Wilson.

Since November 1, 1955, the Department of Terrestrial Magnetism has observed Jupiter at 22 mc almost daily for about seven hours a day. A comparison of longitudes of certain prominent features with the longitudes of the central meridian during an active period shows the radio events rotating with nearly the system II period. A correlation between the presence of the Red Spot and occurrence of radio storms is mentioned with the caution that identification is uncertain and circumstantial. The white region to which C. A. Shain (*Nature*, 176, 856, 1955) attributes the 1950–1951 activity cannot now account for much of the noise observed this season. It may be significant that Shain reported receiving radiation in 1950–1951 during 135° of rotation of Jupiter, while the DTM data show a characteristic rotation angle of the order of 50°.

Data at two other frequencies, 27 mc and 18 mc, available through the courtesy of H. W. Wells, indicate that the Jupiter radiation received is not part of a continuum. Among the three frequencies used at DTM, there is no correlation between the occurrence of bursts, and only a general agreement between the times of prolonged disturbances. The location of the source of these events is predominantly between 280°$_2$ and 60°$_2$ on all frequencies used.

Since January, 1956, the DTM interferometer has been used to observe circular polarization, if present. Many records have been obtained indicating a rather high degree of right-hand, circular polarization, nearly 100 per cent in some cases. One event exhibits some of both the right-hand and left-hand senses, using the radio convention of polarization description.

Losses in Dielectric Image Lines—D. D. King and S. P. Schlesinger, *The Johns Hopkins University*—The dipole mode in a dielectric rod permits an image system in which half the dielectric and its surrounding field are replaced by a metal sheet. If the field is allowed to extend many wavelengths outside the rod, the resulting line has very low losses. The contribution of the image surface to line loss is calculated, and shown to be generally less than the dielectric loss. Radiation from obstacles along the line is also discussed: in closed single-mode waveguides they are useful for matching purposes. Although matching elements are easily constructed for the image line, radiation loss proves difficult to control.

Single Slab Circular Polarization Surface Wave Structure*—Robert C. Hansen, *Hughes Aircraft Company*—A single grounded dielectric slab can support either TM or TE modes, but cannot propagate both with the same velocity. This paper concerns a modification of the single slab which enables either polarization to propagate with the same velocity. Such a structure could transmit a circularly polarized wave, and would be useful in transmission, feeder, and antenna applications.

The structure consists of a grounded dielectric slab with parallel metal plates imbedded in the dielectric, normal to and in

* T. Hatanaka, "The Faraday effect in the earth's ionosphere with special reference to polarization measurements of solar radio emission," Res. Rep. EE 257, School of Elec. Eng., Cornell Univ., Ithaca, N. Y.; August, 1955.

† F. Link, *Bull. Astr. Inst. Czech.*, vol. 7, p. 1; 1956.

‡ B. Elsmore and G. R. Whitfield, *Nature*, vol. 176, p. 457; 1955.

* The work described in this paper was done under Air Force Cambridge Research Center Contract No. AF19(604)-1317.

contact with the ground plane. The plates do not reach the top of the slab. Propagation is *along* the plates, whereas corrugated surfaces propagate across the vanes. For small plate thickness, the TE field is undisturbed; hence, the entire slab thickness controls the velocity. The TM field, however, has an electric field component parallel to the plates, which is shorted out by the plates; thus, only the thickness of slab above the plates controls this mode, and the two modes can be independently controlled.

Since the plates are not a perfect short circuit, a boundary tube analysis is given which finds the higher mode amplitudes, and the variation of effective short circuit with parameters. This analysis sets up a sum of modes in each region, and then solves the resulting sets of simultaneous transcendental equations by a contour integration-residue theory technique. The theory is illustrated by a specific example.

Network Computations in Multimode Waveguide—Leopold B. Felsen, *Microwave Research Institute, Polytechnic Institute of Brooklyn*—Propagation phenomena in a waveguide propagating N modes and containing lumped discontinuities can be described in terms of the behavior (on N transmission lines coupled by lumped networks) of voltage-current (impedance based), incident-reflected waves (scattering basis), or a combination thereof (mixed basis). Such behavior is conveniently analyzed in terms of transfer descriptions which directly relate wave characteristics at one point of the system with those at another. Alternative transfer descriptions in the above-mentioned bases are considered from a unified viewpoint, their individual mutual relationship is described, and conditions imposed by such network properties as reciprocity, conservation of energy, symmetry, etc., are formulated. A table of alternative transfer representations for various specific microwave structures is presented. As an example, the problem of multimode propagation through two transverse discontinuities is considered in detail and evaluated explicitly for the case of small and large discontinuity structures. The former case is of interest to the compensating problem, while the latter constitutes a cavity problem.

Evaluation of Discontinuities in Multimode Circular Waveguide—L. B. Felsen and W. K. Kahn, *Microwave Research Institute, Polytechnic Institute of Brooklyn*—A general formulation for the determination of the network parameters of arbitrary aperture and obstacle discontinuities in multimode waveguide has been applied to the approximate evaluation, in a straightforward manner, of the scattering coefficients of small obstacles and apertures in oversized circular waveguide. Emphasis has been placed on transmission in the TE_{01} mode in a waveguide assumed to propagate all modes up to, but excluding, TE_{02}. Two types of discontinuities have been investigated in detail: (a) angularly symmetric or pseudo-symmetric transverse apertures and obstacles, and (b) nonangularly symmetric structures. Category (a) contains discontinuities which do not couple the TE_{01} mode to any other propagating mode, and comprises centered circular apertures and disks and symmetrical arrangements of symmetrical apertures or obstacles in the waveguide cross section. Category (b) includes noncentered or asymmetrically located apertures or obstacles whose coupling into other modes has been computed.

Accurate and comprehensive measurements have been made via a cavity technique on the discontinuity structures in category (a) and are compared with predicted theoretical values. An extension of the cavity measurement technique to determine TE_{11}-TM_{11} mode coupling is described.

Control of Spurious Modes in Multimode Waveguides by Use of Foam Dielectric Inserts—Samuel P. Morgan, *Bell Telephone Laboratories, Inc.*—When multimode waveguides are used in communications systems, unwanted propagating modes may be generated where the guide changes in size, shape, or direction. If the amplitude and phase of the spurious mode(s) can be determined, it is sometimes possible to insert into the guide properly shaped pieces of low-dielectric-constant material which interact with the desired transmission mode in such a way as to cancel the undesired mode(s). Two examples are described: 1) The cancellation of higher circular electric modes produced by a tapered section joining two round guides of different diameters which carry the TE_{01} mode; 2) the use of a dielectric compensator in a curved section of round guide to permit the broadband transmission of the TE_{01} mode through the bend without undesirable mode conversions.

Helix Waveguide—S. P. Morgan, J. A. Young, *Bell Telephone Laboratories, Inc.*—Helix waveguide, composed of tightly wound turns of insulated copper wire covered with a lossy jacket, shows great promise for use as a communication medium. The properties of this type of waveguide have been investigated using the sheath helix model. Modes whose wall currents follow the highly conducting helix have very low attenuation constants which are essentially the same as for copper pipe. The other modes have very large attenuation constants which are determined by the electrical properties of the jacket. The circular electric mode important for long distance communication has low loss for zero pitch helices. Numerical results for the propagation constants of some of the normal modes in zero pitch helix waveguide as a function of the jacket parameters have been obtained using high speed digital computing machines.

Measurement of Service Fields for VHF Broadcasting—Robert S. Kirby, *National Bureau of Standards*—Current practice in determining service fields of vhf broadcast transmitters involves making mobile field strength recording surveys along generally radial routes from the transmitter. This practice leads to somewhat dubious results inasmuch as the measurements are made along roadbeds using low antennas, and only a small amount of the data obtained is used in making an estimate of a specific field-strength iso-probability contour.

A new method of measurement is proposed and analyzed. This method involves making field strength observations at discrete locations along arcs or complete circles centered on the transmitter. Maximum use is made of the observations as estimators of the population parameters. By sampling at discrete points it becomes feasible to observe the fields at points more representative of potential receiver locations with the proper receiving antenna height. The sampling method has a further advantage of separating out time variations from spatial variations. An example of the determination of an actual television service contour is given.

A Survey of Microwave Near Field Measuring Techniques—J. H. Richmond and T. E. Tice, *Ohio State University*—Various techniques for measuring the near fields of a microwave antenna system and the near-field distortion produced by a radome are discussed. These include the use of a small horn, a small open-ended waveguide loaded with dielectric, a dipole, a short, thin, linear conducting scatterer, a linear scatterer whose scattered energy is modulated at an audio rate to help separate it from the unmodulated incident energy, automatic phase plotters, and a plotter for recording time-quadrature components which provide information equivalent to phase and amplitude measurements. The relative advantages and disadvantages of these techniques are discussed. These techniques are considered with special emphasis on the problem of measuring the distortion due to dielectric obstructions in the near field of an antenna. Test results with various techniques are described and compared.

A 25,000 Megacycle Receiver Employing a Rotary Frequency Shifter—R. L. Cosgriff, R. G. Kouyoumjian, T. E. Tice, D. F. Yaw, *Ohio State University*—The construction and analysis of a simple yet sensitive 25,000-mc measuring system are described. It employs a superheterodyne receiver with an intermediate frequency of 210 cycles and a bandwidth of 4 cycles. A single source of radio-frequency power is used and a continuously rotating waveguide phase shifter is used as a frequency shifter. A small portion of the power from the source is used as a reference signal or "local oscillator" and the remaining signal is shifted in frequency and used as the test signal. This provides the equivalent of a local oscillator with a stability of one-fourth of a cycle in 25×10^9 cycles.

The sensitivity gained through the use of the narrow IF bandwidth is offset by higher crystal mixer noise at the low intermediate frequency. Thus the sensitivity of the receiver is comparable to that of a good superheterodyne receiver of more conventional design. It is believed that the rotary type is less complex and less subject to maintenance difficulties where great frequency stability is essential. It has a linear dynamic range greater than 80 db. It is particularly useful for cw radar reflection studies and for near-field measurements. The advantages and limitations of the system are discussed.

Sensitivity of Microwave Detectors—R. L. Cosgriff, *Ohio State University*—Recently two new types of detectors have come into use in the microwave field. In both cases either a crystal or bolometer is excited by

two signals originating from a common source. One is a fixed amplitude signal and the other is the signal to be measured. In the case of the coherent detector the signal to be measured is modulated and the detector output is proportional to the inphase or quadrature component of this input signal. The second type detector is essentially a low-if-frequency superheterodyne in that the frequency of one of the two input signals to the detector is shifted by a fixed amount by a phase shifter.

If crystals are employed optimum sensitivity in the case of the low-if-frequency detectors results when the fixed signal power P_r causes the noise power in the receiver output to be 4.7 db larger than the noise when the crystal is unexcited. In the optimum case the sensitivity is given by

$$P_{sm} = 1.21\frac{P^2_m}{P_r} \qquad (1)$$

where P_m is the sensitivity of the crystal and receiver using the crystal as a square low device and P_{sm} is the input signal power which causes the desired receiver output power to be equal to the noise power.

An equation similar to (1) results for the sensitivity of these detectors using bolometers. In the case of the bolometer the optimum power due to the fixed amplitude signal is equal the power absorbed by the crystal due to the dc current. Using empirical relationships for the change of resistance with applied power, the sensitivity of the bolometer detector is given by

$$P_{sm} = 0.81\frac{P^2_m}{P_r} \qquad (2)$$

where P^2_m and P_r have the same meaning as in (1) and $2P_r$ is equal to the power due to the dc current when P^2_m is measured. Using (2) one finds that the bolometer should result in detectors of the type herein considered which are considerably more sensitive than that realized using crystal detectors. So far laboratory experiments have not verified this conclusion in that measured sensitivities using crystal and bolometer units are nearly the same.

Line-of-Sight Wave Propagation in a Randomly Inhomogeneous Medium—Bob M. Fannin, *University of Texas*—Theoretical calculations have been made, using the single-scattering approximation, for propagation in a randomly inhomogeneous medium in which the deviations of refractive index from the mean are small. The scattering cross-section concept generally employed evolves from the single-scattering approximation when the additional assumption is made that the "atmospheric blobs" are sufficiently small compared with the range and wavelength that rays to the transmitter or receiver from the various points in a volume several times as large as the average blob size can be taken at parallel. This last restriction is not imposed in this development so that the results are equally valid for large as well as small blobs.

The statistical quantities considered are the variance, correlation function, and power spectrum for the phase and relative amplitude of the field at a point and their difference at two points. The emphasis in this paper is in indicating the transition from the ray treatment results to the scattering cross-section results.

The correlation function for the refractive index is taken to be

$$C(r, \tau) = \overline{\Delta n^2} \exp\left\{-[U^2\tau^2 + 1r - v\tau]^2/1^2\right\}$$

in which r is vector distance, v is the mean wind velocity, and is the time difference. This time as well as space dependent form for the correlation function is employed so that the power spectra can be computed from the original formulation.

Turbulent Mixing Theory Applied to Radio Scattering—Richard A. Silverman, *New York University*—Obukhoff's statistical theory of turbulent mixing is proposed as a replacement for the heuristic theories of Gallet and Villars-Weisskopf, and is applied to the problem of the scattering of radio waves by refractive index fluctuations. In the case of ionospheric scattering, order-of-magnitude agreement with the observed scattered power is obtained if the refractive index fluctuations are attributed to electron density fluctuations produced by turbulent mixing in the lower edge of the E layer. In the case of tropospheric scattering, it appears that order-of-magnitude agreement with the observed scattered power can be obtained, except during the summer months, by attributing the refractive index fluctuations to temperature fluctuations. During the summer months and at low scattering heights, humidity and its fluctuations are expected to play a prominent role. Experimental and theoretical evidence is cited in favor of perennial fractional-degree temperature fluctuations in the troposphere.

The Layered Atmosphere and Scatter Propagation—W. S. Ament and D. L. Ringwalt, *Naval Research Laboratory*—Indirect evidence that tropospheric scatter very often arises from distinct elevated horizontal layers in the atmosphere is found in 1) the radio hole phenomenon, 2) occasional disappearances of radar echoes as the target airplane climbs through the layer, 3) nonmonotonic (wallowing) dependence of scatter field on range (Megaw, Rogers, *et al.*), and 4) refractometer, radiosonde, and other meteorological observations. Dynamical stability of the layer or layers leads apparently to the relatively stable fields reported by Smyth, Bauer, and others. The Booker-Gordon and related theories based on the Born approximation are not well adapted to explain such large meteorological effects on radio fields as 1) and 2); alternative theoretical attacks are suggested in outline. A combined radio field and meteorological measuring program, guided by the foregoing layer concept, is described, and early results presented.

Radio Studies of Atmospheric Turbulence*—J. W. Herbstreit, K. A. Norton, Philip L. Rice, R. B. Muchmore,† M. C. Thompson, and Roger Gallet, *National Bureau of Standards*—A summary is presented in this paper of progress made recently at the National Bureau of Standards, Boulder Laboratories, in understanding the nature of atmospheric turbulence in the troposphere. These studies are motivated by attempts to solve two important engineering problems: 1) the design of radio delay circuits depending upon the forward scatter of radio waves to points far beyond the radio horizon; 2) the determination of the limiting accuracy of a microwave radio direction finding system. Physical reasons are given for preferring a particular mathematical form: $pK_1(p)$* for the correlation function describing the atmospheric turbulence, and experimental radio data are given for propagation paths both well beyond and well within the radio horizon which establish the correctness of the physical reasoning. A third independent source of evidence substantiating the theory is the direct measurement of the fluctuations of the refractive index of the atmosphere by means of a Birnbaum refractometer.

A New Technique for the Study of Scatter Propagation in the Troposphere—W. J. Heikkila, J. H. Chapman, and J. E. Hogarth, *Radio Physics Laboratory, Defence Research Board, Canada*—A radio spectrometer is described which measures the broadening of a radio line due to propagation in the lower atmosphere. The sidebands due to this broadening can overlap the information bands in a communications system, and have the characteristics of noise. These sidebands have been named "propagation noise." It is shown that propagation noise power density varies with f, the frequency difference from the carrier, as k^2/f^2 for values of f in the range 0.05 cps to 20 cps at a carrier frequency of 500 mc. Here k is independent of f. The technique described permits observation of scattering of radio waves over short paths along which meteorological conditions are likely to be uniform, and readily measured.

Troposphere Scattering of Microwaves—C. A. Potter, *U. S. Navy Electronics Laboratory*—Characteristics of X-band and L-band scattered signals were measured in the Arizona desert in 1955. Beam-swinging and antenna aperture comparison were performed at ranges of 46, 103, and 184 miles. Measurements of refractive index fluctuation at a point along the path were taken using temperature sensing elements carried in a tethered balloon. Power spectra of the scattered signals and of refractive index were obtained by punched-card techniques. An approach has been made toward formulation of a model of the tropospheric scattering mechanism as a multiple-scattering process.

Measurements of Signal Levels at UHF and SHF Propagated by the Troposphere over Paths 100 to 618 Miles in Length†—James H. Chisholm and James F. Roche, *Lincoln Laboratory, Massachusetts Institute*

* This work was supported in part by the Air Force Cambridge Research Center, Air Research and Development Command.

† Ramo-Woolridge Corp., Los Angeles 45, Calif.

* $K_1(p)$ is the modified Bessel function of the second kind.

† The research reported in this document was supported jointly by the Army, Navy, and Air Force under contract with the Massachusetts Institute of Technology.

of Technology—Experimental measurements at uhf over paths 94, 188, 350, and 618 miles in length have been made utilizing highly directive paraboloidal antenna systems. Simultaneous measurements at shf were made over the same paths out to 350 miles utilizing the same antennas.

Rates of attenuation vs distance obtained from these experiments have been analyzed to determine the effect of seasonal variations and frequency.

Measurements of the angular scattering for the uhf path, 618 miles in length, were determined by rotating the 60-foot diameter paraboloidal transmitting antenna and recording the resulting signal received on two antennas, one having a 28-foot diameter and the other having a 60-foot diameter.

Measurements of the effective gain of various combinations of transmitting and receiving antenna apertures over these paths are described.

The results obtained at uhf over the 618 mile path are compared with values calculated from current theoretical models of tropospheric scattering.

A New Whistler Dispersion Theory*—R. A. Helliwell, T. F. Bell, and R. L. Smith, *Radio Propagation Laboratory, Stanford University*—Expressions are derived for the group velocity and attenuation rate in the longitudinal extraordinary mode of propagation for frequencies below the gyro-frequency. Detailed graphs of refractive index and the above quantities are shown.

The theory predicts a maximum in the group velocity at a frequency less than or equal to one-fourth of the gyro-frequency. This behavior is not exhibited by the Eckersley approximation, a special case of the theory. The region of validity of the graphs is discussed. Examples are given of their application to the study of whistlers and related low frequency phenomena.

The Application of Nose Whistlers to the Study of the Outer Ionosphere†—R. L. Smith, *Radio Propagation Laboratory, Stanford University*—Assuming that nose whistlers‡ follow lines of the earth's magnetic field and that the group velocity is described by the appropriate dispersion law, we can express the time delay as a function of frequency and ionization along the path. The results of calculations using different models of variation of ionization with height are compared with the data from nose whistler spectrograms.

For a constant density model, the best fit to the experimental data yields an electron density of 800/cc. However, this model is found to be inconsistent with certain features of the experimental data. It is therefore necessary to consider more complicated models. The results of this study are compared with those obtained by other methods.

* The research in this paper was sponsored by the Electronics Research Directorate of the Air Force Cambridge Research Center.

† The research in this paper was sponsored by the Electronics Research Directorate of the Air Force Cambridge Research Center.

‡ R. A. Helliwell, J. H. Crary, J. H. Pope, and R. L. Smith, "The nose whistler—a new high latitude phenomenon," *J. Geophys. Res.*, vol. 61; March, 1956.

Radio Echoes from Auroral Ionization Detected at Relatively Low Geomagnetic Latitudes*—R. L. Leadabrand, A. M. Peterson, *Stanford University*—Radio echoes due to reflection from auroral ionization are consistently seen at the relatively low geomagnetic latitude of Stanford University. These echoes were observed using low power radars at frequencies between 6 and 30 mc. The echoes occur at ranges between 1400 and 4700 km to the north of Stanford. The heights of reflection are between 300 and 1200 km above the surface of the earth. The echoes occurring at great heights may possibly be the result of reflection from the primary auroral particles well outside the earth's ionosphere. The paths which the auroral signals travel over the relatively enormous distance from Stanford to the auroral zone are in most cases greatly influenced by the normal ionospheric layers. The echoes are correlated with periods of high geomagnetic activity but are found to occur most frequently during daylight hours. Typical duration times, on the days when the echoes are found to occur, lie between 1 minute and 3 hours. The diurnal, seasonal, and annual variations in the occurrence frequencies are available from 3 years of experimental observations.

Experiments on Whistlers and Associated Atmospherics†—J. H. Crary and R. A. Helliwell, *Stanford University*—Some recent results of experiments on whistlers and associated atmospherics are described. Stanford whistlers are correlated with impulsive atmospherics recorded on the U.S.S. Atka while she was near Stanford's geomagnetic conjugate point. Six apparent correlations were obtained on December 27, 1954, of which only one was expected on the basis of chance alone. Applying the Eckersley dispersion law the time of origin of each whistler was calculated. The differences between these times and the actual times of occurrence of the corresponding tweeks on the Atka average 0.07 second with a standard deviation of 0.24 second. Since the average delay of the whistlers was about one second, it is concluded that these whistlers were in fact produced by lightning discharges in the southern hemisphere, thus giving support to Storey's theory of the whistler path.

The observation of "short" whistlers with frequency components extending up to at least 25 kilocycles is reported. The results show the practicability of conducting experiments on the whistler mode of propagation using signals from vlf stations or other man-made generators.

A comparison is made of the relative amplitudes of whistlers received on two crossed loops in vertical planes and on a vertical monopole antenna. Although most whistlers were heard with roughly equal amplitude in the three antennas, there were significant differences in some cases.

* This research was supported jointly by the U. S. Army, the Navy, and the Air Force under Contract Nonr 251(07) and DA-04-200-ORD-181 with Stanford University.

† This work was supported in part by the Electronics Research Directorate of the Air Force Cambridge Research Center and in part by the National Science Foundation. The observations on the U.S.S. Atka were made by Amory H. Waite, the official Signal Corps observer, with the cooperation of the CRPL of the National Bureau of Standards, the Signal Corps, and the Navy.

On the Dependence of Whistler Dispersion upon the Geomagnetic Latitude of the Generating Spheric—M. G. Morgan, H. W. Curtis, *Dartmouth College;* H. E. Dinger, *Naval Research Laboratory;* A. W. Sullivan, *University of Florida*—Spherics fixes obtained along the east coast of North America by the Air Weather Service of the U. S. Air Force are identified with individual whistlers observed at one or more locations. The dispersion of these whistlers is determined from spectrograms and compared with the geomagnetic latitude of the spherics.

Other Contributions—M. M. Newman, *Lightning and Transient Research Institute,* and others—(No abstract).

Atomic and Molecular Resonance Devices—H. Plotkin, *Signal Corps Engineering Laboratory*—The use of molecules and resonances in the microwave region as frequency references and as highly selective amplifiers will be discussed. The various systems that have been devised for these purposes may be classified according to several criteria: those in which the referenced molecule enters the measuring field in the form of a beam vs those in which the molecules are part of the gas; systems in which the molecules themselves radiate the useful precise-frequency signal vs those in which the external source is controlled by the narrow molecular response; and finally, systems in which the response is detected by counting selected particles vs those in which absorption of emission of radiation from the molecule is detected. The relative merits of these methods will be discussed from viewpoints of precision signal to noise and practicability.

Atomic and Molecular Frequency Standards for Distance Measuring—Peter Antonucci, *Rome Air Development Center*—This paper will present the aspects that must be considered when an atomic or molecular frequency standard is being used for making distance measurements. It will also compare the advantages gained by using the atomic and molecular frequency standards of those with high-precision crystal.

The paper will cover measurements over long and short periods of time and will bring out the factors which contribute to the errors of both these types of measurements. It will also present one application of this different measuring system to the Navarho Navigation System.

Maser—James P. Gordon, *Bell Telephone Laboratories, Inc.*—An apparatus called the Maser has been developed which allows amplification of microwave power through induced quantum transitions in a beam of unstable ammonia molecules. Theoretically and practically the device allows extremely low noise but also extremely narrow band amplification of microwave signals at the transition frequencies of the molecules. With sufficient regeneration inside a resonant cavity, stable oscillation can be produced, again at the frequencies of the molecular resonances. Long time stability approaching one part in 10^{10} should

be obtainable from a maser oscillator utilizing ammonia as the source of microwave energy. Stable amplification of perhaps 10 db in a bandwidth of several kilocycles has been obtained from presently constructed apparatus. Some experimental details will be discussed; also effects of electric and magnetic fields on the oscillation frequencies.

A Frequency Reduction Technique for Maser Oscillators—Walter H. Higa, *Jet Propulsion Laboratory, California Institute of Technology*—Practical applications of the maser will require a frequency divider to reduce the signal frequency from the *K* band to a region where amplification is readily achieved. The method proposed here utilizes a dual cavity maser which simultaneously generates frequencies of approximately 24 kmc (3, 3 line of NH_3) and 25 kmc (6, 6 line of NH_3); subsequent heterodyning of these two signals will produce a difference frequency of approximately 1 kmc. Stability requirements on the local oscillator used for beating the two output frequencies will be discussed. Advantages and disadvantages of the method will be discussed, and comparison with standard techniques will be made.

Gas Cell Type Frequency Standards and Special Techniques for Linewidth-Reduction and Signal:Noise Increase—T. R. Carver, *Princeton, N. J.*—It is desirable in utilizing atomic resonances as frequency standards of absolute accuracy to obtain very narrow lines and therefore avoid pulling effects of observation equipment. One approach to this problem will be described which utilizes the microwave hyperfine transition of alkali metal vapors, in particular, Rb^{87} at 6834.685 mc/sec. Doppler width is reduced by collision with nonmagnetic buffer gas atoms. To further reduce line width caused by exchange collisions of metal atoms, the technique of optical pumping will be described. The possibility of the use of the resulting device as a molecular oscillator will be discussed.

The Atomichron, an Atomic Frequency Standard—R. T. Daly, *National Company, Inc.*—Progress has been made toward reducing the atomic beam frequency standard to a practical, transportable instrument. Both breadboard and engineering models have achieved a frequency stability of 5 parts in 10^{10} parts for indefinite periods; reproducibility of one part in 10^9 parts. The device consists of a servo controlled quartz crystal oscillator at 5 mc, frequency multiplier and synthesizer delivering a signal to the atomic beam tube to excite the atomic resonance, and a single integrator servo mechanism to control the quartz crystal oscillator. With an atomic resonance "*Q*" of 50 million and a servo velocity constant of 15 it has been possible to achieve the stated results.

Four principal sources of error are found to be:

1) Ambient magnetic field.
2) Phase shifts in the exciting cavity fields through which the atomic beam passes.
3) Even harmonic distortion in the "dithering" of the radio frequency signal applied to excite the atomic beam and sense the servo correction required.
4) Noise accompanying the error sign produced in the atomic beam tuba

Abstracts of Papers From the IRE-URSI Symposium Held October 11-12, 1956—Berkeley, Calif.

Measured Rain Attenuation of 4.3 Millimeter Wavelength Radio Signals—C. W. Tolbert and J. R. Gerhardt, *Electrical Engineering Research Laboratory, The University of Texas*—A series of one-way signal attenuation measurements through rain were made at 4.3 millimeters wavelength over a 1000-foot path at various intervals during the period from November, 1955 through April, 1956. Coordinated rainfall rates and drop size distributions were measured for correlation with the path transmission characteristics. The radio data were recorded continuously for periods of several minutes using either a 4.3 magnetron transmitter with crystal video receiver or a 4.3 mm reflex klystron and a superheterodyne receiver. The rain data were taken at discrete intervals using both tipping bucket and specially designed continuous wire rain gauges and dye-coated filter paper devices. In general it was shown that predictions of signal attenuations based on measured drop size distributions gave results which were consistent with the radio data but that attenuations based on rainfall rates alone, assuming the Laws and Parsons relation between rainfall rates and drop size distributions, could give rise to significant errors for the more intense rainfalls.

Comparison of Predictions of Vector Model of Microwave Reflection from the Ocean with Experimental Results—C. I. Beard, *Applied Physics Laboratory, The Johns Hopkins University*, and F. E. Brooks, Jr., *Electrical Engineering Research Laboratory, The University of Texas*—The vector model of microwave reflection from the ocean* has been extended to predict total signal fluctuations at minima in the interference pattern, as well as maxima, and to predict the shapes of the probability distributions as a function of $h\Psi/\lambda$. For these predictions one requires h, Ψ, and λ for the roughness parameter, $h\Psi/\lambda$, and the polarization of the radiation. A knowledge of the antenna pattern is of course required. The treatment applies to line-of-sight propagation.

A comparison of the theory to experimental results obtained by the Electrical Engineering Research Laboratory of The University of Texas in 1955 at the Gulf of Mexico is given.

Characteristics of Sea Clutter at HF†—R. P. Ingalls and M. L. Stone, *Lincoln Laboratory, Massachusetts Institute of Technology*—The characteristics of sea returns at hf have been the subject of a series of measurements. The initial experiments at 18 and 24 megacycles per second indicated that the Doppler spectrum of the sea return contained a very narrow peak close to the carrier frequency. A similar result has been obtained at a lower frequency by Crombie who also proposed a theoretical model of the clutter generating mechanism.*

This model postulated that most of the clutter return was from sea waves whose wavelength was equal to a half wavelength or multiple of the radio frequency. From hydrodynamic considerations, the velocity of the sea waves is proportional to the square root of the wavelength. The Doppler shift associated with a given carrier frequency is therefore proportional to the square root of the carrier frequency. The Doppler shift of the narrow peaks in the spectrum of the sea return can be derived from these considerations.

A series of Doppler power spectrum and backscattering cross-section measurements have been made at 18 and 24 megacycles using coherent pulsed radar techniques and a narrow band spectrum analyzer. The

* C. I. Beard, I. Katz, and L. M. Spetner, "Phenomenological vector model of microwave reflection from the ocean," IRE TRANS., vol. AP-4, pp. 162–167; April, 1956.

† The research in this document was supported jointly by the Army, Navy, and Air Force under contract with the Mass. Inst. of Tech., Cambridge, Mass.

* D. D. Crombie, *Nature*, vol. 175, p. 681; April 16, 1955.

results supported Crombie's theoretical model of the sea clutter at these frequencies.

The following results have been obtained:

1) The back scattering cross section is on the order of 10^{-4} square meters for a square meter of sea surface.
2) The Doppler spectrum is composed of a peak at the carrier frequency and two narrow sidebands shifted by the amount predicted.
3) The bandwidth of the Doppler shifted sidebands is on the order of 10^{-2} cps.
4) The exact distribution of the clutter power within these spectrum peaks is a function of sea state.

Topics in the Design of Antennas for Scatter*—John Granlund, *Lincoln Laboratory, Massachusetts Institute of Technology*—Unlike the signal received over a line-of-sight path, scatter signals arrive at the receiving site from a continuum of directions with intensities that may be described by a directional pattern similar to an antenna pattern. This paper shows how the mean signal power available at the terminals of a receiving antenna may be expressed in terms of the antenna pattern and of a pattern of incoming power density. Methods of measuring the power density pattern at the receiving site are discussed. Designs maximizing the available power are obtained for two rather general types of antenna when they are illuminated by arbitrary power density patterns. Numerical results, obtained for an assumed Gaussian-shaped power density pattern, suggest that only a very small increase in available power may be obtained by readjusting the pattern of an antenna which was initially adjusted to have maximum plane wave gain in the direction of maximum power density. A large array of small antennas may be subject to "gain loss," but if the connections between array elements are allowed to vary in time at the fading rate, the array will not exhibit "gain loss." Appropriate electronic circuitry for the interconnections is discussed.

HF Field Strength Measurements over Sea Water and Sea Ice†—Stephen J. Fricker and William T. Quinn, Jr., *Lincoln Laboratory, Massachusetts Institute of Technology*—Measurements of field strength of vertically polarized 18 mc waves have been made 1) over sea water off the Massachusetts coast, and 2) over sea water and ice in the vicinity of Thule, Greenland.

The measurements in 1) were made to ranges of 100–300 miles, at altitudes of 600–2000 feet. The method used was to transmit from a ground station and receive on a calibrated receiver mounted in a U. S. Navy blimp. In general, the results agreed with the theoretical curves computed on a 4/3 earth basis for $\Sigma = 80$, $\sigma = 5$ mhos/meter. Between 50 to 150 miles the field often appeared to be a few db below the predicted value, while beyond 200 miles a scatter type field was evident, giving values in excess of the computed levels.

When sea ice is formed, the attenuation rate may be expected to increase if the sea is shielded appreciably. A decrease in the conductivity of the sea water also would give greater attenuation. Measurements were made with a beacon-equipped Navy P2V-5F airplane, with the group equipment at the U. S. Coast Guard Cape Atholl Station. Curves were obtained out to 150 miles, mainly at 5000 feet altitude, under conditions ranging from zero to maximum ice thickness (4 to 5 feet). The curves showed little ice effect, but did have attenuation rates greater than those predicted for a conductivity of 5 mhos/meter. Theoretical curves for smaller conductivity values were compared with the measured curves, and appear to indicate a lower conductivity value for the sea in these regions.

The Effect of Atmospheric Noise on Time-Division Multiplex Teletype*—A. W. Sullivan, *Engineering and Industrial Experiment Station, University of Florida*, and R. F. Brown, *Convair, Fort Worth, Texas*—An experimental study was made of the correlation between the cumulative probability distribution of atmospheric noise and the error-signal distribution occurring in a four-channel time-division multiplex teletype system using frequency-shift modulation. Noise measurements were made at six different predetection bandwidths simultaneously from which six probability distributions were obtained. To a first order approximation these distributions follow the logarithmic-normal probability law and it was found that the error-signal distribution followed the same general law.

The teletype equipment consisted of the AN/FGC-5 Transmitting and Receiving Terminal Groups together with the CV/TRA-31 series Converter. Every effort was made to duplicate normal operating conditions encountered in the usual radio-teletype link.

Empirical curves are presented which show a high degree of correlation between the measures of atmospheric noise and the performance of the system.

Worldwide Lightning Fields and Magnetic Pulsations in the 1 to 150 C/S Band—Philip A. Goldberg, *University of Oregon*—Investigations of geoelectromagnetic activity in the 1 to 150 cps band establish the presence of two different phenomena. Between 30 and 150 cps a continuously fluctuating electromagnetic field with burst-like structure is identified as due to lightning. Waveform details and features of a distinctive diurnal variation show that 1) such fields propagate with only slight attenuation, and 2) the entire worldwide distribution of lightning activity contributes strongly to the rms field at a given location. The attenuation rate is about 1.4 db/1000 km for daytime paths of 5000 and 15,000 km at 100 cps. An ionosphere conductivity of 4×10^{-6} mho-met^{-1} is indicated. Corresponding penetration depths of 25 km suggest that principally upper D and lowest E ionosphere regions support propagation at 100 cps. Between 1 and 5 cps a different class of phenomena is evident from an abrupt increase in spectral intensities to values 50 times greater than in the rest of the band. The indication is that "rapid" 0.01 to 0.1 cps magnetograph pulsations attributed to ionospheric currents have detectable detail up to 5 cps. At a transition frequency between 5 and 30 cps the two phenomena have comparable magnitudes.

Results from the Tornado Season of 1956—Herbert L. Jones, *Oklahoma A. & M. College*—For the first time in the history of sferic research, it is believed, there has been obtained simultaneous recordings of visual lightning strokes and the associated sferics. The high-frequency direction finder recordings show a series of narrow elliptical patterns that occurred at the exact times of the several surges recorded for a stroke recorded by the picture camera. The significance of these results will be discussed.

Several tornadic-type storms were tracked past the immediate vicinity of the Tornado Laboratory. Some interesting relationships were noticed in the simultaneous results from the low and high frequency finders.

Performance of Radio Systems in the Presence of Atmospheric Noise—A. D. Watt and E. L. Maxwell, *National Bureau of Standards, Boulder, Colo.*—The performance of several types of radio systems in the presence of various types of atmospheric noise and thermal noise will be compared with the measured statistical distribution of the noise envelope. The effects of the character of the noise as well as the receiver characteristics upon the resulting errors will be discussed and illustrated by typical examples.

Estimates of External Radio Noise Levels—R. T. Disney, *National Bureau of Standards, Boulder, Colo.*—A recent compilation of available noise date from a number of sources has been made. Using this information, propagation factors, and a knowledge of world-wide thunderstorm activity, a complete new set of expected radio noise levels has been prepared for presentation to CCIR. The methods of handling the data and the considerations given a number of factors that entered into the preparation of these predictions will be discussed. The types of radio noise considered in this report are atmospheric, galactic, and manmade.

Motion of Sporadic-*E* Patches Determined from High Frequency Backscatter Records—Clayton Clark and Allen M. Peterson, *Radio Propagation Laboratory, Stanford University*—New evidence of the motion of "sporadic-E" ionization has been obtained at Stanford University from records of ionospheric sounding equipment which displays ground (or sea) backscatter as mirrored in ionospheric layers or reflecting clouds. Sporadic-E patches of relatively limited geographical extent (order of 10,000 square kilometers) often appear on the records of this apparatus, and their growth and motion can in some cases be followed. Whether this motion is due to physical translation of the ionized material (as by winds) or to some other cause such as motion of an ionizing agency is not known;

* The research in this document was supported jointly by the Army, Navy, and Air Force under contract with the Mass. Inst. of Tech., Cambridge, Mass.
† The research in this document was supported jointly by the Army, Navy and Air Force under contract with the Mass. Inst. of Tech., Cambridge, Mass.
* The research reported in this paper was sponsored by the AF Cambridge Res. Ctr., Cambridge, Mass., under Contract No. AF 19(604)-876.

however, it is of interest to compare observations made by this relatively new technique with earlier ones made by other means.

Detailed observation of E_s clouds or patches showed that the number which can be clearly distinguished as separate events is approximately 2700 in the three-year period. Duration of the individual patches varied from a few minutes to a maximum of 10.5 hours, with a mean value of 3 hours. Every patch was examined for indications of motion. If during a period of one-half hour a given patch did not dissolve or become mingled with other activity so that it could no longer be studied as a unit, it was chosen for plotting. The centroid of the patch, defined as the mean range and the mean angular position in azimuth, was plotted until the patch either moved out of range or was otherwise lost. A total of some 264 such tracks were studied and speed and direction information derived.

Results indicate speeds between 50 and 1000 km/hr with a strong peak near 250 km/hr. Directions of motion observed were predominantly westward but cases occurred in other directions also. Diurnal and seasonal variations of speeds, directions and geographic distributions are presented.

Supporting evidence obtained from the vertical incidence sounder is presented along with a discussion of possible causitive mechanisms involved.

Lunar Tidal Variations in the Sporadic-*E* Layer of the Ionosphere at Stanford, California*—H. Myron Swarm, *Linfield Research Institute, McMinnville, Oregon*, and R. A. Helliwell, *Radio Propagation Laboratory, Stanford University*—Statistical studies of the virtual height of the sporadic-*E* ionospheric layer at Stanford, Calif. have shown the existence of a semidiurnal lunar tidal variation.

Six months' data in 1951 and two months' data in 1953 were analyzed using a digital computer. Maximum amplitude of the semidiurnal lunar variation was found to be about 0.6 km with the maximum occurring about 6 hours after local transit. Consistent results were obtained with both sets of data.

These data are compared with other published semidiurnal E_s and *E*-region tidal data.

Some Characteristics of Equatorial *F*-Region Scattering Deduced from Soundings Made Aboard a Moving Ship†—O. G. Villard, Jr. and P. B. Gallagher, *Radio Propagation Laboratory, Stanford University*—A 17-megacycle scatter-sounder was operated aboard a military transport vessel during a voyage from California to the Marshall Islands (geomagnetic latitude approximately 3° north) and return, March 5–30, 1956. The equipment had a peak power output of one kilowatt and a pulse length variable from 200 to 2000 microseconds. A beam antenna was used, consisting of a three-element Yagi rotatable in azimuth and capable of being tilted so as to direct its major lobe upwards as well as along the horizon.

During the evening hours, at geomagnetic latitudes less than 15 degrees, a strong echo was obtained from ionization believed to be the *F*-region scatter observed by Booker and Wells at Huancayo, Peru, and first reported in 1938. The echo was present at times when the f_0F_2 was as low as 11 or 12 megacycles. The measurements suggest 1) that the ionization is not, in general, field-aligned; 2) that it is in the form of a horizontal layer, and 3) that its time of appearance is a function of the geomagnetic latitude of the observing station.

Whistler and Dawn Chorus Occurrence above the Auroral Zone—H. W. Curtis and M. G. Morgan, *Dartmouth College*—Observations were made in June and July, 1956, at Thule and Sondrestron, Greenland, and at Frobisher Bay, Baffin Island. Comparisons on these measurements with data from Knob Lake, Quebec (in the auroral zone) and from the U. S. East Coast network of Whistler recording stations indicates that Dawn Chorus extends far north of the auroral zone and of latitudes at which Whistlers are only faintly detectable; but not to the geomagnetic pole.

Nose Whistler Observations at Seattle*—R. L. Smith and R. A. Helliwell, *Radio Propagation Laboratory, Stanford University*—A new type of whistler called the "nose" whistler was discovered recently at College, Alaska (geomagnetic latitude 65°), and a theory of its origin was given.† Observations using special equipment were made at Seattle, Washington (geomagnetic latitude 53°), during March and April, 1956, to check the theory. Several examples of nose whistlers were found, for which the nose frequencies were about 15 kc, a value closely in accord with the theory. Each record shows an associated whistler component of the "classical" (*i.e.*, no nose observable) type arriving slightly ahead of the nose whistler. In one case a simultaneous recording was obtained at Stanford (geomagnetic latitude 44°) and showed only the classical component of the whistler.

These results support the hypothesis that classical whistlers are simply the lower frequency components of nose whistlers and that the nose frequency is determined primarily by the electron gyrofrequency at the top of the path. They provide new evidence that whistler pairs result from the concentration of whistler energy at different geomagnetic latitudes. It is shown that nose whistler data capable of giving much more detailed information on the distribution of charge along the ray path than can be extracted from classical whistlers.

The cooperation and assistance of R. F. Chase and H. M. Swarm in connection with field work are gratefully acknowledged.

An "Unusual" Solar-Terrestrial Relationship—Kurt Toman, *GRD, Air Force Cambridge Research Center*—Daily values of the final Zurich sunspot number (Z) and the planetary K-index (ΣK_p) were correlated. The number of selected pairs was essentially constant. The studies were extended over the last sunspot cycle. Positive and negative correlation coefficients were obtained. The former are prevalent during the period of sunspot maximum. During sunspot minimum limited intervals of a negative correlation between Z and ΣK_p became apparent. The negative correlation was found to be significant as the correlogram revealed the solar rotational period of 28½ days.

One interval of negative correlation between Z and ΣK_p was investigated in more detail.

This analysis may bring us closer to a physical interpretation of solar-terrestrial relationships than correlation studies extended over long periods are likely to provide us with.

On the Interpretation of Long-Range Radio Echoes from Auroral Ionization*—Sidney Stein and O. G. Villard, Jr., *Stanford University*—Ever since the inception of continuous scatter-sounder recordings at Stanford University, long-range radio echoes from the auroral zone have been detected.† These long-range echoes are attributable to reflections from ionization associated with the aurora.‡

Long-range propagation paths from Stanford into the auroral zone via the *E* layer and *F* layer were investigated to determine the loci of perpendicular intersection between the ray paths and the terrestrial magnetic field lines. Range histograms for auroral-zone echoes were obtained for the different radio frequencies of operation. Comparisons were made between the experimental histograms and the ranges predicted by the propagation modes that occur at each frequency, in order to determine the altitudes of reflection.

Through analysis of scatter-sounder PPI recordings of individual long-range auroral-zone echoes, the propagation mode can frequently be deduced. The altitude of perpendicular intersection of the ray path with the magnetic field at the range of the auroral-zone echo was determined for many cases.

A conclusion from this study is: long-range auroral-zone echoes result from long-range propagation into the auroral region with reflection from ionization situated at *E*-region heights. This result is in accord with the investigations of auroral echoes performed by other experimenters at high latitudes.

Diurnal Variations of Signal Level and Scattering Heights for VHF Propagation—Albert D. Wheelon, *The Ramo-Wooldridge*

* This research was sponsored by the Electronics Research Directorate of the AF Cambridge Res. Ctr., Cambridge, Mass.

† This work was supported jointly by the U. S. Army, Navy, and Air Force under contract with Stanford Univ., Stanford, Calif.

* This work was supported in part by the Electronics Res. Directorate of the AF Cambridge Res. Ctr. and in part through an IGY Natl. Sci. Foundation Grant.

† J. H. Crary, J. H. Pope, and R. L. Smith, "The 'nose' whistler—a new high-latitude phenomenon," *J. of Geophys. Res.*, vol. 61, pp. 139–142; 1956.

* This work was supported jointly by the U. S. Army, Navy, and Air Force under contract with Stanford Univ., Stanford, Calif.

† A. M. Peterson and R. L. Leadabrand, "Long-range radio echoes from auroral ionization," *J. of Geophys. Res.*, vol. 59, p. 306; 1954.

‡ R. L. Leadabrand, "Radio Echoes from Auroral Ionization Detected at Relatively Low Geomagnetic Latitudes," Tech. Rep. No. 98, Radio Propagation Lab., Stanford Univ., Stanford, Calif.; 1955.

Corporation—The scattering of vhf radio waves in the ionospheric E layer is identified with turbulent fluctuations of the electron plasma. The theory of gradient mixing is applied to the afternoon and early evening periods, for which solar control is thought to dominate meteoric contributions. The scattering cross section for this process depends on ionospheric conditions only through the ambient electron

$$\sigma = r_0^2 \left(\frac{dN}{dh}\right)^2 \left[\frac{4\pi}{\lambda} \sin\frac{\theta}{2}\right]^{-5}$$

density-height profile $N(h)$. The variation of field strength scattered from a given height is thus related to diurnal variations in the D and E layers.

Using available estimates for electron density and recombination coefficients in the lower ionosphere, it is found that the afternoon decay of signal strength and simultaneous increase of scattering height can be understood. The observation of two scattering levels on short paths and the lack of a midday maximum on very long paths are also predictable. The signal behavior on hf and vhf scatter during sudden ionospheric disturbances can be correlated with this model, as can the diurnal variation of the power ratio of 50 and 108 mc signals. A brief discussion of the meteoric component is also presented.

Observations of Forward Scattering of 43.5 MC/S Radio Waves from Meteor Trails Over a 690-KM from Palo Alto, California to San Diego, California—T. J. Keary and H. J. Wirth, *U. S. Navy Electronics Laboratory, San Diego, Calif.*—Since the summer of 1955 the Stanford University Radio Propagation Laboratory has operated at Palo Alto, California a 43.5 mc radio-transmitter with output power of a few hundred watts broadly directed toward San Diego by a 3-element Yagi antenna. At the San Diego terminal of the 690-km path, the Navy Electronics Laboratory has monitored the RPL transmissions, using a similar 3-element Yagi antenna connected to conventional receiving and recording equipment.

Signal spikes observed to erupt intermittently above the noise level are interpreted as being produced by forward scattering of the transmitted radiation by ionized trails of meteors. Analysis of the records reveals the following:

1) Rates of occurrence of signal spikes are about four times as high in early morning (0600) as in the late afternoon (1800).

2) Intervals between signal spikes have a Poisson distribution as expected from statistical considerations.

3) Distribution of durations of exponentially decaying signal spikes at $1/e$ times peak amplitudes shows a maximum at 0.2 sec, a value considerably shorter than originally anticipated.

4) Distribution of amplitudes indicates that the number of echoes N having amplitude greater than A is given approximately by $N = 1/A^m$. There is some evidence that exponent m has a diurnal variation, being higher in early morning hours than in late afternoon hours.

The Results of Some Rocket Experiments for Electron Density Distribution—James C. Ulwick, *Ionospheric Physics Laboratory, Geophysics Research Directorate, Air Force Cambridge Research Center*—The rocket experiments are based on the measurements of the delay of a pulsed signal as function of the position of the rocket. The analysis has been made for the smooth horizontally stratified ionosphere using the IRM 704 electronic computer.

The data from three rocket flights are presented. They are limited to E-region heights. Preliminary results of the same flights have been reported before. A comparison of the electron density curves obtained for the same ionosphere at different frequencies, different ground stations, and different legs of the rocket trajectory allows to estimate the accuracy of the results and to judge the influence of local irregularities.

Measurements with Voice Transmissions by Ionospheric Scatter on 38.6 MC—I. H. Gerks, *Collins Radio Co.*, and R. M. Wundt, *Propagation Laboratory, Air Force Cambridge Research Center*—This paper describes some results of an experimental program aimed at the investigation of propagation characteristics and modulation techniques particularly for voice transmissions by ionospheric scatter in the vhf range.

An experimental link using a frequency of 38.6 mc has been set up by Air Force Cambridge Research Center and Collins Radio Company between Cedar Rapids, Iowa, and Scituate, Mass. Versatile equipment has been designed providing for transmission and reception of voice signals by am, fm, and single-sideband modulation, and of frequency-shift telegraphy signals. On SSB two voice channels are available. SSB transmissions are made with suppressed carrier which is reclaimed at the receiver in order to maintain the exact relationship of the different frequencies in the sideband. Dual space diversity is used at the receiver and a diversity combiner of the ratio squarer type is used giving an improvement of 3 db over the switching type combiner. Voice transmissions with SSB and fm are being compared during 24-hour periods and signal strength and signal-to-noise ratios are measured at the same time. The effect of space diversity on SSB transmission is investigated. Tape recordings of typical voice transmissions will be demonstrated. Measurements of phase coherence in a narrow radio-frequency band with a width of 0.8 kc to 3.2 kc are being made using SSB modulation, and with a bandwidth up to 20 kc with the AM suppressed carrier method.

Bandwidth Limitations of the Ionosphere for Through Transmission—R. B. Muchmore and A. D. Wheelon, *GMRD, The Ramo-Wooldridge Corporation*—It is known that long-distance scatter propagation via the ionosphere has a bandwidth limitation produced by the random scattering process. It is shown here that there is a similar limitation for line-of-sight transmission through the ionosphere but that allowable bandwidth for coherent transmission is, in general, much greater for through transmission than for beyond line-of-sight scatter. Expressions are derived for the bandwidth of the medium for both near and far zone limits. The near zone bandwidth is independent of the parameters of the medium; the far zone bandwidth is a function of the height and depth of the ionosphere, the fluctuation scale length, and the wavelength. The theoretically derived results are compared with the results on radio star scintillation obtained by Burrows and Little.

On Meteor Echoes from Underdense Trails at Very High Frequencies*—Morton Loewenthal, *Lincoln Laboratory, Massachusetts Institute of Technology*—The behavior of underdense meteor echoes is investigated in the frequency region where the time for the meteor to produce the reflecting trail is of the same order of magnitude or smaller than the decay time given for trails in which the finiteness of the meteor velocity is ignored. The theory involves the properties of Fresnel integrals or error functions of complex arguments. Results were obtained by programming the computation on the Whirlwind II Computer and from these computations it is possible to determine the effects of diffusion. The results clearly indicate the transition from the infinite velocity extreme to the case of severe diffusion both of which can be handled by elementary methods. In addition to results reported, early data will be presented on the turning points, maximum and minimum, in the presence of diffusion, and also the effects of diffusion on the duration and frequency spectra of the echoes.

Measurements in an Aircraft of 50-Mc Field Strength Along a 1500-Mile Path†—William G. Abel, *Lincoln Laboratory, Massachusetts Institute of Technology*—Variations in the strength of signals from a high-power cw transmitter at El Campo, Texas were measured in an aircraft flying between El Campo and Round Hill, Mass. Usable signals were received continuously from the transmitter site to distances somewhat in excess of 1000 miles. Measurements were made both along the great circle path and off-path and at several different altitudes.

Changes in the fading rate and rate of attenuation of the received signal were observed as the aircraft was flown successively through the line-of-sight field, diffraction field, tropospheric scatter field, and ionospheric scatter field. The change from one propagation mode to another was smooth without abrupt changes in field strength level and with a gradual increase in fading rate as the transition region was traversed.

Average rates of field-strength attenuation for the several propagation modes were determined from these measurements.

Discussion—What are the most easily measured characteristics of terrestrial radio

* The research in this document was supported jointly by the Army, Navy, and Air Force under contract with the Mass. Inst. of Tech., Cambridge, Mass.
† The research in this document was supported jointly by the Army, Navy, and Air Force under contract with the Mass. Inst. of Tech., Cambridge, Mass.

noise from which the interference to different types of communication systems can be determined?—*CRPL Boulder Laboratories, University of Florida, and others.*

The Role of Stratospheric Scattering in Radio Communication—H. G. Booker and W. E. Gordon, *Cornell University*—On the mixing-in-gradient hypothesis of incoherent scattering of radio waves in a dry atmosphere the intensity of the irregularities in dielectric constant depends on the excess of the temperature gradient above that appropriate to an adiabatic atmosphere. In going from the upper troposphere to the stratosphere, there is a significant increase in this gradient-excess and consequently a significant increase in the intensity of irregularities in dielectric constant. The decrease in intensity with increase of height measured by Crain* in the troposphere does not, therefore, indicate reliably the intensity to be expected above the tropopause.

Calculations have been made concerning the effect of stratospheric, as distinct from tropospheric, scattering. Stratospheric scattering is expected to predominate over tropospheric scattering at ranges greater than about 700 km. At a range of 1000 km the transmission-loss due to stratospheric scattering agrees reasonably well with observations reported by Norton, Rice, and Vogler,† and by Chisholm and Roche.‡ The effect of stratospheric scattering at a frequency of 180 mc is such that the minimum signal observed at this frequency over the path from Cedar Rapids, Iowa to Sterling, Va. could conceivably have been stratospheric in origin, with ionospheric scattering being predominant at certain times, for example, during SID's.

A Study of Propagation Conditions at Vero Beach, Florida—C. A. Hines, *Wright Air Development Center*—This paper presents a summary of the results of a study of the degraded propagation environment of the eastern coast of Florida. The data were taken on May 22–25, 1956. Signal intensity measurements were made at 3300 mc in level flights at various altitudes from 1000 to 10,000 feet. Extensive refractive index data were obtained in the form of vertical profiles, high-altitude microfluctuations, and near-the-water microfluctuation. During the course of the tests, signal strength measurements showed "standard" propagation on May 22 and 25. On May 23 and 24, the data show short-term fades, radio holes, and beyond-the-horizon signals of such intensity (only a few db below free-space) as to exclude the probability of a high-altitude scatter mechanism being a major contributing factor. A near-the-surface mechanism such as "low quality ducting" is indicated.

Overwater Refractive Index Measurements from the Sea Surface to 15,000 Feet—C. A. Hines, *Wright Air Development Center*, and C. M. Crain, *The University of Texas*—This paper describes the results of refractive index measurements made from near the surface of the sea to altitudes of 15,000 feet off the East Coast of Florida. The low altitude measurements were obtained with microwave refractometer mounted on an adjustable height boom on a boat and the other measurements, both fluctuations and profiles, were made using airplane carried refractometers. The measurements were made by the Propagation Section of WADC concurrently with a series of air-to-ground 3000-mc propagation measurements described in a companion paper by Hines. Particular emphasis is given to the boat measurements where rapid fluctuations greater than 20 N units were common at altitudes of 30 feet above the surface. These measurements and similar measurements made by the University of Texas from a drilling platform in the Gulf of Mexico illustrate the extreme nonhomogeneity of the refractive index structure common at low altitudes near sources of water vapor.

Recent Observations of Thin and Horizontally Stratified Elevated Dielectric Layers in the Troposphere with Implications for Short Wave Tropospheric Propagation Beyond the Horizon*—J. R. Bauer, J. H. Meyer, J. T. Prohaska and F. A. Wilson, *Lincoln Laboratory, Massachusetts Institute of Technology*—Recent airborne measurements of gross refractive index profiles of the troposphere and the fine structures of elevated layers are reported. Many of the observed layers were stratified over distances in excess of two hundred miles and are shown to follow the curvature of the earth to a remarkable degree. Because moisture and temperature measurements were conducted simultaneously with the refractive index measurements, some relationships regarding the nature of the rapid changes in the composition of the atmosphere across elevated layers are reported. While most of the layers described are of the well-known subsidence (shelf) type, the existence of extremely thin step-function-like layers with very sharp upper and lower edges is also established. Relatively strong elevated layers found in the spring are compared with extremely weak ones observed in very dry winter air at sub-zero temperatures.

The possible role of these thin, horizontally stratified layers in the propagation of short waves well beyond the horizon is discussed.

A Note on the Effect of Weather Fronts on VHF and UHF Transmission Beyond the Horizon—D. R. Hay, J. W. B. Day and L. A. Maynard, *Defence Research Board, Radio Physics Laboratory, Ottawa, Ont., Canada*—The effect of weather fronts on vhf and uhf signals transmitted beyond the horizon is being studied on two experimental paths. A preliminary analysis indicates that the passage of a weather front through the transmission path is accompanied by a marked increase in signal fading rate. Measurements on the signal amplitude distribution and frequency spectrum during the frontal passage are being carried out as an extension of the experimental program.

* C. M. Crain, "Survey of airborne microwave refractometer measurements," PROC. IRE, vol. 43, pp. 1405–1411; October, 1955.

† K. A. Norton, P. L. Rice, and L. E. Vogler, "The use of angular distance in estimating transmission loss and fading range for propagation through a turbulent atmosphere over irregular terrain," PROC. IRE, vol. 43, pp. 1488–1526; October, 1955.

‡ Chisholm and Rice, URSI meeting, Washington, D. C.; May, 1956.

* The research in this document was supported jointly by the Army, Navy, and Air Force under contract with the Mass. Inst. of Tech., Cambridge, Mass.

Contributors

Carlos M. Angulo (S'50–A'52–M'52) was born in Pinto (Madrid), Spain, in 1921. He received the degree of Ingeniero de Telecomunicacion from the Escuela Oficial de Telecomunicacion in Madrid, in 1946; the M.E.E. degree in communication engineering in 1951, and the D.E.E. degree in electrophysics in 1955, both from the Polytechnic Institute of Brooklyn, New York.

C. M. Angulo

From 1946 to 1948, Dr. Angulo worked as an assistant technical director of Transradio Espanola S.A. in Madrid, engaging in radio telegraphy and radio telephony. In 1947 he became a research associate of the Spanish Council of Scientific Research in Madrid, working in electrcacoustics. Dr. Angulo joined the Polytechnic Institute of Brooklyn as a research associate in 1949 and as instructor of electrical engineering in 1950. His research during this period was in microwaves. He became an assistant professor of engineering at Brown University, Providence, R. I., in 1952 and associate professor in 1955, where he is at present doing research in antennas and propagation while teaching.

During the summer of 1956, Dr. Angulo was a visiting research associate professor at the Control Systems Laboratory of the University of Illinois, working in propagation problems.

He is a member of Tau Beta Pi, Sigma Xi, and the American Association for the Advancement of Science.

❖

For a photograph and biography of Bob M. Fannin, see page 672 of the October, 1956 issue of IRE Transactions on Antennas and Propagation.

❖

For a photograph and biography of Leopold B. Felsen, see page 96 of the January, 1956 issue of Transactions of the PGAP. Dr. Felsen's position at the Polytechnic Institute of Brooklyn has been changed to that of Research Associate Professor.

❖

John Searcy Hollis (S'49–A'50–M'55) was born in Collier, Ga., on November 6, 1918. Mr. Hollis was employed by Warner Robins Air Service Command from 1942 to 1944, where he headed an aircraft radio maintenance school and was later general foreman of the aircraft radio and radar maintenance shops. After service in the United States Navy in 1944 and 1945, he studied at the Georgia Institute of Technology, receiving the B.E.E. degree with highest honor in 1950 and the M.S.E.E. degree in 1956.

J. S. Hollis

Mr. Hollis joined the staff of the Engineering Experiment Station at Georgia Tech in 1948, where he is now a special research engineer in the Radar Development Branch and is directing programs on specialized scanning techniques.

Mr. Hollis is a member of Eta Kappa Nu, Tau Beta Pi, and Phi Kappa Phi, and is an associate member of Sigma Xi.

❖

F. Sheppard Holt was born in Washington, D.C., July 12, 1920. He received the A.B. degree from Kenyon College in 1941. From 1942 to 1943 he was a research associate in the Theoretical Group, M.I.T. Radiation Laboratory, and from 1943 to 1946 he held a commission in the U.S. Navy. He attended the Graduate School at M.I.T. from 1946 to 1950 concurrently serving as an Instructor in the M.I.T. mathematics department. Since receiving the Ph.D. in applied mathematics in 1950, he has worked as a mathematician in the Antenna Laboratory of the Air Force Cambridge Research Center. He now holds the position of assistant professor in mathematics at Tufts University and works part time for the Air Force Cambridge Research Center.

F. S. Holt

❖

Kenneth H. Jehn was born in Paterson, N. J., on April 10, 1917. He received the B.S. degree from Rutgers University in 1942 and the M.S. degree in meteorology from New York University in 1949. During World War II, he served as a weather officer in the Army Air Forces, including one year as instructor of meteorology at New York University. In September 1946, Mr. Jehn joined the staff of the Electrical Engineering Research Laboratory at The University of Texas as a research meteorologist, where he has been engaged in research in micrometeorology, radio meteorology, and radio climatology. During this time he also developed the present academic program in meteorology, first as instructor and now as assistant professor of meteorology and nominal head of the meteorology program in the Department of Aeronautical Engineering at The University of Texas.

K. H. Jehn

Mr. Jehn is a professional member of the American Meteorological Society, and a member of the American Association for the Advancement of Science, the Ecological Society of America, Phi Beta Kappa, and Sigma Xi.

❖

Edward I. King (S'55–A'56) was born on July 10, 1932, in Pittsburgh, Pa. He was graduated from the University of Florida in 1955 with the degree of Bachelor of Electrical Engineering. While at the University of Florida he worked part-time with the Atmospheric Noise Research Laboratory. Upon graduation he joined the staff of Bell Telephone Laboratories in the electronic switching development department. He is now on active duty with the U. S. Navy.

E. I. King

Mr. King is a member of Phi Eta Sigma and Phi Kappa Phi.

❖

Maurice W. Long (S'47–A'51–SM'55) was born on April 20, 1925, in Madisonville, Ky. Mr. Long spent 1943 to 1946 in the U. S. Navy. He received the B.E.E. degree from the Georgia Institute of Technology in 1946 and the M.S.E.E. degree from the University of Kentucky in 1948. The next two years were spent in graduate studies at the University of Kentucky and Columbia University.

M. W. Long

Mr. Long was employed for part of 1946 and 1947 and the summer of 1948 as a research assistant at the Georgia Institute of Technology. From 1947 to 1949 he was an instructor of electrical engineering at the University of Kentucky. Since 1950 he has been at the Engineering Experiment Station

of the Georgia Institute of Technology where he is presently head of the Radar Development Branch.

Mr. Long is a member of Sigma Pi Sigma and Sigma Xi.

❖

Alex Mayer was born in Romania and entered the United States in 1930. He received the B.S. degree in physics from College of the City of New York in 1943, and the M.S. and Ph.D. degrees in physics from New York University in 1950 and 1954, respectively. From 1944 to 1946 he served in the armed forces first as sound-range and radio repairman, then as physics and mathematics instructor at the Philippine Institute for the Armed Forces, Manila. From 1946 to 1949 he was an instructor in the Physics Department at C.C.N.Y. From 1950 to 1954 he was a research assistant as well as instructor in the Physics Department at N.Y.U., where his research activities were in the fields of electromagnetic diffraction theory and gaseous electronics. As a senior engineer in the Microwave Group of the M/R Division of Raytheon Mfg. Co., he was engaged in antenna research from 1954 to 1956. He is presently with a communications techniques group at the Lincoln Laboratory of M.I.T.

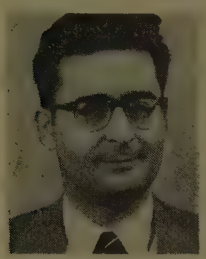

A. MAYER

❖

Leslie G. McCracken (S'47–A'48–SM'55) was born in Philadelphia, Pa., in 1925. He received the B.S. degree in electrical engineering from the Massachusetts Institute of Technology in 1945, the M.S. degree in electrical engineering from Lehigh University in 1947, and the Ph.D. degree from the Pennsylvania State University in 1952.

L. G. MCCRACKEN

From 1943 to 1946, he served in the U. S. Naval Reserve. In 1947 he accepted an appointment in the Ordnance Research Laboratory at the Pennsylvania State College. There he held the position of research assistant in the electronics section until 1949, when he joined the staff of the electrical engineering department of the Pennsylvania State College.

Since 1951 he has been associated with the Naval Research Laboratory, Washington, D. C., where he is a consultant in the Search Radar Branch, Radar Division, engaged in studies of wave propagation phenomena and search radar performance.

Since September, 1956 he has been serving as an associate professor of electrical engineering at Lehigh University. Dr. McCracken is a member of Eta Kappa Nu, Sigma Xi, and Alpha Phi Omega.

❖

Yasuto Mushiake (A'55) was born in Okayama-ken, Japan, in 1921. He graduated from Tohoku University, Sendai, Japan in 1944, and continued his graduate study there for five years, receiving the degree of Doctor of Engineering in 1954.

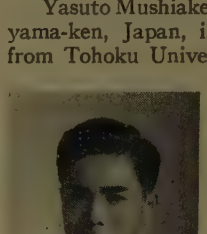

Y. MUSHIAKE

Since 1949 he has been an Assistant Professor in the Electrical Communications Department of the Tohoku University. In 1954 he left Japan temporarily to enter the Antenna Laboratory of The Ohio State University as a research associate. After 20 months of research work in the United States he returned to the Tohoku University in 1956.

Dr. Mushiake has designed various tv receiving antennas in Japan, and he is one of the co-authors of the book "Yagi-Uda Antenna," and others. He received the Ohm Technical Prize in 1953.

He is a member of the Institute of Electrical Engineers of Japan, and the Institute of Electrical Communication Engineers of Japan.

❖

G. P. Ohman was born in Sweden, on December 15, 1918. He received the B.S. degree in electrical engineering from the Illinois Institute of Technology in 1943, and the M.S. degree from the University of Maryland in 1948.

G. P. OHMAN

Except for a short period in the Navy during the war, he has been affiliated with the U. S. Naval Research Laboratory, Washington, D. C., since 1943. His work has been mostly in the broad field of radar with emphasis on test equipments, navigational aids, and currently on experimental high resolution radar systems. In recent years he has also been associated with the University of Maryland on a part-time basis as lecturer in electrical engineering.

Mr. Ohman is a member of Phi Kappa Phi, Tau Beta Pi, and Eta Kappa Nu.

❖

Arthur A. Oliner (M'47–SM'52) was born in Shanghai, China, on March 5, 1921. He received the B.A. degree from Brooklyn College in 1941, and the Ph.D. degree in physics from Cornell University in 1946. From 1941 to 1944, he was a graduate teaching assistant in the physics department at Cornell University, and later participated in an Office of Scientific Research and Development project at Cornell from 1944 to 1945.

A. A. OLINER

Since 1946, Dr. Oliner has been with the Microwave Research Institute of the Polytechnic Institute of Brooklyn, where he has been engaged in research in a variety of topics in the microwave field. While on a leave of absence, he spent the summer of 1952 at the Microwave Laboratory of Hughes Aircraft Company, Culver City, Calif. He has also taught graduate courses in physics and electrical engineering, and is a Research Associate Professor at the Institute.

He is a member of American Physical Society and Sigma Xi. He is also a member of the IRE Committee on Antennas and Waveguides, and the Administrative Committee of the Professional Group on Microwave Theory and Techniques.

❖

Samuel Sensiper (S'39–A'42–SM'47) was born in Elmira, N. Y., on April 26, 1919. He received the S.B. degree in electrical engineering from the Massachusetts Institute of Technology in 1939, the E.E. degree from Stanford University in 1941, and the Sc.D. degree in electrical engineering from the Massachusetts Institute of Technology in 1951.

S. SENSIPER

From 1939 to 1941 he was a research and teaching assistant at Stanford. From 1941 to 1948 he was employed by the Sperry Gyroscope Company. From 1949 to 1951 he was a staff member of the Research Laboratory of Electronics at the Massachusetts Institute of Technology. Since 1951 Dr. Sensiper has been at the Hughes Aircraft Company, formerly in the Microwave Laboratory, and now in the Electron Tube Laboratory.

Dr. Sensiper received a World War II Certificate of Commendation from the Bureau of Ships and was an Industrial Electronics Fellow at M.I.T. from 1947 to 1948.

He is a member of Sigma Xi, RESA, and Eta Kappa Nu.

❖

Alan J. Simmons was born in New York, N. Y., on October 14, 1924. He received the B.S. degree in physics and chemistry from Harvard University in 1945, and the M.S. degree in electrical engineering from the

Massachusetts Institute of Technology in 1948. While in the U. S. Navy during 1944–1945, he attended the radar schools at Harvard and M.I.T.

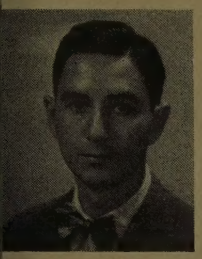

A. J. SIMMONS

From 1946 to 1948 Mr. Simmons was a research assistant at the Research Laboratory for Electronics, M.I.T. Since that time he has been working on microwave antennas and allied problems in the microwave antennas and components branch at the Naval Research Laboratory, Washington, D. C.

❖

Arnold W. Sullivan was born on September 20, 1923, in DeFuniak Springs, Fla. He received the B.E.E. degree in 1947, and the M.S.E. degree in electrical engineering in 1950, both from the University of Florida. Since 1948 he has been a member of the faculty of the University of Florida and has served as a leader of research projects dealing with investigations of atmospheric radio noise problems. He is now an associate professor of electrical engineering.

A. W. SULLIVAN

Mr. Sullivan is a member of the IRE subcommittees on Basic Measurements and on Atmospherics. He is a member of the USA National Committee and chairman of Commission IV of URSI in the United States.

❖

Douglas N. Travers (A'52) was born on June 27, 1928, in San Antonio, Texas. He received the B.E. degree in electrical engineering from The Johns Hopkins University in 1951. From 1951 to the present, he has been with the Southwest Research Institute in San Antonio, working in the communications research section on the development of various experimental high frequency shore and shipboard direction finders. Mr. Travers is an associate member of the Research Society of America and is a registered professional engineer.

D. N. TRAVERS

❖

Osamu Tukizi was born in Takamatu, Japan, on December 17, 1915. He received the B.S. degree in physics from the University of Kyûsyû in 1944.

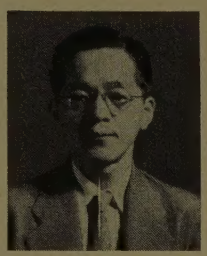

O. TUKIZI

Upon graduation, from the University of Kyûsyû, he joined the Physical Institute of Radio Waves (in Tokyo), which was reorganized in 1949 as the Electrical Communication Laboratory. Mr. Tukizi has been engaged throughout in theoretical research of tropospheric propagation.

From July, 1955 to January, 1956, he took advanced study of propagation at the Laboratoire National de Radioélectricité in France.

❖

Victor Twersky (S'47–A'50–M'56) was born August 10, 1923 in Lublin, Poland. He received the B.S. degree in 1947 from the City College of New York, the A.M. degree in 1948 from Columbia University, and the Ph.D. degree in 1950 from New York University; his major subject in each school was physics.

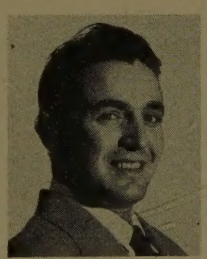

V. TWERSKY

From 1943 to 1946 Dr. Twersky was in the U. S. Army, where he served primarily as a photographer and as head of a photographic section.

He was a teaching assistant in physics in 1949, and a research associate of the Institute of Mathematical Sciences (Division of Electromagnetic Research) of New York University from 1950 to 1953. He also worked as a physicist at the Nuclear Development Associates during 1951 to 1952. He has been an engineering specialist with the Sylvania Electronic Defense Laboratory since 1953, and is also a lecturer in mathematics at Stanford University. His major interests in physics have been acoustics, electromagnetic theory, and multiple scattering of waves.

Other work, begun in 1946 in the Biology Department of CCNY, includes development of acoustic guidance devices for the blind, and research on the physical basis of obstacle perception by audition.

Dr. Twersky is a fellow of the American Physical Society, a member of the New York Academy of Sciences, the Acoustical Society of America, AAAS, FAS, RESA, National Commission II URSI, and a past member of the West Coast IRE Committee on Antennas and Waveguides.

❖

Robert E. Webster (A'53) was born in Montgomery, Ala., on January 11, 1928. He received the Bachelor of Engineering degree from Vanderbilt University, Nashville, Tenn., in 1950 and the Master of Science degree from The Ohio State University, Columbus, Ohio, in 1951.

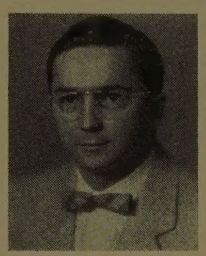

R. E. WEBSTER

Since 1951 he has been a research associate at the Antenna Laboratory of The Ohio State University. His major interests have been in vehicular antennas and radomes.

He is a member of Tau Beta Pi and Sigma Xi.

❖

Jui Lin Yen (S'53–A'54) was born in Canton, China, on November 29, 1925. He received the B.S. degree in electrical engineering from Chao Tung University, China in 1948. In 1950 he received the M.A.S. degree and in 1953 the Ph.D. degree in engineering physics from University of Toronto.

J. L. YEN

In 1953 Dr. Yen joined the staff of University of Toronto where he is now a lecturer in electrical engineering and recently became engaged in the field of radio astronomy.

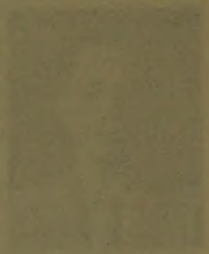

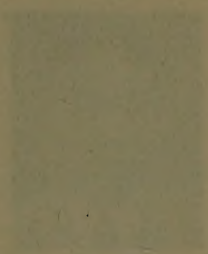

INSTITUTIONAL LISTINGS

The IRE Professional Group on Antennas and Propagation is grateful for the assistance given by the firms listed below, and invites application for Institutional Listing from other firms interested in the field of Antennas and Propagation.

ANDREW CORPORATION, 363 E. 75th St., Chicago 19, Illinois
Antennas, Antenna Systems, Coaxial Transmission Lines, Design, Development, Production

ANTLAB, 4950 North High St., Columbus 14, Ohio
Antenna Pattern Range Measuring Systems

COLLINS RADIO COMPANY, Cedar Rapids, Iowa
Antenna Design and Propagation Research Related for Airborne and Ground Communication Systems.

DEVELOPMENTAL ENGINEERING CORP., 1001 Conn. Ave, N.W., Washington, D. C. and Leesburg, V
Research, Development, Installation of Antennas and Antenna Equipment for Super Power Stations

DORNE AND MARGOLIN, INC., 30 Sylvester Street, Westbury, L. I., New York
Antenna Research and Development—Radiation Pattern Measuring Services.

THE GABRIEL LABORATORIES, Div. of the Gabriel Co., 135 Crescent Road, Needham Heights 94, Ma
Research and Development of Antenna Equipment for Government and Industry.

HUGHES AIRCRAFT COMPANY, Culver City, California
Research, Development, Mfr.: Radar, Missiles, Antennas, Radomes, Tubes, Solid State Physics, Computers

JANSKY & BAILEY, INC., 1339 Wisconsin Ave. N.W., Washington 7, D.C.
Radio & Electronic Engineering; Antenna Research & Propagation Measurements; Systems Design & Evaluatic

MARYLAND ELECTRONIC MANUFACTURING CORPORATION, College Park, Md.
Antenna and System Development and Production for Civil and Military Requirements.

THE RAMO-WOOLDRIDGE CORPORATION, Los Angeles 45, California

TRANSCO PRODUCTS, INC., 12210 Nebraska Ave., Los Angeles 25, Calif.
Antenna Design and Production—Radiation Pattern Measuring Services

WHEELER LABORATORIES, INC., 122 Cutter Mill Road, Great Neck, New York
Consulting Services, Research and Development, Microwave Antennas and Waveguide Components

The charge for an Institutional Listing is $25.00 per issue or $75.00 for four consecutive issues. Application may be made to the Technical Secretary, The Institute of Radio Engineers, 1 East 79th Street, New York 21, N.Y.